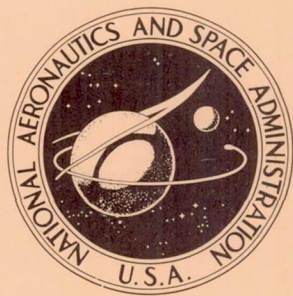


NASA TECHNICAL NOTE



NASA TN D-5314

NASA TN D-5314

CASE FILE COPY

SUBSONIC PERFORMANCE
CHARACTERISTICS OF A LARGE-SCALE
1.075-PRESSURE-RATIO TIP-TURBINE
CRUISE-FAN PROPULSION SYSTEM

by Francis J. Capone and Harry T. Norton, Jr.

Langley Research Center

Langley Station, Hampton, Va.

SUBSONIC PERFORMANCE CHARACTERISTICS OF
A LARGE-SCALE 1.075-PRESSURE-RATIO TIP-TURBINE
CRUISE-FAN PROPULSION SYSTEM

By Francis J. Capone and Harry T. Norton, Jr.

Langley Research Center
Langley Station, Hampton, Va.

NATIONAL AERONAUTICS AND SPACE ADMINISTRATION

For sale by the Clearinghouse for Federal Scientific and Technical Information
Springfield, Virginia 22151 - CFSTI price \$3.00

SUBSONIC PERFORMANCE CHARACTERISTICS OF
A LARGE-SCALE 1.075-PRESSURE-RATIO TIP-TURBINE
CRUISE-FAN PROPULSION SYSTEM

By Francis J. Capone and Harry T. Norton, Jr.
Langley Research Center

SUMMARY

An investigation has been conducted in the Langley 16-foot transonic tunnel to determine internal and external performance characteristics of a large-scale 1.075-pressure-ratio tip-turbine cruise fan. The intent of this investigation was to determine trends rather than absolute levels in performance since the fan was originally designed as a low-pressure-ratio lift fan. The effects of geometry change and exit-area variation on performance were determined with three fan cowls, afterbodies, and nozzle-exit plugs. The gas generator was closely coupled to the fan and resulted in a gas-generator nacelle that extended forward and below the fan nacelle. Eight configurations were investigated at Mach numbers from 0 to 0.85 and at an angle of attack of 0° . The test Reynolds number based on the fan diameter (36.00 inches (91.44 cm)) varied from 3.90×10^6 to 11.25×10^6 .

The results showed that the fan operated at the design pressure ratio or near design fan rotational speeds for all configurations. Only changes in exit area affected internal performance. The average overall fan efficiency (ratio of fan developed power to power absorbed by the fan turbine) was 62.5 percent for all configurations. As a result of the low pressure ratio of the fan, the fan was found to operate over a wide range of fan mass-flow rates, to have a rapid fall-off in thrust with free-stream Mach number, and to perform over a large range of free-stream Mach number for a given nozzle area. There was a 20-percent increase in thrust and a 20-percent decrease in specific fuel consumption for the complete propulsion system over values for the basic gas generator at the higher Mach numbers. Static thrust was found to be in slight error due to flow in the wind tunnel induced by the fan exhaust.

Because the net thrust decreased rapidly with increasing free-stream Mach number (due to low-pressure-ratio fan), the drag-minus-thrust coefficients became positive for all the configurations tested above a Mach number of 0.50. Those configurations with the longer nacelles had lower nacelle-drag coefficients, partly because of less flow spillage about the fan cowl. Increasing exit area decreased fan-nacelle drag due to a decrease in

afterbody drag and an increase in plug thrust. All the configurations exhibited lower drag-rise Mach numbers than predicted from fan-nacelle design probably attributable to interference drag caused by the fairing between the fan and gas-generator nacelles. This interference drag was a result of pressures being much less than free-stream static pressure and premature supercritical flows developing on the fairing.

The close agreement between windmill external pressure distributions measured on the full-size model with pressures measured on a 1/5-scale flow-through model, both in the same wind tunnel, is taken to indicate that wind-tunnel-wall interference and blockage effects were negligible.

INTRODUCTION

The National Aeronautics and Space Administration has been conducting extensive research on V/STOL aircraft that utilize tip-turbine-driven lift fans (refs. 1 to 7). This propulsion system uses the exhaust products of a gas generator (turbojet engine) to drive turbine blades mounted around the periphery of a ducted fan. Conversion of the high disk loading of the turbojet gas generator to the lower disk loading of the fan results in an increase in static thrust for the same power input. Reference 5 presents results for a full-scale model of a current VTOL aircraft that has a lift fan in each wing, a pitch-control fan mounted in the nose (needed for transitional flight), and a conventional turbojet for cruise.

A lift fan can also be used for subsonic cruise by rotating the fan 90° to function essentially as a turbofan engine with a bypass ratio that can vary from 8:1 to 15:1. In this way, at low forward speeds, the thrust of the driving gas generator is augmented and the cruise-fan specific fuel consumption can be less than that for a conventional turbojet or turbofan engine of lower bypass ratio (ref. 8). Reference 7 presents test results for a V/STOL transport configuration that has both lift and lift-cruise fan engines. Low-speed results for an isolated 1.1-pressure-ratio lift-cruise fan are presented in reference 9. (Pressure ratio is the ratio of stagnation pressure aft of the fan to stagnation pressure ahead of the fan.)

The present investigation utilized the X-376, 36.00-inch-diameter (91.44-cm) pitch-control fan of reference 5 and was concerned with extending cruise-fan internal and external performance data to high subsonic Mach numbers. This investigation was not intended, however, to determine absolute levels of performance but rather to indicate trends in internal and external performance due to external changes in geometry and variation of nozzle-exit area. This approach was used because the tip-turbine fan of this investigation was designed as a lift fan (i.e., pitch-control fan of ref. 5) and not as a cruise fan since the fan design pressure ratio was only 1.075. Lower cruise performance would be expected since a cruise fan with a pressure ratio of 1.3 is desirable for near

optimum performance when take-off thrust and cruise fuel consumption is considered (ref. 10).

There are, however, some advantages in testing an available large-scale propulsion system (even though it may not be optimum for cruise) rather than small-scale tests. Inasmuch as model Reynolds number in large-scale tests are comparable to flight Reynolds number, boundary-layer effects in both the internal and external flows are similar. Also the effects of performance of hot gas mixing and nonuniform flow conditions behind the fan are more realistic.

The propulsion system of this investigation was a tip-turbine cruise fan with a close-coupled gas generator. The nacelle housing the gas generator extended forward and was below the fan nacelle with a fairing section between the two. Three fan cowls (inlets) and afterbodies were investigated in order to determine the effects of geometry changes on performance. Since an increase in flight Mach number requires a decrease in fan duct exit area in order to obtain the proper static pressure across the fan for a fixed fan blade angle and rotational speed, three nozzle plugs were provided to vary the nozzle-exit area. For actual flight applications, the nozzle plug might be a two-position plug, its diameter being varied by means of an inflatable rubber centerbody as suggested in reference 8.

This investigation was conducted in the Langley 16-foot transonic tunnel and results are included for eight configurations at Mach numbers from 0 to 0.85 and an angle of attack of 0° . The test Reynolds number based on the fan diameter of 36.00 inches (91.44 cm) varied from 3.90×10^6 to 11.25×10^6 . Results are also included for a non-powered 1/5-scale model of one of the configurations. This model was investigated in order to determine wind-tunnel-wall interference and blockage effects.

One of the configurations of the present investigation was also tested at angle of attack and these results are presented in reference 11.

SYMBOLS

Model forces and moments are referred to an axis system shown in figure 1 where the origin is at the intersection of the fan axis of rotation with the fan-rotor reference plane. In addition, fan flow parameters (such as pressures, mass-flow rate, thrust, etc.) were computed at various locations within the cruise fan. These locations have been designated as instrumentation planes and are identified in figure 1 to conform with usage adopted by the engine manufacturer. Dimensions are given in both U.S. Customary Units and the International System of Units (SI). Conversion factors (based on ref. 12) relating the two systems are found in table I. Table II presents various constants used. A

discussion of procedures used to compute fan performance characteristics is given in appendix A. Symbols used in this report are as follows:

- A cross-sectional area, ft^2 (meters 2)
- A_{max} reference area based on fan-cowl maximum diameter at plane 10.3 as given in table II (does not include gas generator cross section), ft^2 (meters 2)
- C_A axial-force coefficient measured by force balance, $\frac{\text{Axial force}}{q_{\infty} A_{\text{max}}}$
- $C_{D,B}$ fan bullethead pressure-drag coefficient, $\sum_{x/l=0}^1 -C_p \frac{A_l}{A_{\text{max}}}$
- $C_{D,f}$ skin-friction drag coefficient
- $C_{D,\beta}$ fan-nacelle-afterbody pressure-drag coefficient, $\sum_{x/l=a}^{1.0} -C_p \frac{A_l}{A_{\text{max}}}$,
where $a = x/l$ at station 10.3 (see fig. 1)
- $C_{D,\pi}$ nacelle-drag coefficient as defined in appendix A, $\frac{D_n}{q_{\infty} A_{\text{max}}}$
- $C_{F,\text{plug}}$ plug thrust coefficient, $\sum_{x/l=1.0}^b C_p \frac{A_l}{A_{\text{max}}}$, where b is the value of x/l at the end of the plug (see fig. 1)
- C_m pitching-moment coefficient measured by force balance, $\frac{\text{Pitching moment}}{q_{\infty} A_{\text{max}} d_{\text{max}}}$
- C_N normal-force coefficient measured by force balance, $\frac{\text{Normal force}}{q_{\infty} A_{\text{max}}}$
- C_p pressure coefficient, $\frac{p_l - p_{\infty}}{q_{\infty}}$
- $C_{p,\text{min}}$ minimum pressure coefficient

$C_{p, \text{sonic}}$	pressure coefficient for sonic flow
$c_{p, a}$	specific heat for air, $\frac{\text{Btu}}{\text{lbm} \cdot ^\circ\text{R}} \left(\frac{\text{joules}}{\text{kilogram} \cdot ^\circ\text{K}} \right)$
$c_{p, g}$	specific heat for gas-generator exhaust, $\frac{\text{Btu}}{\text{lbm} \cdot ^\circ\text{R}} \left(\frac{\text{joules}}{\text{kilogram} \cdot ^\circ\text{K}} \right)$
D_n	net drag, $F_n + (D - F)$, lbf (newtons)
D_r	ram drag, lbf (newtons)
$(D - F)$	drag minus thrust measured by force balance, lbf (newtons)
d	diameter, in. (cm)
d_{max}	fan-nacelle maximum diameter of station 10.3, 50 in. (127.00 cm)
$F_{5.1}$	ideal gas-generator exhaust thrust, lbf (newtons)
$F_{5.6}$	ideal fan-turbine exhaust thrust, lb (newtons)
$F_{11.0}$	ideal fan thrust, lbf (newtons)
F_g	total ideal gross thrust for cruise-fan propulsion system, $(F_{5.6} + F_{11.0})$, lbf (newtons)
$F_{g, E}$	gas-generator ideal gross thrust, lbf (newtons)
F_n	net thrust for cruise-fan propulsion system, $F_g - D_r$, lbf (newtons)
$F_{n, E}$	gas-generator net thrust, $F_{g, E} - D_{r, E}$, lbf (newtons)
F_{meas}	static thrust measured by force balance, lbf (newtons)
g	gravitational acceleration, ft/sec ² (meters/sec ²)
l	length of fan cowl plus afterbody, in. (cm)

M	free-stream Mach number
M_l	local Mach number where l can be replaced by instrumentation plane number
M_{tip}	fan-blade rotational tip Mach number
\dot{m}	mass-flow rate, lbm/sec (kilograms/sec)
\dot{m}_f	mass-flow rate of fuel, lbm/sec (kilograms/sec)
\dot{m}_∞/\dot{m}_i	ratio of free-stream mass-flow rate to capture-area mass-flow rate
N	rotational speed, percent of full speed except where noted
P_F	fan ideal power at station 11.0, hp (kilowatts)
P_R	fan ideal power, hp (kilowatts)
P_T	total ideal power output of fan turbine, hp (kilowatts)
$P_{5.1}$	ideal power available from gas-generator discharge, hp (kilowatts)
$P_{5.6}$	ideal power absorbed by fan turbine from gas-generator discharge, hp (kilowatts)
p	static pressure, lbf/ft ² (newtons/meter ²)
p_t	stagnation pressure, lbf/ft ² (newtons/meter ²)
$p_{t,b}$	boundary-layer stagnation pressure, lbf/ft ² (newtons/meter ²)
$\left(\frac{\bar{p}_{t,11.0}}{\bar{p}_{t,10.0}}\right)_{eff}$	effective fan pressure ratio (see appendix A)
q_∞	free-stream dynamic pressure, lbf/ft ² (newtons/meter ²)
R	gas constant, ft/ ^o R (joules/kilogram- ^o K)

R_T	fan-turbine power-absorption ratio, $P_{5.6}/P_{5.1}$
r	radius, in. (cm)
sfc	specific fuel consumption, per hour
T	absolute static temperature, $^{\circ}R$ ($^{\circ}K$)
T_t	absolute stagnation temperature, $^{\circ}R$ ($^{\circ}K$)
V	velocity, ft/sec (meters/sec)
x	longitudinal distance (in the results presented, x is measured from the fan-nacelle leading edge; in the configuration ordinates (fig. 7), however, x -values are measured as shown in the separate sketches), in. (cm)
x_A	afterbody length (fig. 7(d))
x_{EN}	distance from gas-generator-nacelle leading edge to gas-generator-compressor face (fig. 7(g))
x_{FC}	fan-cowl length (fig. 7(b))
y	vertical distance, in. (cm)
β	afterbody boattail angle, deg
γ	ratio of specific heat for air
γ_g	ratio of specific heat for gas-generator exhaust gas
δ	static-pressure correction parameter for correction to standard sea-level conditions, $p_{\infty}/2116.2$ ($p_{\infty}/101\ 325$)
δ_t	stagnation-pressure correction parameter for correction to standard sea-level conditions, $p_{t,\infty}/2116.2$ ($p_{t,\infty}/101\ 325$)
η_F	overall fan efficiency, $P_F/P_{5.6} = P_{11.0}/P_{5.6}$

η_R	fan-rotor efficiency, 0.82 (assumed value)
η_S	fan-stage efficiency, P_F/P_T
θ	meridian angle as defined in figure 2, deg
$\sqrt{\sigma}$	stagnation-temperature correction parameter for correction to standard sea-level conditions, $\sqrt{T_{t,\infty}/518.69} \left(\sqrt{T_{t,\infty}/288.05} \right)$
ρ	density, lbm/ft ³ (kilograms/meter ³)

Subscripts:

∞	free stream
2.0	gas-generator compressor face
5.1	gas-generator turbine-discharge plane
5.6	fan-tip-turbine discharge plane
9.0	fan-inlet leading edge
10.0	fan-inlet measuring plane
10.3	fan-rotor reference plane
10.6	fan-rotor-discharge measuring plane
11.0	fan-discharge measuring plane aft of stators
b	boundary layer
E	gas generator
e	exit
eff	effective

F	fan
i	geometric capture area
l	local
max	maximum
static	static conditions where $M \approx 0$

A bar over a symbol indicates an average value.

APPARATUS AND PROCEDURE

Model Installation

A sketch showing the installation of the cruise-fan propulsion system in the Langley 16-foot transonic tunnel is presented as figure 2. Figure 3 shows a simplified sketch of the cruise-fan assembly, and photographs of some of the configurations are given as figure 4. The model was sting supported so that the fan-nacelle center line was 25.00 inches (63.50 cm) above the tunnel center line. (See fig. 2.) All model geometry is referenced to the fan-rotor reference plane, plane 10.3 (fig. 1), and plane 10.3 is hereinafter used to refer to this location. For this investigation, the propulsion system was mounted in the wind tunnel in an inverted position. For an actual flight application, the gas generator would be on top rather than on the bottom. All references made to model geometry are according to the wind-tunnel installation.

As a means of increasing the structural integrity of the model, guy wires were attached to the sting by two fixtures which protruded through holes at the rear of the gas-generator nacelle. (See rear view of fig. 4(b).) A flexible seal between the fixtures and the gas-generator nacelle prevented any air leakage. A second set of guy wires was attached directly to the sting downstream of the gas-generator nacelle. (See front view of fig. 4(b).)

Configurations

A three-digit configuration code is used to identify the various configurations as follows:

X	X	X
Fan cowl (inlet)	Afterbody	Plug

Thus, configuration 144 used fan cowl 1, afterbody 4, and plug 4. Sketches of the eight configurations tested are shown in figure 5, and the geometric characteristics of these configurations are summarized in figure 6.

Propulsion System

The propulsion system of this model consisted of the X-376 tip-turbine fan (pitch-control fan of ref. 5), driven by a modified T58-GE-6A gas generator. Figure 4(c) shows the gas generator in relation to the fan. In this photograph, the transition ducts and bellows have not yet been installed.

Fan.- The fan was a single-stage, tip-turbine-driven fan designed for a pressure ratio of 1.075. The rotor contained 36 fan blades and the tip-mounted turbine buckets. The fan tip diameter was 36.00 inches (91.44 cm) and the hub diameter was 16.20 inches (41.15 cm). Design rotational speed of the fan was 4074 revolutions per minute. A bulletnose fairing for the fan hub was provided to smooth the flow entering the fan. Bulletnose ordinates are given in figure 7(a). The fan rotor without the bulletnose can be seen in the photograph of figure 4(d). A single set of 52 stator vanes were part of the rear fan frame and can be seen in the photograph of figure 4(e).

The tip-turbine buckets were located radially outboard on the fan-rotor blade tips. The gas-generator exhaust was admitted through a scroll to the fan tip turbines. The scroll of this partial-admission turbine covered the lower 167° of the circumferential arc; the remainder of the turbine arc was inactive. The tip-turbine diameter was 41.60 inches (105.66 cm). The scroll can be seen with insulation about it in figure 4(d).

Gas generator.- The gas generator was a modified T58-GE-6A turboshaft gas turbine engine and used JP-4 as a fuel. The modification consisted of removing the power turbine assembly. Design speed of this gas generator is 26 300 revolutions per minute. A flow-straightening and bellows section were provided between the gas generator and fan scroll inlet. (See fig. 3.)

The fan flow and turbine flow were then discharged into a common annular chamber before entering the exhaust nozzle system. (See figs. 3, 4(e), and 4(f).)

Model Components

In order to simplify the description of the various model components, each of the model components or surface has been defined in figure 3 and ordinates are given in figure 7. A more complete description of these surfaces now follows.

Fan cowl and inlet.- The fan cowl and inlet include that portion of the fan nacelle (excluding gas-generator nacelle) that is forward of plane 10.3 (fig. 3). The fan cowl is

the external surface and the fan inlet is the internal surface. Fan-cowl and inlet ordinates are given in figure 7(b) and ordinates for the fairing between the fan-cowl and gas-generator nacelle are given in figure 7(c).

Three fan cowls were tested during this investigation. The design of the two longest fan cowls was based on the methods of references 13 and 14 to have NACA series 1 inlet shapes with critical Mach numbers of 0.81 (cowl 1) and 0.71 (cowl 2). The data of reference 13 did not extend to the proportions desired for the shortest cowl and its critical Mach number was estimated to be 0.55 (cowl 3). All three cowls had a maximum diameter of 50 inches (127.00 cm) occurring at plane 10.3. The large diameter was necessary to accommodate the scroll and to keep the nacelle symmetrical. Future cruise fans would probably have smaller full admission scrolls (active over 360° of arc) that would result in a smaller diameter nacelle for the same-diameter fan (ref. 8). Internal flow areas for the three fan inlets are given as figure 8(a).

Afterbody, nozzle shroud, and plug.- The afterbody is defined as the external portion of the fan nacelle that is aft of plane 10.3 (fig. 3); the internal contour is defined as the nozzle shroud. Afterbody and nozzle-shroud ordinates are given in figure 7(d) and ordinates for the fairing between the afterbody and gas-generator nacelle are presented in figure 7(e). The external contours of the three afterbodies were circular-arc segments terminating with boattail angles of $\beta = 10^\circ$ (afterbody 4), 12° (afterbody 1), and 14.5° (afterbody 2). (See fig. 6.)

The nozzle shroud consisted of a cold and a hot side. (See fig. 7(d).) The cold side consisted of the upper 173° of the shroud and the hot side, the remaining 187° . The hot side was fabricated to allow for expansion due to the heating effects of the fan-turbine flow. A flow splitter of the same radius as the shroud cold side and located circumferentially the same as the hot side was provided in order that fan-turbine exhaust-gas pressure and temperature could be measured before mixing occurred with the cold fan flow. The nozzle shroud geometry including the flow splitter can be seen in figure 4(e).

Three plugs were provided in order to vary the exit area of a particular configuration. Plug ordinates are given in figure 7(f). The three exit areas investigated, 433 in^2 (2793 cm^2), 566 in^2 (3652 cm^2), and 770 in^2 (4968 cm^2), were sized for operation at Mach numbers of 0.80, 0.45, and 0.17, respectively. Internal flow areas for the various afterbody-plug combinations are given as figure 8(b).

Gas-generator nacelle and inlet.- The gas-generator nacelle is defined as the external surface of the fairing enclosing the gas generator, force balance, and sting up to the flexible seal (fig. 3). The gas-generator inlet was the internal surface up to the gas-generator compressor face. Contours for the gas-generator nacelle up to the cylindrical section were established, again by the design technique of reference 13. The

design critical Mach number was 0.81 and the NACA inlet designation was 1-50-110. Ordinates for the gas-generator nacelle and inlet are presented in figure 7(g) and the bullethead ordinates can be found in figure 7(h). The internal flow area for the gas-generator inlet is shown in figure 8(c). The flexible seal insured no leakage between the end of the gas-generator nacelle and the nacelle-to-sting transition section which was attached to the sting (fig. 3).

Instrumentation

Model forces were measured with a six-component internally located strain-gage balance. An externally wrapped water jacket was used about the balance to maintain a constant balance temperature. Pressure measurements up to a maximum of 485 were made, depending on the configuration, and were recorded on 12 pressure-scanning devices, each capable of scanning 48 pressures. Each pressure-scanning device contained a single pressure transducer. The outputs of the force balance and pressure-scanning units were digitized and recorded on punch cards. A part of the pressure instrumentation was used for determining static-pressure distributions over the various model surfaces. The remainder of the pressure instrumentation was used for determining flow properties at the various instrumentation planes (fig. 1) throughout the model as follows:

Plane	Type	Number	θ , deg
2.0	Stagnation	15	22.5, 112.5, 202.5
2.0	Static	9	22.5, 112.5, 202.5
2.0	Boundary layer	6	22.5, 112.5, 202.5
5.1	Stagnation	6	0, 180
5.6	Stagnation	8	{ 112.5, 137, 157.5, 180 202.5, 225, 247.5, 270
10.0	Stagnation	24	45, 135, 225, 315
10.0	Static	24	45, 135, 225, 315
10.0	Boundary layer	16	45, 135, 225, 315
10.6	Stagnation	24	67.5, 157.5, 247.5, 337.5
11.0	Stagnation	24	67.5, 157.5, 247.5, 337.5
11.0	Boundary layer	12	157.5, 337.5

Gas-generator and fan-turbine exhaust stagnation temperatures were measured with chromel-alumel thermocouple probes and were recorded on continuous strip-chart recorders. Gas-generator rotational speed was measured with a tachometer generator and fan rotational speed was determined from a variable-reluctance magnetic pickup. Gas-generator fuel mass-flow rate was determined from calibration curves based on corrected inlet flow rates for the T58-GE-6A gas generator. (See appendix A.) In addition, gas-generator fuel and oil pressure, gas-generator and fan vibration, fan-blade stresses, and nacelle-cavity temperatures were monitored continually to insure safe operation.

Wind Tunnel and Tests

The investigation was conducted in the Langley 16-foot transonic tunnel, which is a single-return atmospheric wind tunnel with a slotted, octagonal test section. The speed range of this tunnel is from a Mach number of 0.20 to 1.30. Maximum Mach number for this investigation was 0.85 for configuration 144.

Fan-blade stresses higher than allowable limited testing of configuration 243 to $M = 0.40$ and configurations 112 and 322 to $M = 0.65$. These configurations have a larger exit area than the other configurations tested and the high stresses were attributed to operation of the fan at off-design conditions not normally encountered in a typical fan operating envelope.

The following procedure was used in recording data. First, the wind tunnel was brought to the desired speed and a fan windmill data point was taken. The gas generator was started and brought to idle condition (about 55 to 60 percent of rated speed) and another data point was taken. Then three power-on data points were taken, the last being usually at approximately maximum uncorrected gas-generator speed (usually 98 to 101 percent). It required about 30 seconds to record a data point because of the pressure-scanning equipment used.

Boundary-layer transition strips were not affixed to any portions of the model during the investigation.

Corrections

No corrections for wind-tunnel-wall interference or blockage effects were applied to the data. However, it is believed that the magnitude of these corrections is negligible since a comparison of windmill pressure distributions between configuration 123 and a 1/5-scale flow-through model of configuration 123 shows good agreement. These results are discussed in appendix B.

Axial force was corrected to the condition of free-stream static pressure acting across the flexible seal. This correction varied from -0.002 to 0.005 in terms of a seal-force coefficient $(\text{Seal force}/q_{\infty}A_{\text{max}})$.

RESULTS

Table III is an index to the results of this investigation, which are presented in figures 9 to 81. In general, typical pressure distributions have been presented in order to show trends. Only data taken at windmill and maximum obtainable fan-rotational-speed conditions are presented and only the maximum obtainable fan speed is noted in the figures. Windmill fan speed can be obtained from figure 13.

The pressure profiles of figures 14 to 29 have been plotted as a function of r/r_{max} where $r = 0$ is the fan-nacelle center line. For the fan-inlet and rotor-discharge profiles, $r_{\text{max}} = 18.00$ inches (45.72 cm) and $r/r_{\text{max}} = 0.45$ for the fan bulletnose. For the fan-discharge profiles, $r_{\text{max}} = 19.35$ inches (49.15 cm) and $r/r_{\text{max}} = 0.422$ for the exit plug.

The pressure distributions presented as figures 44 to 69 have been plotted as a function of x/l where l is the fan-cowl length plus afterbody length (total fan-nacelle length) for each configuration and this length is given in figure 6. The origin of the coordinate system in these data figures is the leading edge of the fan cowl for that particular configuration. Thus, $x/l = 0$ is the fan-cowl (or inlet) leading edge and $x/l = 1.0$ is the nozzle exit. For the fan-nacelle pressure distributions presented in figures 44 to 51, the outer surface corresponds to the fan cowl and afterbody while the inner surface corresponds to the fan-inlet and nozzle-shroud surfaces. Similar terminology is used for the gas-generator pressure distributions of figures 60 to 67. That is, $x/l = 0$ represents the leading edge of the fan cowl. The location of plane 10.3 has also been identified in these figures.

DISCUSSION

Gas-Generator Flow Characteristics

Some selected gas-generator inlet pressure profiles for configuration 244 are presented in figure 9. These results are typical of all the configurations and show excellent inlet pressure recovery and uniform velocity profiles at the gas-generator-compressor face. Figures 10 and 11 present gas-generator and fan-turbine exhaust stagnation-pressure profiles, respectively. These profiles, again, are for configuration 244 and are at the same test conditions as the inlet distributions presented in figure 9. In addition, data are presented at a lower gas-generator rotational speed. The circumferential drop

in fan-turbine exhaust pressure (fig. 11) is primarily associated with the flow having to travel a greater distance to the outer extremities of the scroll.

Gas-generator and fan-turbine exhaust-temperature characteristics for the various configurations are shown in figure 12. Again, only selected data are presented to show trends in these temperatures. On the average there is a drop of about 10 percent in stagnation temperature from the gas-generator turbine through the fan tip turbines that is caused by the expansion of the flow through the tip turbine and the accompanying extraction of energy needed to drive the fan.

Some gas-generator performance data are presented in figure 13 for the various configurations. Shown are gas-generator air-mass-flow rate and power characteristics. Also shown are variation of fan speed and fan-turbine expansion ratio $\bar{p}_{t,5.6}/\bar{p}_{t,5.1}$ with gas-generator rotational speed. Total gas-generator mass-flow rate can be obtained by adding the fuel-flow rate given in appendix A to the values of corrected air-mass-flow rate given in figure 13.

Fan Internal-Flow Characteristics

Fan-inlet pressure profiles.- Fan-inlet stagnation- and static-pressure profiles are presented in figures 14 to 21 for the various configurations. These data, at windmill and maximum-obtainable fan rotational speed for selected Mach numbers, are representative of flow conditions in the three inlets. Increasing fan speed from windmill to maximum-obtainable speed changed the static-pressure level and influenced boundary-layer depth. Because the pressure probes for inlet 3 were located 2.75 inches (4.24 cm) behind the inlet leading edge, they may be influenced by both radial and axial components of the flow.

The data of figures 14 to 21 generally show that fan-rotor inlet velocity decreases from the hub to the tip. This higher velocity at the hub is primarily due to local acceleration of the flow over the bulletnose. Increases in Mach number do not appreciably affect inlet performance and all three inlets exhibit excellent pressure recovery with little loss associated with the boundary layer. Losses in effective fan-inlet stagnation pressure $(\bar{p}_{t,10.0})_{\text{eff}}$ were less than 0.3 percent.

Fan-rotor and fan-discharge pressure profiles.- Fan-rotor and fan-discharge stagnation-pressure profiles are presented in figures 22 to 29. These data are at the same test conditions as the inlet pressure profiles given in figures 14 to 21. The stagnation pressures at windmill conditions were essentially equal at all the meridian stations; consequently, data at only one meridian station are presented at windmill conditions. The meridian station at $\theta = 157.5^\circ$ for $p_{t,11.0}/p_{t,\infty}$ was chosen in order to show windmill boundary-layer conditions.

The pressures at plane 11.0 were numerically averaged to give the effective fan pressure ratio. The large pressure drop at the fan-blade tips is probably due to operation of the tips in a stall region. The fan-blade tips are also influenced by boundary-layer and tip-clearance effects. These conditions are especially prevalent at low Mach numbers where the largest percentage pressure drop occurs. Because the Mach number is increased and the fan is operating at conditions nearer optimum, and thus at a more uniform blade loading, the pressure profiles at each meridian station tend to flatten out and become the same. (For example, compare figs. 22(a), (b), and (c).) Those pressures at $\theta = 157.5^\circ$ and 247.5° are generally higher than at the other two meridian stations and may be due to leakage of hot gas from the scroll. The lower pressure levels for configurations 112 and 322 at $M = 0.65$ (figs. 27(c) and 28(c)) are due to operation of the fan at about 76 to 77 percent speed.

Fan Performance Characteristics

Static thrust.— Static thrust measured by the force balance for the configurations tested is presented in figure 30 and is plotted as a function of $N_F/\sqrt{\sigma}$ and $(N_F/\sqrt{\sigma})^2$ which allows extrapolation to 100 percent fan speed. Maximum measured thrust for configuration 243 (which was sized for $M = 0.17$) was 1450 pounds (6450 N). By extrapolation to 100 percent fan speed, a maximum thrust of 1530 pounds (6807 N) might be expected.

Also shown in figure 30 are the static-thrust ratios $F_{\text{meas}}/F_{n,\text{static}}$ (ratio of measured to computed static thrust). These ratios have been presented for corrected fan speeds greater than 60 percent and have not been presented for configuration 113 since these data may be influenced by a plug mechanical instability which limited the maximum attainable static $N_F/\sqrt{\sigma}$ to about 72 percent. The static-thrust data for configuration 113, however, have been presented. These static-thrust ratios, which range from about 0.84 to 0.91, are believed to be lower than would be expected because of a wind-tunnel flow that was induced by the fan discharge at static conditions. The higher thrust ratios for configuration 243 would be expected since its exit was designed for take-off (Mach number 0.17). The fan discharge caused an induced velocity through the wind tunnel that was estimated by observers to be about 22 to 30 feet per second (6.70 to 9.15 m/sec). This induced flow existed mainly as a core in the center of the wind tunnel and was not present in the tunnel walls.

An estimate has been made of the induced ram drag based on the induced free-stream velocity of 22 feet per second (6.70 m/sec) and fan mass-flow rate at maximum fan speed. The ram drag at this induced free-stream velocity was about 6 percent of the ideal static thrust. Because of this induced velocity, it is believed that the measured static-thrust levels presented in figure 30 are 6 to 10 percent too low.

Fan airflow, pressure ratio, and thrust characteristics.- Fan airflow rates, effective pressure ratio, and thrust characteristics are presented for the various configurations in figures 31 to 38. As can be seen, the fan operated at or near the design pressure ratio of 1.075 at maximum corrected fan speeds. At high Mach numbers (0.7 and 0.8) up to 90 percent of the gross thrust is used to overcome the large amount of ram drag which is due to the high bypass fan. External geometry changes (except exit area) have no effect on these parameters.

Fan-turbine power-absorption ratio, fan-stage efficiency, and overall fan efficiency.-

Fan-turbine power-absorption ratio $R_T = P_{5.6}/P_{5.1}$; fan-stage efficiency $\eta_s = P_F/P_T$; and overall fan efficiency $\eta_F = P_F/P_{5.6}$ are presented in figure 39. Appendix A contains a more complete description of these quantities. An increase in the exit area requires a larger input from the gas generator. Maximum overall fan efficiencies η_F , which range from 61 to about 64 percent, occur at the approximate Mach number for which that exit was sized. For example, $\eta_{F,max}$ occurs at $M = 0.2$ for configuration 243; at $M = 0.5$ for configurations 112 and 322; and at $M = 0.65$ to $M = 0.85$ for configurations 144, 244, 344, 123, and 113. At a constant $N_F/\sqrt{\sigma}$ greater than 85 percent, there is a sharp increase in η_F as Mach number is increased from static conditions to the Mach number for which a particular exit area was designed. The Mach number effect present in these data can be removed by plotting efficiency as a function of M/M_{tip} .

Specific-fuel-consumption and net-thrust-augmentation characteristics.- Specific-fuel-consumption and net-thrust-augmentation ratios are shown in figures 40 and 41, respectively. It should be noted that one is the reciprocal of the other; however, both have been included for the convenience of the reader. These data are summarized in figure 42 and have been presented at $N_F/\sqrt{\sigma} = 90$ percent. The advantages of coupling the large-bypass-ratio fan are quite evident especially at static conditions. At the higher Mach numbers, there is about a 20-percent increase in thrust for the complete propulsion system over the thrust for the basic gas generator. (See fig. 42.)

Thrust-ratio characteristics.- A summary of the thrust ratio $\frac{F_{n,max}}{(F_{n,max})_{static}}$

is presented in figure 43. The thrust ratios presented are based on the maximum value of F_n for any particular configuration at a given Mach number, and the data for all configurations of a particular exit area were averaged. The value of $(F_{n,max})_{static}$ was that which was measured (appendix A) for configuration 243. The dependence of thrust levels on exit area and Mach number is illustrated in this figure. The large reduction in net thrust with increase in free-stream Mach number is due primarily to the low pressure ratio of the fan, which results in a relatively low value of discharge

velocity, such that the difference between the exit velocity and V_{∞} becomes very small as Mach number is increased. Fans with a higher pressure ratio would not have as great a reduction in net thrust.

Some comments concerning the two-position inflatable plug proposed in reference 8 can be made. A nozzle system of this type would be simpler than, for example, a nozzle system with a variable exit. However, it would be expected that during part of the flight regime, the two-position-plug nozzle system would not be as efficient as a variable exit system which would operate at an exit area that gave optimum performance for a particular flight speed. If, for example, the present propulsion system were operated with only the three exit areas investigated (a three-position nozzle), one would change exit area at $M = 0.30$ and $M = 0.55$ for optimum performance (for this propulsion system only). However, if the nozzle system used only a two-position inflatable plug, then losses in thrust of 6 to 10 percent would occur when the exit area was changed at $M = 0.3$. (See fig. 43.) These losses are approximately the same as those predicted in reference 8. Similarly, the data of figure 42 can be used to predict losses in specific fuel consumption and thrust augmentation.

Another important observation from these data is the relatively wide range of free-stream Mach numbers which can be obtained with a given fixed nozzle area. This Mach number range is due to the wide range of mass-flow rates at which this low-pressure-ratio fan operates. (See fig. 43.)

Surface Pressure Distributions

Surface pressure distributions for the various configurations are presented in figures 44 to 67. These distributions include: fan cowl and inlet, afterbody, and nozzle shroud (figs. 44 to 51); bullethead and plug (figs. 52 to 59); and gas-generator nacelle and inlet (figs. 60 to 67).

In general, fan operation had little or no effect on the external fan cowl and afterbody pressure distributions except in the vicinity of the cowl leading edge, where fan operation at times made the negative pressure peaks at the cowl lip less negative. (See figs. 44 to 51.) This effect occurred at low Mach numbers where mass-flow ratio has greatest variation with fan rotational speed. (See fig. 69.) At windmill conditions (lower mass-flow ratio), more spillage occurs and probably causes the higher cowl-lip suction.

A comparison of the pressure distributions for configurations 144, 244, and 344 (figs. 45, 46, and 47, respectively) showed that although the external pressure distributions over the fan cowls are quite different, afterbody pressure distributions are nearly the same with configuration 344 (shortest fan cowl), having the most negative afterbody pressure coefficient. The shorter fan cowls exhibit a more rapid expansion of the flow

over the cowl and, hence, higher negative pressure peaks. Also, the flow experiences a sudden compression in the vicinity of the cowl maximum diameter.

Another condition typical of the external flow is the difference in afterbody pressure recovery on the fairing between the afterbody and gas-generator nacelle ($\theta = 150^\circ$). This lower pressure region (more negative pressure coefficient in fairing) is a possible source of high interference pressure drag.

The plug pressure distributions for all the configurations except 112 and 322 are characterized by an overexpansion of the flow as it leaves the nozzle. (See figs. 52 to 59.) These configurations use the large plugs (plugs 3 and 4), and the overexpansion probably results from a more rapid acceleration of the flow over these larger plugs. Comparison of the plug pressure distributions at $\theta = 0^\circ$ and $\theta = 180^\circ$ (figs. 52 to 59) shows little asymmetry of the flow due to mixing of the cold fan flow and hot fan-turbine exhaust.

Operation of the fan also had little effect on gas-generator nacelle pressures except at the nacelle leading edge where increases in fan speed decreased the magnitude of the gas-generator nacelle-lip suction. (See figs. 60 to 67.) These results indicate that as the flow over the top of the gas-generator nacelle ($\theta = 0^\circ$) approaches the fan nacelle, it approaches stagnation conditions. In addition, a local acceleration of the flow on the cylindrical part of the gas-generator nacelle is induced by the flow field of the entire fan nacelle.

Aerodynamic Characteristics

Aerodynamic characteristics as measured by the force balance for the various configurations tested are presented in figure 68. The thrust has not been removed from the coefficients presented. At Mach numbers greater than 0.50, the drag of all the configurations (except 243 which was not tested above $M = 0.40$) was larger than the thrust. However, this was to be expected since this particular propulsion system as stated in the INTRODUCTION was not originally intended for use as a cruise fan because of the low-pressure-ratio fan. Previously, this propulsion system was noted to experience large decreases in net thrust with increase in free-stream Mach numbers.

Operation of the fan generally caused small changes in normal force and large increases in pitching moment with increasing fan speed. Pitching moment varied nearly linearly with fan speed.

Drag Characteristics

The variation of mass-flow ratio (capture-area ratio) with fan speed and the variation of nacelle-drag coefficient with mass-flow ratio are presented in figures 69 and 70,

respectively. Nacelle-drag coefficient as defined in appendix A is

$$C_{D,\pi} = \frac{D_n}{q_\infty A_{\max}} = \frac{F_n + (D - F)}{q_\infty A_{\max}}$$

where

$$F_n = \text{Net thrust} = (F_{11.0} + F_{5.6}) - D_r$$

$$(D - F) = \text{Measured drag minus thrust}$$

The nacelle-drag data at windmill conditions have been summarized in figure 71. Also shown in this figure are the gas-generator skin-friction drag coefficient and the total skin-friction drag coefficients for each configuration. Skin-friction drag with a fully turbulent boundary layer and zero heat transfer assumed was computed by the Sommer and Short method as given in reference 15.

Those configurations employing the fan cowls 1 or 2 had the lowest drag. In order to determine some of the reasons for the differences between configurations, afterbody pressure drag and plug thrust coefficients have been presented in figures 72 and 73, respectively. The fan-nacelle afterbody is defined in figures 7(d) and 7(e). The force coefficients in figures 72 and 73 were obtained from integration of the pressures acting on these surfaces as outlined in appendix A. Since there is little change in the afterbody pressure distributions with fan operation (figs. 44 to 51), only windmill afterbody drag coefficients have been presented in figure 72 ($C_{D,\beta}$ varied ± 5 percent from values presented with fan operation). Note that plug thrust is for only the external portion of the plug downstream of the nozzle exit.

The differences between $C_{D,\pi}$ for configurations 144 (long cowl) and 244 (medium cowl) are due primarily to differences in skin friction. The small difference between $C_{D,\beta}$ for configurations 144 and 344 (or 244 and 344) is offset by the lower values of $C_{D,f}$ for configuration 344 (short cowl). However, the drag of configuration 344 is considerably greater than that of configurations 144 and 244. This result is probably due to an increase in the amount of inlet-flow spillage (configuration 344 operates at lower \dot{m}_∞/\dot{m}_1) and the pressure drag on the fan inlet. Both fan inlets 1 and 2 develop some thrust in the inlets due to positive pressures acting on the diverging surface of the fan inlet. Whether this is a net thrust for the inlet and cowl depends upon the balance that exists between the cowl-lip thrust and the additive drag. (Theoretically, the cowl-lip thrust cancels the additive drag at subsonic speeds.)

Although the afterbody drag of both afterbodies 1 and 2 is almost twice as large as that of afterbody 4 (due to greater projected area, figs. 5 and 6), approximately the same amount of thrust is developed on the plugs for configurations 123 and 113 so that approximately the same nacelle drag results for these configurations as for configuration 144. (See figs. 72 and 73.)

An effect of exit-area variation can be seen by comparing configurations 113 and 112. Afterbody drag is lower and plug thrust is higher for configuration 112 and results in lower nacelle drag. (See figs. 71, 72, and 73.) The lower plug thrust for configuration 113 is a result of the overexpansion of the flow leaving the nozzle. (Compare figs. 56 and 57.) This overexpansion also influences afterbody pressures on configuration 113 by causing these pressures to be more negative with a corresponding increase in afterbody drag. (See fig. 72.)

Although a similar effect might be expected in a comparison of afterbody drag of configurations 123 and 322, afterbody drag (fig. 72) for configuration 322 is higher. However, afterbody pressures are probably influenced more by the flow developed over the shorter fan cowl as is the case with configurations 144 and 344.

Other small differences between the nacelle-drag coefficients for different configurations are due to differences in the nozzle frictional losses that are not taken into account in the analysis presented. The differences between these losses are believed to be quite small.

All the configurations exhibited lower drag-rise Mach numbers than predicted from nacelle design considerations. The lower drag-rise Mach number can be partly attributed to the fairing between the fan and the gas-generator nacelles. In order to illustrate this result, the fan-nacelle-lip peak negative pressure coefficients $C_{p,min}$ have been plotted as a function of Mach number and are presented in figure 74. Shown are $C_{p,min}$ for three meridian angles, $\theta = 0^\circ$, 90° , and 150° , for configurations 144, 244, and 344. (Other configurations show similar effects.) The pressure orifices at $\theta = 150^\circ$ are located along the center of the fairing. Also shown is the pressure coefficient necessary for sonic flow. Since supercritical flow is undesirable because of associated drag increases due to shock formation and possible flow separation, it becomes necessary not to accelerate the flow along the nacelle above sonic conditions. For fan cowl 1 (configuration 144) and $\theta = 0^\circ$, the Mach number for critical flow is 0.79 and indicates that the design procedures used are sufficient for designing isolated nacelles since the design Mach number M_{cr} was 0.81. The critical Mach number for the gas generator is about 0.82 (design Mach number was 0.81).

However, the critical Mach number is decreased at the other meridian stations shown and is about 0.71 at $\theta = 150^\circ$ (about a 10-percent reduction) so that reductions in

critical Mach number due to fairing interference are indicated. The same is also true for configuration 244 (medium cowl). Reference 11 showed that for configuration 113, the fan-nacelle critical Mach number was lowered to 0.65 at an angle of attack of 5° and a free-stream Mach number of 0.70. Although the critical Mach number is the same at all the meridian angles for configuration 344 (short cowl), $C_{p,\min}$ is higher at $\theta = 150^\circ$ up to the critical Mach number. These larger negative pressures along the fairing also affect afterbody pressure recovery and, hence, afterbody drag. This effect on afterbody drag is shown in the lower part of figure 72 where the ratio of fairing afterbody drag to total afterbody drag is shown. The tick marks indicate the ratio of fairing projected areas to total afterbody projected area. As can be seen, the fairing drag is from 2.5 to 9.0 percent higher than might be expected on the basis of fairing projected area for an assumed symmetric pressure distribution about the entire afterbody.

The results of references 9 and 16 would tend to indicate that the values of nacelle-drag coefficient for the present investigation are high. Data from reference 16 were obtained for isolated nacelles which were supported from the front by a pipe that extended into the throat of the wind tunnel. High-pressure air was brought through the pipe to serve as the fan flow. During the investigation of reference 9, section drag coefficients were obtained from integrations of the boundary-layer total pressures at the fan-nacelle trailing edge. These results indicate a section drag coefficient that varies from 0.11 along the meridian containing the gas-generator nacelle to 0.04 along the meridian located 180° from the gas generator (similar to isolated nacelle meridian). These results would indicate that although low nacelle-drag coefficients can be obtained for isolated nacelles (ref. 16), addition of a close-coupled gas-generator nacelle can increase nacelle drag due to skin friction and can cause possible adverse interference effects. The importance of properly simulating inlet conditions is also evident. For the test setup of reference 16, the inlet mass-flow ratio is 1.0 and, hence, the effects of flow spillage inherent with operating inlets at lower mass-flow ratios were not present.

In addition, the nacelle-drag coefficients presented herein also include the nozzle and plug frictional losses that were not included in the calculation of fan thrust because of the location of the pressure instrumentation (appendix A). These losses are usually associated with internal performance and had they been taken into account, the computed thrust would be lower and, hence, would result in lower nacelle-drag coefficients. The coefficients of the present investigation are also based on the fan-nacelle maximum area rather than the total cross-sectional area represented by both the fan and gas-generator nacelles. Addition of the gas-generator-nacelle cross-sectional area would increase the total cross-sectional area about 15 percent.

CONCLUDING REMARKS

An investigation has been conducted in the Langley 16-foot transonic tunnel to determine internal and external performance characteristics of a large-scale 1.075-pressure-ratio tip-turbine cruise fan. The effects of geometric change and exit-area variation on performance for eight configurations were investigated at Mach numbers from 0 to 0.85 and at an angle of attack of 0^0 . Geometric variation was accomplished by using three fan cowls, afterbodies, and nozzle-exit plugs. The test Reynolds number based on the fan diameter (36.00 inches (91.44 cm)) varied from 3.90×10^6 to 11.25×10^6 .

The results showed that the fan operated at the design pressure ratio at or near design fan rotational speeds for all configurations. Only changes in exit area affected internal performance. The average overall fan efficiency (ratio of fan developed power to power absorbed by the fan turbine) was 62.5 percent for all configurations. Because of the low pressure ratio of the fan, the fan was found to operate over a wide range of fan mass-flow rates, to have a rapid fall-off in thrust with free-stream Mach number, and to perform over a large range of free-stream Mach numbers for a given nozzle area. A 20-percent increase in thrust and a 20-percent decrease in specific fuel consumption was obtained for the complete propulsion system over that for the basic gas generator at the higher Mach numbers. Static thrust was found to be in slight error due to flow in the wind tunnel induced by the fan exhaust.

Because the net thrust decreased rapidly with increasing free-stream Mach number (as a result of the low-pressure-ratio fan), the drag-minus-thrust coefficients became positive for all the configurations tested above a Mach number of 0.50. Those configurations with the longer nacelles had lower nacelle-drag coefficients attributable, in part, to less flow spillage about the fan cowl. Increasing the exit area decreased the fan-nacelle drag because of a decrease in afterbody drag and an increase in plug thrust. All the configurations exhibited lower drag-rise Mach numbers than predicted from fan-nacelle design, probably because of interference drag caused by the fairing between the fan and gas-generator nacelles. This interference drag was a result of pressures being much less than free-stream static pressure and premature supercritical flows developing on the fairing.

The close agreement between windmill external pressure distributions measured on the full-size model with pressures measured on a 1/5-scale flow-through model, both in the same wind tunnel, is taken to indicate that wind-tunnel-wall interference and blockage effects were negligible.

Langley Research Center,
National Aeronautics and Space Administration,
Langley Station, Hampton, Va., March 19, 1969,
721-03-00-02-23.

APPENDIX A

DATA REDUCTION PROCEDURE FOR FAN PERFORMANCE CALCULATIONS

This appendix is intended to give a brief description of the data reduction procedure used to obtain fan performance characteristics from measured quantities. The equations used assume U.S. Customary Units in order to avoid confusion. Conversion factors to the International System of Units (SI), based on reference 12, are found in table I. Table II presents various constants used.

From figure 1 and the section on SYMBOLS, the following notation is found to summarize the flow conditions measured at various locations through the model:

<u>Plane</u>		<u>Symbol</u>
∞	free-stream stagnation pressure	$P_{t,\infty}$
∞	free-stream static pressure	P_{∞}
2.0	gas-generator compressor-face stagnation pressure	$P_{t,2.0}$
2.0	gas-generator compressor-face static pressure	$P_{2.0}$
2.0	gas-generator compressor-face boundary-layer pressure	$P_{t,b,2.0}$
5.1	gas-generator turbine-discharge stagnation pressure	$P_{t,5.1}$
5.6	fan-tip-turbine-discharge stagnation pressure	$P_{t,5.6}$
10.0	fan-inlet stagnation pressure	$P_{t,10.0}$
10.0	fan-inlet static pressure	$P_{10.0}$
10.0	fan-inlet boundary-layer pressure	$P_{t,b,10.0}$
10.6	fan-rotor-discharge pressure	$P_{t,10.6}$
11.0	fan-discharge pressure	$P_{t,11.0}$
11.0	fan-discharge boundary-layer pressure	$P_{t,b,11.0}$

It should be noted that several measurements of each type pressure were made. The number of these measurements is summarized in the previous section on APPARATUS. The pressures measured at each plane (except plane ∞) were numerically averaged and are denoted with a bar over the symbol. The pressure probes were arranged so that each probe surveyed approximately the same annular area. Flow conditions at both the gas generator and fan inlet (planes 2.0 and 10.0, respectively) were computed by

APPENDIX A - Continued

the following procedure. (For simplicity the symbols used are for plane 10.0; however, calculations at plane 2.0 are identical except as otherwise noted.)

The effective fan-inlet stagnation pressure is defined as

$$(\bar{p}_{t,10.0})_{\text{eff}} = \frac{A_{10.0}(\bar{p}_{t,10.0}) + A_{b,10.0}(\bar{p}_{t,b,10.0})}{A_{10.0} + A_{b,10.0}} \quad \text{lb/ft}^2 \quad (\text{A1})$$

where $A_{10.0}$ and $A_{b,10.0}$ are flow areas assigned to the boundary-layer-free core and boundary layer, respectively and represent areas surveyed by the respective pressure survey rakes, and $(A_{10.0} + A_{b,10.0})$ is the total flow area. To compute gas-generator inlet conditions, similar area terms are used. The average static and stagnation pressures are used to compute the Mach numbers in the core and boundary layer. Thus,

$$M_{10.0} = \sqrt{\frac{2}{\gamma - 1} \left[\left(\frac{\bar{p}_{10.0}}{\bar{p}_{t,10.0}} \right)^{-\frac{\gamma-1}{\gamma}} - 1 \right]} \quad (\text{A2})$$

and

$$M_{b,10.0} = \sqrt{\frac{2}{\gamma - 1} \left[\left(\frac{\bar{p}_{10.0}}{\bar{p}_{t,b,10.0}} \right)^{-\frac{\gamma-1}{\gamma}} - 1 \right]} \quad (\text{A3})$$

The fan-inlet flow coefficient is then defined as

$$\frac{(A_{10.0})_{\text{eff}}}{A_{10.0} + A_{b,10.0}} = \frac{A_{10.0}(M_{10.0}) + A_{b,10.0}(M_{b,10.0})}{(A_{10.0} + A_{b,10.0})(M_{10.0})}$$

Fan-inlet static temperature is computed from

$$T_{10.0} = \frac{T_{t,10.0}}{\frac{T_{t,10.0}}{T_{10.0}} + \left(\frac{\gamma - 1}{2} \right) (M_{10.0})^2} = \frac{T_{t,\infty}}{1 + \left(\frac{\gamma - 1}{2} \right) (M_{10.0})^2} \quad ^\circ\text{R} \quad (\text{A4})$$

APPENDIX A - Continued

where the stagnation temperature $T_{t,10.0}$ at plane 10.0 is assumed to be equal to $T_{t,\infty}$. Fan-inlet density and velocity are then

$$\rho_{10.0} = \frac{\bar{p}_{10.0}}{RT_{10.0}} \quad \text{lbm/ft}^3 \quad (\text{A5})$$

and

$$V_{10.0} = M_{10.0} \sqrt{g\gamma RT_{10.0}} \quad \text{ft/sec} \quad (\text{A6})$$

Finally fan-inlet mass-flow rate was calculated by the following expression:

$$\dot{m}_{10.0} = \rho_{10.0} (V_{10.0}) (A_{10.0} + A_{b,10.0}) \left[\frac{(A_{10.0})_{\text{eff}}}{A_{10.0} + A_{b,10.0}} \right] \quad \text{lbm/sec} \quad (\text{A7})$$

As was stated previously, similar calculations were performed to arrive at the gas-generator mass-flow rate except that the fuel (JP-4) mass-flow rate must be added to the air mass-flow rate so that the total gas-generator mass-flow rate is

$$\dot{m}_{5.1} = \dot{m}_{2.0} + \dot{m}_f \quad \text{lbm/sec} \quad (\text{A8})$$

where \dot{m}_f is the fuel mass-flow rate and is obtained from a calibration curve of corrected air mass-flow rate for the T58-GE-6A gas generator as given by the following table:

$\frac{\dot{m}_{2.0}\sqrt{\sigma}}{\delta},$ lbm/sec	$\dot{m}_f,$ lbm/sec
4.0	0.0308
6.0	.0570
8.0	.0911
10.0	.1320
12.0	.1812
14.0	.2365
16.0	.2935
18.0	.3503

APPENDIX A - Continued

Next, fan-discharge effective stagnation pressure at plane 11.0 is found in a manner similar to the fan-inlet effective pressure

$$(\bar{p}_{t,11.0})_{\text{eff}} = \frac{A_{11.0}(\bar{p}_{t,11.0}) + A_{b,11.0}(\bar{p}_{t,b,11.0})}{A_{11.0} + A_{b,11.0}} \quad \text{lbf/ft}^2 \quad (\text{A9})$$

and the fan effective pressure ratio is then

$$\left(\frac{\bar{p}_{t,11.0}}{\bar{p}_{t,10.0}} \right)_{\text{eff}} = \frac{(\bar{p}_{t,11.0})_{\text{eff}}}{(\bar{p}_{t,10.0})_{\text{eff}}} \quad (\text{A10})$$

Fan-discharge stagnation temperature is

$$T_{t,11.0} = \frac{T_{t,10.0}}{\eta_R} \left[\left(\frac{\bar{p}_{t,11.0}}{\bar{p}_{t,10.0}} \right)_{\text{eff}}^{\frac{\gamma-1}{\gamma}} - 1 \right] + T_{t,10.0} \quad ^\circ\text{R} \quad (\text{A11})$$

where

$$\eta_R = 0.82 \text{ (assumed)}$$

and

$$T_{t,10.0} = T_{t,\infty}$$

A single representative value of the rotor efficiency η_R can be used for simplicity, since the thrust varies as the square root of the temperature and a precise determination of this parameter is not absolutely essential for adequate accuracy in the thrust level in view of the small variation of $T_{t,11.0}$.

Fan ideal thrust when discharging to free-stream static pressure is then calculated by the following relationship:

$$F_{11.0} = \dot{m}_{10.0} \sqrt{\frac{2(778.26)(c_{p,a})(T_{t,11.0})}{g} \left\{ 1 - \left[\frac{p_\infty}{(\bar{p}_{t,11.0})_{\text{eff}}} \right]^{\frac{\gamma-1}{\gamma}} \right\}} \quad \text{lbf} \quad (\text{A12})$$

APPENDIX A - Continued

Similarly, gas-generator ideal thrust and fan-turbine ideal thrust are found

$$F_{5.1} = \dot{m}_{5.1} \sqrt{\frac{2(778.26)(c_{p,g})(T_{t,5.1})}{g} \left[1 - \left(\frac{p_{\infty}}{\bar{p}_{t,5.1}} \right)^{\frac{\gamma_g - 1}{\gamma_g}} \right]} \quad \text{lbf} \quad (\text{A13})$$

and

$$F_{5.6} = \dot{m}_{5.1} \sqrt{\frac{2(778.26)(c_{p,g})(T_{t,5.6})}{g} \left[1 - \left(\frac{p_{\infty}}{\bar{p}_{t,5.6}} \right)^{\frac{\gamma_g - 1}{\gamma_g}} \right]} \quad \text{lbf} \quad (\text{A14})$$

Total ram drag is defined as

$$D_r = D_{r,F} + D_{r,E} = \frac{V_{\infty}(\dot{m}_{10.0} + \dot{m}_{2.0})}{g} \quad \text{lbf} \quad (\text{A15})$$

where V_{∞} is the free-stream velocity and can be determined from M and $T_{t,\infty}$.

Gross ideal thrust for the cruise-fan propulsion system

$$F_g = F_{11.0} + F_{5.6} \quad \text{lbf} \quad (\text{A16})$$

and cruise-fan propulsion net thrust (including gas generator) is

$$F_n = F_g - D_r \quad \text{lbf} \quad (\text{A17})$$

Gas-generator net thrust is defined as

$$F_{n,E} = F_{5.1} - D_{r,E} = F_{g,E} - D_{r,E} \quad (\text{A18})$$

The net aerodynamic drag for the cruise-fan propulsion system as it is supported on the force balance is

$$D_n = F_n + (D - F) \quad \text{lbf} \quad (\text{A19})$$

APPENDIX A - Continued

where the quantity $(D - F)$ is the drag minus thrust measured by the force balance and includes the aerodynamic drag of both the fan nacelle and gas-generator nacelle. Nacelle-drag coefficient is then defined as

$$C_{D,\pi} = \frac{D_n}{q_\infty A_{\max}} \quad (\text{A20})$$

where A_{\max} is the fan-nacelle cross-sectional area based on a fan-nacelle maximum diameter of 50 inches (127.00 cm) and does not include the gas-generator cross-sectional area. It should be noted that although the calculation of fan gross thrust does include frictional losses up to the planes of the pressure instrumentation (planes 5.6 and 11.0), it does not contain frictional losses through the rest of the nozzle and over the plug. Because of the omission of these losses, the determination of the net aerodynamic drag is conservative inasmuch as these losses are usually associated with internal performance. It is obvious that the axial-force coefficient presented is

$$C_A = \frac{(D - F)}{q_\infty A_{\max}} \quad (\text{A21})$$

and that the terms drag and axial force can be used interchangeably since these data are presented at an angle of attack of 0° . Body-axis coefficients have been used in the present report since they are the basic force data presented in reference 11 where the effects of angle of attack were determined. The analysis for removing the thrust effects from measured force data at angle of attack is also found in reference 11.

Various ideal power terms based on complete isentropic expansion and efficiencies based on these powers are now defined. The ideal power available from the gas-generator discharge is

$$P_{5.1} = \frac{778.26}{550} c_{p,g} T_{t,5.1} \dot{m}_{5.1} \left[1 - \left(\frac{p_\infty}{\bar{p}_{t,5.1}} \right)^{\frac{\gamma_g - 1}{\gamma_g}} \right] \quad \text{hp} \quad (\text{A22})$$

The ideal power absorbed by the fan turbine from the gas-generator discharge is

$$P_{5.6} = \frac{778.26}{550} c_{p,g} T_{t,5.1} \dot{m}_{5.1} \left[1 - \left(\frac{\bar{p}_{t,5.6}}{\bar{p}_{t,5.1}} \right)^{\frac{\gamma_g - 1}{\gamma_g}} \right] \quad \text{hp} \quad (\text{A23})$$

APPENDIX A - Continued

The total ideal power output of the fan turbine that could be delivered to the fan rotor is

$$P_T = \frac{778.26}{550} c_{p,g} \dot{m}_{5.1} (T_{t,5.1} - T_{t,5.6}) \quad \text{hp} \quad (\text{A24})$$

Ideal power output of the fan rotor (not computed) is

$$P_R = \frac{778.26}{550} c_{p,a} T_{t,10.0} \dot{m}_{10.0} \left[\left(\frac{\bar{p}_{t,10.6}}{\bar{p}_{t,10.0}} \right)^{\frac{\gamma-1}{\gamma}} - 1 \right] \quad \text{hp} \quad (\text{A25})$$

The ideal power contained in the airstream computed at station 11.0 is defined as

$$P_F = \frac{778.26}{550} c_{p,a} T_{t,10.0} \dot{m}_{10.0} \left[\left(\frac{\bar{p}_{t,11.0}}{\bar{p}_{t,10.0}} \right)^{\frac{\gamma-1}{\gamma}} - 1 \right] \quad \text{hp} \quad (\text{A26})$$

Based on the previously presented power terms, the following efficiencies are defined:

Turbine efficiency

$$\eta_T = \frac{P_{5.6}}{P_T} \quad (\text{A27})$$

Fan-rotor efficiency

$$\eta_R = \frac{P_R}{P_T} \quad (\text{A28})$$

Fan-stage efficiency

$$\eta_S = \frac{P_F}{P_T} \quad (\text{A29})$$

Overall fan efficiency

$$\eta_F = \frac{P_F}{P_{5.6}} \quad (\text{A30})$$

It should be noted that η_R was assumed to be 0.82 for the calculation of $T_{t,11.0}$ since P_R was not determined.

APPENDIX A - Continued

The fan-turbine power-absorption ratio is

$$R_T = \frac{P_{5.6}}{P_{5.1}} \quad (A31)$$

where the difference between $P_{5.1}$ and $P_{5.6}$ is excess power and is still available in the discharge from the turbine for producing thrust.

Fan-rotor-tip Mach number can be found by

$$M_{tip} = \frac{\left(\frac{4074 N_F}{100} \right) \frac{\pi d_F}{60}}{\sqrt{g \gamma R T_\infty}} \quad (A32)$$

where N_F is fan rotational speed in percent full speed (4074 rpm is fan maximum design speed) and d_F is fan diameter.

Fan-inlet mass-flow ratio (capture-area ratio) is defined as

$$\frac{\dot{m}_\infty}{\dot{m}_i} = \frac{\dot{m}_{10.0}}{\rho_i V_i A_i} = \frac{\dot{m}_{10.0}}{\rho_\infty V_\infty A_\infty} \quad (A33)$$

where the assumption $\rho_\infty V_\infty = \rho_i V_i$ is made.

Specific fuel consumption for the gas generator and fan is, respectively,

$$(sfc)_E = \frac{3600 \dot{m}_f}{F_{n,E}} \quad \text{per hr} \quad (A34)$$

and

$$(sfc)_F = \frac{3600 \dot{m}_f}{F_n} \quad \text{per hr} \quad (A35)$$

and the specific-fuel-consumption ratio is

$$\frac{(sfc)_F}{(sfc)_E} \quad (A36)$$

The net-augmentation ratio is simply

$$\frac{F_N}{F_{N,E}} \quad (A37)$$

APPENDIX A - Continued

and it can be seen that the net-augmentation ratio is the reciprocal of the specific-fuel-consumption ratio. The gross augmentation ratio is $F_g/F_{5.1}$.

The thrust ratio is

$$\frac{F_{n,max}}{(F_{n,max})_{static}} \quad (A38)$$

where $F_{n,max}$ is the maximum net thrust for any configuration at a given Mach number, and $(F_{n,max})_{static}$ is the maximum static thrust at 100 percent fan speed of configuration 243, which is 1530 pounds (6807 N). This value is obtained by extrapolating the static thrust of configuration 243 to 100 percent fan speed (fig. 30). The exit area of configuration 243 was sized to simulate take-off or maximum static thrust conditions.

The static thrust ratio is

$$\frac{F_{meas}}{F_{n,static}} \quad (A39)$$

where F_{meas} is the measured static thrust and $F_{n,static}$ is the ideal static net thrust for a particular configuration.

Fan and gas-generator performance parameters have been corrected to standard sea-level conditions (ref. 17) by the following relationships:

$$\delta = \frac{p_{\infty}}{14.696} \quad (A40)$$

$$\delta_t = \frac{p_{t,\infty}}{14.696} \quad (A41)$$

$$\sqrt{\sigma} = \sqrt{\frac{T_{t,\infty}}{518.69}} \quad (A42)$$

Component pressure forces on the afterbody and plug were obtained in the drag or thrust direction by assigning to each pressure orifice an incremental area projected on a plane normal to the fan-nacelle center line and by numerically summing the incremental forces.

The afterbody is defined in figures 7(d) and 7(e) and thus the afterbody drag includes the drag of the afterbody to the gas-generator nacelle fairing. The afterbody drag

APPENDIX A - Concluded

coefficient is

$$C_{D,\beta} = \sum_{x/l=a}^{1.0} - \frac{C_p A_l}{A_{\max}} \quad (A43)$$

where $a = x/l$ at plane 10.3 for each configuration.

Because pressures on the plug are usually above free stream, it is desirable to define a plug thrust coefficient rather than a drag coefficient. The plug thrust coefficient is based on that portion of the plug downstream of the nozzle exit. Thus, the plug thrust coefficient is

$$C_{F,\text{plug}} = \sum_{x/l=1.0}^b \frac{C_p A_l}{A_{\max}} \quad (A44)$$

where $b = x/l$ corresponding to end of plug.

APPENDIX B

DISCUSSION OF SCALE MODEL INVESTIGATION

Model and Procedure

In an effort to determine qualitatively the wind-tunnel-wall interference effects, a 1/5-scale flow-through model of configuration 123 was constructed of wood with a plastic overlay. A sketch of the 1/5-scale model is presented in figure 75 and a photograph of the model in the Langley 16-foot transonic tunnel is shown as figure 76. Nondimensional ordinates can be found in figure 7. The fan nozzle shroud was made symmetrical using the contours of the cold side.

The model was designed with separate fan and gas-generator ducts. No attempt was made to simulate the pressure losses associated with the flow through both the actual fan and gas generator while they are windmilling. However, mass-flow ratio was determined for the simulated fan flow and good agreement was found with that of the full-scale configuration under windmill conditions over the Mach number range investigated. (See fig. 77.) No measurements were made of the flow through the gas-generator duct. Pressure tubing was routed from the fan nacelle into the gas-generator duct and out of the model in the annulus between this duct and the sting. This arrangement resulted in more solid blockage of the gas-generator duct than is indicated in the sketch of figure 75.

The model was tested at Mach numbers from 0.30 to 0.80. Surface pressures and fan-duct stagnation pressures were measured and recorded on the same type of system as was used for the full-scale tests. Boundary-layer transition was fixed at the fan bullethead, inlet, and nacelle and on the gas-generator nacelle. A transition strip 0.1 inch (0.25 cm) wide was located 0.85 inch (2.16 cm) back of the leading edges and consisted of No. 80 carborundum grains cemented in a thin coat of clear shellac.

Results and Discussion

A comparison of fan-cowl-plus-afterbody pressures is presented in figure 78. With the exception of the forward portion of the fan cowl (up to $x/l = 0.15$), good to excellent agreement was found in the levels of pressure coefficients over the Mach number range investigated. There are some probable reasons, other than a windmilling fan effect, for the discrepancies over the forward portion of the nacelle. First, the curvature may not be identical. The full-scale fan nacelle was fabricated with a fiber-glass shell over a frame structure which resulted in a wavy surface. On the other hand, the 1/5-scale model was made of mahogany covered with plastic and had a smooth surface with no waviness. Secondly, in this area, where pressure gradients are very steep, slight errors in locating the pressure orifices can also cause apparent discrepancies. For

APPENDIX B - Concluded

example, at $x/l = 0$ where the largest differences occur, the orifice measuring stagnation pressure on the 1/5-scale model indicates a lower pressure coefficient than might be expected. Also, another probable cause of these discrepancies is the difference in Reynolds number.

Figure 79 presents comparisons of the bulletnose-plus-plug pressure distributions. Good to excellent agreement was found especially with the plug pressures.

Gas-generator-nacelle pressure distributions are compared in figure 80. Here again the same problems encountered with the leading-edge area of the fan nacelle are probably the causes for disagreement in the same region on the gas-generator nacelle. However, from $x/l = -0.50$ to $x/l = 0.92$, the agreement is good. The discrepancy that exists at $x/l = 1.08$ is caused by the placement of the pressure orifice on the 1/5-scale model at the start of engine-nacelle boattail and the consequent effects of expansion about the boattail. The cylindrical section on the 1/5-scale model should have extended about 1.2 inches (2.75 cm) farther downstream from this last orifice since the nacelle extended 6 inches (15.24 cm) beyond the last orifice on the full-scale configuration.

Bulletnose and afterbody drag coefficient and plug thrust coefficient are compared in figure 81 and show excellent agreement. Bulletnose drag coefficient was computed by a method similar to that of the afterbody drag coefficient as shown in appendix A.

From a comparison of pressure distributions and computed pressure drag coefficients between a 1/5-scale and full-scale configuration of the tip-turbine cruise fan, it is concluded that for the range of Mach numbers investigated, tunnel-wall-interference effects are negligible. This result is evident by the good agreement in the measured surface pressure distributions. The only discrepancies occur at the leading edge of both the fan and engine nacelle and these could probably be due to inaccurately duplicating the full-scale model and Reynolds number effects.

Comparison of computed pressure drags or thrust also shows excellent agreement.

REFERENCES

1. Aoyagi, Kiyoshi; Hickey, David H.; and deSavigny, Richard A.: Aerodynamic Characteristics of a Large-Scale Model With a High Disk-Loading Lifting Fan Mounted in the Fuselage. NASA TN D-775, 1961.
2. Maki, Ralph T.; and Hickey, David H.: Aerodynamics of a Fan-in-Fuselage Model. NASA TN D-789, 1961.
3. deSavigny, Richard A.; and Hickey, David H.: Aerodynamic Characteristics in Ground Effect of a Large-Scale Model With a High Disk-Loading Lifting Fan Mounted in the Fuselage. NASA TN D-1557, 1963.
4. Hickey, David H.; and Hall, Leo P.: Aerodynamic Characteristics of a Large-Scale Model With Two High Disk-Loading Fans Mounted in the Wing. NASA TN D-1650, 1963.
5. Kirk, Jerry V.; Hickey, David H.; and Hall, Leo P.: Aerodynamic Characteristics of a Full-Scale Fan-in-Wing Model Including Results in Ground Effect With Nose-Fan Pitch Control. NASA TN D-2368, 1964.
6. Chambers, Joseph R.; and Grafton, Sue B.: Static and Dynamic Longitudinal Stability Derivatives of a Powered 0.18-Scale Model of a Fan-in-Wing VTOL Aircraft. NASA TN D-4322, 1968.
7. Hall, Leo P.; Hickey, David H.; and Kirk, Jerry V.: Aerodynamic Characteristics of a Large-Scale V/STOL Transport Model With Lift and Lift-Cruise Fans. NASA TN D-4092, 1967.
8. Kutney, John T.: Propulsion System Development for V/STOL Transports. J. Aircraft, vol. 3, no. 6, Nov.-Dec. 1966, pp. 489-497.
9. Giulianetti, Demo J.; Biggers, James C.; and Corsiglia, Victor R.: Wind-Tunnel Test of a Full-Scale, 1.1 Pressure Ratio, Ducted Lift-Cruise Fan. NASA TN D-2498, 1964.
10. Fasching, W. A.; and Asmus, F. J.: High Bypass Lift/Cruise Fan. The State of the Art. [Preprint] 650202, Soc. Automot. Eng., Apr. 1965.
11. Capone, Francis J.: Subsonic Aerodynamic Characteristics of a Large-Scale 1.075 Pressure-Ratio Tip-Turbine Cruise-Fan Propulsion System at Angle of Attack. NASA TN D-5316, 1969.
12. Mechtly, E. A.: The International System of Units - Physical Constants and Conversion Factors. NASA SP-7012, 1964.

13. Baals, Donald D.; Smith, Norman F.; and Wright, John B.: The Development and Application of High-Critical-Speed Nose Inlets. NACA Rept. 920, 1948. (Supersedes NACA ACR L5F30a.)
14. Nichols, Mark R.; and Keith, Arvid L., Jr.: Investigation of a Systematic Group of NACA 1-Series Cowlings With and Without Spinners. NACA Rep. 950, 1949. (Supersedes NACA RM L8A15.)
15. Peterson, John B., Jr.: A Comparison of Experimental and Theoretical Results for the Compressible Turbulent-Boundary-Layer Skin Friction With Zero Pressure Gradient. NASA TN D-1795, 1963.
16. Fasching, W. A.; and Kutney, John: Lift/Cruise Fan Exhaust System Research Program. TRECOM Tech. Rep. 64-49, U.S. Army Transp. Res. Command (Fort Eustis, Va.), Sept. 1964.
17. Hesse, Walter J.; and Mumford, Nicholas V. S., Jr.: Jet Propulsion for Aerospace Applications. Second ed., Pitman Pub. Corp., 1964.

TABLE I.- CONVERSION FACTORS

Physical quantity	U.S. Customary Unit	Conversion factor	SI unit
Acceleration	ft/sec ²	3.04800×10^{-1}	meters/sec ²
Area	ft ²	9.290304×10^{-2}	meters ²
Mass density	lbm/ft ³	16.018463	kilograms/meter ³
Force	lbf	4.4482216152605	newtons
Gas constant	ft/ ^o R	5.38032026	joules/kilogram- ^o K
Length	ft	3.048×10^{-1}	meters
Length	in.	2.54×10^{-2}	meters
Mass-flow rate	lbm/sec	4.5359237×10^{-1}	kilogram/sec
Pressure	lbf/ft ²	47.880258	newtons/meter ²
Power	hp	7.4569987×10^2	watts
Specific fuel consumption	lbm/lbf-hr	9.8066	kilograms/newton-hr
Specific heat	Btu/lbm- ^o R	4.184×10^3	joules/kilogram- ^o K
Temperature	^o R	5.555×10^{-1}	^o K
Time	sec	1.000	seconds
Velocity	ft/sec	3.04800×10^{-1}	meters/sec

TABLE II.- CONSTANTS

Symbol	U.S. Customary Units	SI units
A_{\max}	13.646 ft ²	1.268 meters ²
$c_{p,a}$	0.2430 Btu/lb-°R	1016.7 joules/kilogram-°K
$c_{p,g}$	0.2764 Btu/lb-°R	1156.5 joules/kilogram-°K
d_{\max}	50 in.	1.270 meters
g	32.174 ft/sec ²	9.80665 meters/sec ²
R	53.35 ft/°R	287.040 joules/kilogram-°K
γ	1.400	1.400
γ_g	1.330	1.330
η_R	0.820	0.820

TABLE III.- LIST OF DATA FIGURES

Figure	Configuration	Remarks	Page
9	244	Gas-generator-inlet pressure-ratio profiles	65
10	244	Gas-generator-turbine-discharge total-pressure-ratio profiles	66
11	244	Fan-turbine-discharge total-pressure-ratio profiles	67
12	All	Gas-generator and fan-turbine exhaust temperature	68
13	All	Gas-generator performance characteristics	70
14	144	Fan-inlet pressure profiles	78
15	244	Fan-inlet pressure profiles	81
16	344	Fan-inlet pressure profiles	84
17	123	Fan-inlet pressure profiles	87
18	113	Fan-inlet pressure profiles	90
19	112	Fan-inlet pressure profiles	93
20	322	Fan-inlet pressure profiles	96
21	243	Fan-inlet pressure profiles	99
22	144	Fan-rotor-discharge and fan-discharge pressure profiles	101
23	244	Fan-rotor-discharge and fan-discharge pressure profiles	104
24	344	Fan-rotor-discharge and fan-discharge pressure profiles	107
25	123	Fan-rotor-discharge and fan-discharge pressure profiles	110
26	113	Fan-rotor-discharge and fan-discharge pressure profiles	113
27	112	Fan-rotor-discharge and fan-discharge pressure profiles	116
28	322	Fan-rotor-discharge and fan-discharge pressure profiles	119
29	243	Fan-rotor-discharge and fan-discharge pressure profiles	122
30	All	Measured static thrust and static-thrust ratios	124
31	144	Fan performance characteristics	125
32	244	Fan performance characteristics	127
33	344	Fan performance characteristics	129
34	123	Fan performance characteristics	131
35	113	Fan performance characteristics	133
36	112	Fan performance characteristics	135
37	322	Fan performance characteristics	137
38	243	Fan performance characteristics	139

TABLE III.- LIST OF DATA FIGURES - Continued

Figure	Configuration	Remarks	Page
39	All	Fan-turbine power-absorption ratio and fan-stage efficiency	141
40	All	Specific-fuel-consumption ratio	145
41	All	Net-thrust-augmentation ratio	146
42	All	Summary of specific-fuel-consumption and net-thrust-augmentation-ratio characteristics	147
43	All	Summary of thrust-ratio characteristics	148
44	144	Fan-nacelle external and internal pressure distributions	149
45	244	Fan-nacelle external and internal pressure distributions	155
46	344	Fan-nacelle external and internal pressure distributions	162
47	123	Fan-nacelle external and internal pressure distributions	168
48	113	Fan-nacelle external and internal pressure distributions	174
49	112	Fan-nacelle external and internal pressure distributions	179
50	322	Fan-nacelle external and internal pressure distributions	185
51	243	Fan-nacelle external and internal pressure distributions	191
52	144	Fan-bulleenose-plus-plug pressure distributions	194
53	244	Fan-bulleenose-plus-plug pressure distributions	196
54	344	Fan-bulleenose-plus-plug pressure distributions	200
55	123	Fan-bulleenose-plus-plug pressure distributions	204
56	113	Fan-bulleenose-plus-plug pressure distributions	206
57	112	Fan-bulleenose-plus-plug pressure distributions	208
58	322	Fan-bulleenose-plus-plug pressure distributions	212
59	243	Fan-bulleenose-plus-plug pressure distributions	216
60	144	Gas-generator-nacelle internal and external pressure distributions	220
61	244	Gas-generator-nacelle internal and external pressure distributions	222
62	344	Gas-generator-nacelle internal and external pressure distributions	224
63	123	Gas-generator-nacelle internal and external pressure distributions	226
64	113	Gas-generator-nacelle internal and external pressure distributions	228
65	112	Gas-generator-nacelle internal and external pressure distributions	230
66	322	Gas-generator-nacelle internal and external pressure distributions	232
67	243	Gas-generator-nacelle internal and external pressure distributions	234

TABLE III.- LIST OF DATA FIGURES – Concluded

Figure	Configuration	Remarks	Page
68	All	Aerodynamic characteristics	236
69	All	Mass-flow-ratio characteristics	247
70	All	Nacelle-drag-coefficient characteristics	248
71	All	Summary of windmill nacelle-drag coefficient	250
72	All	Afterbody-drag characteristics	252
73	All	Plug thrust coefficient	253
74	All	Variation of fan-cowl minimum pressure coefficient	254
77	123	Comparison between full-scale and 1/5-scale model of mass-flow ratio	257
78	123	Comparison between full-scale and 1/5-scale model of fan-nacelle pressure distributions	258
79	123	Comparison between full-scale and 1/5-scale model of bulletnose-plus-plug pressure distributions	264
80	123	Comparison between full-scale and 1/5-scale model of gas-generator-nacelle pressure distributions	270
81	123	Comparison between full-scale and 1/5-scale model of bulletnose and afterbody-drag coefficient and plug thrust coefficient	276

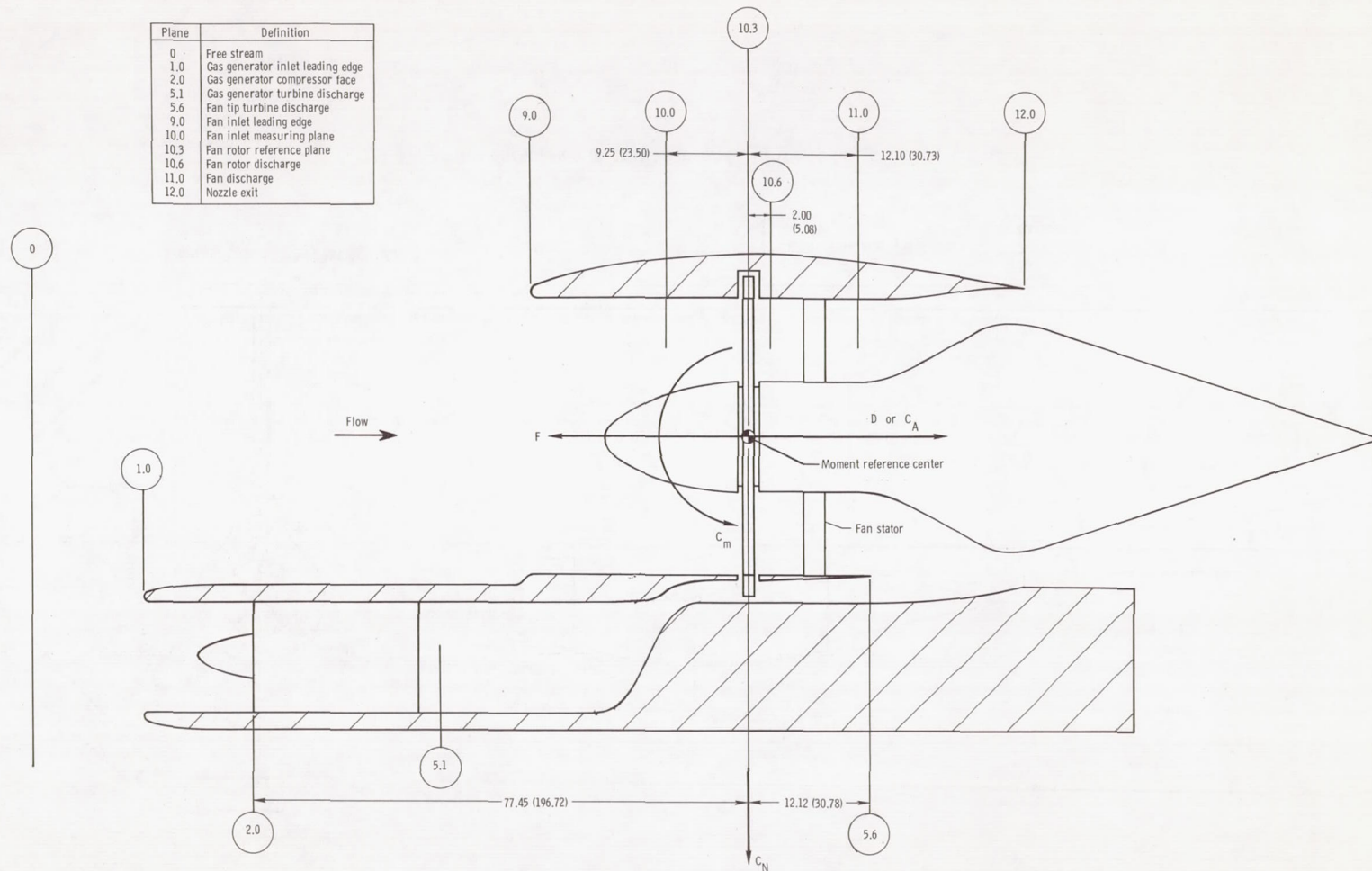


Figure 1.- Cruise-fan-forces sign convention and definition and location of instrumentation planes. All dimensions are in inches (parenthetical dimensions in centimeters).

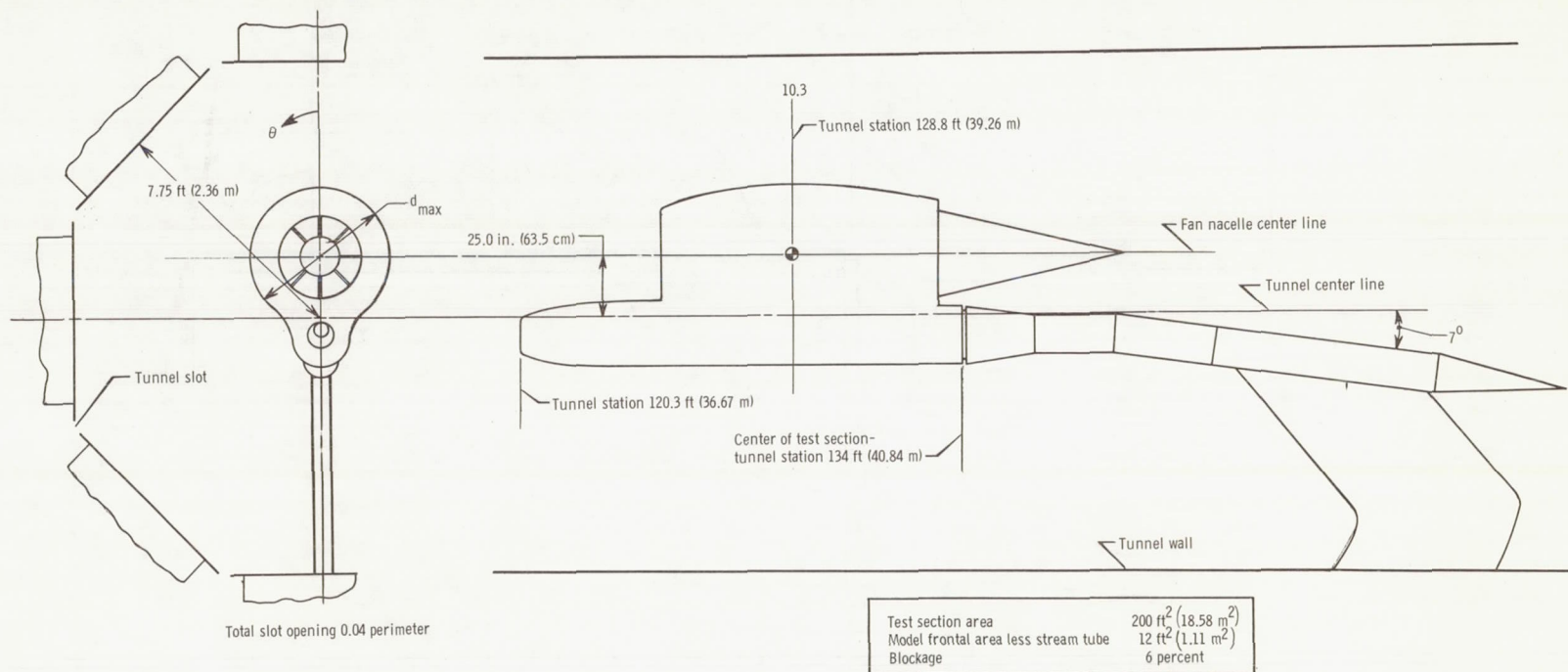


Figure 2.- Installation of cruise-fan model in the 16-foot transonic tunnel.

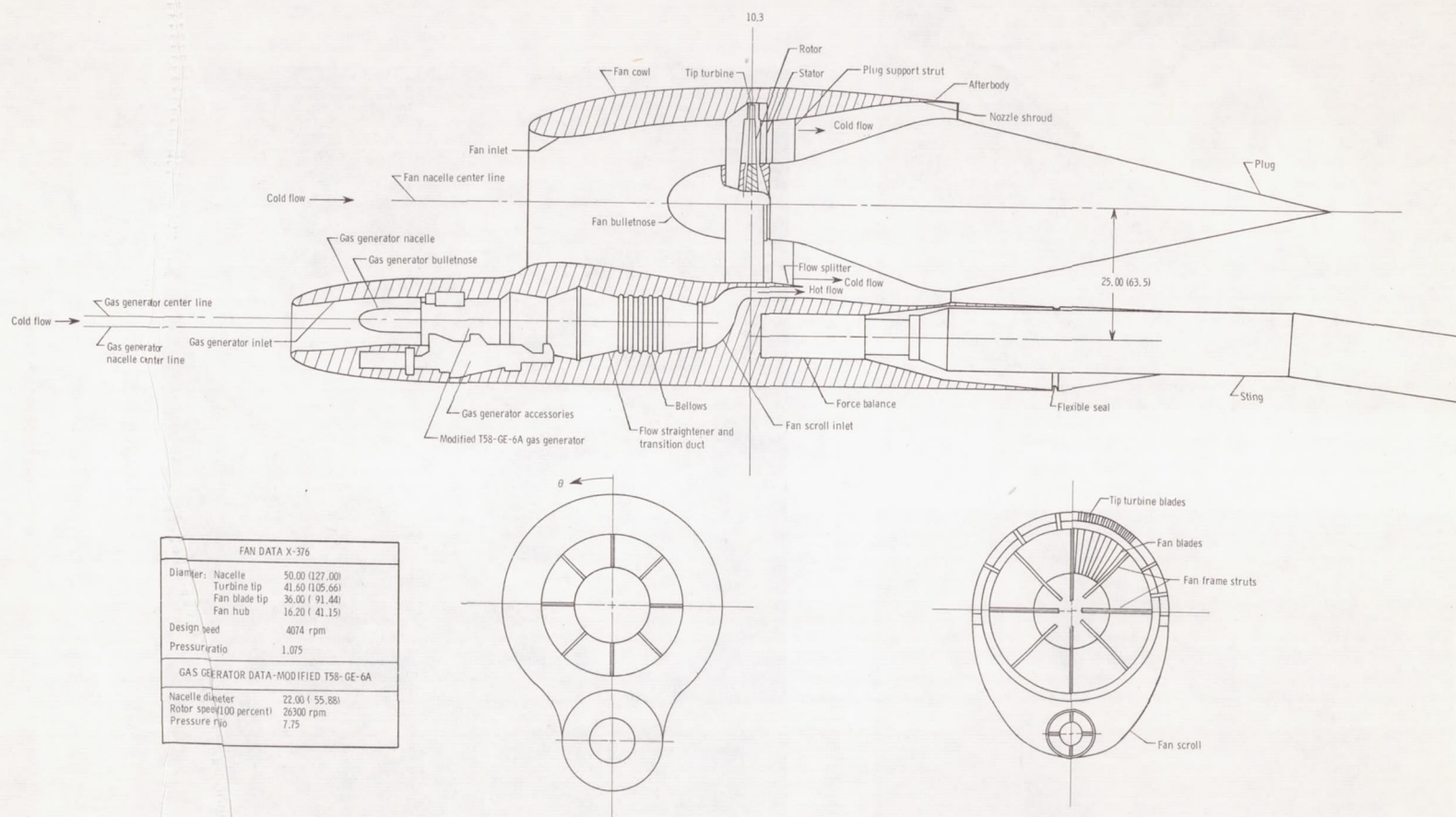
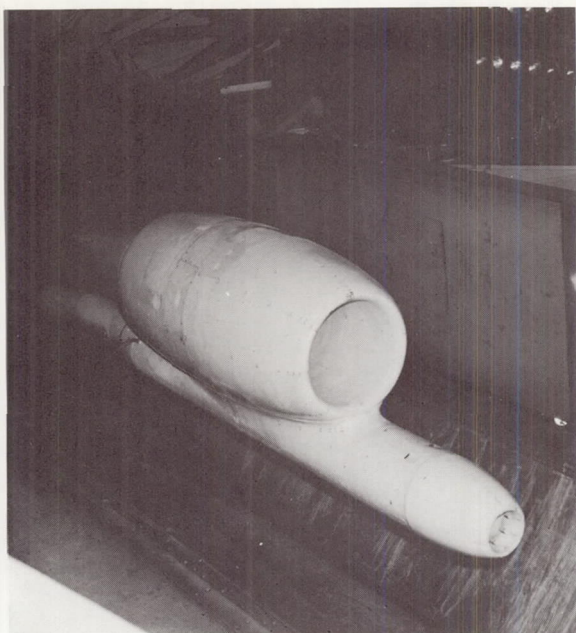
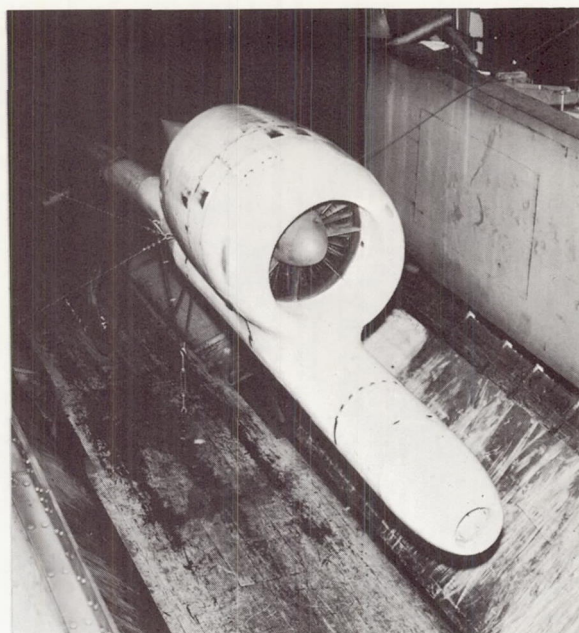


Figure 3.- Sketch of cruise-fan assembly. All dimensions in inches (parentetical dimensions in centimeters) unless otherwise noted.



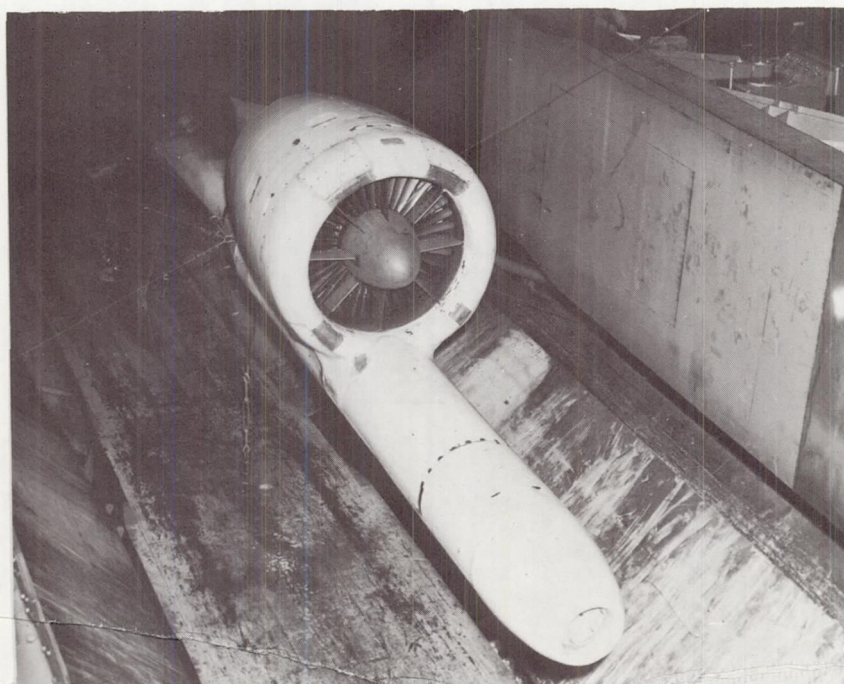
Configuration 144

L-65-4552



Configuration 244

L-65-4525

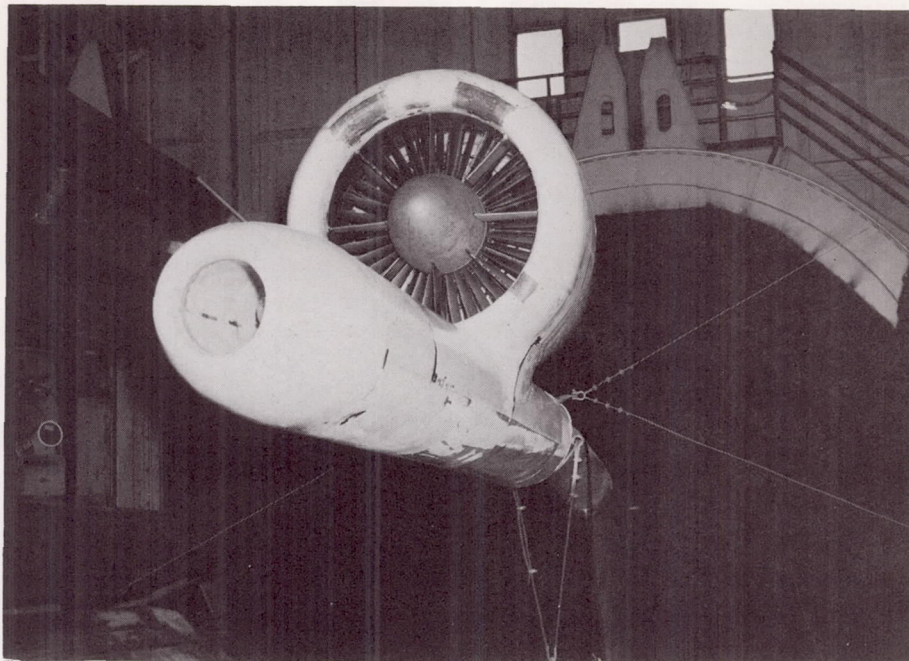


Configuration 322

L-65-4639

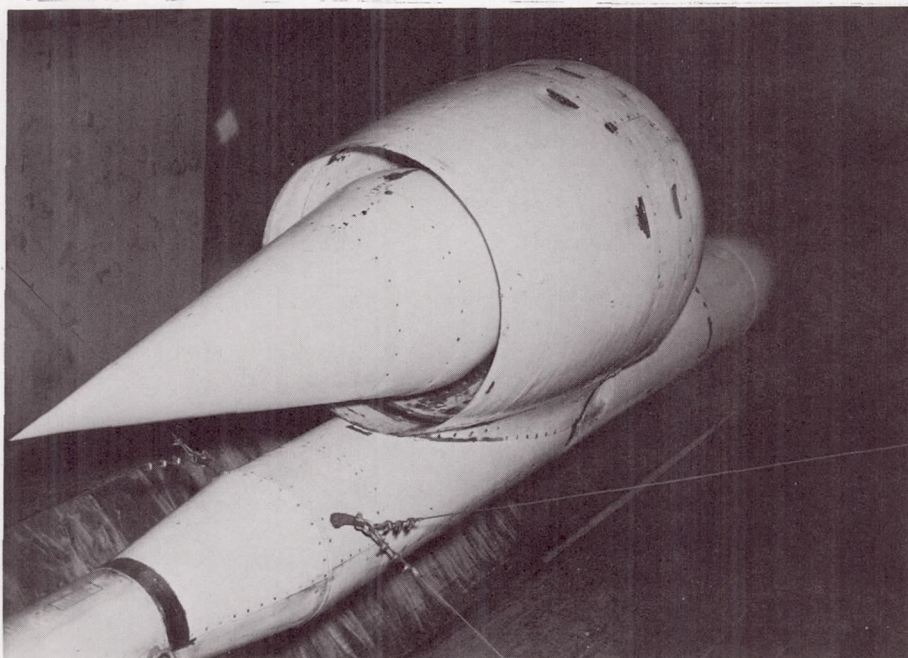
(a) Configurations 144, 244, and 322.

Figure 4.- Photographs of model.



Front view

L-65-4638

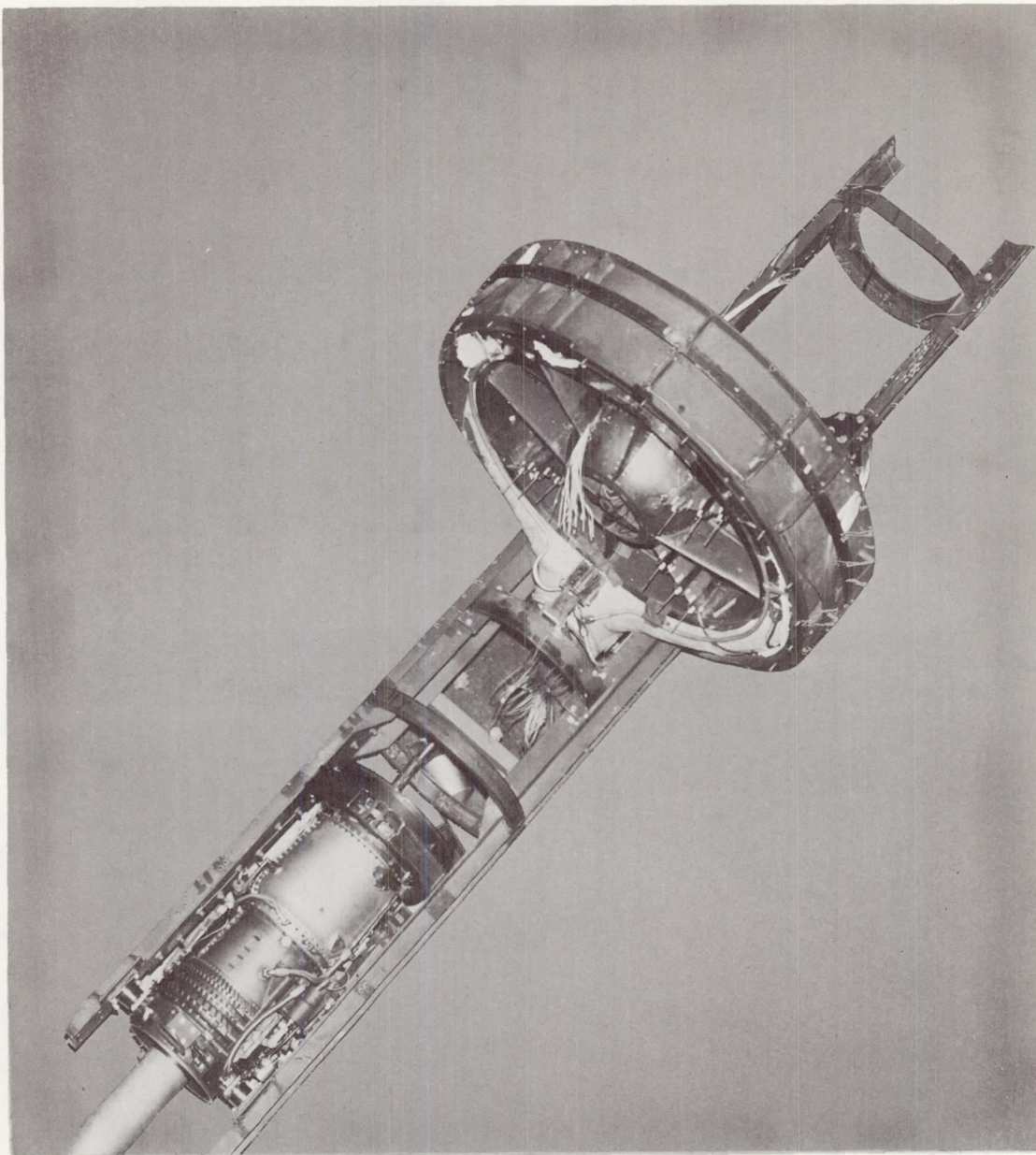


Rear view

L-65-4640

(b) Configuration 322 showing guy wires.

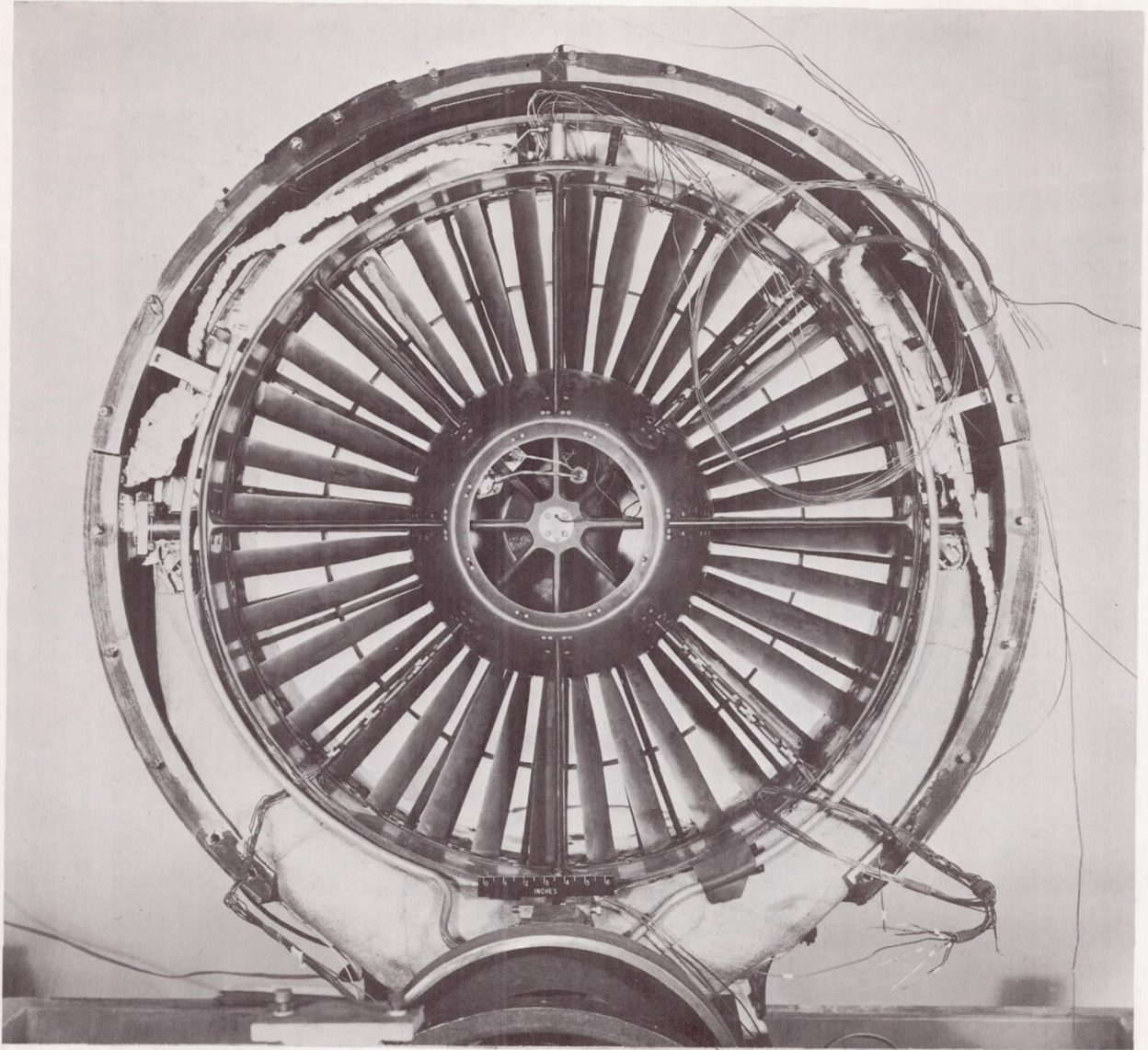
Figure 4.- Continued.



(c) Top view showing gas generator and fan, without transition sections.

L-63-8705

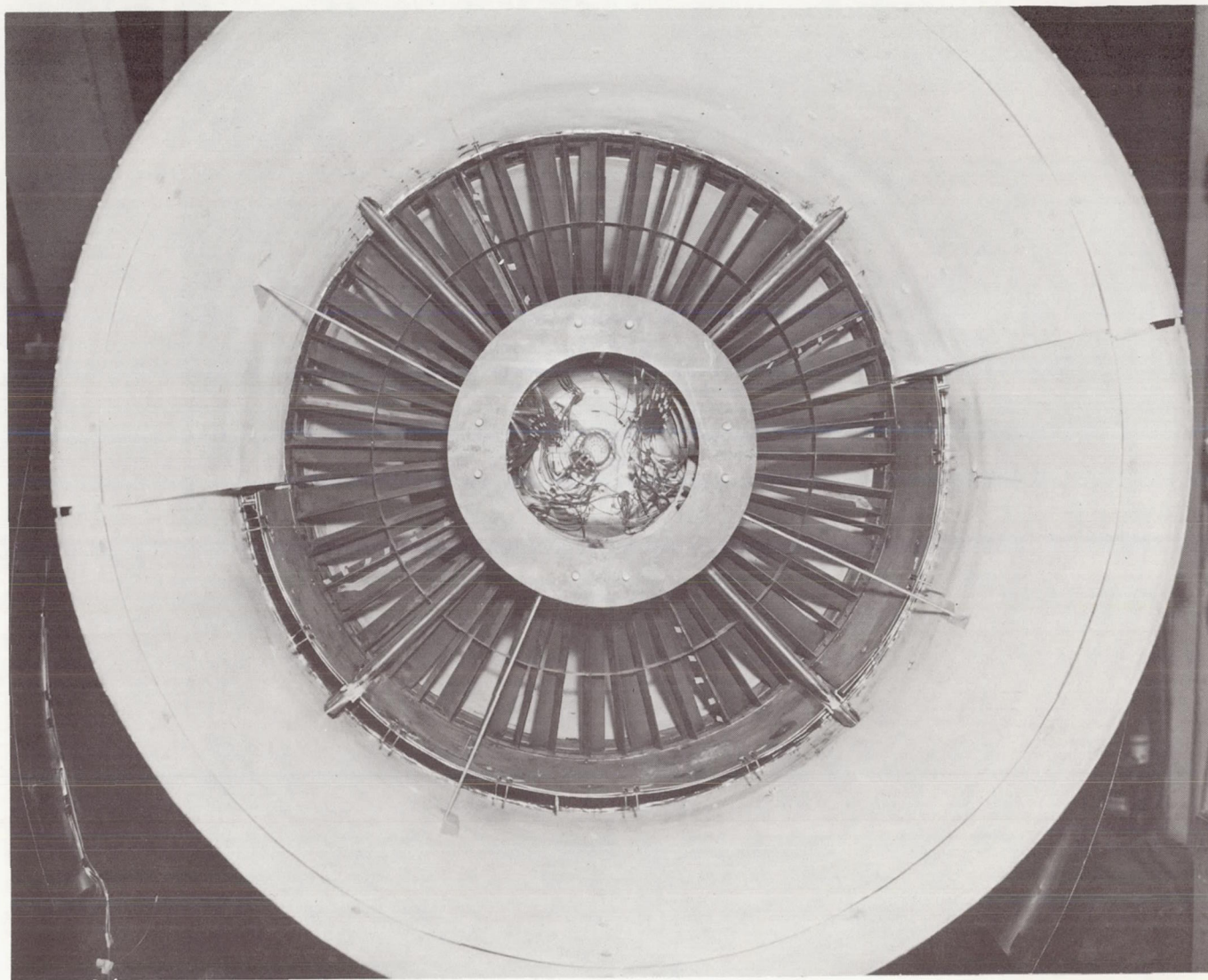
Figure 4.- Continued.



(d) Front view showing scroll and fan rotor.

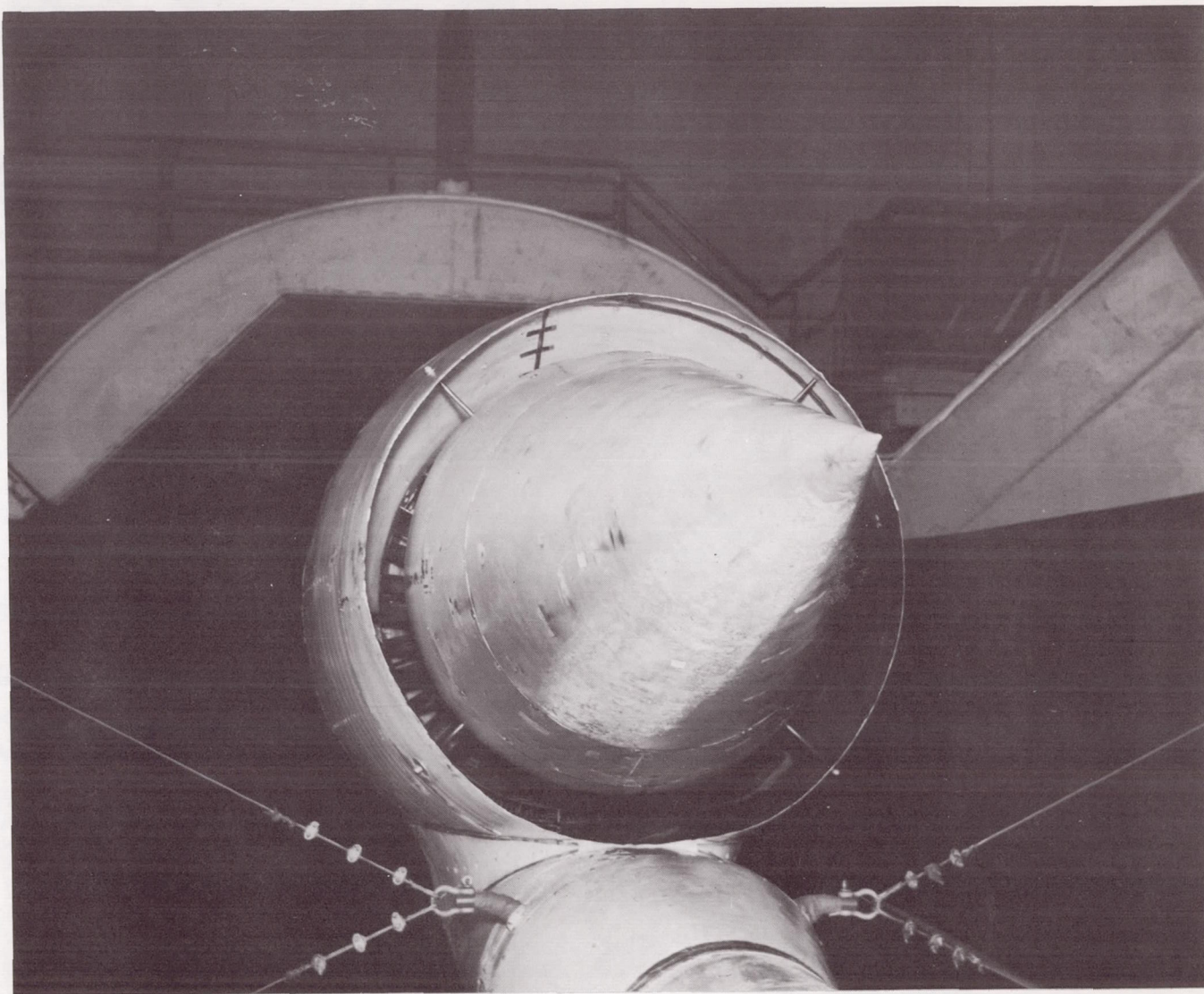
L-63-8451

Figure 4.- Continued.



(e) Rear view showing fan stators and flow splitter plate.

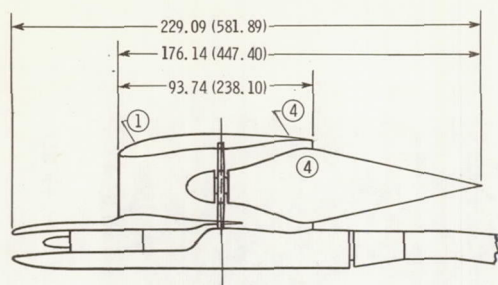
L-63-9681



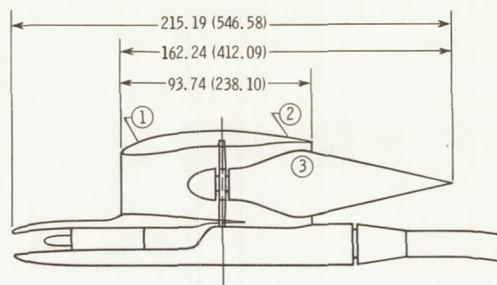
(f) Configuration 243; view of fan turbine blades.

L-65-4787

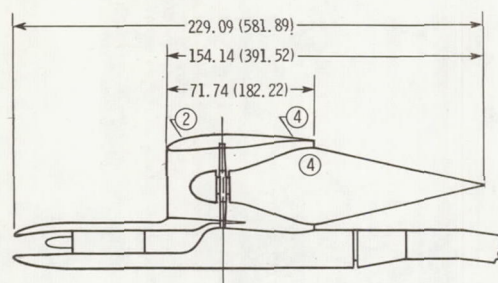
Figure 4.- Concluded.



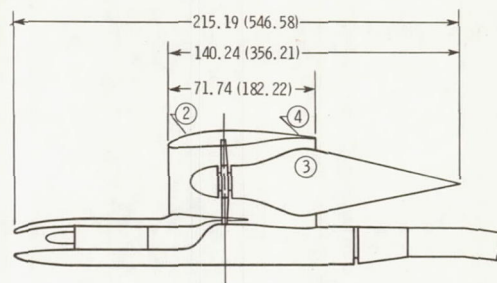
Configuration 144, $A_e = 433 \text{ in}^2 (2793 \text{ cm}^2)$



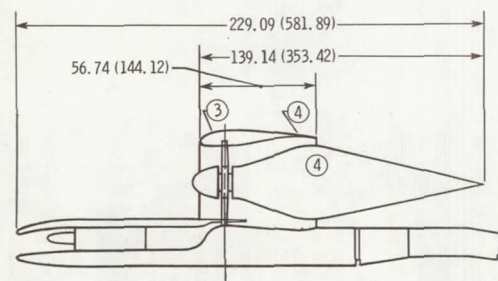
Configuration 123, $A_e = 433 \text{ in}^2 (2793 \text{ cm}^2)$



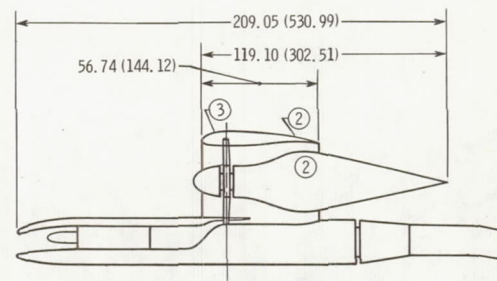
Configuration 244, $A_e = 433 \text{ in}^2 (2793 \text{ cm}^2)$



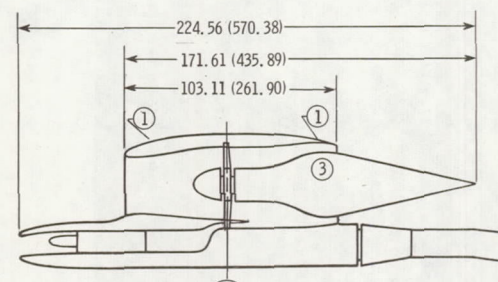
Configuration 243, $A_e = 770 \text{ in}^2 (4968 \text{ cm}^2)$



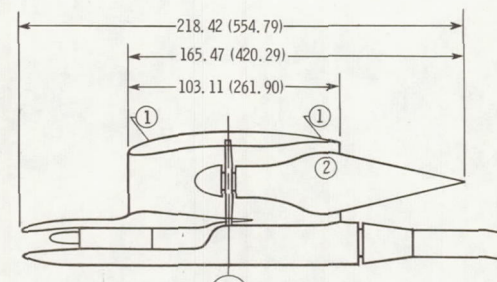
Configuration 344, $A_e = 433 \text{ in}^2 (2793 \text{ cm}^2)$



Configuration 322, $A_e = 566 \text{ in}^2 (3652 \text{ cm}^2)$

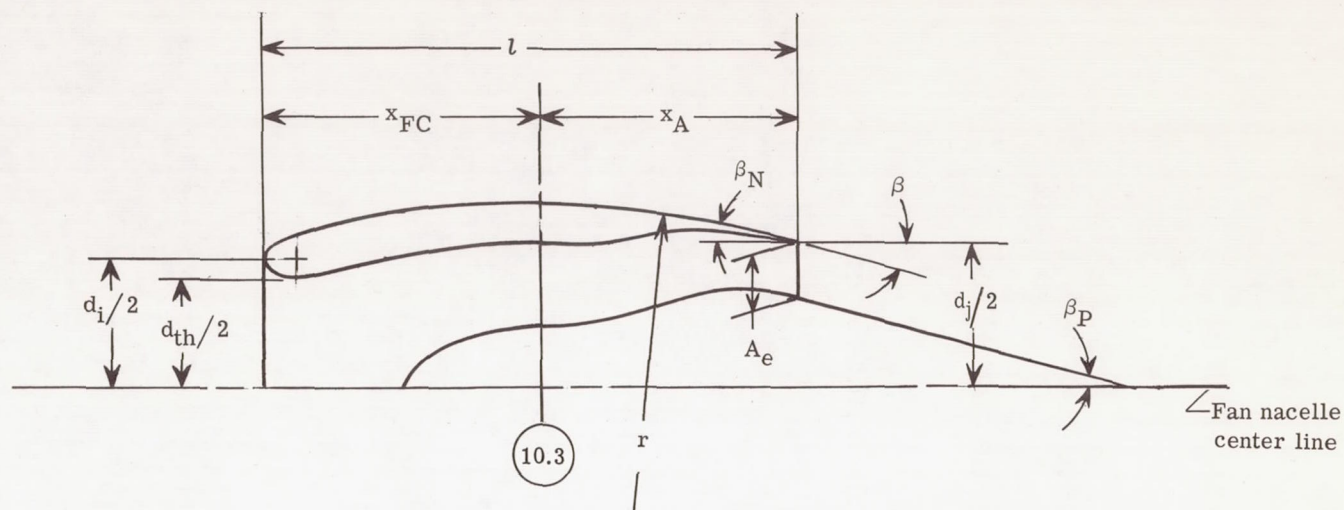


Configuration 113, $A_e = 433 \text{ in}^2 (2793 \text{ cm}^2)$



Configuration 112, $A_e = 566 \text{ in}^2 (3652 \text{ cm}^2)$

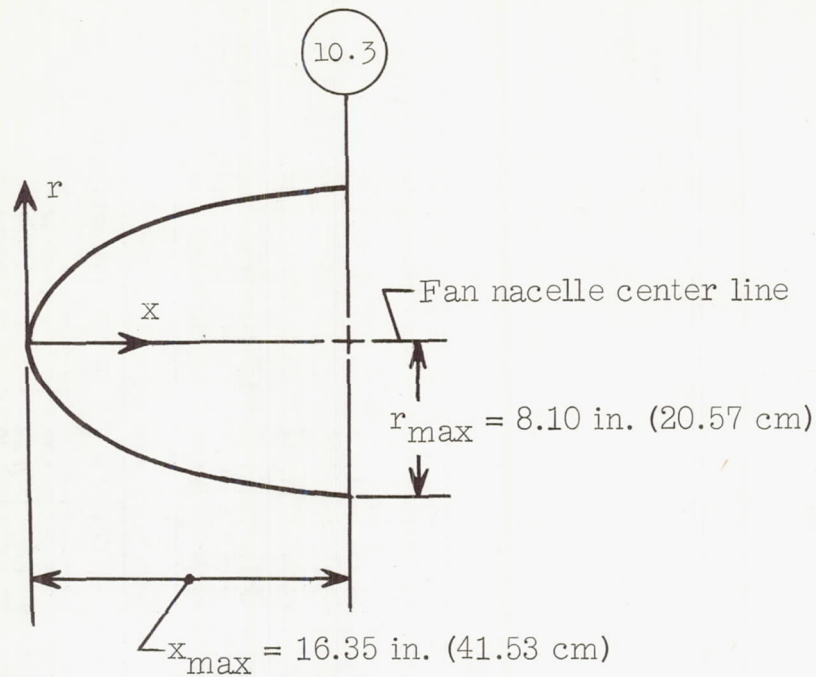
Figure 5.- Sketches of various configurations tested. All dimensions in inches (parentetical dimensions in centimeters) unless otherwise noted. Note that plane 10.3 and configuration component code numbers are shown circled.



Configuration	A_e (in. ²)	A_e (cm ²)	M_{CR}	x_{FC} (in.)	x_{FC} (cm)	x_A (in.)	x_A (cm)	l (in.)	l (cm)	β , deg	l/d_{max}	d_i/d_{th}
144	433	2793	0.81	49.00	124.46	44.74	113.64	93.74	238.10	10	1.87	1.133
244	433	2793	.71	27.00	68.58	44.74	113.64	71.74	182.22	10	1.43	1.133
344	433	2793	.55	12.00	30.48	44.74	113.64	56.74	144.12	10	1.13	1.133
123	433	2793	.81	49.00	124.46	44.74	113.64	93.74	238.10	14.5	1.87	1.133
113	433	2793	.81	49.00	124.46	54.11	137.44	103.11	261.90	12	2.06	1.133
112	566	3652	.81	49.00	124.46	54.11	137.44	103.11	261.90	12	2.06	1.133
322	566	3652	.55	12.00	30.48	44.74	113.64	56.74	144.12	14.5	1.13	1.133
243	770	4968	.71	27.00	68.58	44.74	113.64	71.74	182.22	10	1.43	1.133

Configuration	A_j/A_e	d_j (in.)	d_j (cm)	β_P , deg	β_N , deg	r/d_{max}	NACA inlet designation
144	3.478	43.86	111.40	12.5	6.5	4.10	1-64-98
244	3.478	43.86	111.40	12.5	6.5	4.10	1-72-64
344	3.478	43.86	111.40	12.5	6.5	4.10	1-81-18
123	3.478	39.84	101.19	12.5	11.5	3.57	1-64-98
113	3.478	39.84	101.19	12.5	11.5	5.25	1-64-98
112	2.661	39.84	101.19	12.5	11.5	5.25	1-64-98
322	2.661	39.84	101.19	12.5	11.5	3.57	1-81-18
243	1.956	43.86	111.40	12.5	6.5	4.10	1-72-64

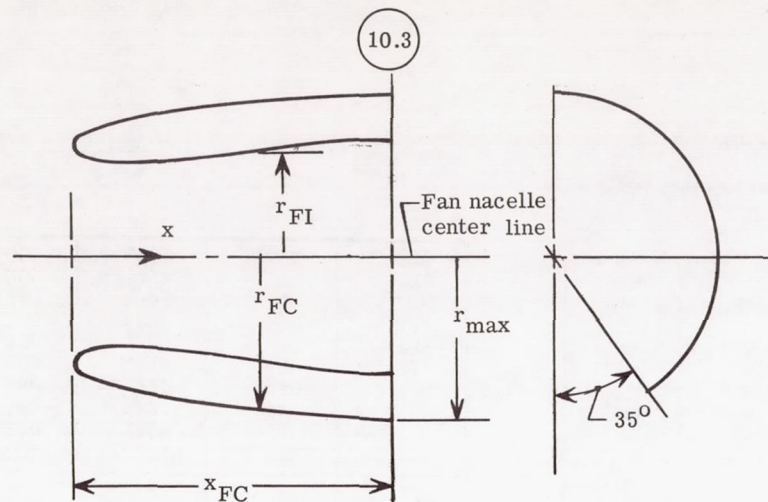
Figure 6.- Summary of cruise-fan geometrical characteristics.



x/x_{\max}	r/r_{\max}
0.000	0.000
.028	.220
.056	.289
.085	.356
.141	.465
.281	.637
.470	.795
.705	.940
.893	.998
1.000	1.000

(a) Fan-bulldog nose ordinates.

Figure 7.- Geometric characteristics of various model components.



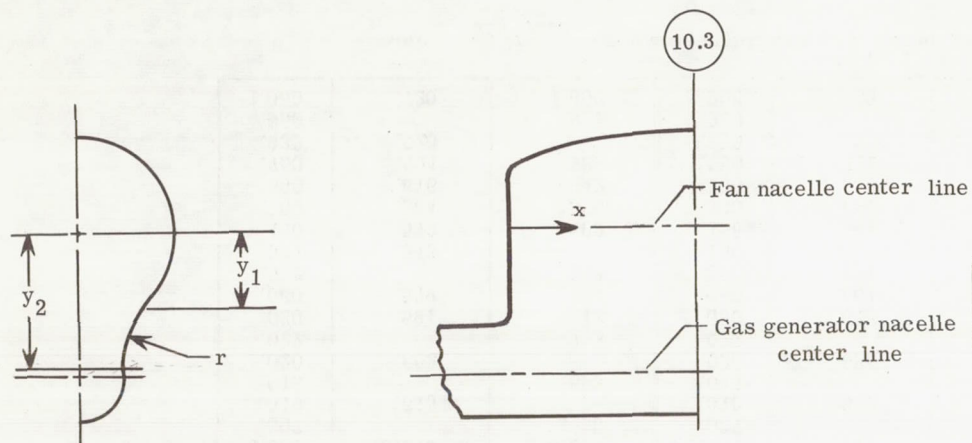
	x_{FC} (in.)	x_{FC} (cm)	r_{max} (in.)	r_{max} (cm)
Fan cowl 1	49.00	124.46	25.00	63.50
2	27.00	68.58	25.00	63.50
3	12.00	30.48	25.00	63.50

Fan cowl 1			Fan cowl 2			Fan cowl 3		
x/x_{FC}	r_{FI}/r_{max}	r_{FC}/r_{max}	x/x_{FC}	r_{FI}/r_{max}	r_{FC}/r_{max}	x/x_{FC}	r_{FI}/r_{max}	r_{FC}/r_{max}
0.000	0.649	0.649	0.000	0.727	0.727	0.000	0.816	0.816
.007		.680	.007		.751	.010		.838
.010	.615		.010	.698		.015	.787	
.015		.693	.015		.762	.020		.848
.020	.602		.020	.686		.030	.779	.856
.022		.703	.022		.771	.060	.765	.879
.030	.594	.713	.030	.678	.779	.090	.755	.890
.060	.579	.744	.060	.661	.802	.150	.741	.914
.092		.768	.090	.651	.821	.300	.723	.954
.097	.573		.150		.851	.392	.720	.986
.150	.573	.809	.158	.644		.500	.720	
.300	.584	.876	.300	.654	.905	.727	.720	.999
.500	.616	.942	.500	.686	.953	.750		1.000
.750	.694	.989	.750	.718	.989	.950		1.000
.933	.720		.879	.720		1.000	.720	
.950		.998	.950		.999			
1.000	.720	1.000	1.000	.720	1.000			

Note: r_{FC}/r_{max} ordinates applicable $\pm 145^\circ$ from vertical, for other $\pm 35^\circ$ see figure 7(c).

(b) Fan inlet and cowl ordinates.

Figure 7.- Continued.



	x_{FC} (in.)	x_{FC} (cm)	r_{max} (in.)	r_{max} (cm)
Fan cowl 1	49.00	124.46	25.00	63.50
2	27.00	68.58	25.00	63.50
3	12.00	30.48	25.00	63.50

Note: Radius of fairing intersects gas generator and fan cowl radii at points y_1 and y_2 . x_{FC} and r_{max} are defined in figure 7(b).

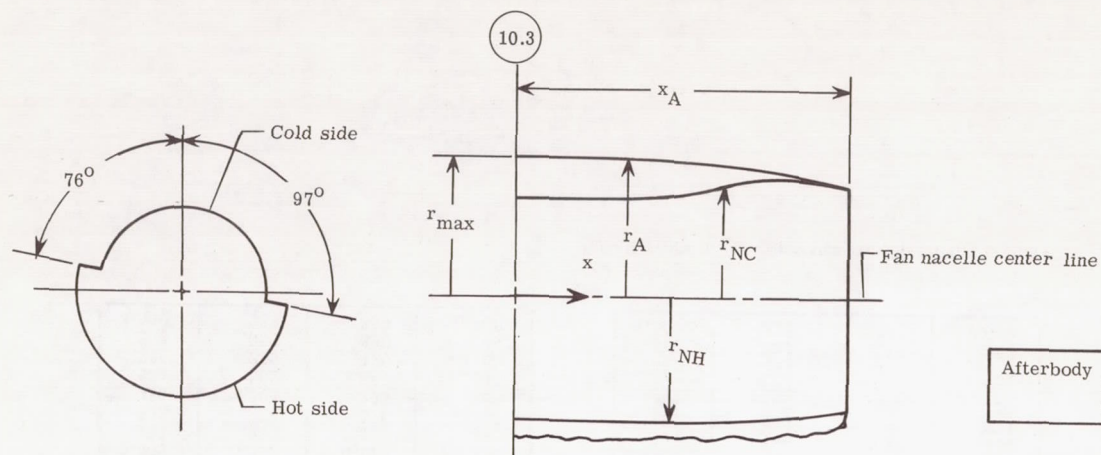
Fan cowl 1			
x/x_{FC}	y_1/x_{FC}	y_2/x_{FC}	r/r_{max}
0.000	0.331	0.367	0.072
.030	.308	.401	.106
.060	.331	.417	.108
.090	.341	.430	.108
.150	.349	.439	.112
.300	.360	.459	.132
.500	.370	.500	.191
.750	.396	.543	.316
.950	.418	.571	.328
1.000	.421	.573	.340

Fan cowl 2			
x/x_{FC}	y_1/x_{FC}	y_2/x_{FC}	r/r_{max}
0.000	0.667	0.667	0.000
.060	.626	.828	.144
.090	.639	.841	.154
.150	.650	.857	.163
.300	.669	.883	.178
.500	.698	.939	.226
.750	.722	.994	.289
.950	.750	1.037	.316
1.000	.765	1.041	.340

Fan cowl 3			
x/x_{FC}	y_1/x_{FC}	y_2/x_{FC}	r/r_{max}
0.000	1.500	1.500	0.000
.030	1.579	1.883	.098
.060	1.600	1.933	.112
.090	1.617	1.967	.124
.150	1.650	2.021	.138
.300	1.675	2.171	.216
.500	1.683	2.300	.311
.750	1.708	2.325	.324
.950	1.713	2.329	.332
1.000	1.721	2.342	.340

(c) Ordinates of fairing from fan cowl to gas-generator nacelle.

Figure 7.- Continued.



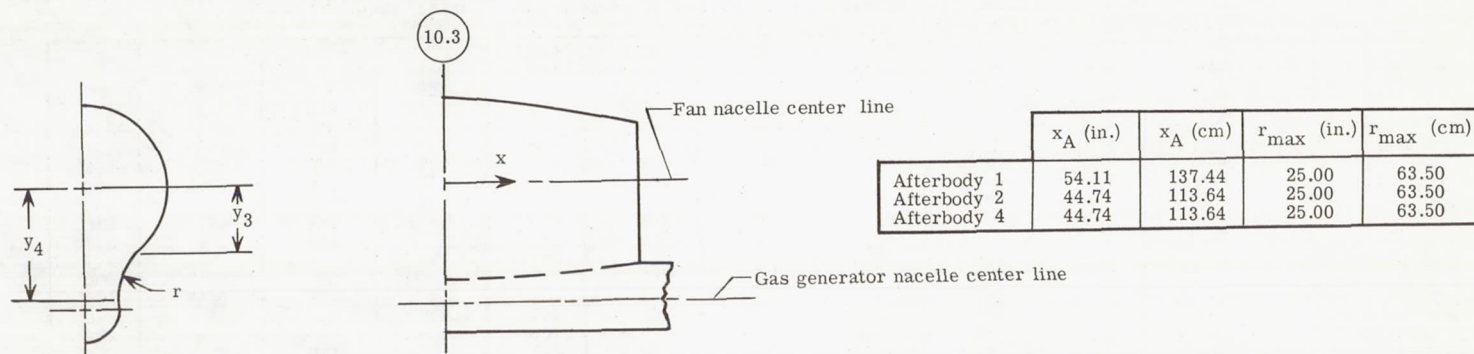
	x_A (in.)	x_A (cm)	r_{max} (in.)	r_{max} (cm)
Afterbody 1	54.11	137.44	25.00	63.50
2	44.74	63.50	25.00	63.50
4	44.74	63.50	25.00	63.50

Afterbody 1				Afterbody 2				Afterbody 4			
x/x_A	r_{NC}/r_{max}	r_{NH}/r_{max}	r_A/r_{max}	x/x_A	r_{NC}/r_{max}	r_{NH}/r_{max}	r_A/r_{max}	x/x_A	r_{NC}/r_{max}	r_{NH}/r_{max}	r_A/r_{max}
0.000	0.720	0.833	1.000	0.000	0.720	0.833	1.000	0.000	0.720	0.833	1.000
.111			.997	.095			.996	.096			1.000
.185	.720	.833		.112	.720	.833		.173	.732	.833	
.221			.988	.191			.990	.191			.999
.388			.965	.268	.720	.833		.294	.768	.833	
.397	.720	.833		.334			.974	.334			.996
.506	.749	.833		.402	.749	.833		.405	.802	.845	
.554			.930	.477			.948	.478			.984
.617	.782	.833		.536	.782	.833		.540	.843	.865	
.710	.782	.833		.648	.810	.833		.651	.878	.888	
.775			.863	.668			.899	.669			.957
.801	.782	.833		.759	.833	.833		.730	.902	.902	
.843	.829	.829	.838	.809	.829	.829		.774	.910	.910	
.889	.818	.818		.859			.831	.783			.935
.935	.798	.798		.865	.818	.818		.825	.914	.914	
.981	.777	.777	.779	.921	.798	.798		.875	.906	.906	
1.000	.768	.768	.772	.966	.777	.777		.978	.877	.877	.887
				.977			.780	1.000	.872	.872	.876
				1.000	.768	.768	.772				

Note: r_A/r_{max} coordinates applicable $\pm 145^\circ$ from vertical, for other $\pm 35^\circ$ see figure 7(e).

(d) Fan afterbody and nozzle shroud ordinates.

Figure 7.- Continued.



Note: Radius of fairing intersects gas generator nacelle and afterbody radii at points y_3 and y_4 .
 x_A and r_{\max} defined in figure 7(d).

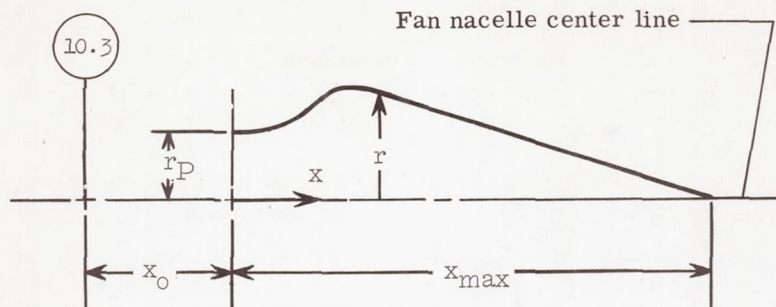
Afterbody 1			
x/x_A	y_3/x_A	y_4/x_A	r/r_{\max}
0.000	0.382	0.519	0.340
.111	.378	.517	.332
.222	.374	.516	.328
.388	.365	.495	.280
.554	.362	.481	.240
.775	.359	.420	.100
.843	.358	.390	.044
1.000	.357	.357	0.000

Afterbody 2			
x/x_A	y_3/x_A	y_4/x_A	r/r_{\max}
0.000	0.462	0.650	0.340
.095	.456	.640	.332
.191	.453	.628	.324
.334	.447	.615	.320
.477	.432	.543	.212
.668	.431	.515	.172
.859	.431	.475	.052
1.000	.431	.431	0.000

Afterbody 4			
x/x_A	y_3/x_A	y_4/x_A	r/r_{\max}
0.000	0.462	0.628	0.340
.096	.460	.627	.340
.191	.459	.626	.340
.334	.458	.625	.340
.478	.464	.610	.240
.669	.473	.550	.088
.859	.477	.517	.044
1.000	.489	.489	0.000

(e) Afterbody to gas generator nacelle fairing ordinates.

Figure 7.- Continued.



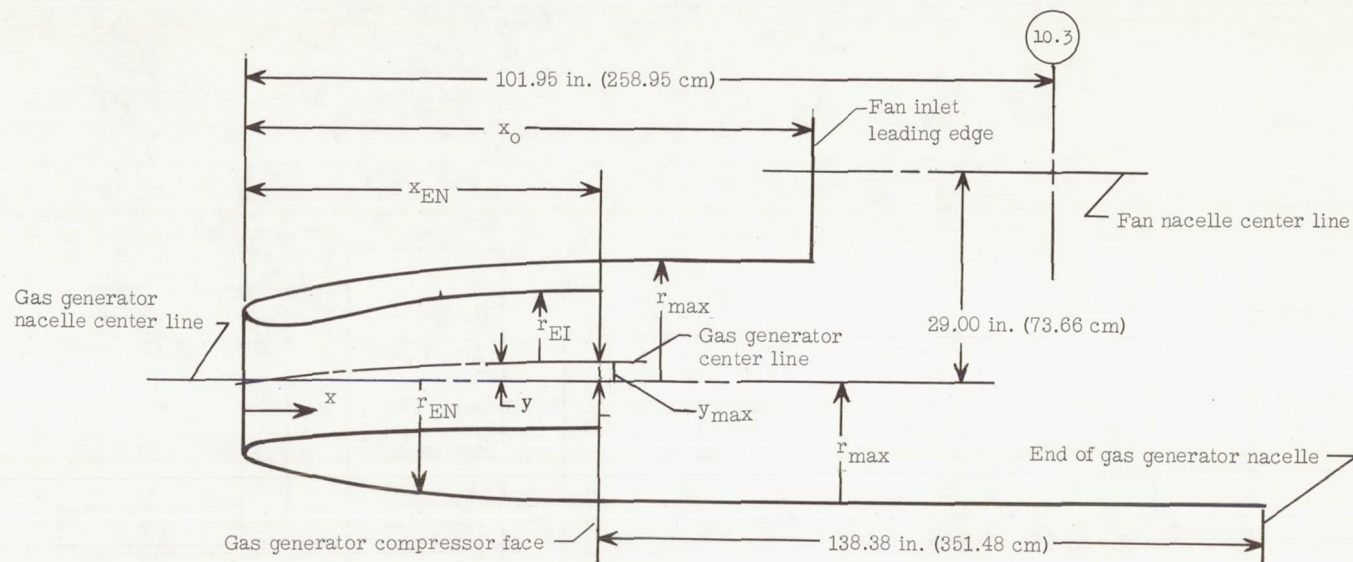
	Plug 2	Plug 3	Plug 4
x/x_{max}	r/r_P	r/r_P	r/r_P
0.000	1.000	1.000	1.000
.060	1.154	1.188	1.122
.120	1.387	1.455	1.417
.180	1.618	1.726	1.723
.240	1.823	1.954	2.029
.300	1.806	1.923	2.263
.310	1.786	1.901	2.270
.320	1.764	1.875	2.263
.330	1.743	1.846	2.244
.340	1.716	1.825	2.213
.350	1.690	1.798	2.179
.360	1.665	1.770	2.146
.480	1.353	1.440	1.756
.600	1.041	1.106	1.341
.720	.728	.773	.938
.840	.416	.440	.538
1.000	0.000	0.000	0.000

	x_{max} (in.)	x_{max} (cm)	r_P (in.)	r_P (cm)
Plug 2	96.14	244.20	8.16	20.73
3	102.28	259.79	8.16	20.73
4	123.90	314.71	8.16	20.73

Plug	Afterbody	x_0 (in.)	x_0 (cm)
2	1	20.33	51.64
2	2	10.96	27.84
3	1	20.33	51.64
3	2	10.96	27.84
3	4	10.96	27.84
4	4	3.24	8.23

(f) Plug ordinates.

Figure 7.- Continued.



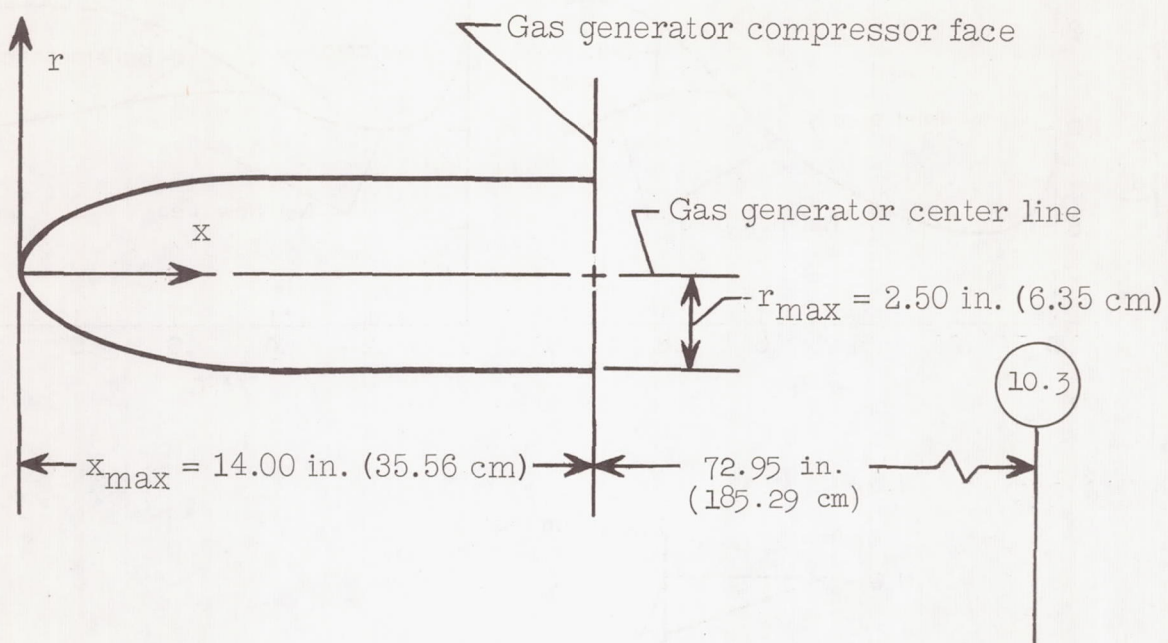
Gas generator inlet		
x/x_{EN}	y/y_{max}	r_{EI}/r_{max}
0.000	0.000	0.512
.014	0	.471
.027	0	.456
.043	0	.452
.082	.030	.450
.166	.150	.454
.330	.350	.465
.661	.850	.486
1.000	1.000	.487

Gas generator nacelle	
x/x_{EN}	r_{EN}/r_{max}
0.000	0.512
.041	.632
.083	.689
.166	.771
.331	.876
.661	.989
1.000	1.000

Fan inlet	x_0 (in.)	x_0 (cm)
1	52.95	134.49
2	74.95	190.37
3	89.95	228.47

	Inch	Centimeter
x_{EN}	29.02	73.71
y_{max}	2.50	6.35
r_{max}	11.00	27.94

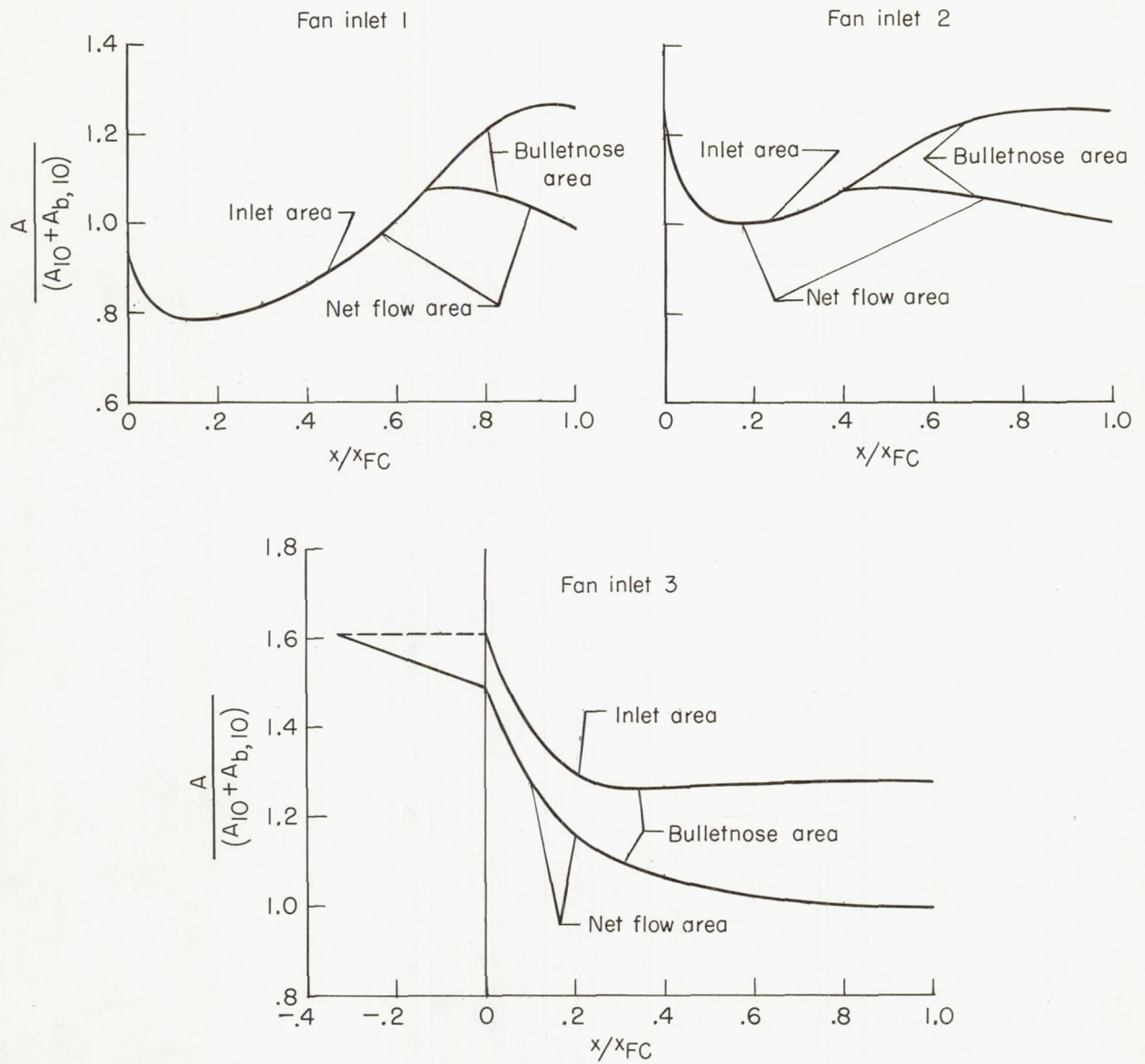
(g) Gas generator inlet and nacelle ordinates.



x/x_{\max}	r/r_{\max}
0.000	0.000
.071	.600
.143	.800
.214	.920
.357	1.000
1.000	1.000

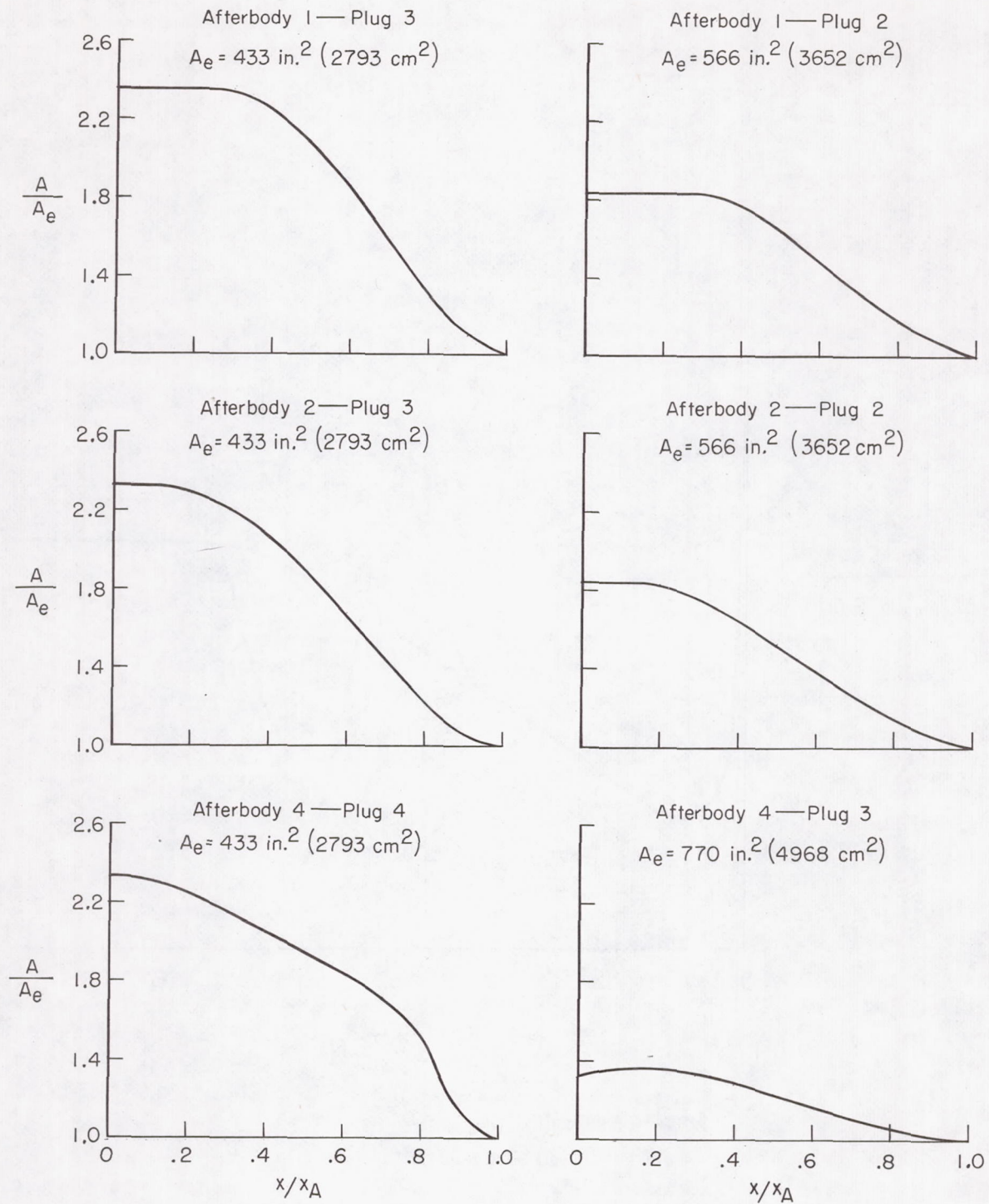
(h) Gas generator bulletnose ordinates.

Figure 7.- Concluded.



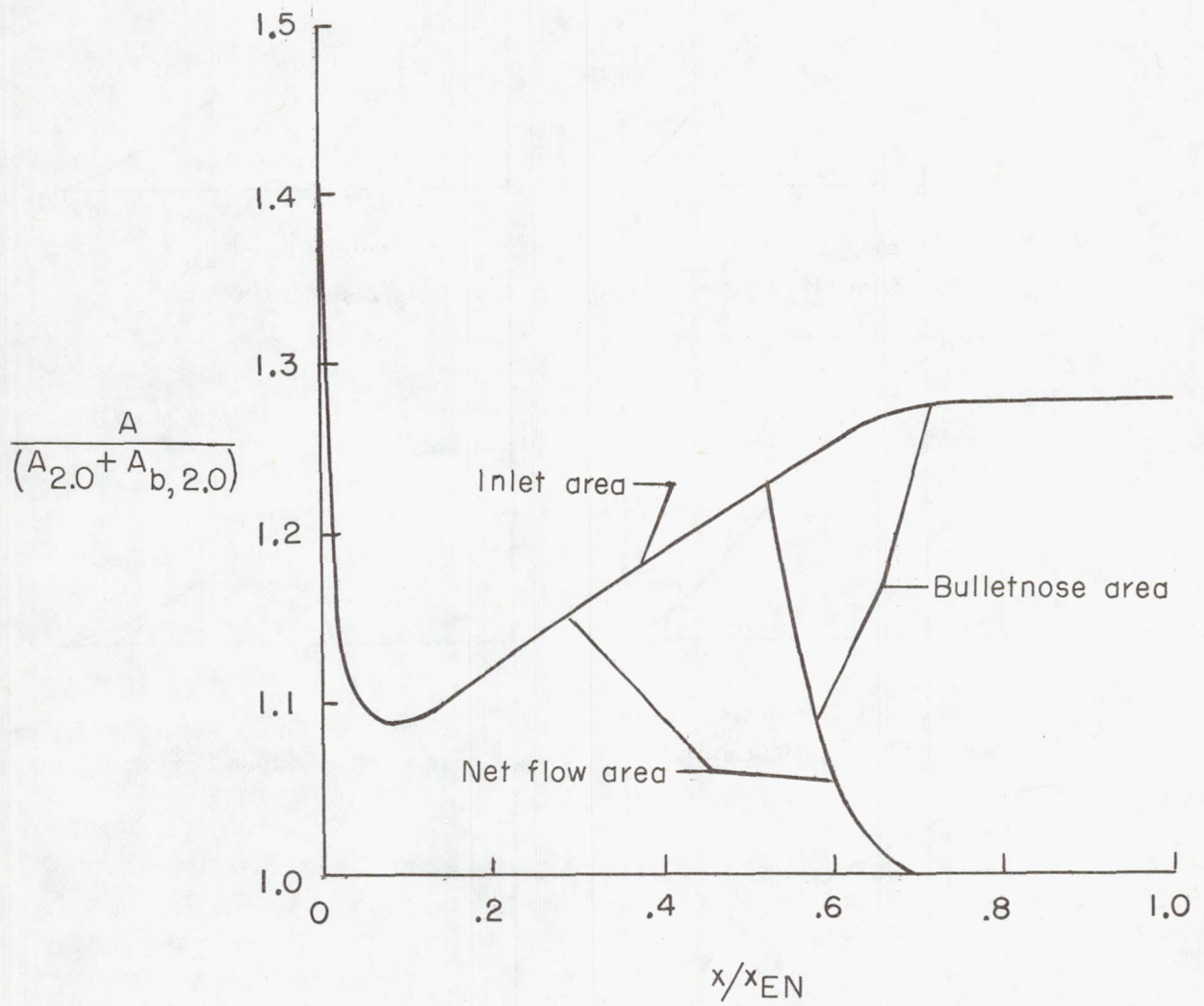
(a) Fan-inlet cross-sectional areas, $(A_{10} + A_{b,10.0}) = 812 \text{ in.}^2$ (5293 cm^2).

Figure 8.- Internal-flow areas.



(b) Nozzle-flow areas.

Figure 8.- Continued.



(c) Gas-generator inlet, $(A_{2.0} + A_{b,2.0}) = 70.6 \text{ in.}^2 \text{ (455 cm}^2\text{)}.$

Figure 8.- Concluded.

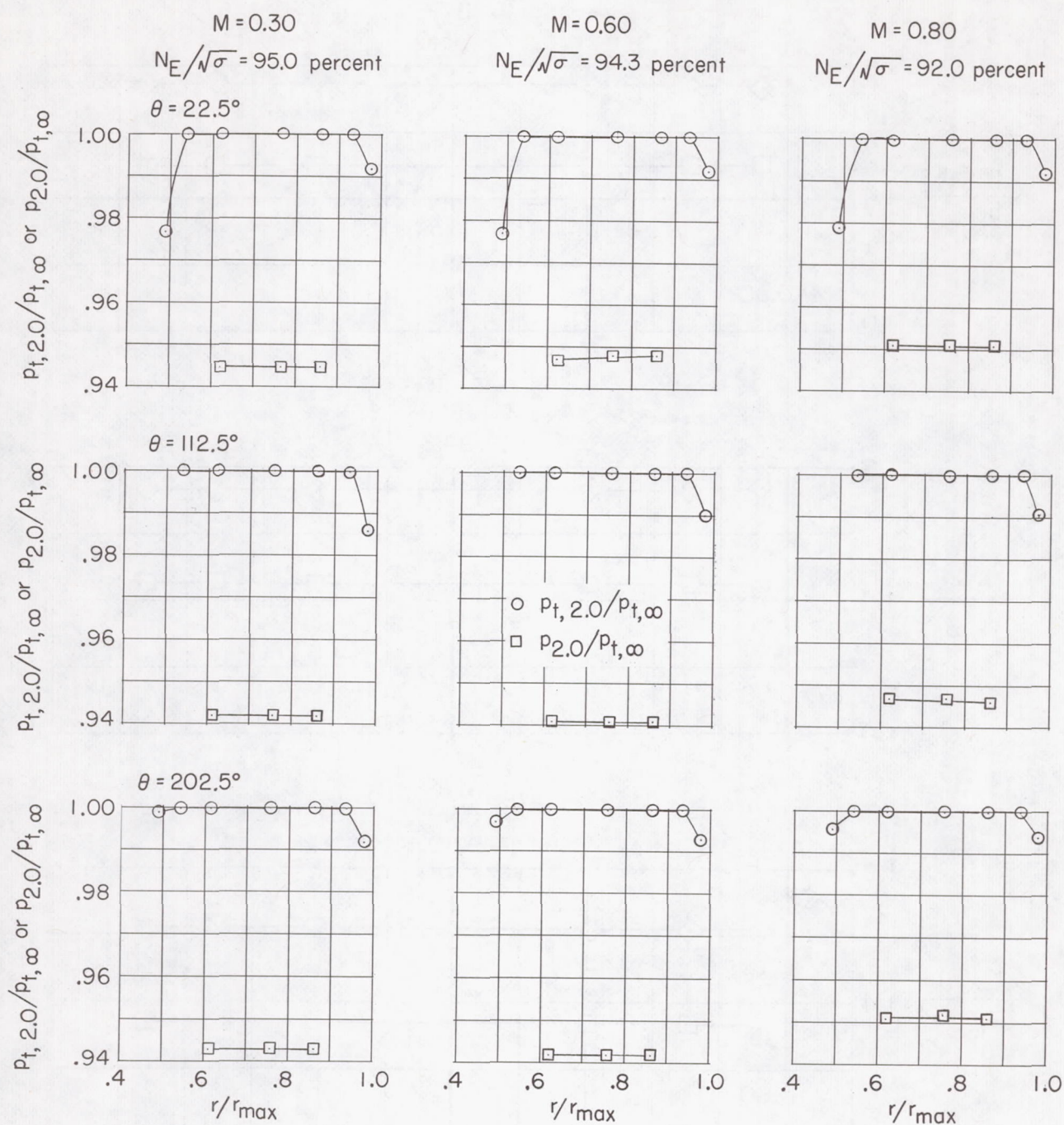


Figure 9.- Typical gas-generator-inlet pressure-ratio profiles. Data are for configuration 244 where $r/r_{\max} = 0$ is gas-generator center line and $r/r_{\max} = 0.466$ is the gas-generator bulletnose.

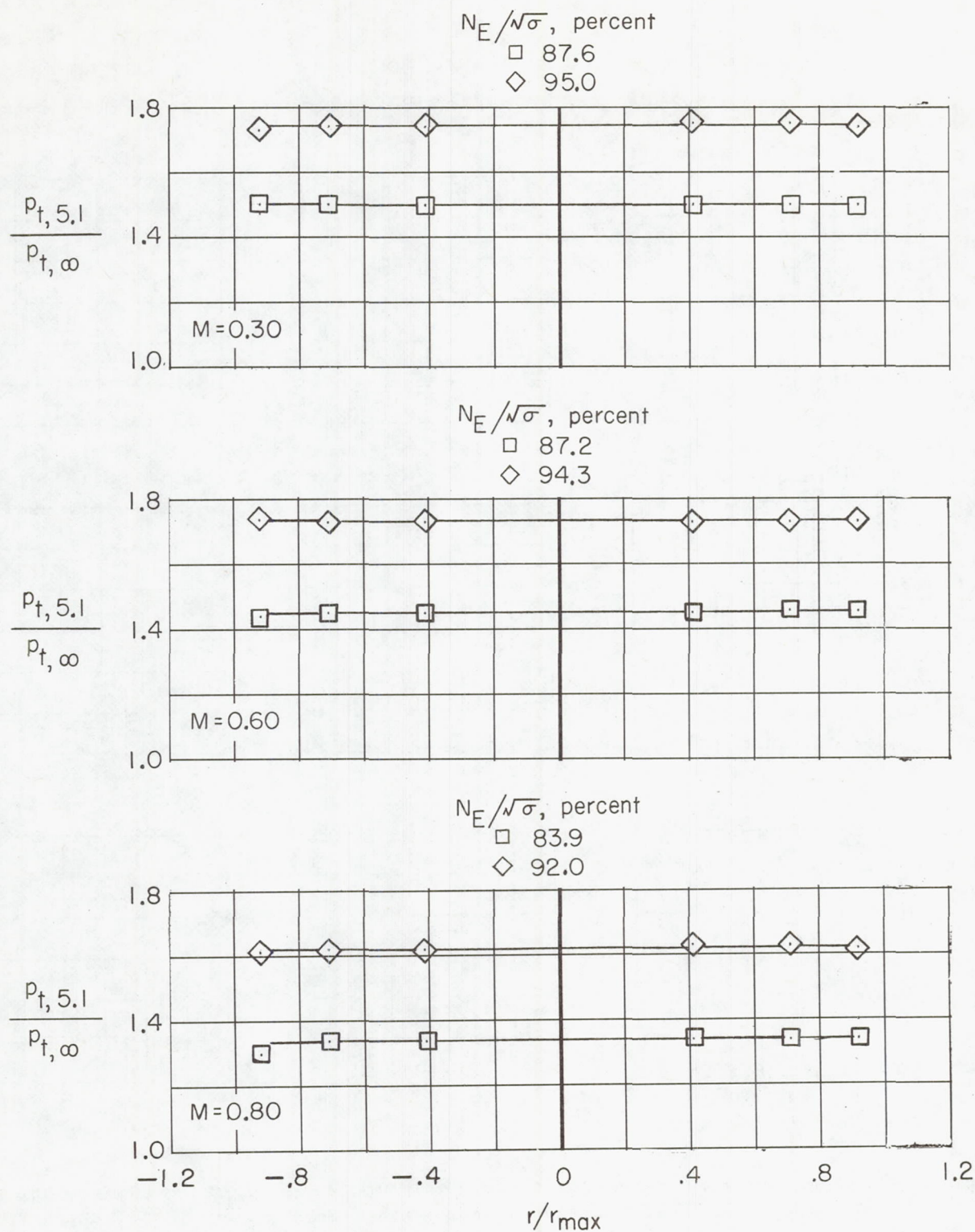


Figure 10.- Typical gas-generator-exhaust total-pressure-ratio profiles. Data are for configuration 244 where $r/r_{\max} = 0.92$ is at $\theta = 0^\circ$.

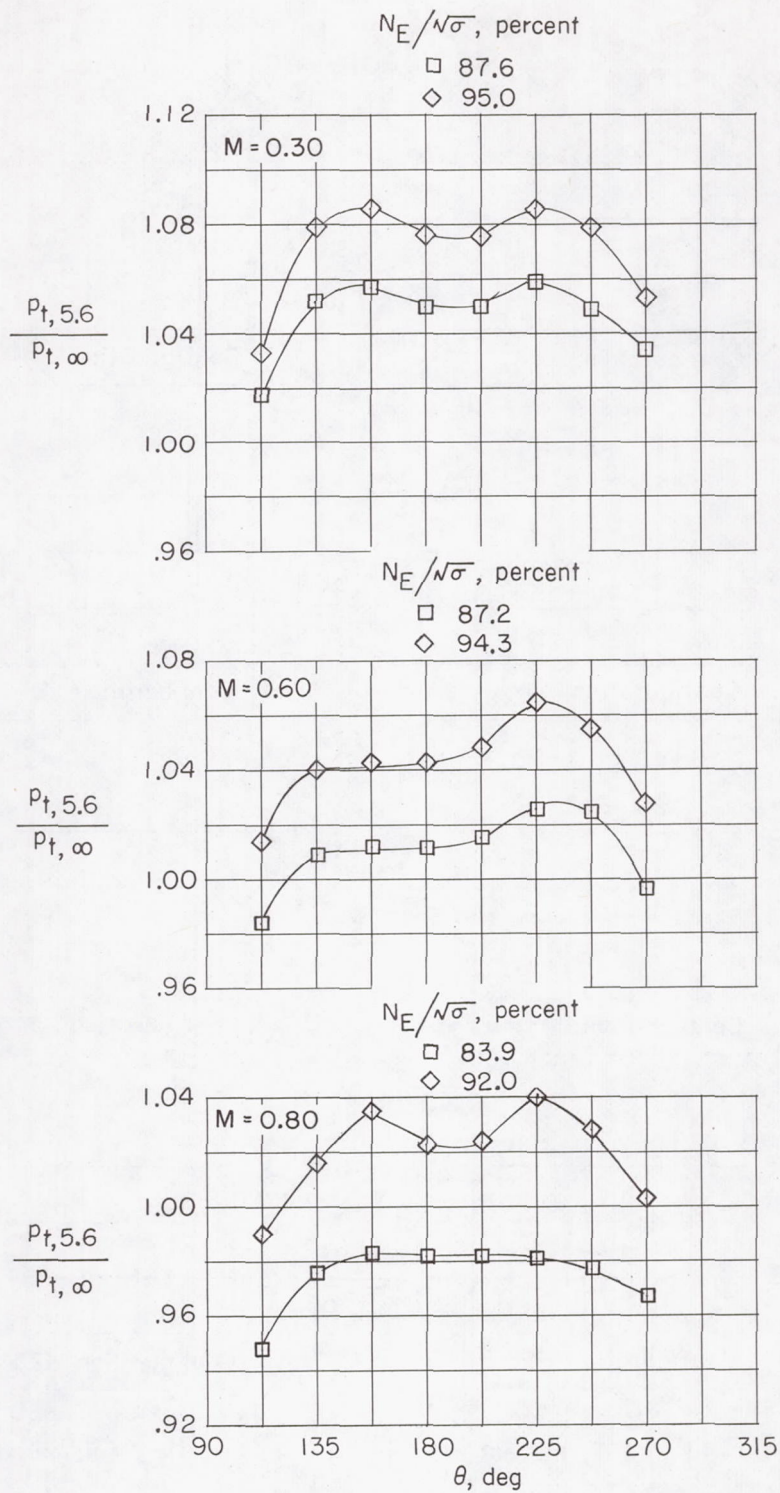
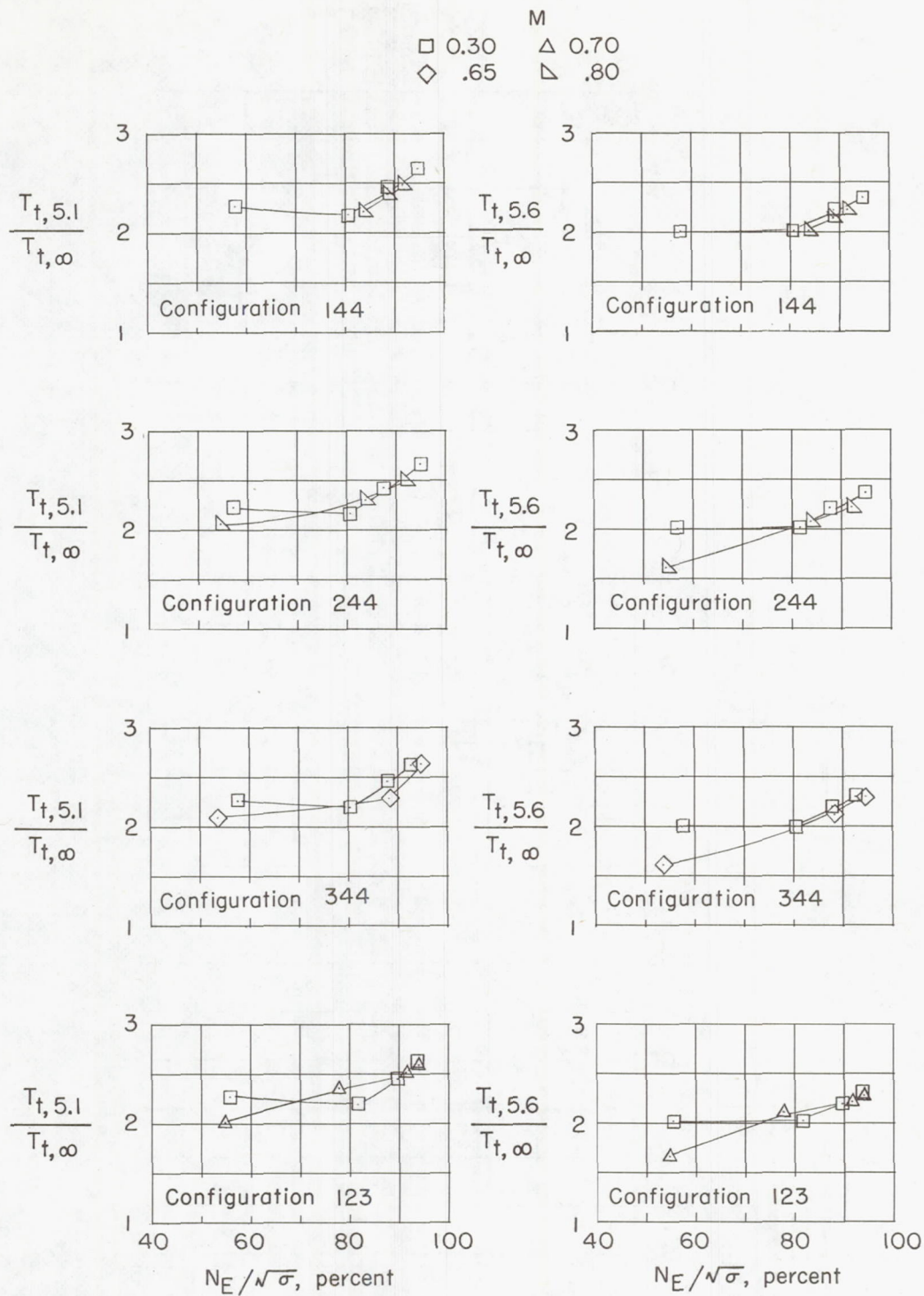
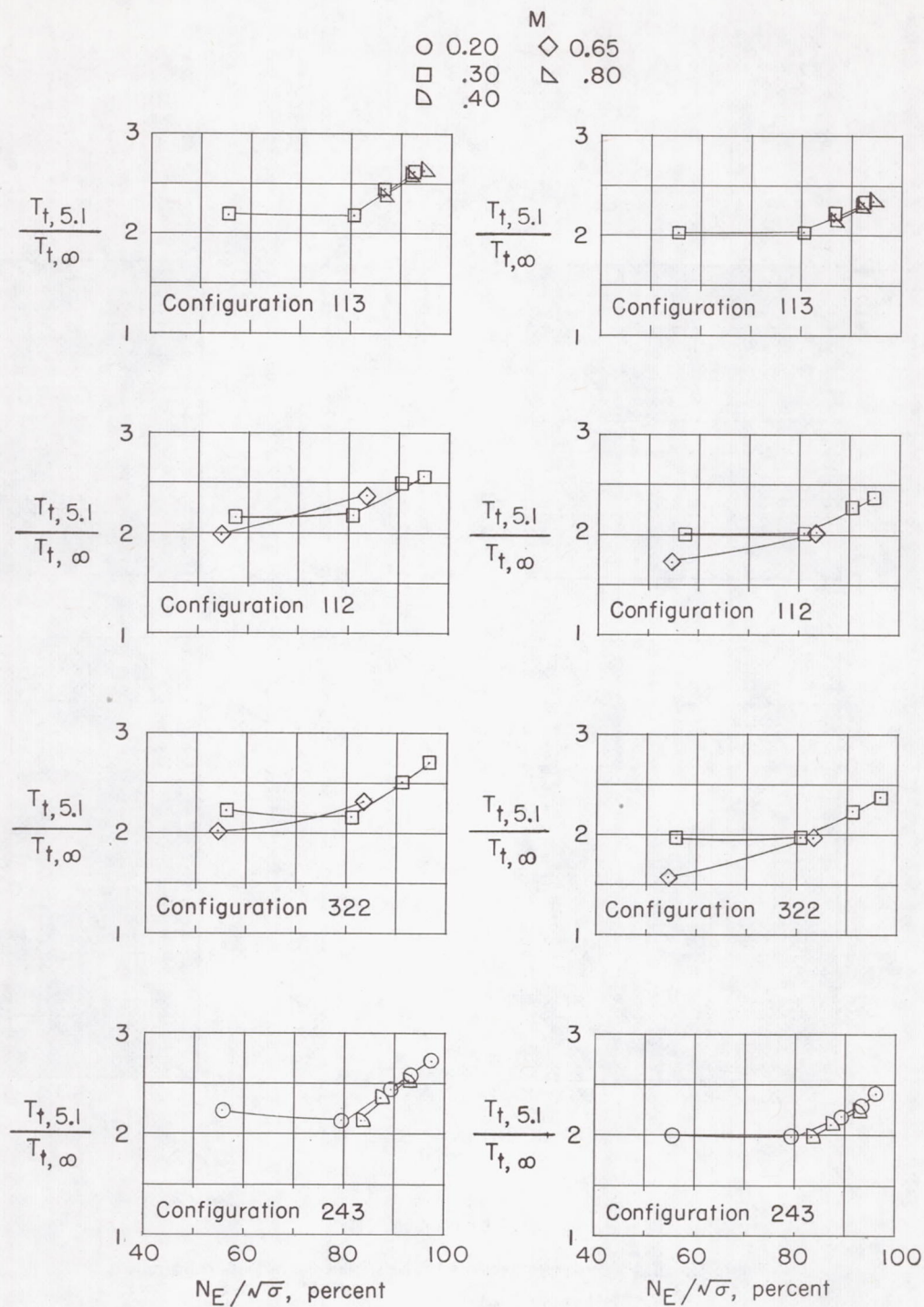


Figure 11.- Typical fan-turbine-exhaust total-pressure-ratio profiles. Data are for configuration 244. Pressure probes located at $r = 19.40$ in. (49.28 cm).



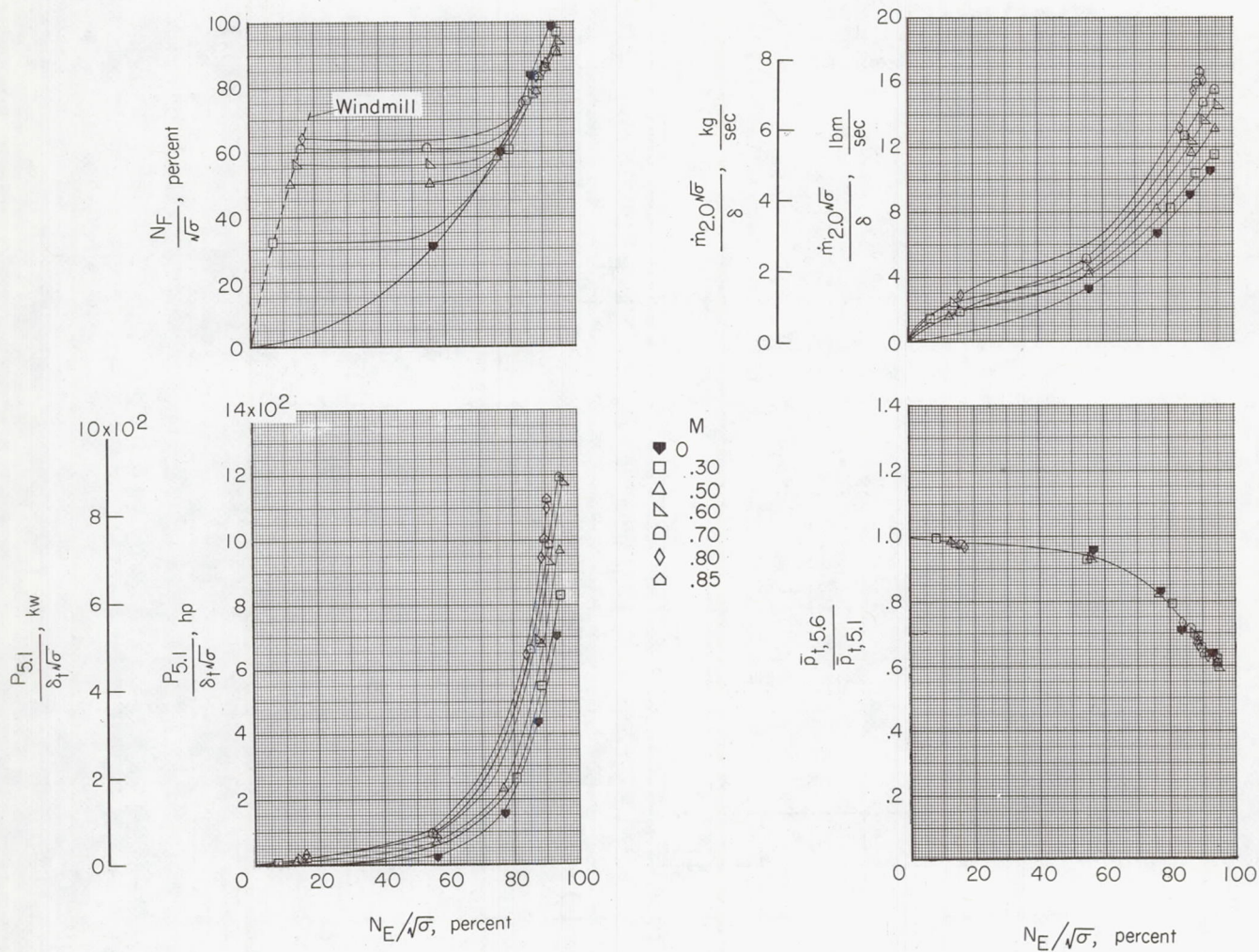
(a) Configurations 144, 244, 344, and 123.

Figure 12.- Variation of gas-generator and fan-turbine exhaust temperature with gas-generator speed.



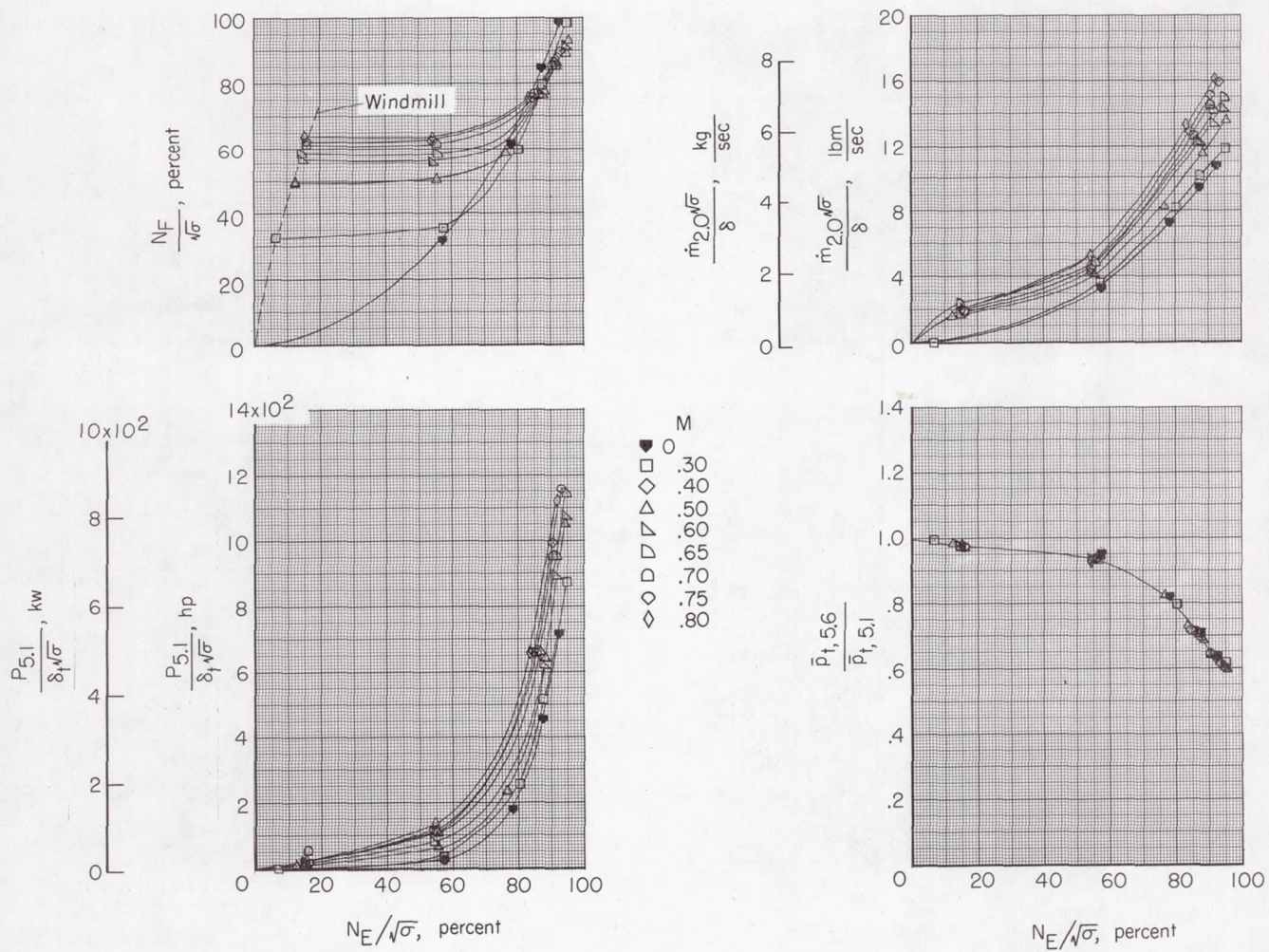
(b) Configurations 113, 112, 322, and 243.

Figure 12.- Concluded.



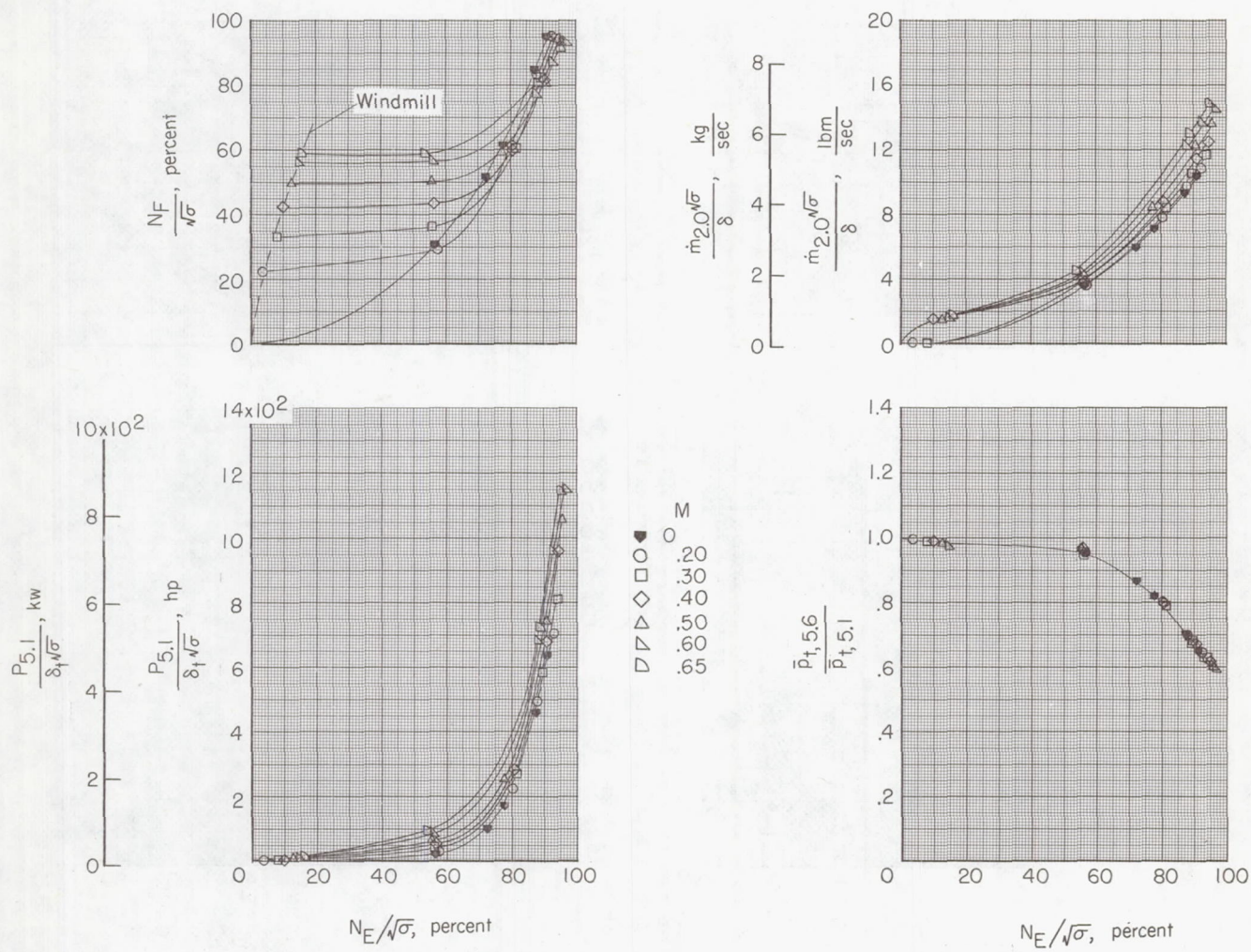
(a) Configuration 144.

Figure 13.- Gas-generator performance characteristics for various configurations.



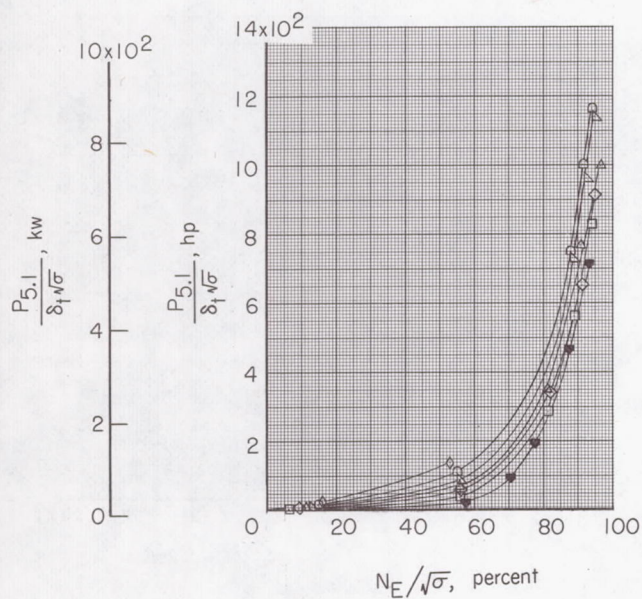
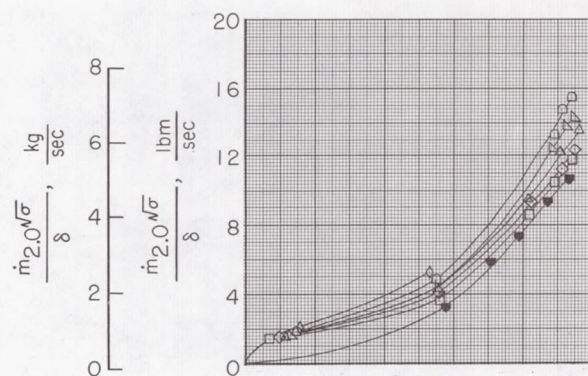
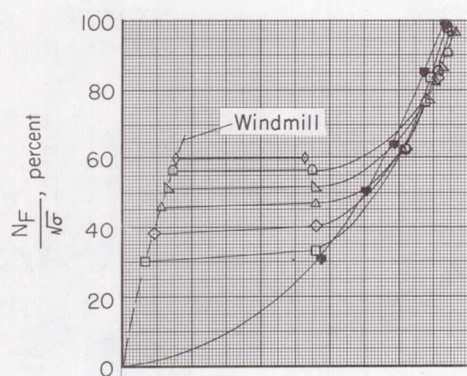
(b) Configuration 244.

Figure 13.- Continued.



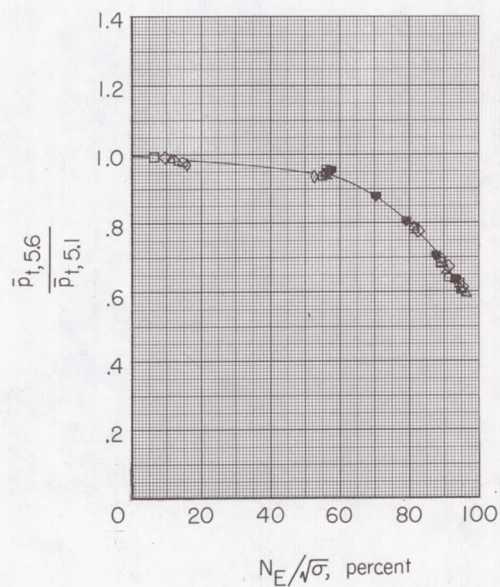
(c) Configuration 344.

Figure 13.- Continued.



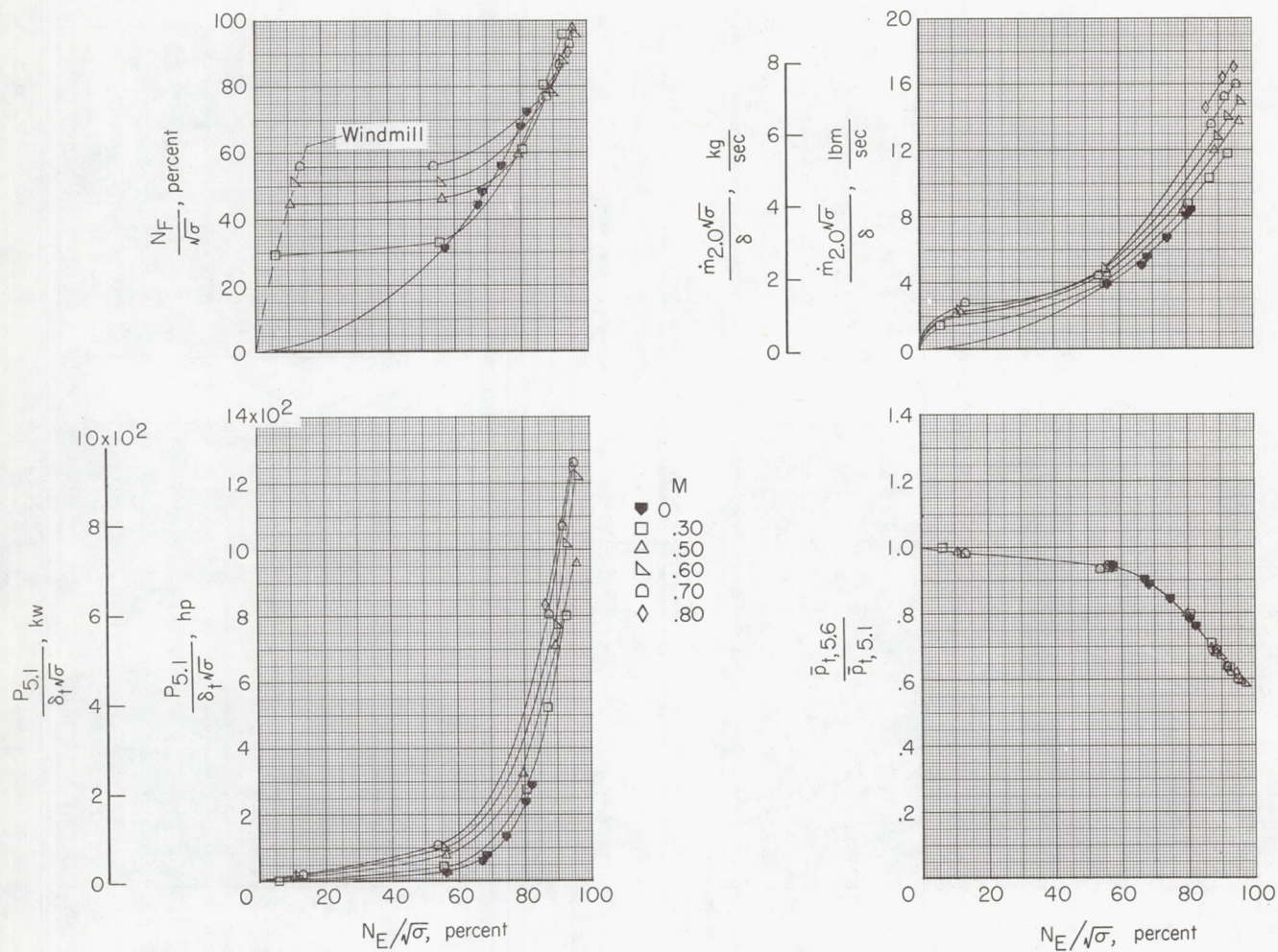
M

- .30
- .40
- ◇ .50
- ▽ .60
- ◻ .70
- ◇ .80



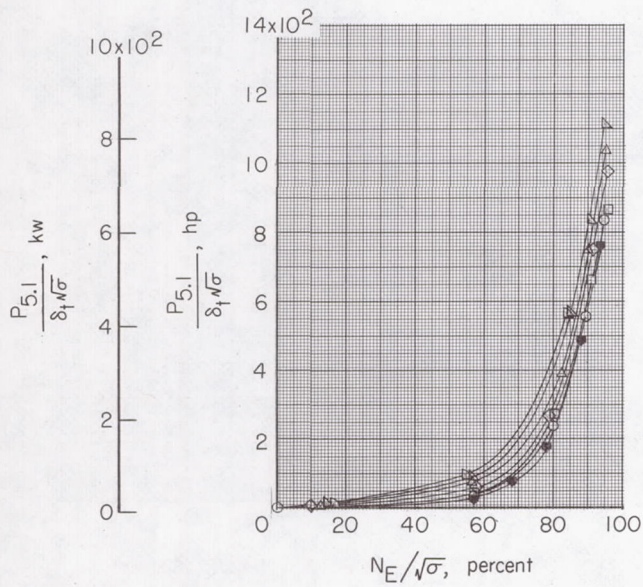
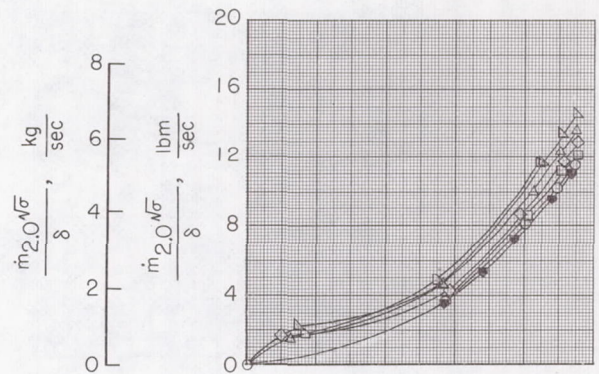
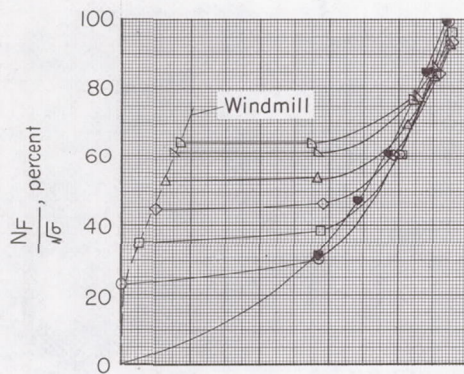
(d) Configuration 123.

Figure 13.- Continued.

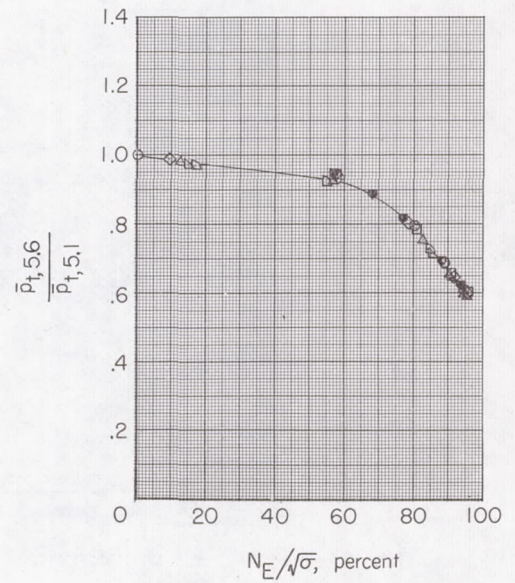


(e) Configuration 113.

Figure 13.- Continued.

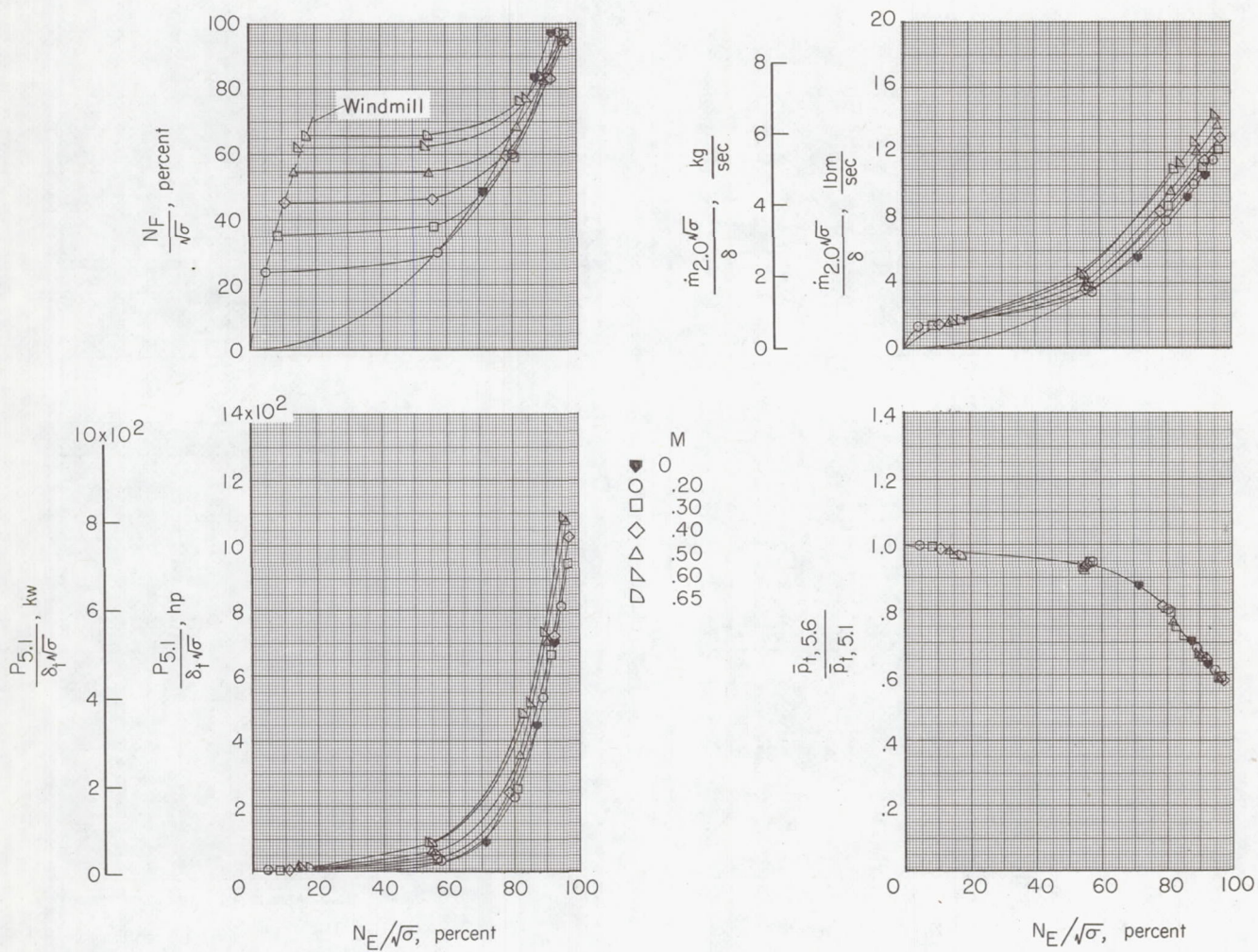


M
 0.20
 0.30
 0.40
 0.50
 0.60
 0.65



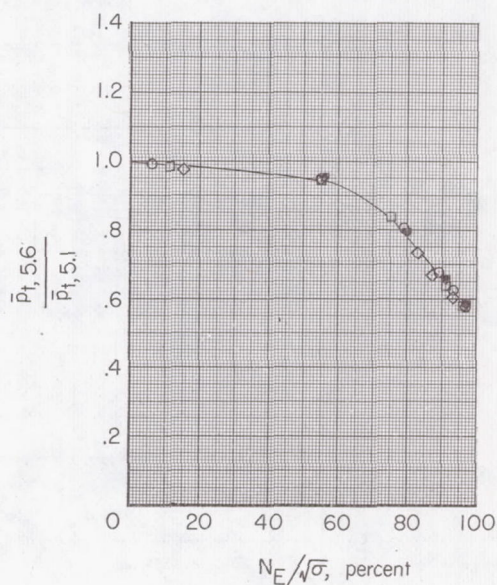
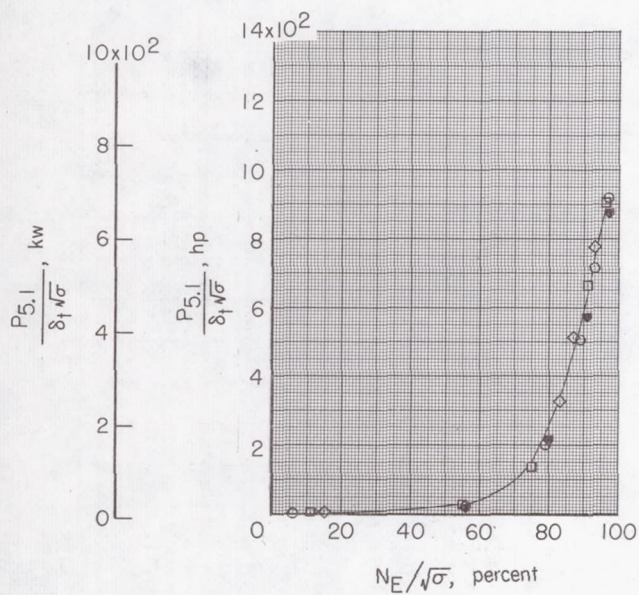
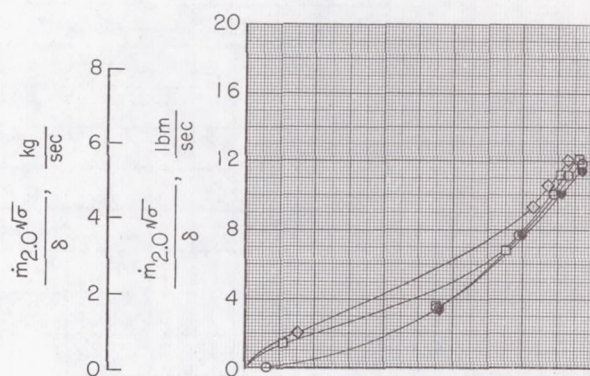
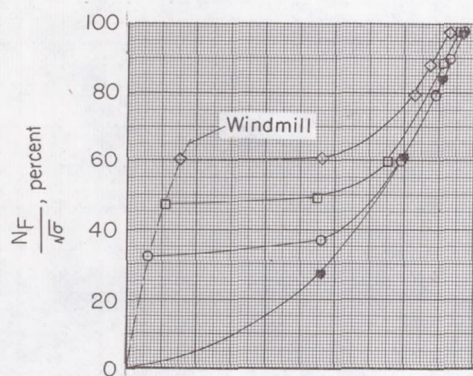
(f) Configuration 112.

Figure 13.- Continued.



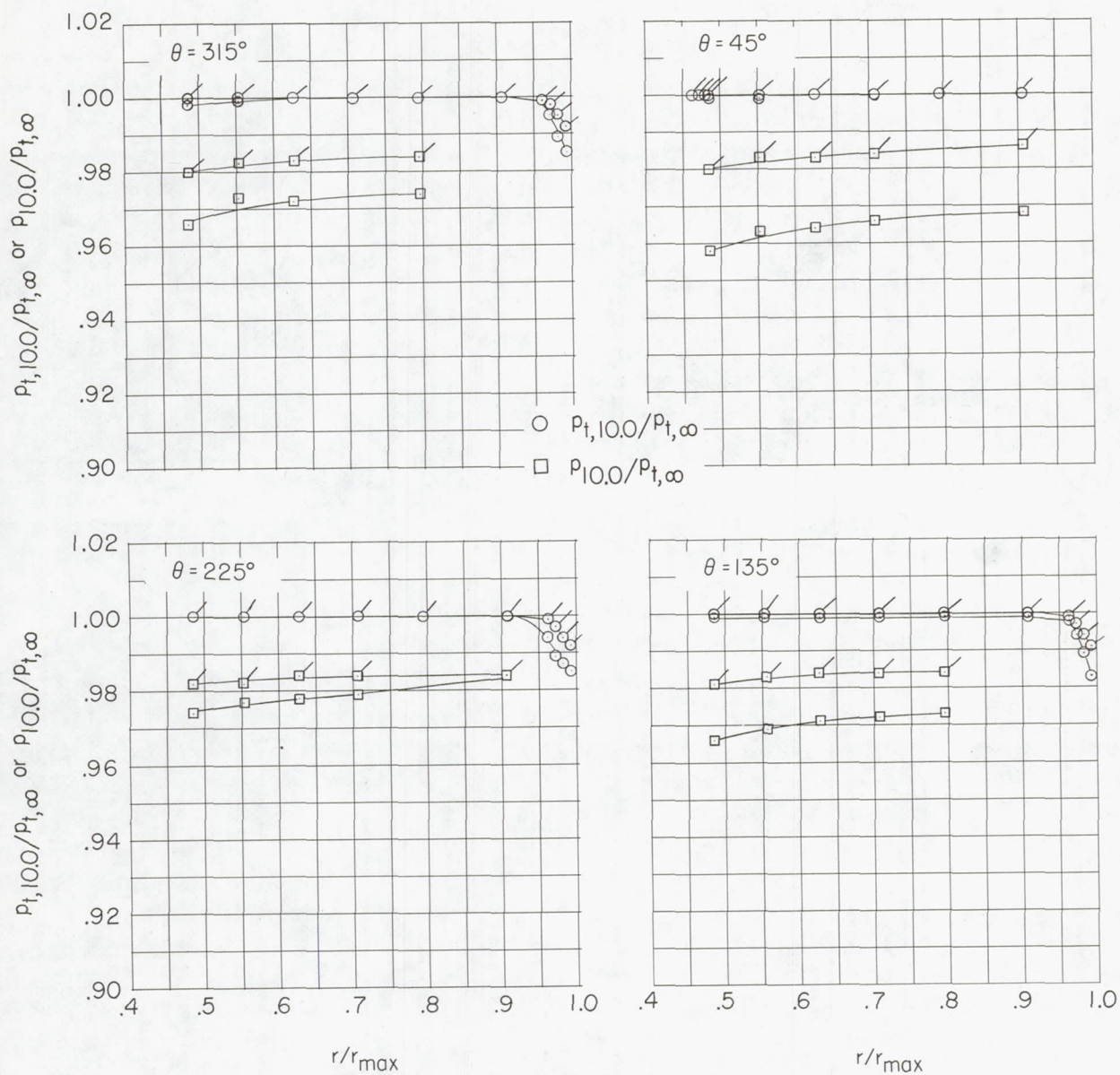
(g) Configuration 322.

Figure 13.- Continued.



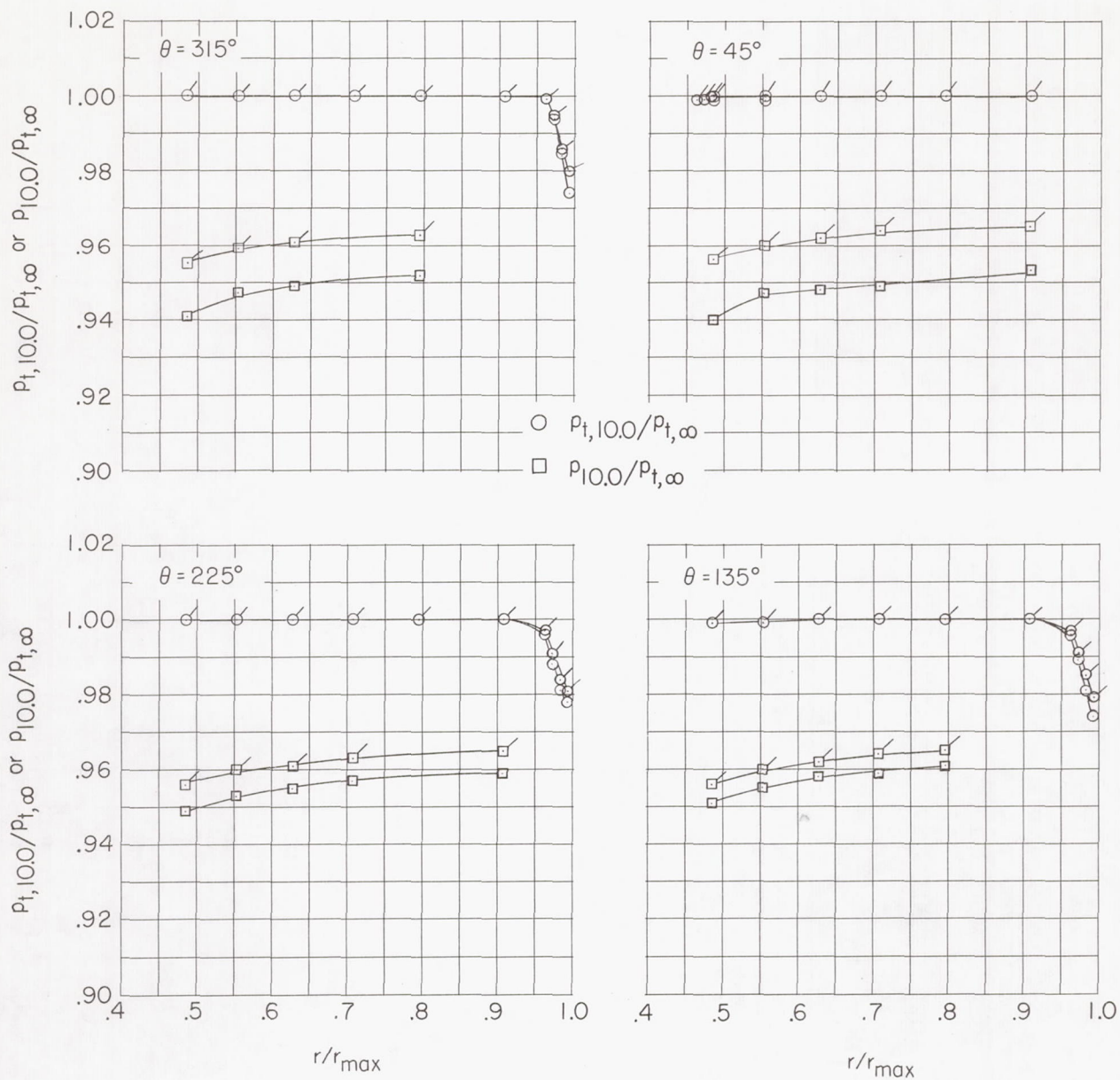
(h) Configuration 243.

Figure 13.- Concluded.



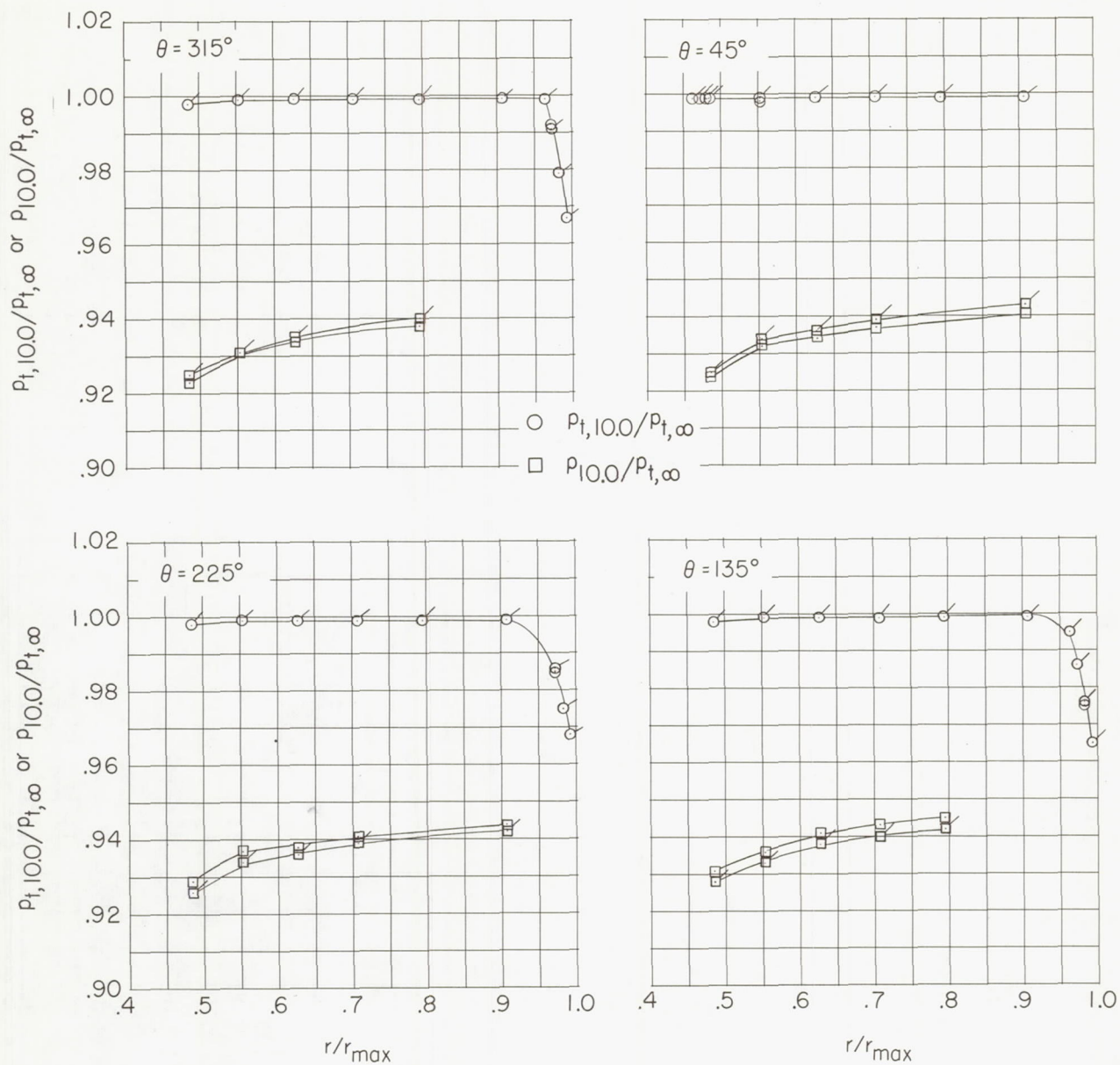
(a) $M = 0.30$; $N_F/\sqrt{\sigma} = 97.0$ percent.

Figure 14.- Fan-inlet total- and static-pressure profiles for configuration 144. Flagged data indicate windmill conditions.
($r/r_{\max} = 0.45$ for fan bulletnose.)



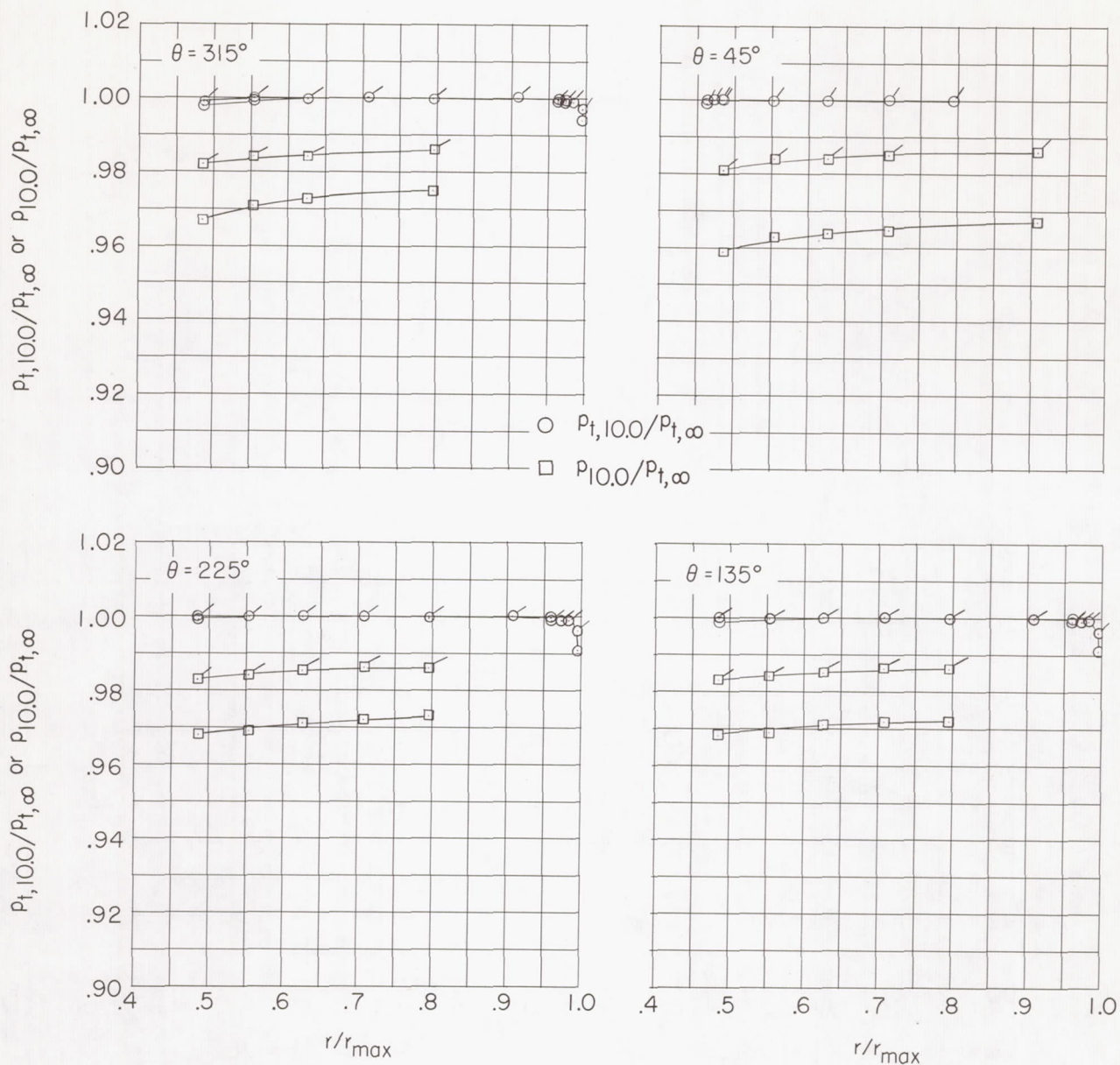
(b) $M = 0.50$; $N_F/\sqrt{\sigma} = 90.6$ percent.

Figure 14.- Continued.



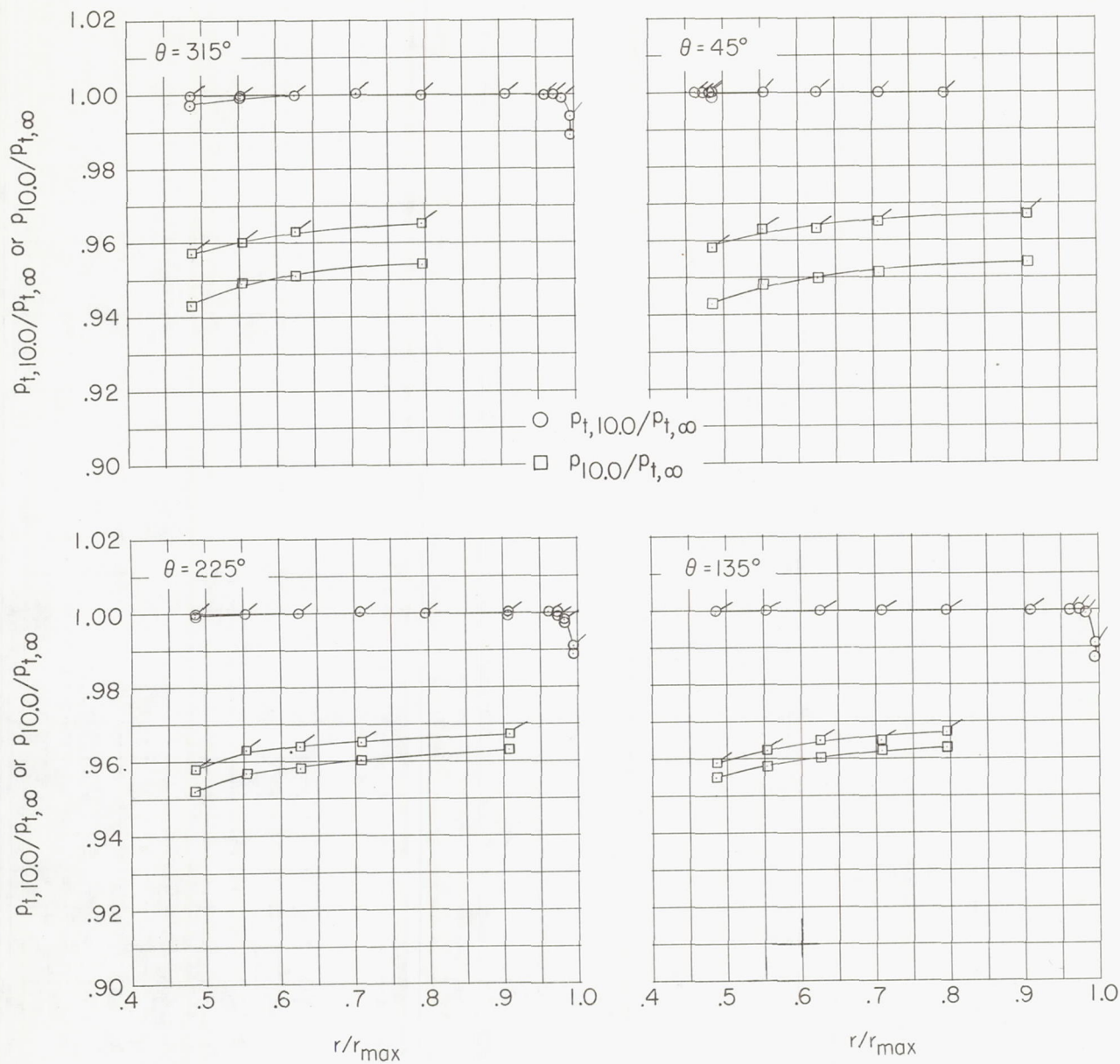
(c) $M = 0.80$; $N_F/\sqrt{\sigma} = 91.5$ percent.

Figure 14.- Concluded.



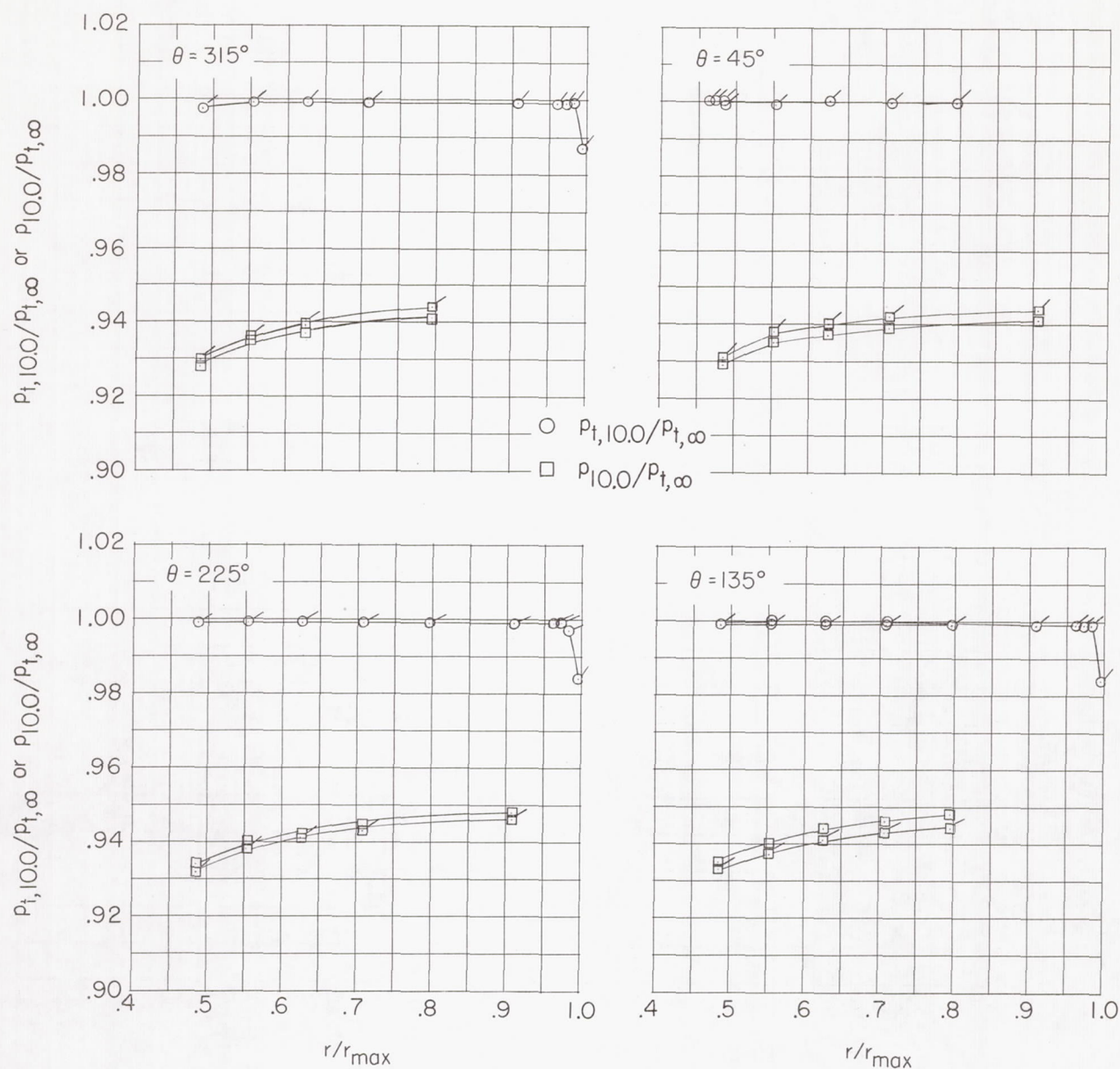
(a) $M = 0.30$; $N_F/\sqrt{\sigma} = 98.5$ percent.

Figure 15.- Fan-inlet total- and static-pressure profiles for configuration 244. Flagged data indicate windmill conditions.
($r/r_{\max} = 0.45$ for fan bullethead.)



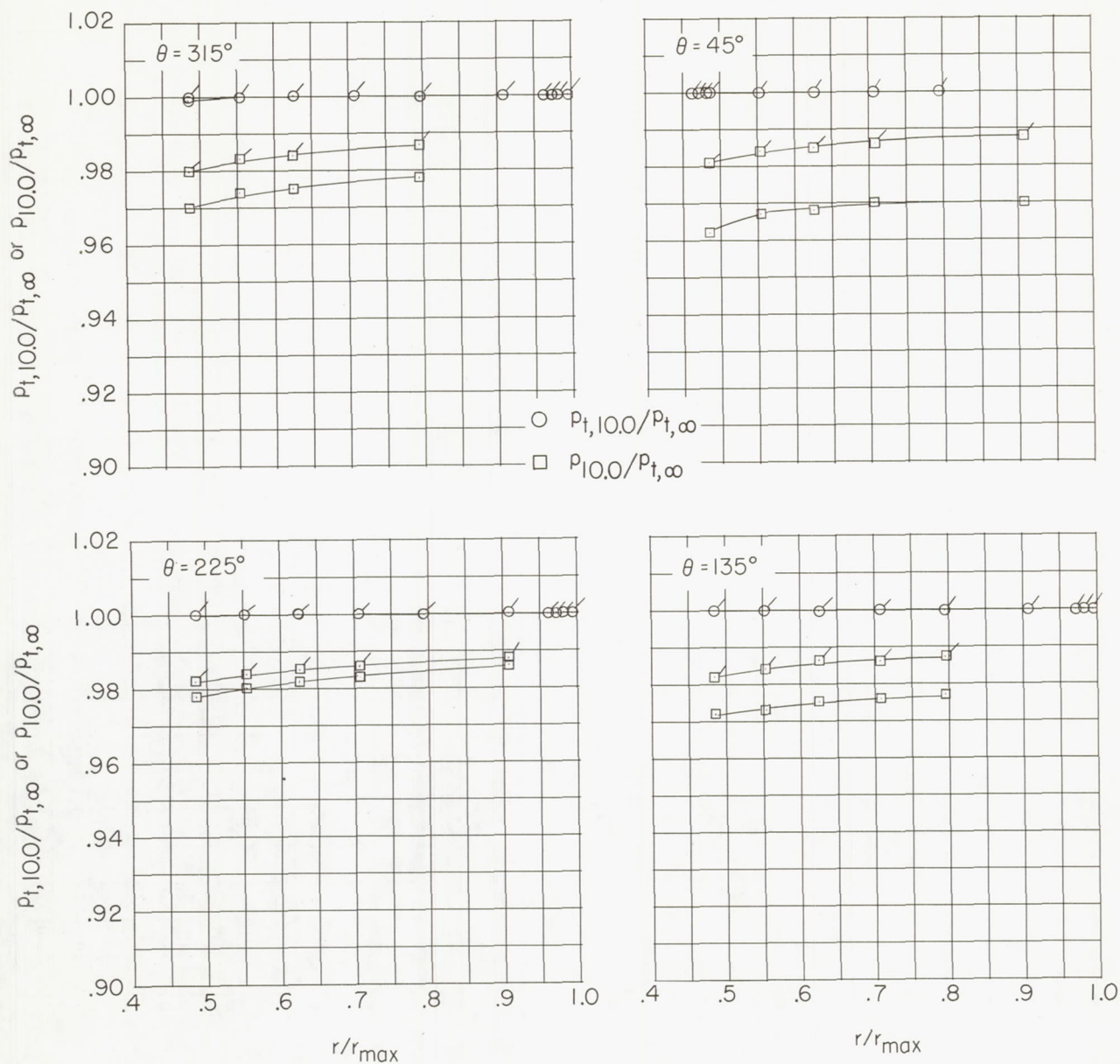
(b) $M = 0.50$; $N_F/\sqrt{\sigma} = 93.9$ percent.

Figure 15.- Continued.



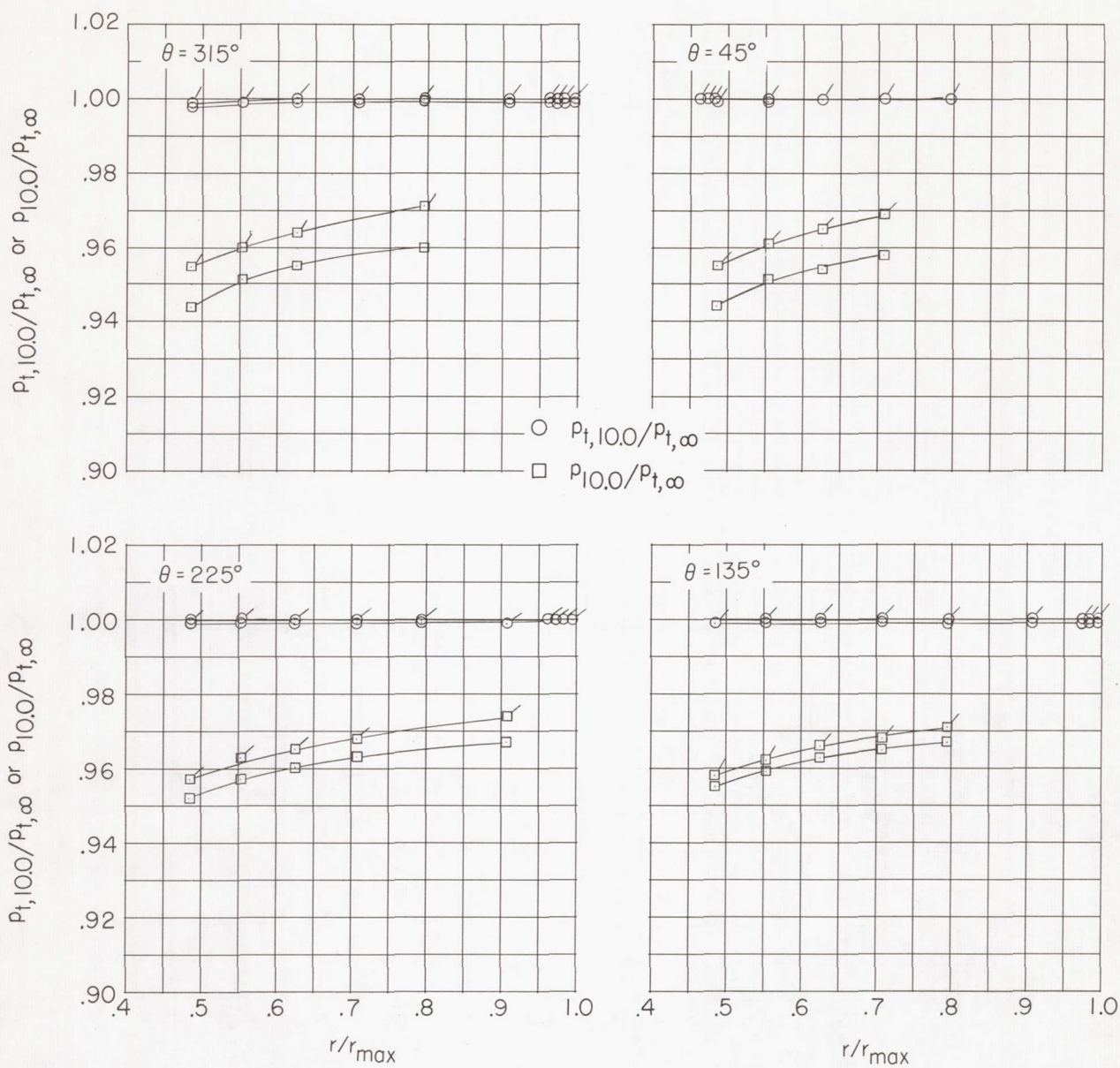
(c) $M = 0.80$; $N_F/\sqrt{\sigma} = 87.5$ percent.

Figure 15.- Concluded.



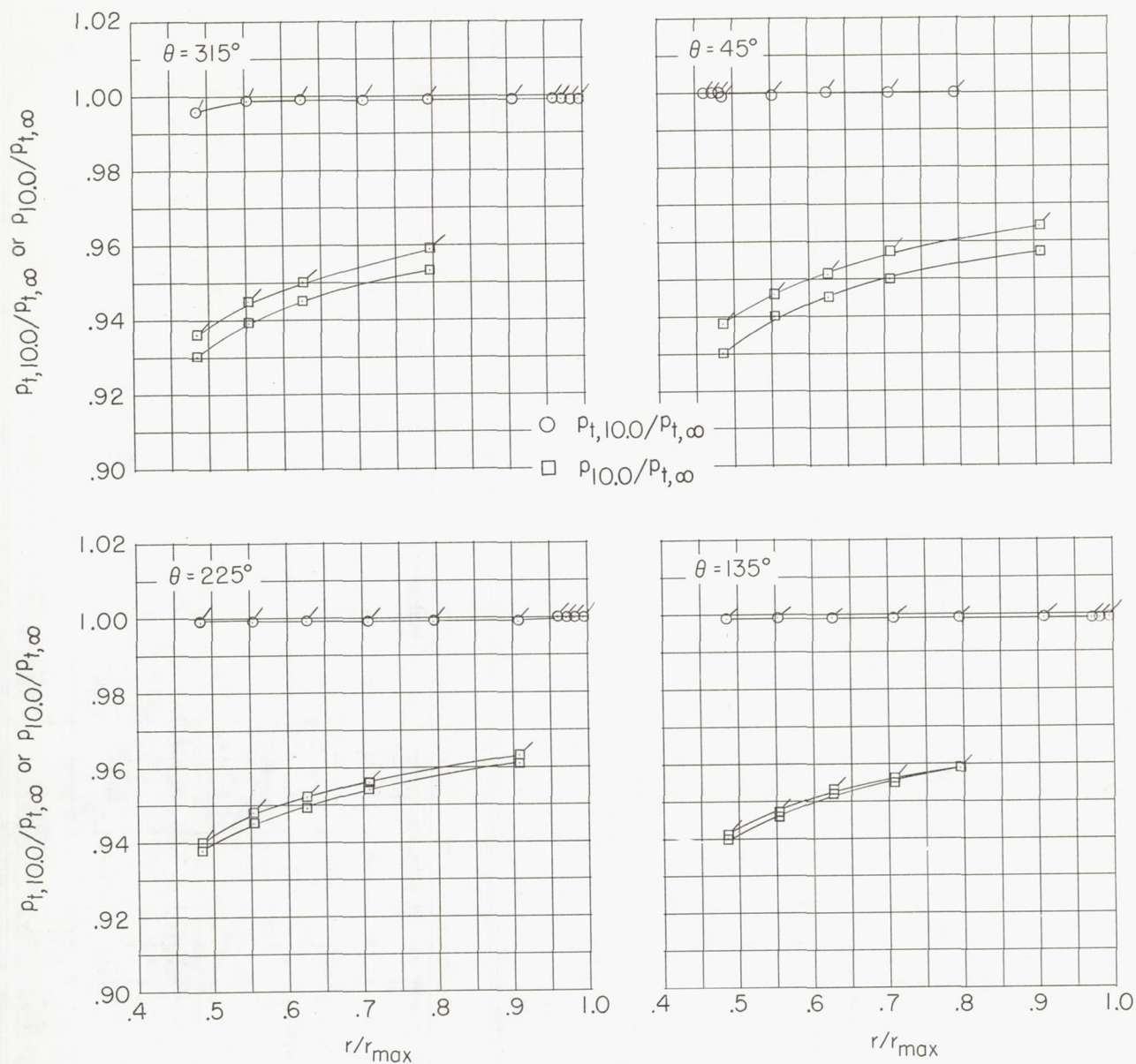
(a) $M = 0.30$; $N_F/\sqrt{\sigma} = 94.8$ percent.

Figure 16.- Fan-inlet total- and static-pressure profiles for configuration 344. Flagged data indicate windmill conditions.
($r/r_{\max} = 0.45$ for fan bullethead.)



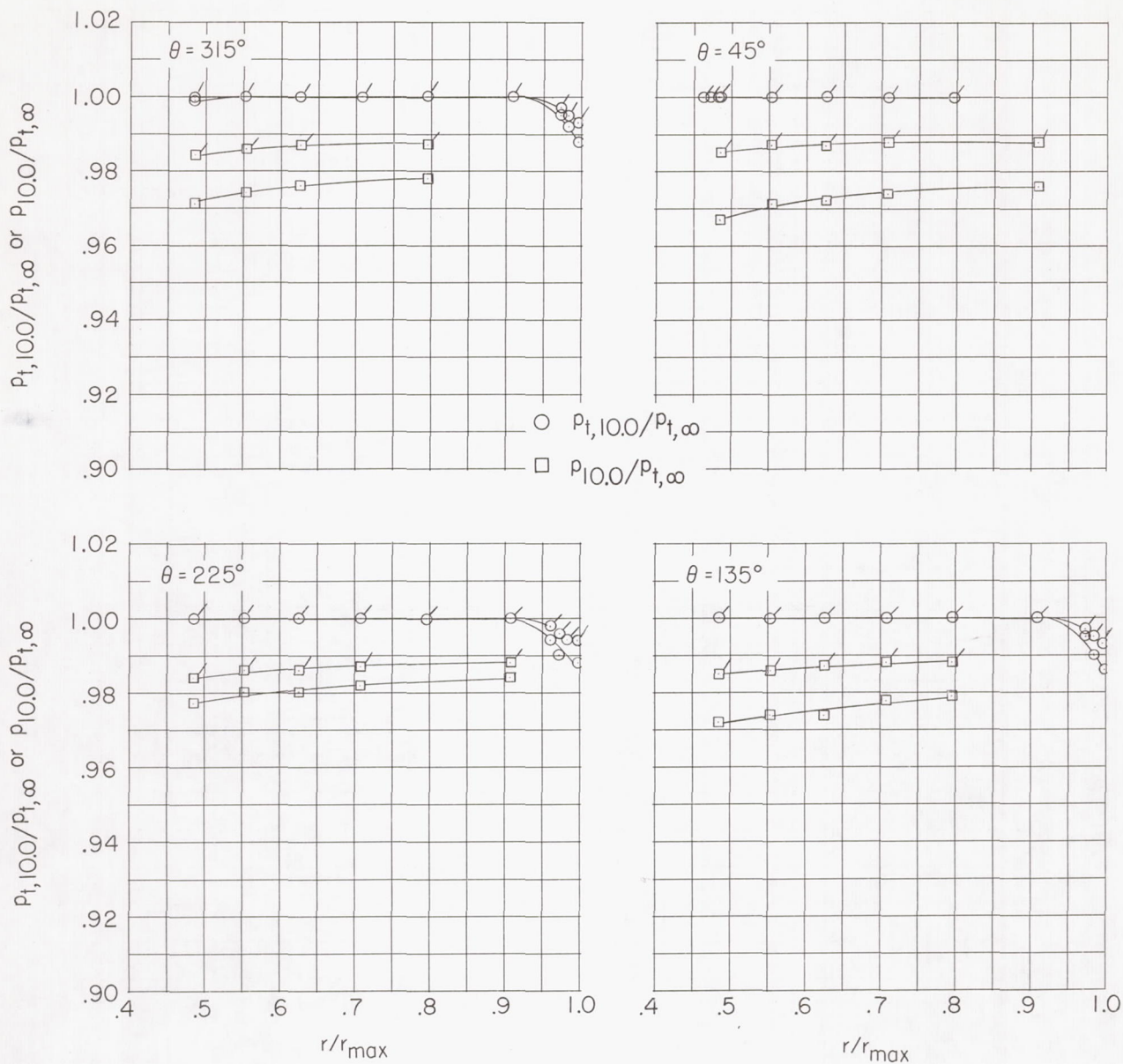
(b) $M = 0.50$; $N_F/\sqrt{\sigma} = 93.5$ percent.

Figure 16.- Continued.



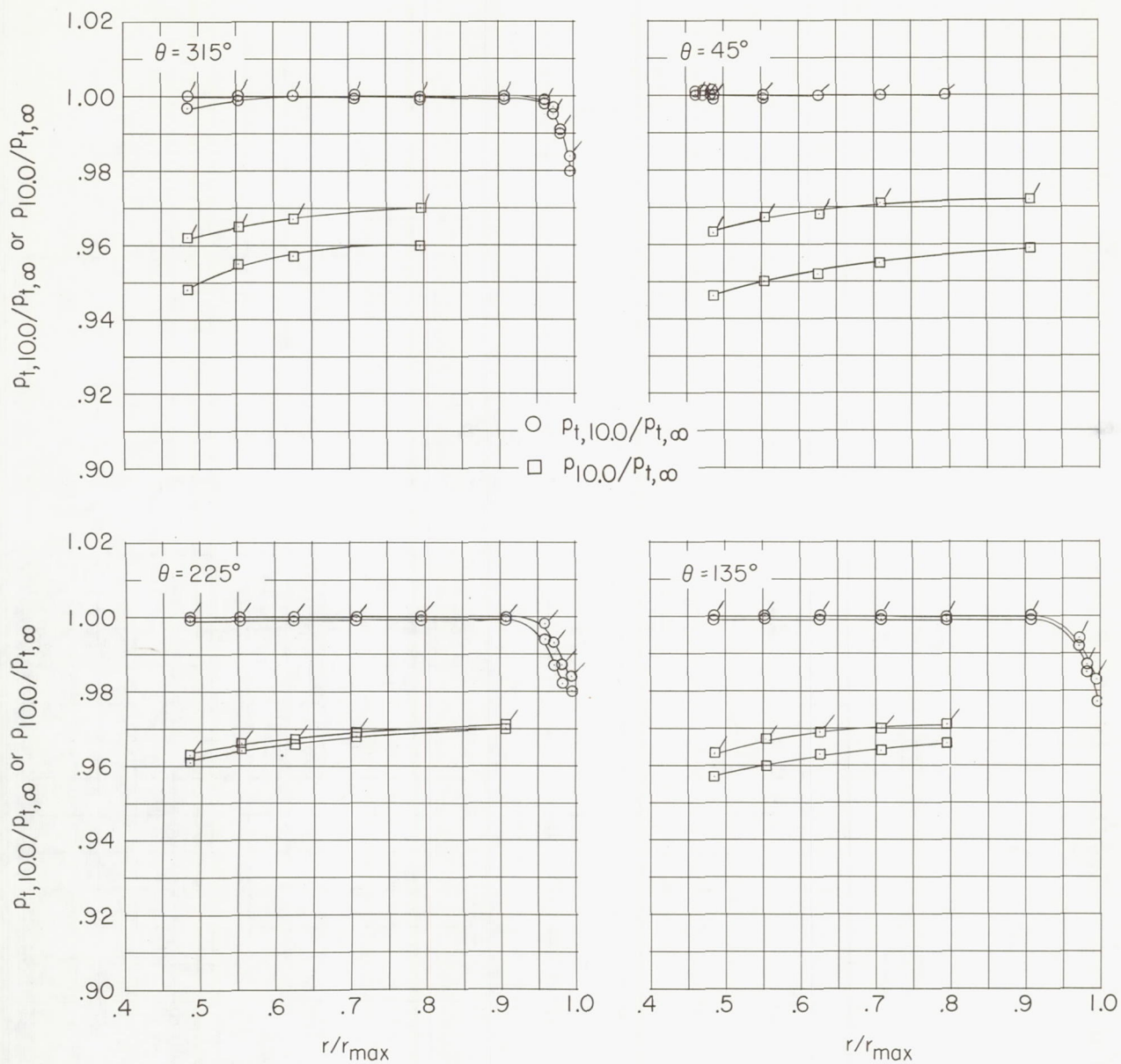
(c) $M = 0.65$; $N_F/\sqrt{\sigma} = 91.7$ percent.

Figure 16.- Concluded.



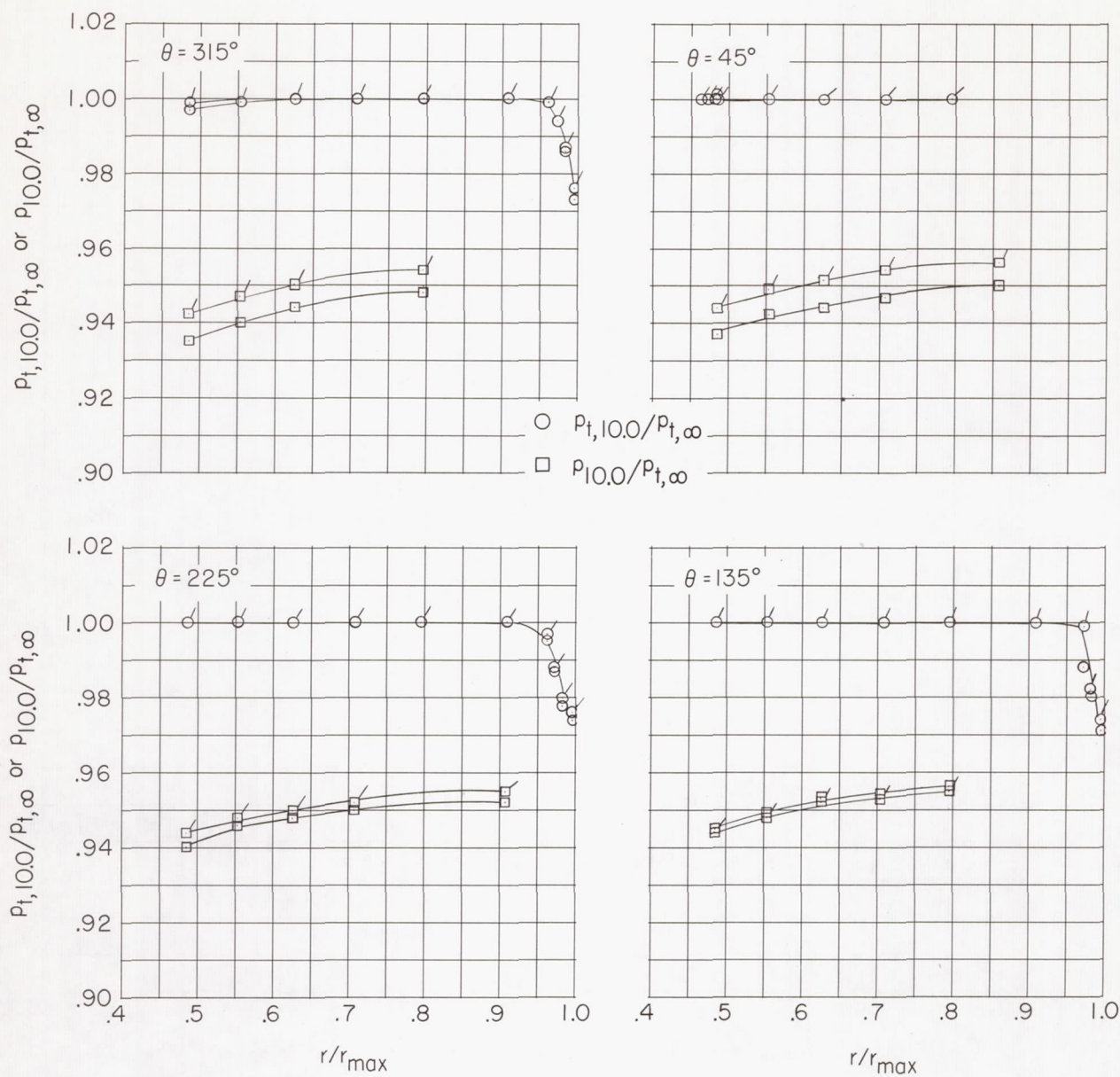
(a) $M = 0.30$; $N_F/\sqrt{\sigma} = 98.1$ percent.

Figure 17.- Fan-inlet total- and static-pressure profiles for configuration 123. Flagged data indicate windmill conditions.
($r/r_{\max} = 0.45$ for fan bullethead.)



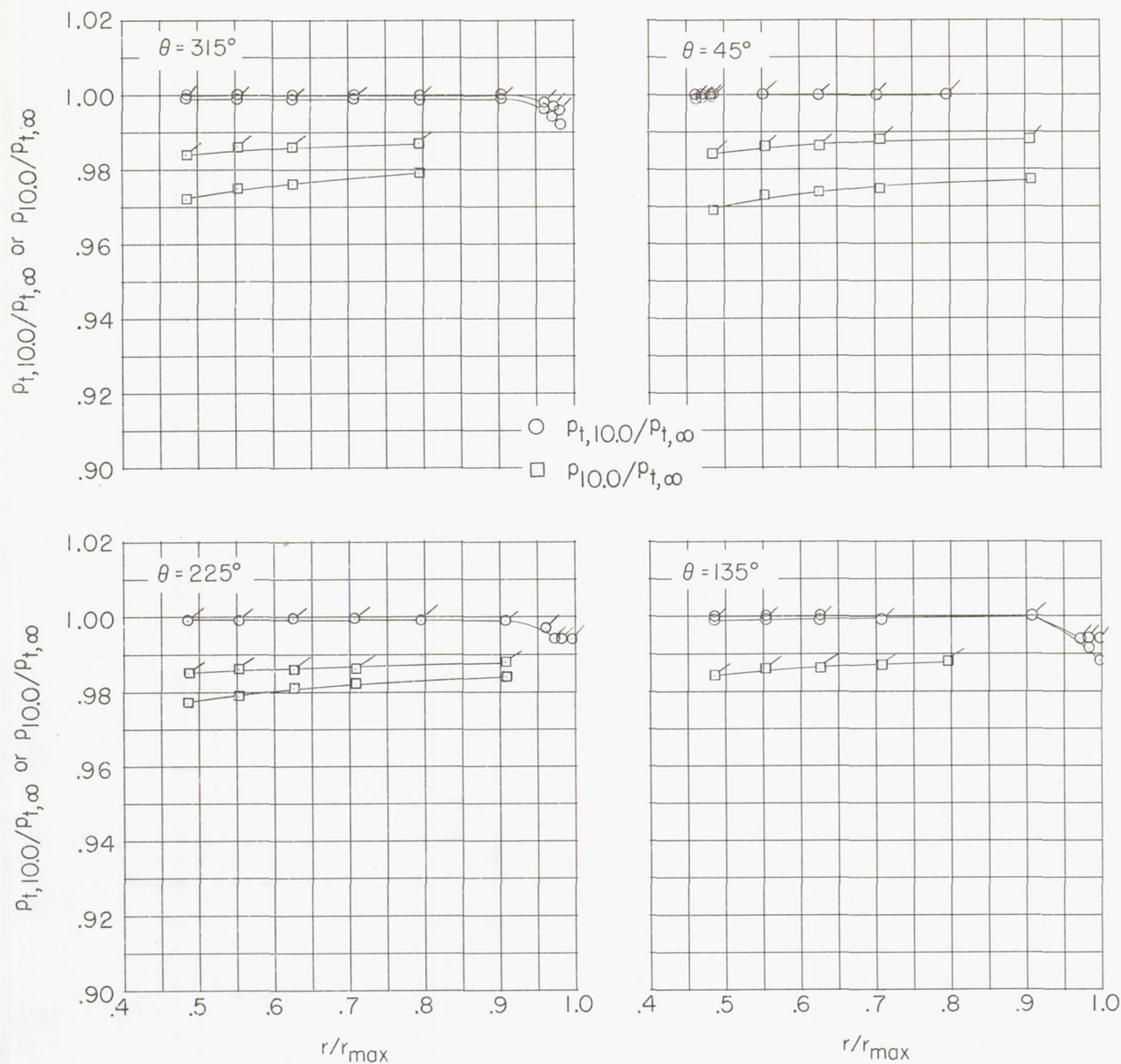
(b) $M = 0.50$; $N_F/\sqrt{\sigma} = 96.8$ percent.

Figure 17.- Continued.



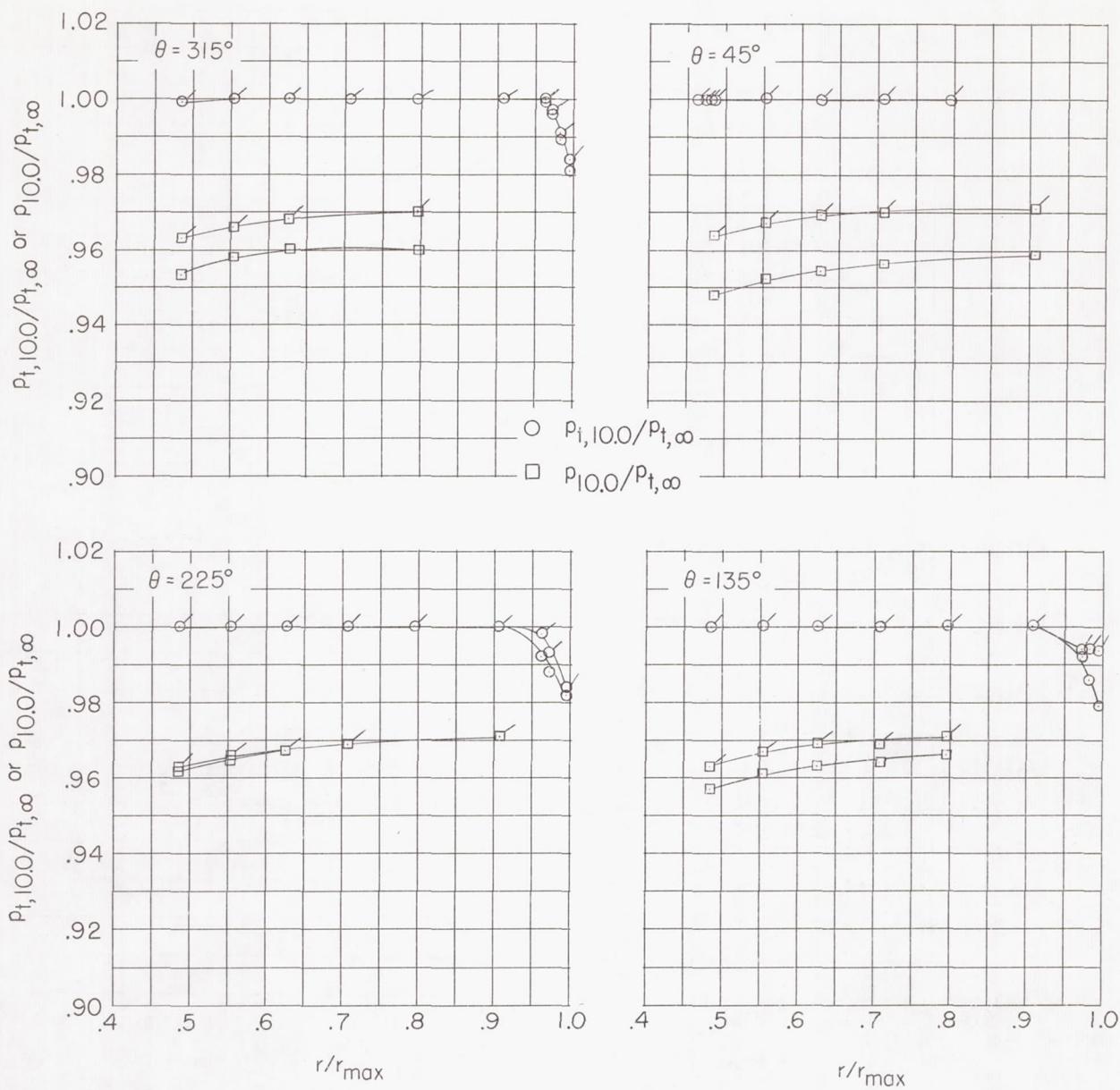
(c) $M = 0.70$; $N_F/\sqrt{\sigma} = 90.6$ percent.

Figure 17.- Concluded.



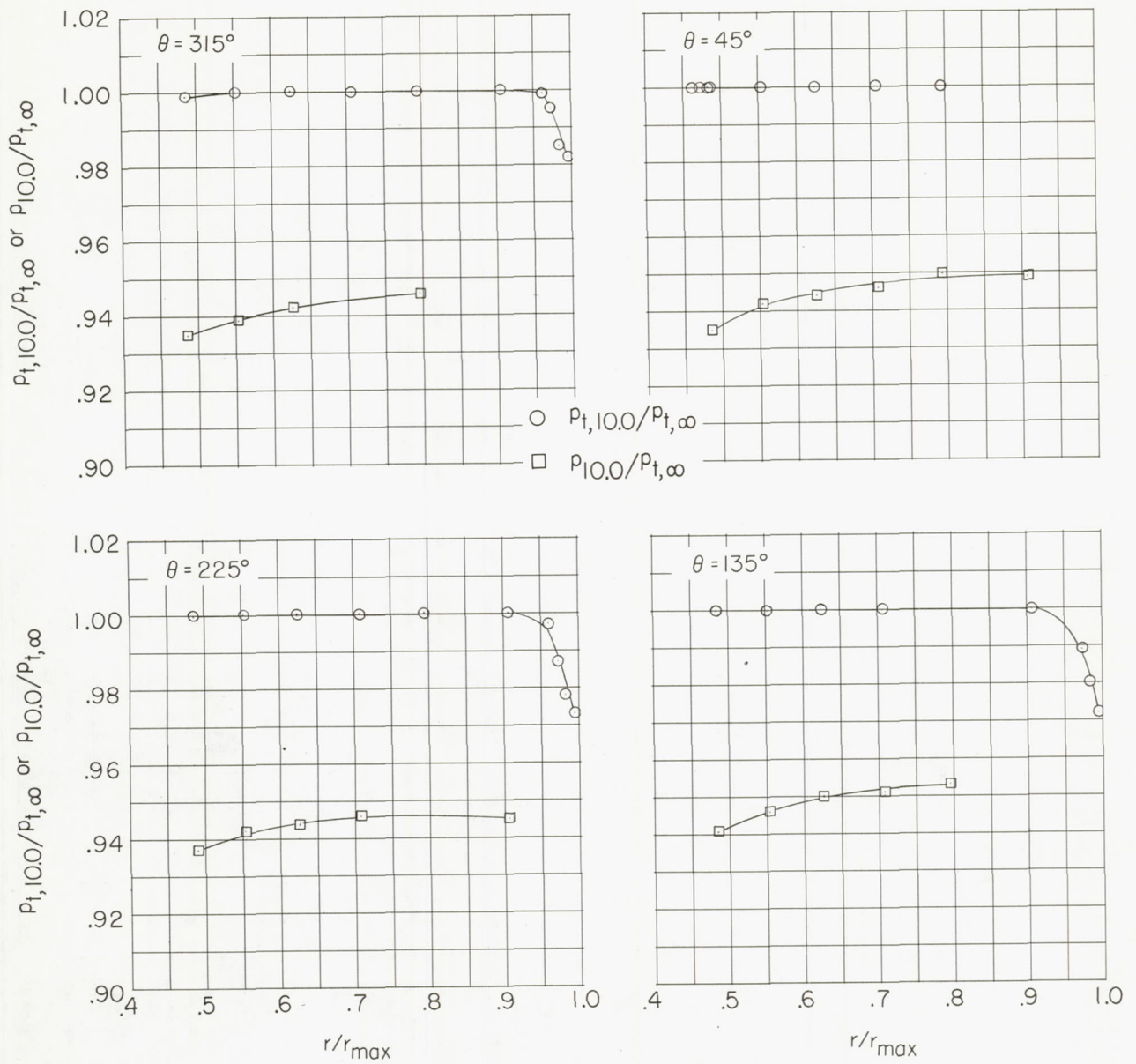
(a) $M = 0.30$; $N_F/\sqrt{\sigma} = 92.6$ percent.

Figure 18.- Fan-inlet total- and static-pressure profiles for configuration 113. Flagged data indicate windmill conditions. ($r/r_{\max} = 0.45$ for fan bulletnose.)



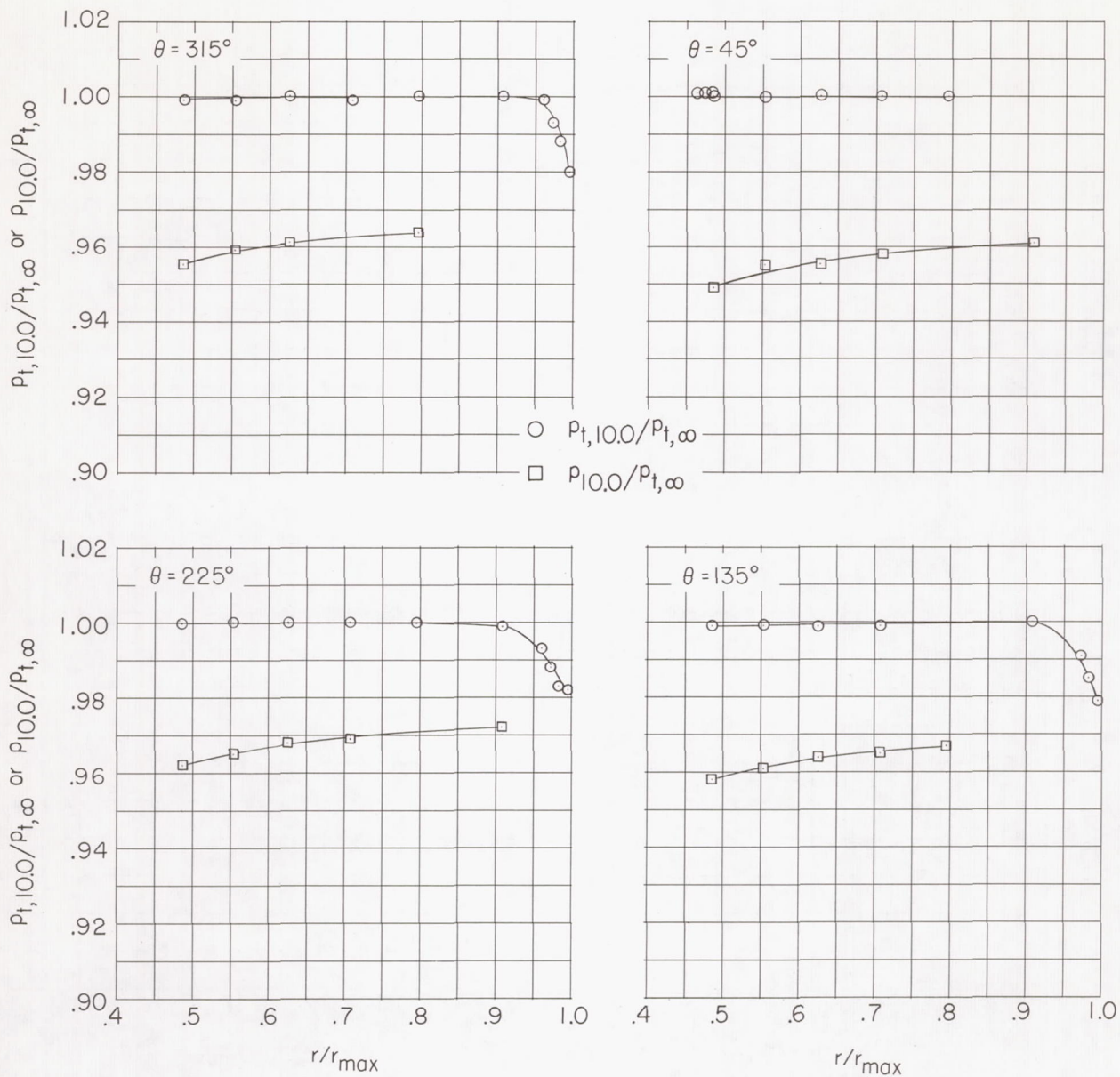
(b) $M = 0.50$; $N_F/\sqrt{\sigma} = 95.9$ percent.

Figure 18.- Continued.



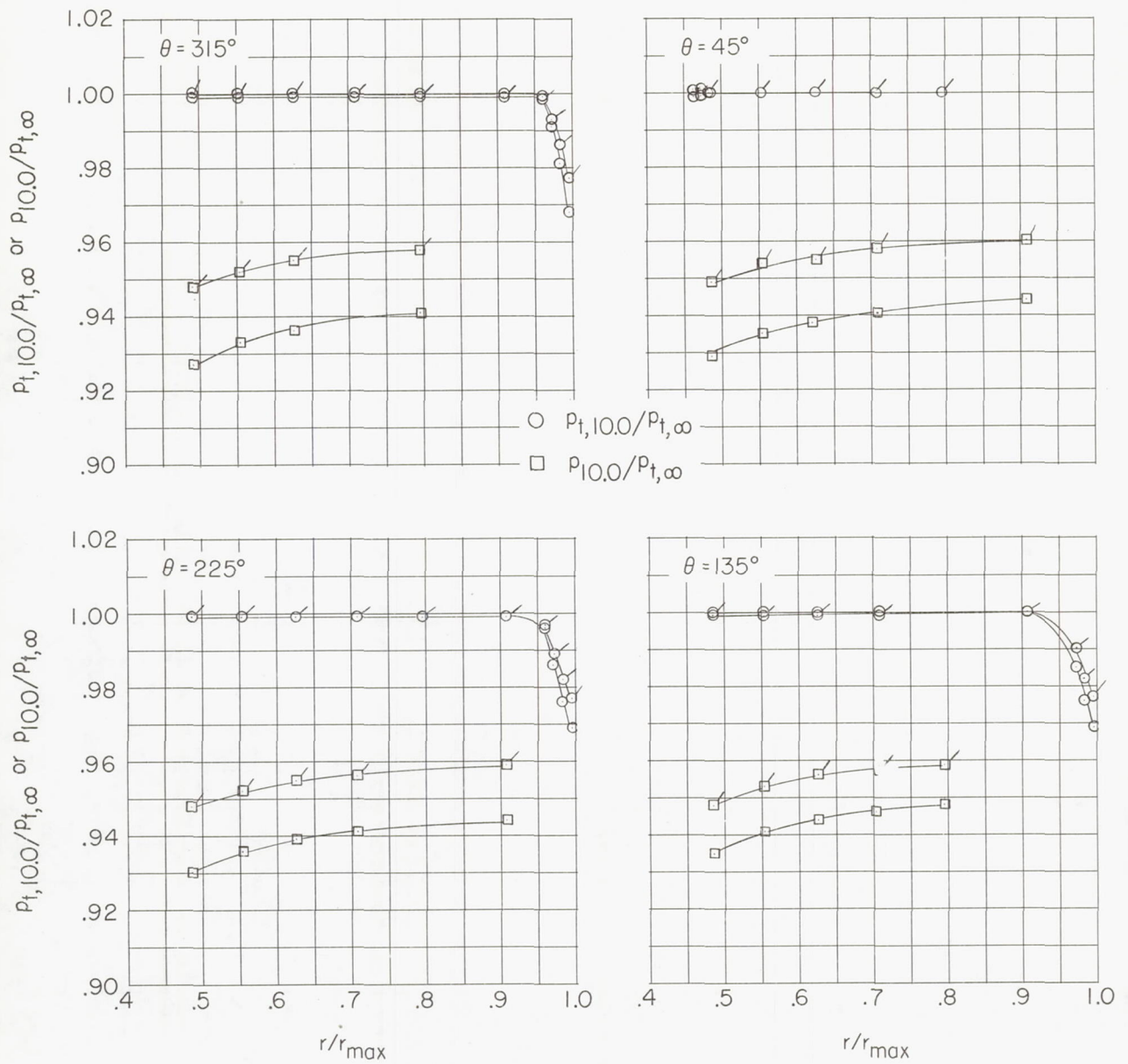
(c) $M = 0.80$; $N_F/\sqrt{\sigma} = 90.8$ percent.

Figure 18.- Concluded.



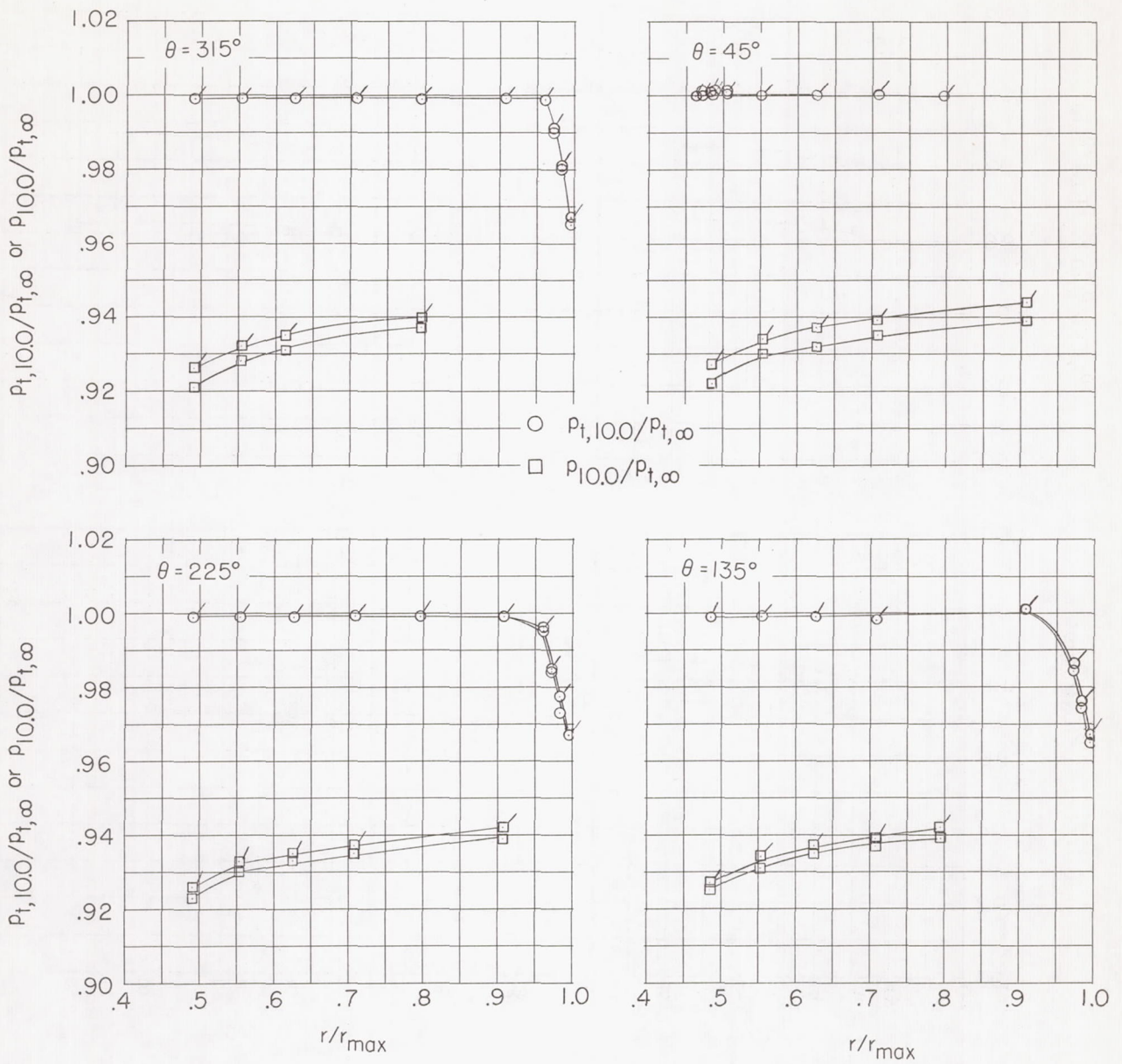
(a) $M = 0.30$; $N_F/\sqrt{\sigma} = 96.8$ percent.

Figure 19.- Fan-inlet total- and static-pressure profiles for configuration 112. Flagged data indicate windmill conditions.
($r/r_{\max} = 0.45$ for fan bulletnose.)



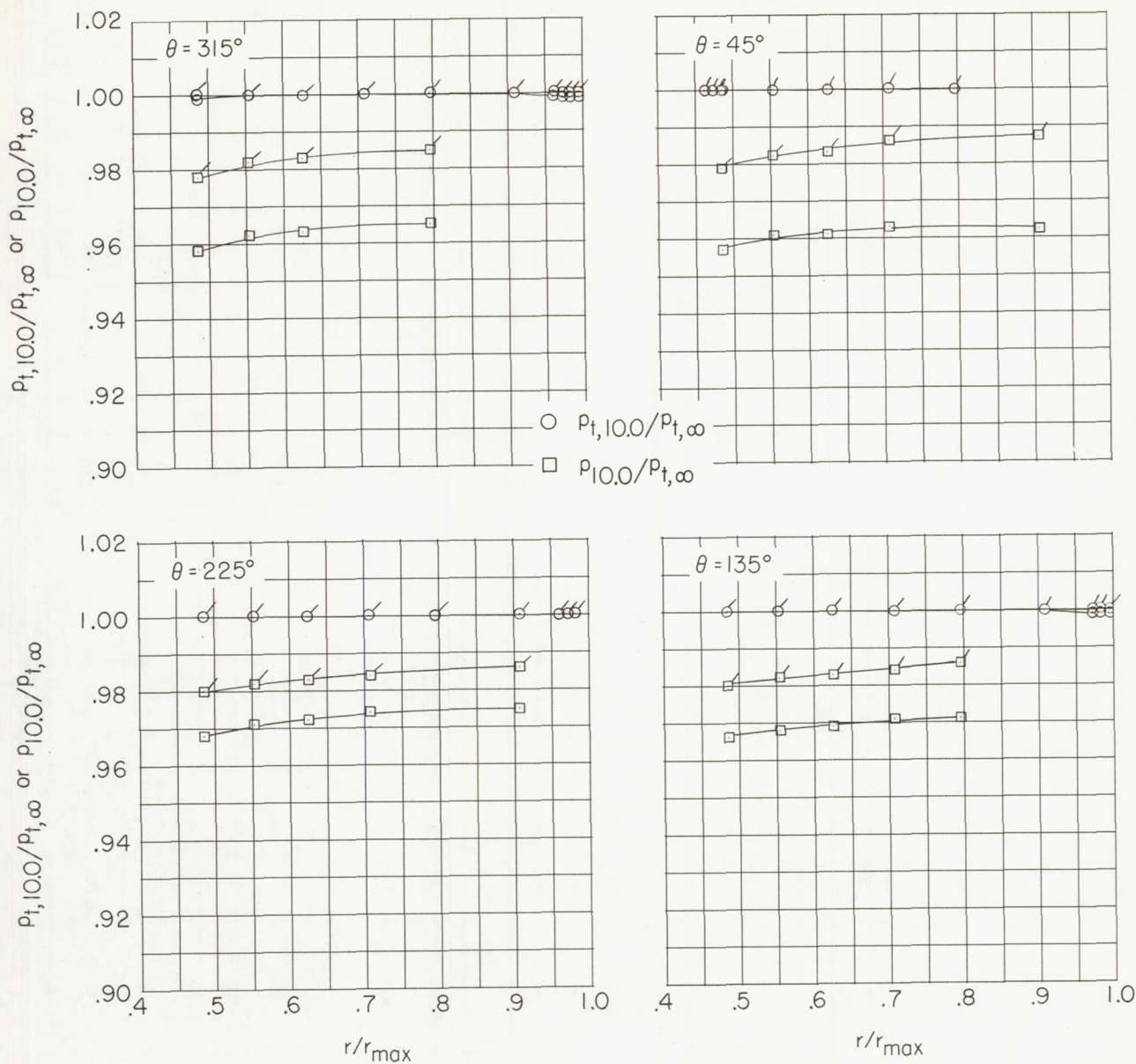
(b) $M = 0.50$; $N_F/\sqrt{\sigma} = 92.9$ percent.

Figure 19.- Continued.



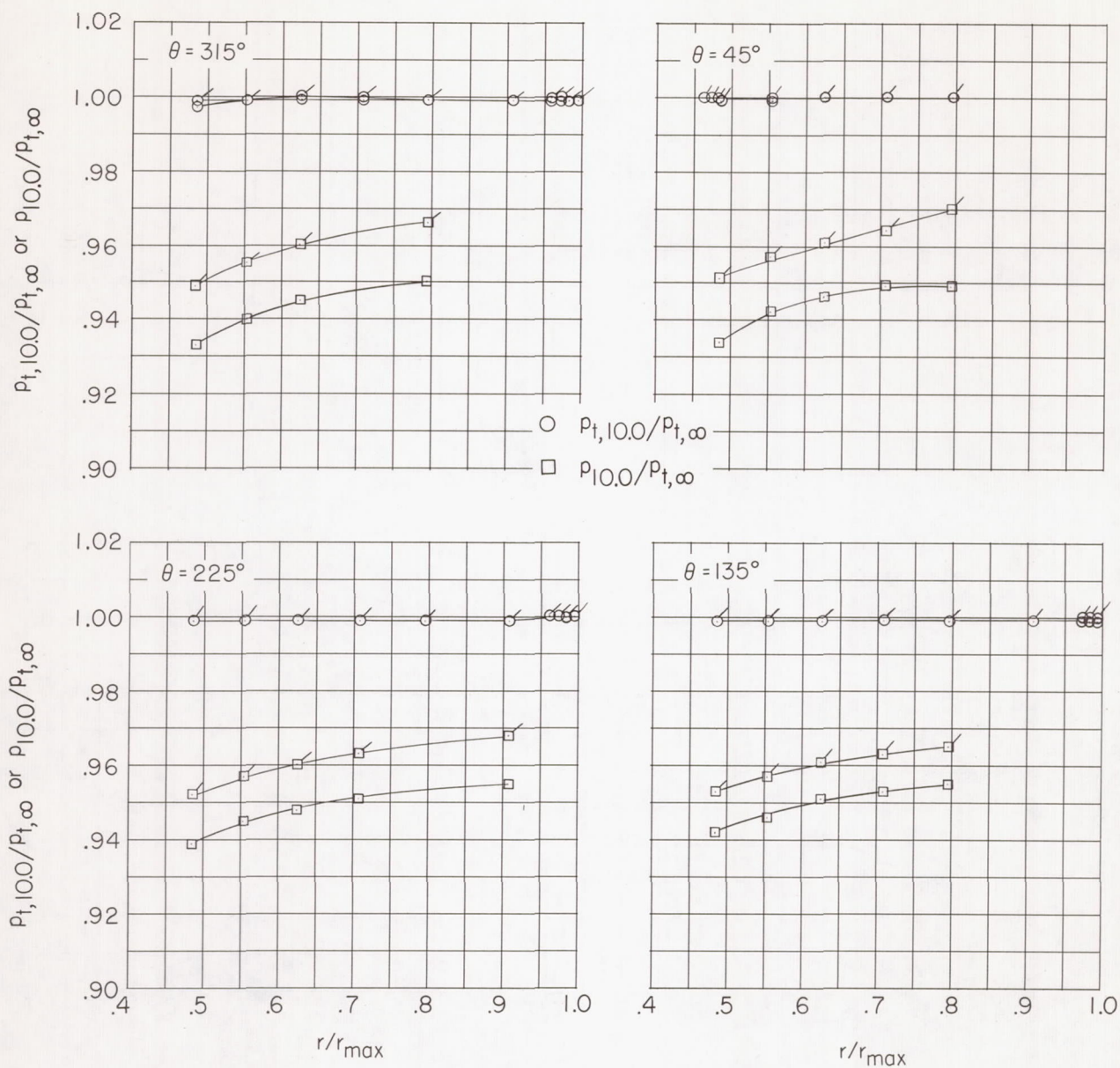
(c) $M = 0.65$; $N_F/\sqrt{\sigma} = 77.0$ percent.

Figure 19.- Concluded.



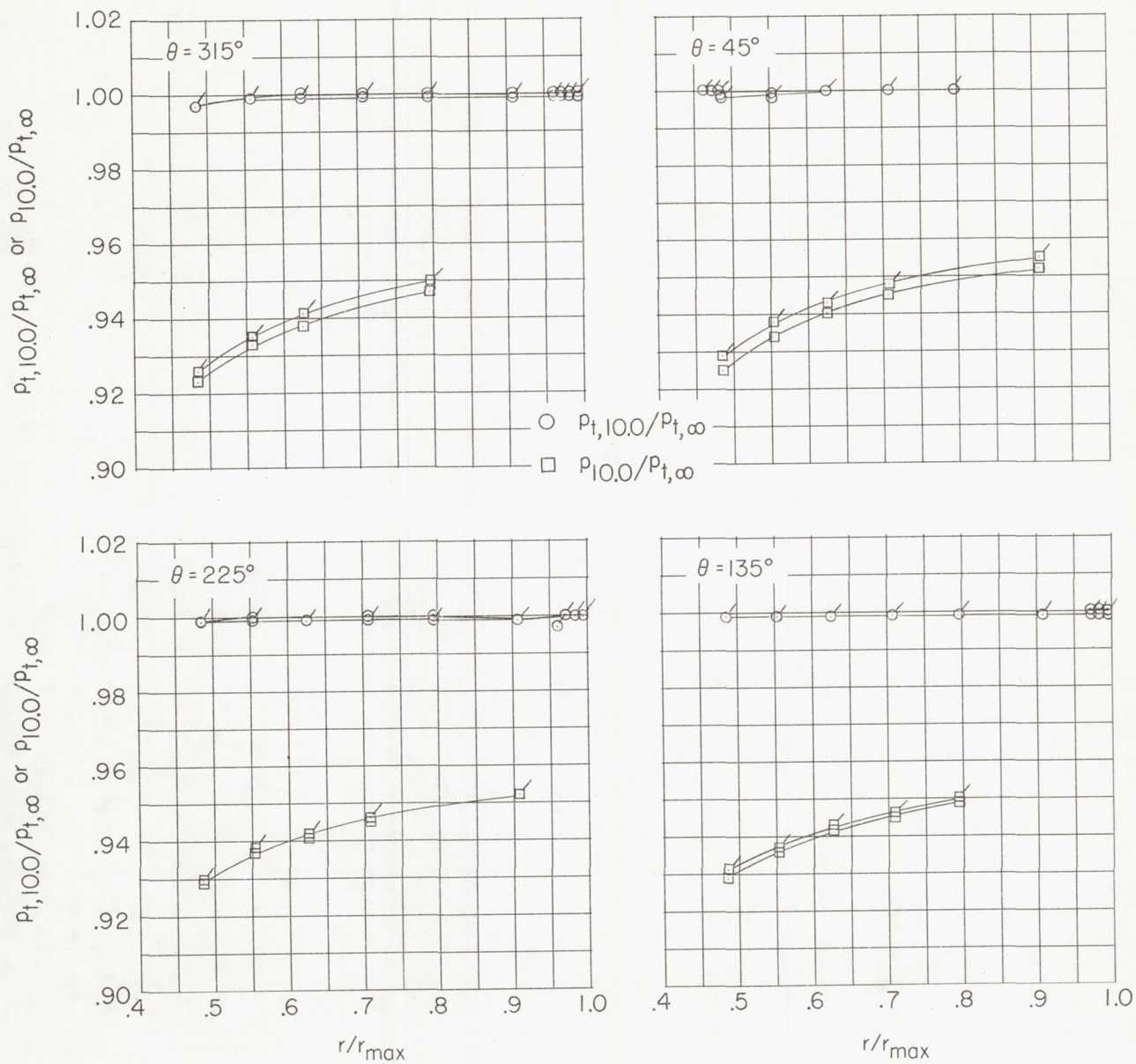
(a) $M = 0.30$; $N_F/\sqrt{\sigma} = 97.5$ percent.

Figure 20.- Fan-inlet total- and static-pressure profiles for configuration 322. Flagged data indicate windmill conditions.
($r/r_{\max} = 0.45$ for fan bulletnose.)



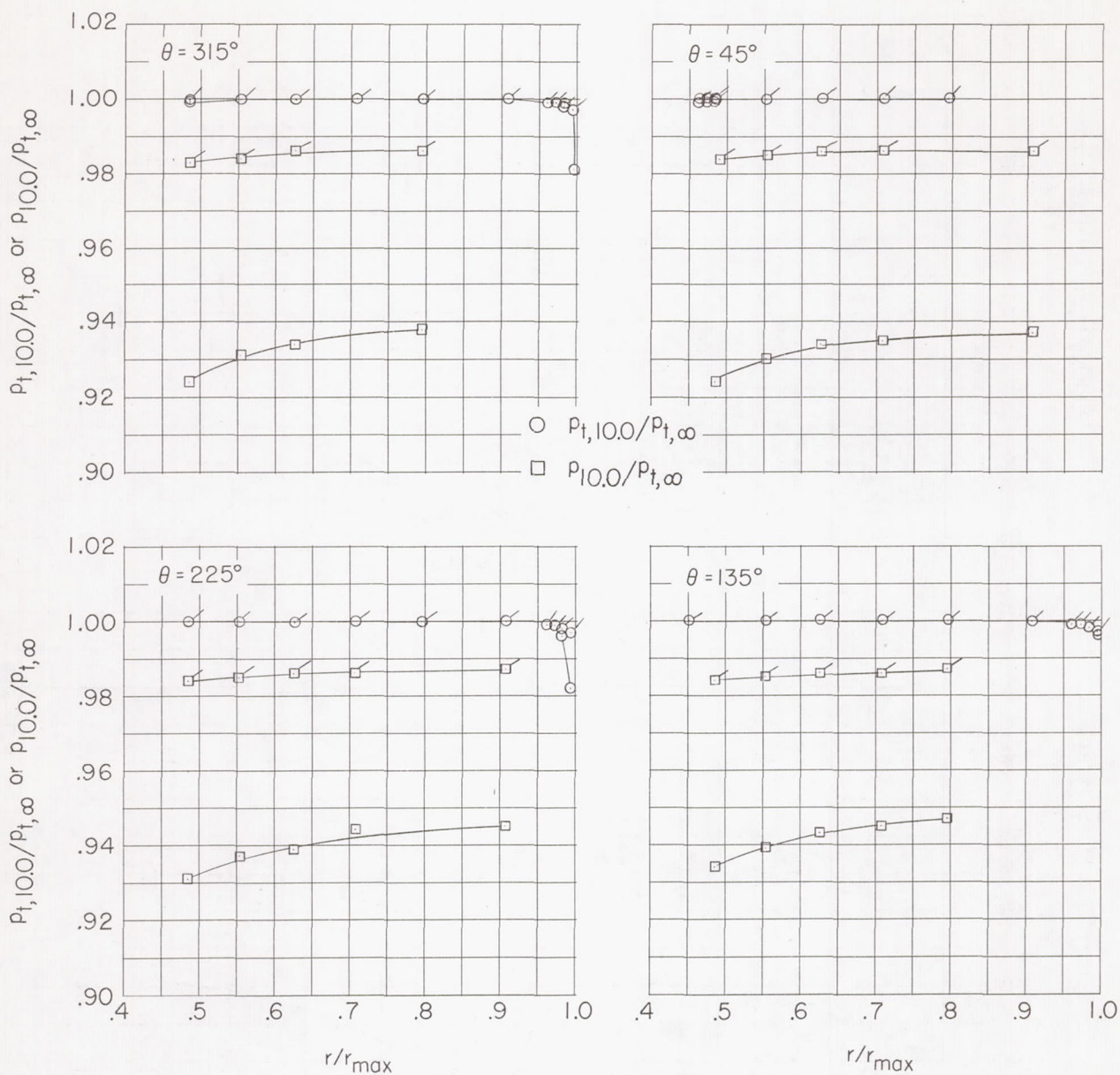
(b) $M = 0.50$; $N_F/\sqrt{\sigma} = 94.4$ percent.

Figure 20.- Continued.



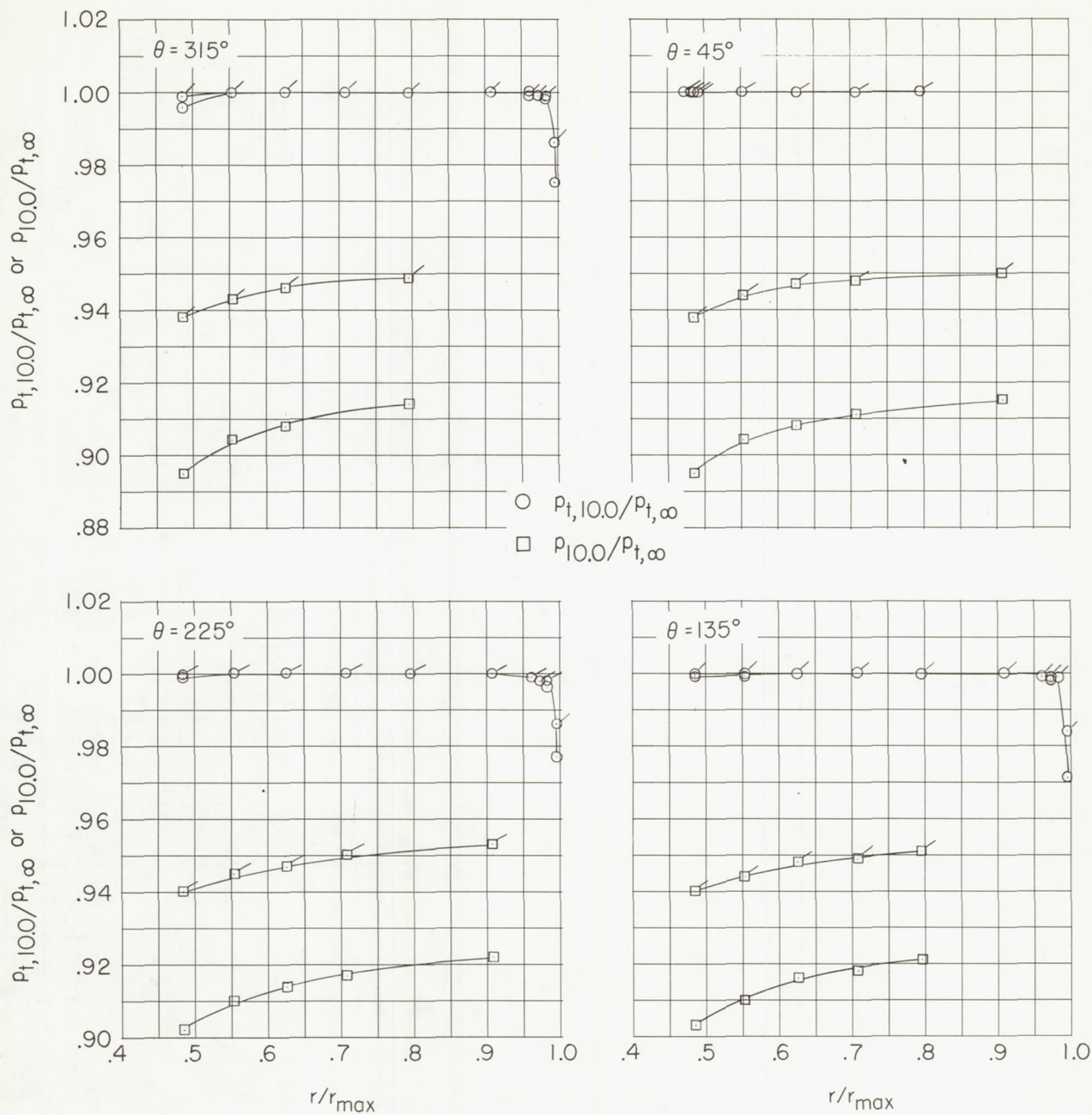
(c) $M = 0.65$; $N_F/\sqrt{\sigma} = 76.5$ percent.

Figure 20.- Concluded.



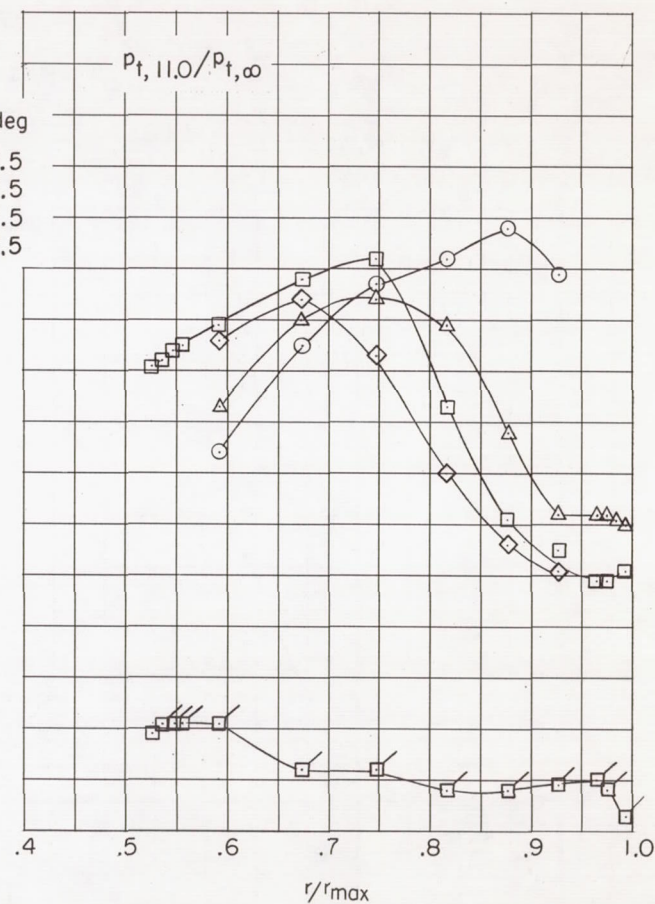
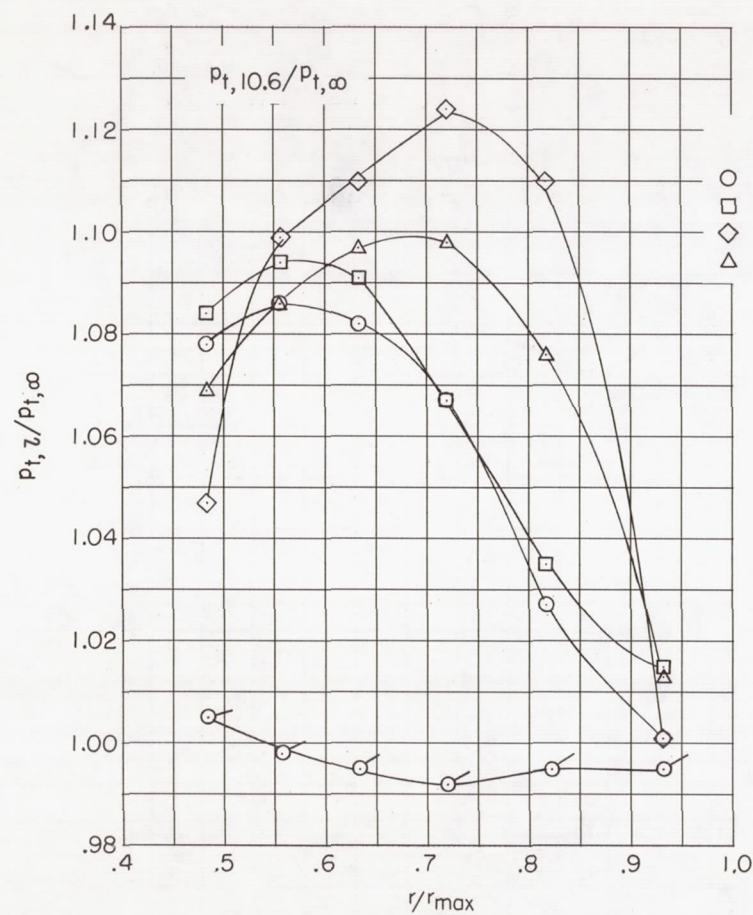
(a) $M = 0.20$; $N_F/\sqrt{\sigma} = 97.2$ percent.

Figure 21.- Fan-inlet total- and static-pressure profiles for configuration 243. Flagged data indicate windmill conditions.
($r/r_{\max} = 0.45$ for fan bulletnose.)



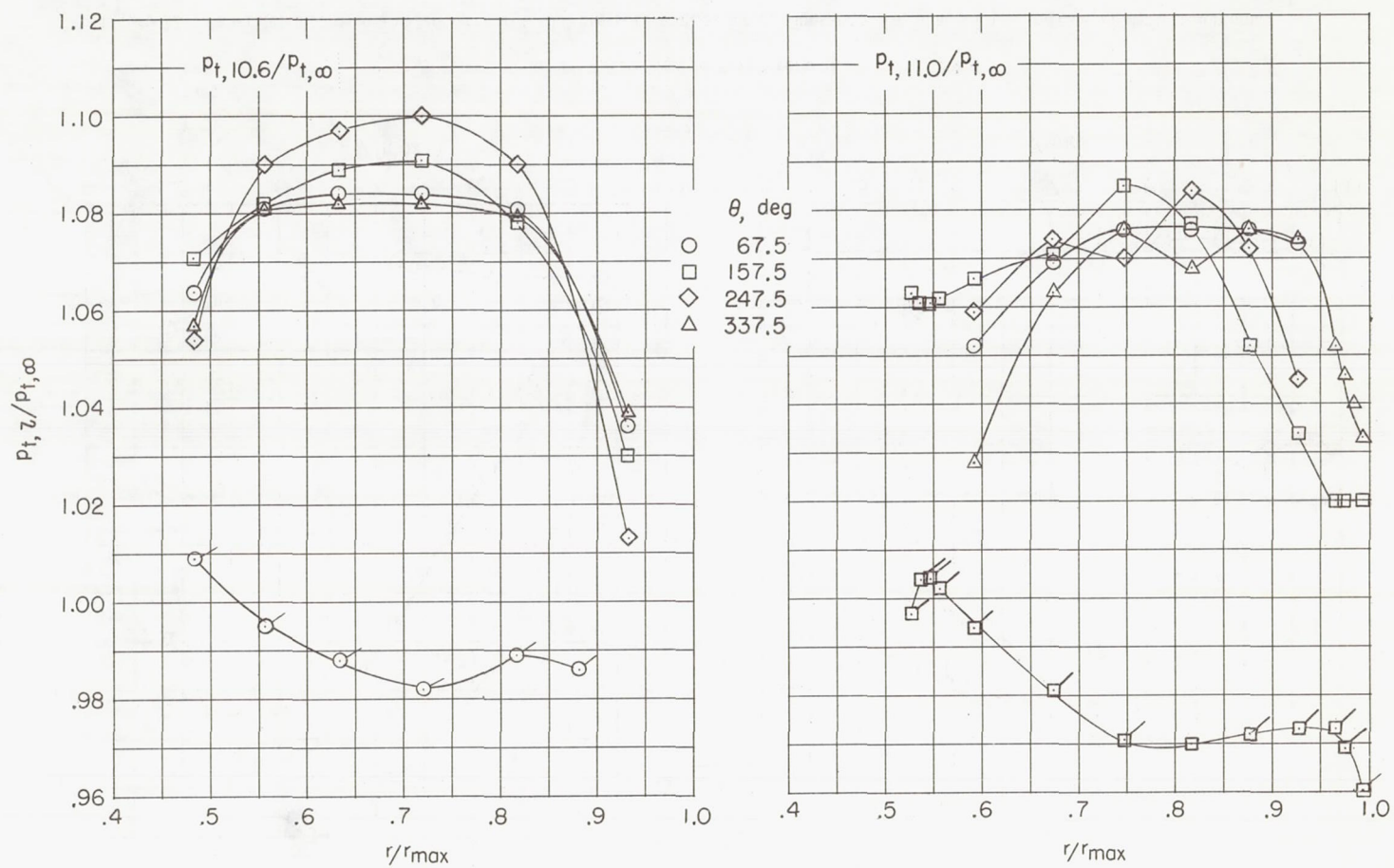
(b) $M = 0.40$; $N_F/\sqrt{\sigma} = 97.1$ percent.

Figure 21.- Concluded.



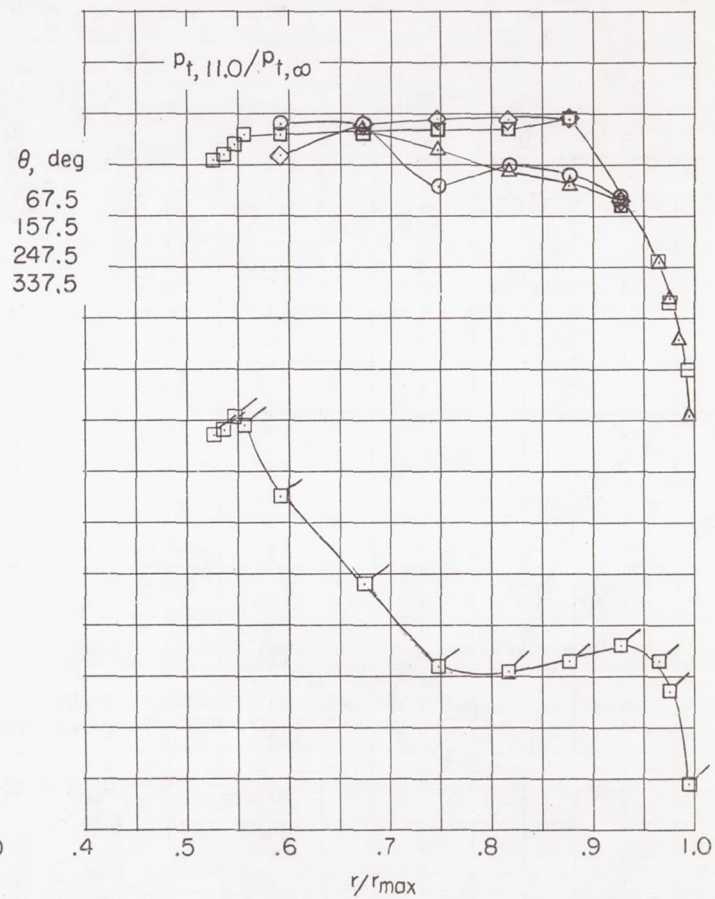
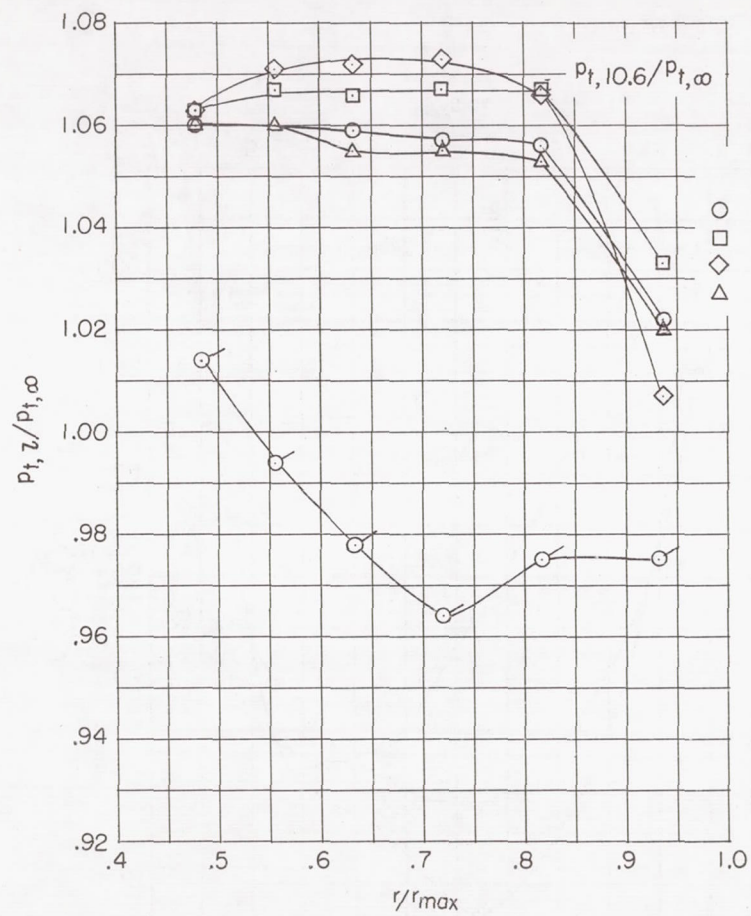
(a) $M = 0.30$; $N_F/\sqrt{\sigma} = 97.6$ percent.

Figure 22.- Fan-rotor-discharge and fan-discharge total-pressure profiles for configuration 144. Flagged data indicate windmill conditions.



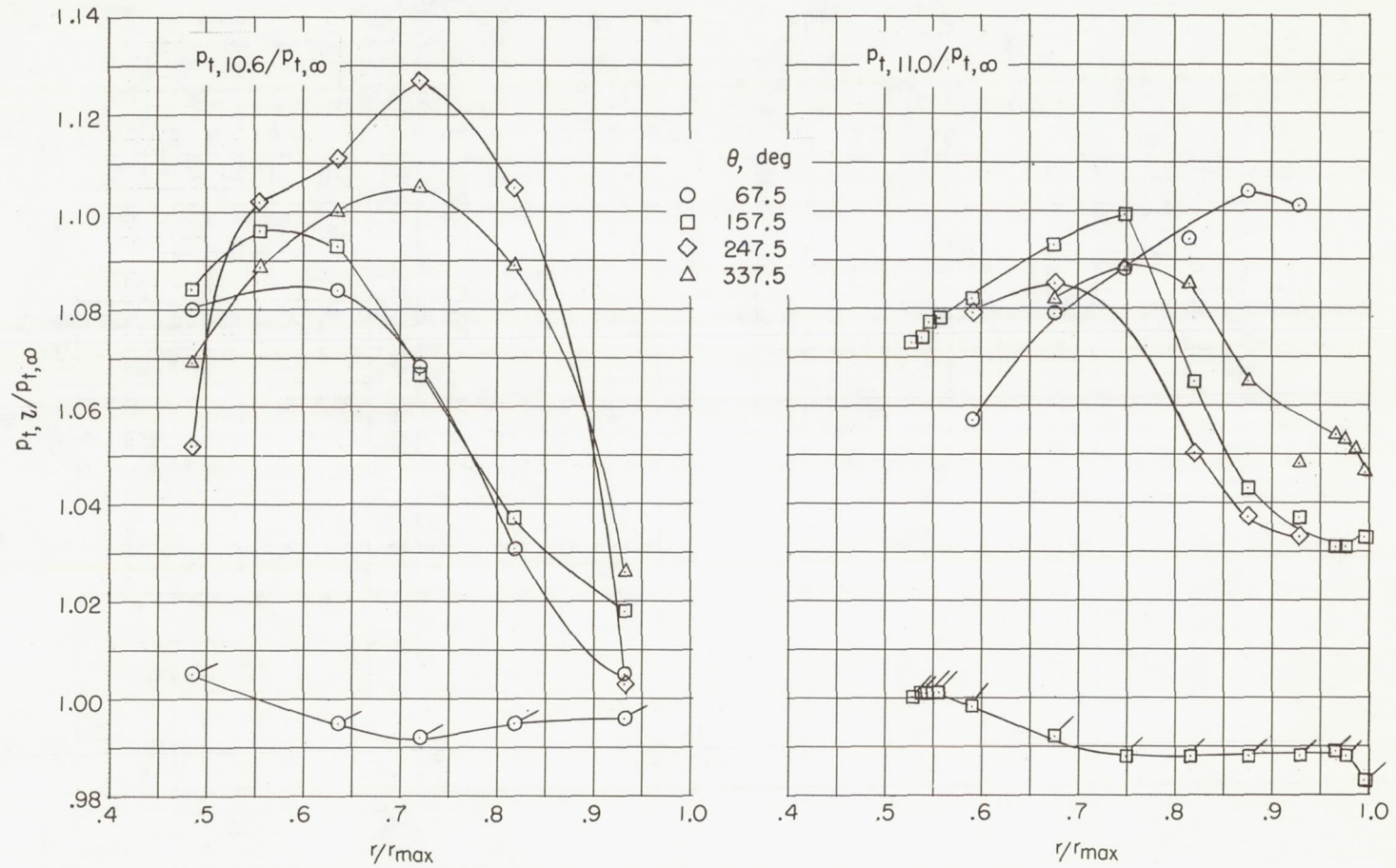
(b) $M = 0.50$; $N_F / \sqrt{\sigma} = 90.6$ percent.

Figure 22.- Continued.



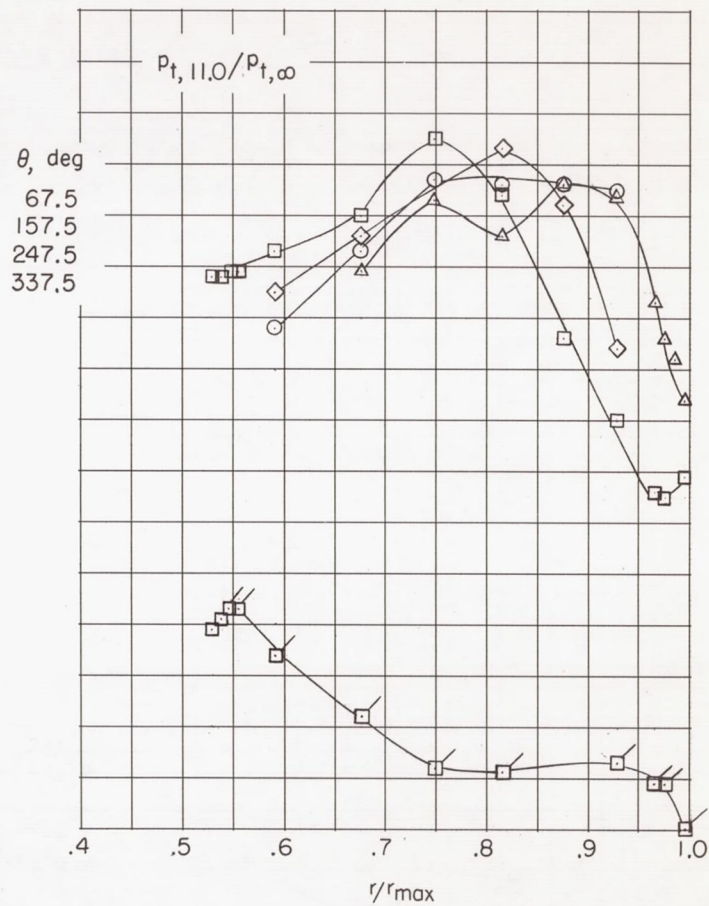
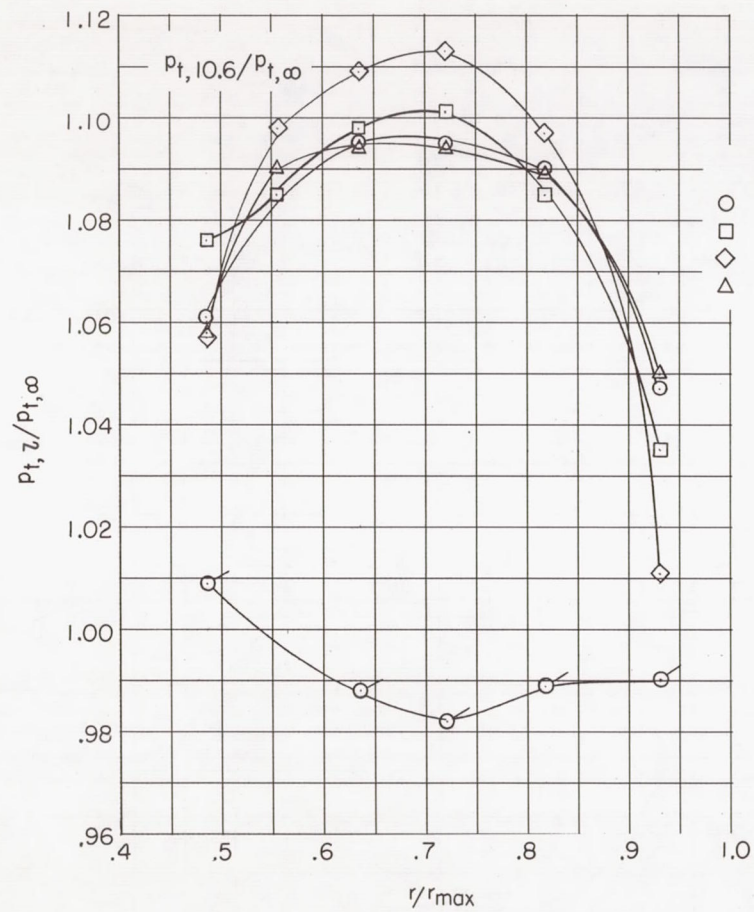
(c) $M = 0.80$; $N_F/\sqrt{\sigma} = 91.5$ percent.

Figure 22.- Concluded.



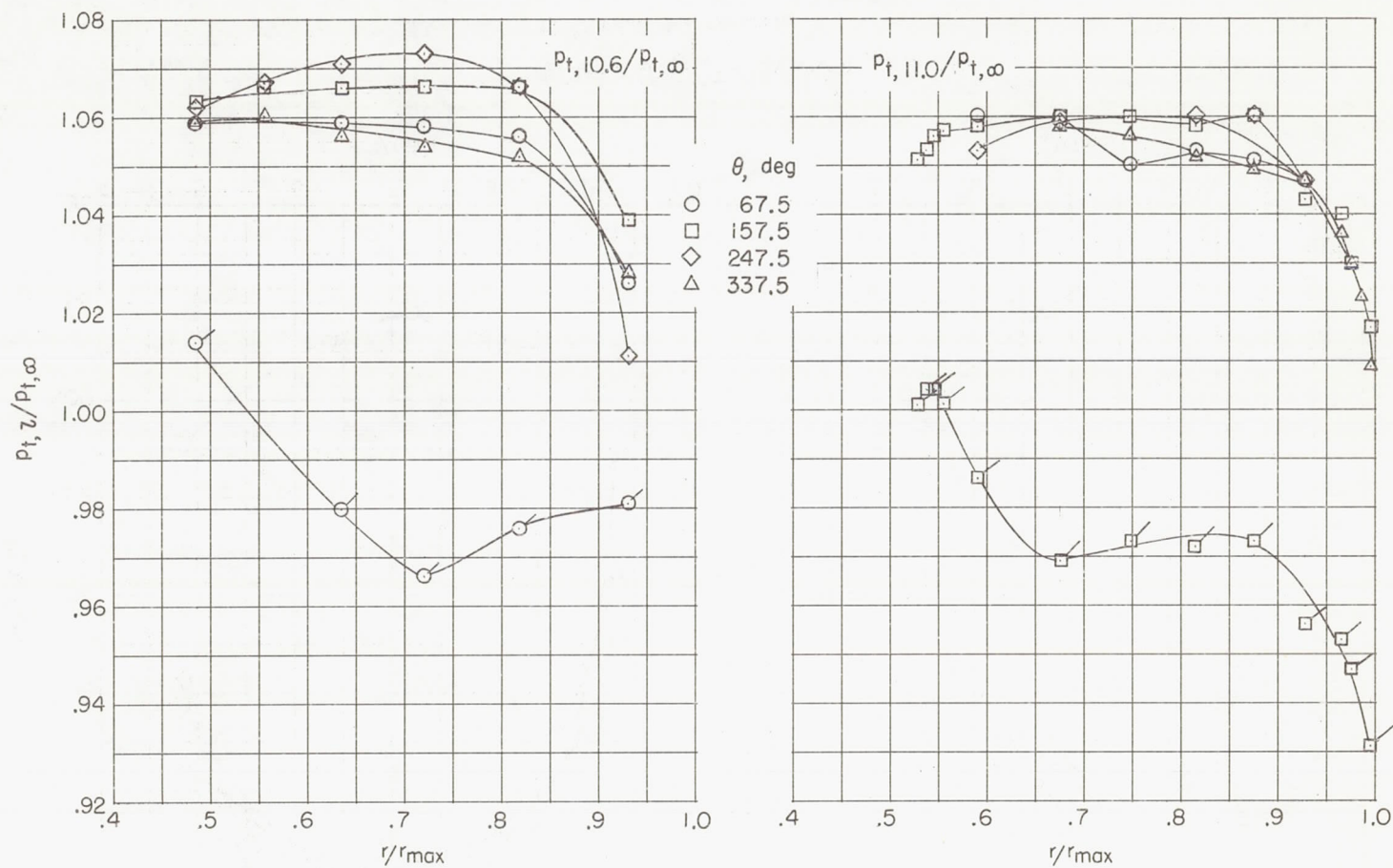
(a) $M = 0.30$; $N_F/\sqrt{\sigma} = 98.5$ percent.

Figure 23.- Fan-rotor-discharge and fan-discharge total-pressure profiles for configuration 244. Flagged data indicate windmill conditions.



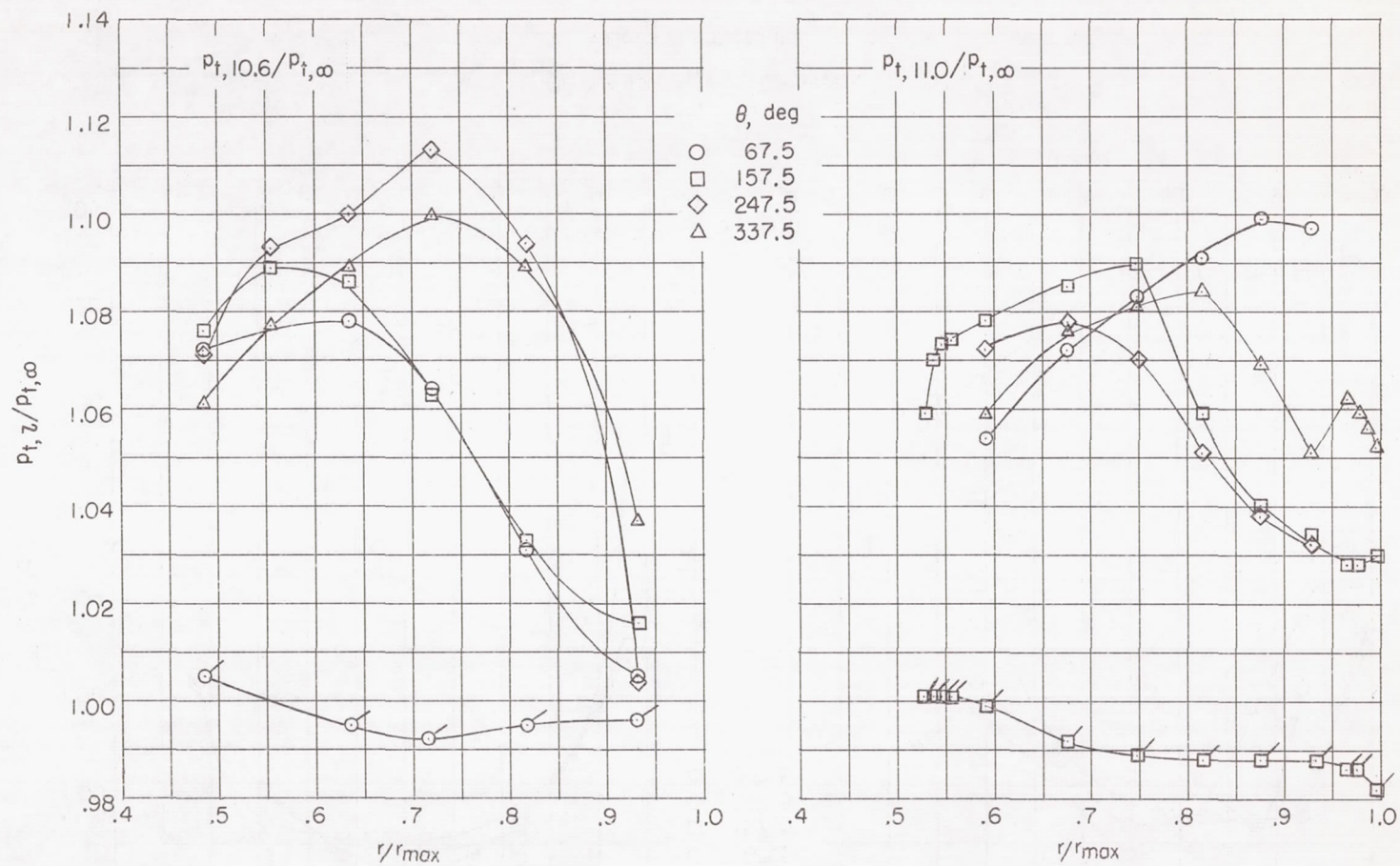
(b) $M = 0.50$; $N_F/\sqrt{\sigma} = 93.9$ percent.

Figure 23.- Continued.



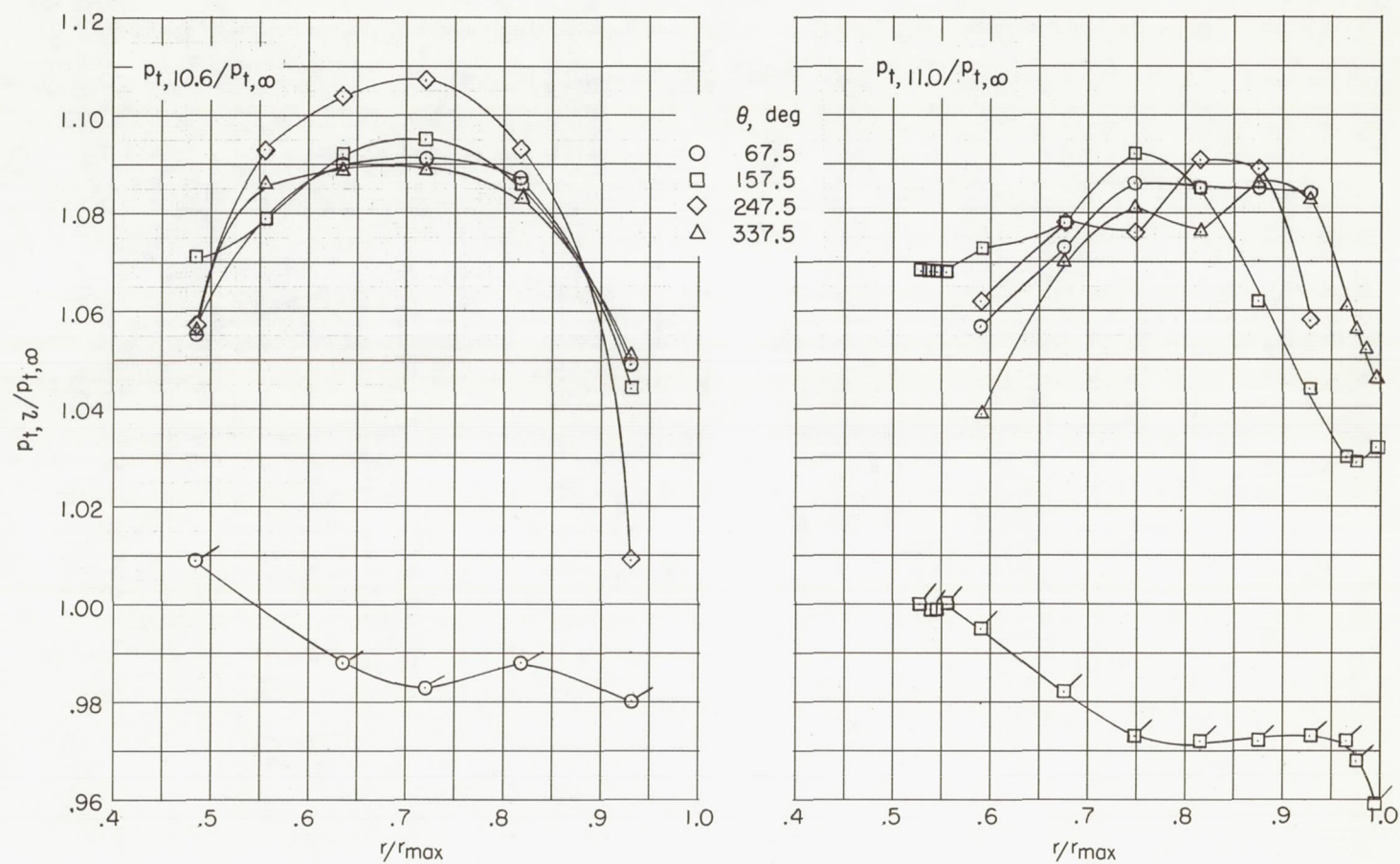
(c) $M = 0.80$; $N_F / \sqrt{\sigma} = 87.5$ percent.

Figure 23.- Concluded.



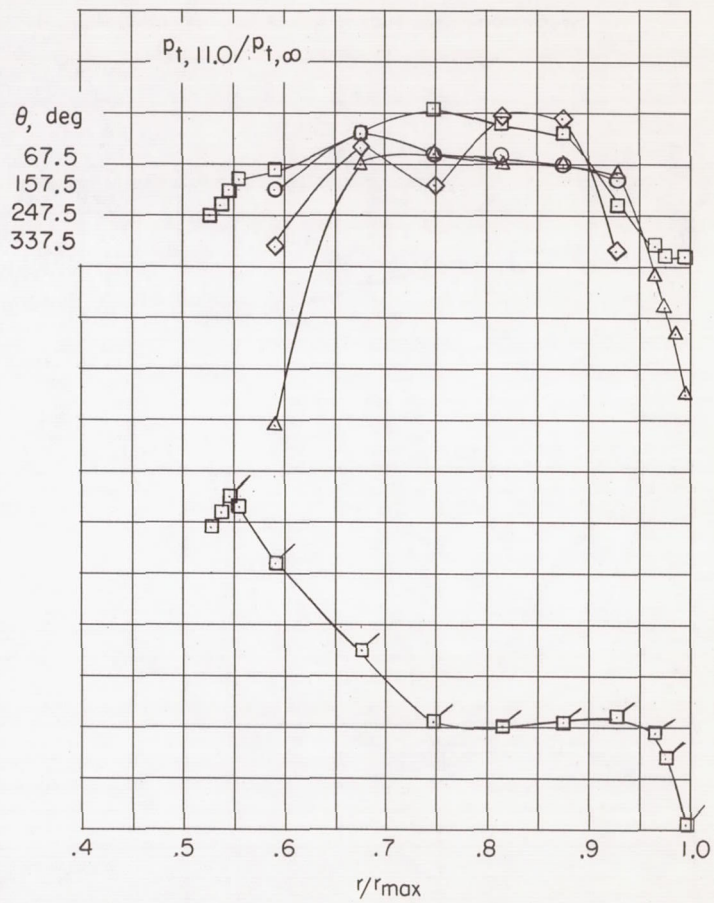
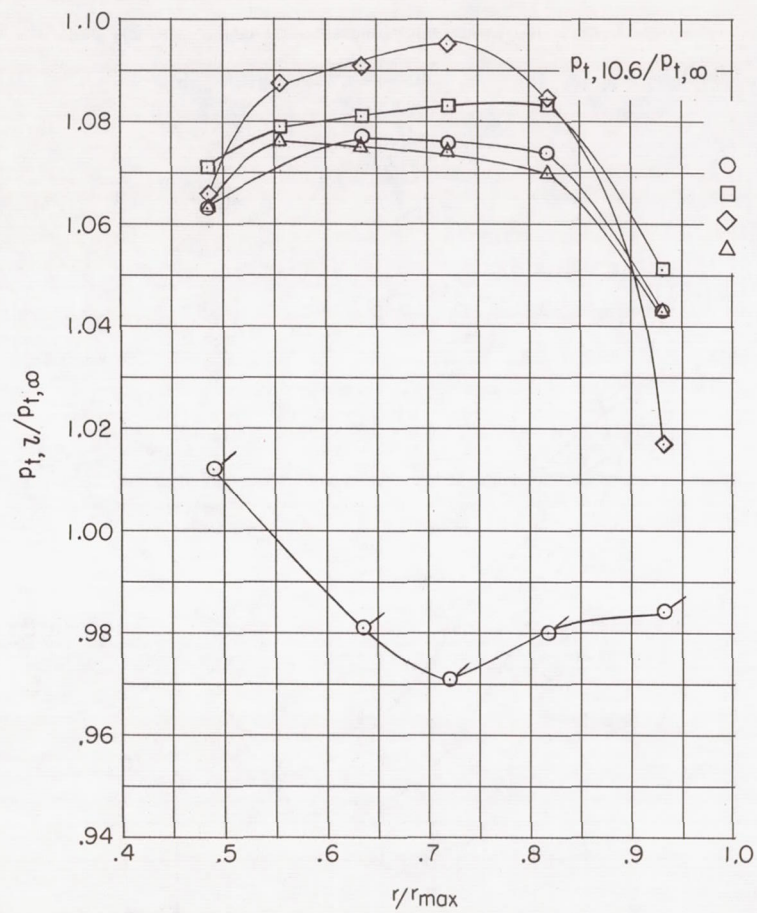
(a) $M = 0.30$; $N_F/\sqrt{\sigma} = 94.8$ percent.

Figure 24.- Fan-rotor-discharge and fan-discharge total-pressure profiles for configuration 344. Flagged data indicate windmill conditions.



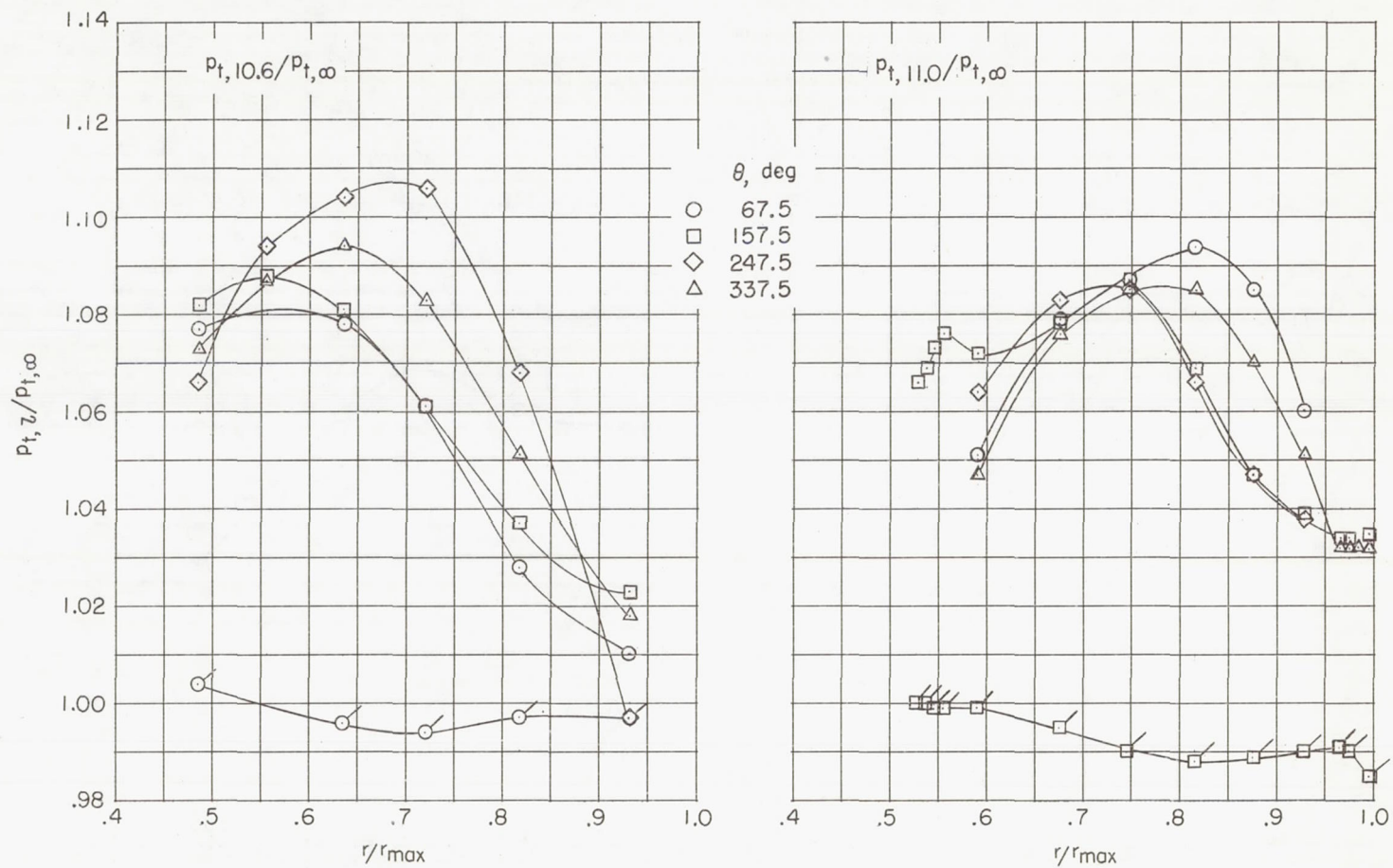
(b) $M = 0.50$; $N_F/\sqrt{\sigma} = 93.5$ percent.

Figure 24.- Continued.



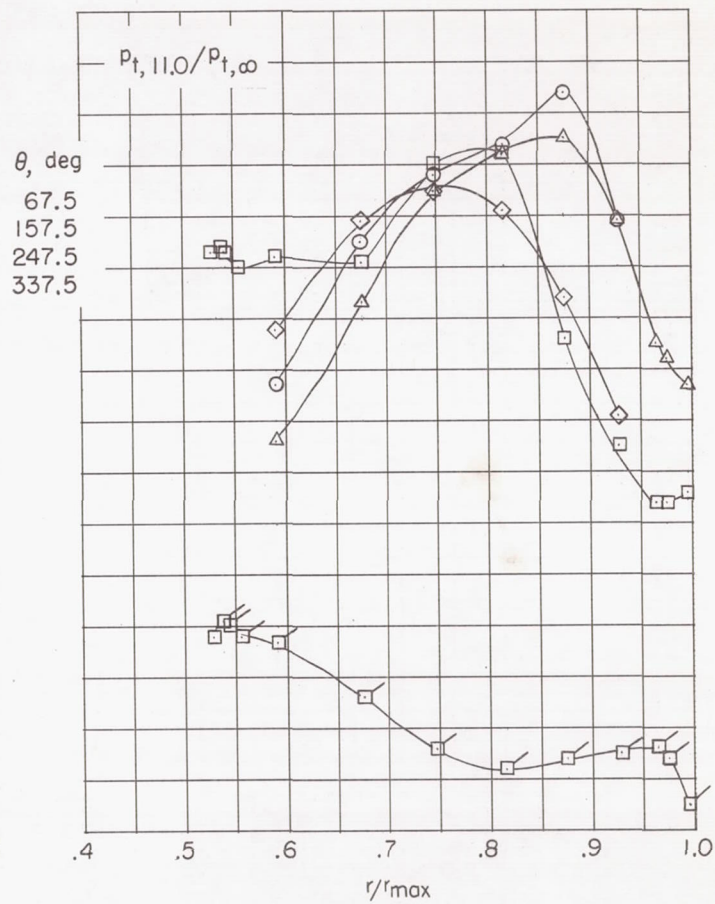
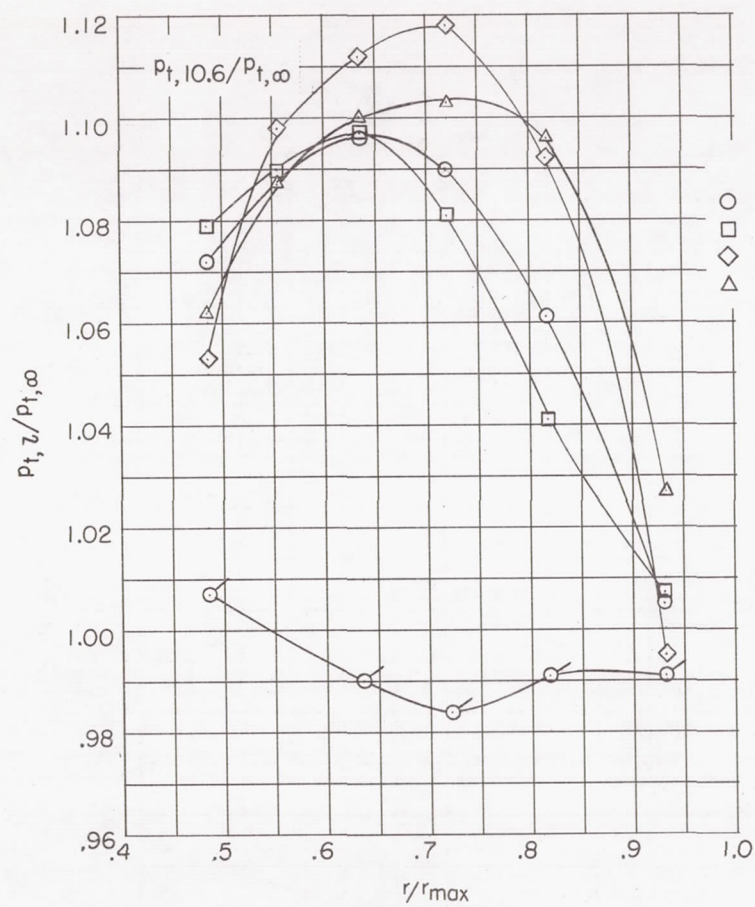
(c) $M = 0.65$; $N_F/\sqrt{\sigma} = 91.7$ percent.

Figure 24.- Concluded.



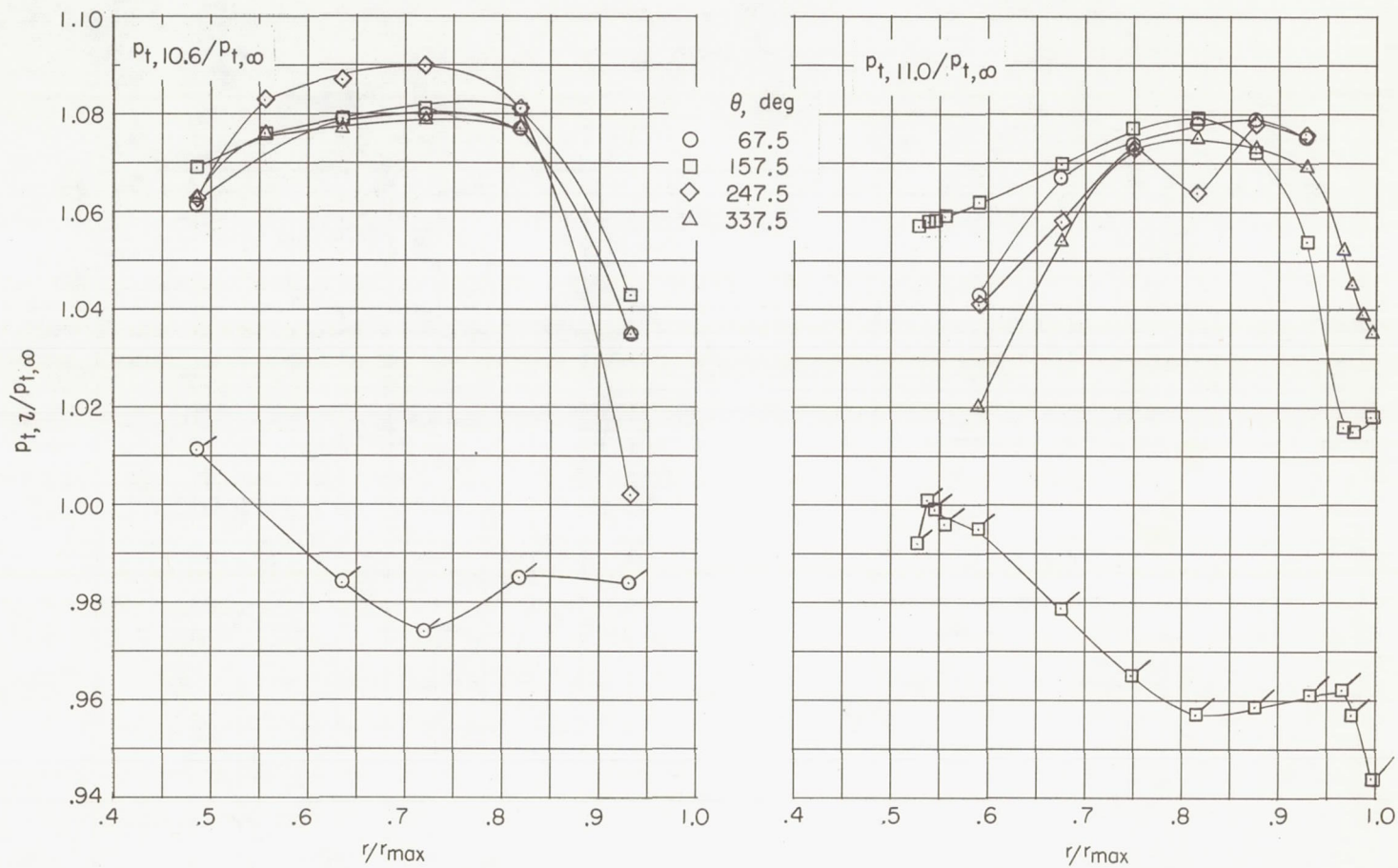
(a) $M = 0.30$; $N_F/\sqrt{\sigma} = 98.1$ percent.

Figure 25.- Fan-rotor-discharge and fan-discharge total-pressure profiles for configuration 123. Flagged data indicate windmill conditions.



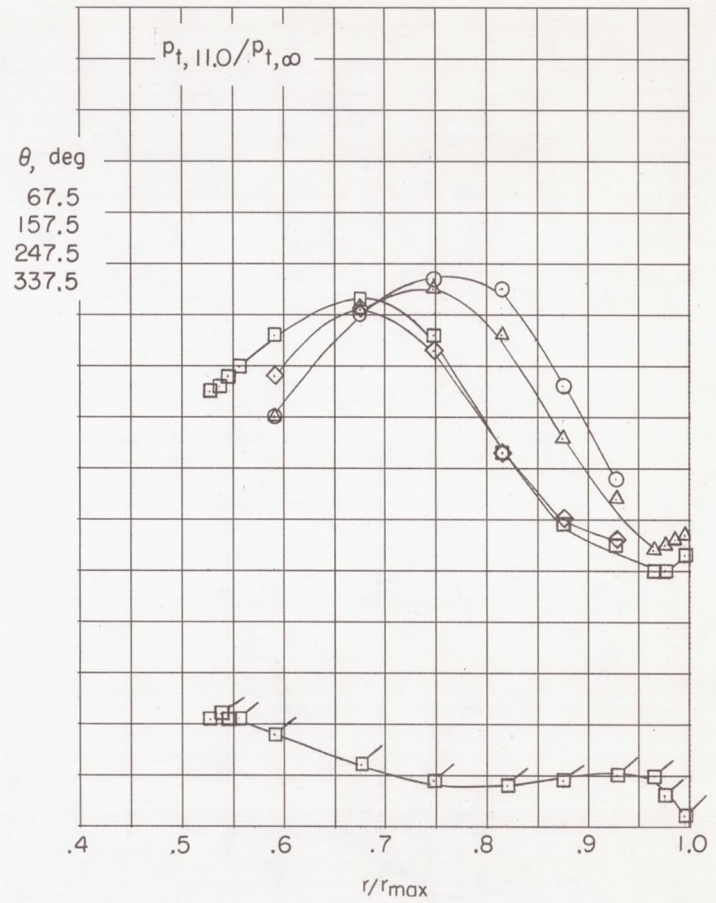
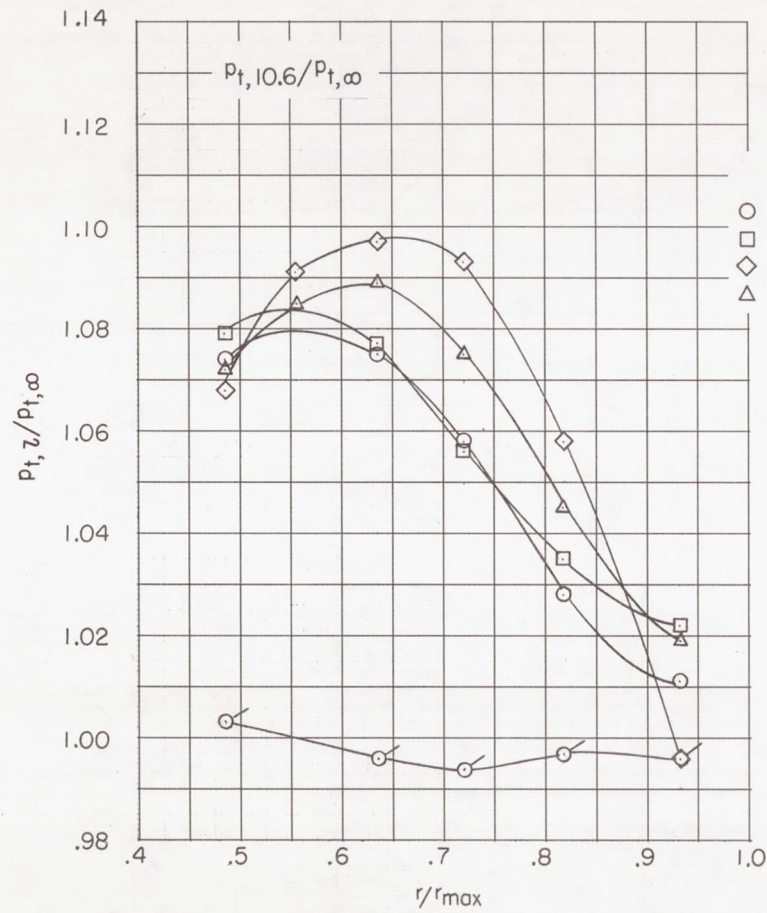
(b) $M = 0.50$; $N_F/\sqrt{\sigma} = 96.8$ percent.

Figure 25.- Continued.



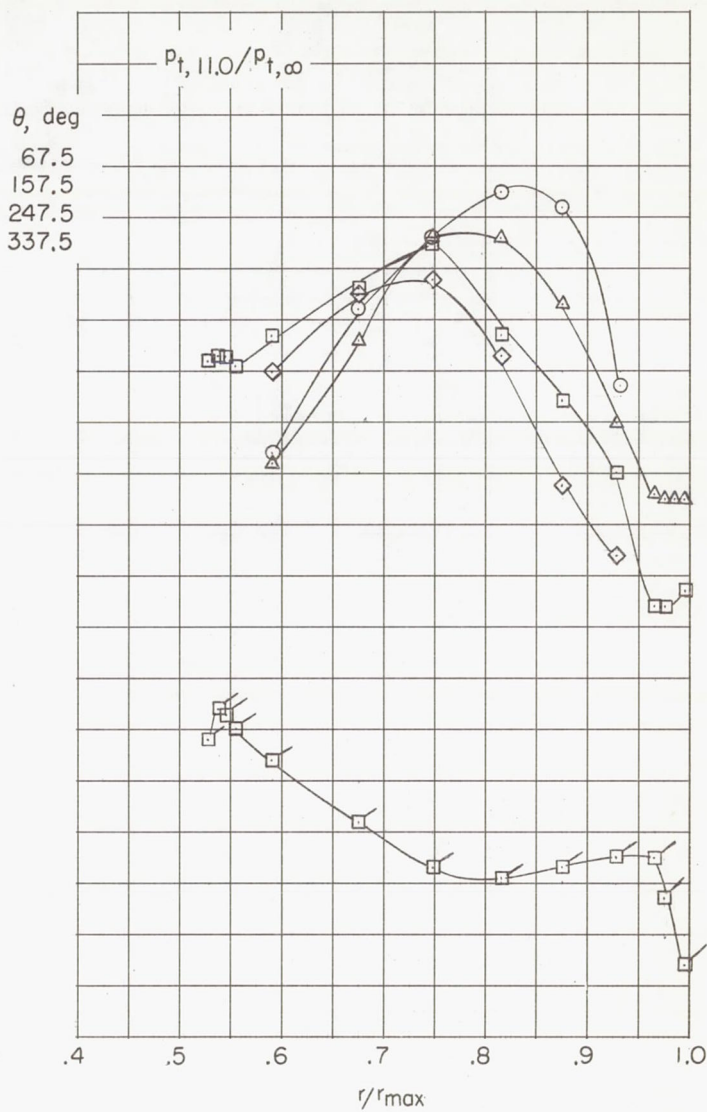
(c) $M = 0.70$; $N_F / \sqrt{\sigma} = 90.6$ percent.

Figure 25.- Concluded.



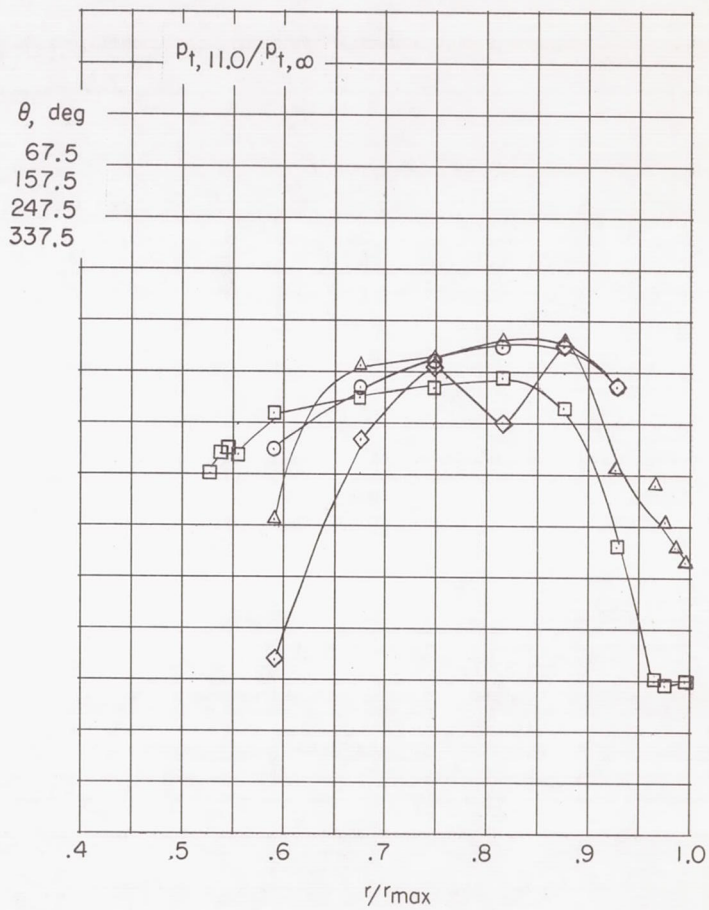
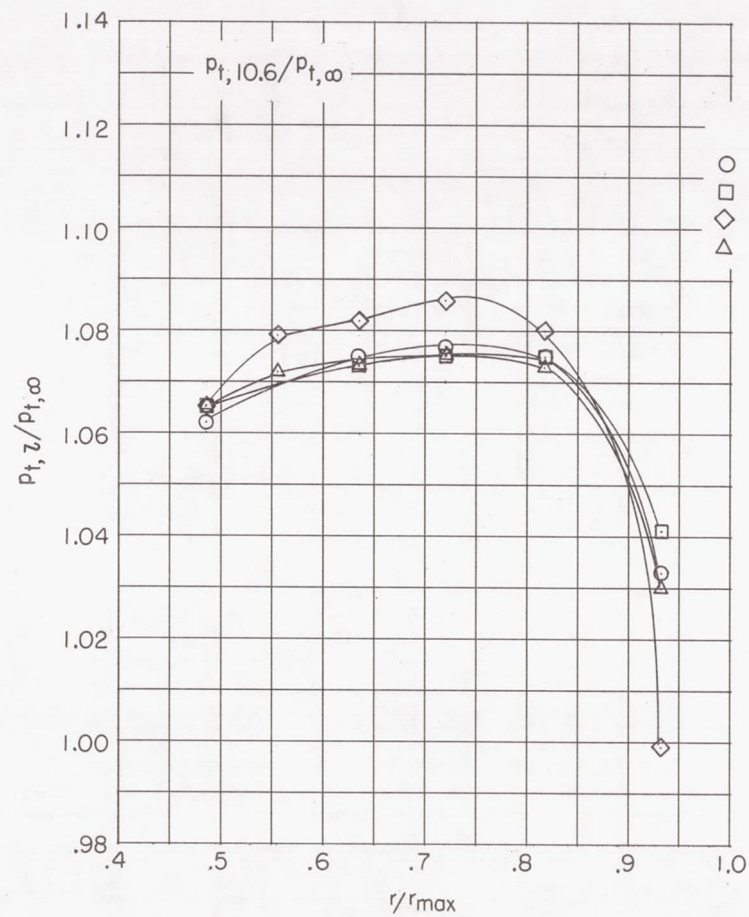
(a) $M = 0.30$; $N_F/\sqrt{\sigma} = 92.6$ percent.

Figure 26.- Fan-rotor-discharge and fan-discharge total-pressure profiles for configuration 113. Flagged data indicate windmill conditions.



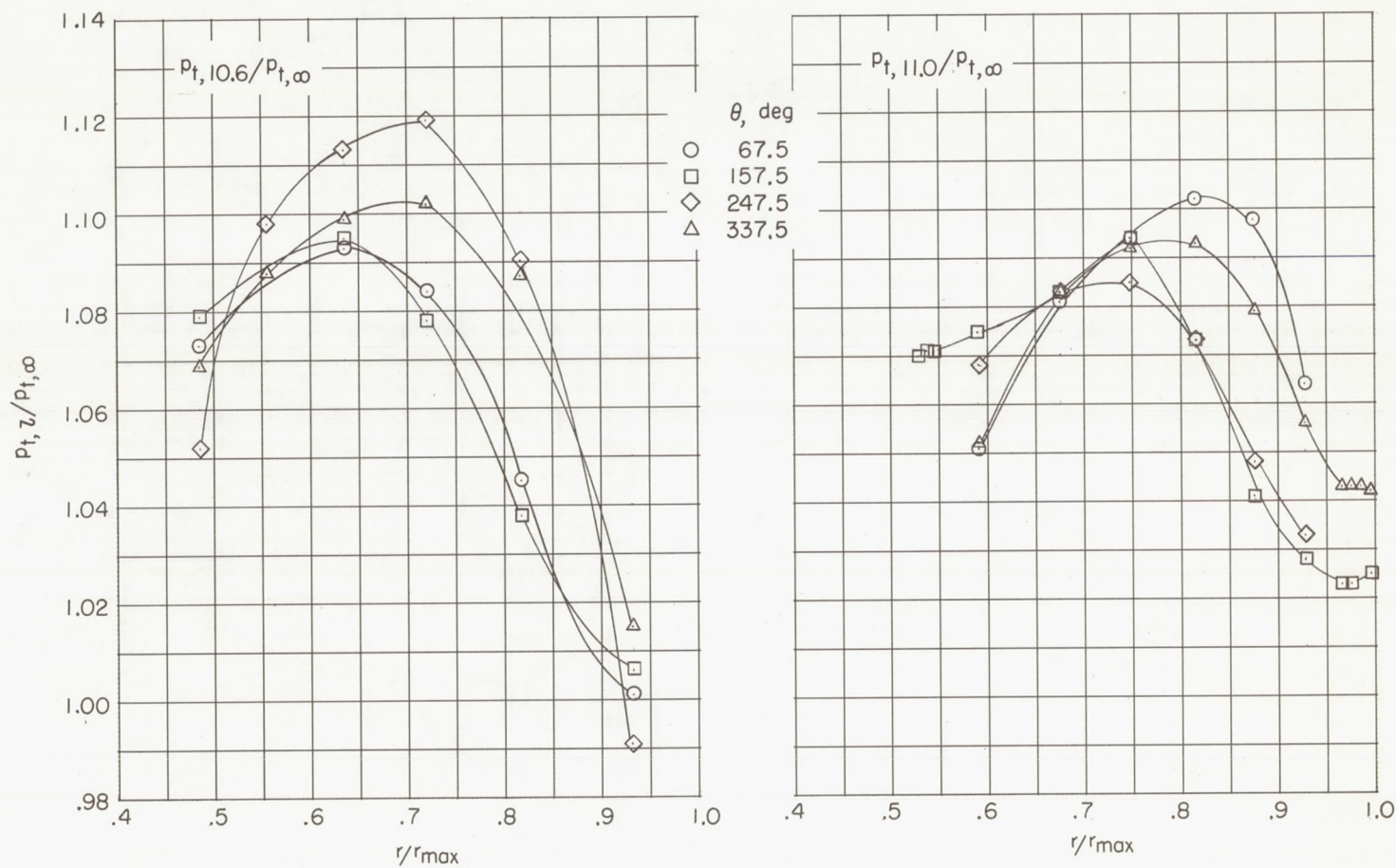
(b) $M = 0.50$; $N_F/\sqrt{\sigma} = 95.9$ percent.

Figure 26.- Continued.



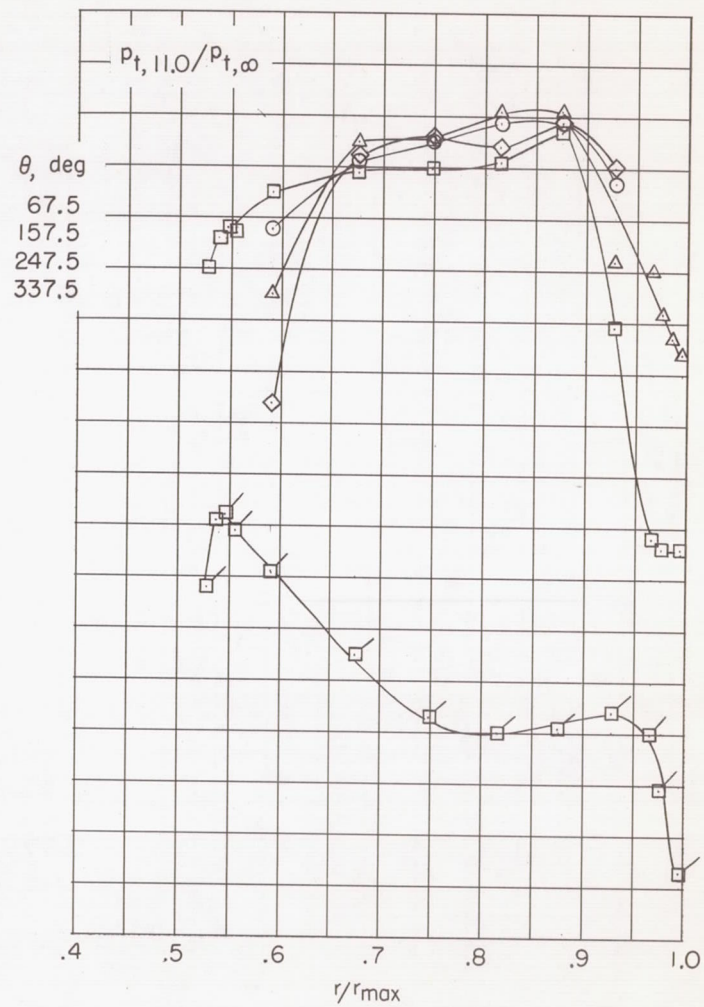
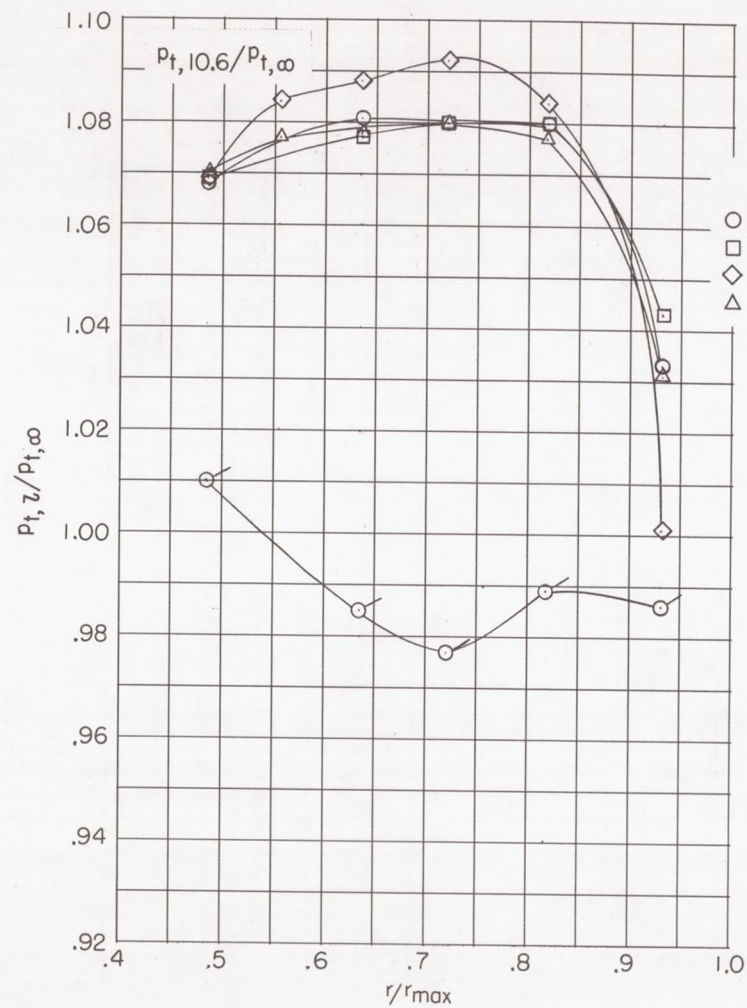
(c) $M = 0.80$; $N_F/\sqrt{\sigma} = 90.8$ percent.

Figure 26.- Concluded.



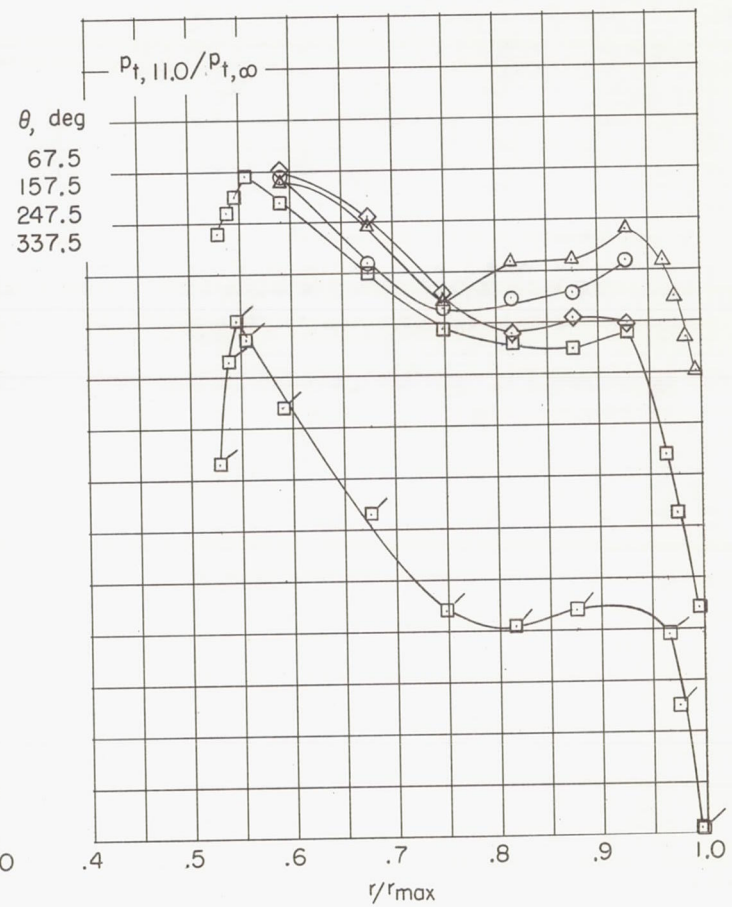
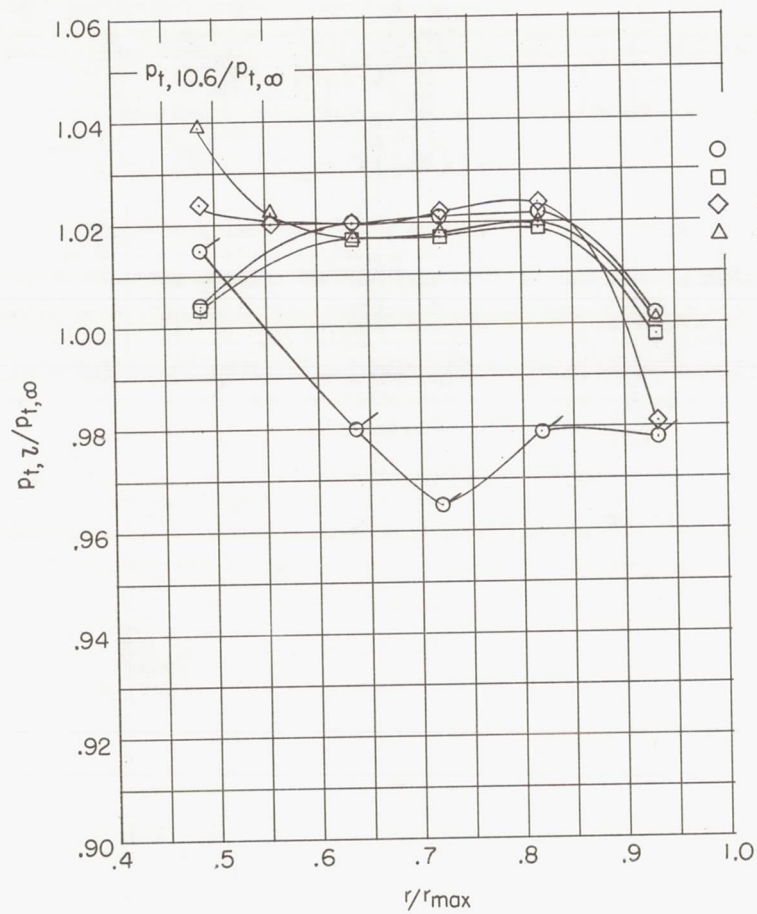
(a) $M = 0.30$; $N_F/\sqrt{\sigma} = 96.8$ percent.

Figure 27.- Fan-rotor-discharge and fan-discharge total-pressure profiles for configuration 112. Flagged data indicate windmill conditions.



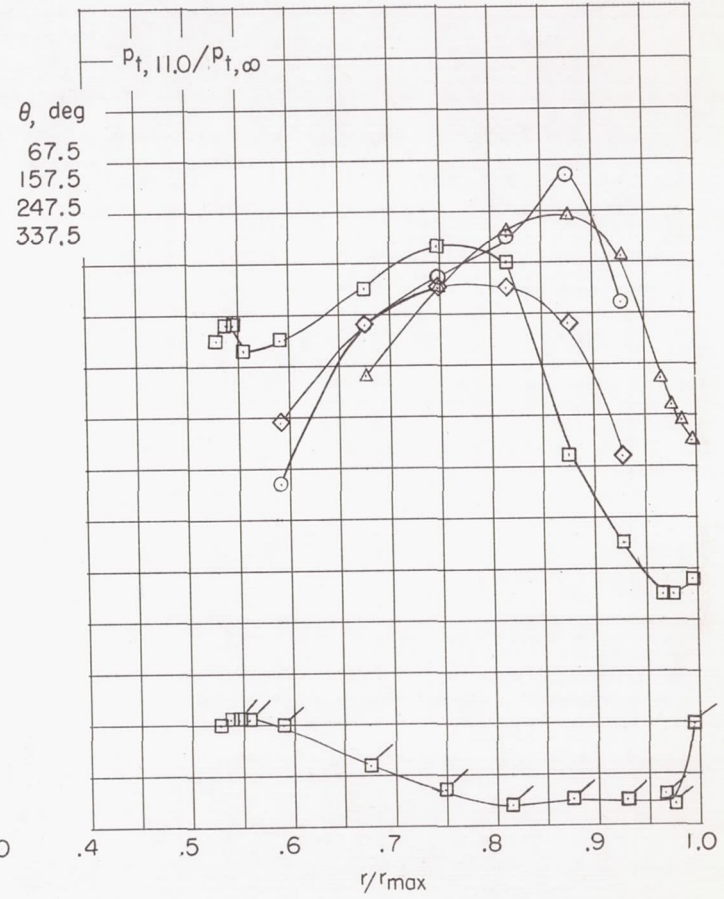
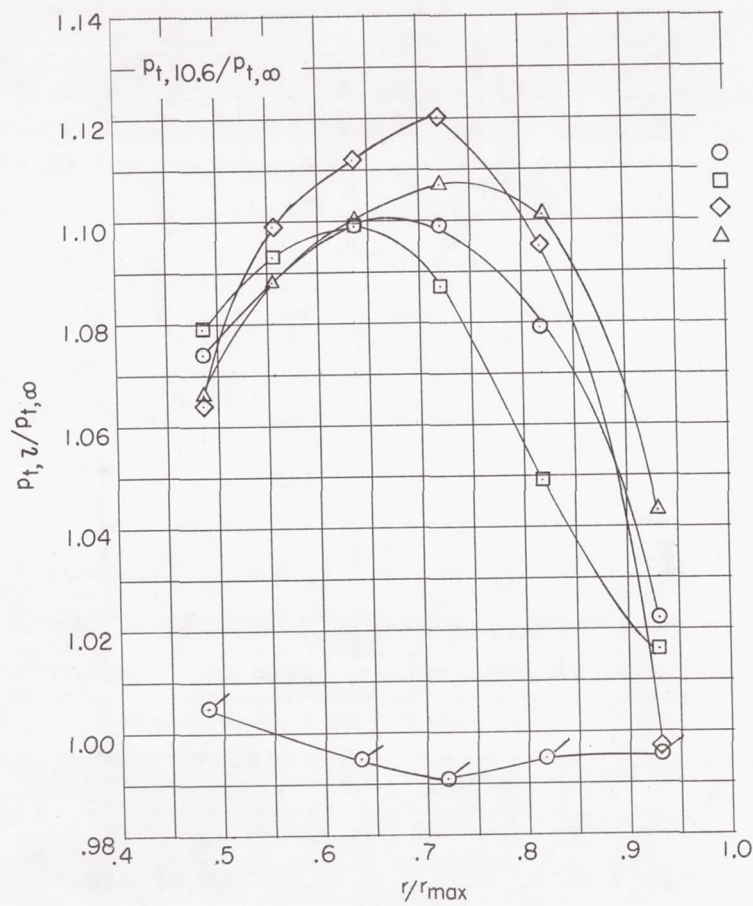
(b) $M = 0.50$; $N_F/\sqrt{\sigma} = 92.9$ percent.

Figure 27.- Continued.



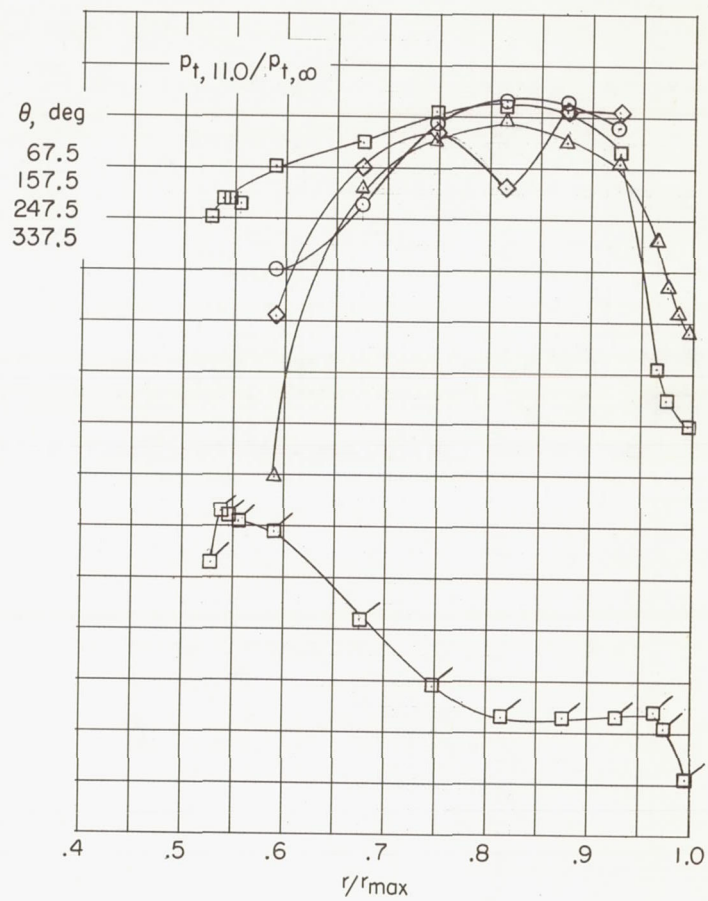
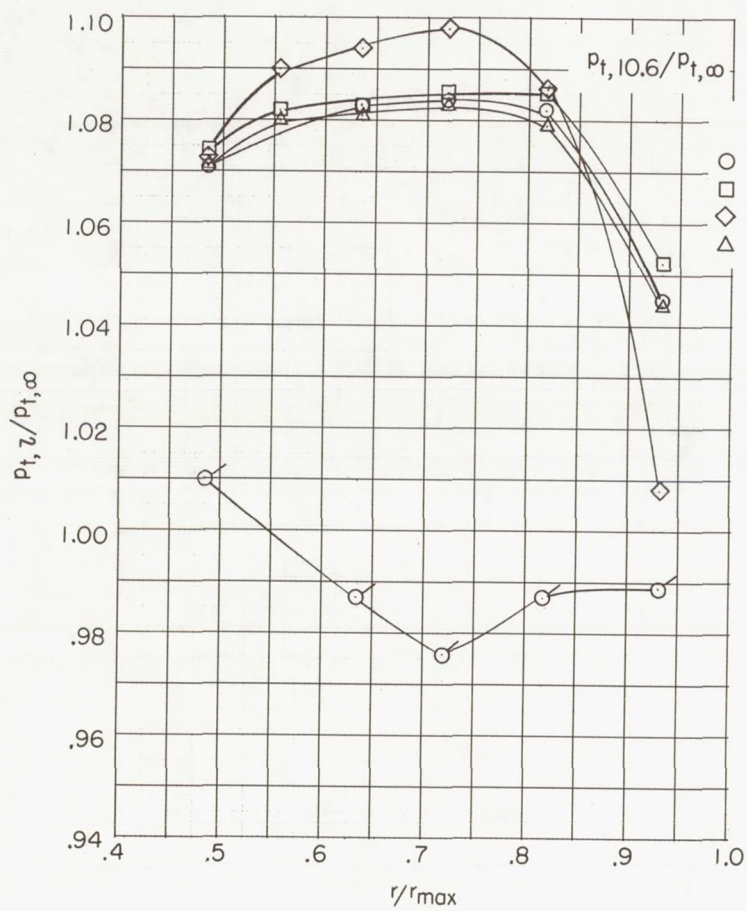
(c) $M = 0.65$; $N_F/\sqrt{\sigma} = 77.0$ percent.

Figure 27.- Concluded.



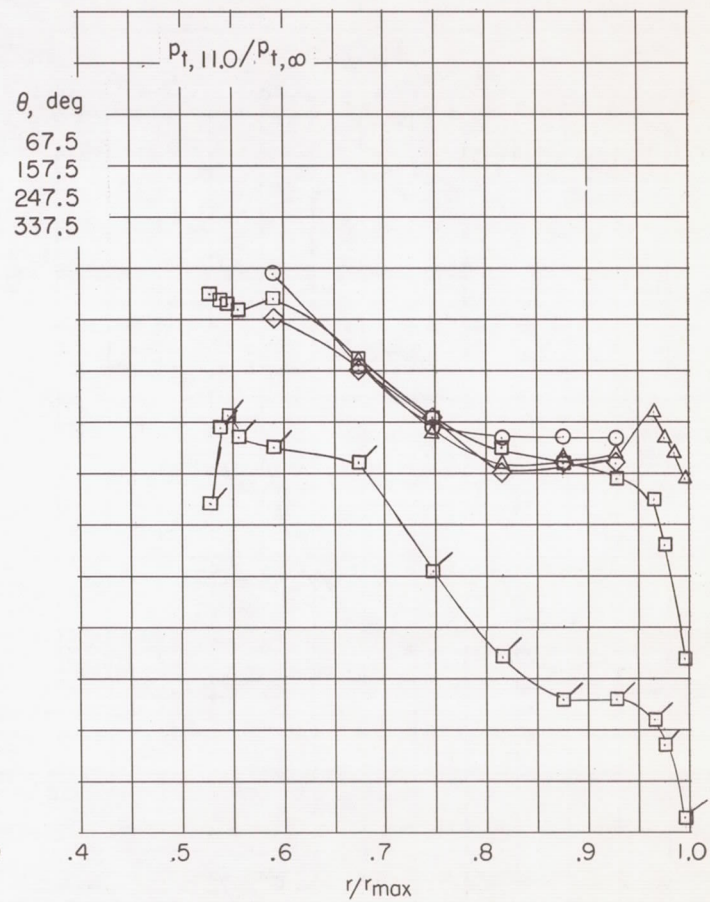
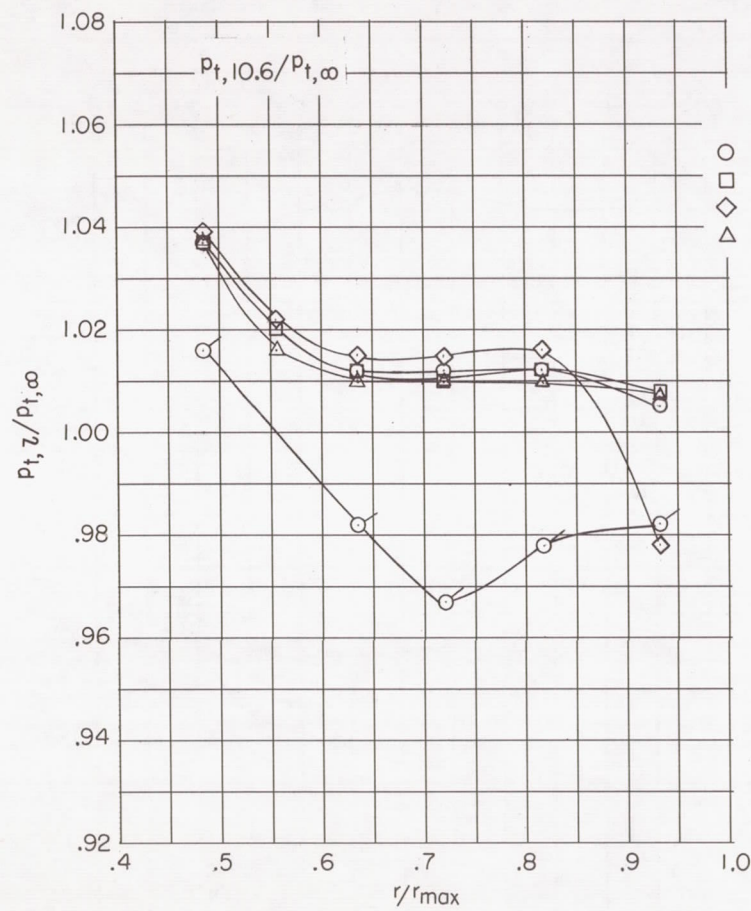
(a) $M = 0.30$; $N_F/\sqrt{\sigma} = 97.5$ percent.

Figure 28.- Fan-rotor-discharge and fan-discharge total-pressure profiles for configuration 322. Flagged data indicate windmill conditions.



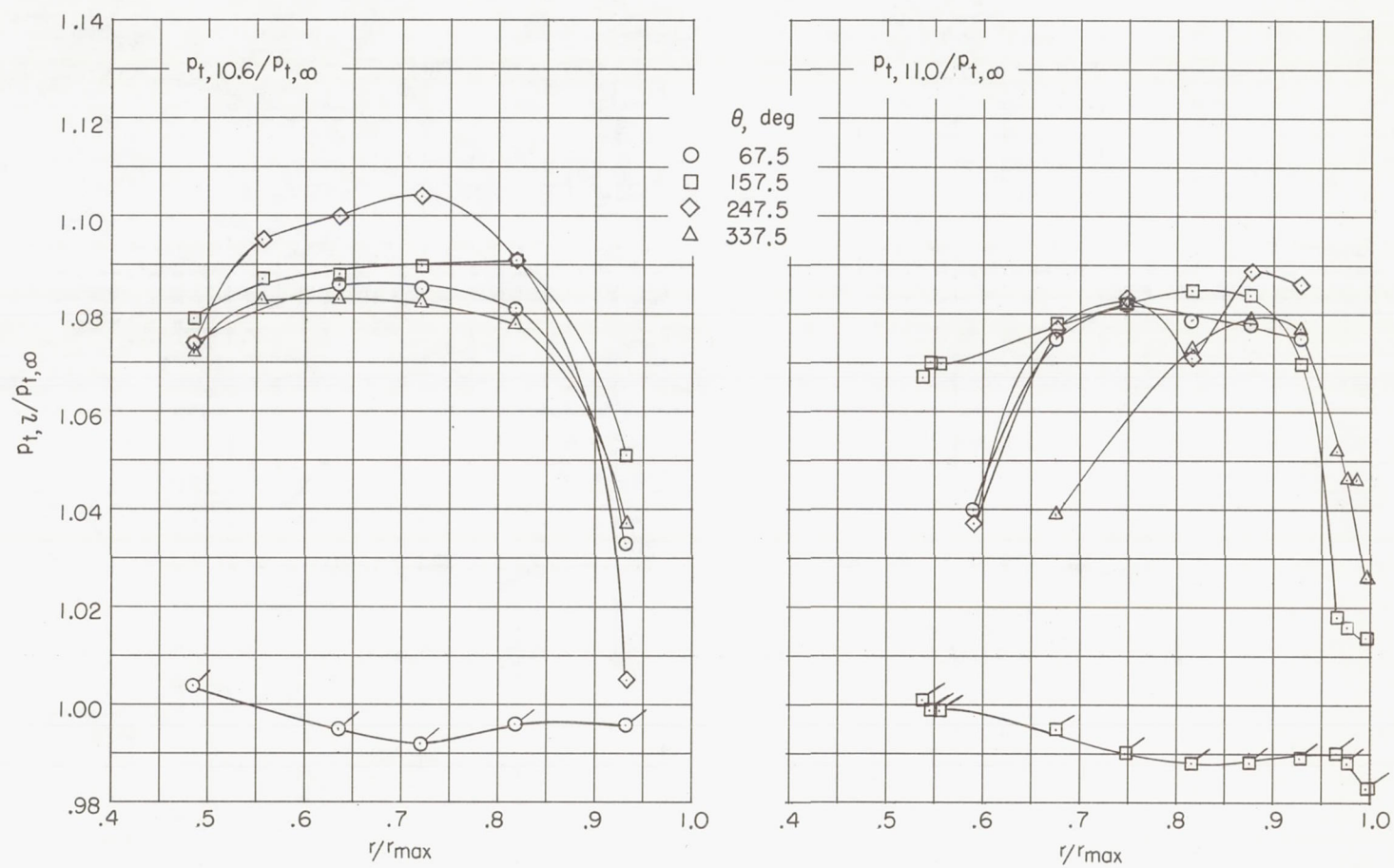
(b) $M = 0.50$; $N_F/\sqrt{\sigma} = 94.4$ percent.

Figure 28.- Continued.



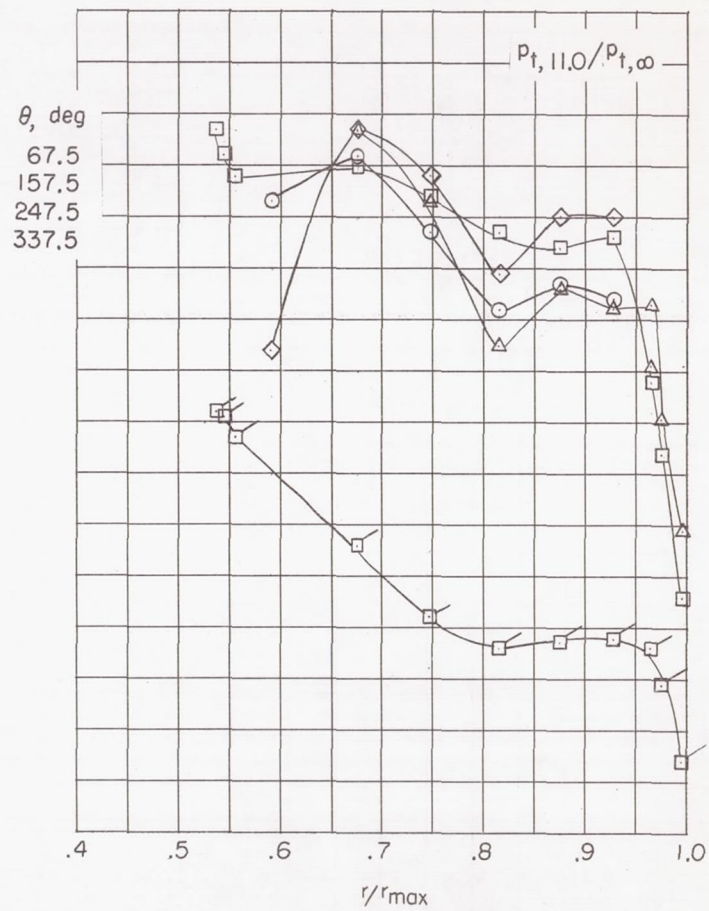
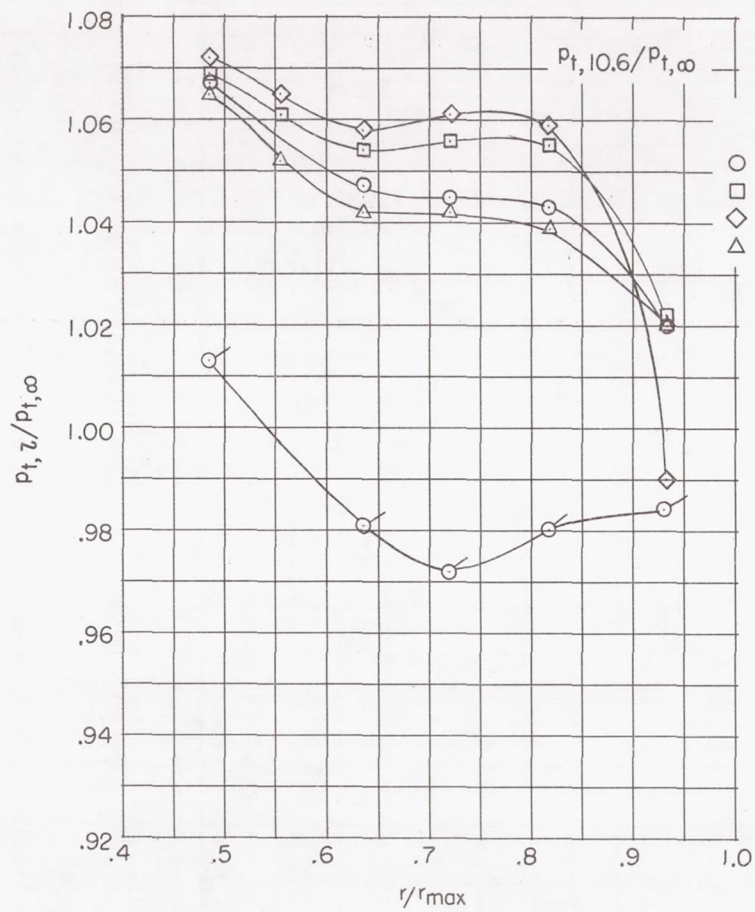
(c) $M = 0.65$; $N_F/\sqrt{\sigma} = 76.5$ percent.

Figure 28.- Concluded.



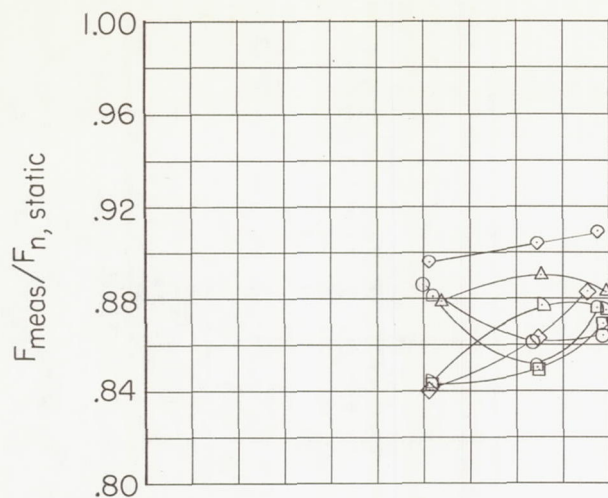
(a) $M = 0.20$; $N_F/\sqrt{\sigma} = 97.2$ percent.

Figure 29.- Fan-rotor-discharge and fan-discharge total-pressure profiles for configuration 243. Flagged data indicate windmill conditions.



(b) $M = 0.40$; $N_F/\sqrt{\sigma} = 97.1$ percent.

Figure 29.- Concluded.



Configuration	A_e (in.)	A_e (cm)
○ 144	433	2793
□ 244	433	2793
◇ 344	433	2793
△ 123	433	2793
▷ 113	433	2793
▷ 112	566	3652
▷ 322	566	3652
◇ 243	770	4968

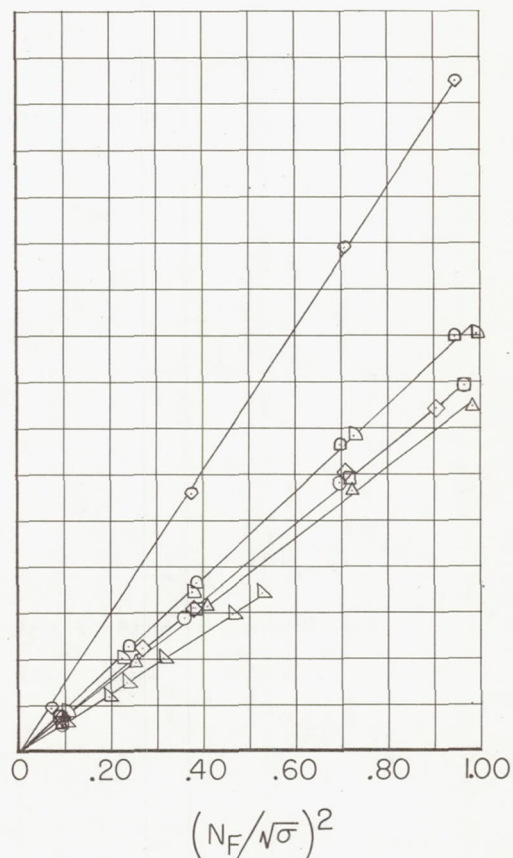
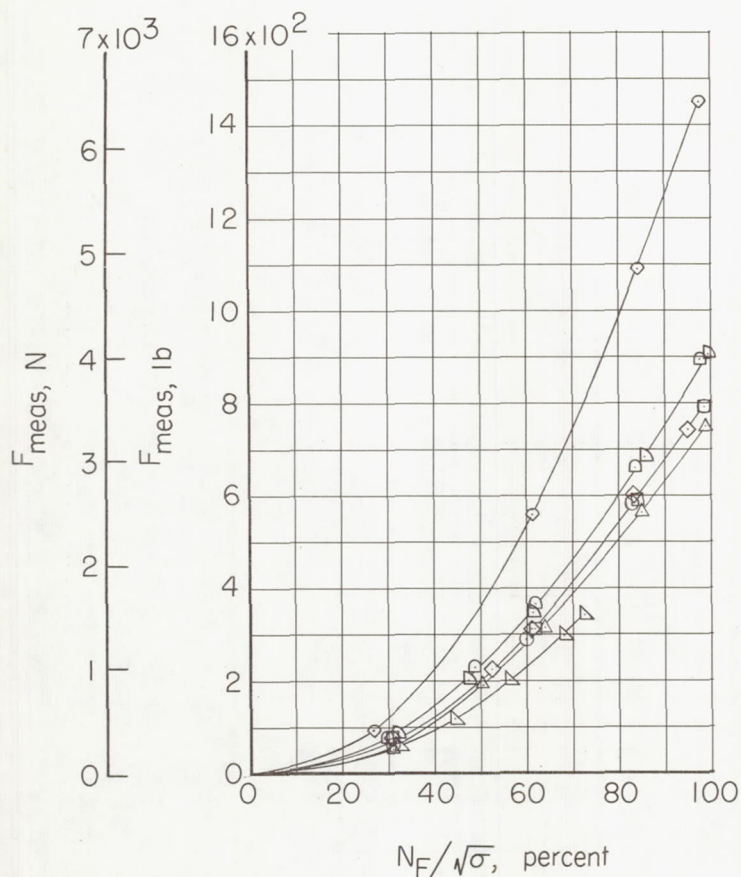
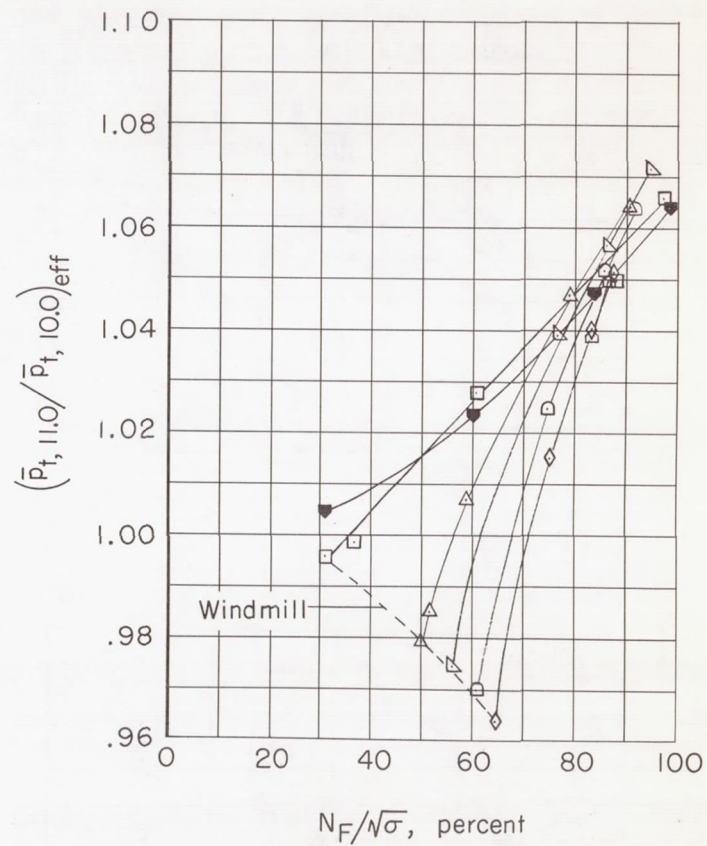
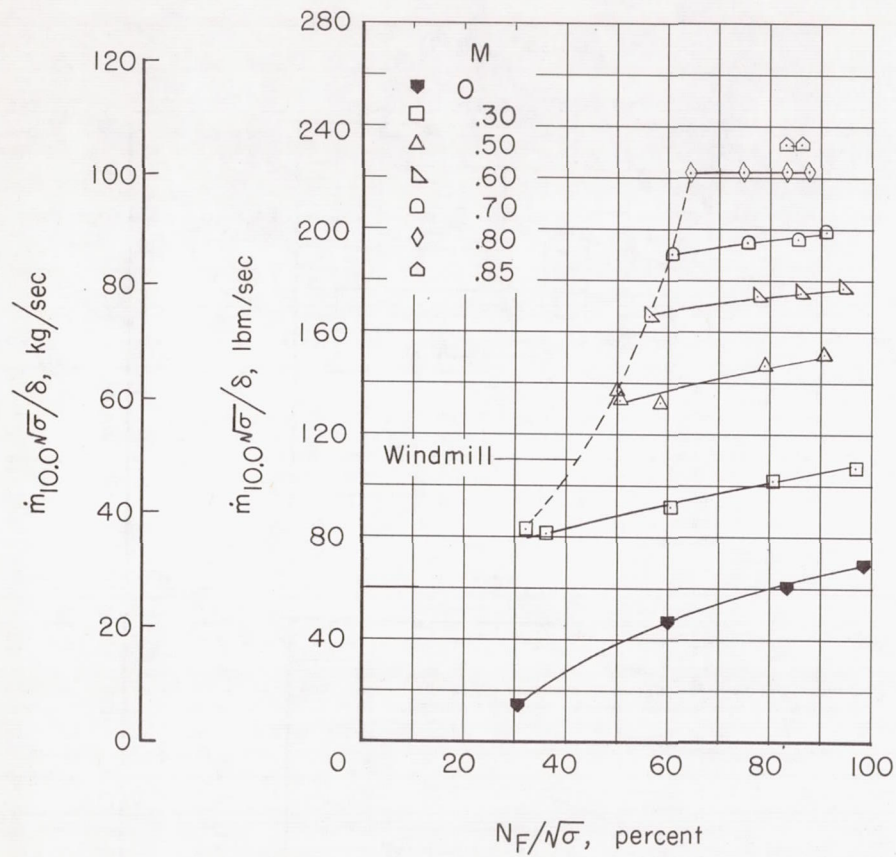
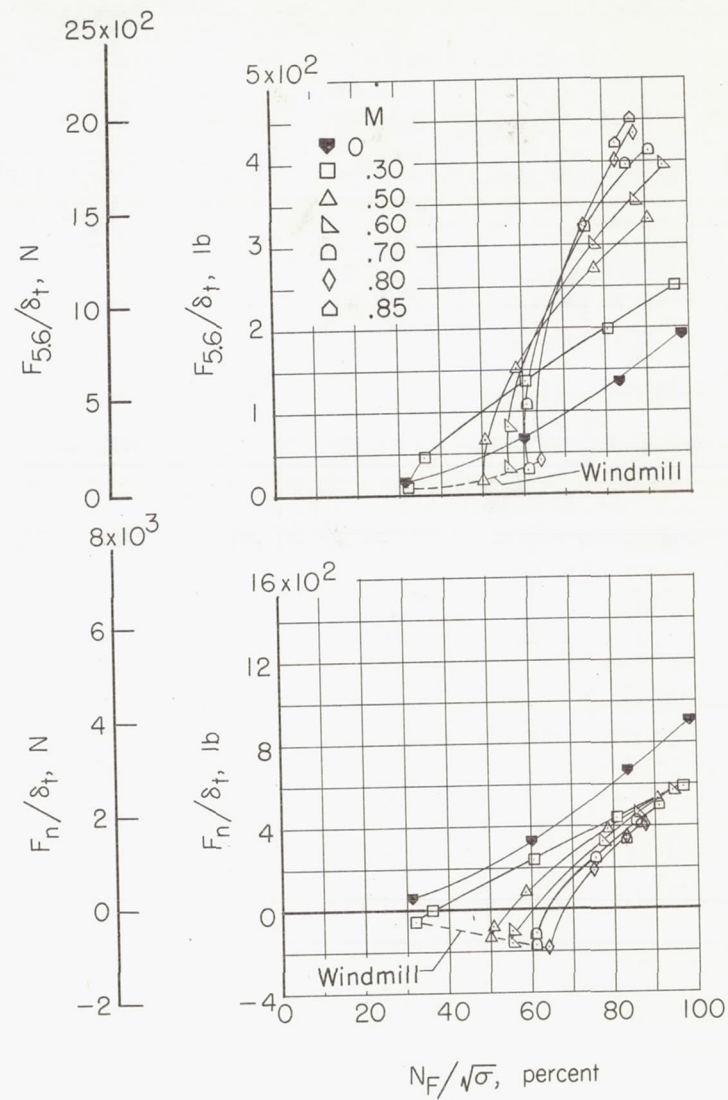
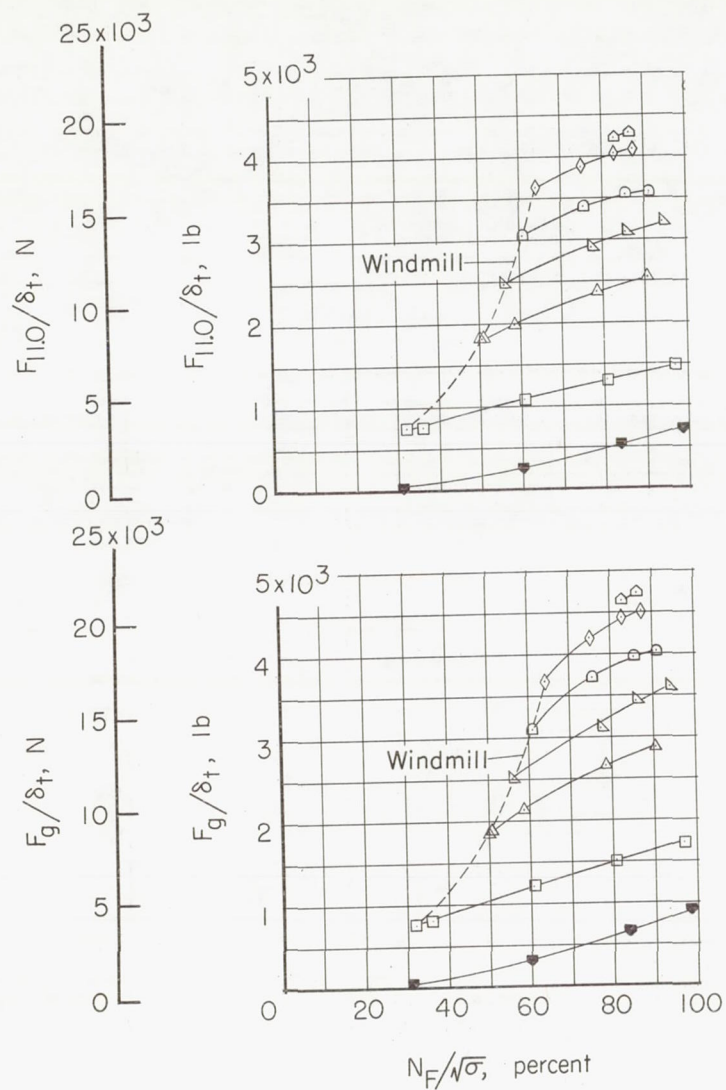


Figure 30.- Measured static-thrust and static-thrust-ratio characteristics for various configurations tested.



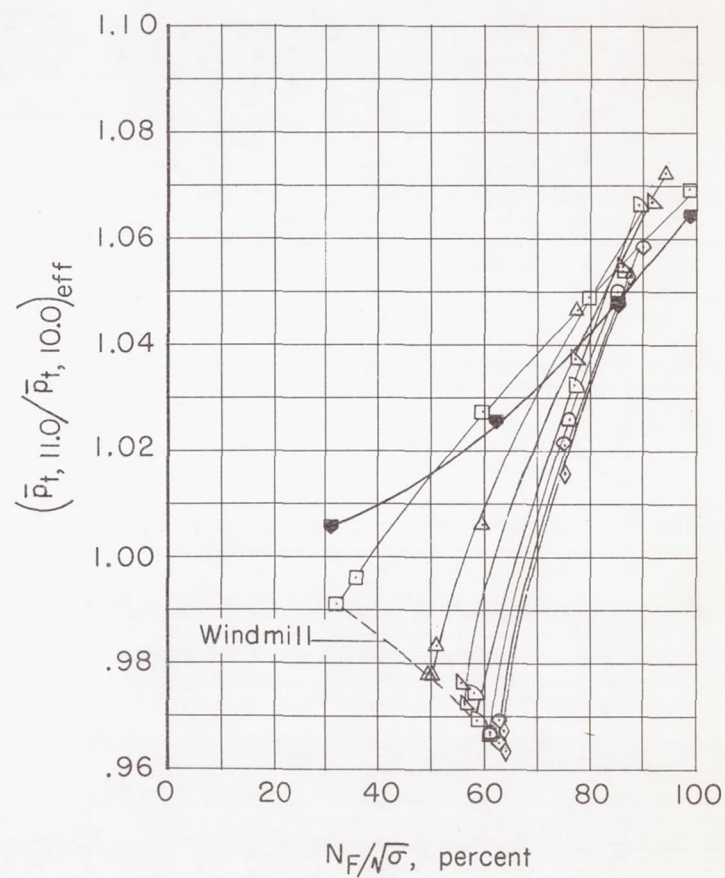
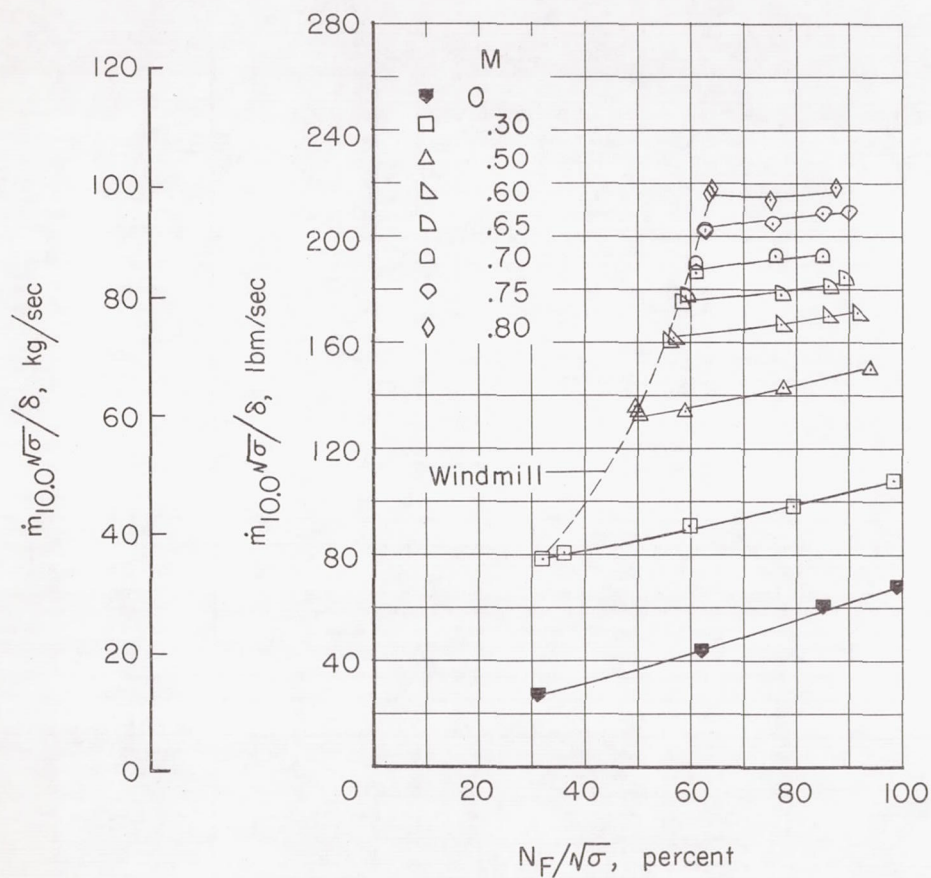
(a) Fan mass-flow rate and pressure ratio.

Figure 31.- Fan performance characteristics for configuration 144.



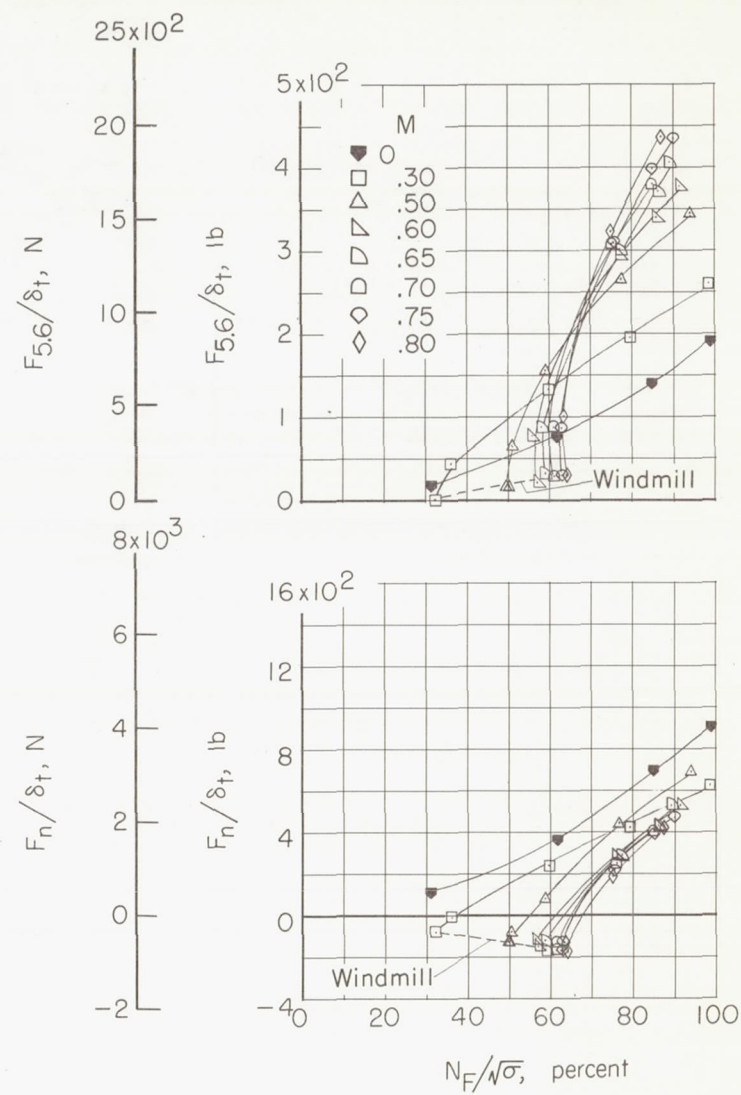
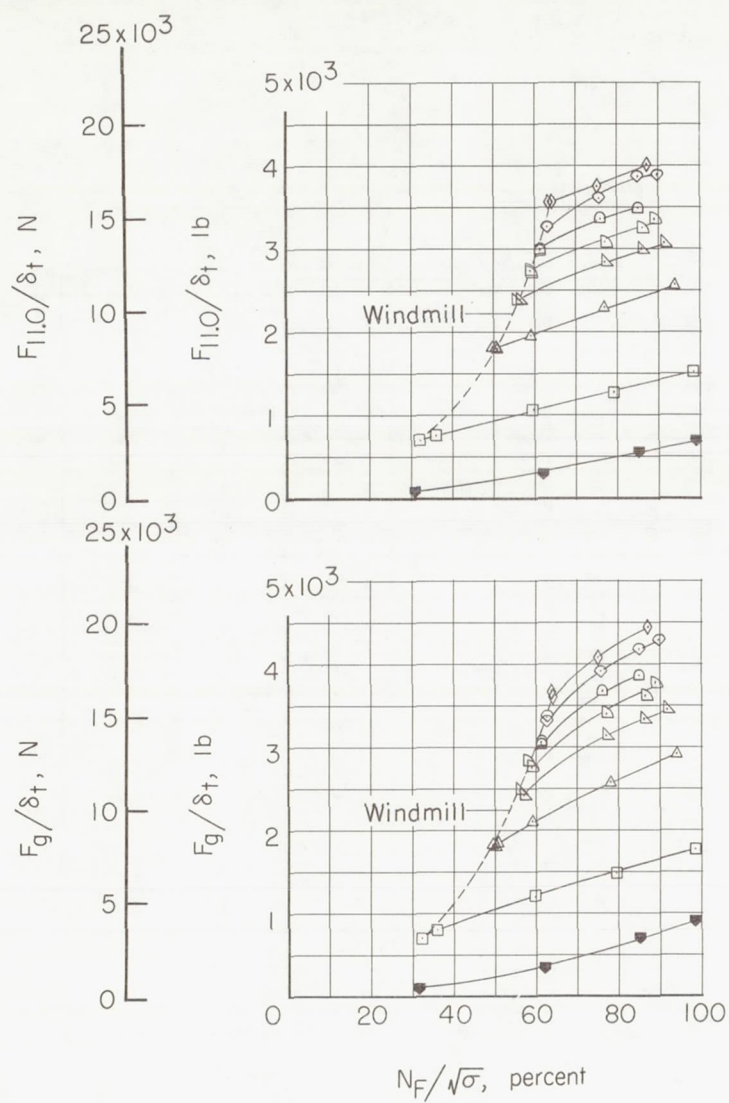
(b) Fan thrust characteristics.

Figure 31.- Concluded.



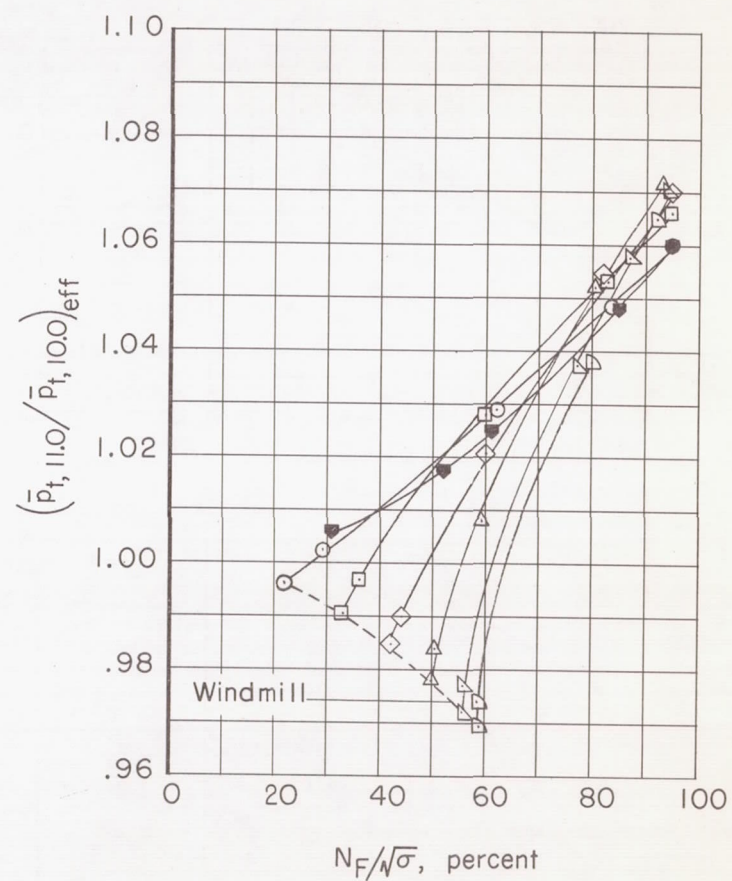
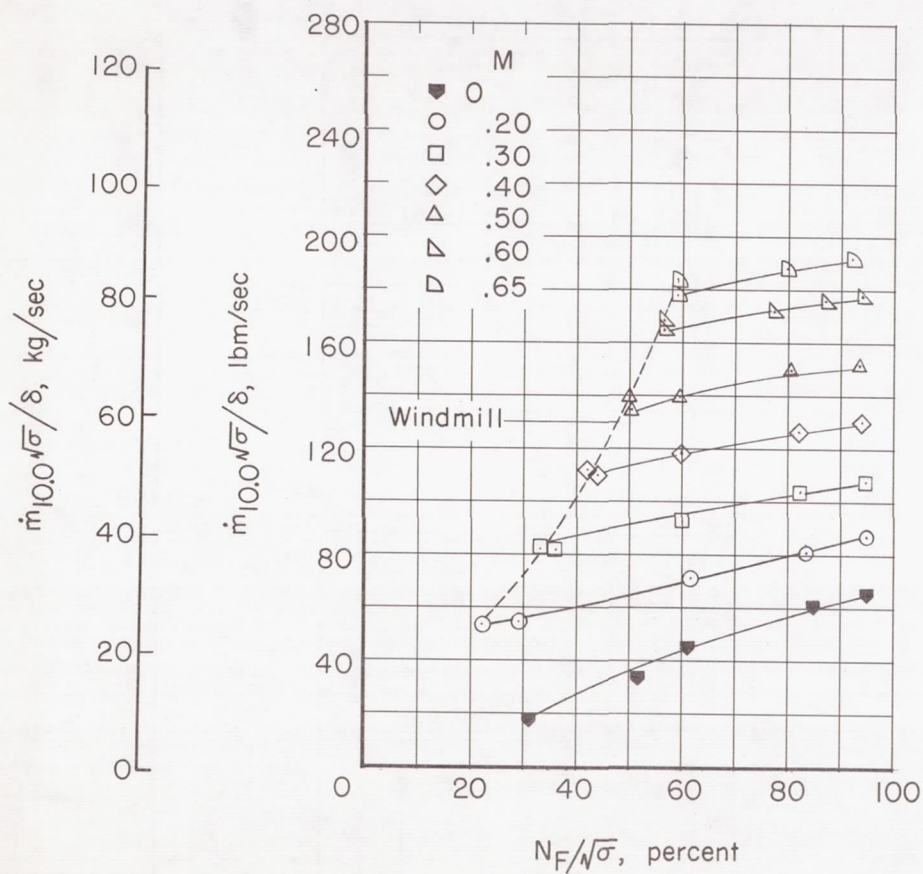
(a) Fan mass-flow rate and pressure ratio.

Figure 32.- Fan performance characteristics for configuration 244.



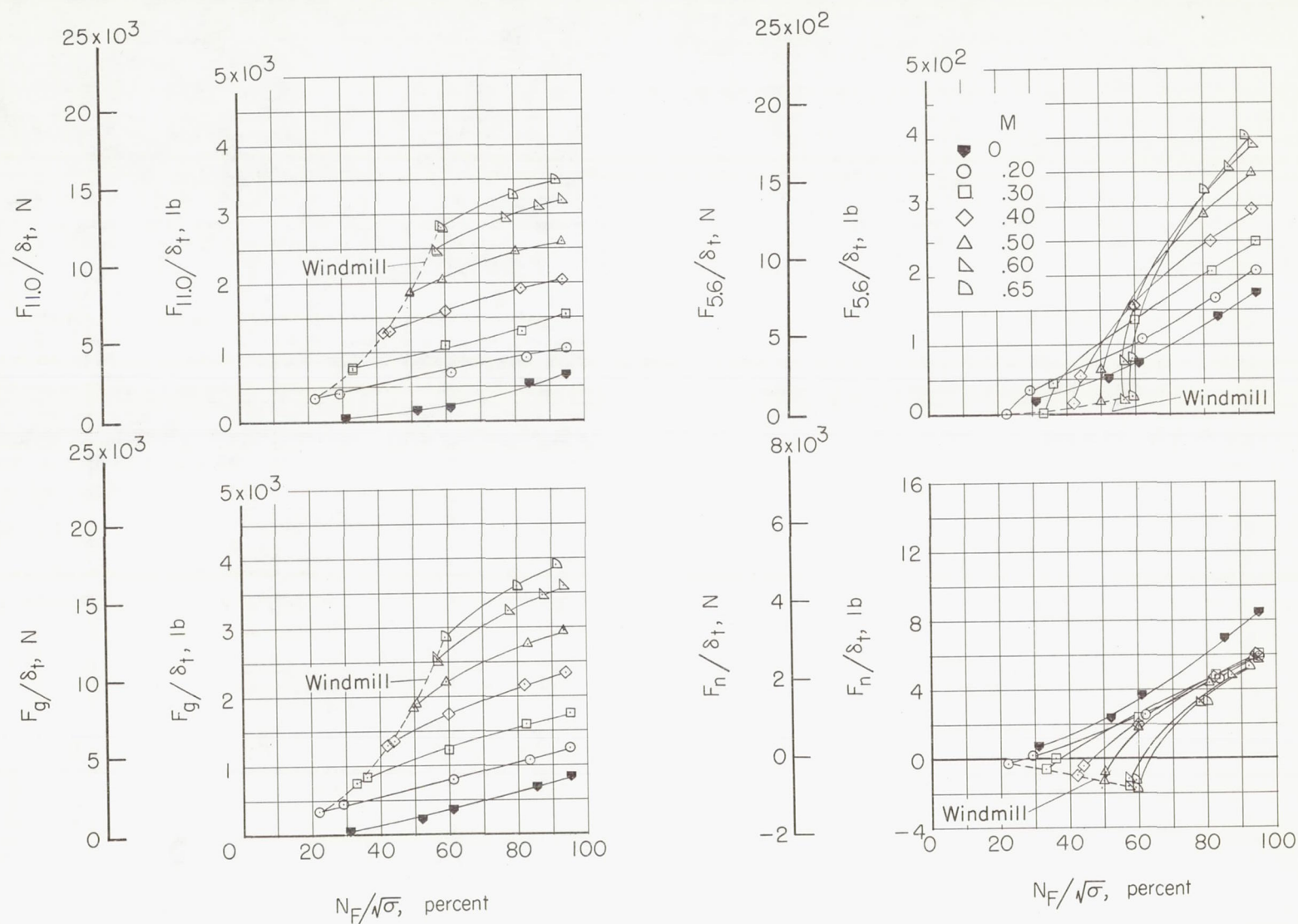
(b) Fan thrust characteristics.

Figure 32.- Concluded.



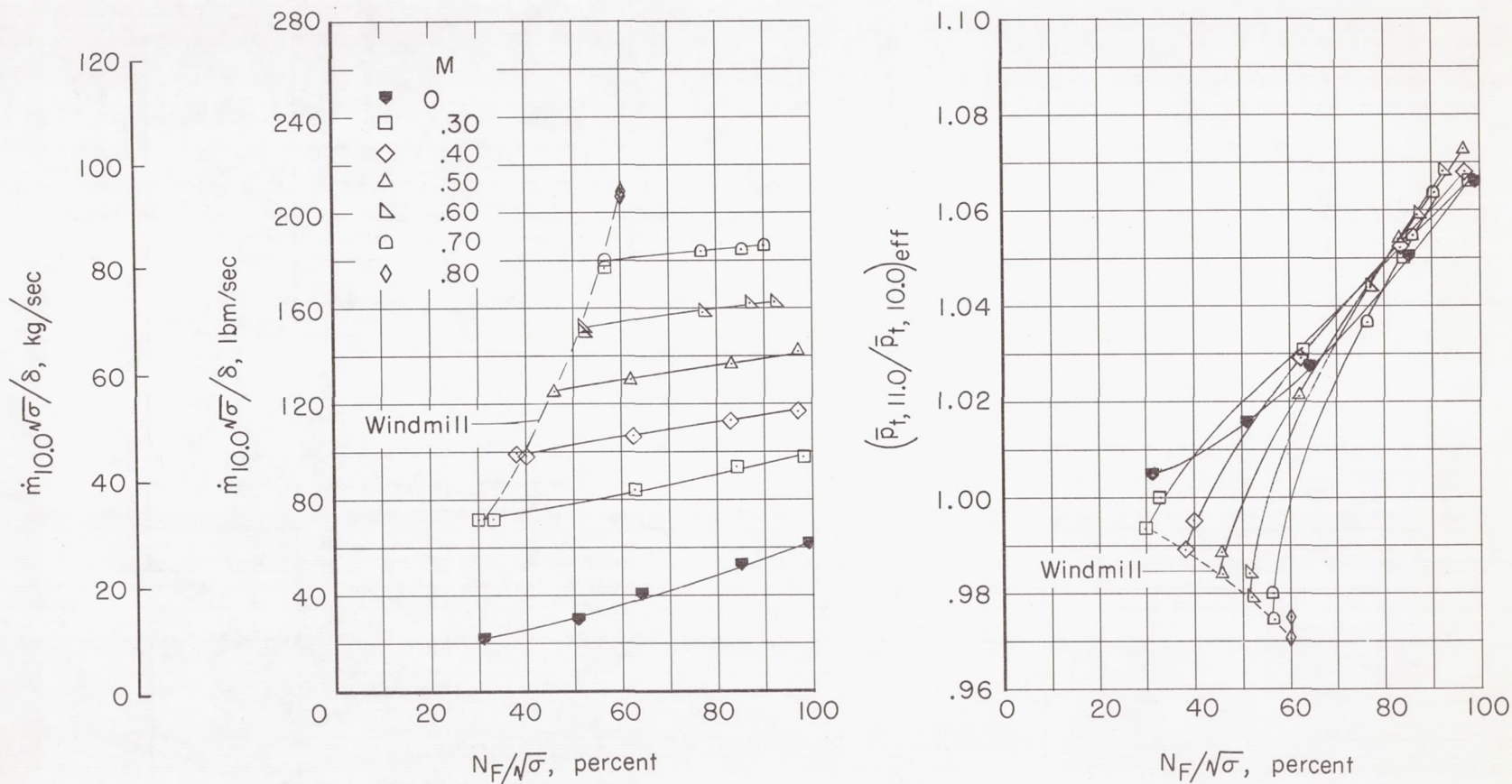
(a) Fan mass-flow rate and pressure ratio.

Figure 33.- Fan performance characteristics for configuration 344.



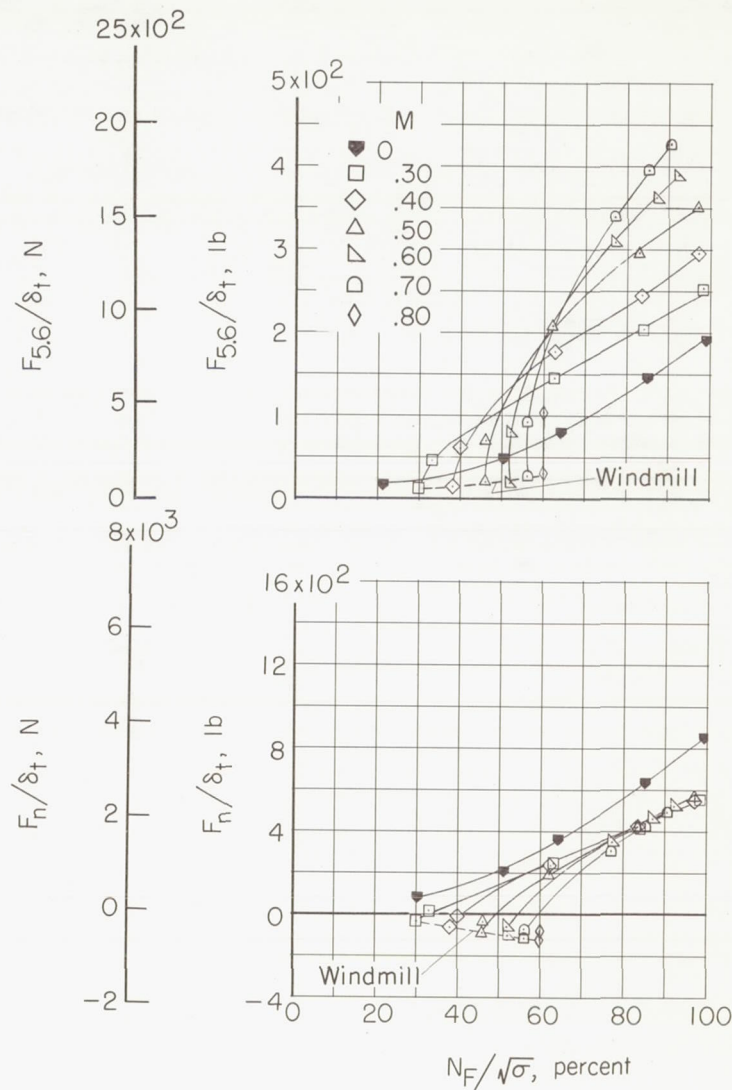
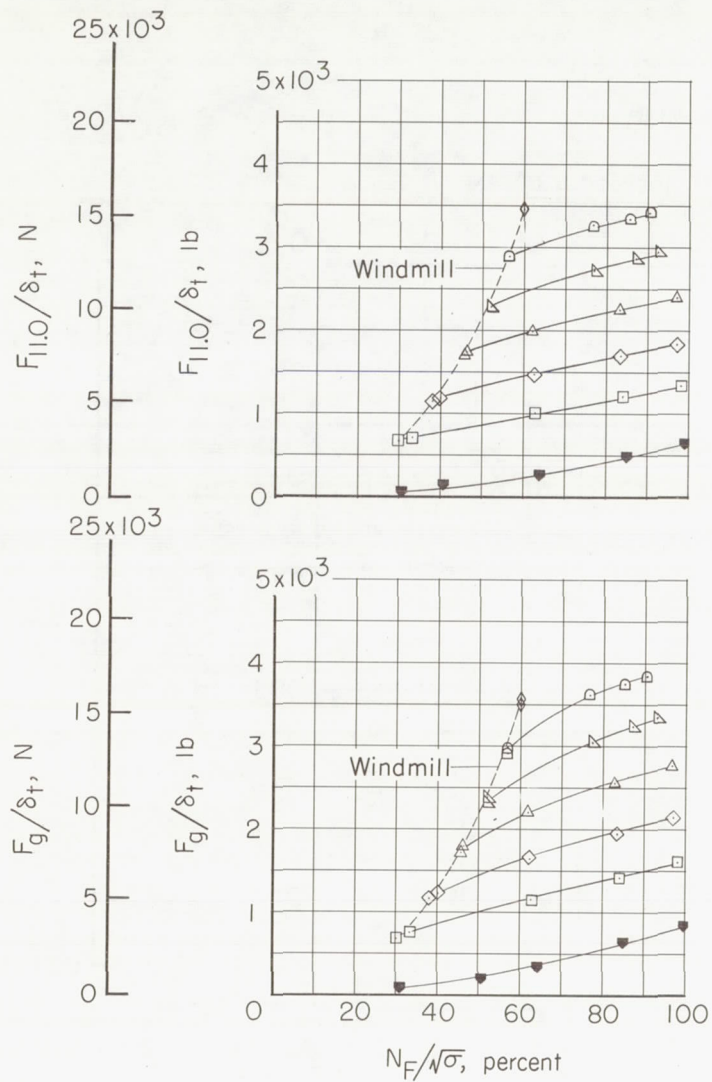
(b) Fan thrust characteristics.

Figure 33.- Concluded.



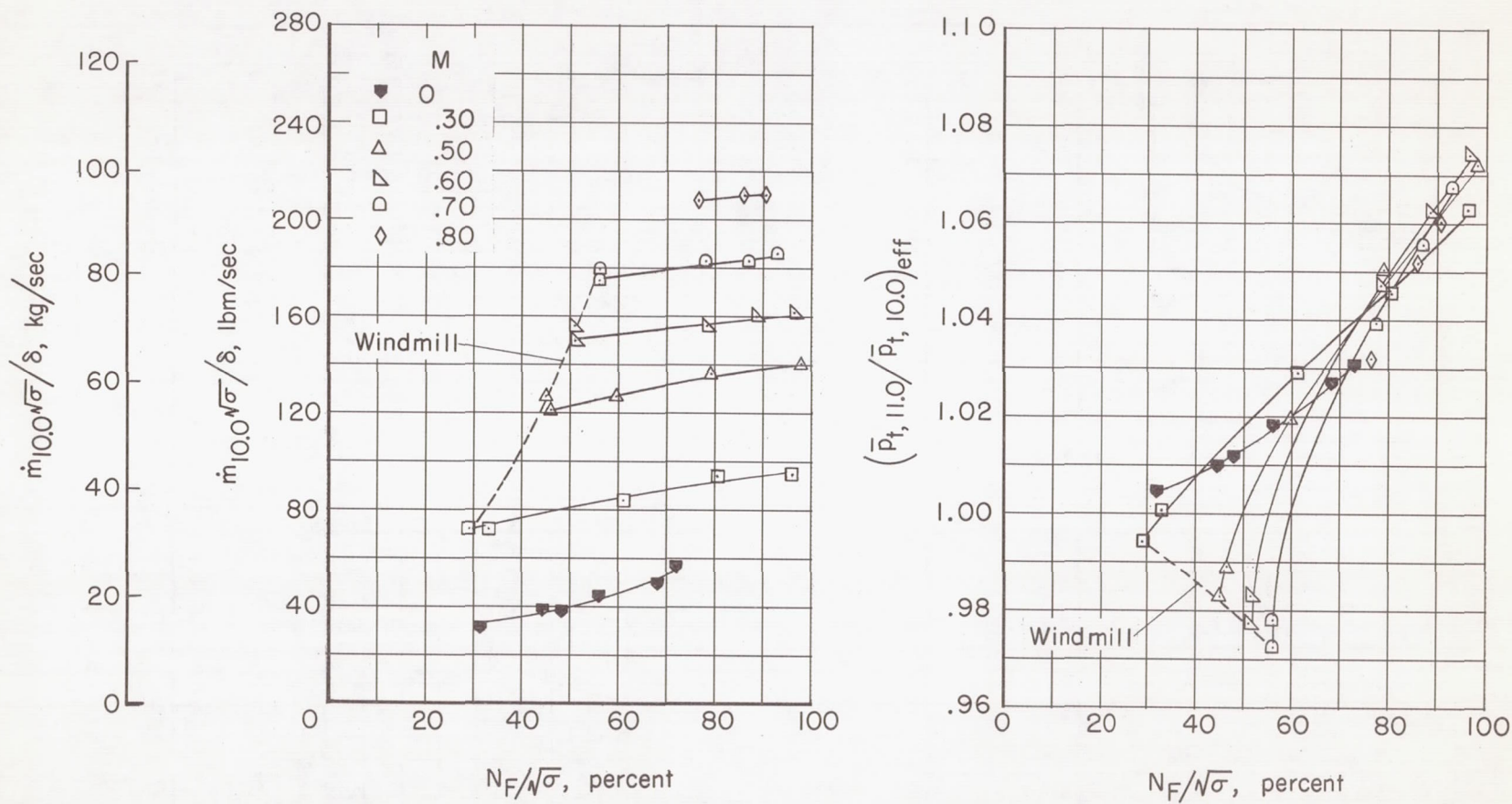
(a) Fan mass-flow rate and pressure ratio.

Figure 34.- Fan performance characteristics for configuration 123.



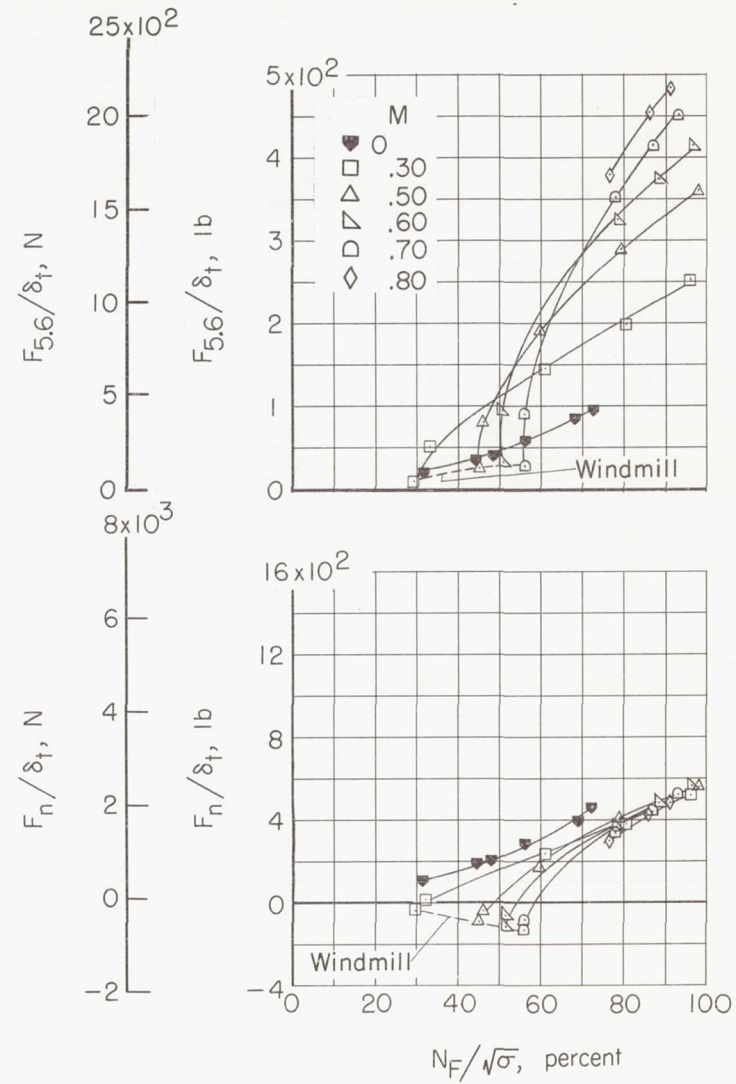
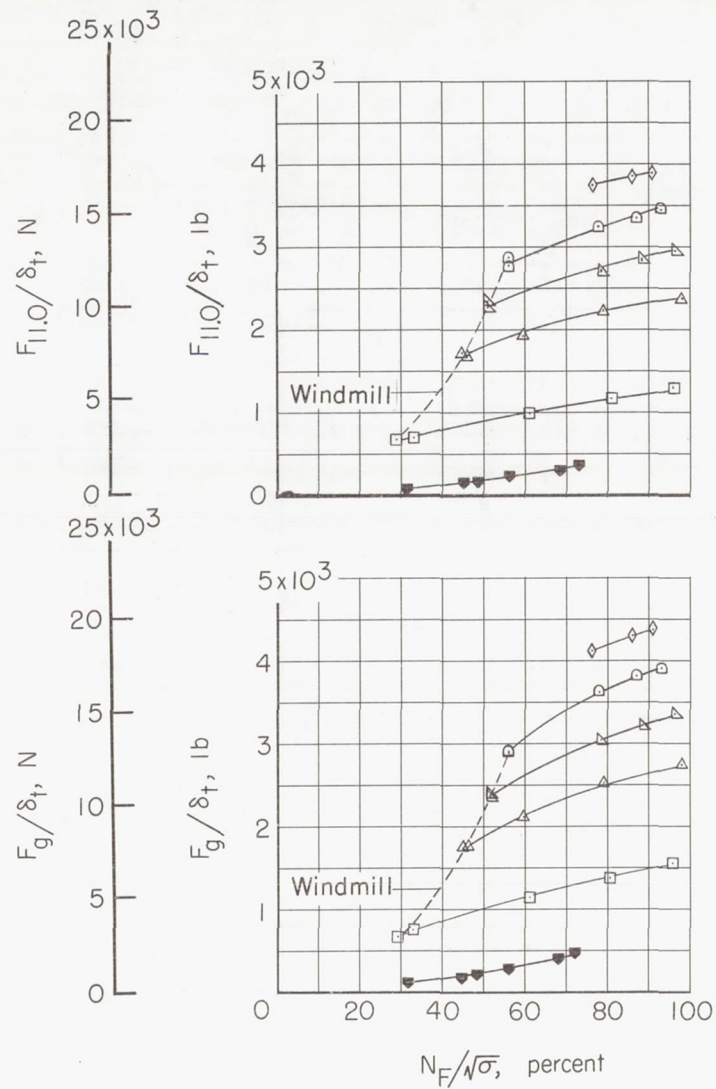
(b) Fan thrust characteristics.

Figure 34.- Concluded.



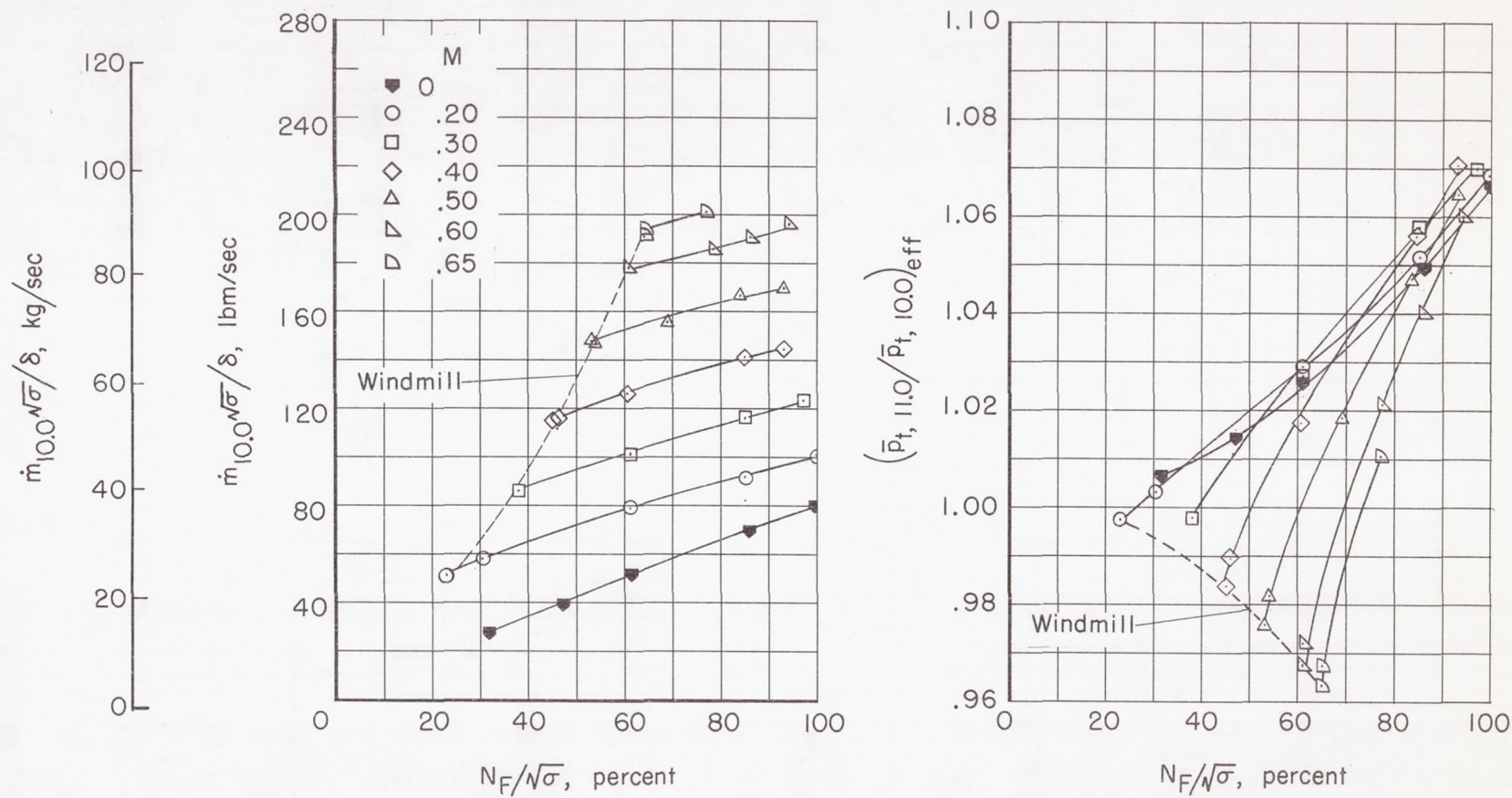
(a) Fan mass-flow rate and pressure ratio.

Figure 35.- Fan performance characteristics for configuration 113.



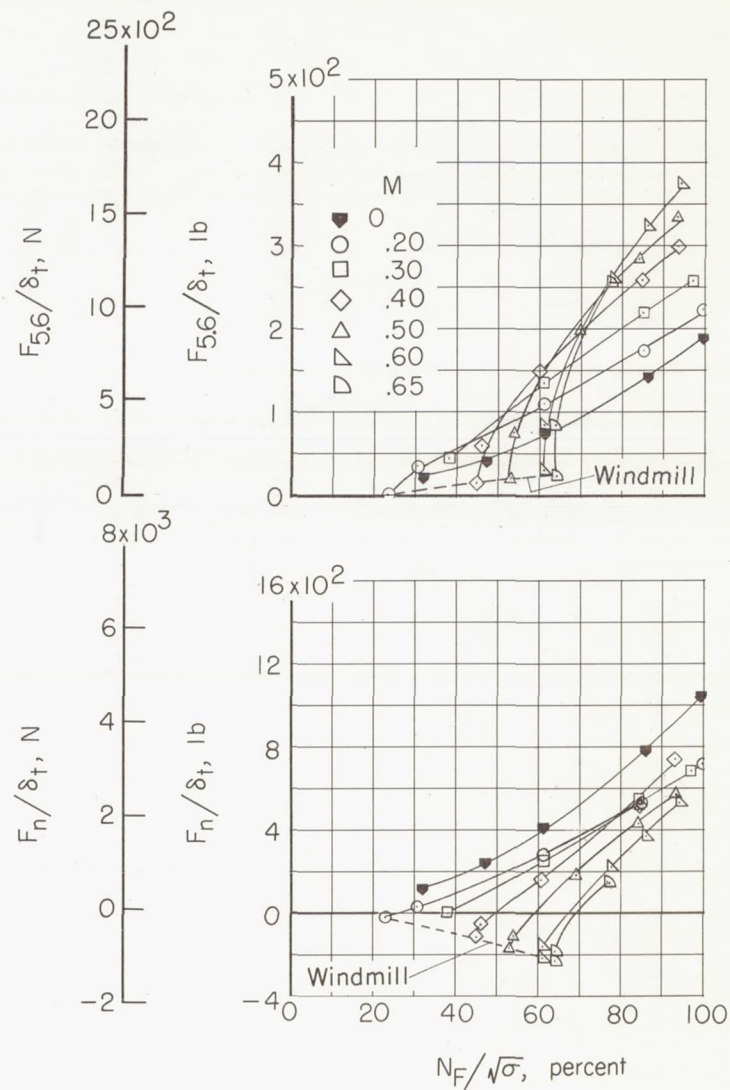
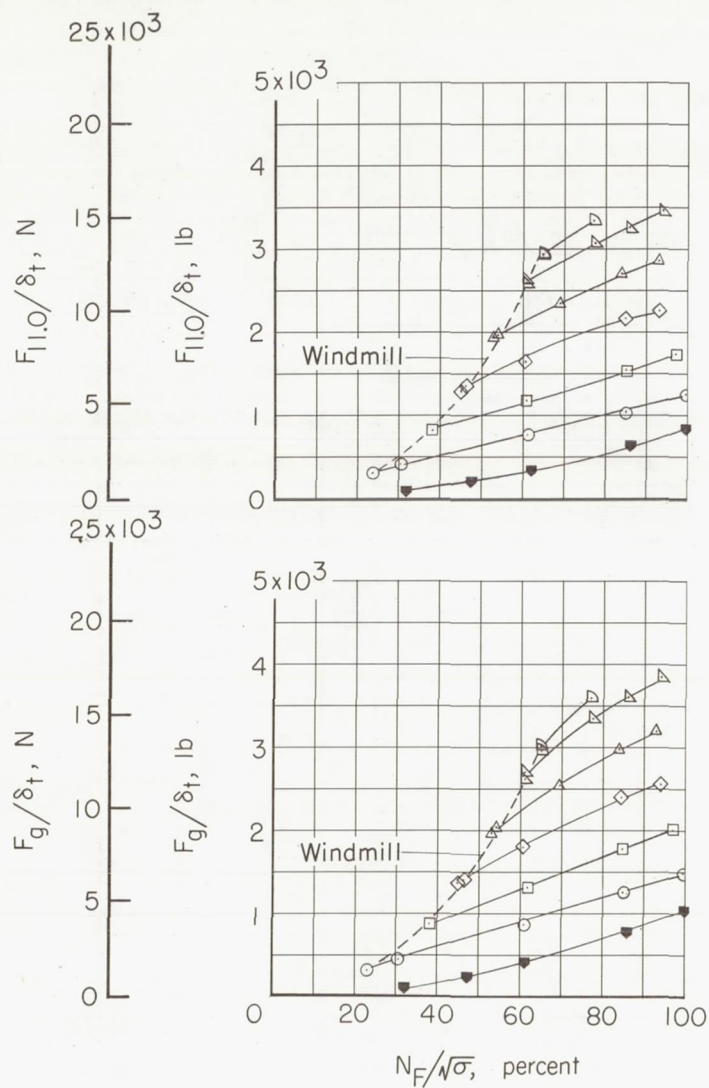
(b) Fan thrust characteristics.

Figure 35.- Concluded.



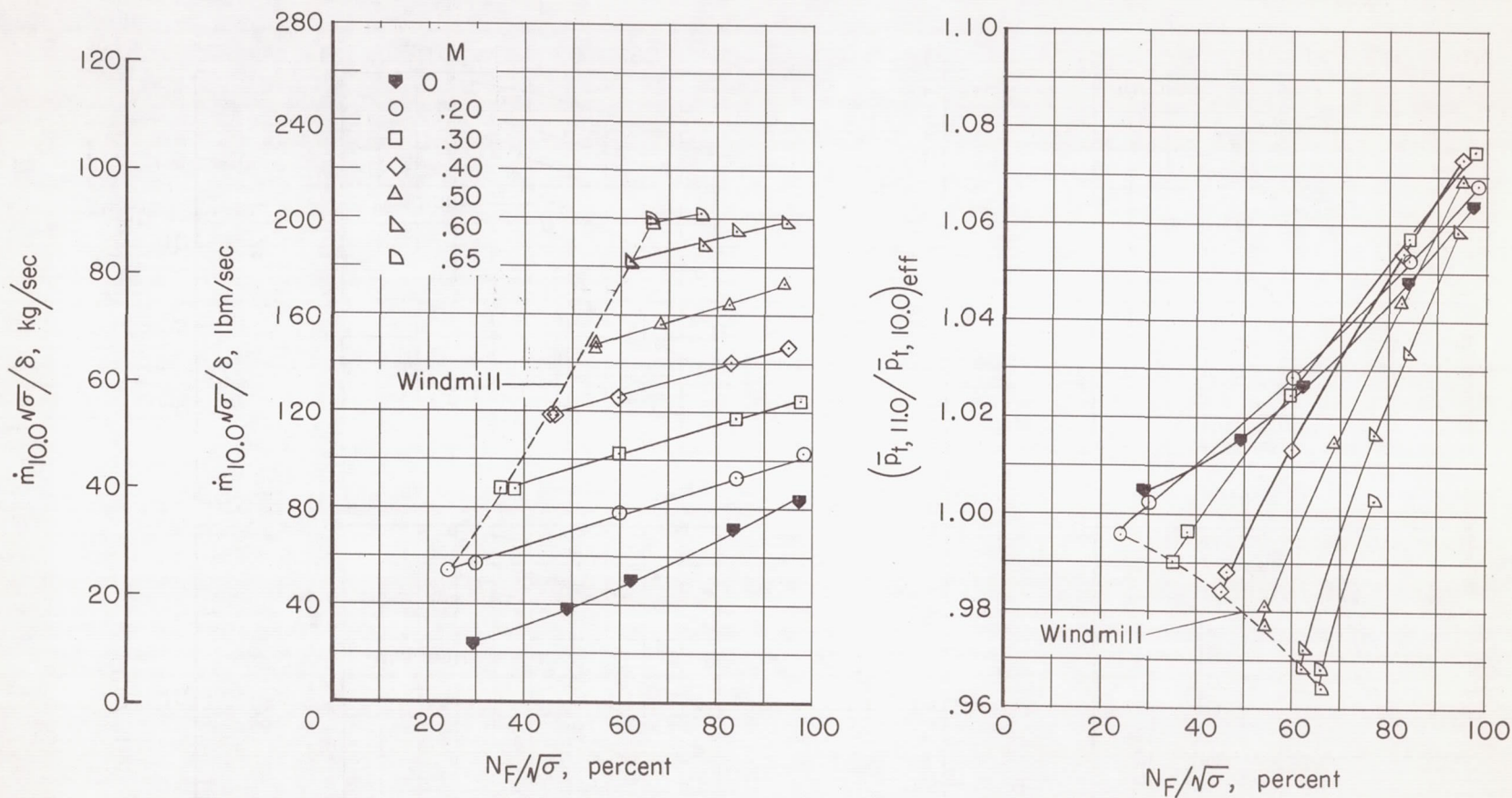
(a) Fan mass-flow rate and pressure ratio.

Figure 36.- Fan performance characteristics for configuration 112.



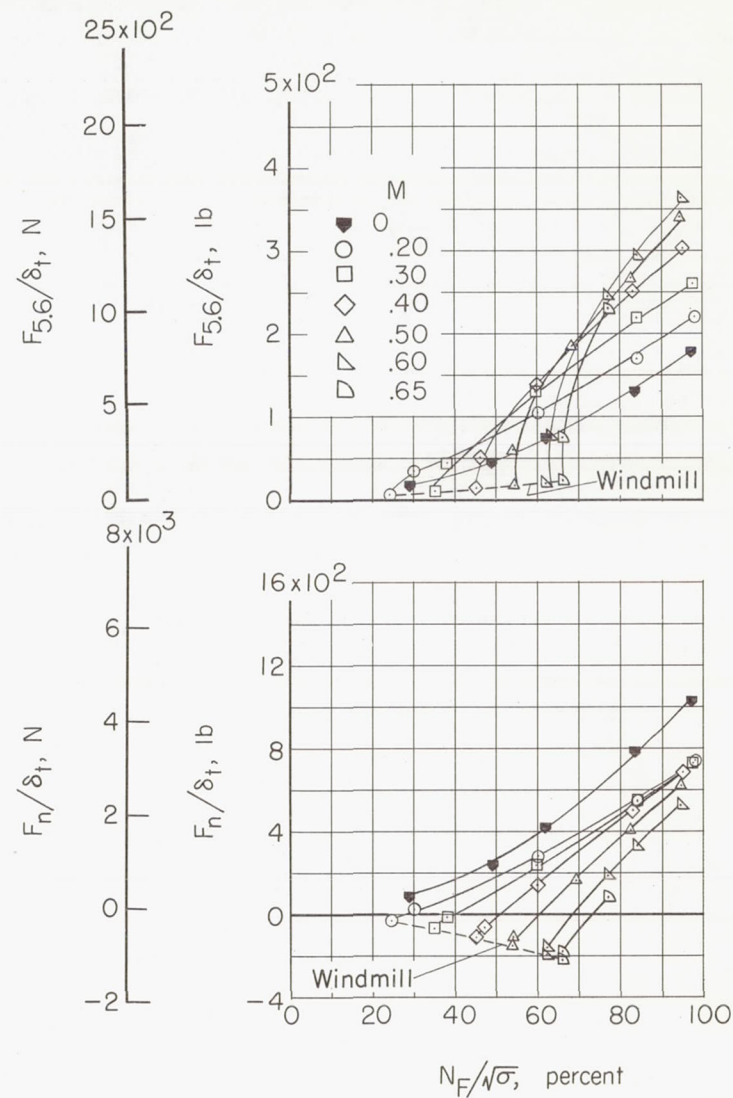
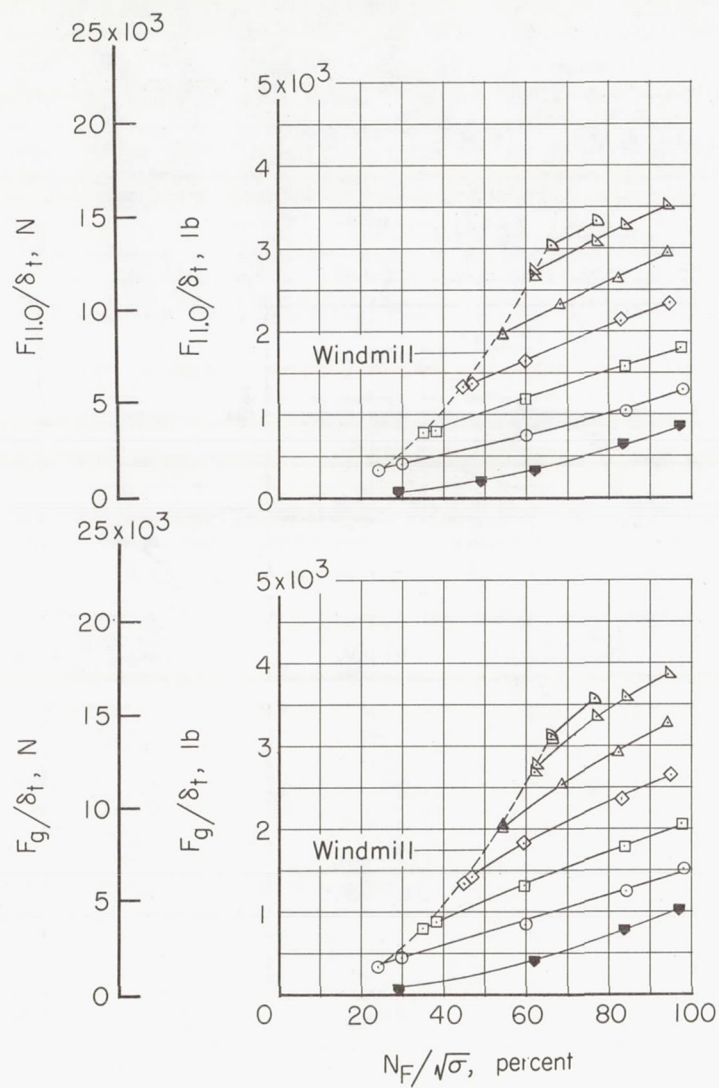
(b) Fan thrust characteristics.

Figure 36.- Concluded.



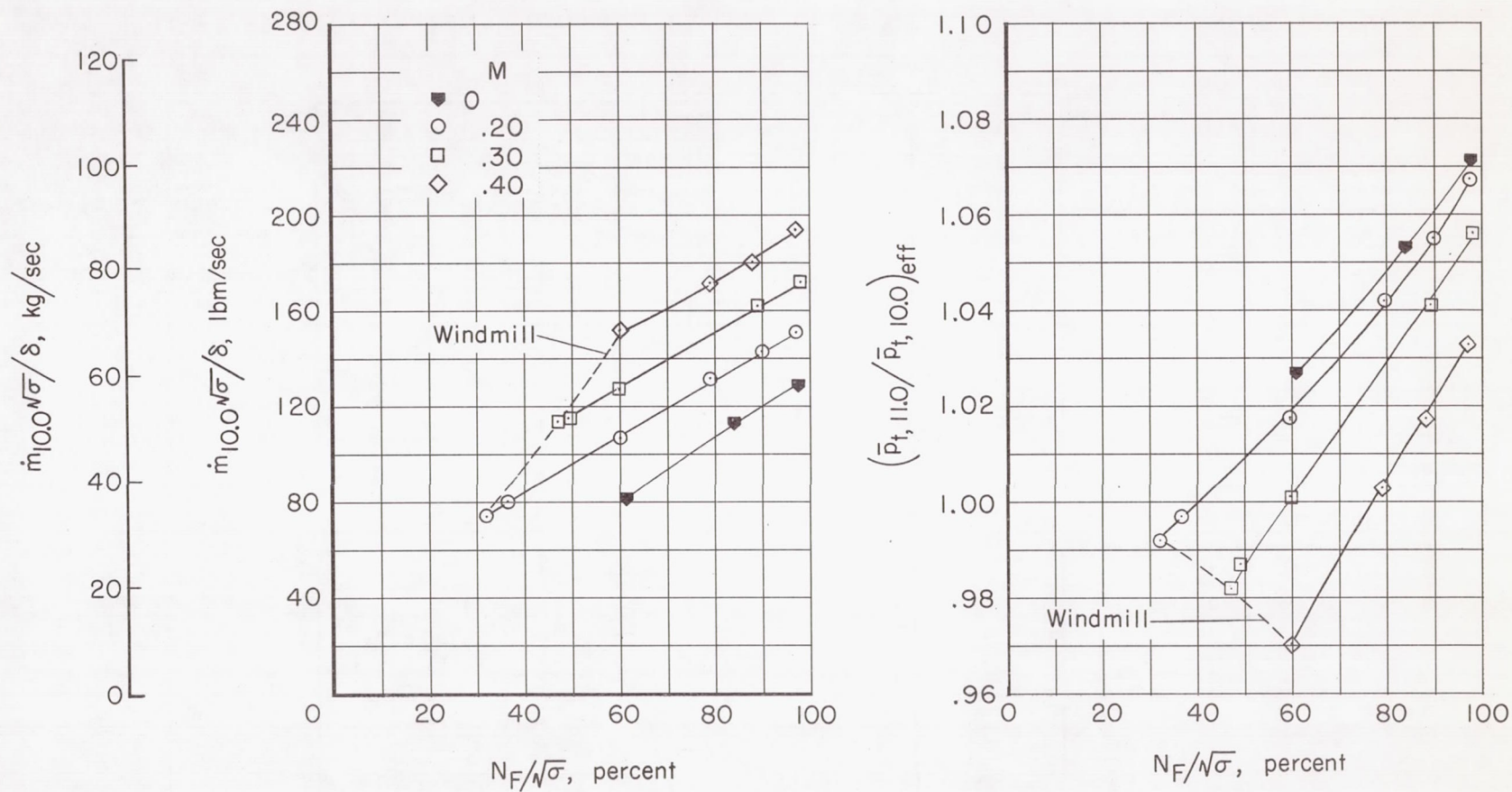
(a) Fan mass-flow rate and pressure ratio.

Figure 37.- Fan performance characteristics for configuration 322.



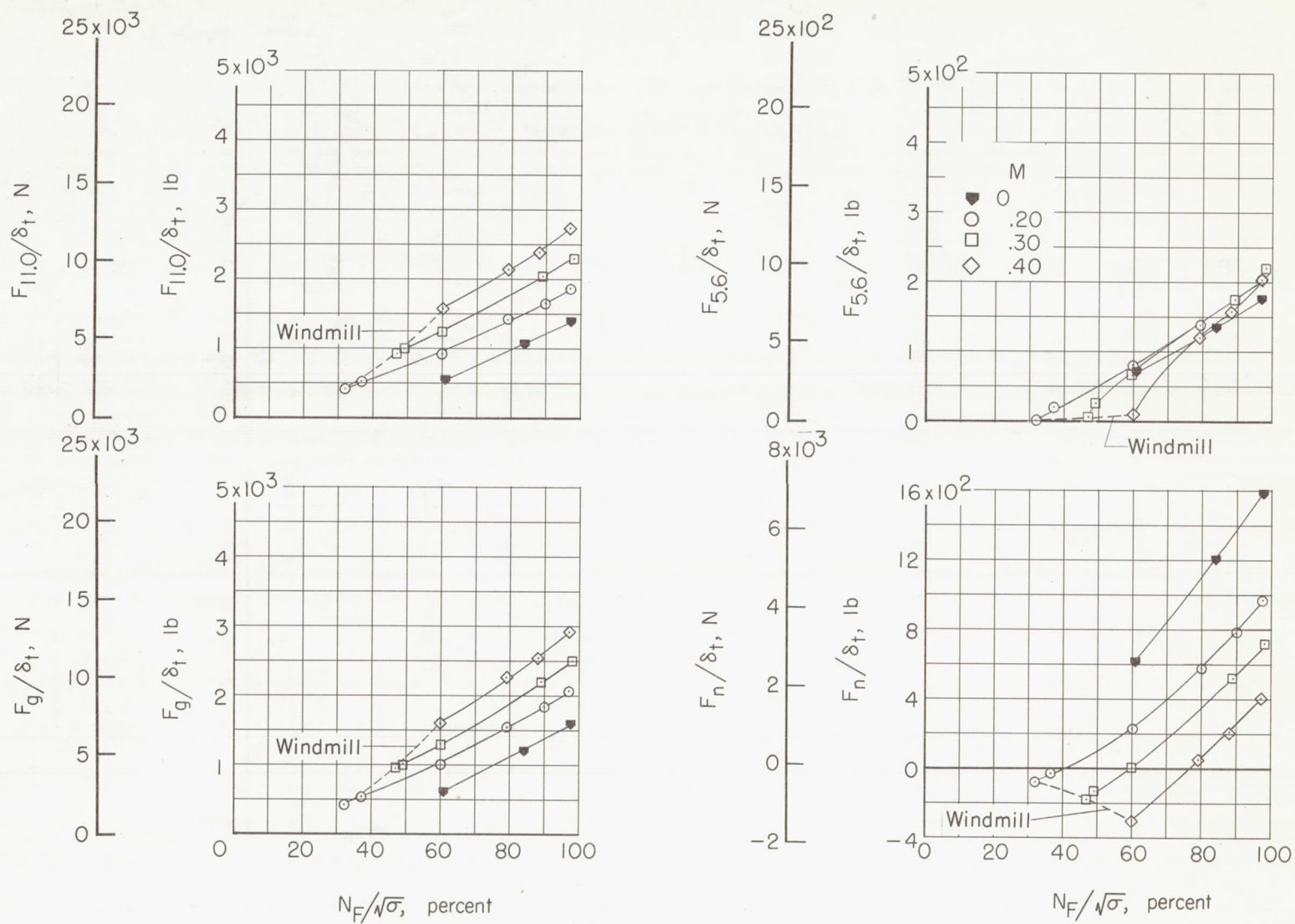
(b) Fan thrust characteristics.

Figure 37.- Concluded.



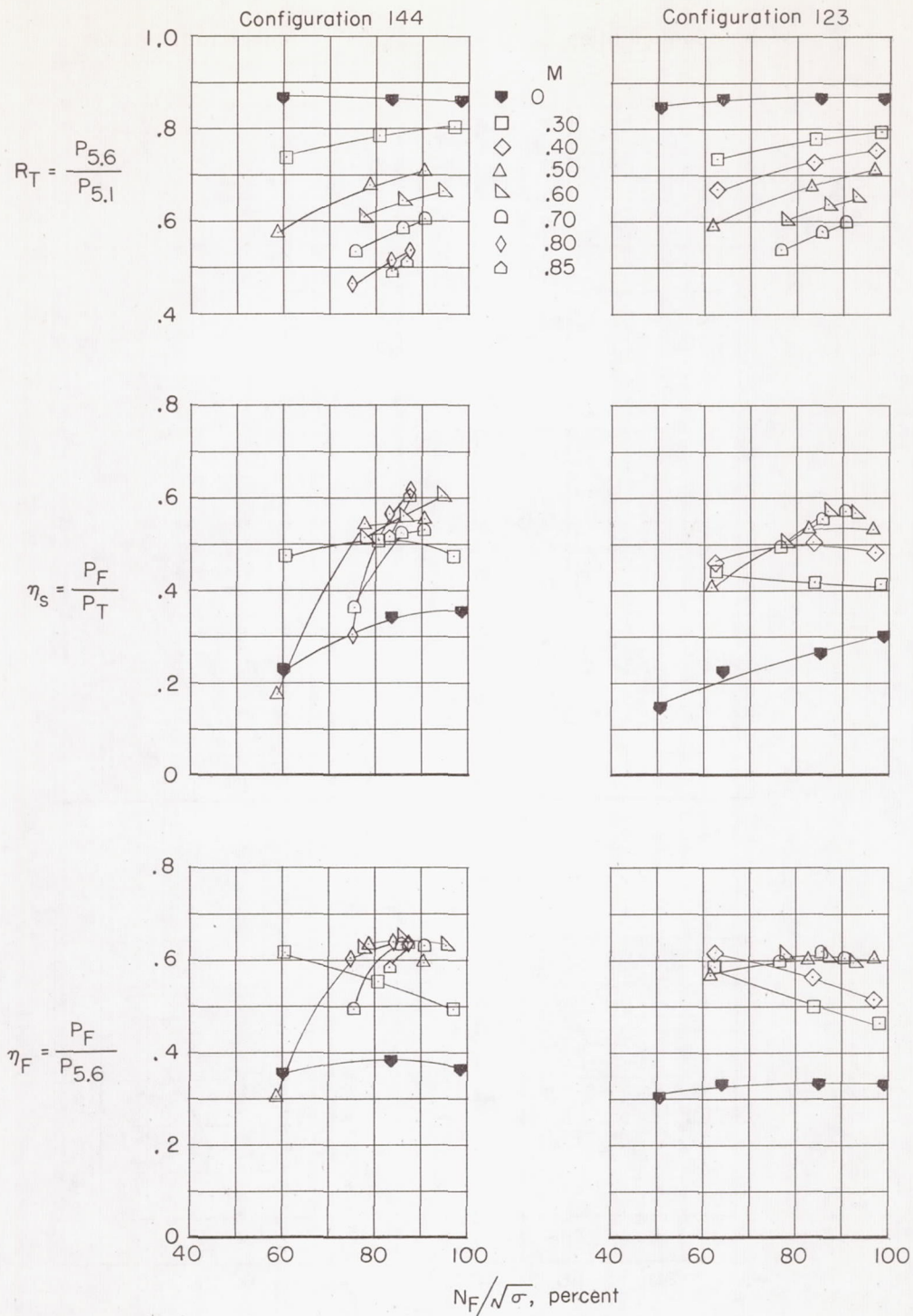
(a) Fan mass-flow rate and pressure ratio.

Figure 38.- Fan performance characteristics for configuration 243.



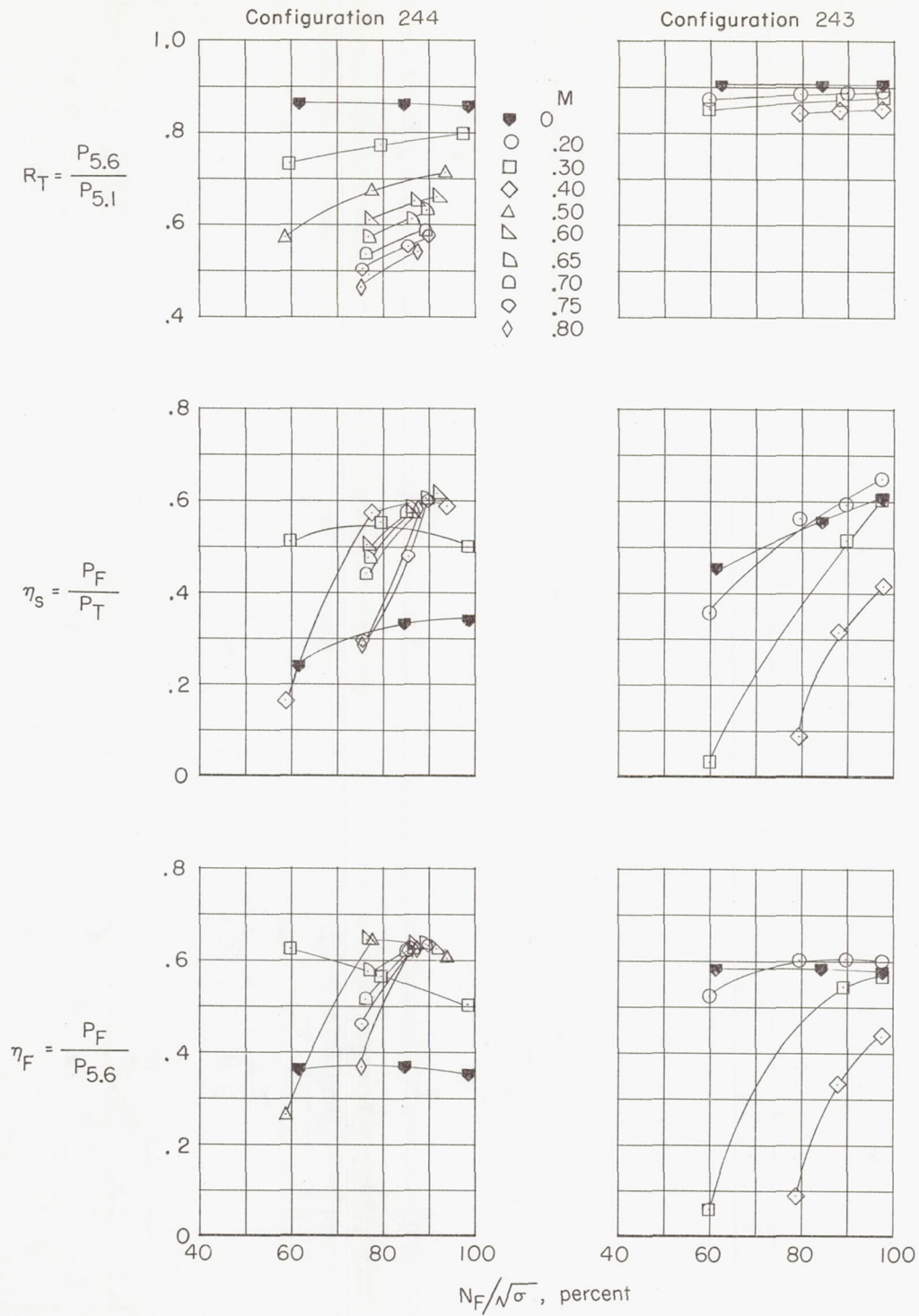
(b) Fan thrust characteristics.

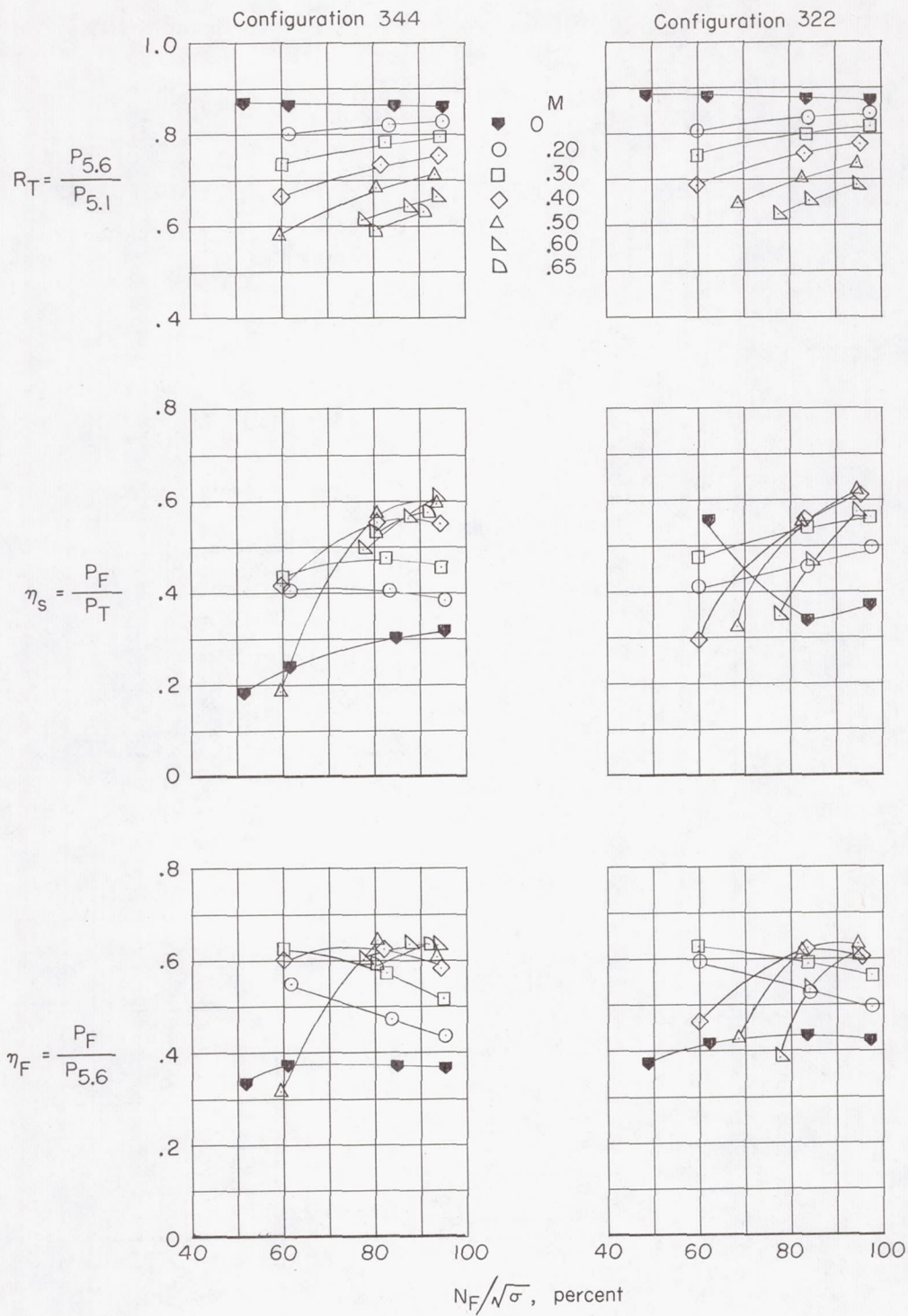
Figure 38.- Concluded.



(a) Configurations 144 and 123.

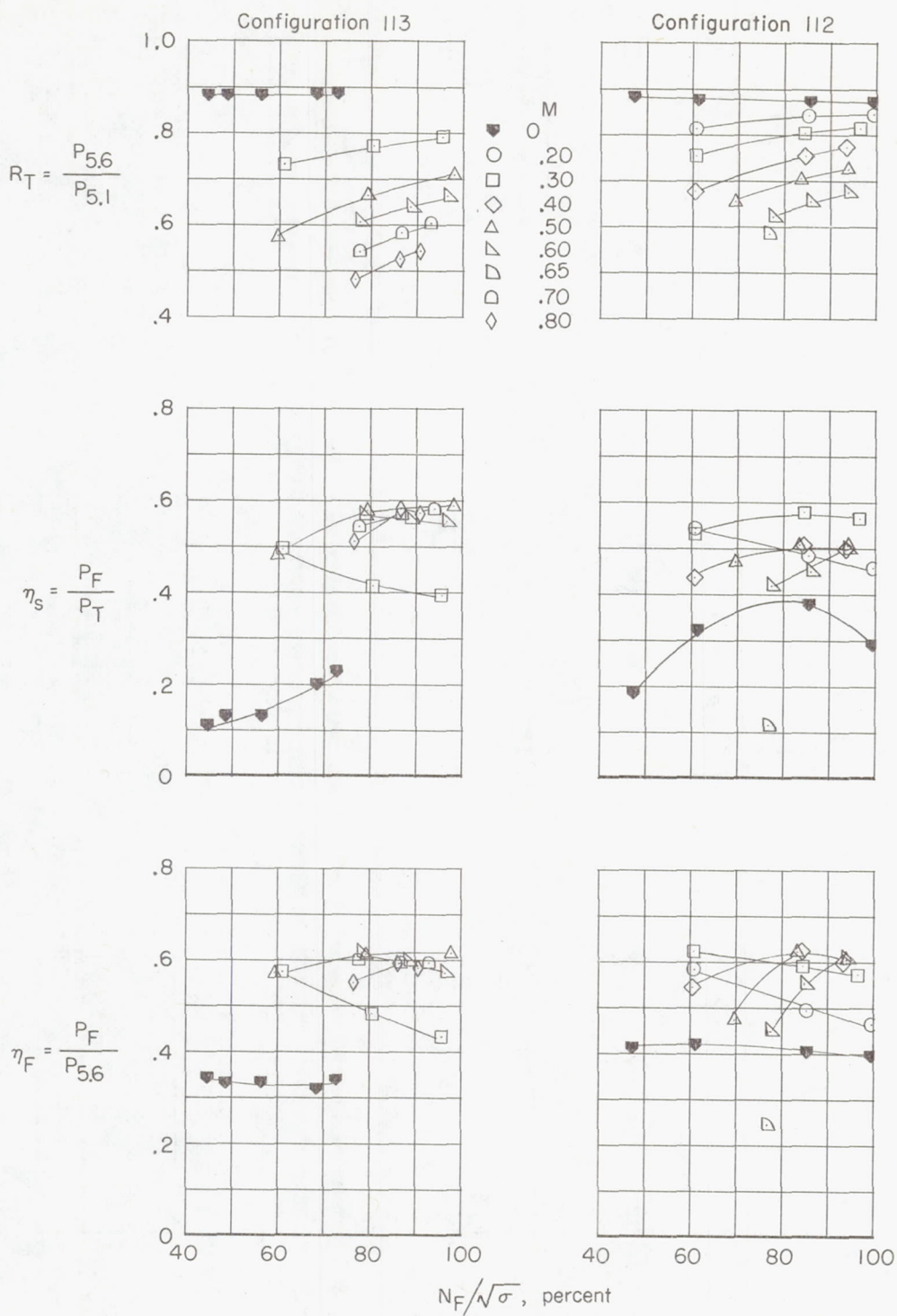
Figure 39.- Fan-turbine power-absorption ratio, fan-stage efficiency, and overall fan-efficiency characteristics for the various configurations tested.





(c) Configurations 344 and 322.

Figure 39.- Continued.



(d) Configurations 113 and 112.

Figure 39.- Concluded.

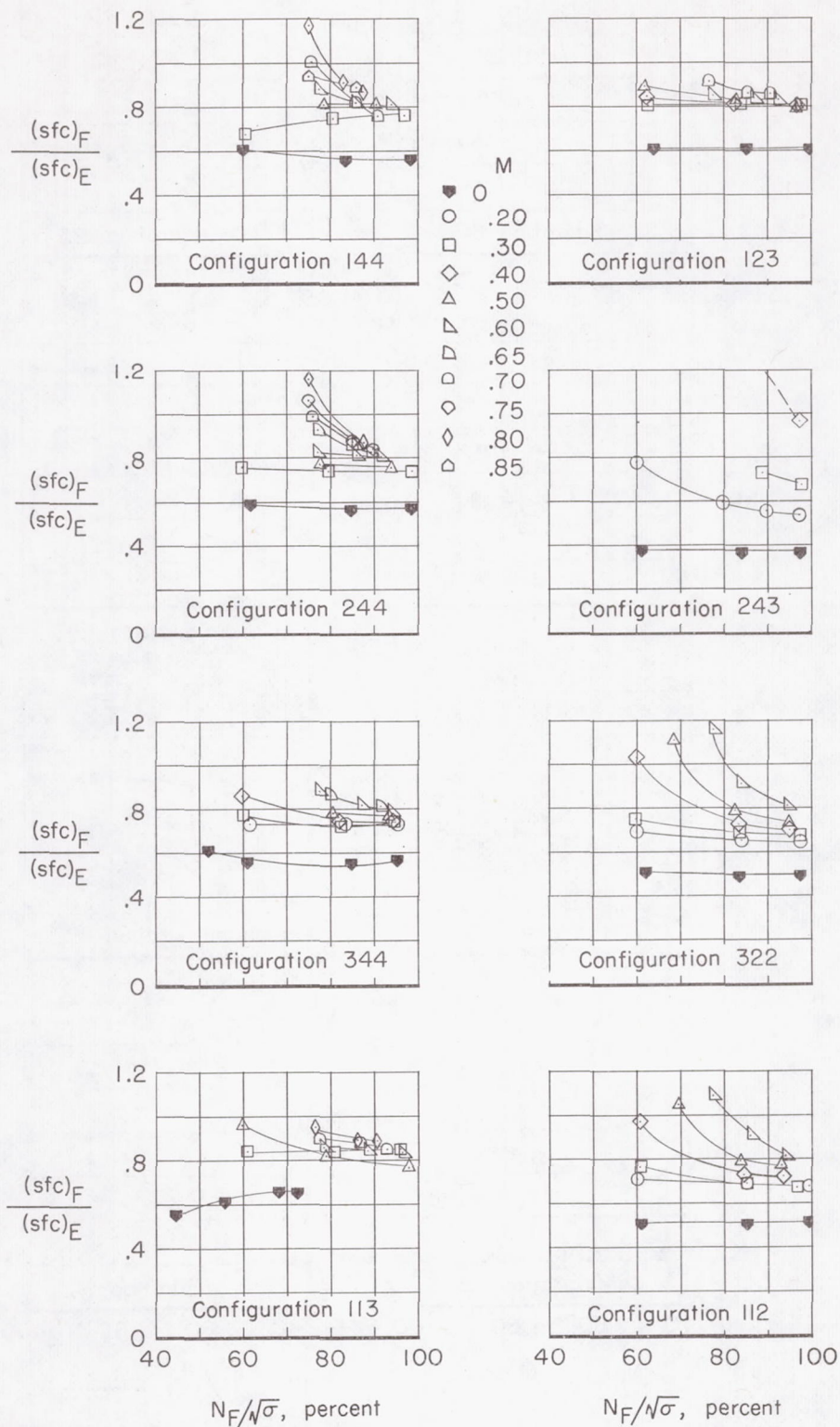


Figure 40.- Specific-fuel-consumption ratios for the various configurations tested.

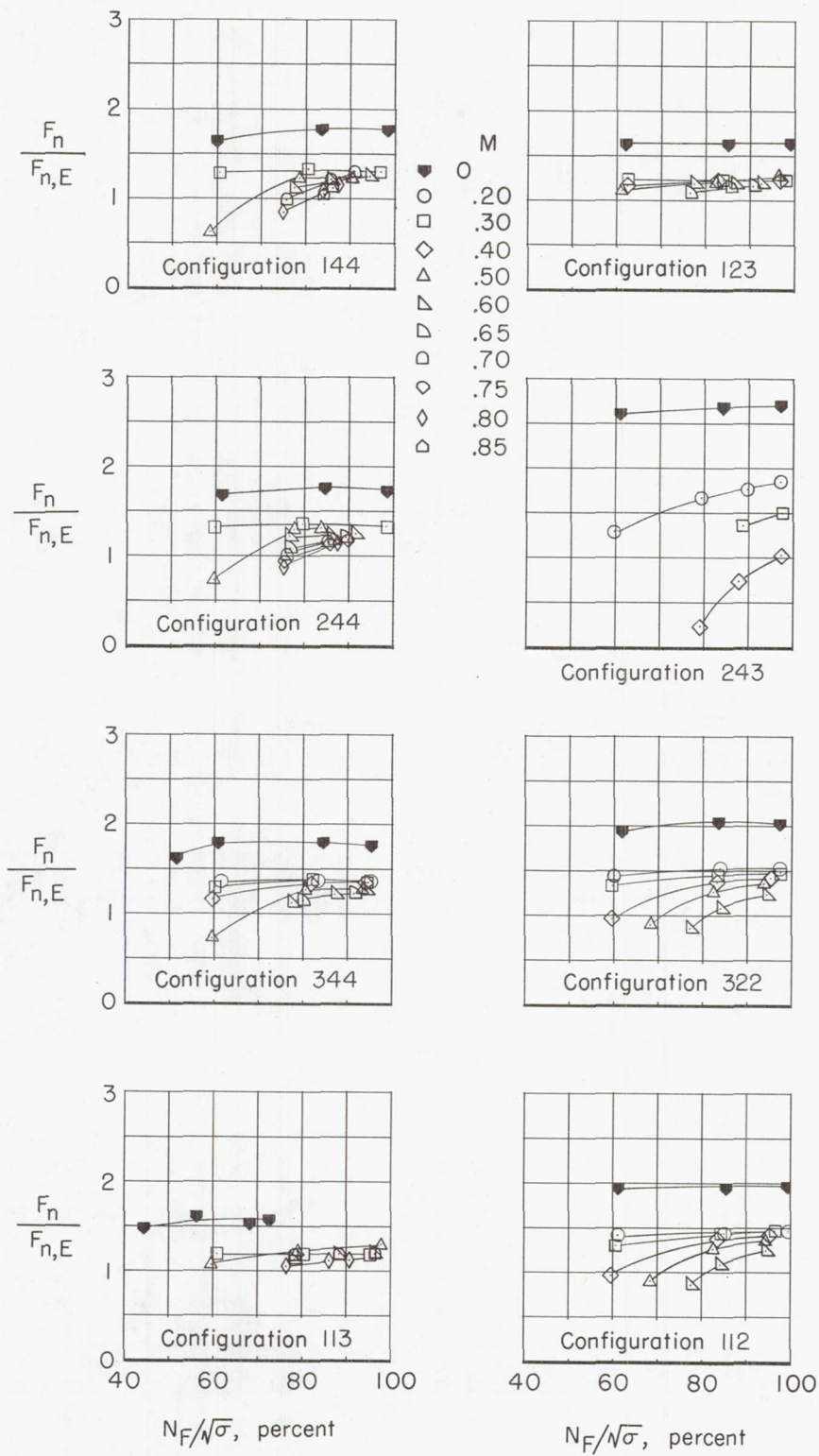


Figure 41.- Net-augmentation ratios for the various configurations tested.

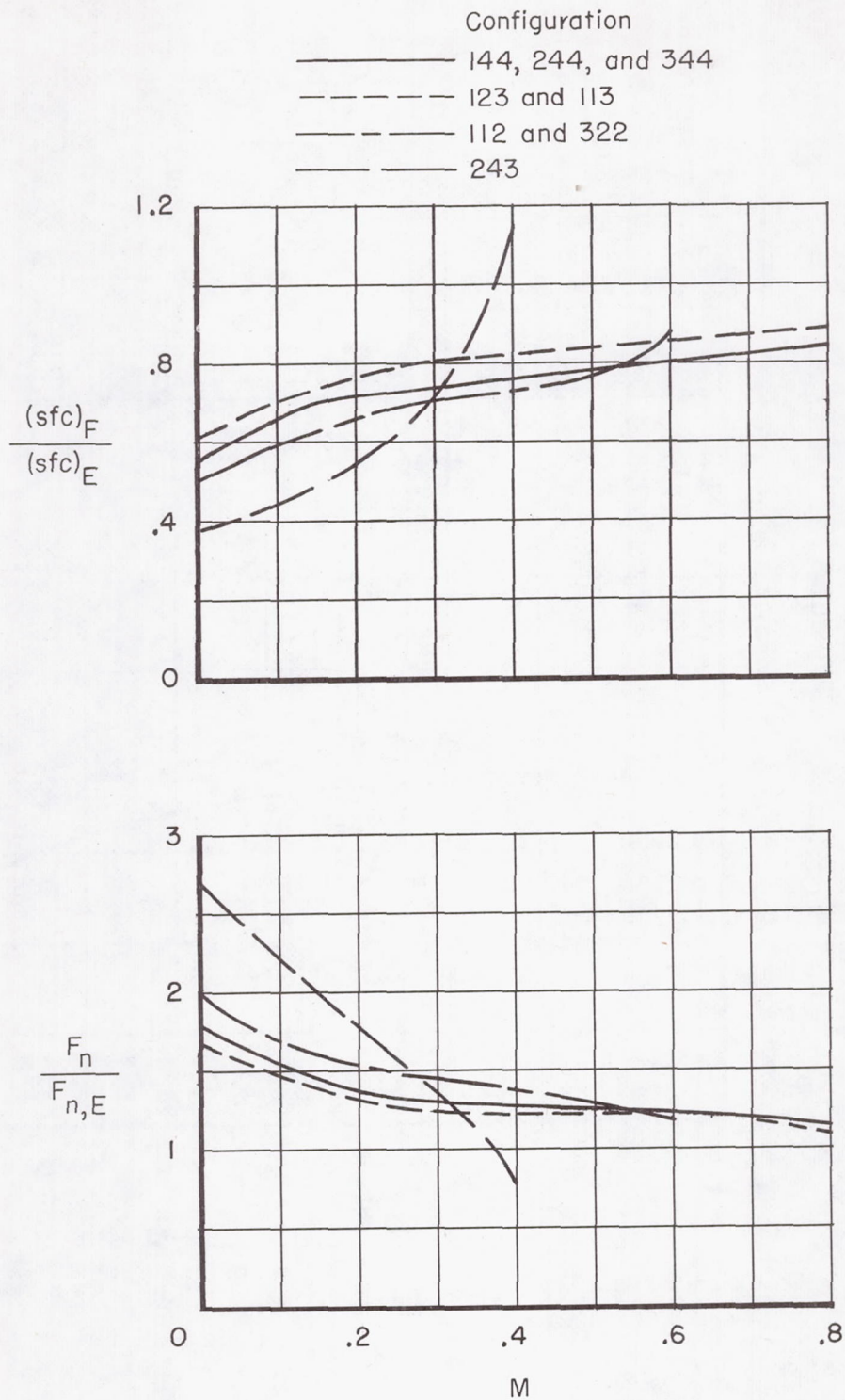


Figure 42.- Summary of specific-fuel-consumption-ratio and net-augmentation-ratio characteristics for the various configurations tested.
 $N_F/\sqrt{\sigma} = 90$ percent.

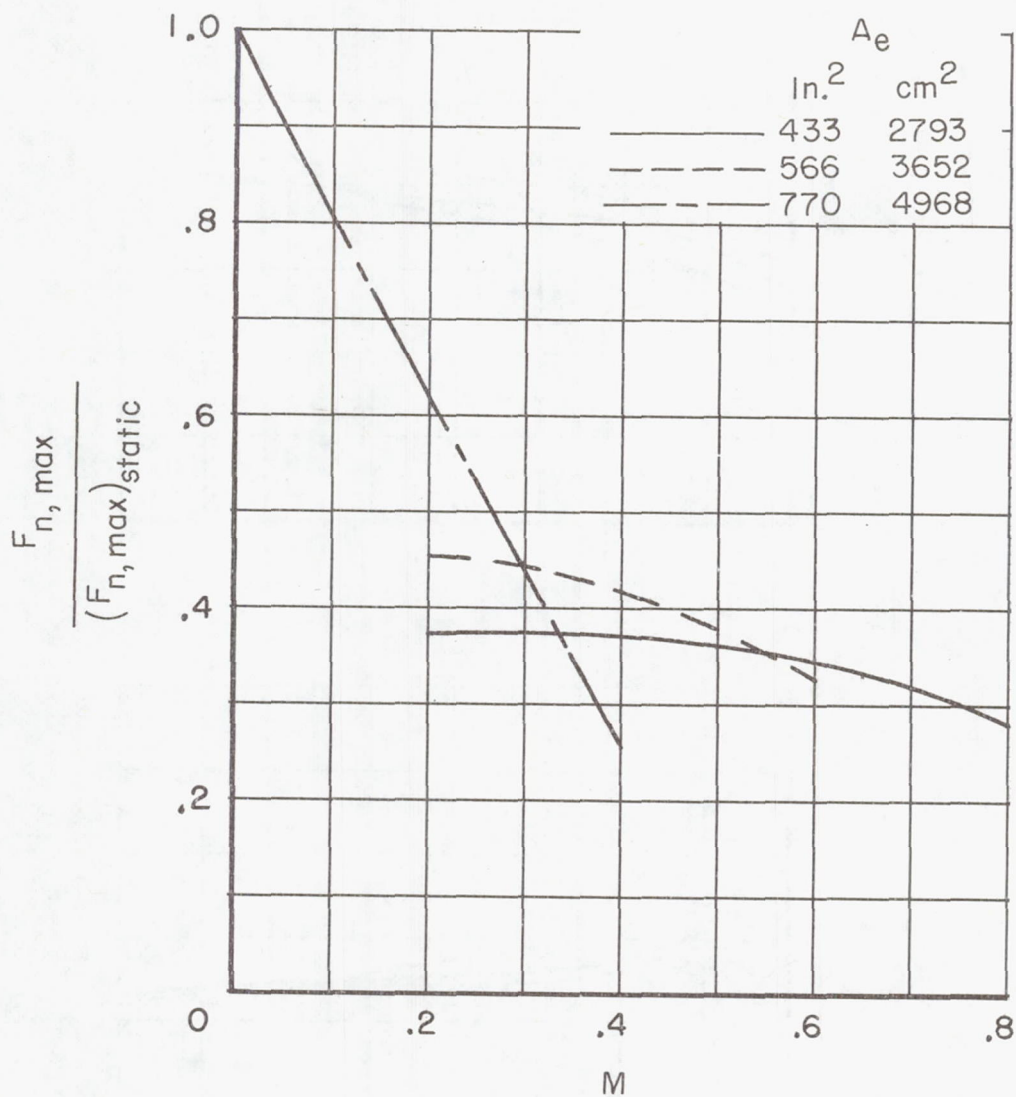
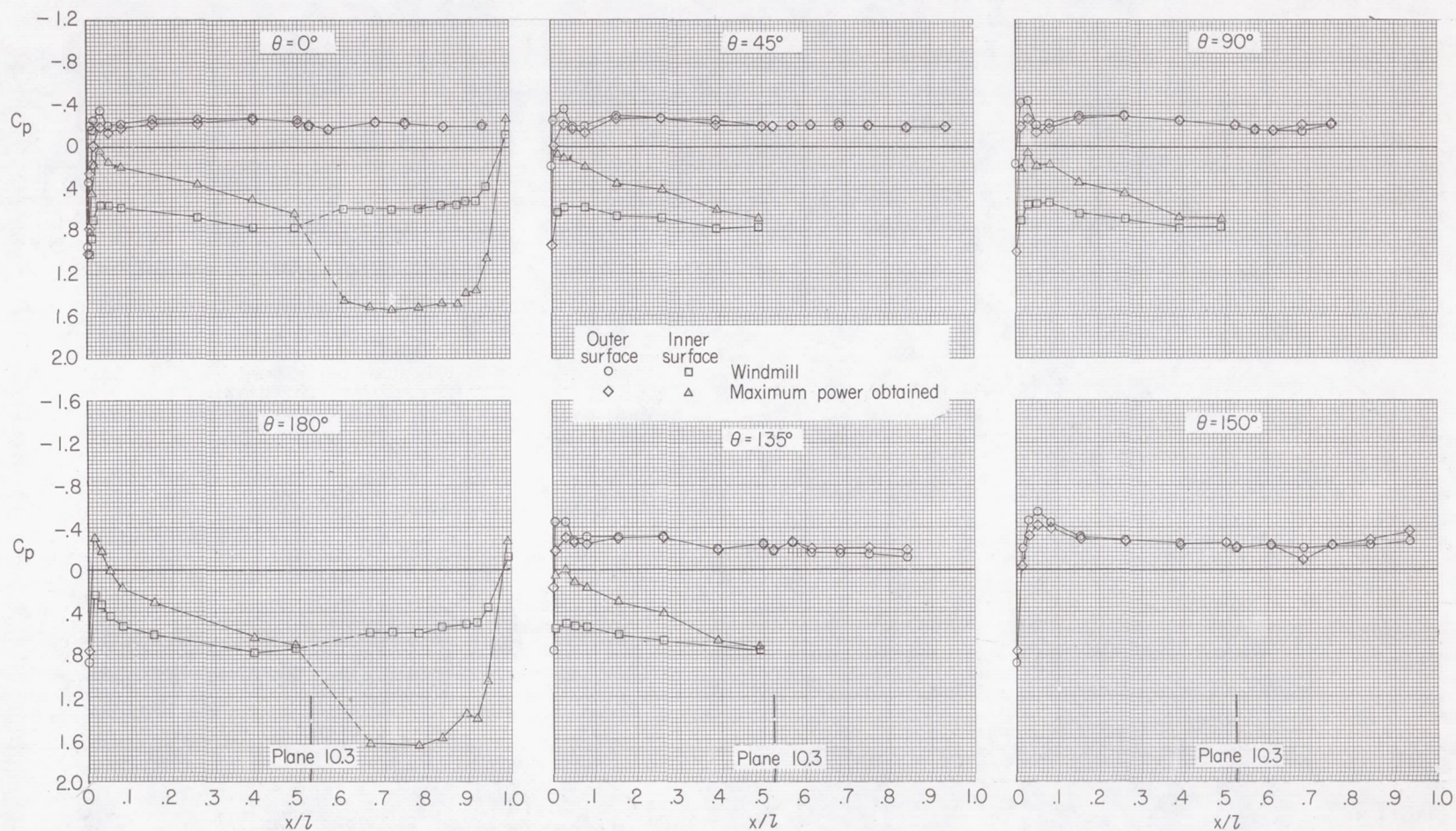
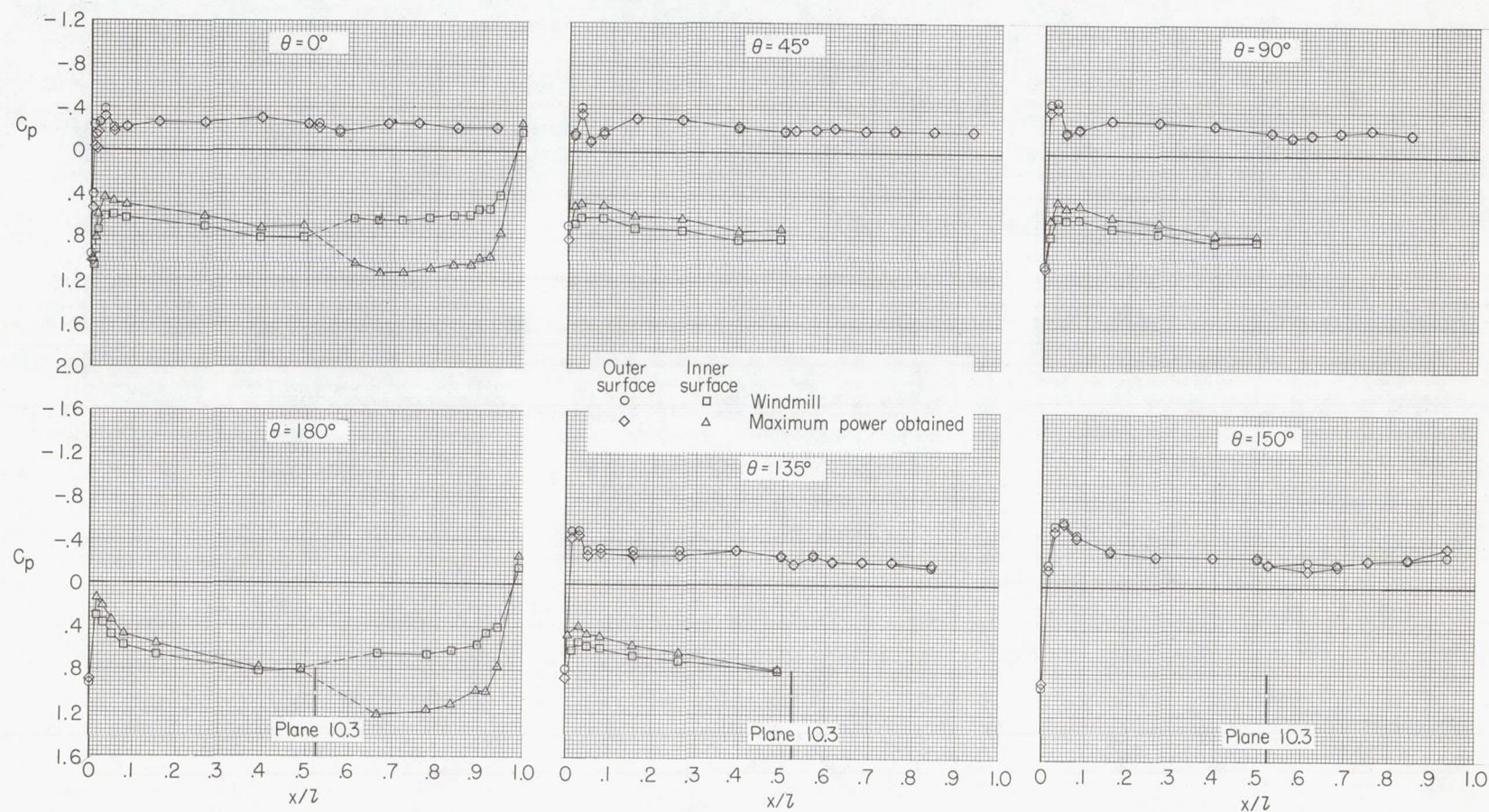


Figure 43.- Summary of thrust-ratio characteristics. $(F_{n, \max})_{\text{static}}$ is for configuration 243 and is 1530 lb (6807 N).



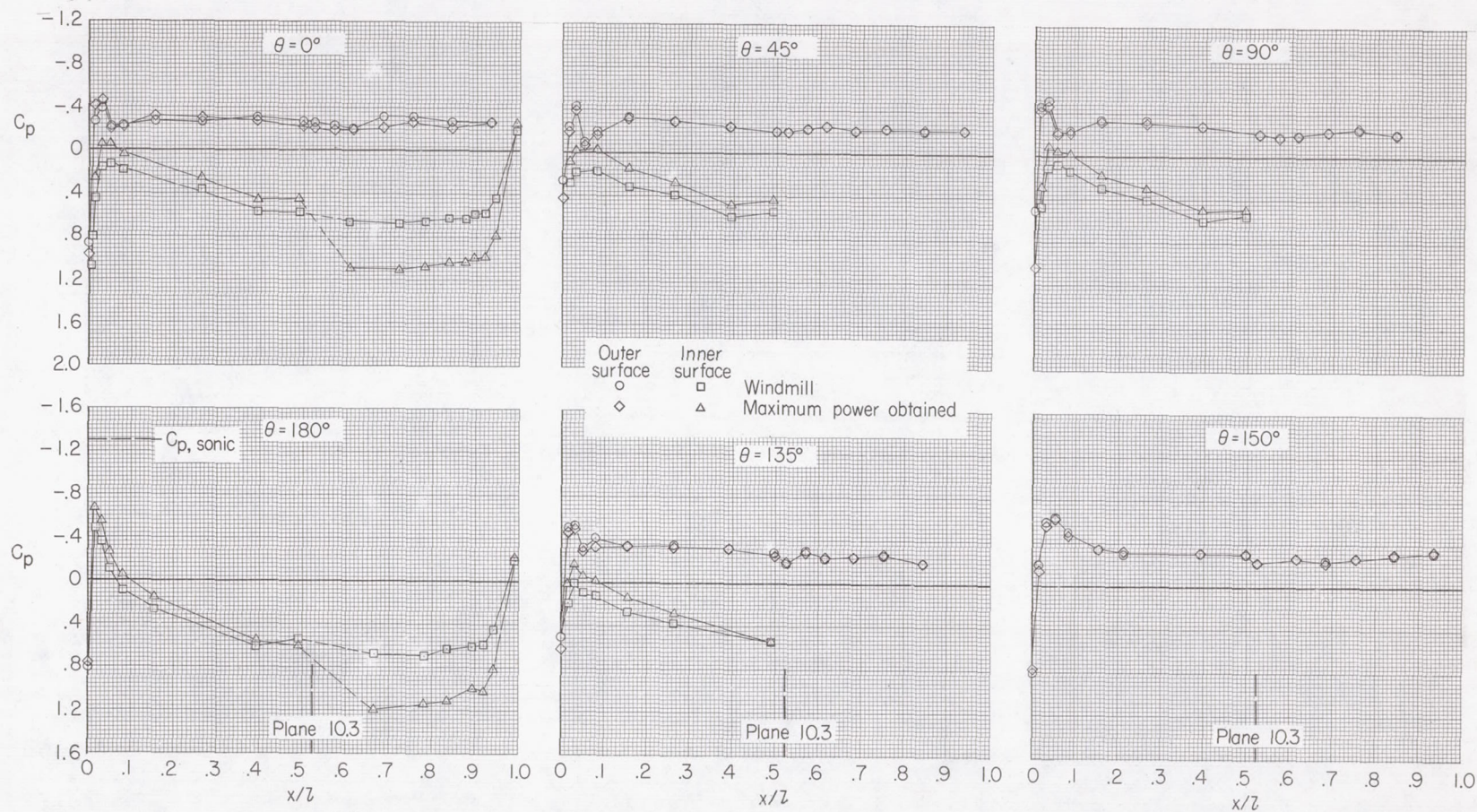
(a) $M = 0.30$; $N_F/\sqrt{\sigma} = 97.0$ percent.

Figure 44.- Fan-nacelle pressure distributions for configuration 144.



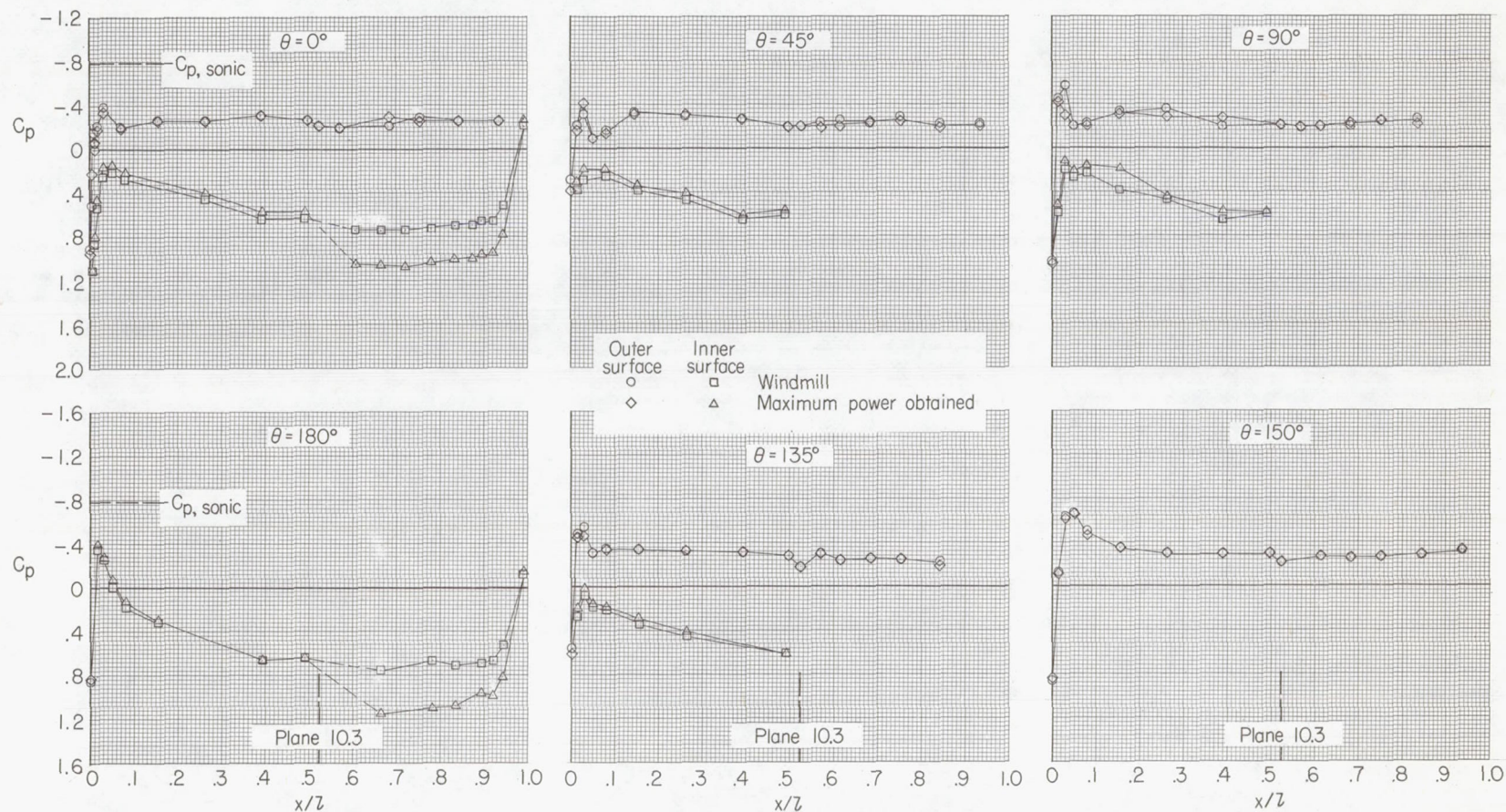
(b) $M = 0.50$; $N_F/\sqrt{\sigma} = 90.6$ percent.

Figure 44.- Continued.



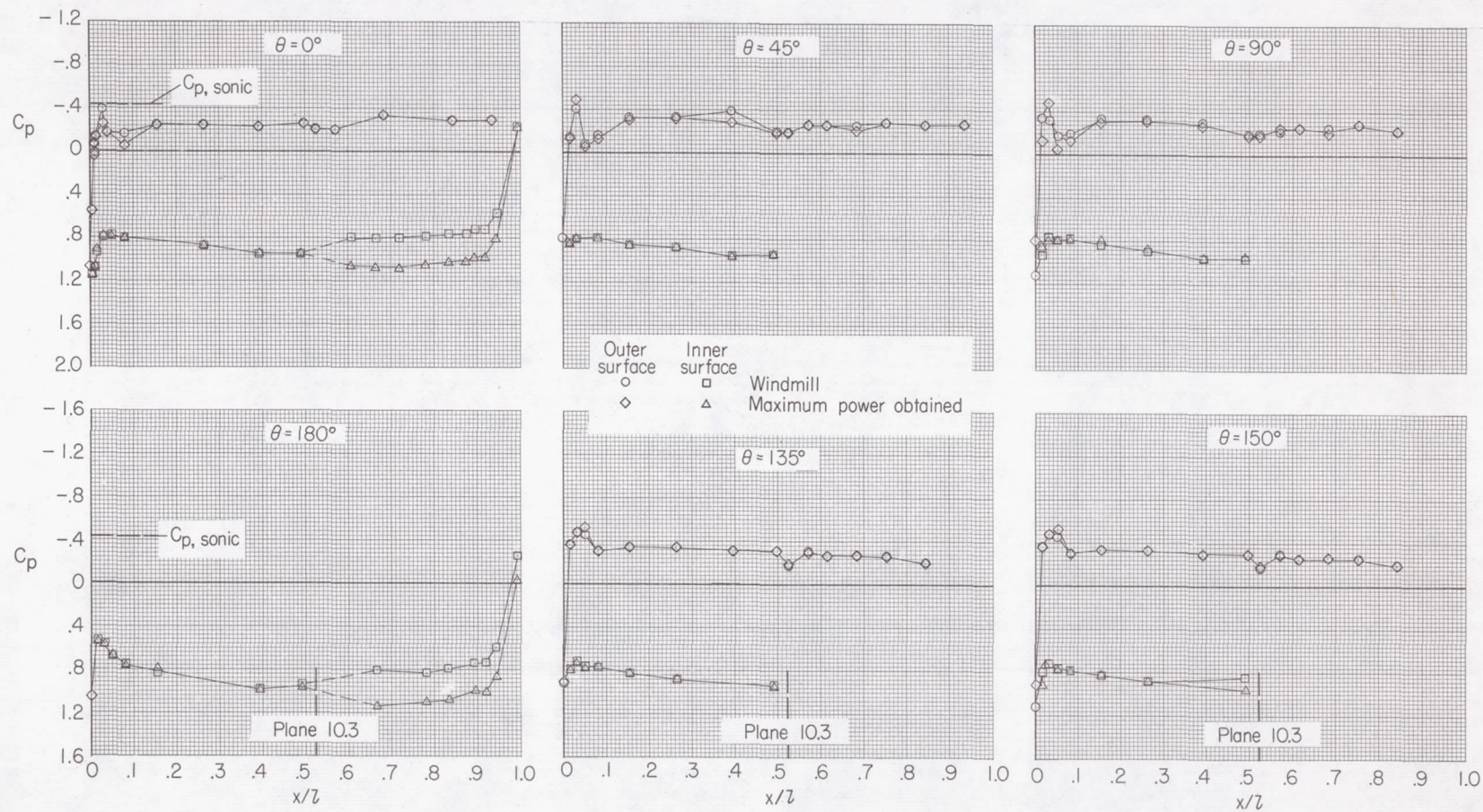
(c) $M = 0.60$; $N_F/\sqrt{\sigma} = 94.2$ percent.

Figure 44.- Continued.



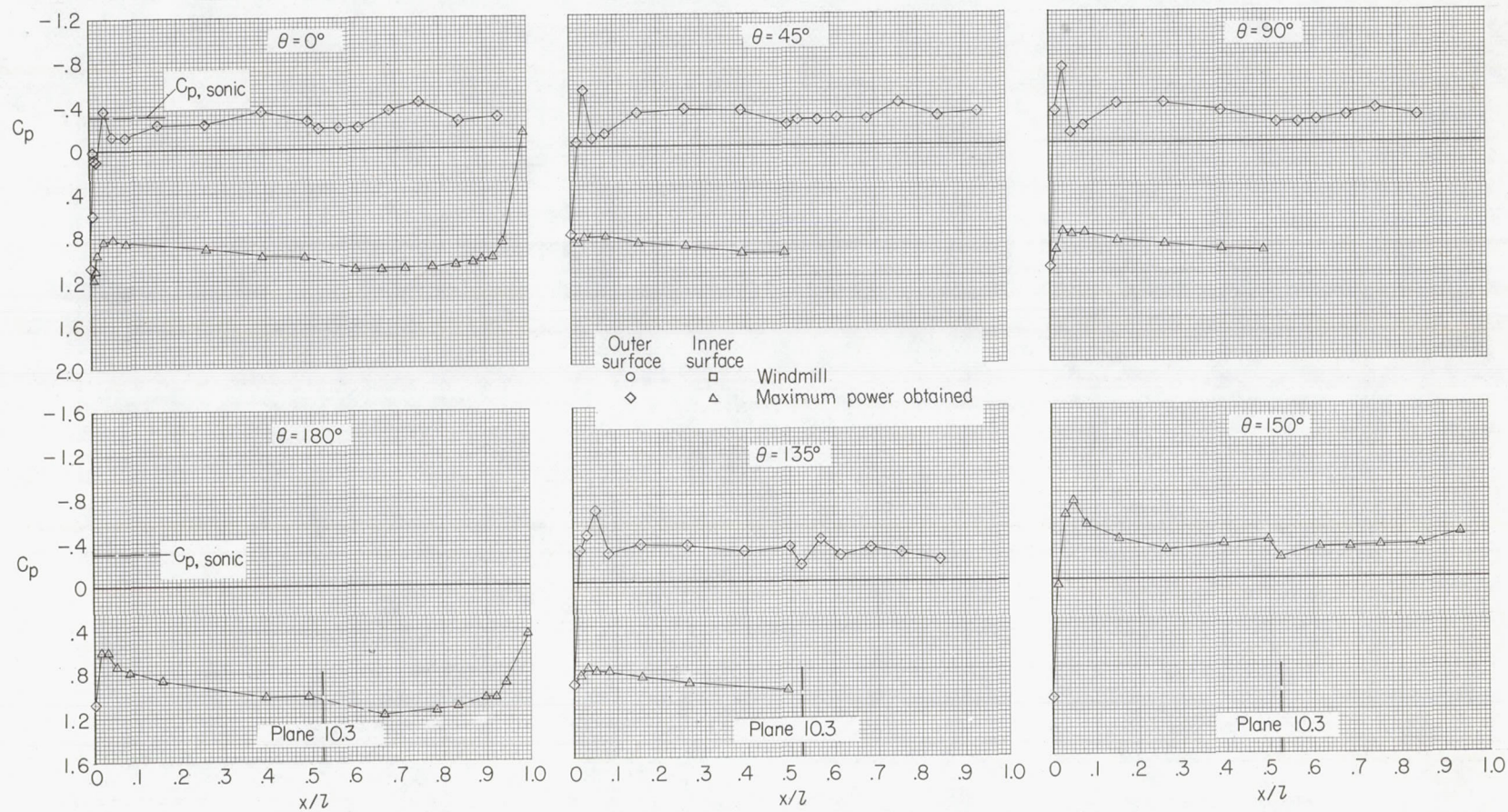
(d) $M = 0.70$; $N_F/\sqrt{\sigma} = 91.1$ percent.

Figure 44.- Continued.



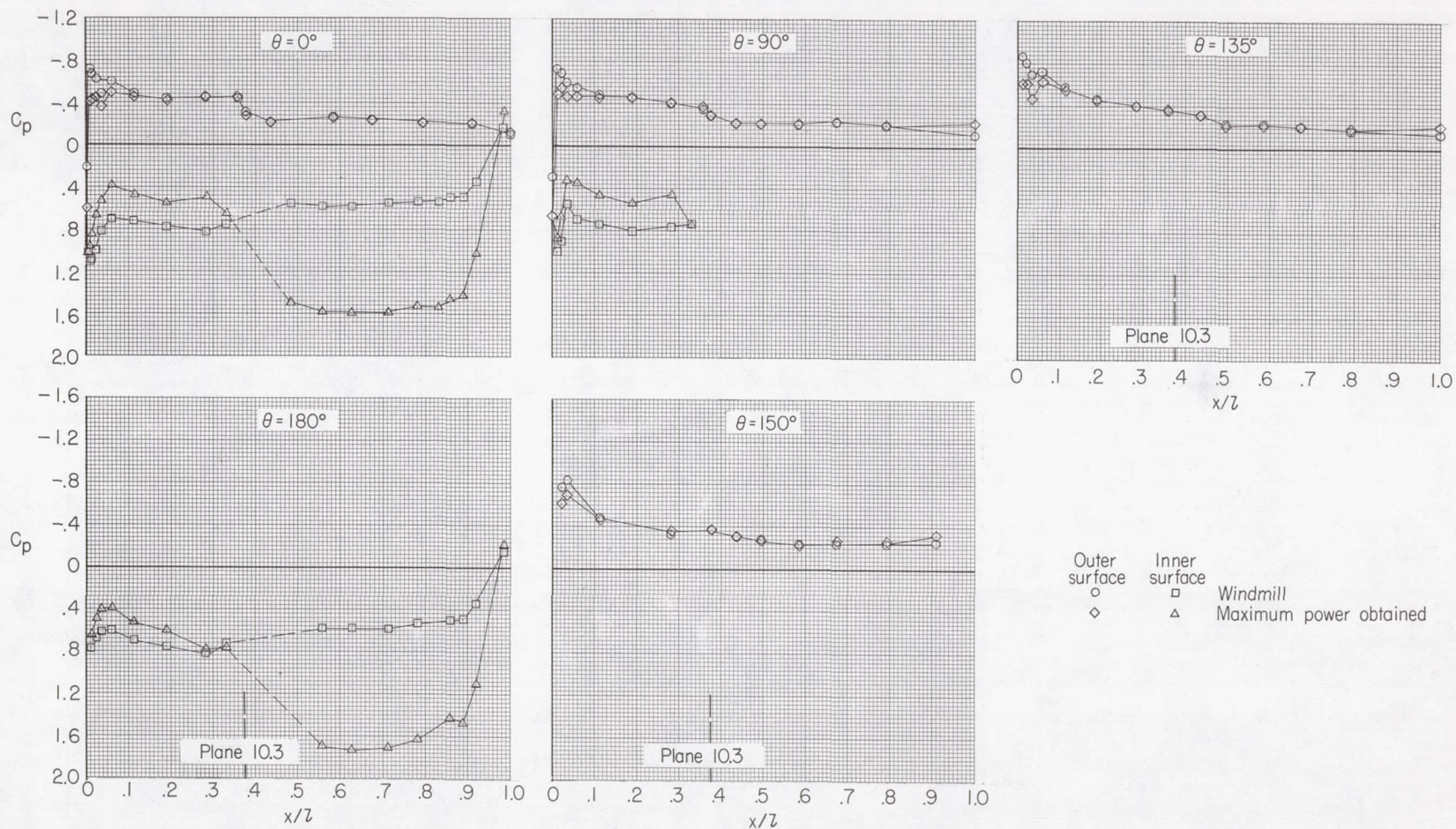
(e) $M = 0.80$; $N_F/\sqrt{\sigma} = 87.6$ percent.

Figure 44.- Continued.



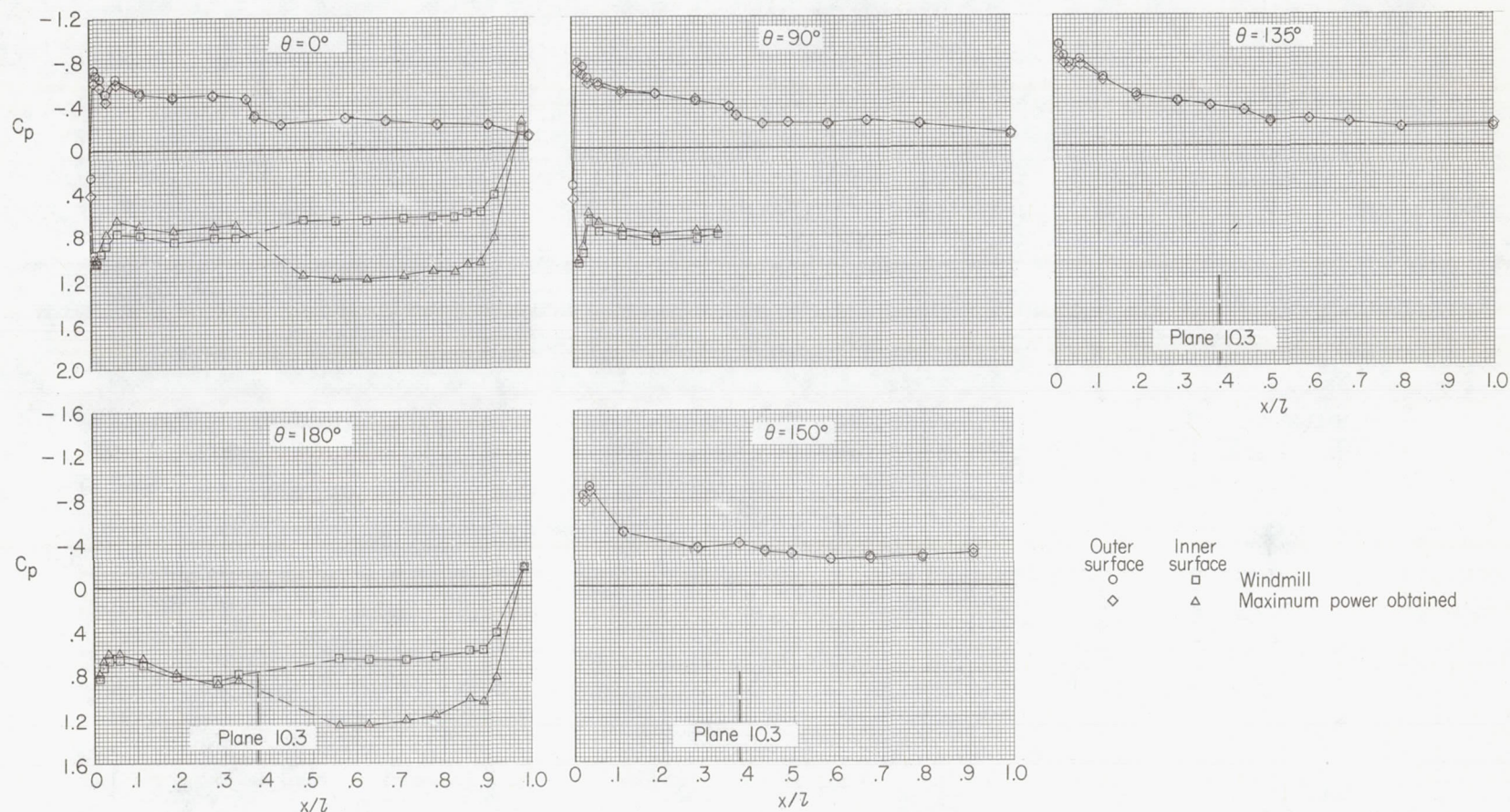
(f) $M = 0.85$; $N_F/\sqrt{\sigma} = 86.3$ percent.

Figure 44.- Concluded.



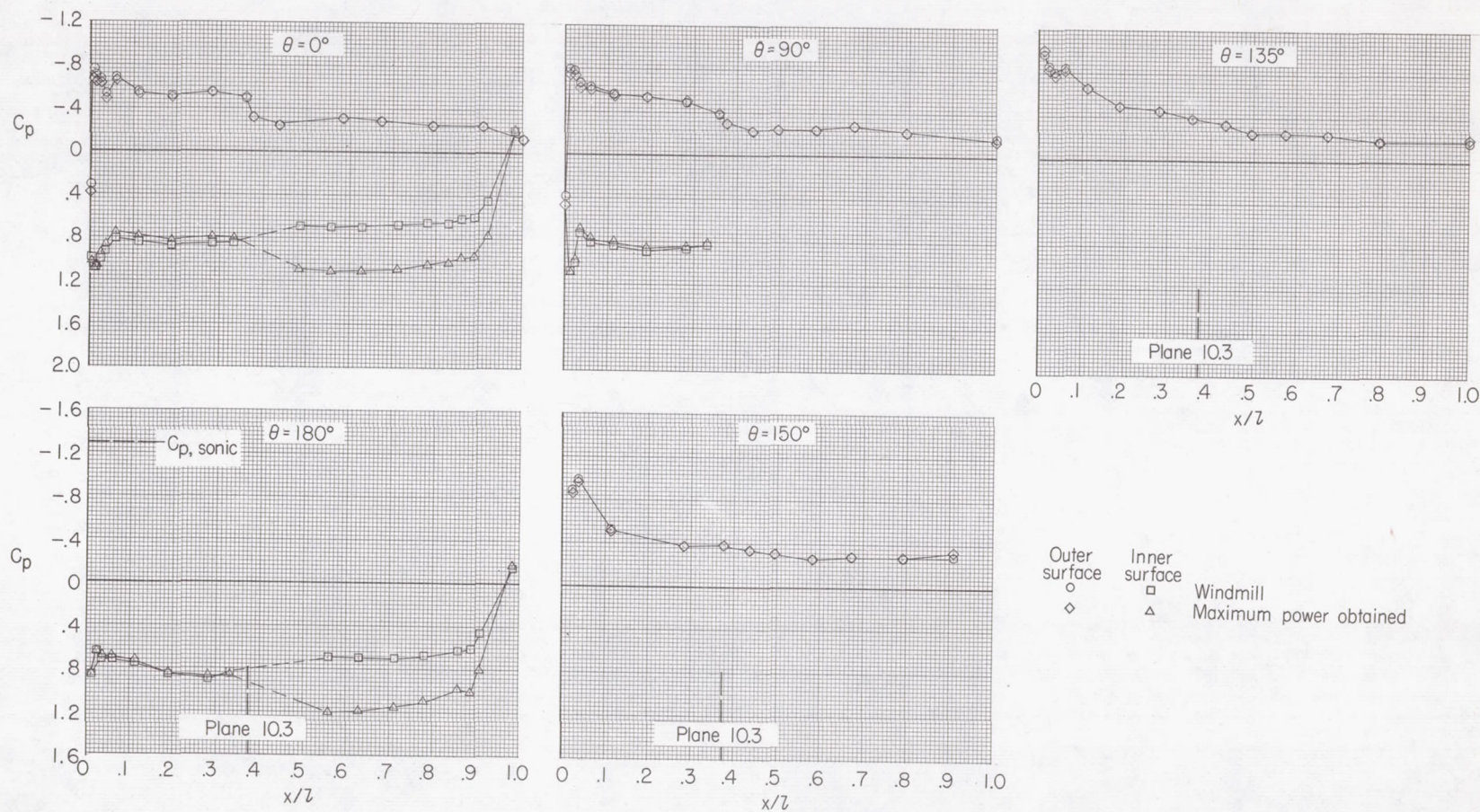
(a) $M = 0.30$; $N_F/\sqrt{\sigma} = 98.5$ percent.

Figure 45.- Fan-nacelle pressure distributions for configuration 244.



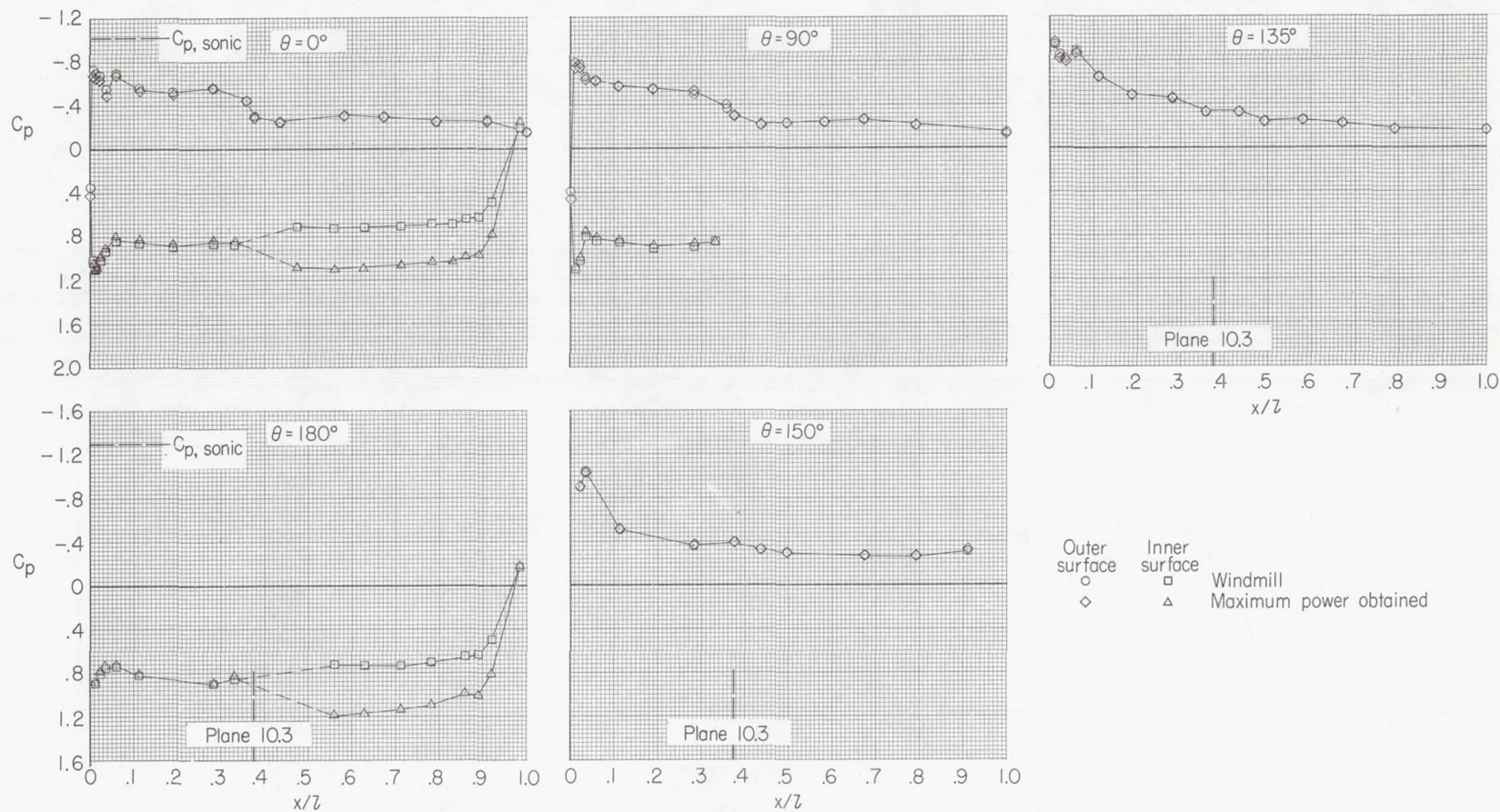
(b) $M = 0.50$; $N_F/\sqrt{\sigma} = 93.9$ percent.

Figure 45.- Continued.



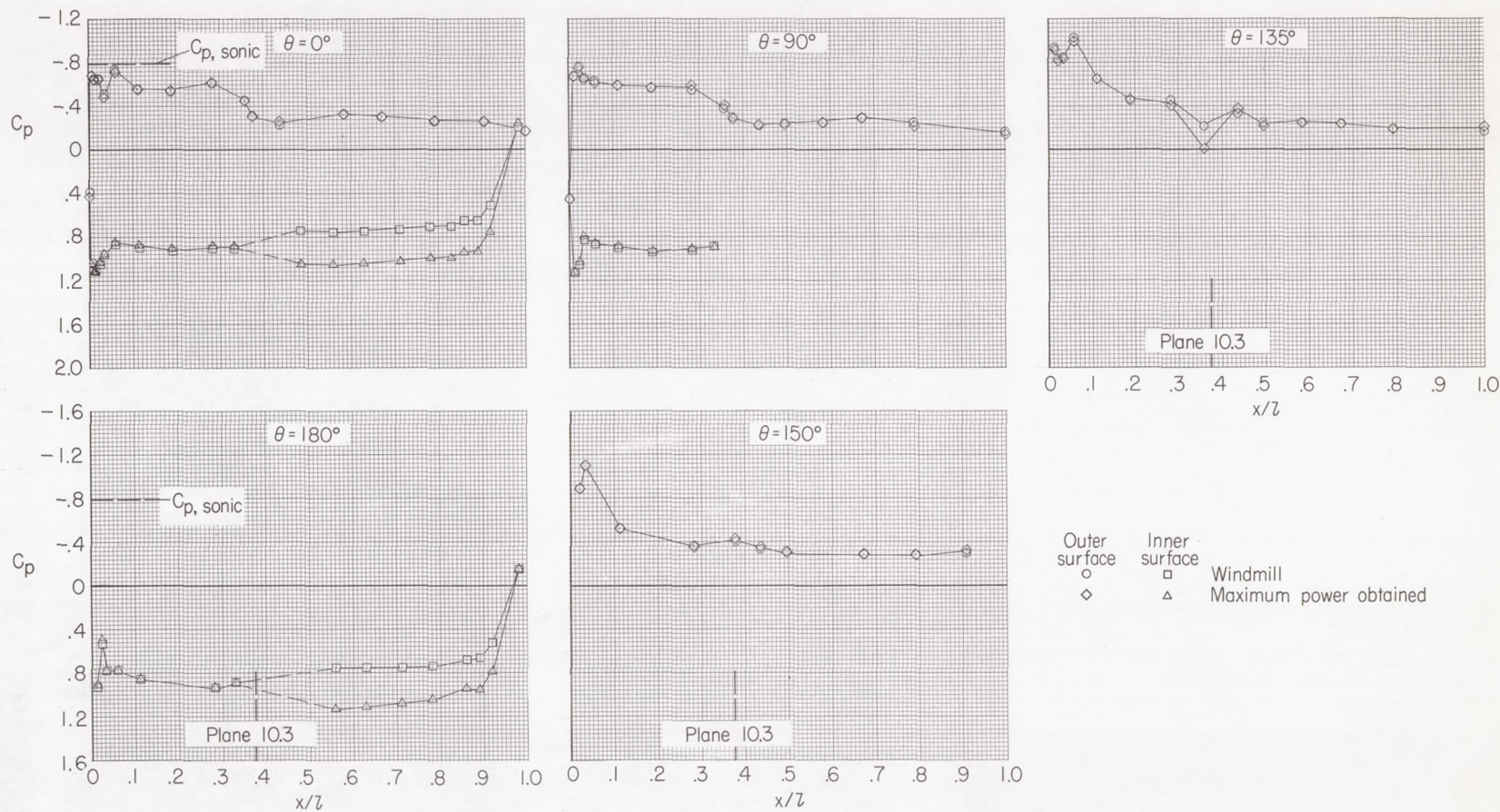
(c) $M = 0.60$; $N_F/\sqrt{\sigma} = 91.4$ percent.

Figure 45.- Continued.



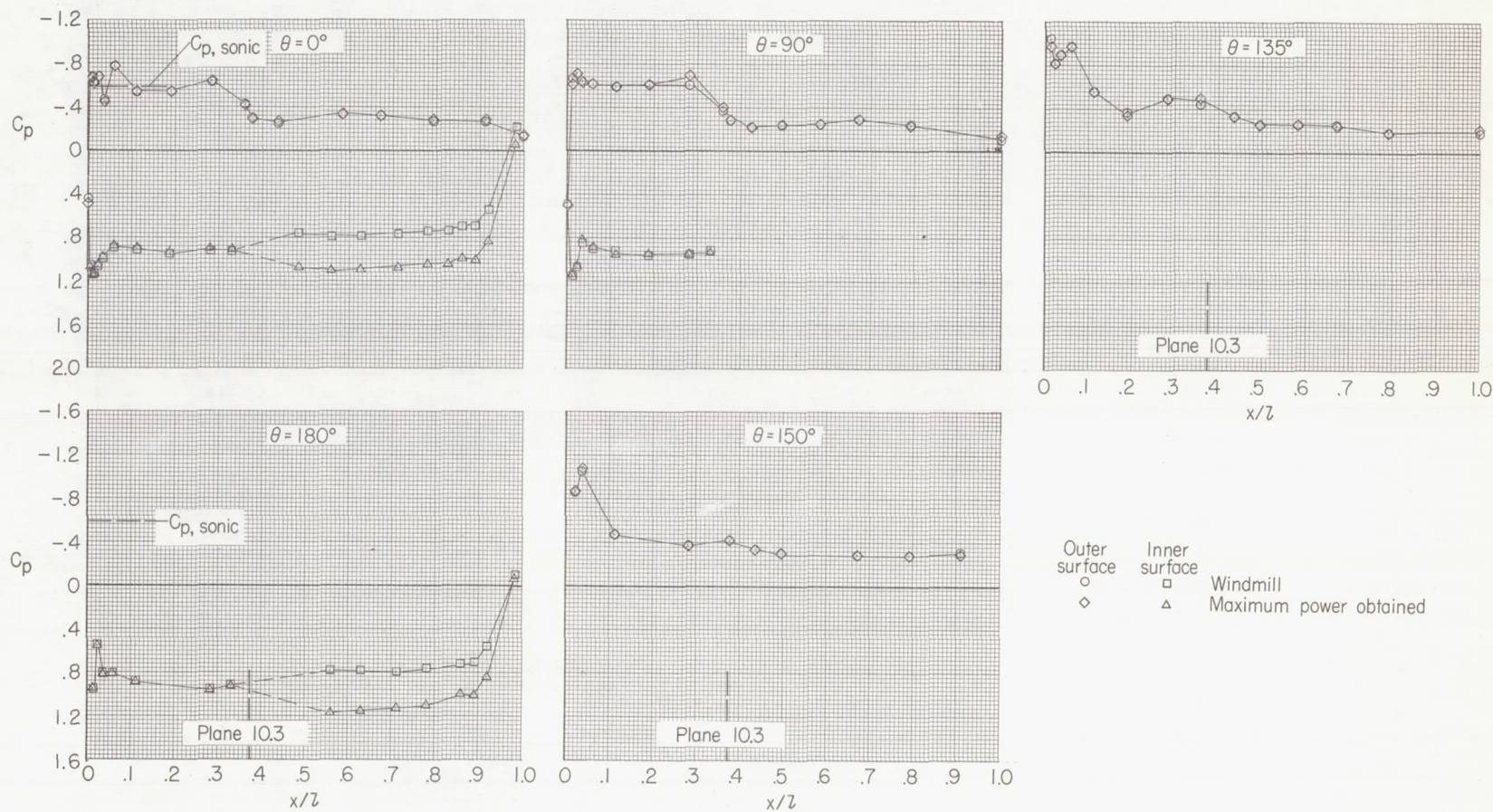
(d) $M = 0.65$; $N_F/\sqrt{\sigma} = 89.1$ percent.

Figure 45.- Continued.



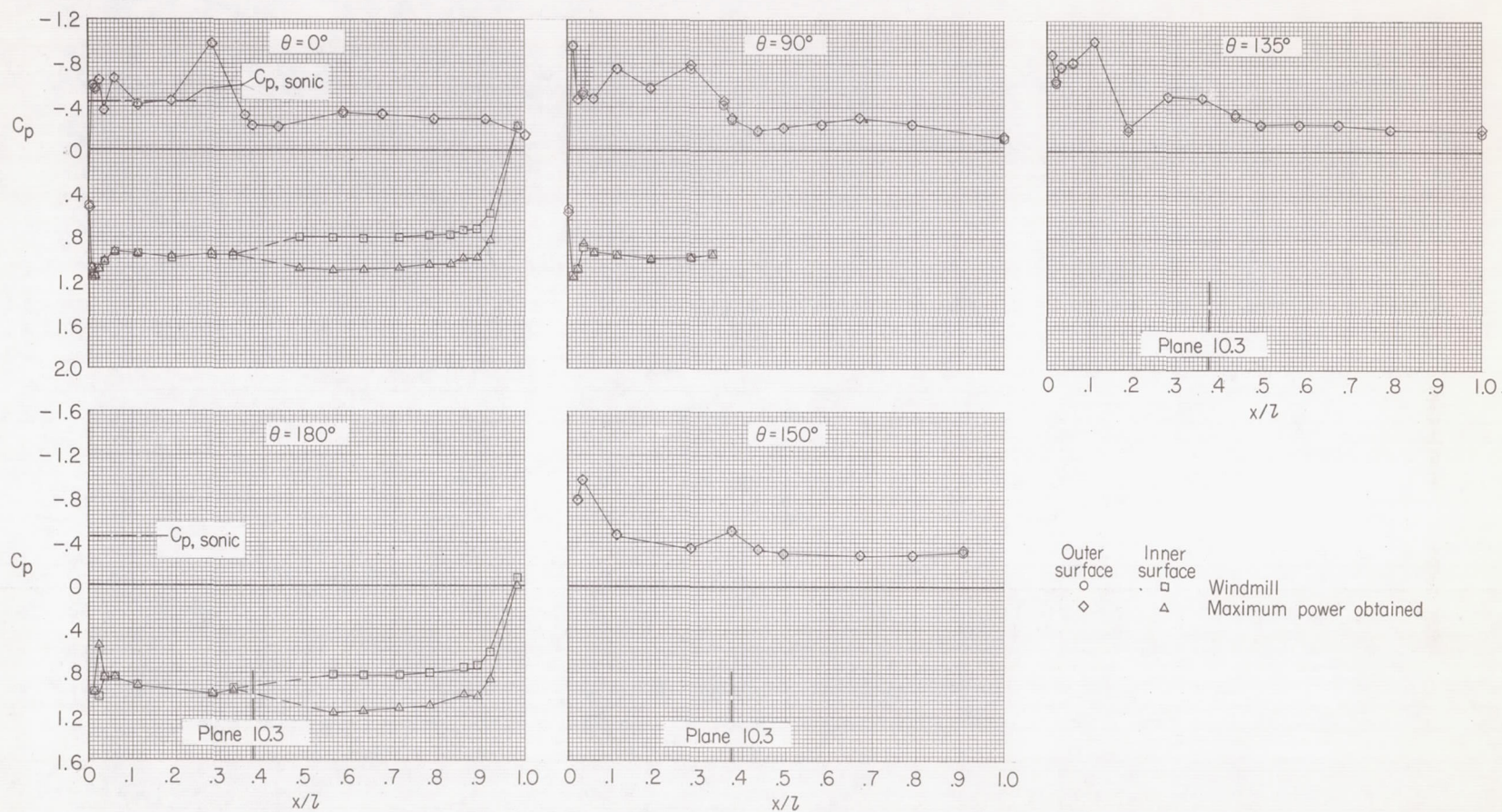
(e) $M = 0.70$; $N_F/\sqrt{\sigma} = 85.1$ percent.

Figure 45.- Continued.



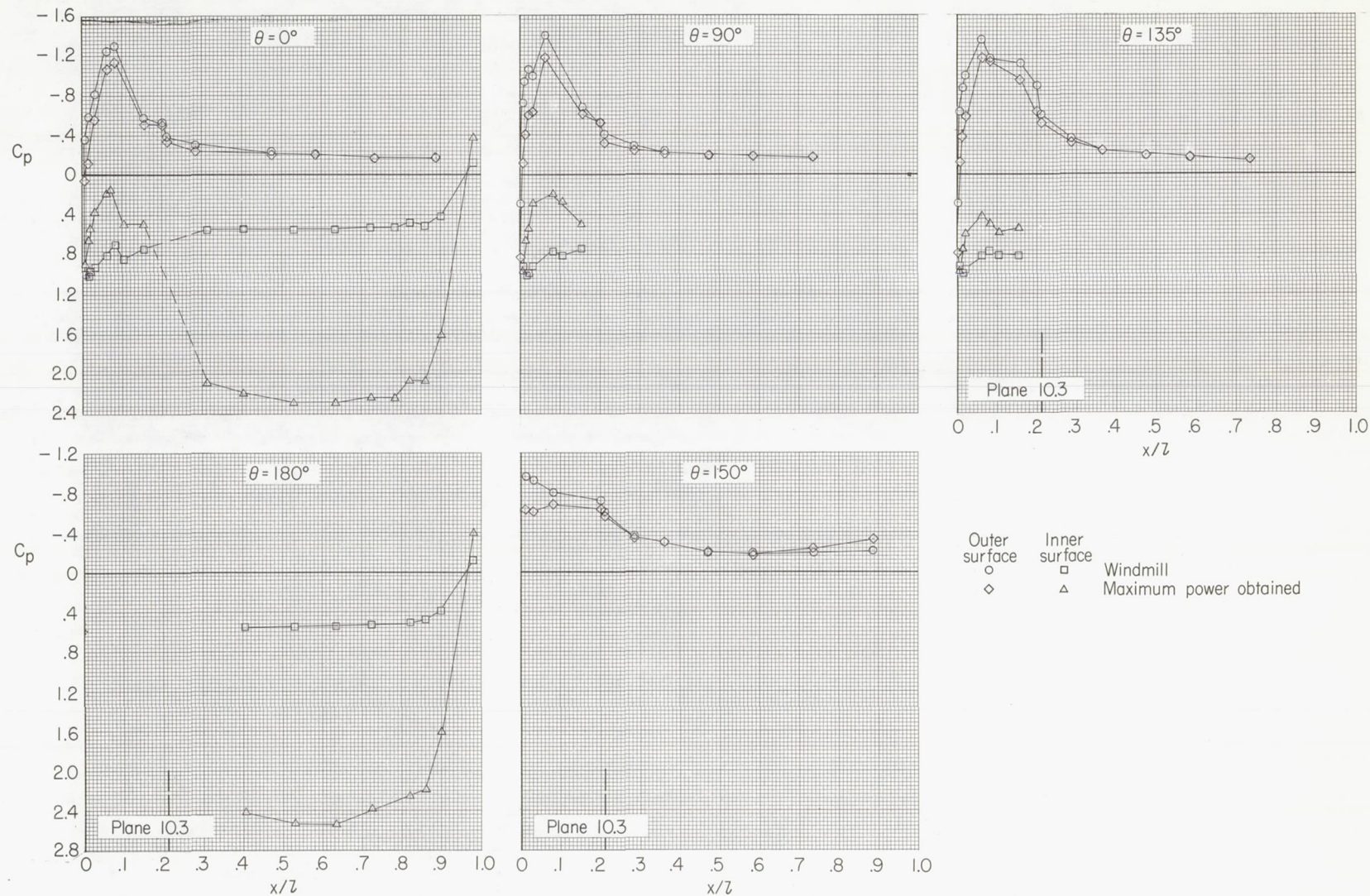
(f) $M = 0.75$; $N_F/\sqrt{\sigma} = 89.8$ percent.

Figure 45.- Continued.



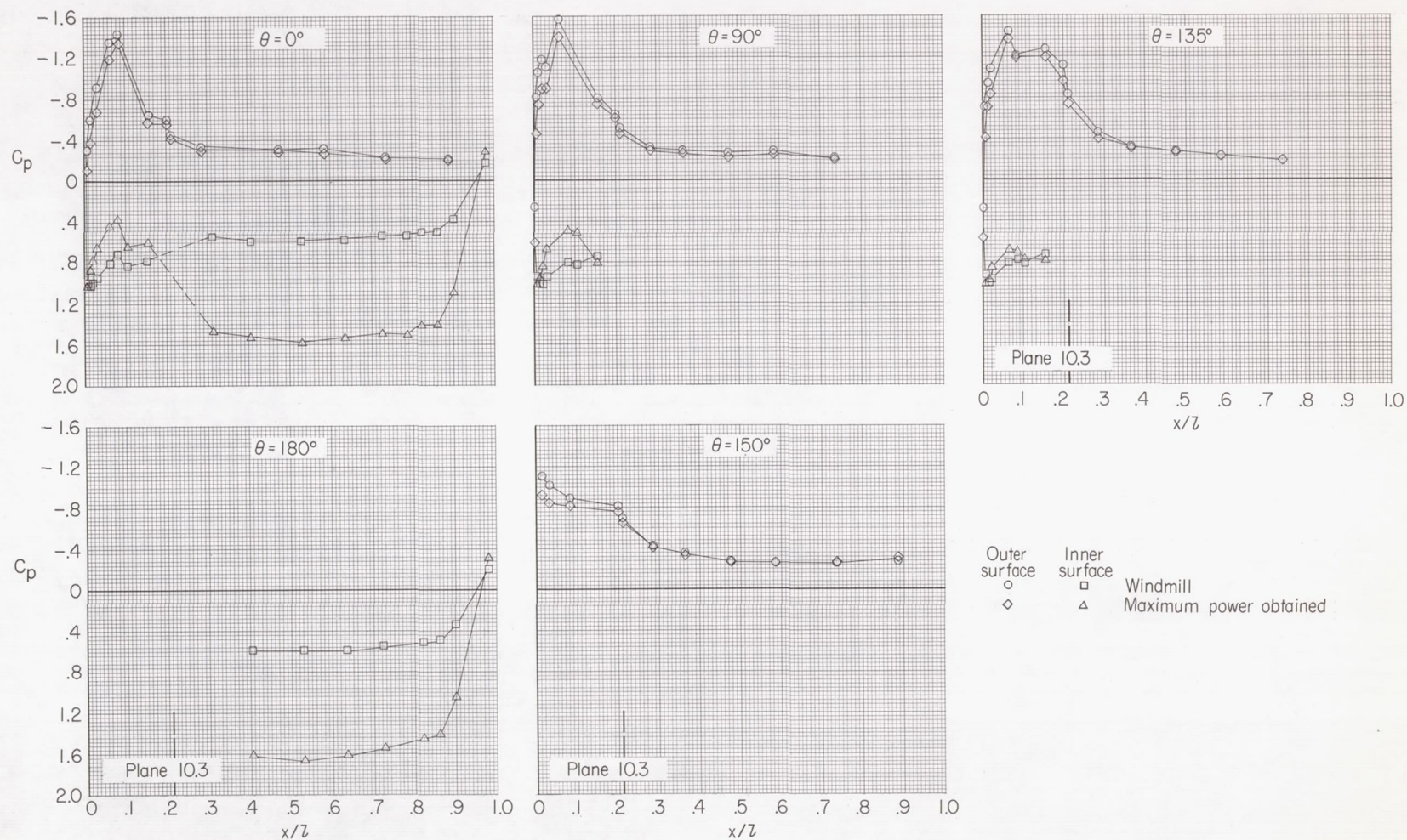
(g) $M = 0.80$; $N_F/\sqrt{\sigma} = 87.5$ percent.

Figure 45.- Concluded.



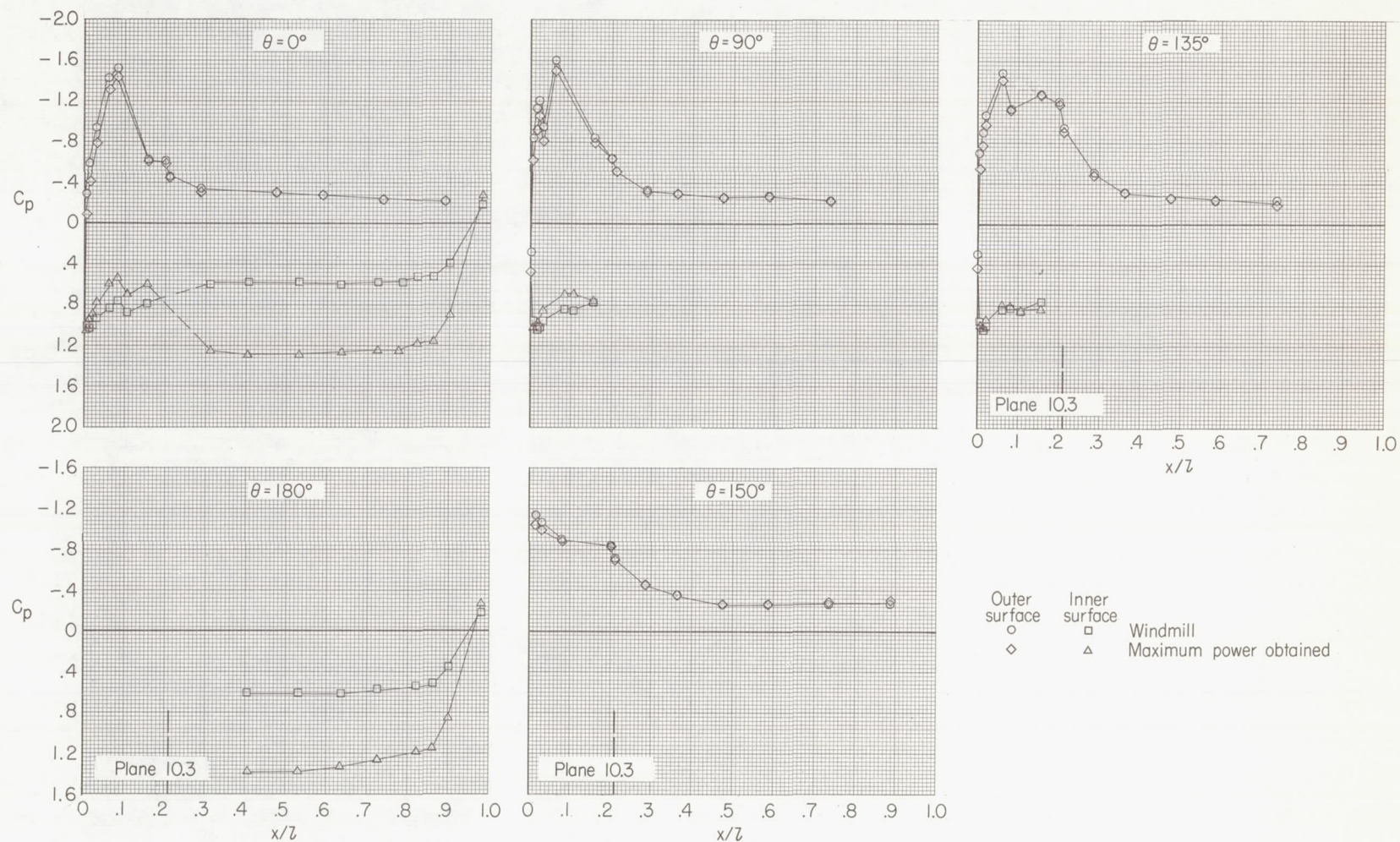
(a) $M = 0.20$; $N_F/\sqrt{\sigma} = 95.3$ percent.

Figure 46.- Fan-nacelle pressure distributions for configuration 344.



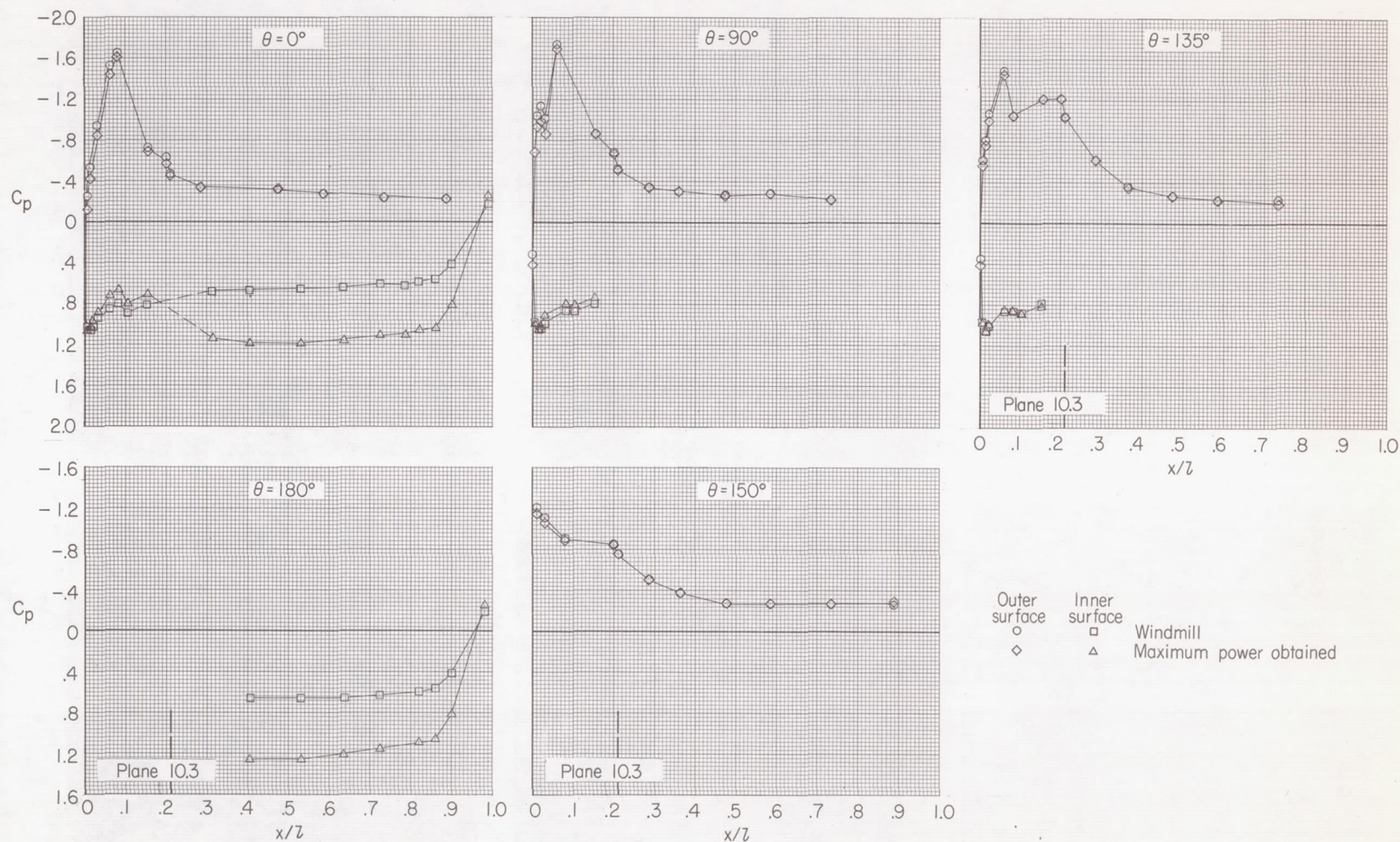
(b) $M = 0.30$; $N_F/\sqrt{\sigma} = 94.8$ percent.

Figure 46.- Continued.



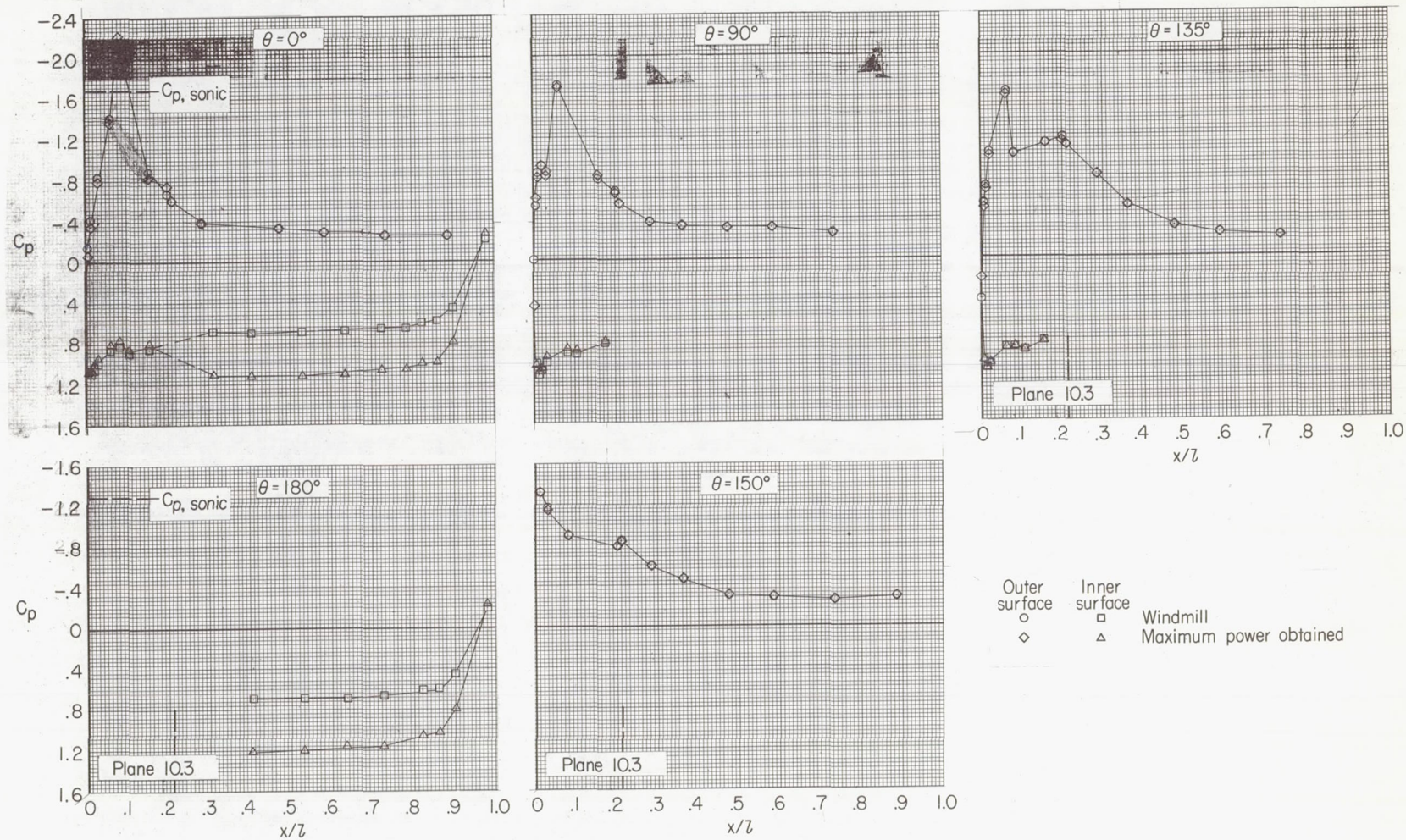
(c) $M = 0.40$; $N_F/\sqrt{\sigma} = 94.2$ percent.

Figure 46.- Continued.



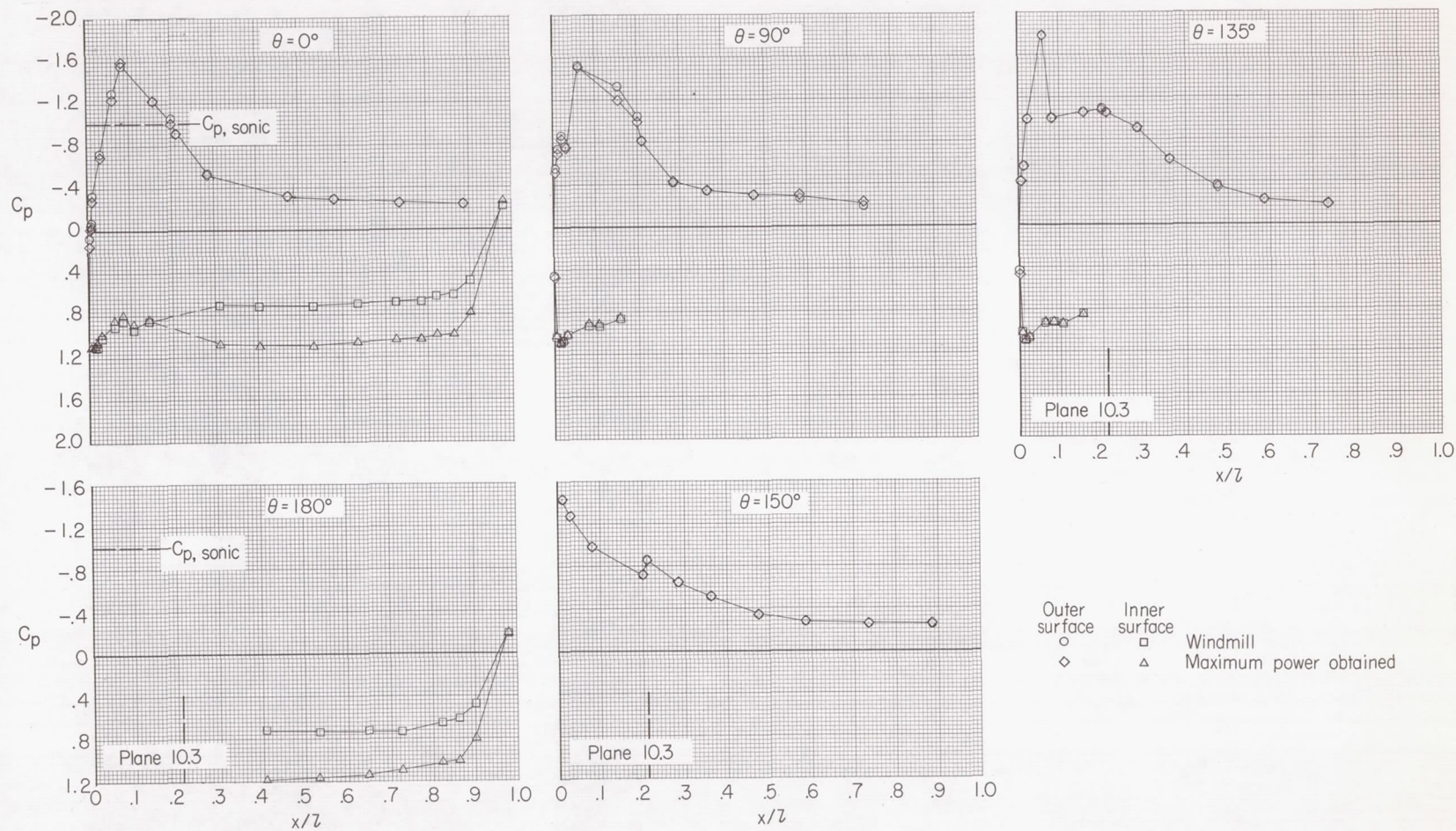
(d) $M = 0.50$; $N_F/\sqrt{\sigma} = 93.5$ percent.

Figure 46.- Continued.



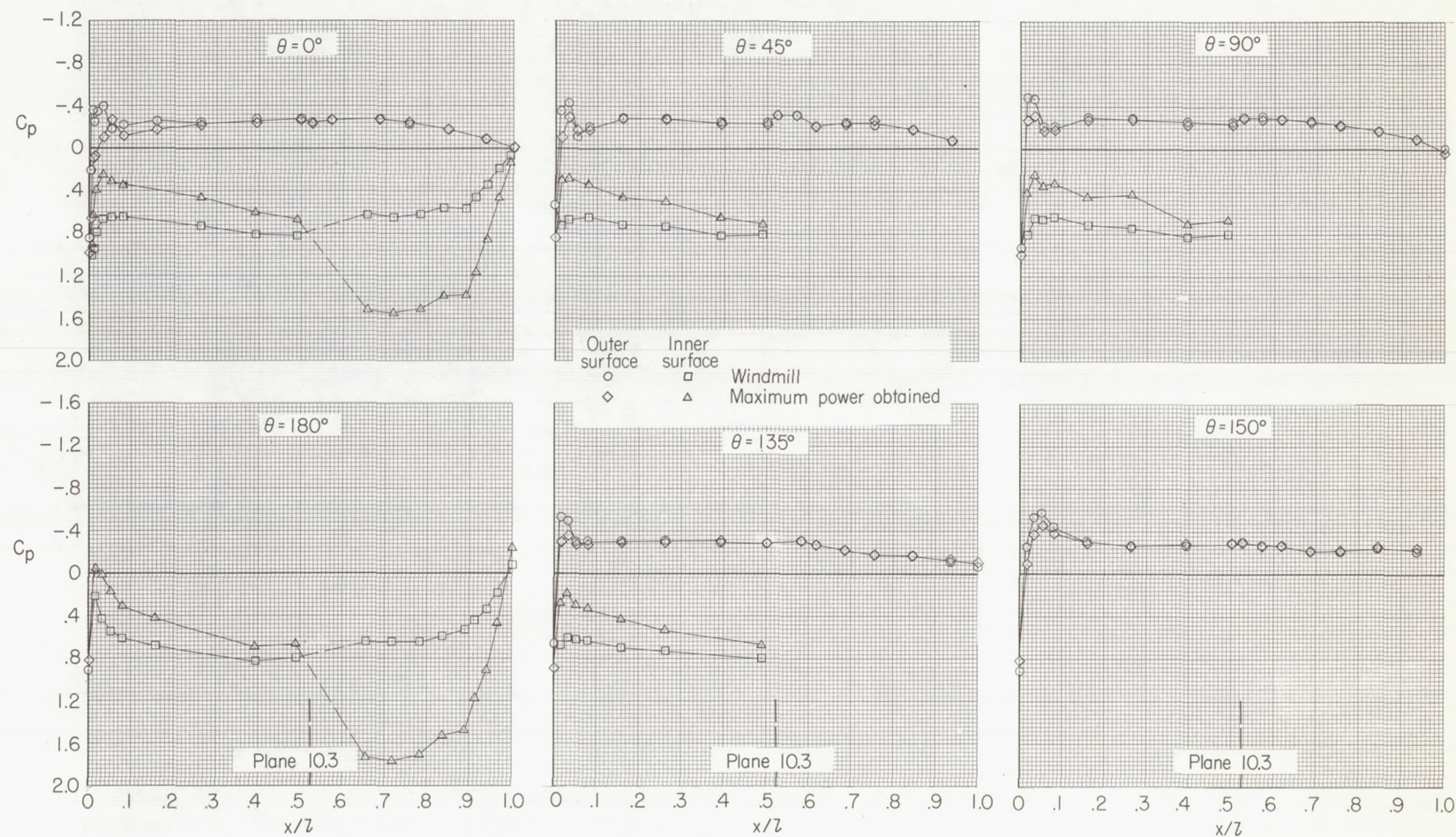
(e) $M = 0.60$; $N_F/\sqrt{\sigma} = 93.8$ percent.

Figure 46.- Continued.



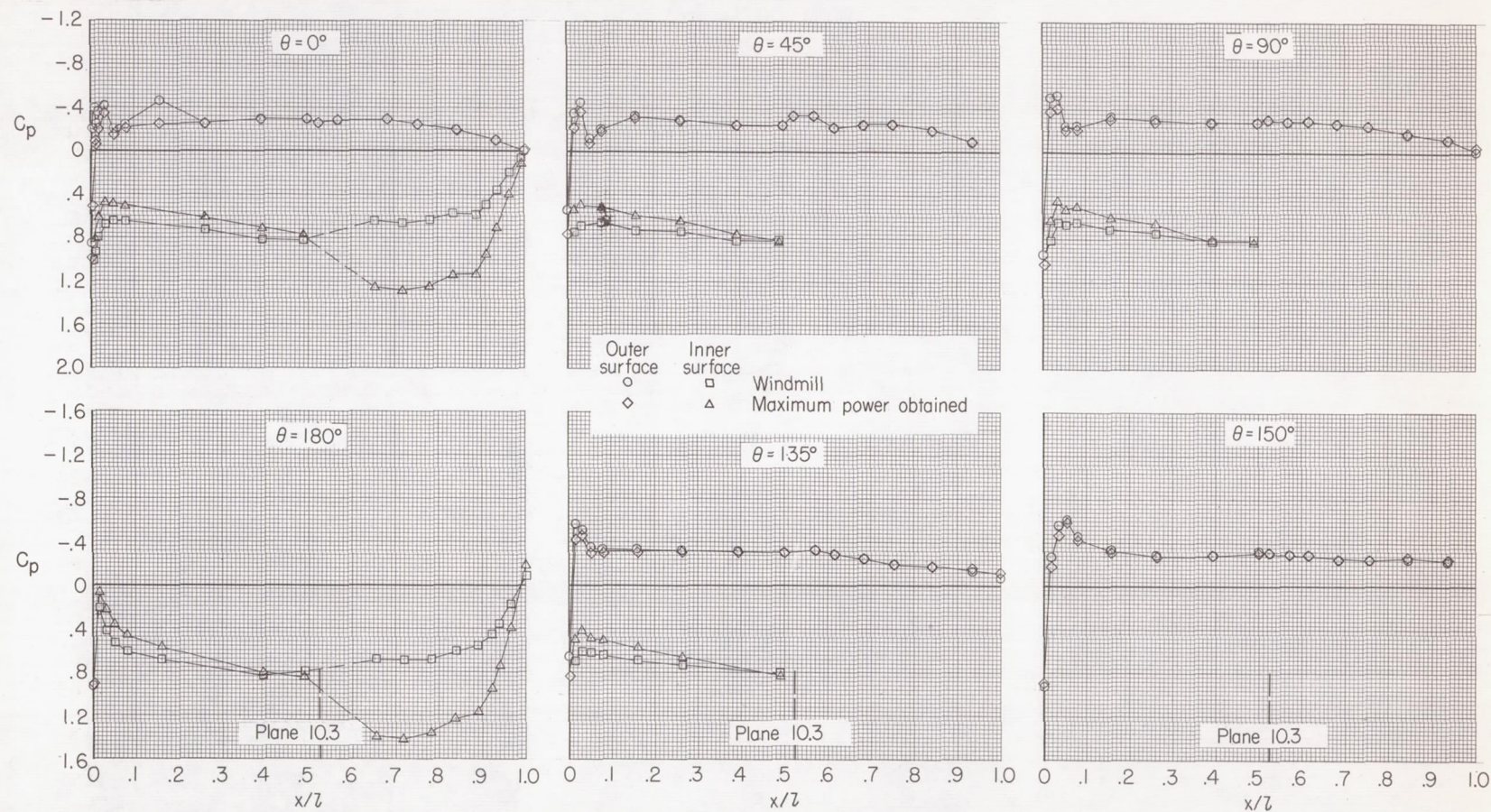
(f) $M = 0.65$; $N_F/\sqrt{\sigma} = 91.7$ percent.

Figure 46.- Concluded.



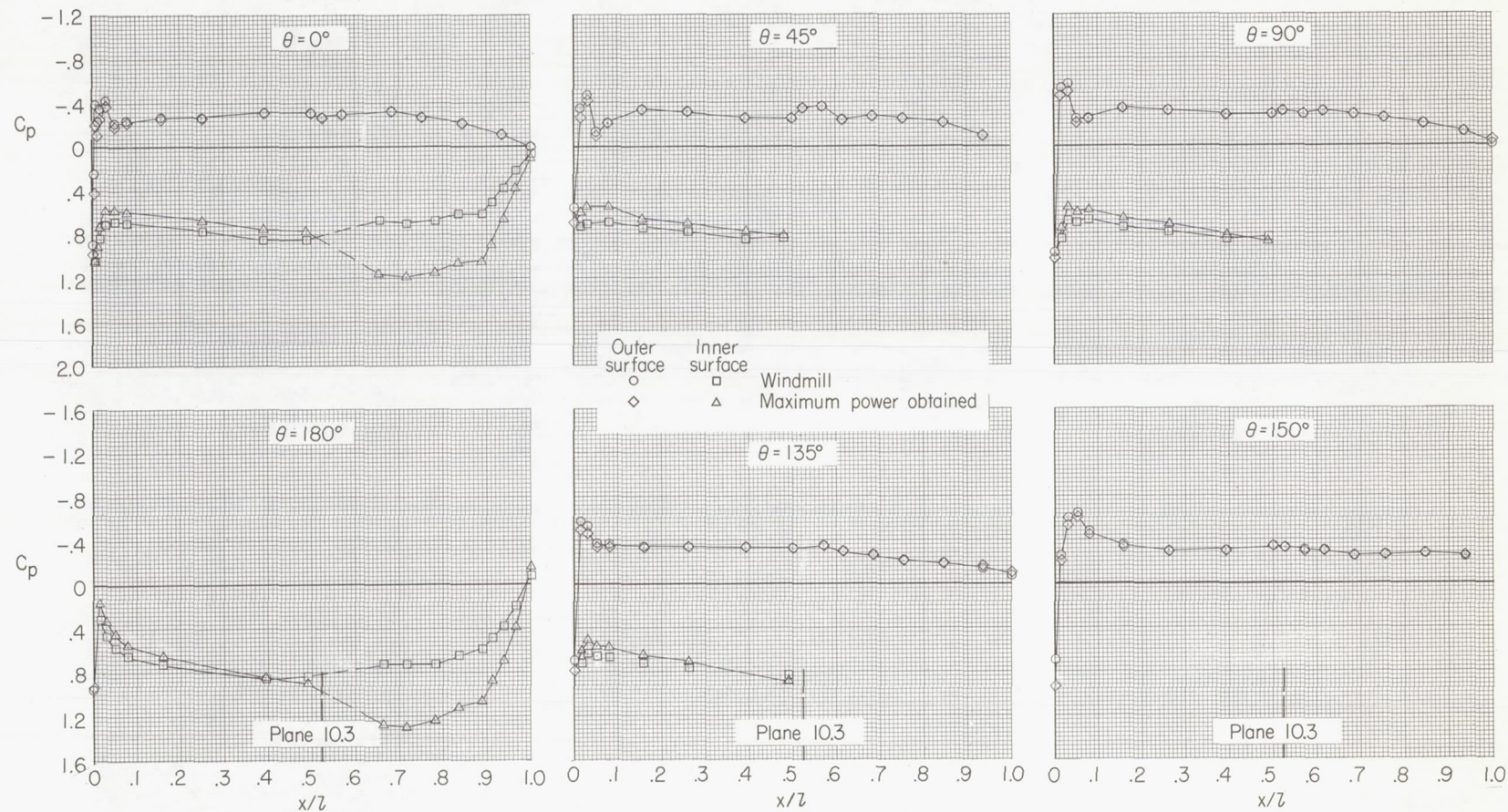
(a) $M = 0.30$; $N_F/\sqrt{\sigma} = 98.1$ percent.

Figure 47.- Fan-nacelle pressure distributions for configuration 123.



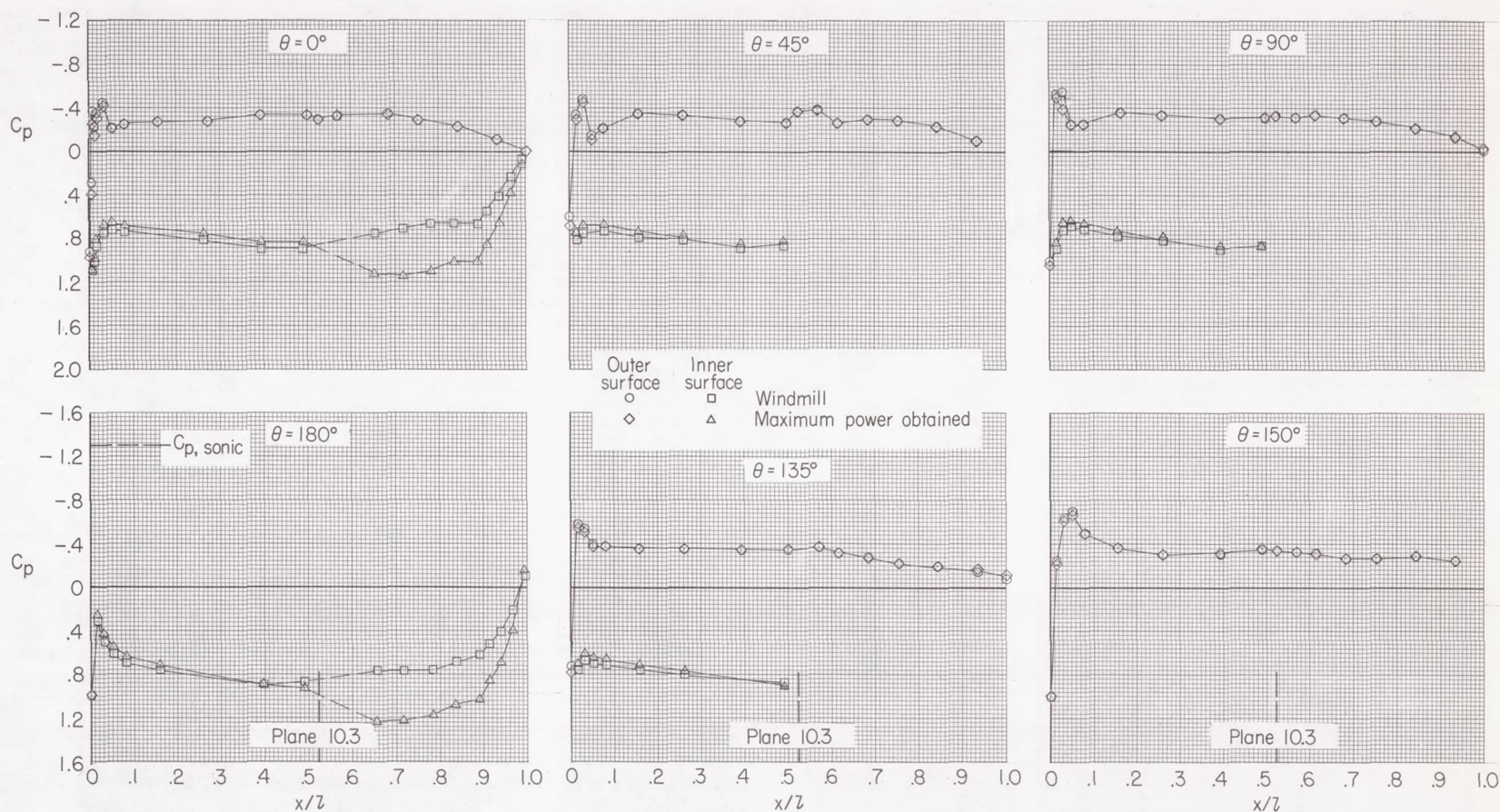
(b) $M = 0.40$; $N_F/\sqrt{\sigma} = 97.0$ percent.

Figure 47.- Continued.



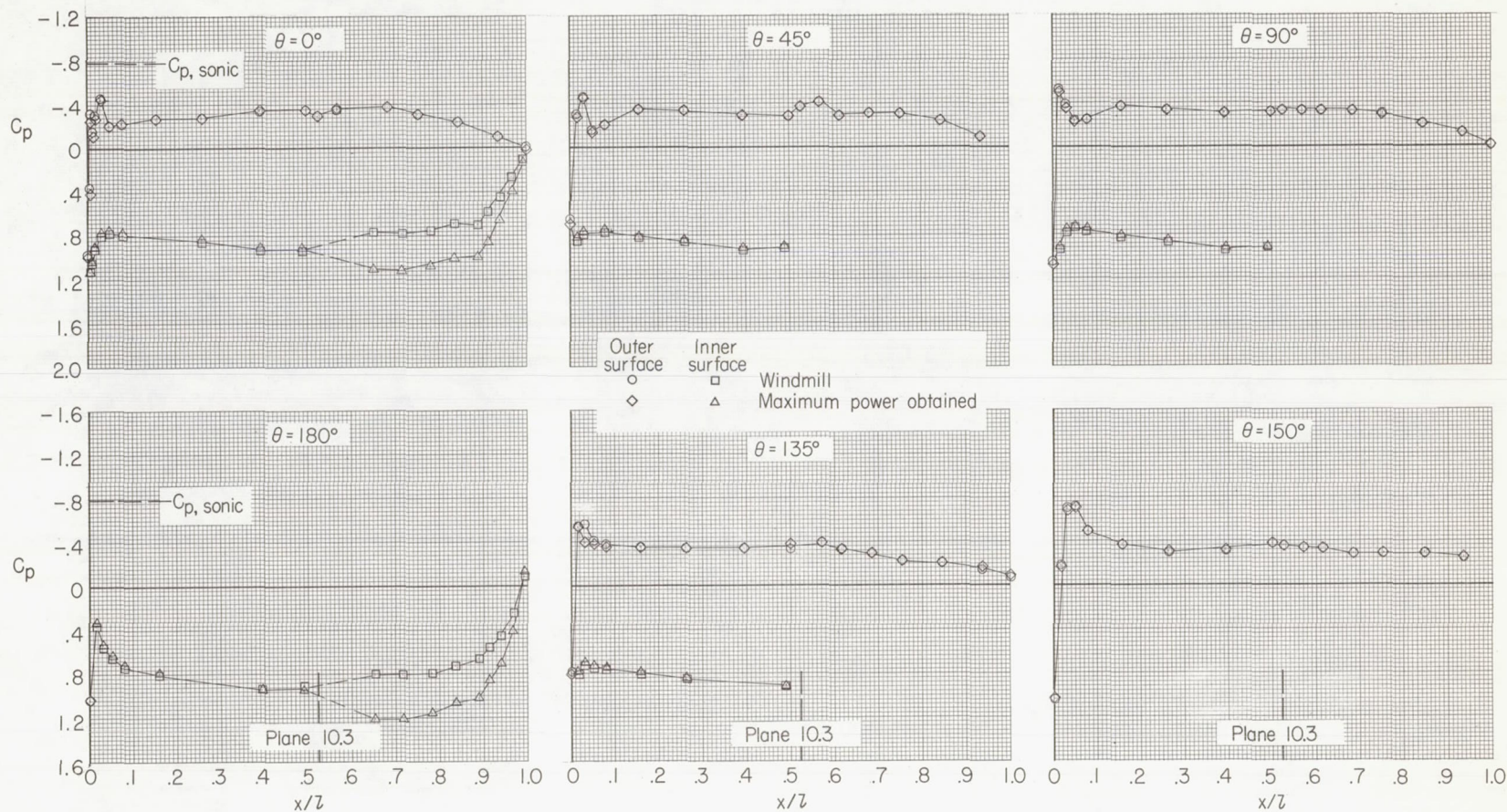
(c) $M = 0.50$; $N_F/\sqrt{\sigma} = 96.8$ percent.

Figure 47.- Continued.



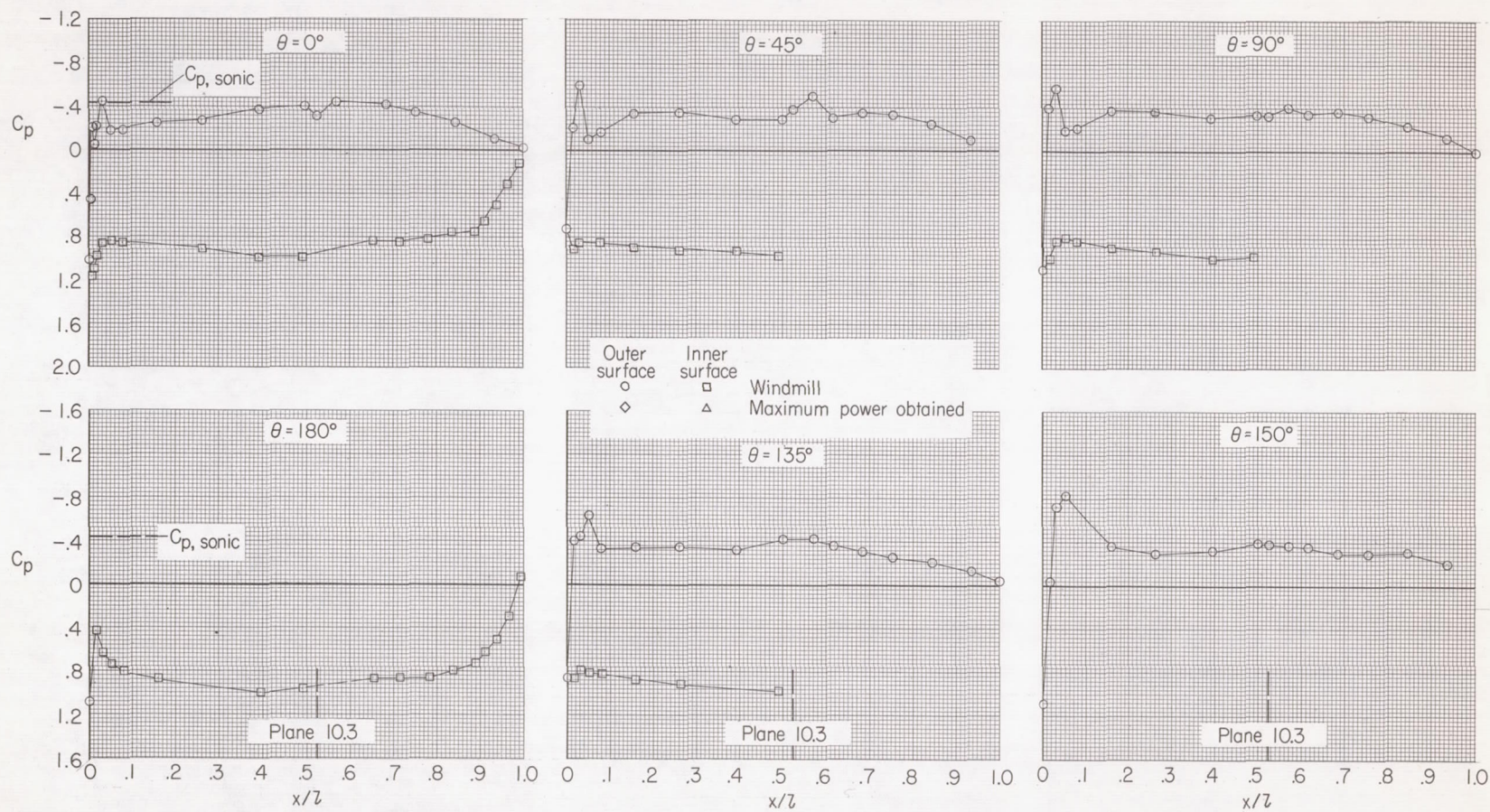
(d) $M = 0.60$; $N_F/\sqrt{\sigma} = 92.4$ percent.

Figure 47.- Continued.



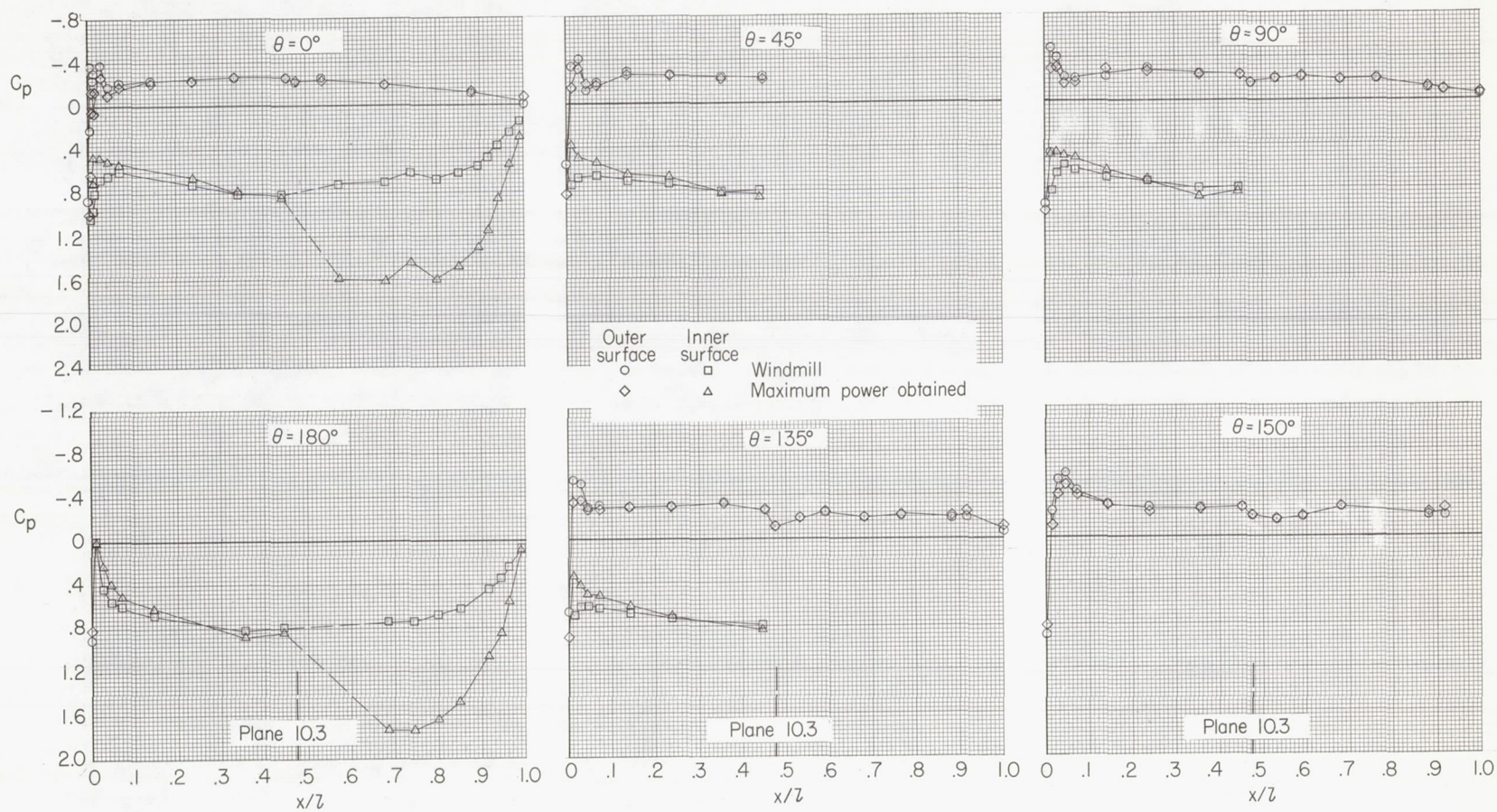
(e) $M = 0.70$; $N_F/\sqrt{\sigma} = 90.6$ percent.

Figure 47.- Continued.



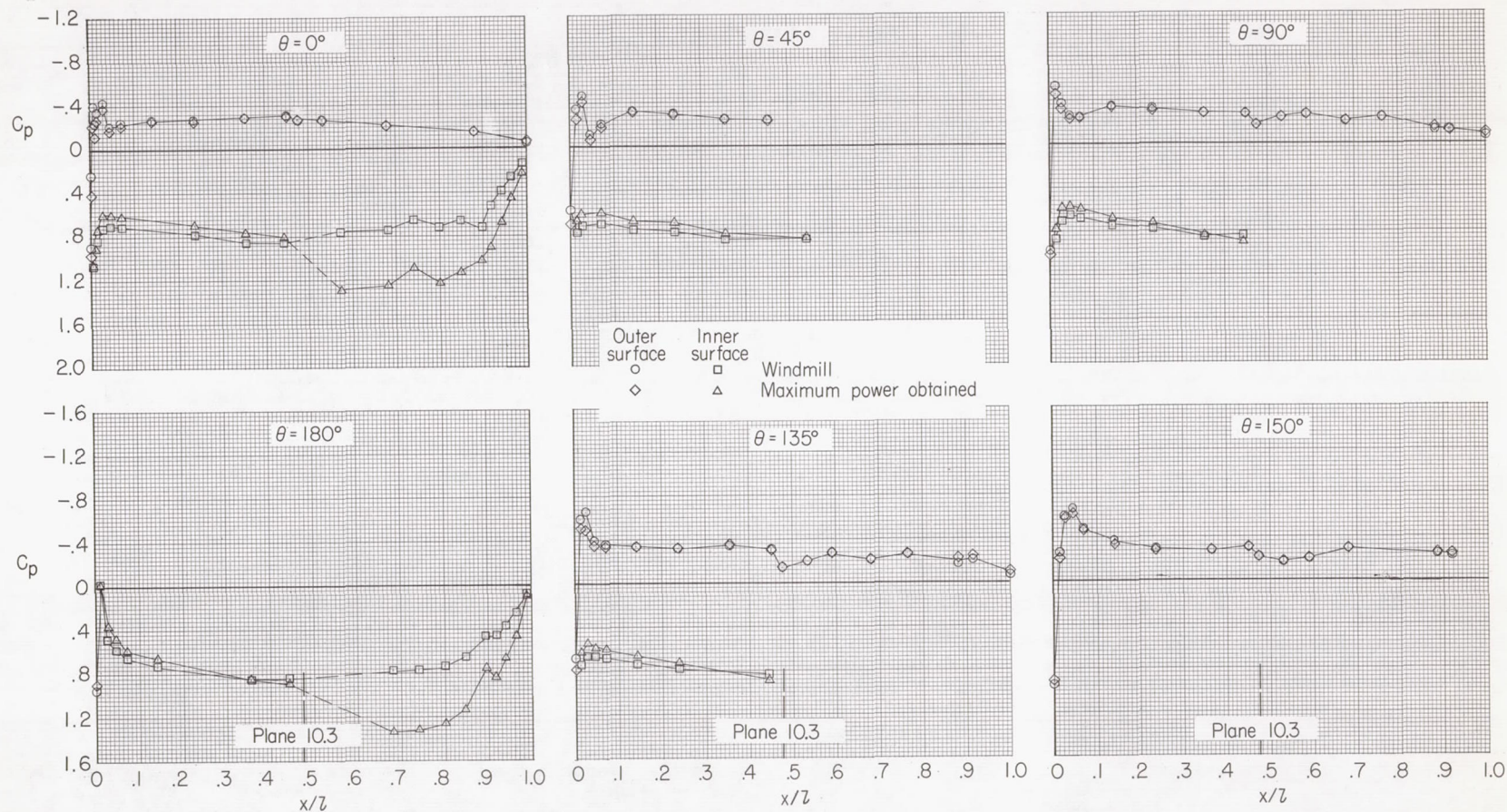
(f) $M = 0.80$.

Figure 47.- Concluded.



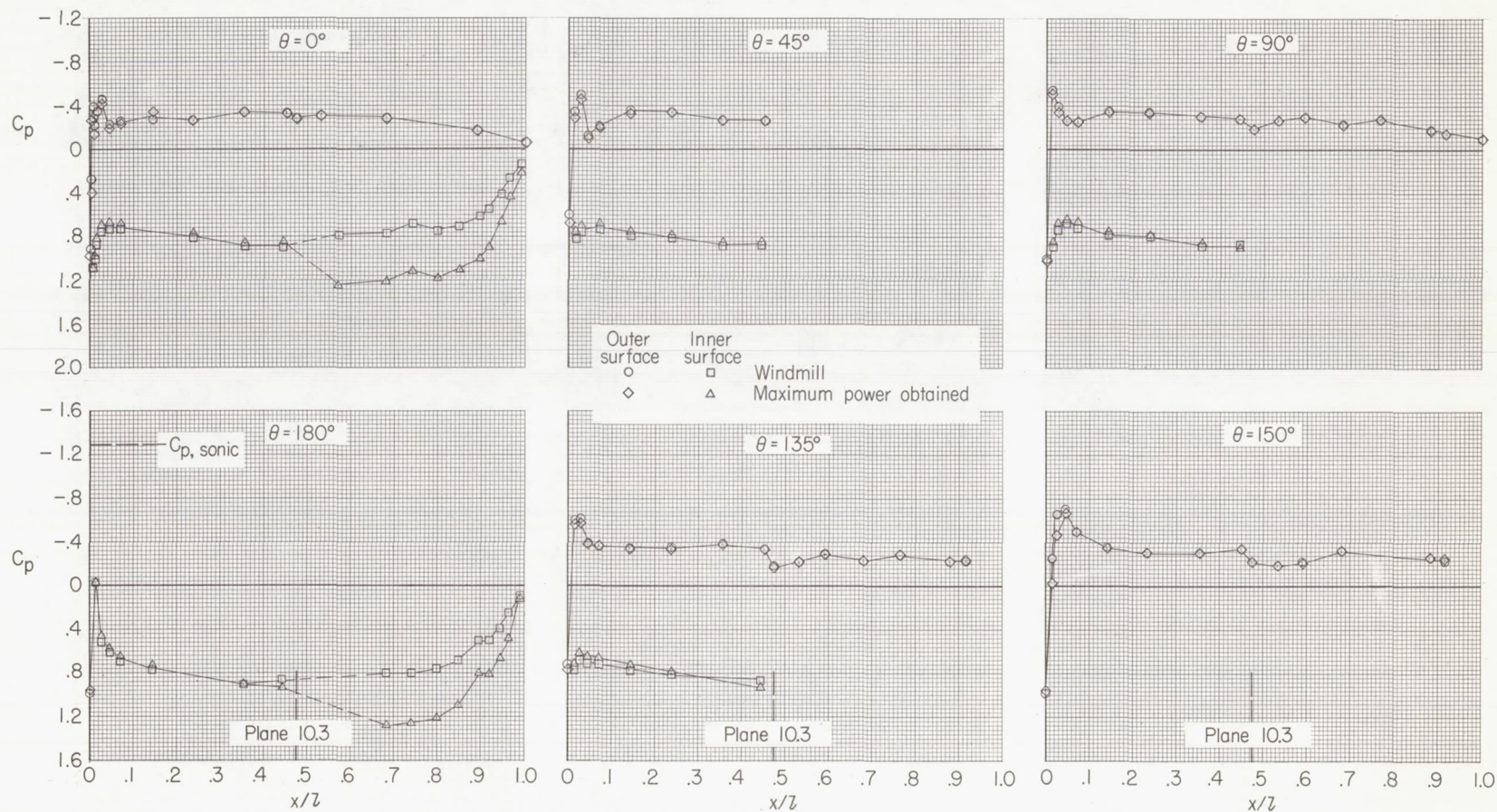
(a) $M = 0.30$; $N_F/\sqrt{\sigma} = 95.8$ percent.

Figure 48.- Fan-nacelle pressure distributions for configuration 113.



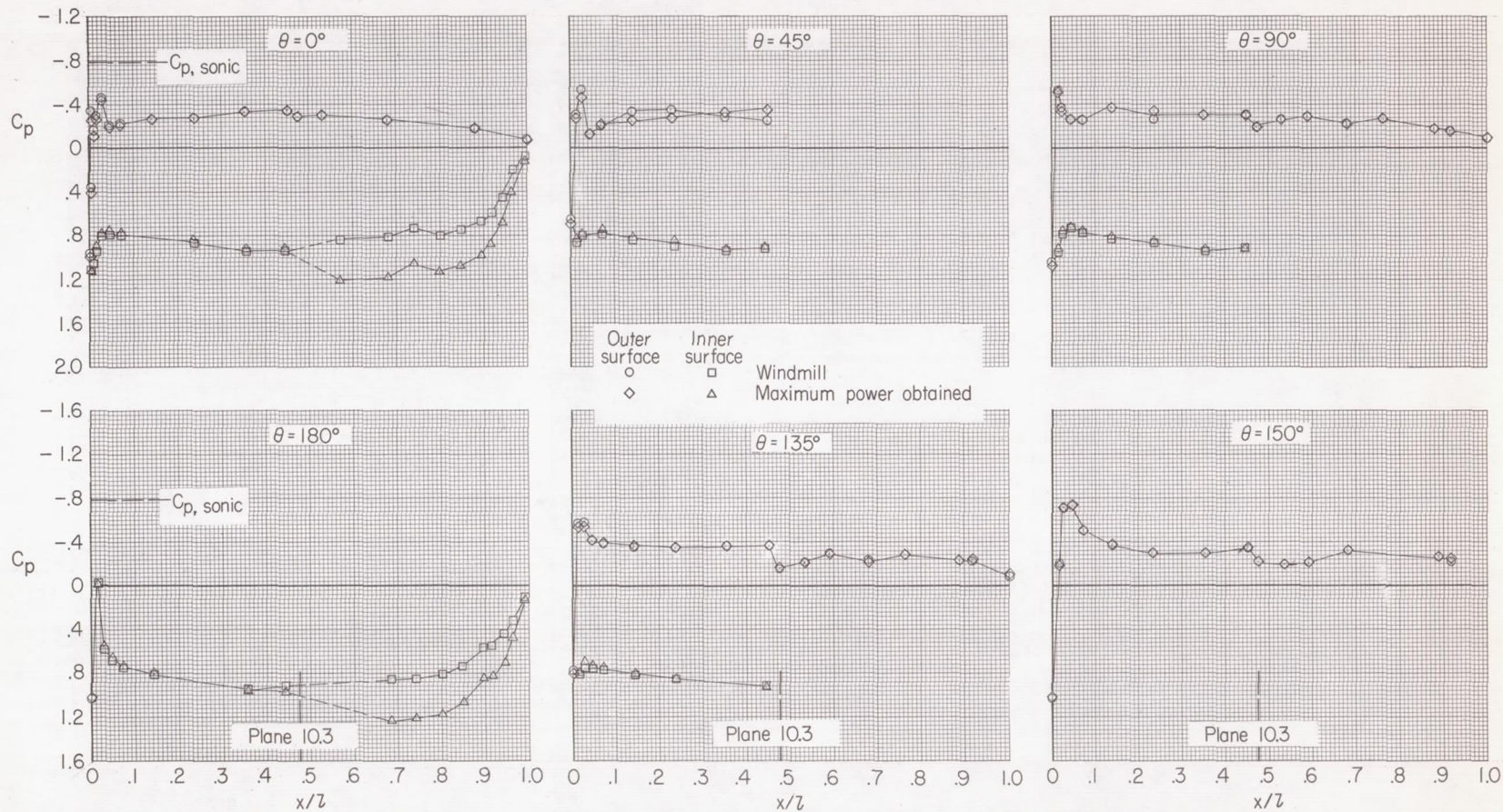
(b) $M = 0.60$; $N_F/\sqrt{\sigma} = 98.0$ percent.

Figure 48.- Continued.



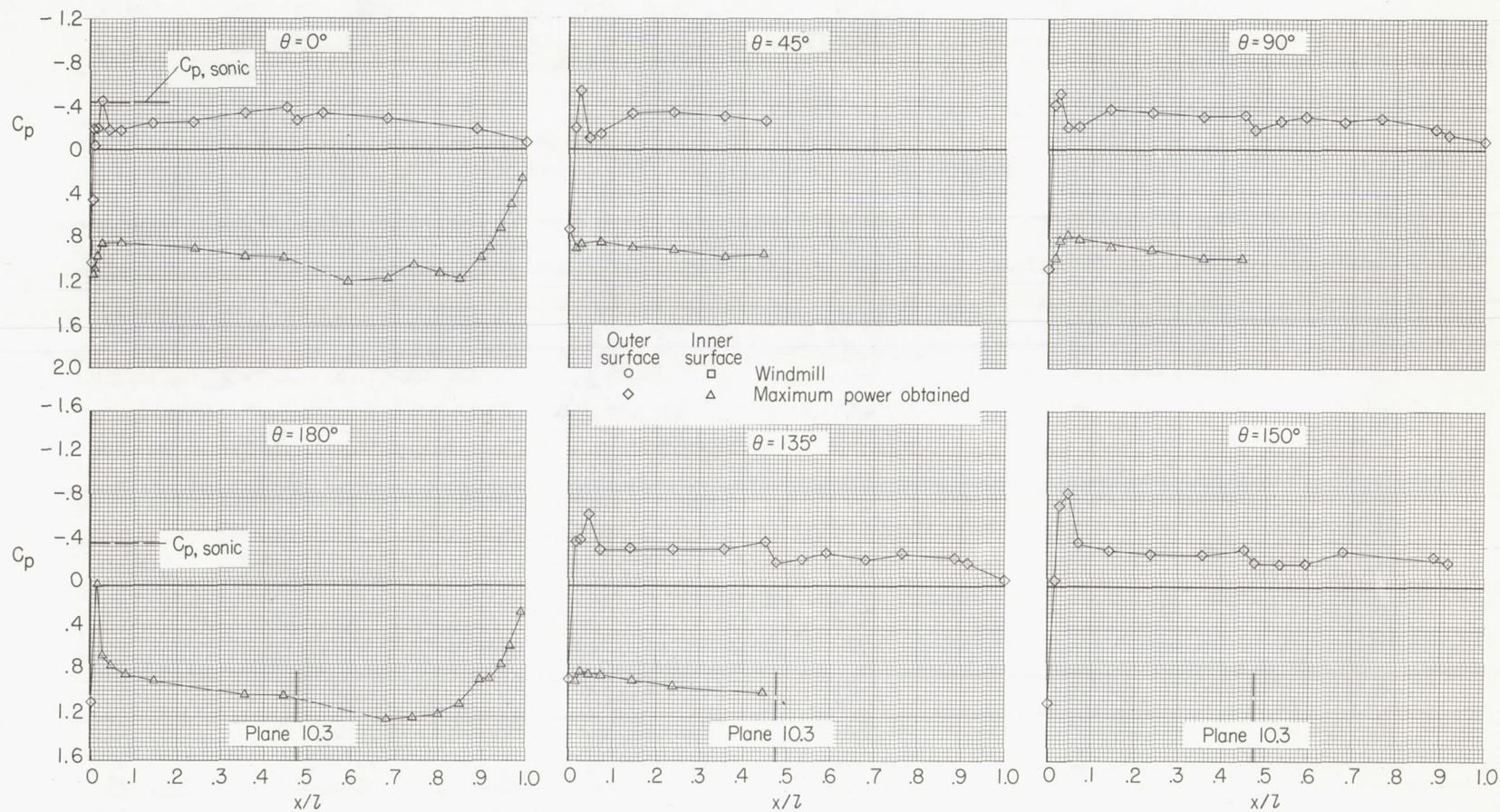
(c) $M = 0.60$; $N_F/\sqrt{\sigma} = 96.4$ percent.

Figure 48.- Continued.



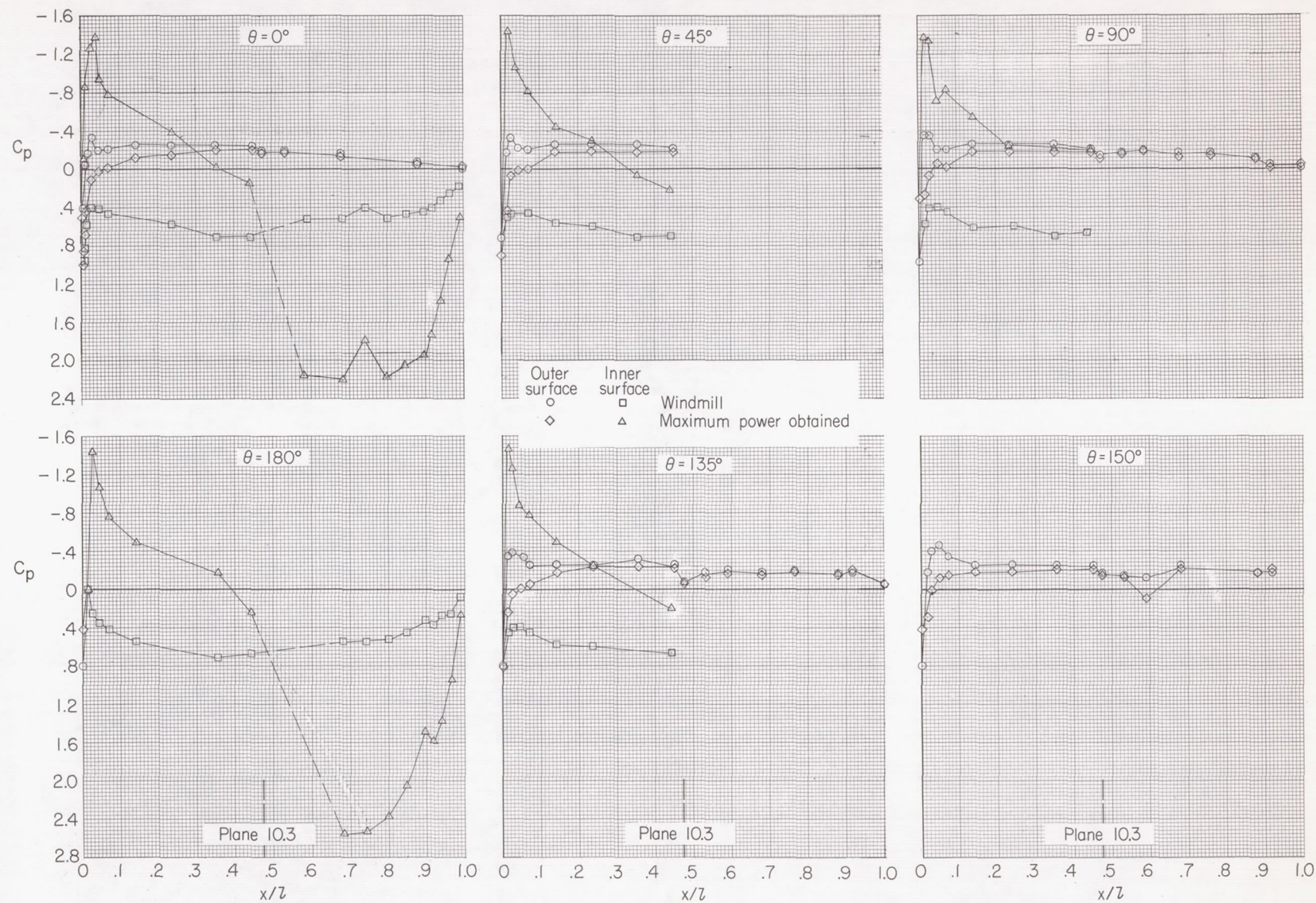
(d) $M = 0.70$; $N_F/\sqrt{\sigma} \approx 93.0$ percent.

Figure 48.- Continued.



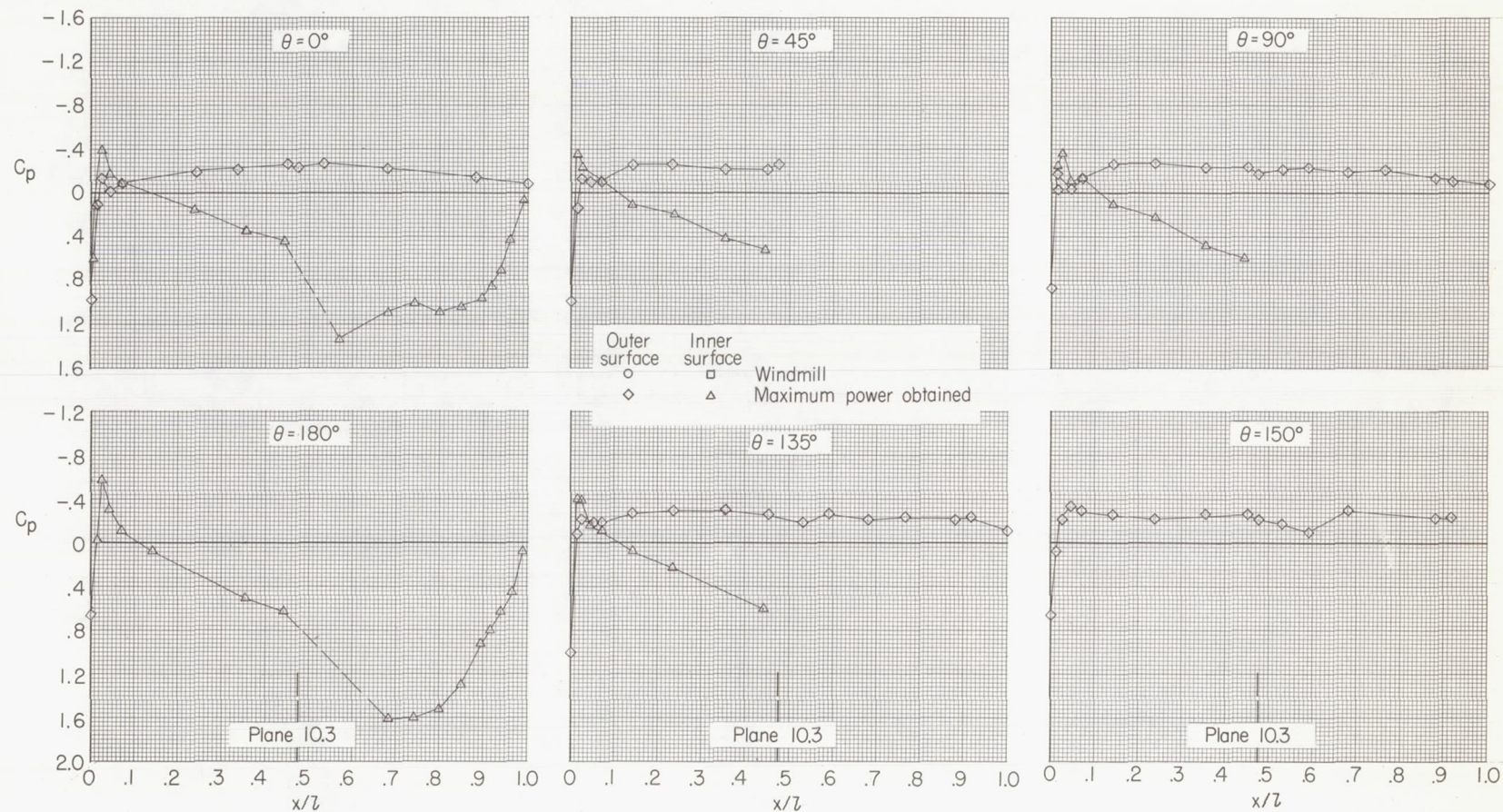
(e) $M = 0.80$; $N_F/\sqrt{\sigma} = 90.8$ percent.

Figure 48.- Concluded.



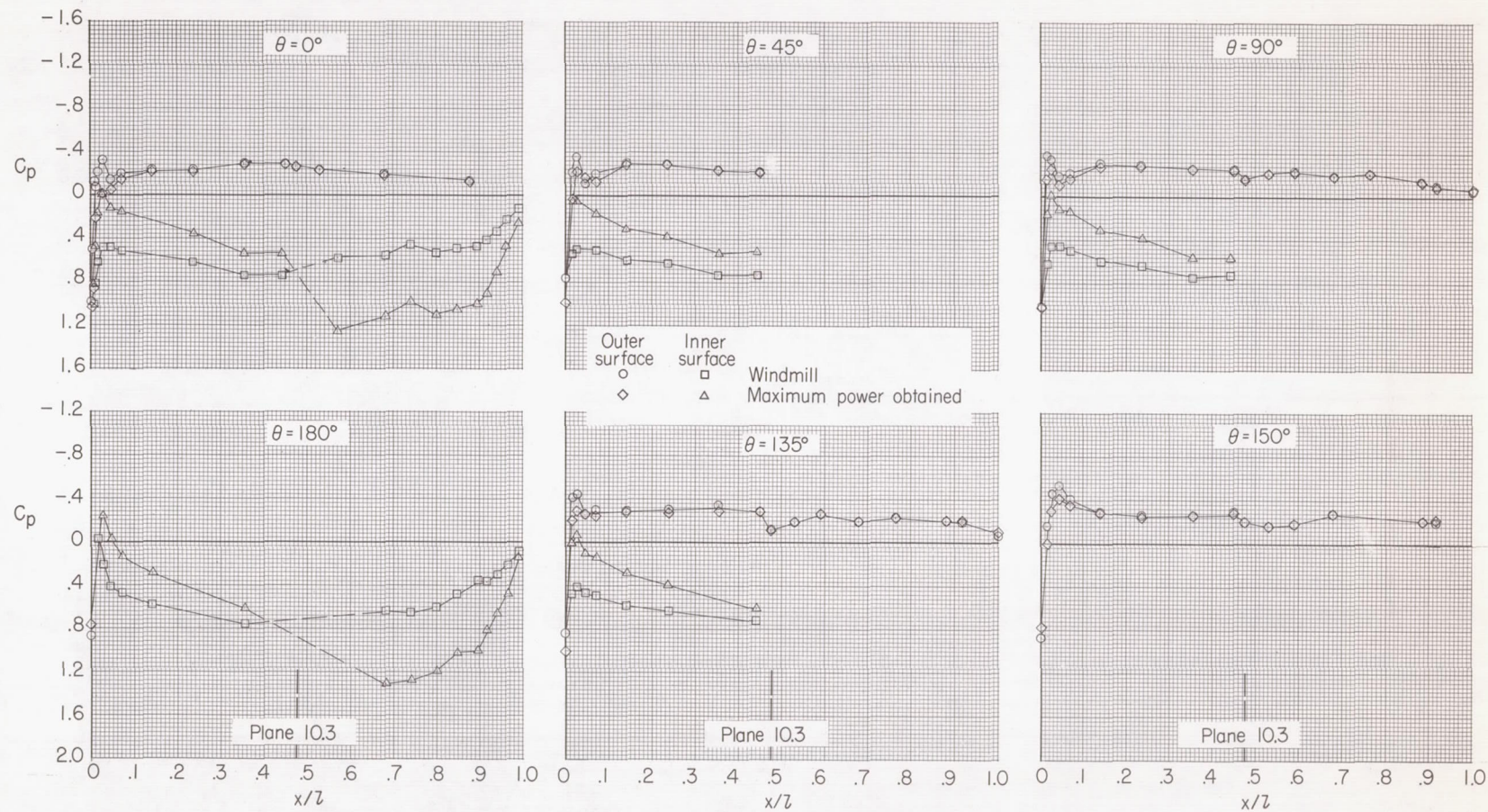
(a) $M = 0.20$; $N_F/\sqrt{\sigma} = 99.6$ percent.

Figure 49.- Fan-nacelle pressure distributions for configuration 112.



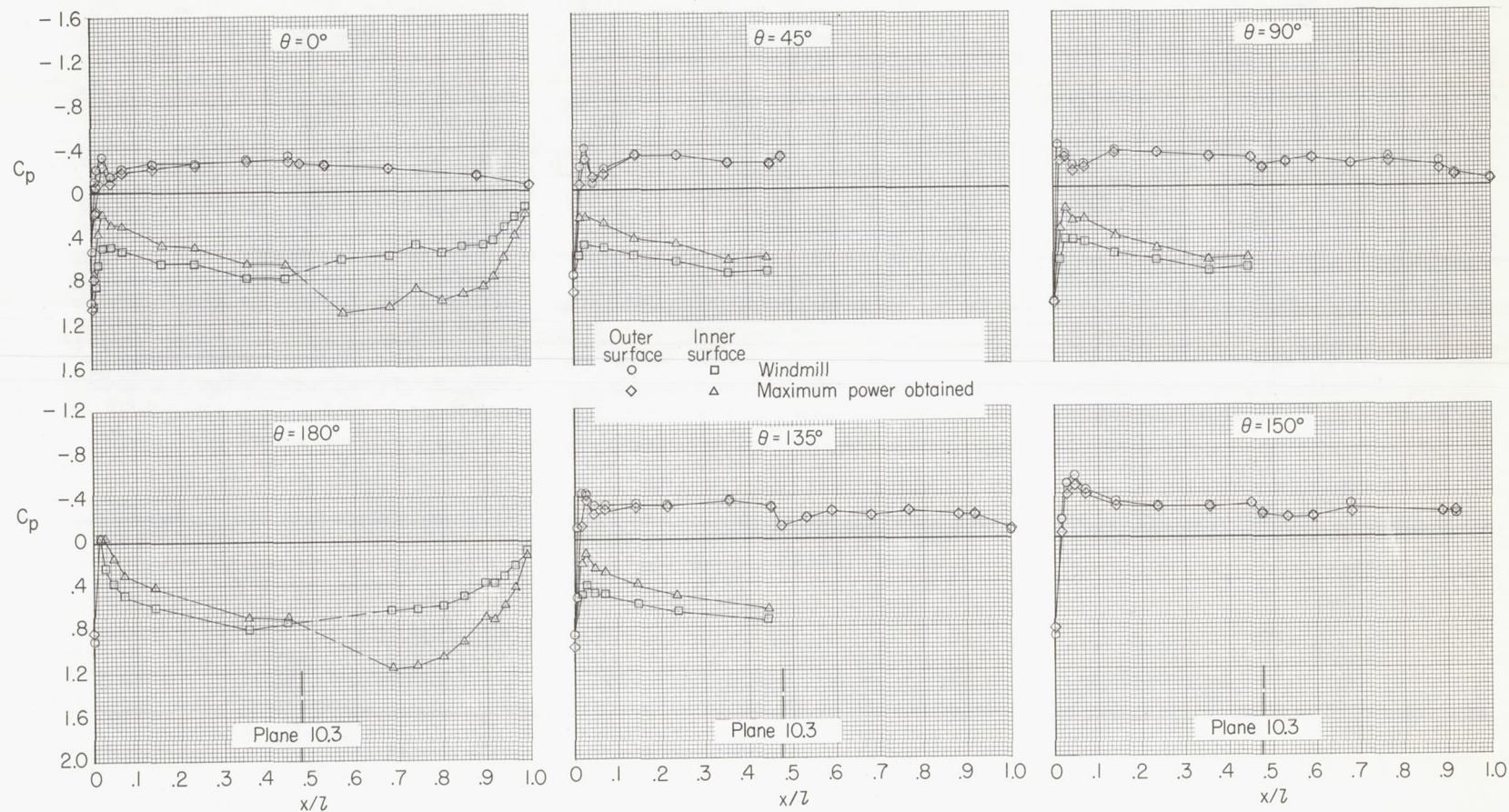
(b) $M = 0.30$; $N_F/\sqrt{\sigma} = 96.8$ percent.

Figure 49.- Continued.



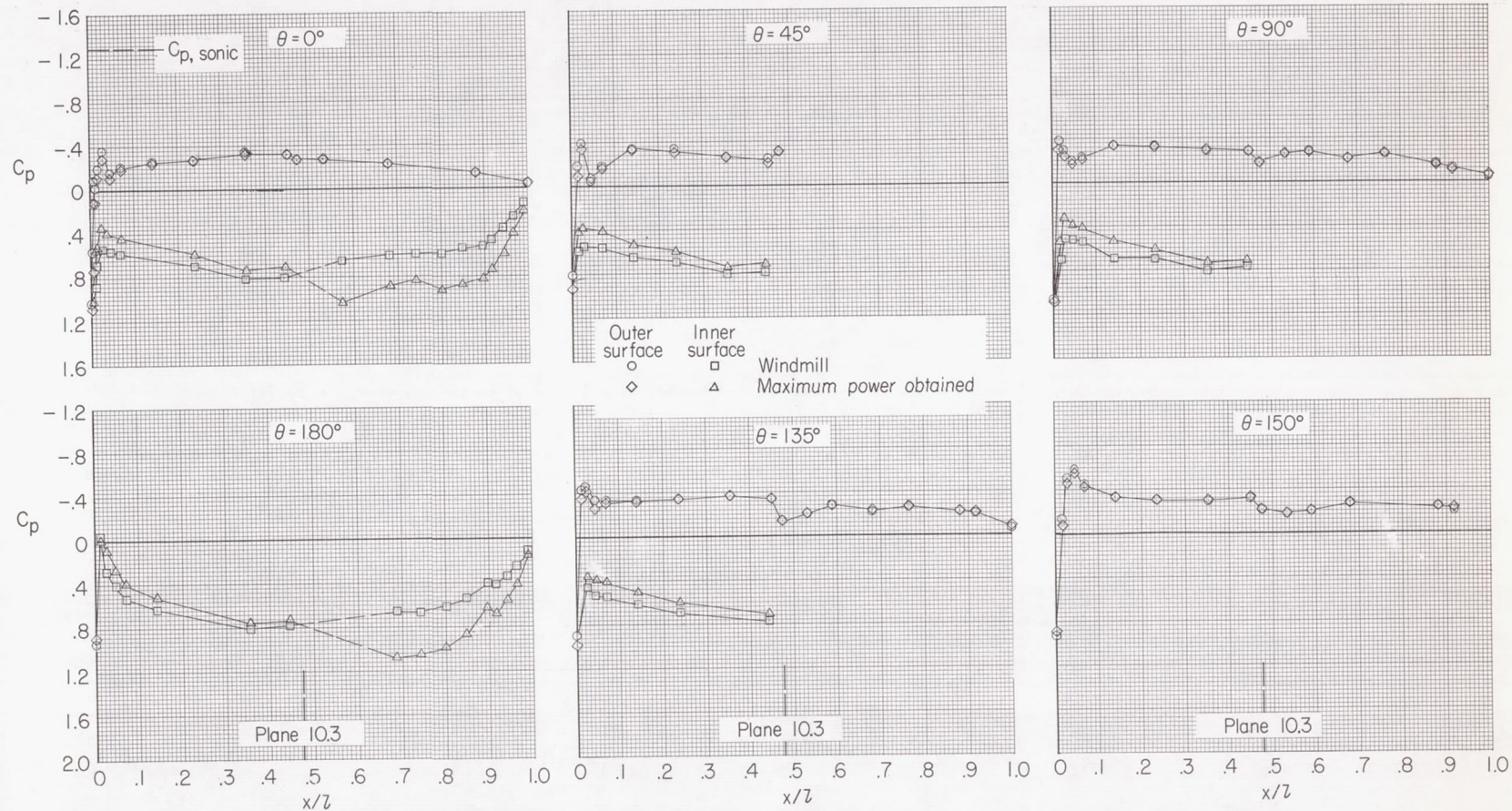
(c) $M = 0.40$; $N_F/\sqrt{\sigma} = 93.3$ percent.

Figure 49.- Continued.



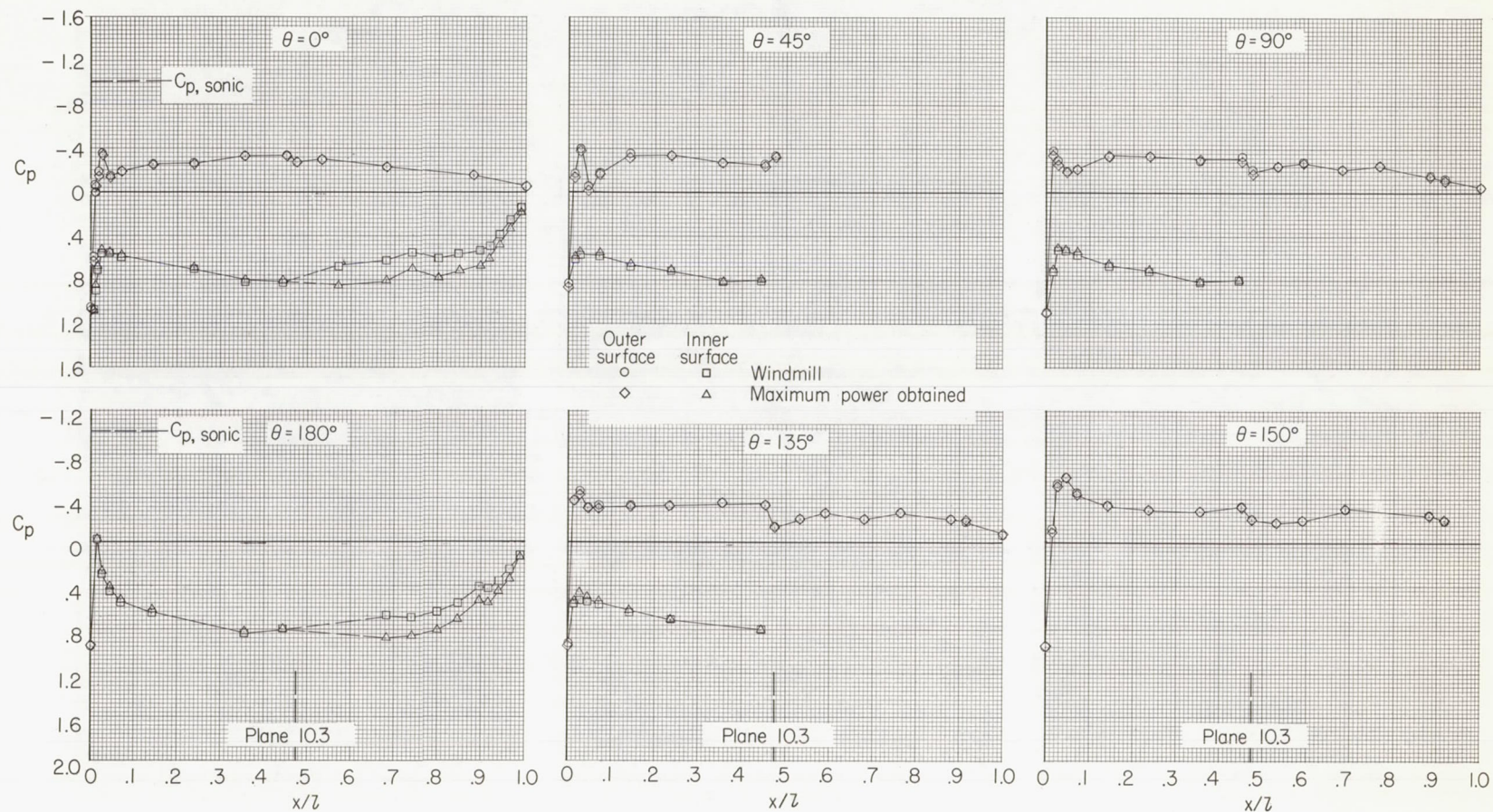
(d) $M = 0.50$; $N_F/\sqrt{\sigma} = 92.9$ percent.

Figure 49.- Continued.



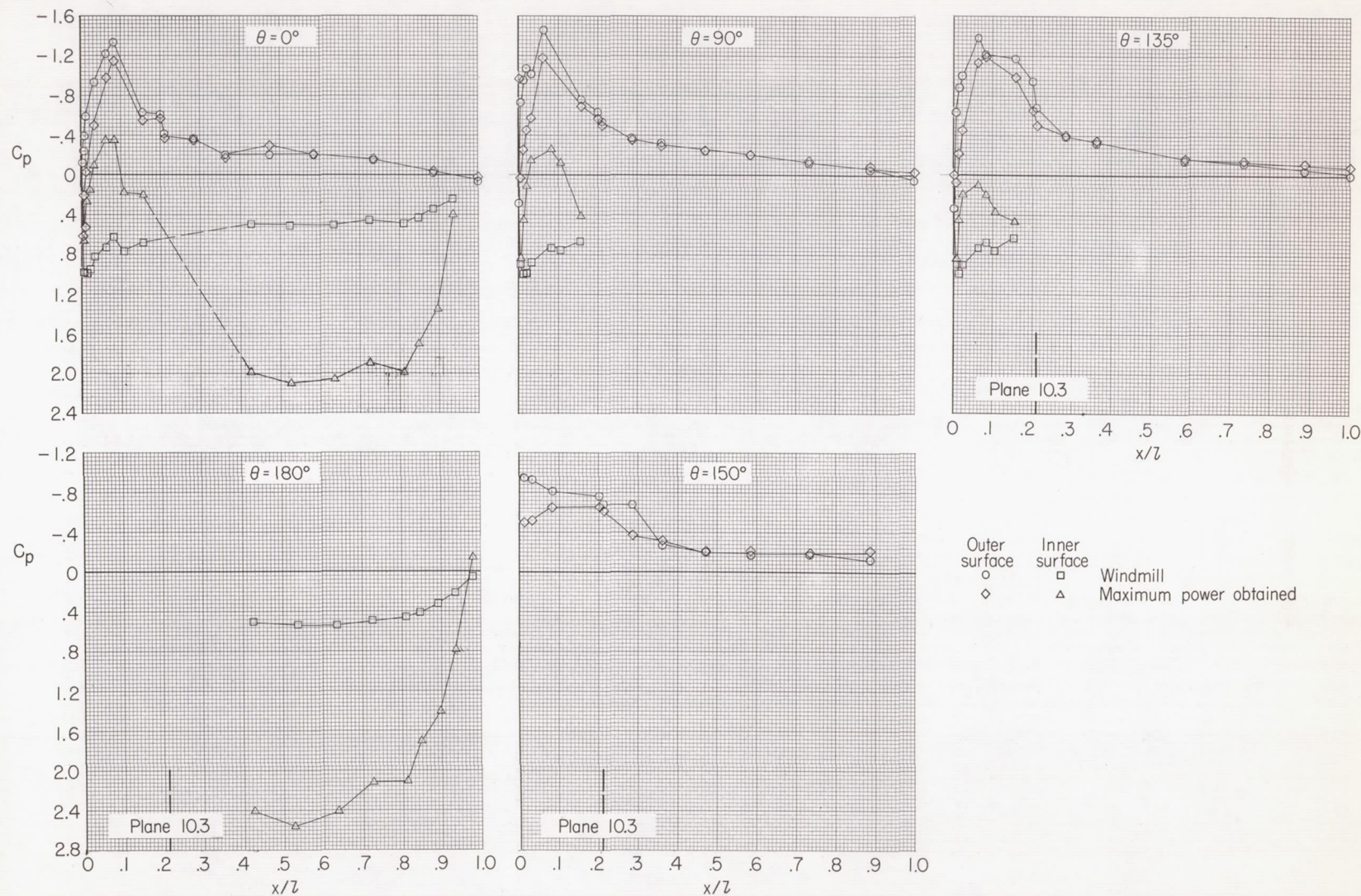
(e) $M = 0.60$; $N_F/\sqrt{\sigma} = 94.0$ percent.

Figure 49.- Continued.



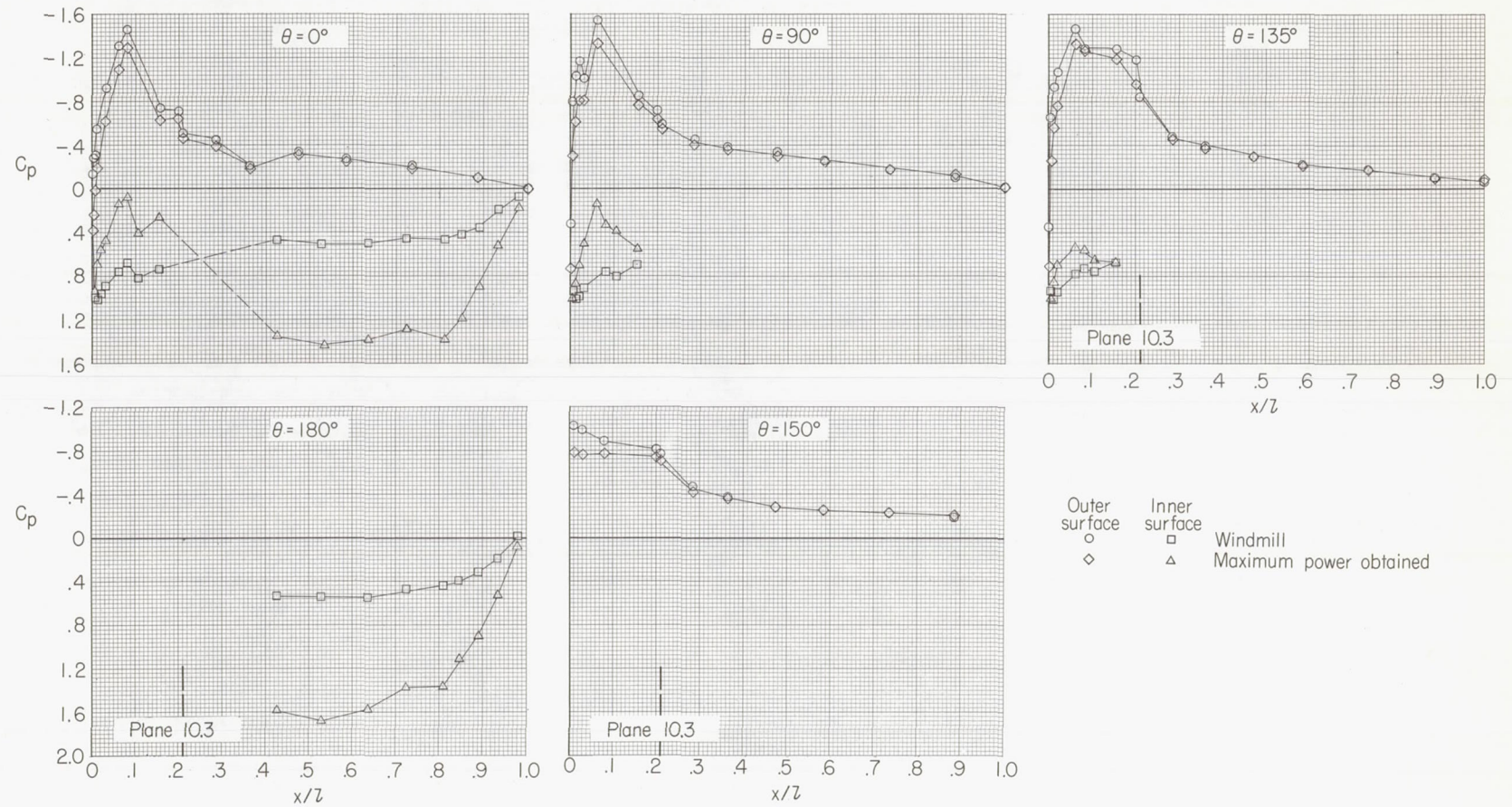
(f) $M = 0.65$; $N_F/\sqrt{\sigma} = 77.0$ percent.

Figure 49.- Concluded.



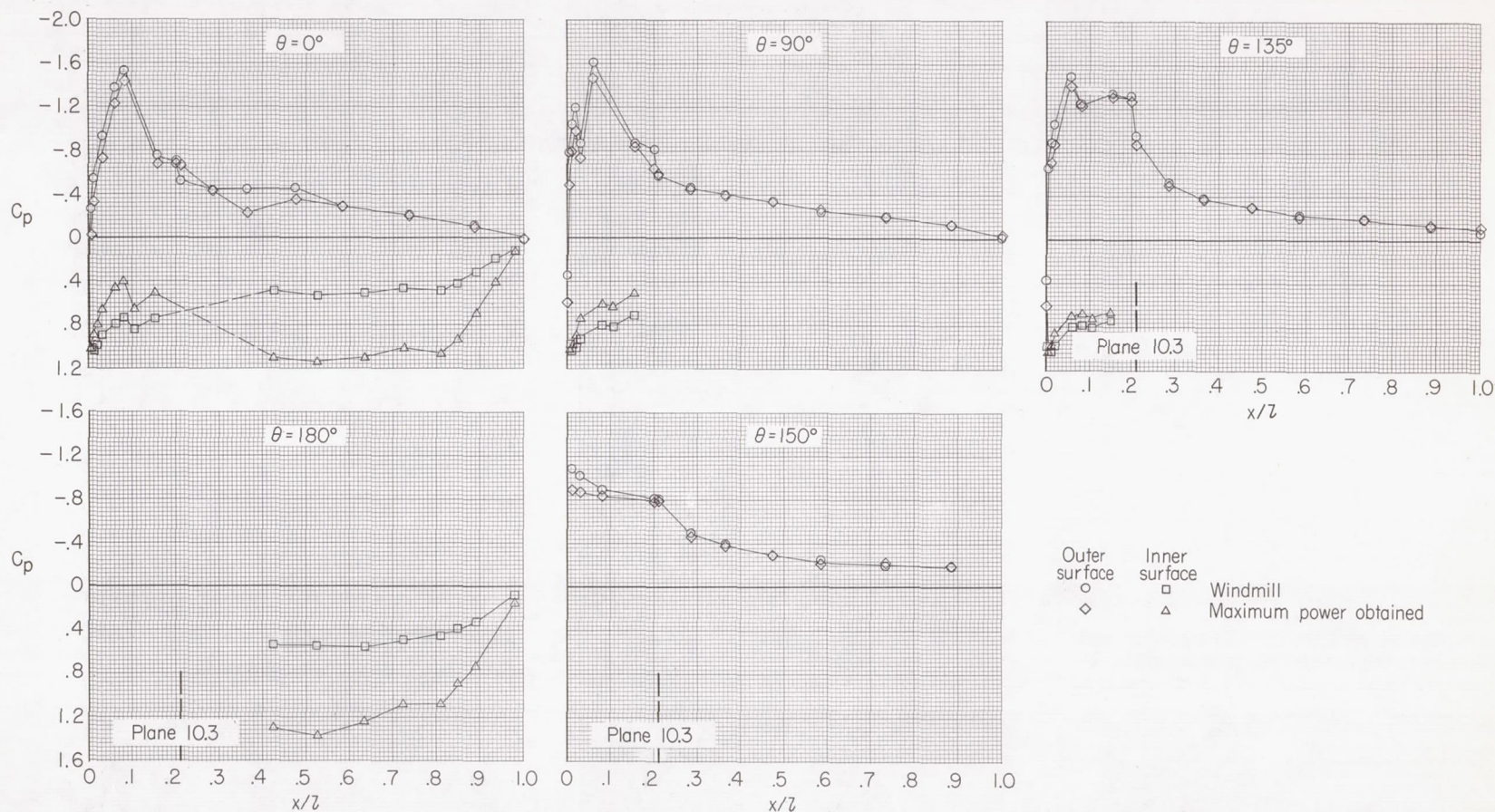
(a) $M = 0.20$; $N_F/\sqrt{\sigma} = 97.8$ percent.

Figure 50.- Fan-nacelle pressure distributions for configuration 322.



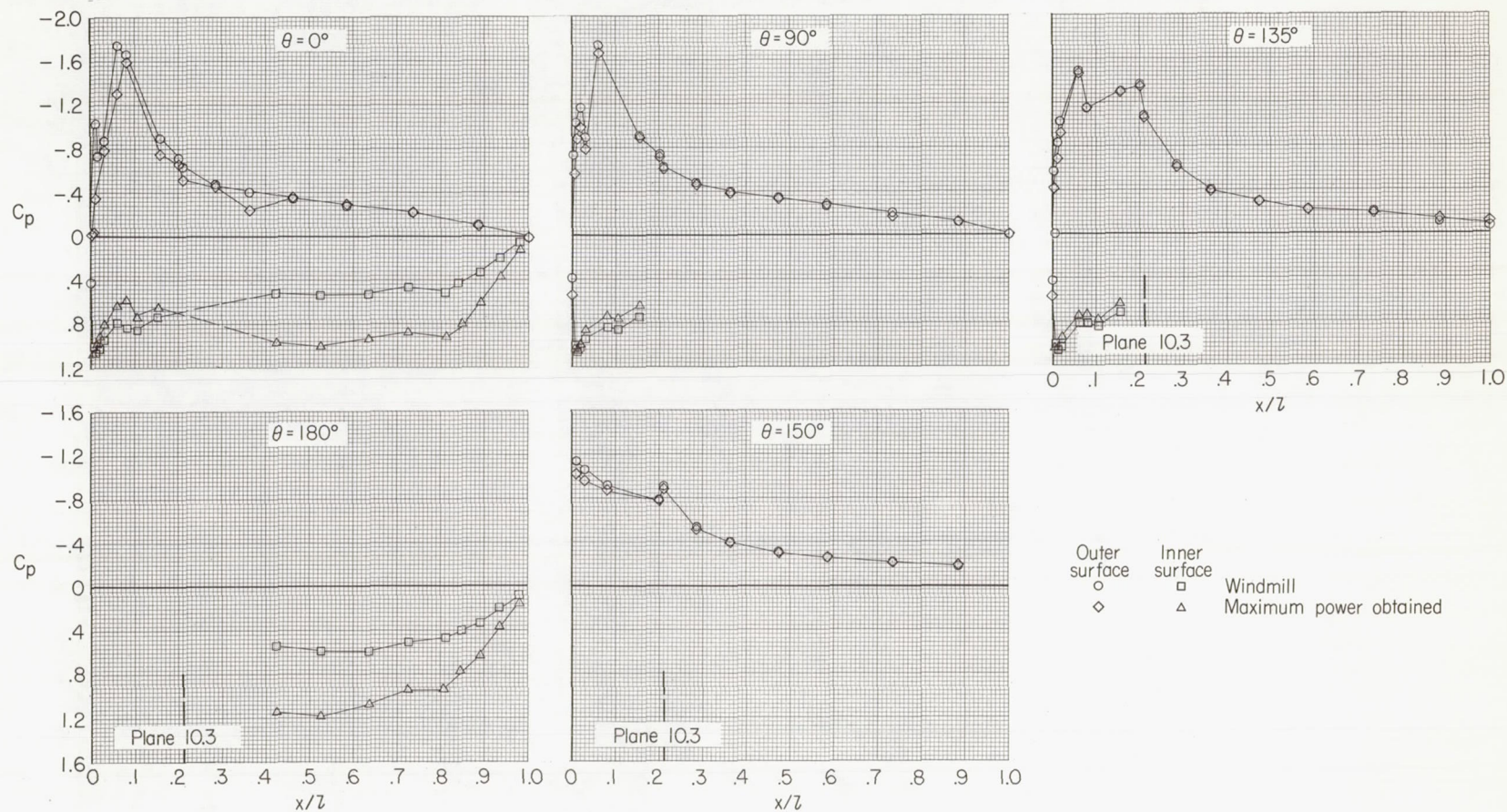
(b) $M = 0.30$; $N_F/\sqrt{\sigma} = 97.5$ percent.

Figure 50.- Continued.



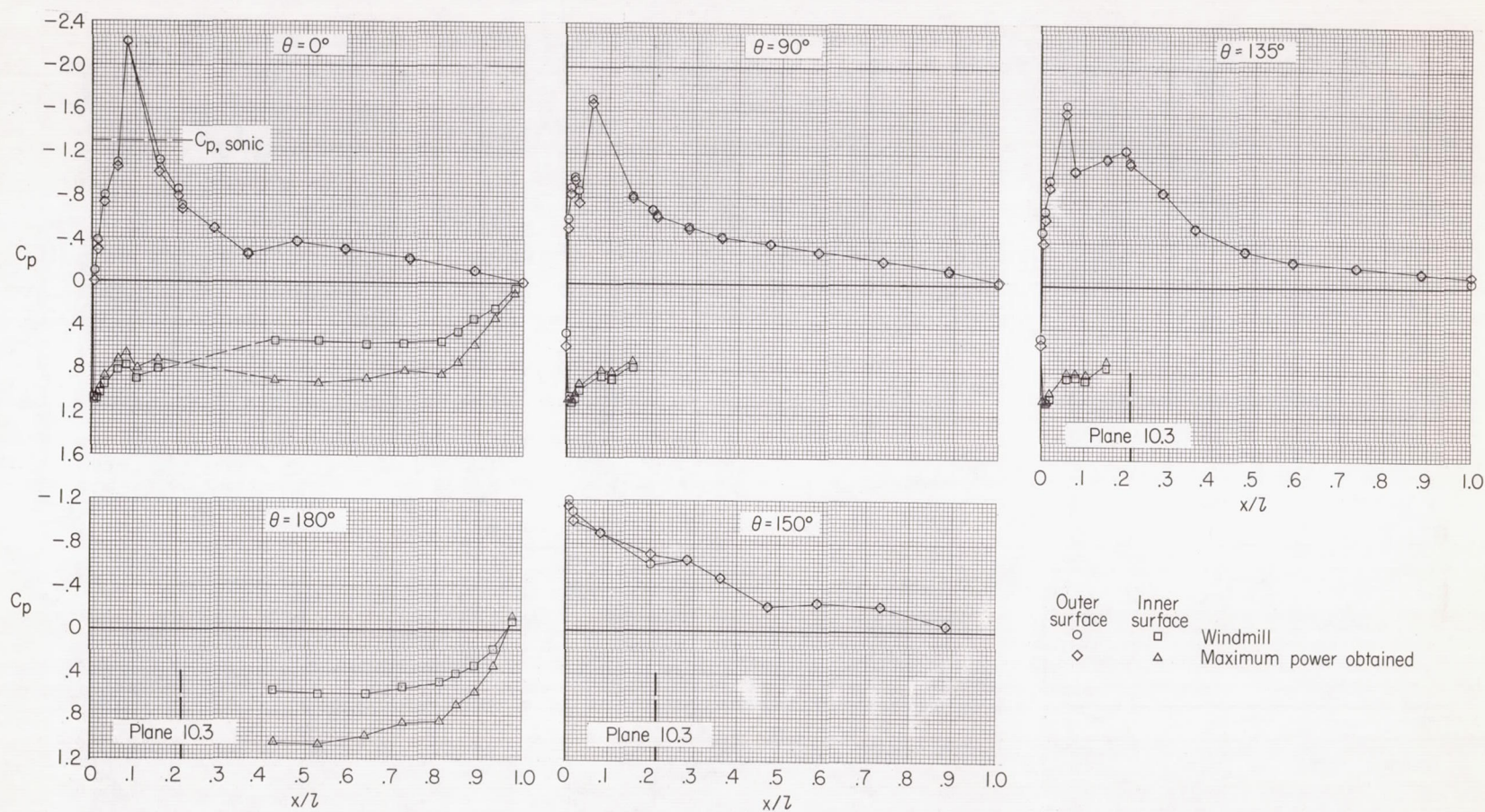
(c) $M = 0.40$; $N_F/\sqrt{\sigma} = 95.2$ percent.

Figure 50.- Continued.



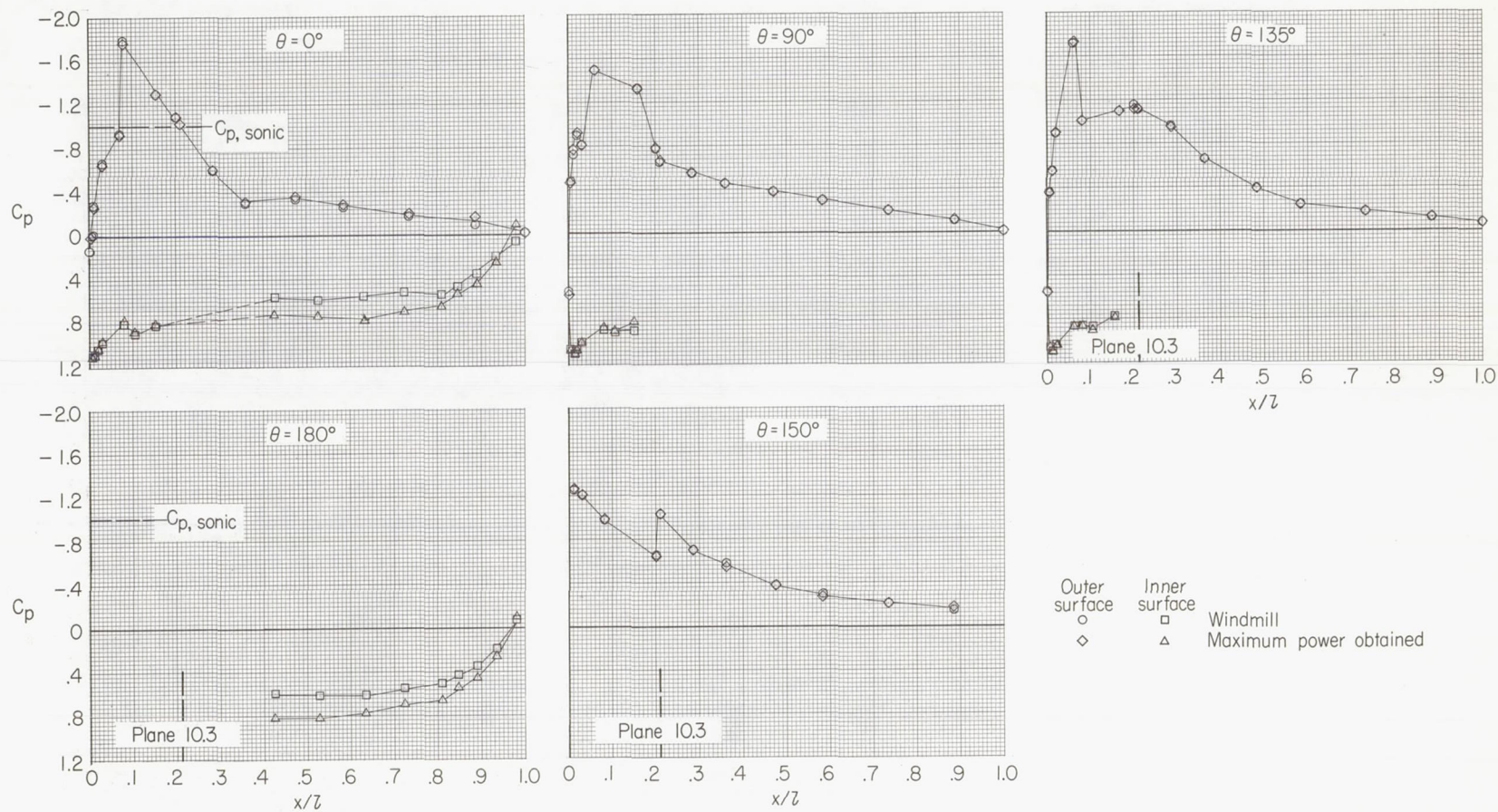
(d) $M = 0.50$; $N_F/\sqrt{\sigma} = 94.4$ percent.

Figure 50.- Continued.



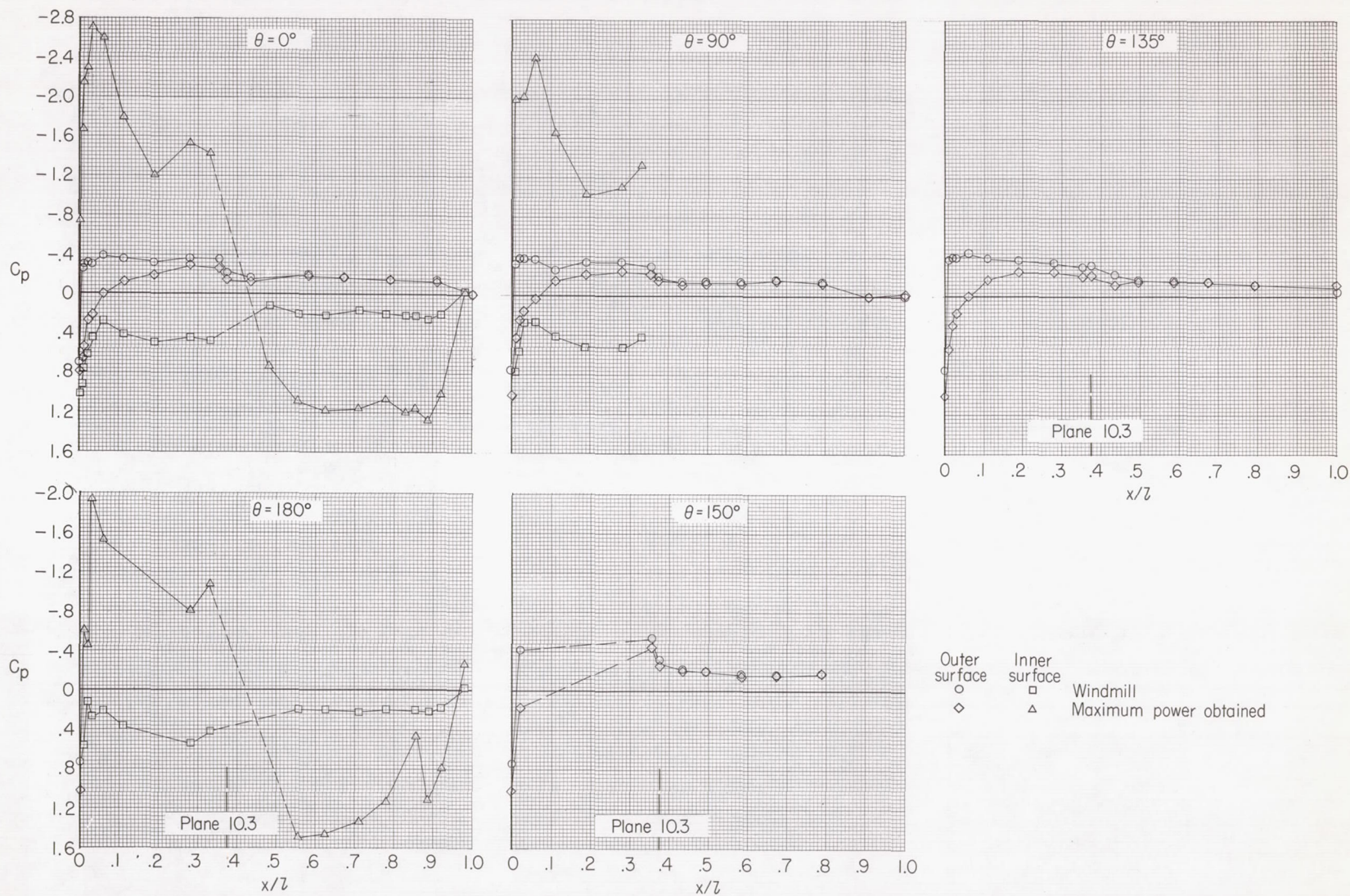
(e) $M = 0.60$; $N_F/\sqrt{\sigma} = 94.5$ percent.

Figure 50.- Continued.



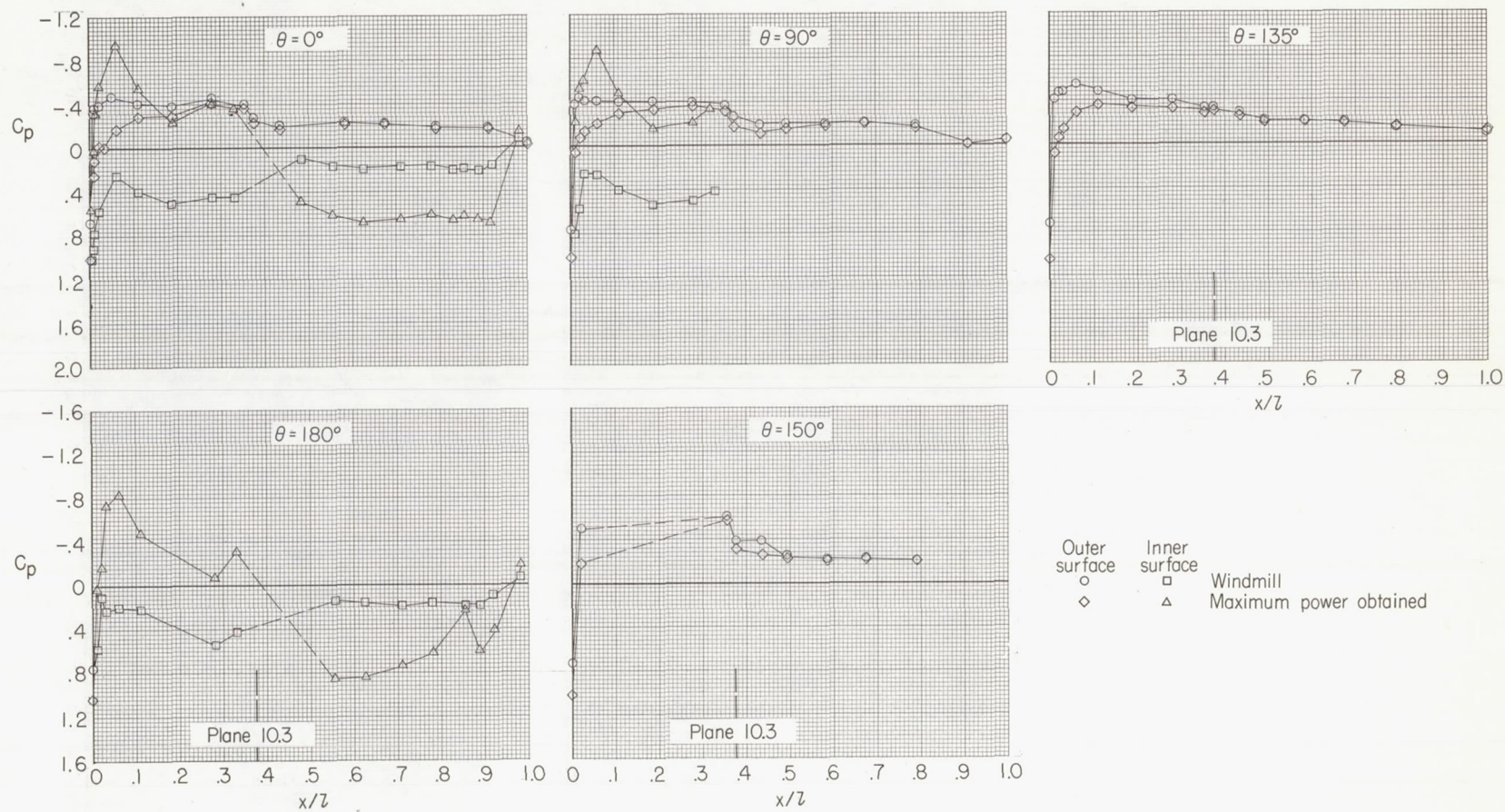
(f) $M = 0.65$; $N_F/\sqrt{\sigma} = 76.5$ percent.

Figure 50.- Concluded.



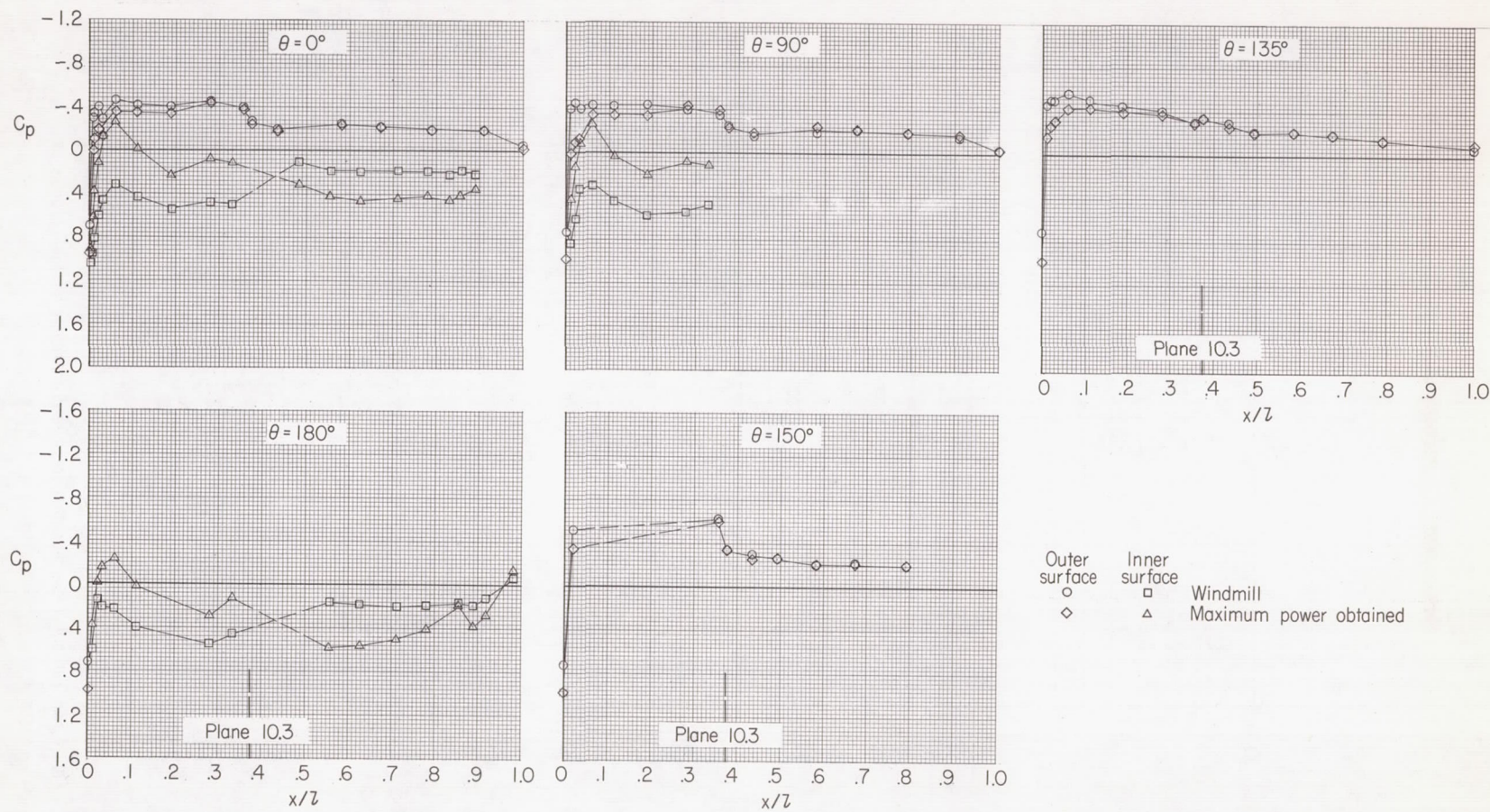
(a) $M = 0.20$; $N_F/\sqrt{\sigma} = 97.1$ percent.

Figure 51.- Fan-nacelle pressure distributions for configuration 243.



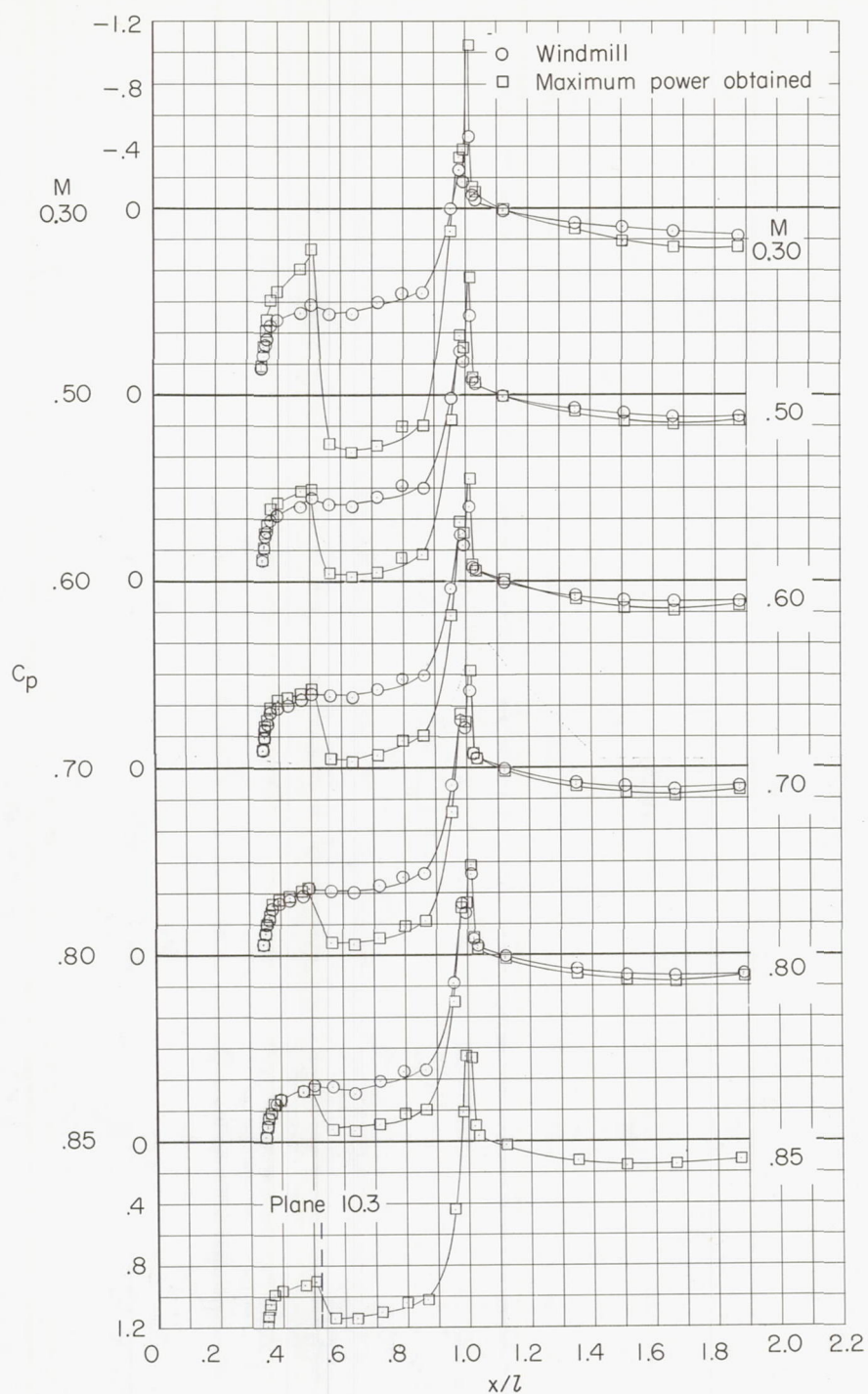
(b) $M = 0.30$; $N_F/\sqrt{\sigma} = 97.7$ percent.

Figure 51.- Continued.



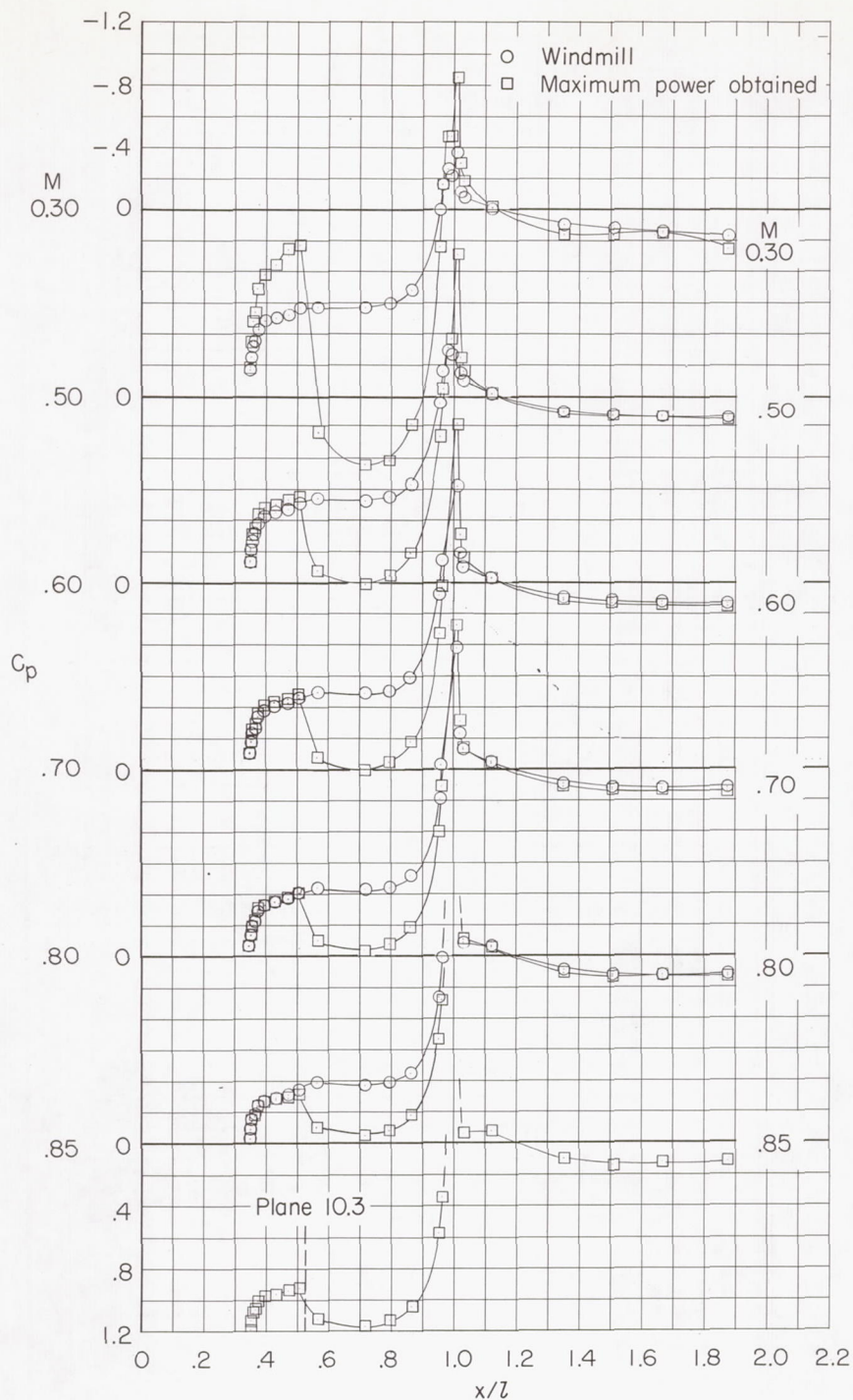
(c) $M = 0.40$; $N_F/\sqrt{\sigma} = 97.1$ percent.

Figure 51.- Concluded.



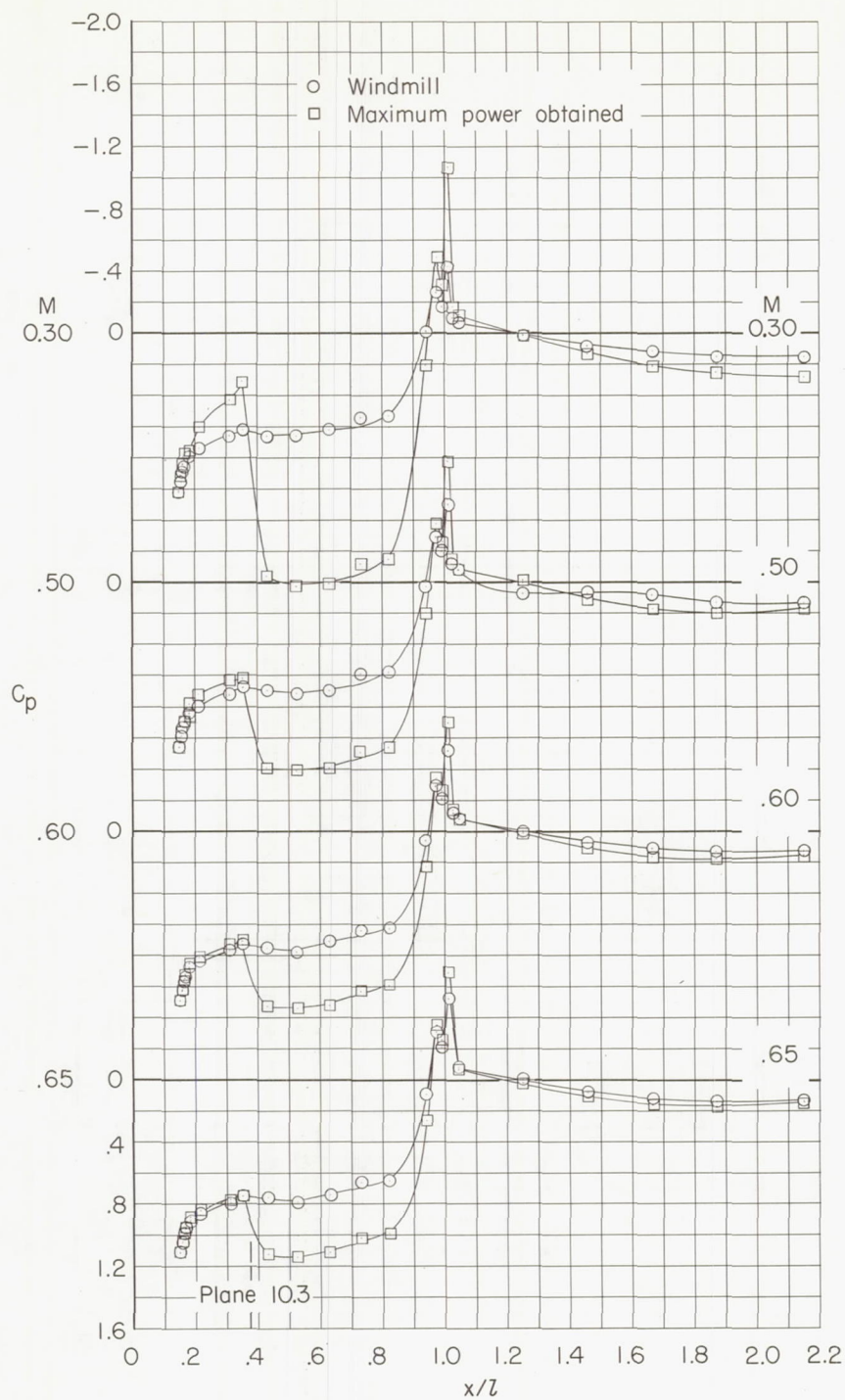
(a) $\theta = 0^\circ$.

Figure 52.- Fan-bulldnose-plus-plug pressure distributions for configuration 144.



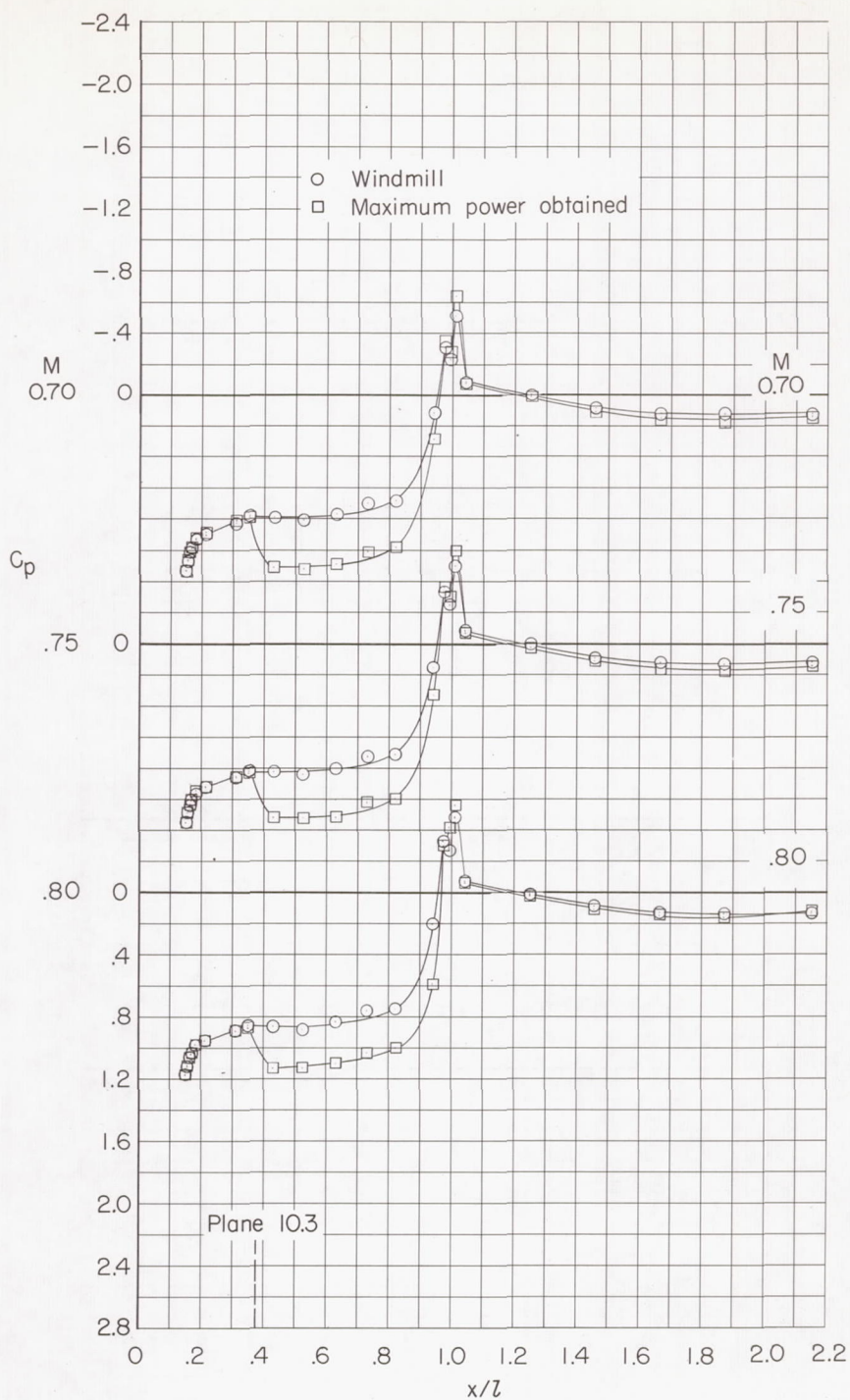
(b) $\theta = 180^\circ$.

Figure 52.- Concluded.



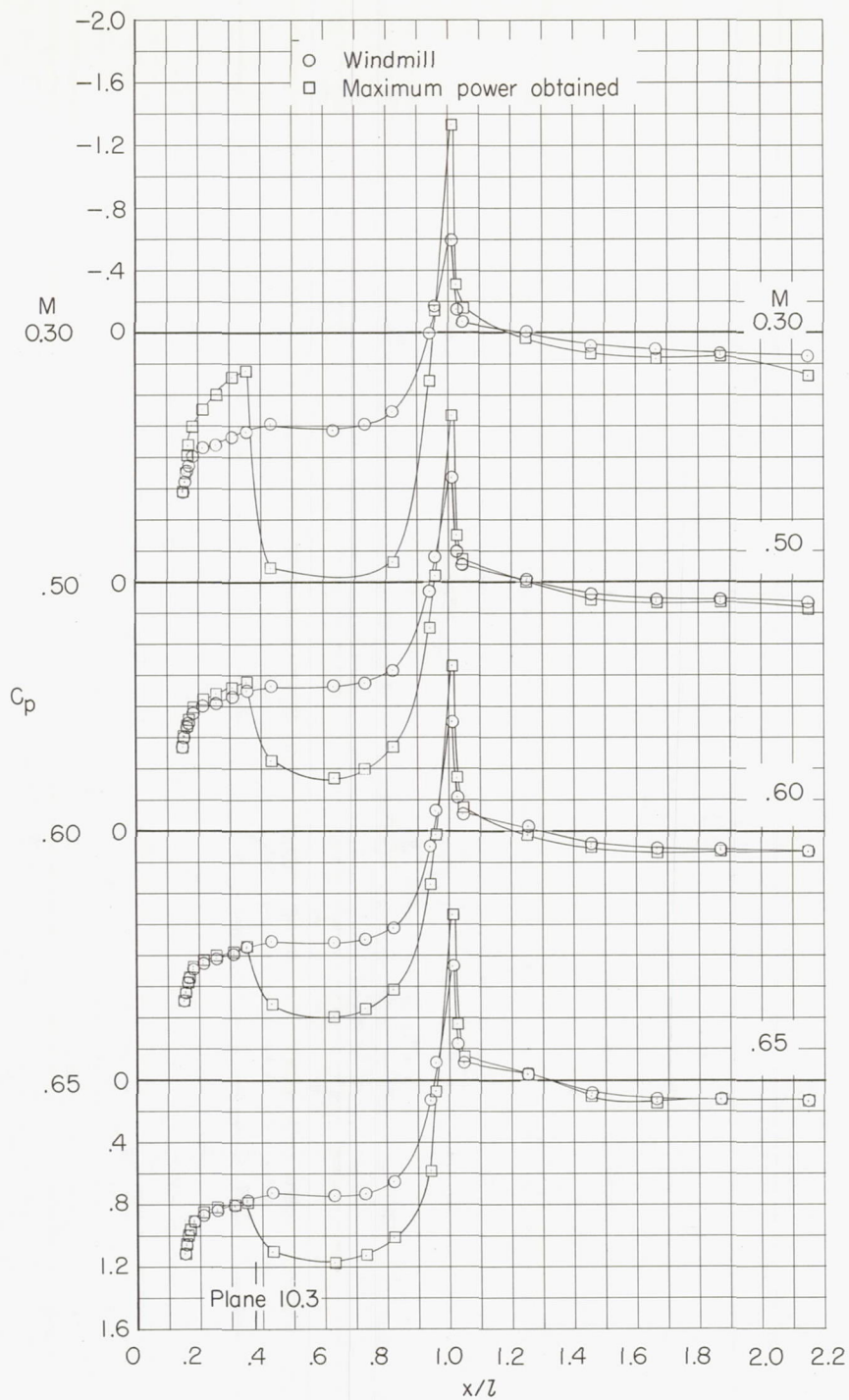
(a) $\theta = 0^\circ$.

Figure 53.- Fan-bulb-nose-plus-plug pressure distributions for configuration 244.



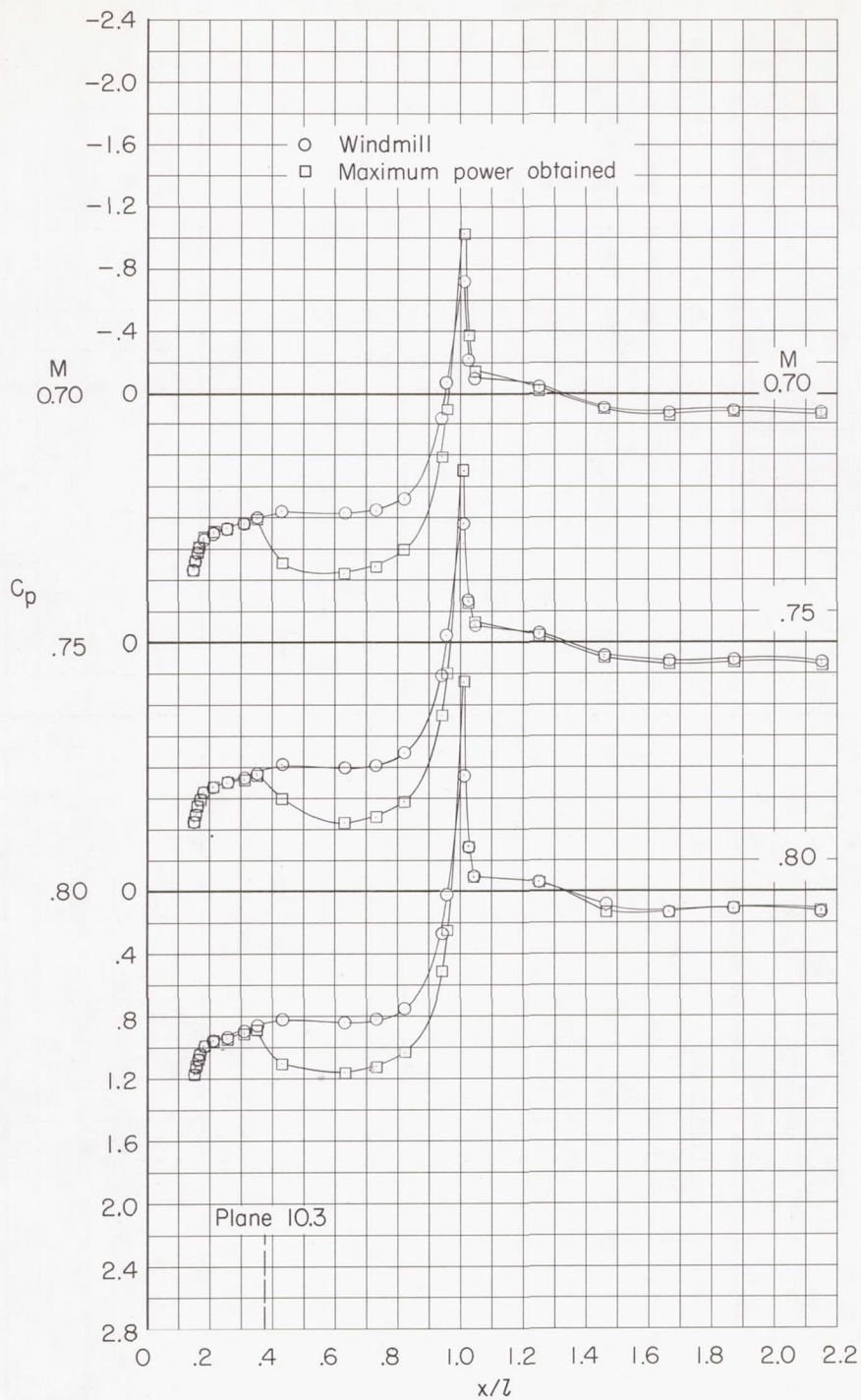
(a) $\theta = 0^\circ$. Concluded.

Figure 53.- Continued.



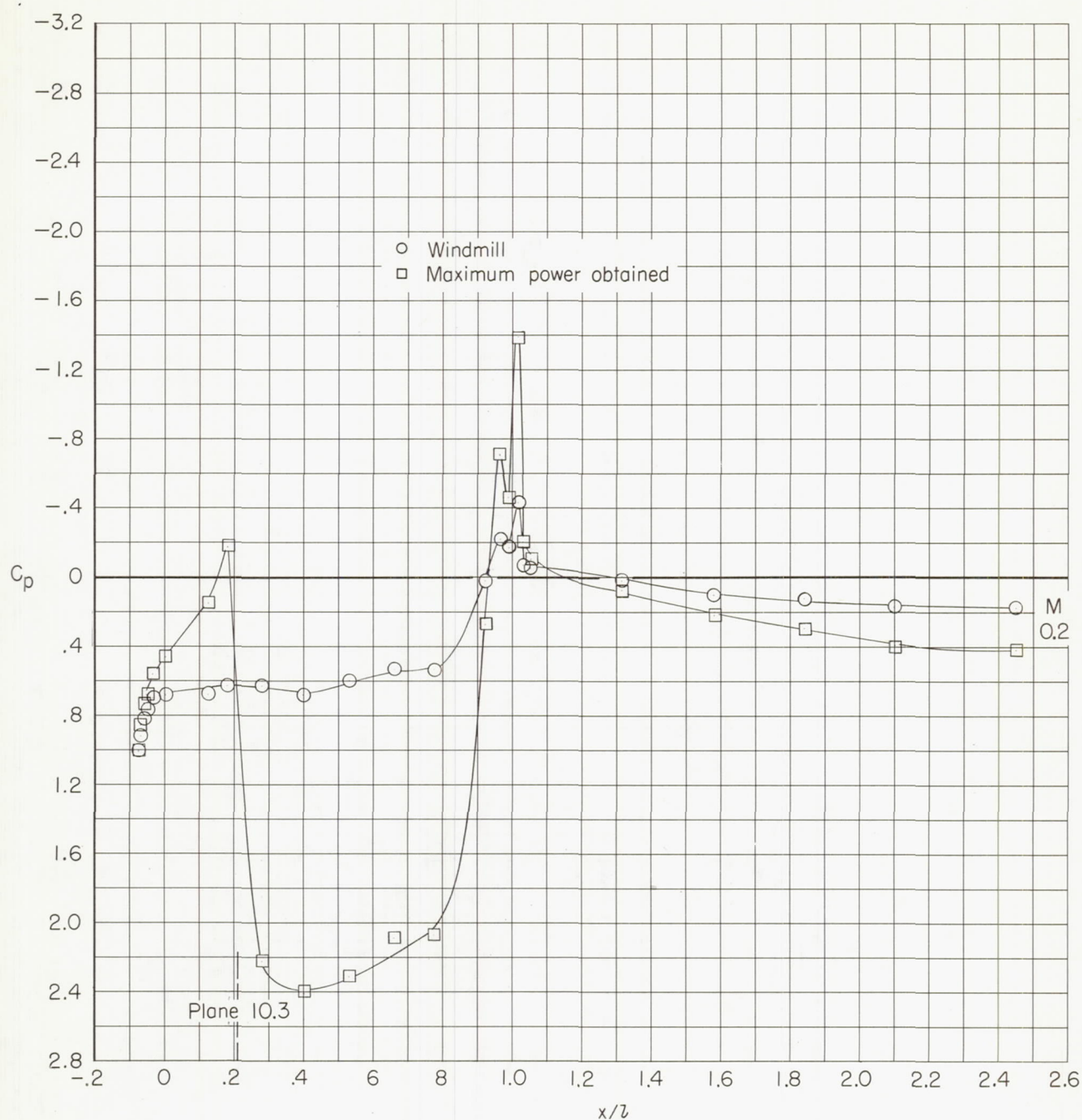
(b) $\theta = 180^\circ$.

Figure 53.- Continued.



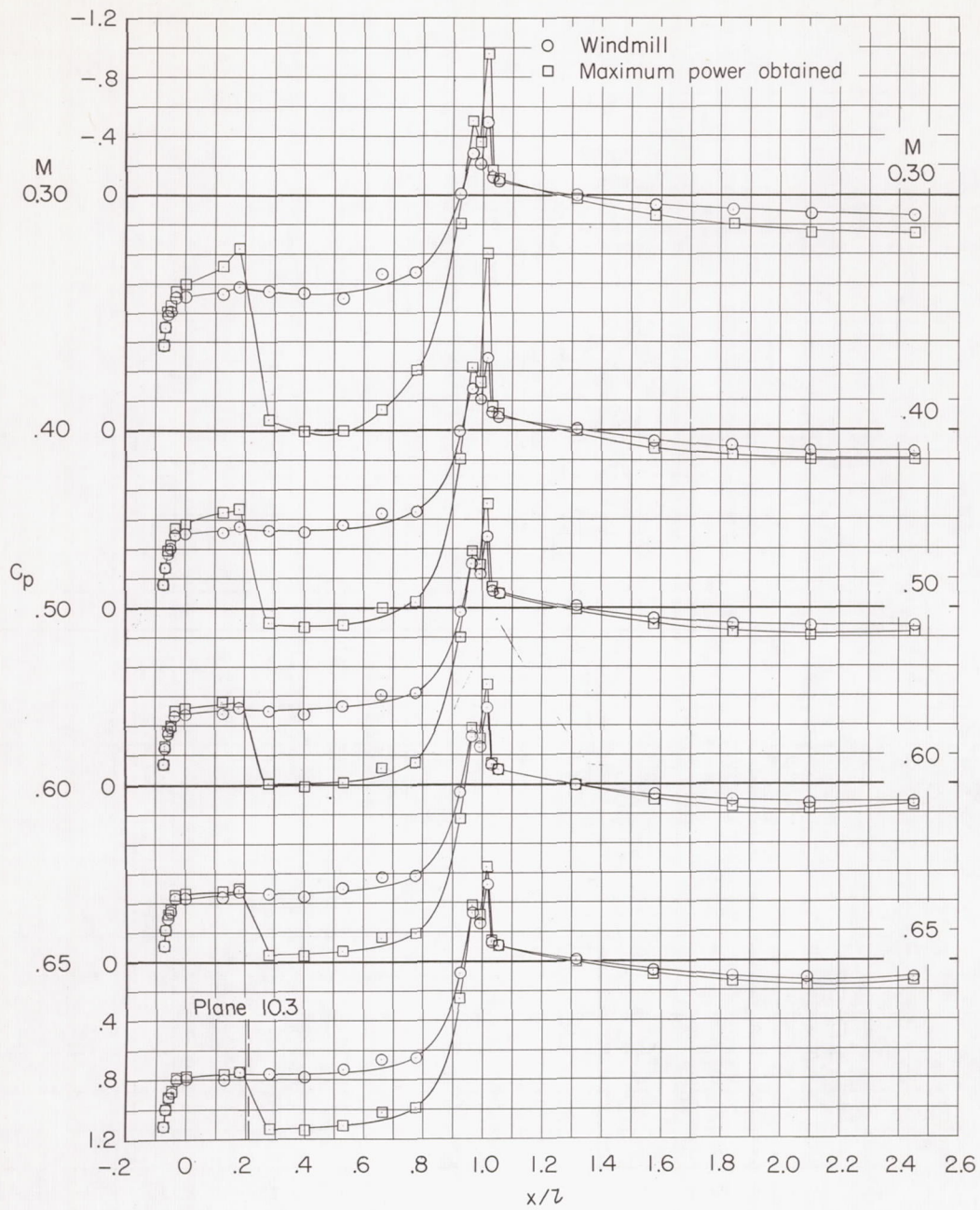
(b) $\theta = 180^\circ$. Concluded.

Figure 53.- Concluded.



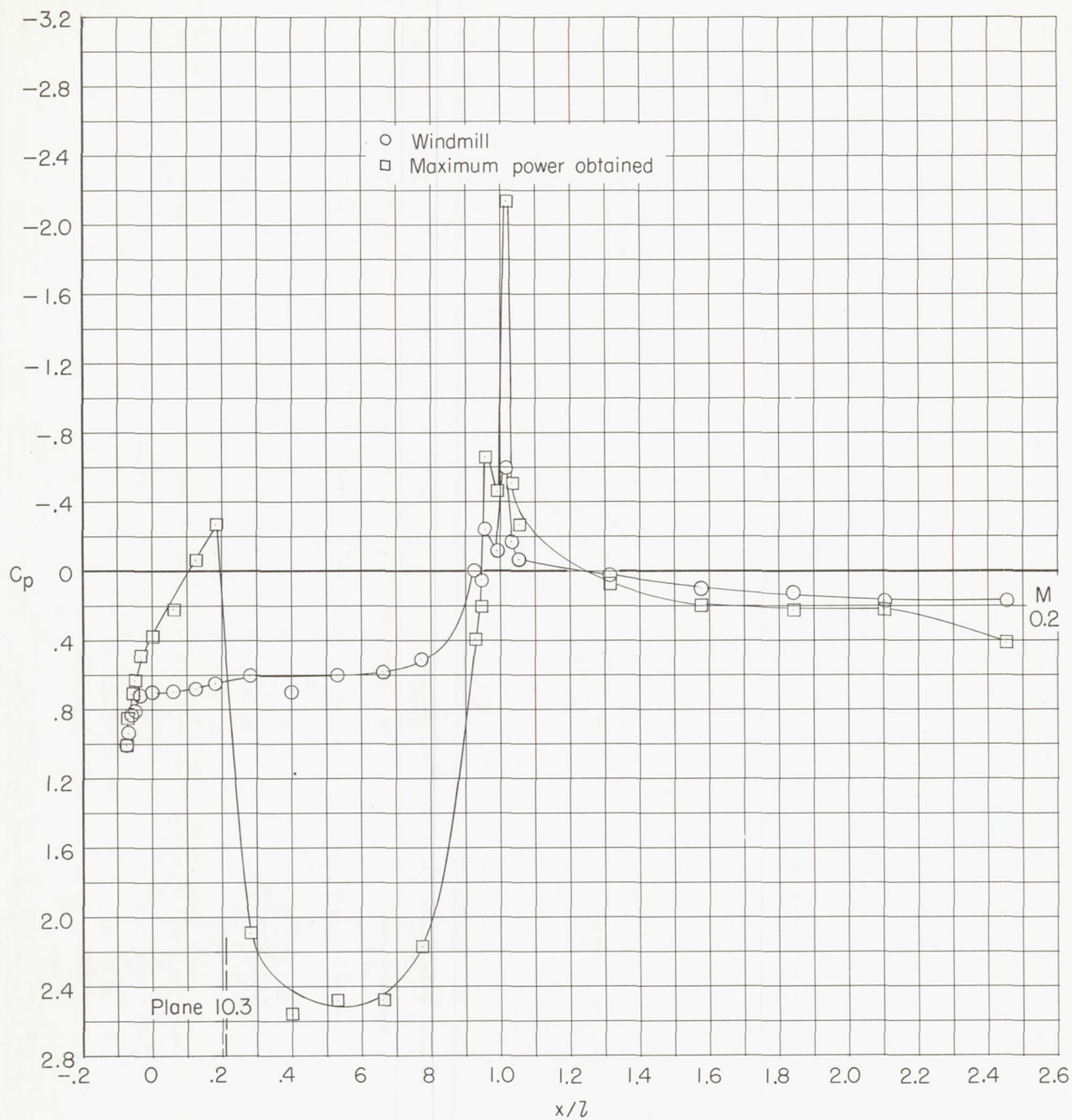
(a) $\theta = 0^\circ$.

Figure 54.- Fan-bullesnose-plus-plug pressure distributions for configuration 344.



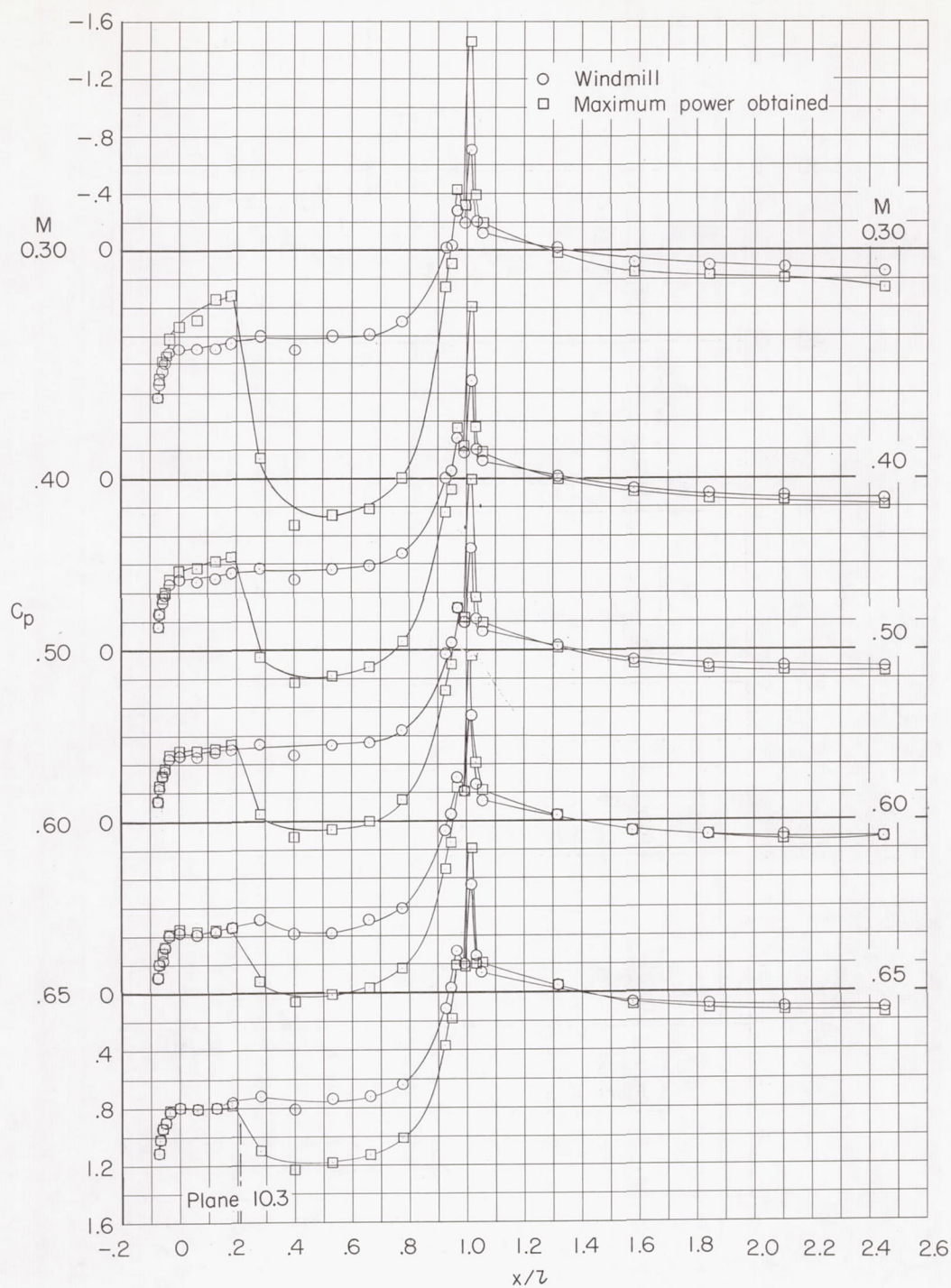
(a) $\theta = 0^\circ$. Concluded.

Figure 54.- Continued.



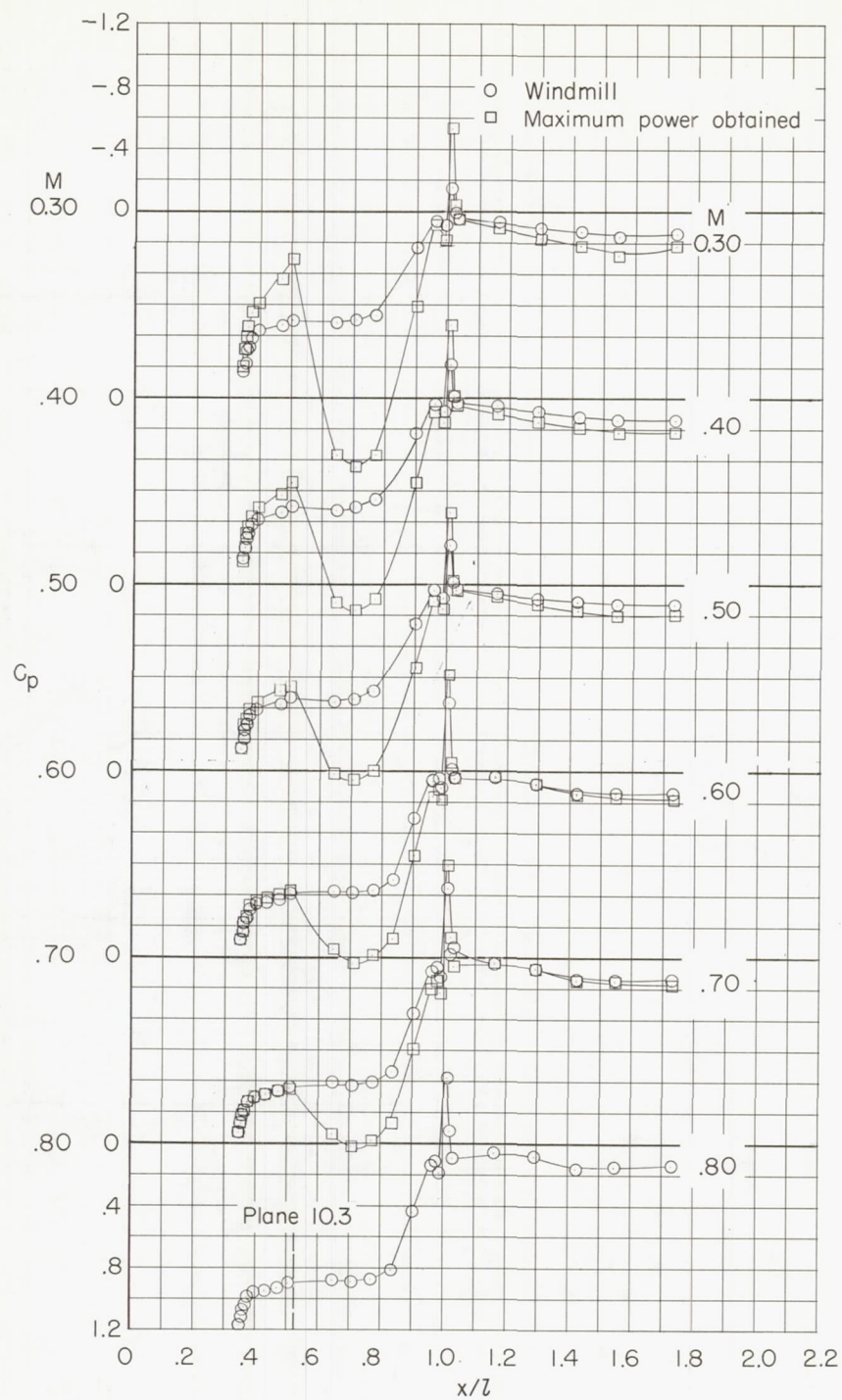
(b) $\theta = 180^\circ$.

Figure 54.- Continued.



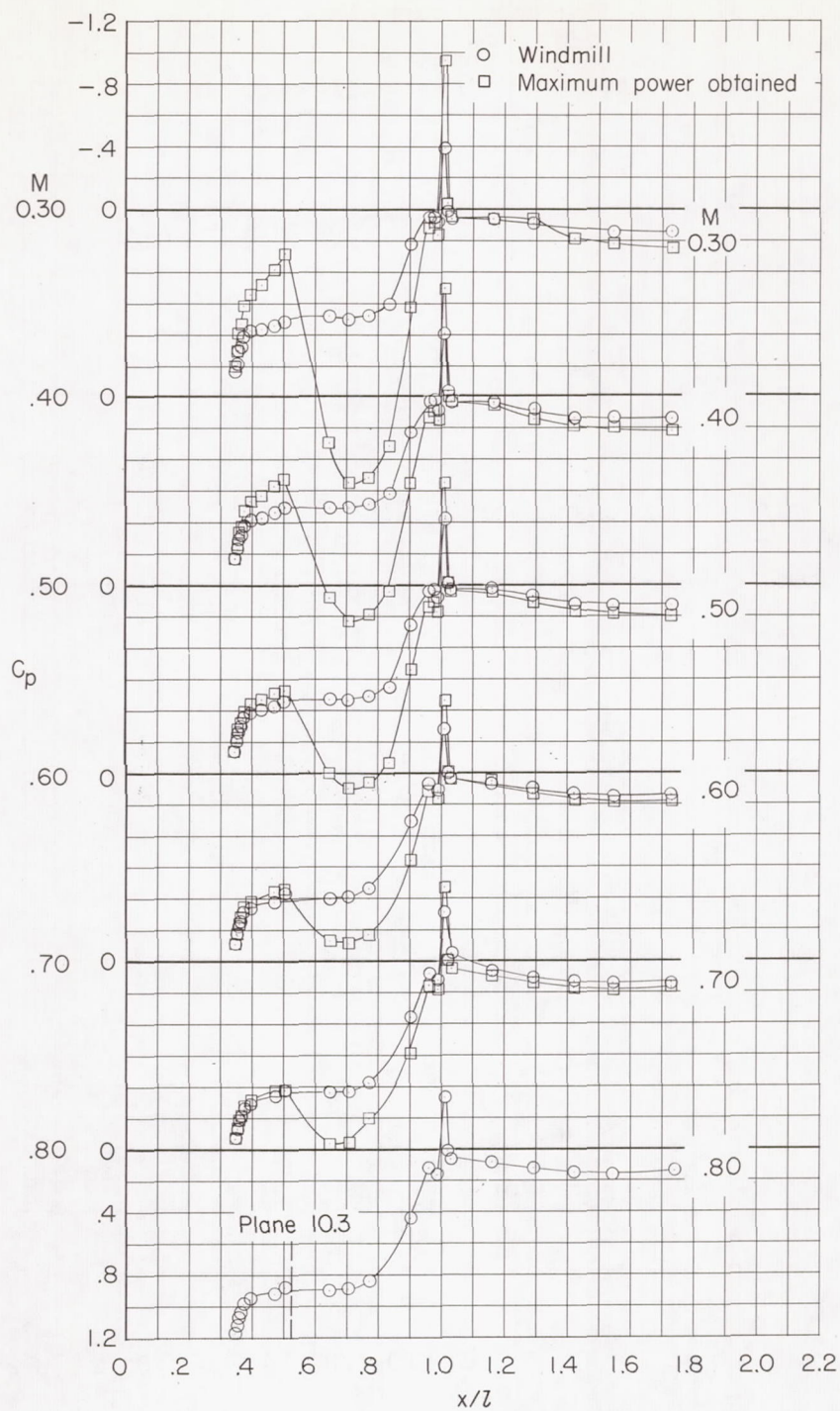
(b) $\theta = 180^\circ$. Concluded.

Figure 54.- Concluded.



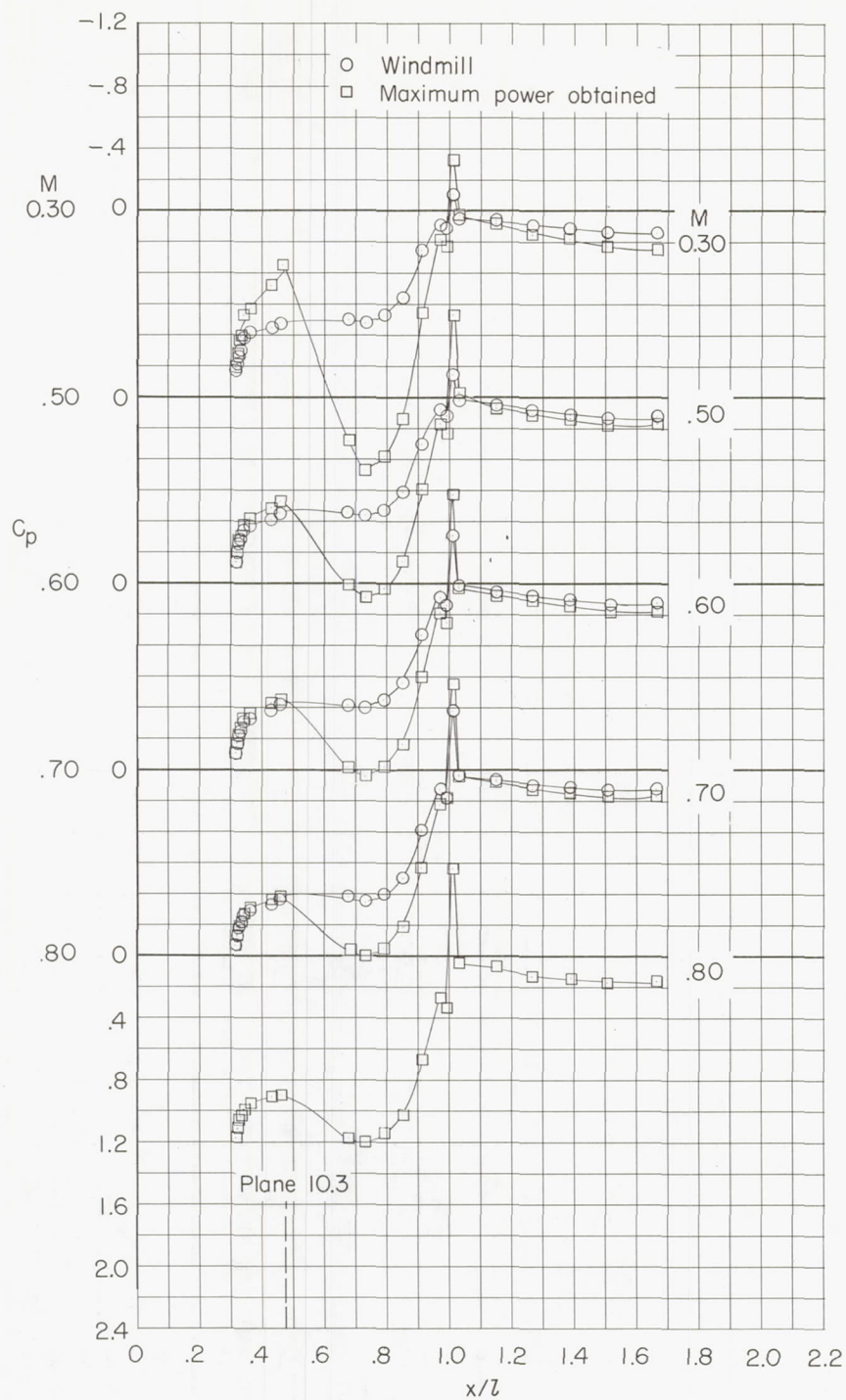
(a) $\theta = 0^\circ$.

Figure 55.- Fan-bulldnose-plus-plug pressure distributions for configuration 123.



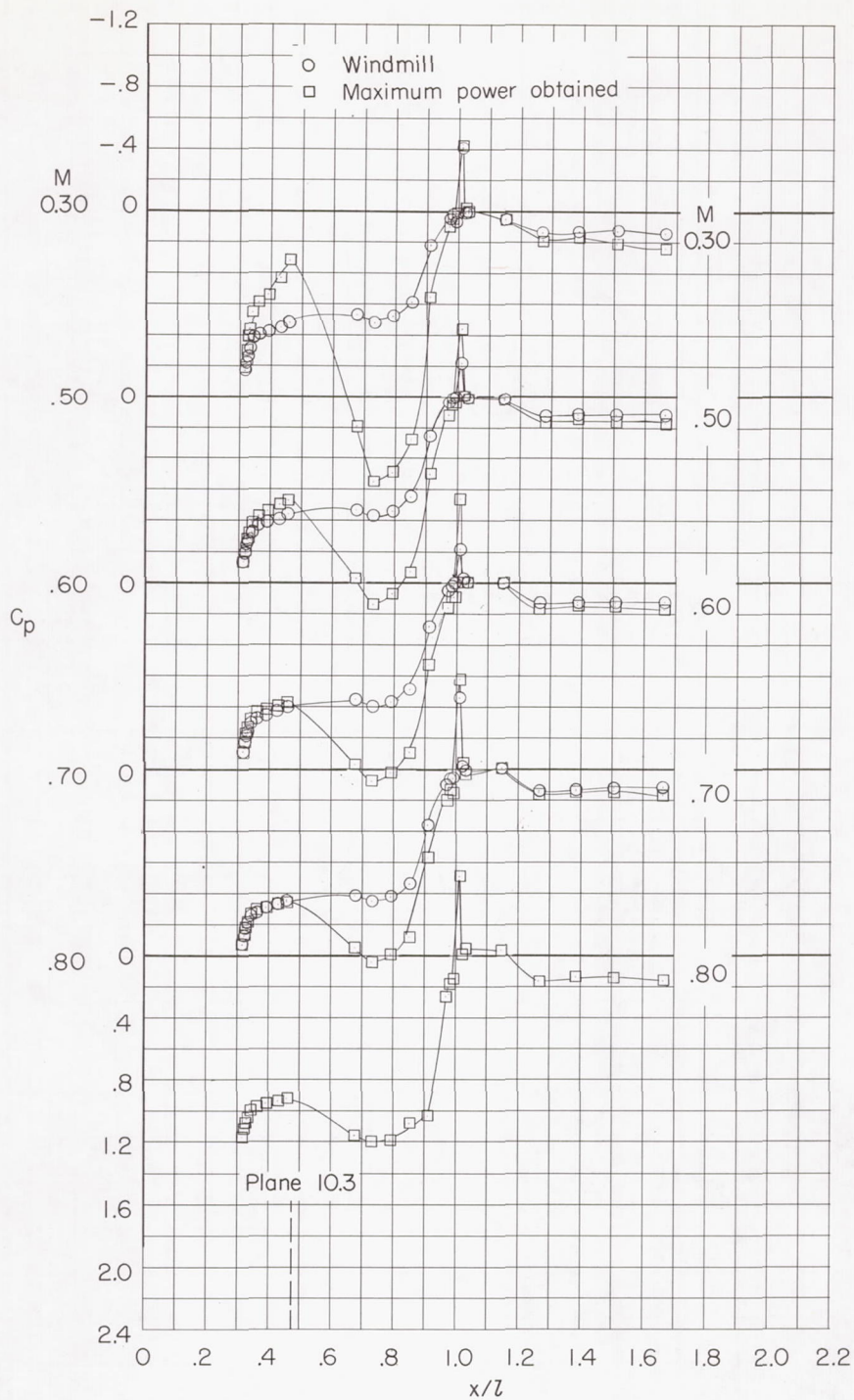
(b) $\theta = 180^\circ$.

Figure 55.- Concluded.



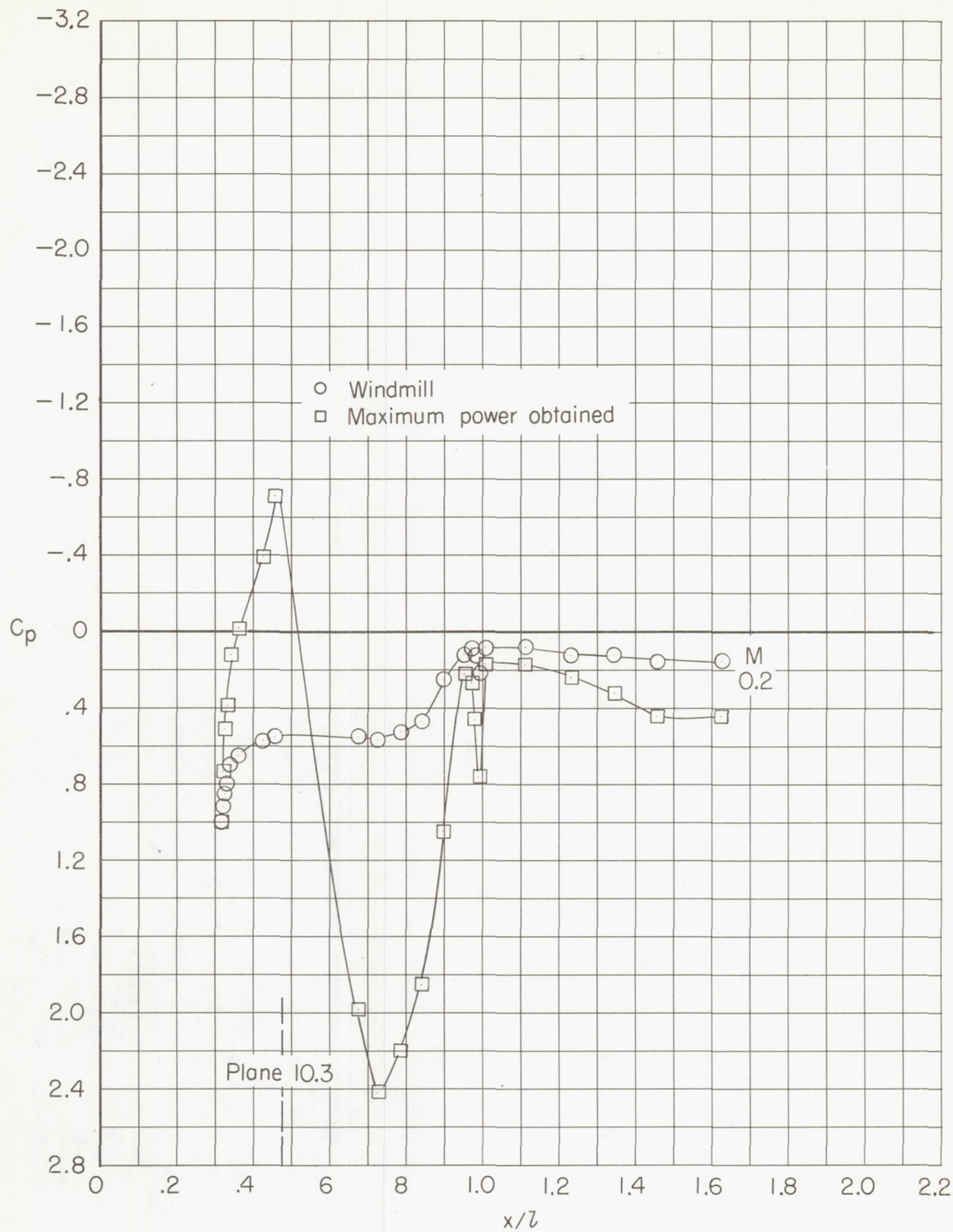
(a) $\theta = 0^\circ$.

Figure 56.- Fan-bulb-nose-plus-plug pressure distributions for configuration 113.



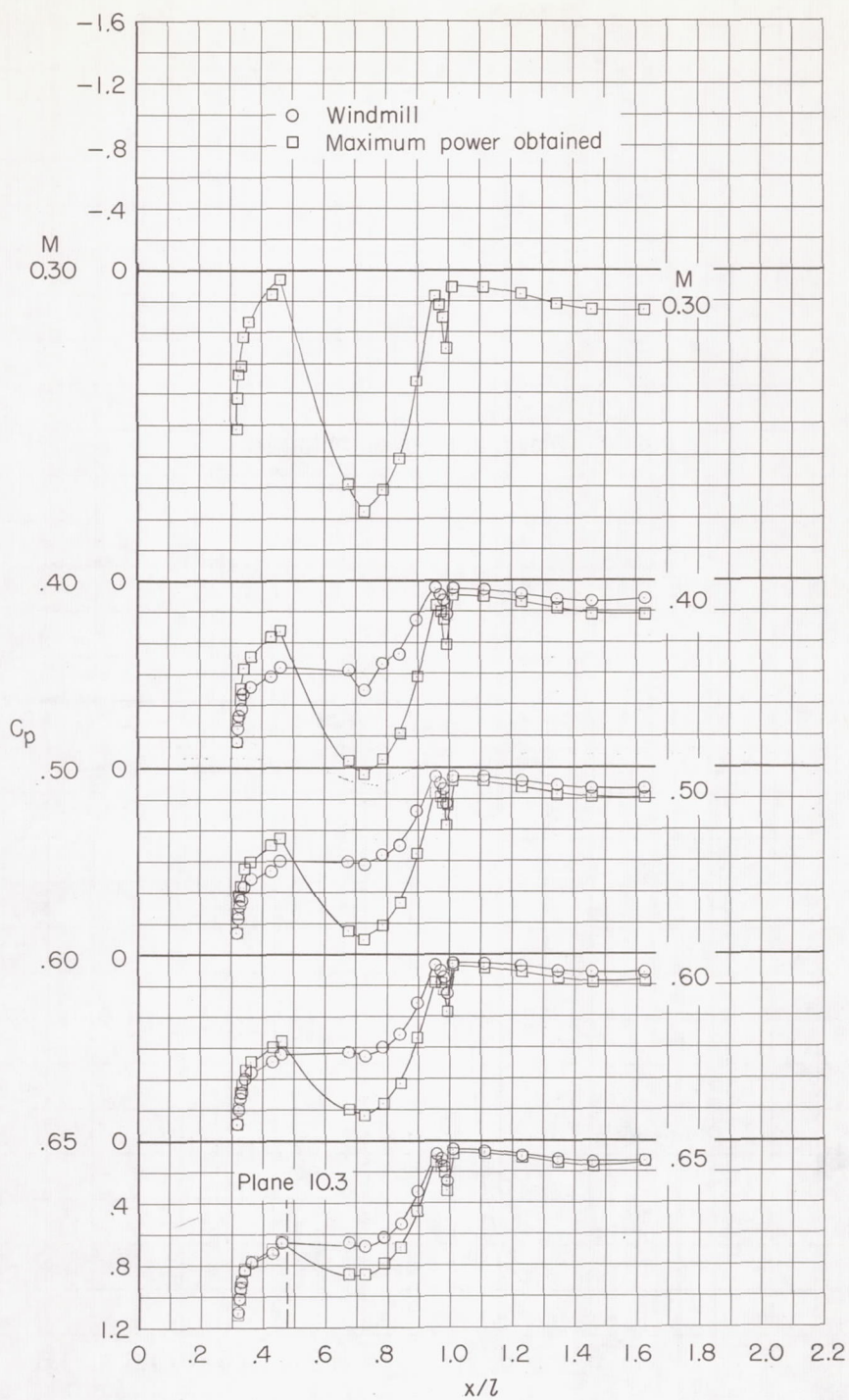
(b) $\theta = 180^\circ$.

Figure 56.- Concluded.



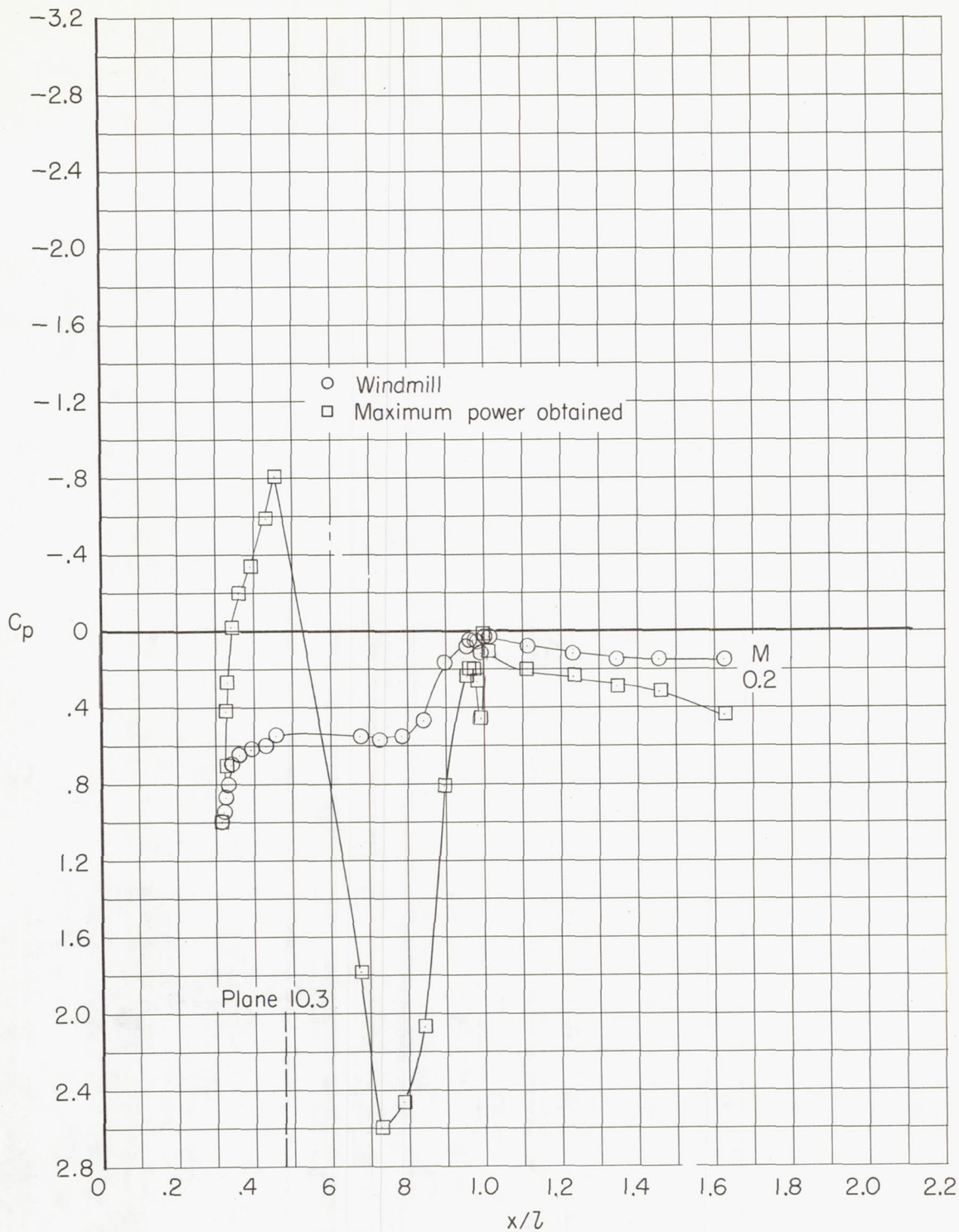
(a) $\theta = 0^\circ$.

Figure 57.- Fan-bulb-nose-plus-plug pressure distributions for configuration 112.



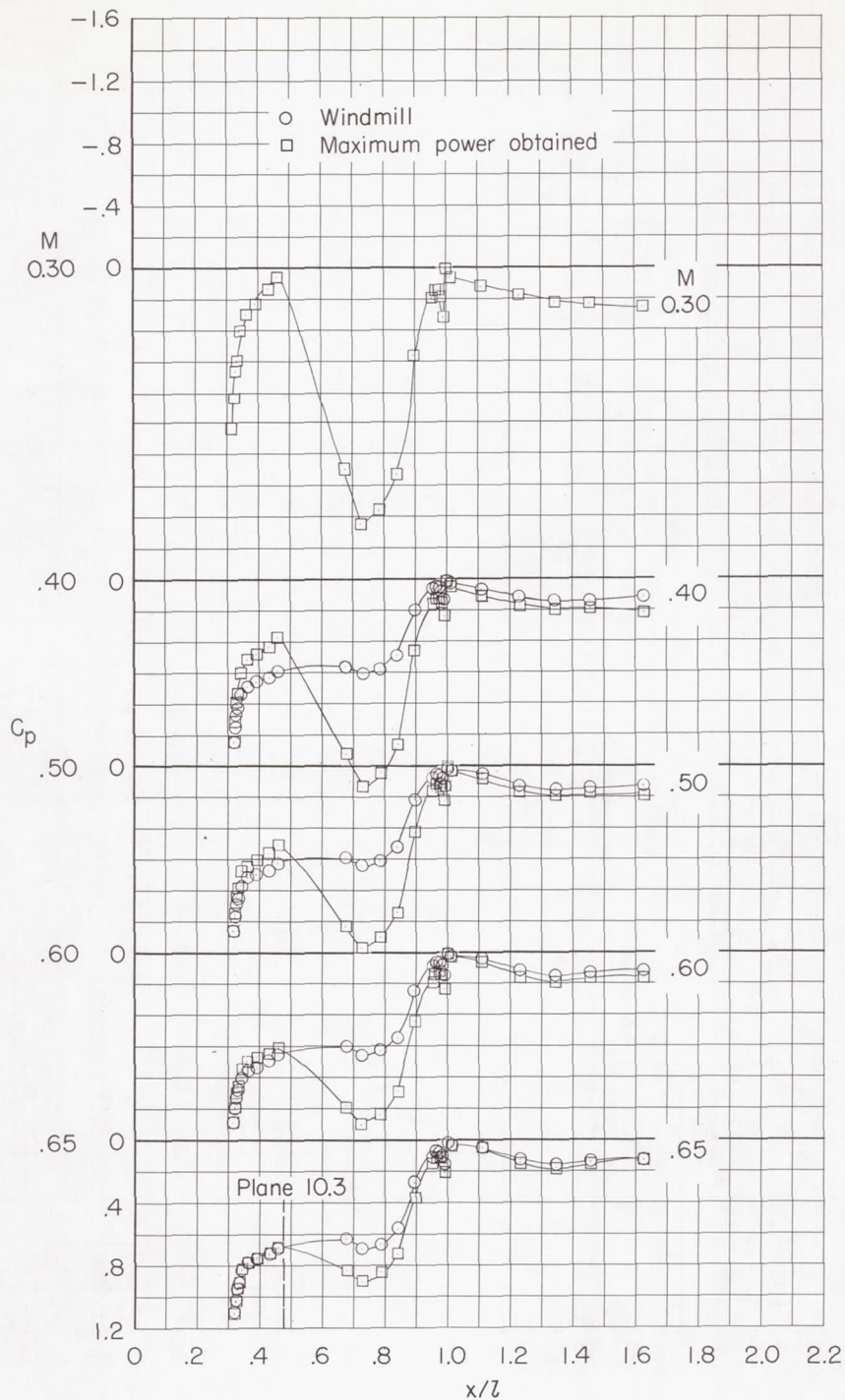
(a) $\theta = 0^\circ$. Concluded.

Figure 57.- Continued.



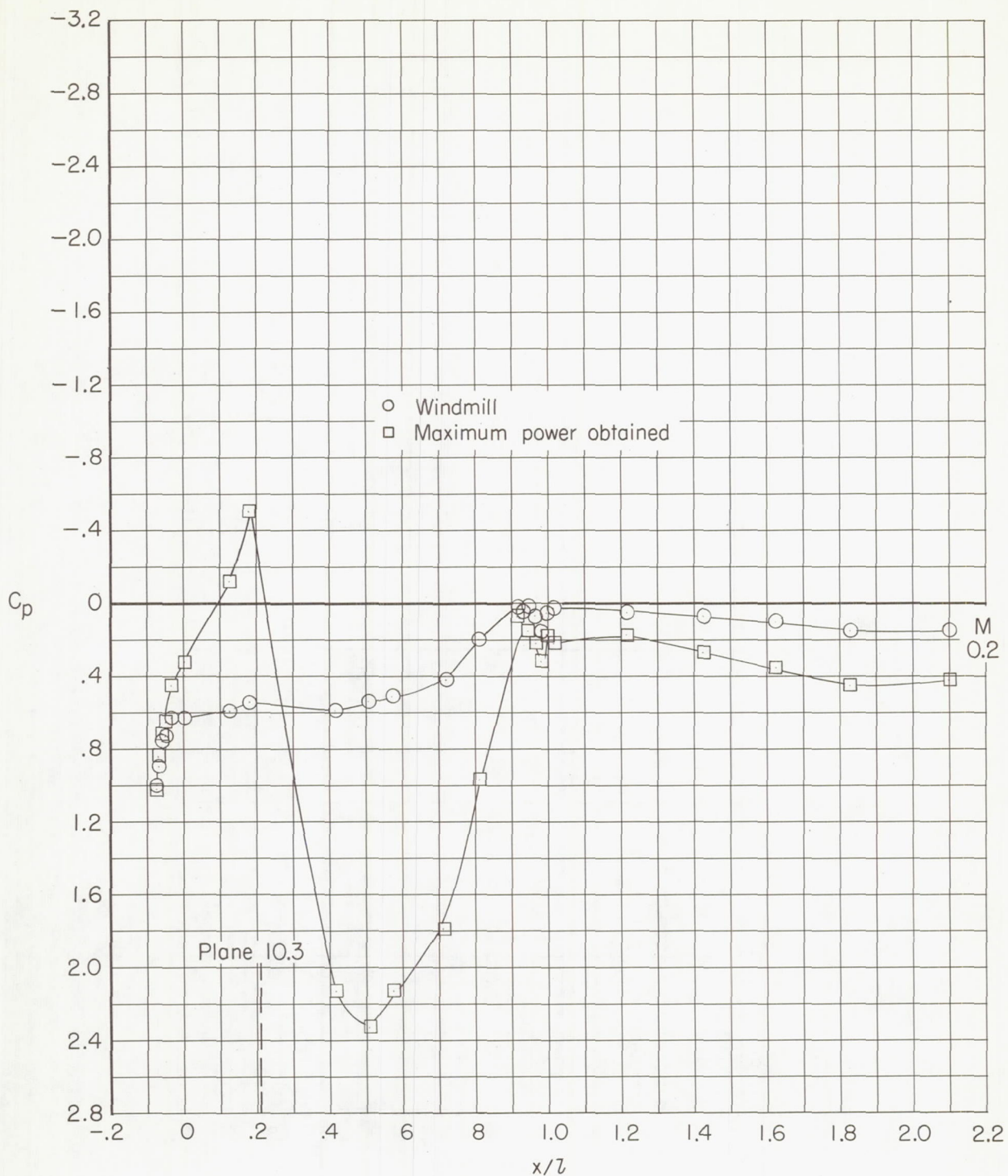
(b) $\theta = 180^\circ$.

Figure 57.- Continued.



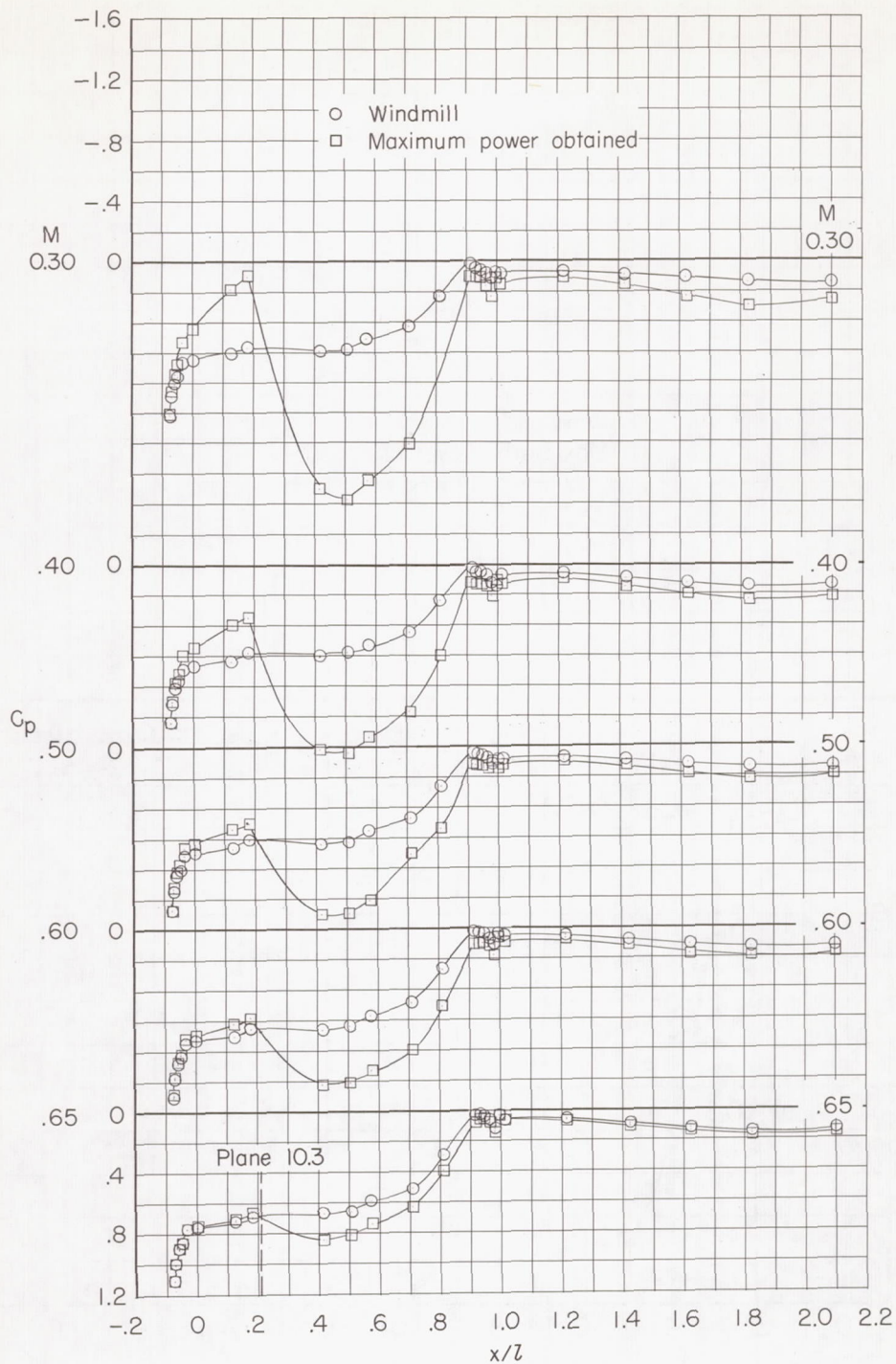
(b) $\theta = 180^\circ$. Concluded.

Figure 57.- Concluded.



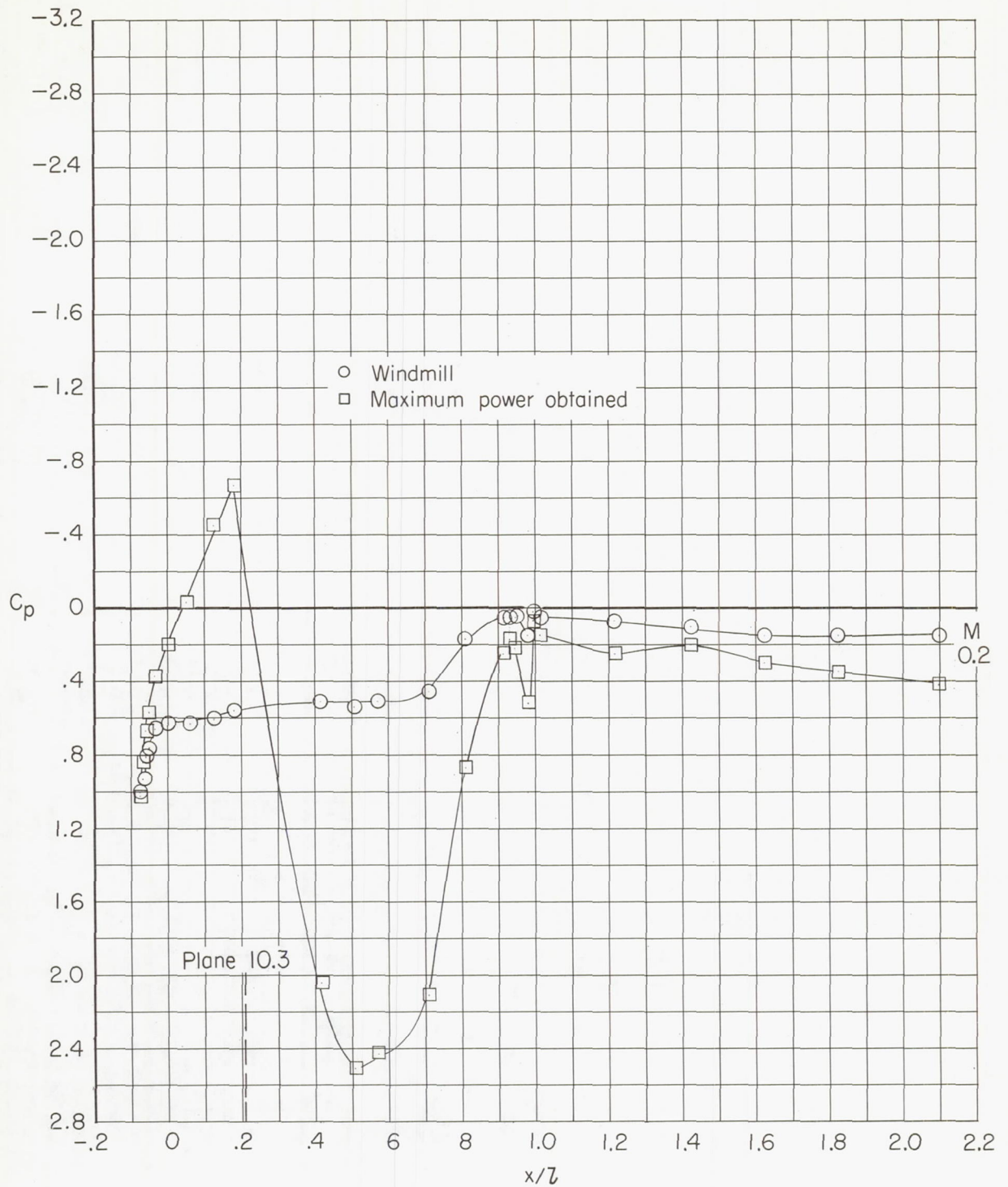
(a) $\theta = 0^\circ$.

Figure 58.- Fan-bulldose-plus-plug pressure distributions for configuration 322.



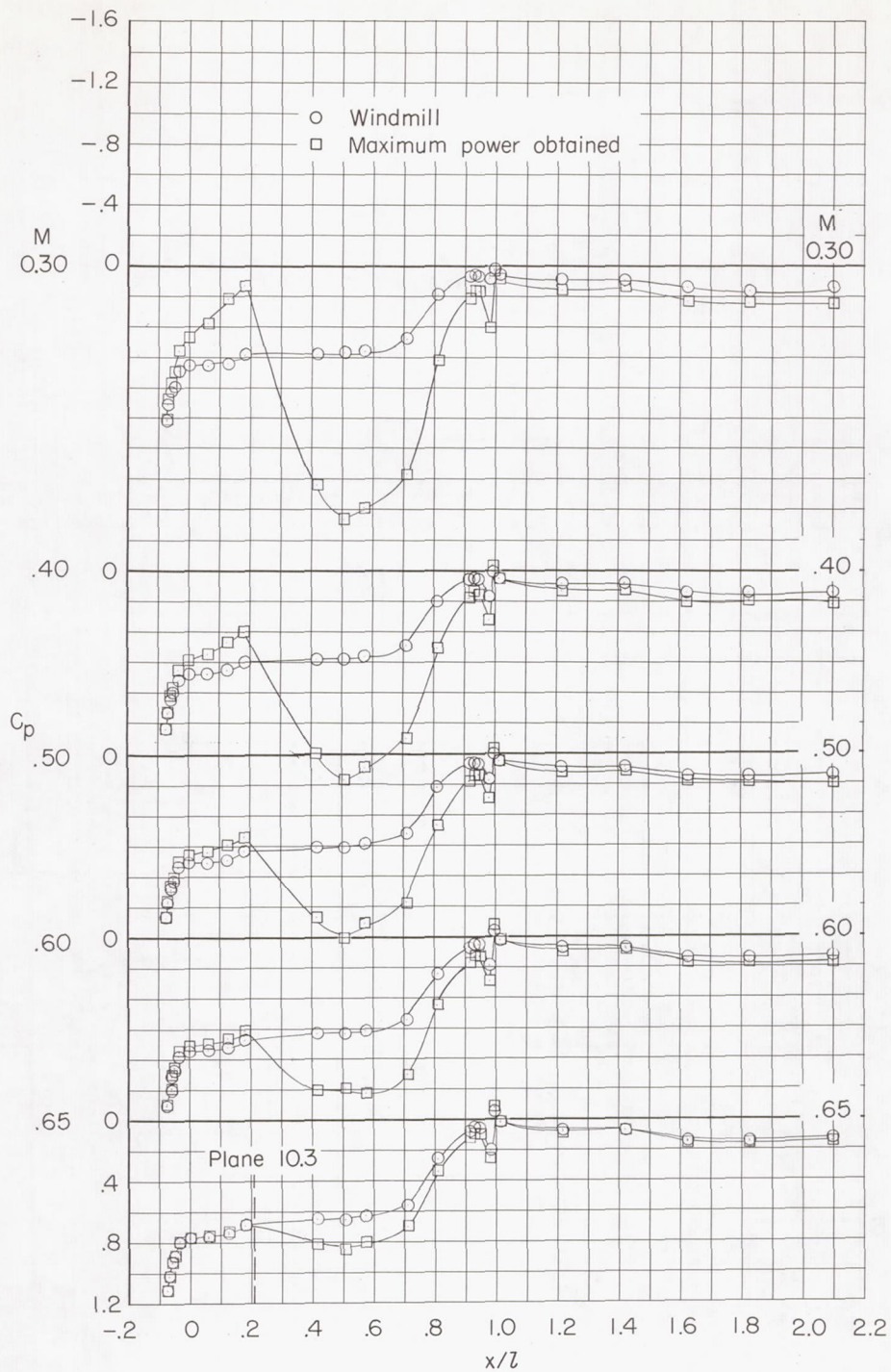
(a) $\theta = 0^\circ$. Concluded.

Figure 58.- Continued.



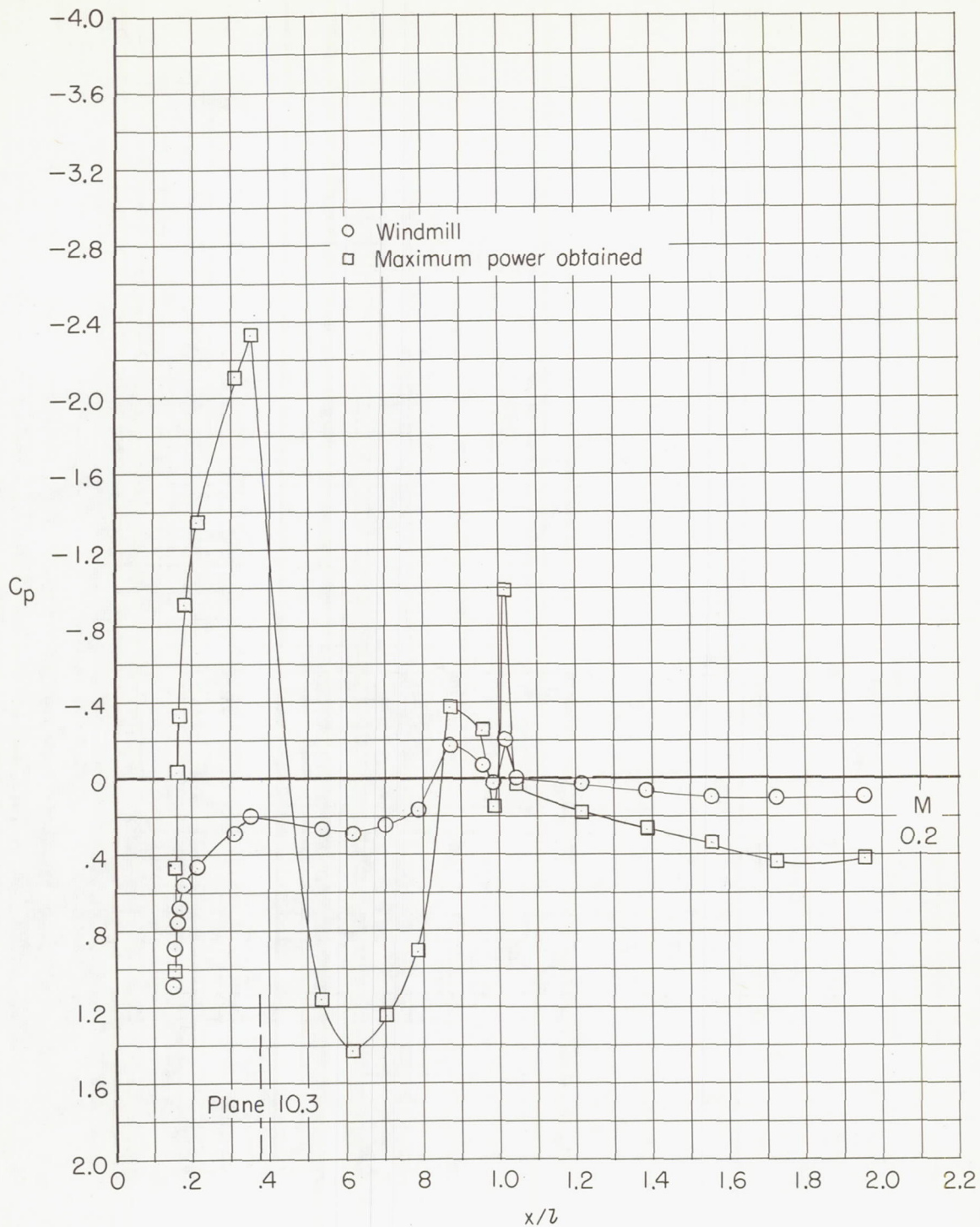
(b) $\theta = 180^\circ$.

Figure 58.- Continued.



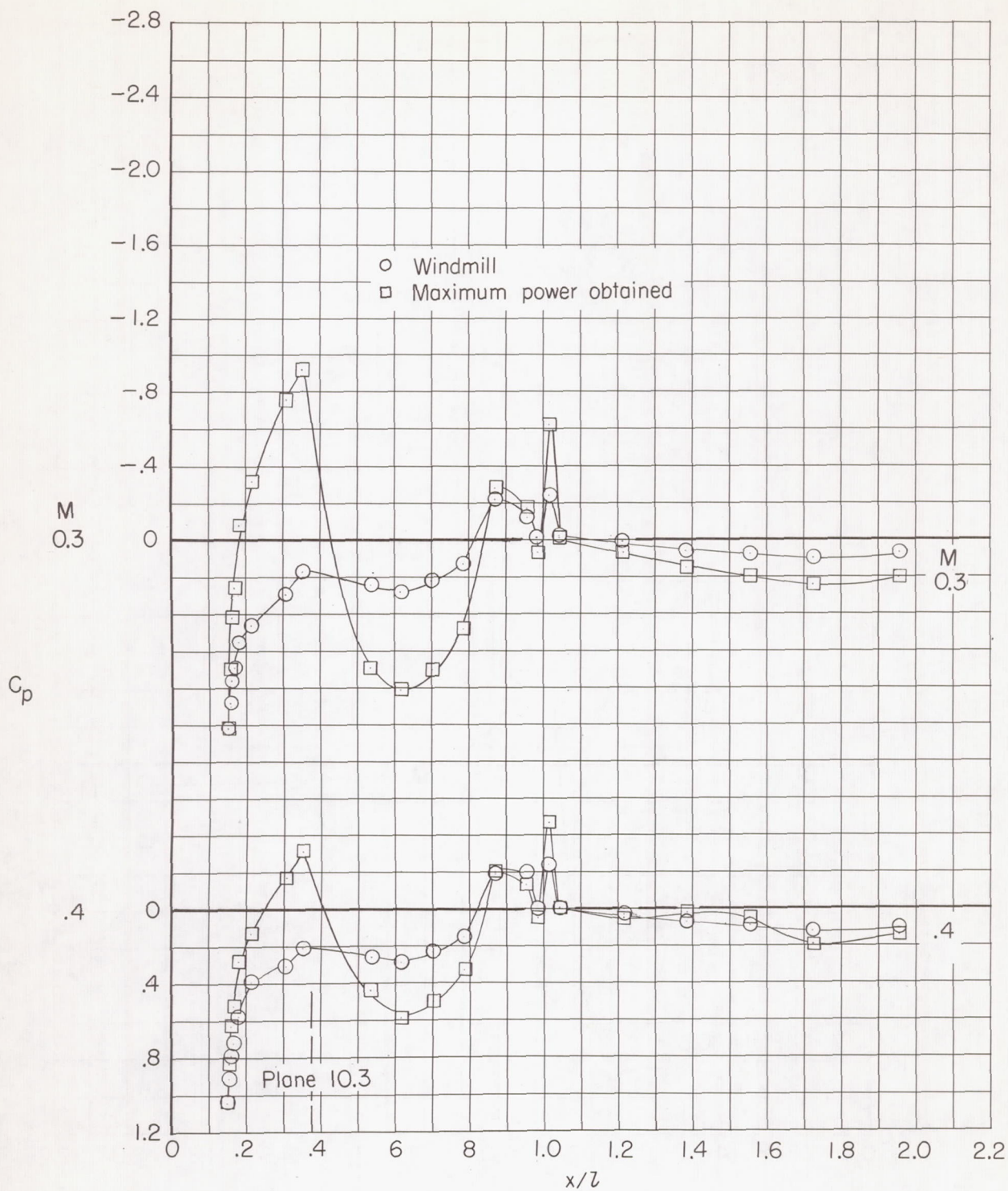
(b) $\theta = 180^\circ$. Concluded.

Figure 58.- Concluded.



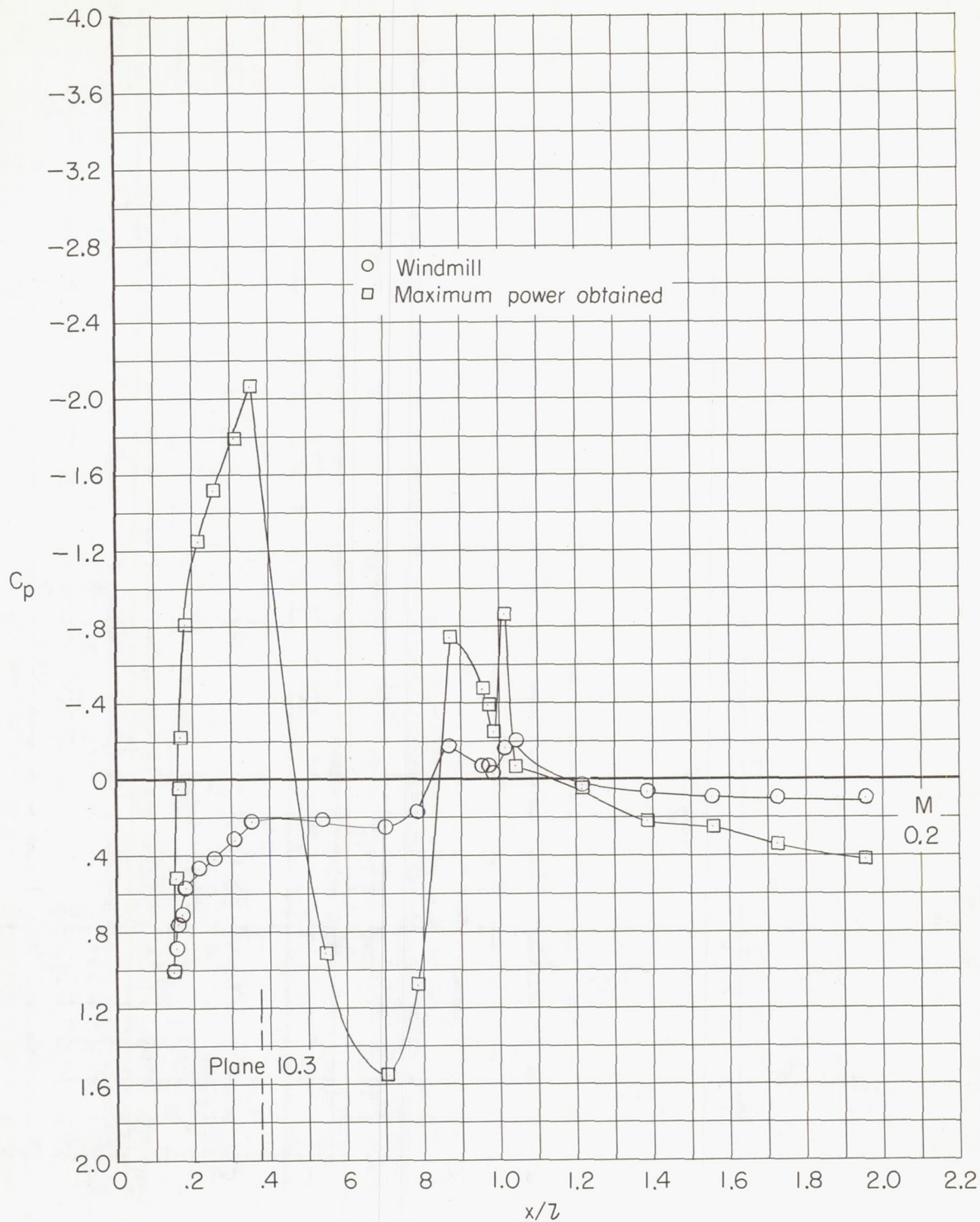
(a) $\theta = 0^\circ$.

Figure 59.- Fan-bulb-nose-plus-plug pressure distributions for configuration 243.



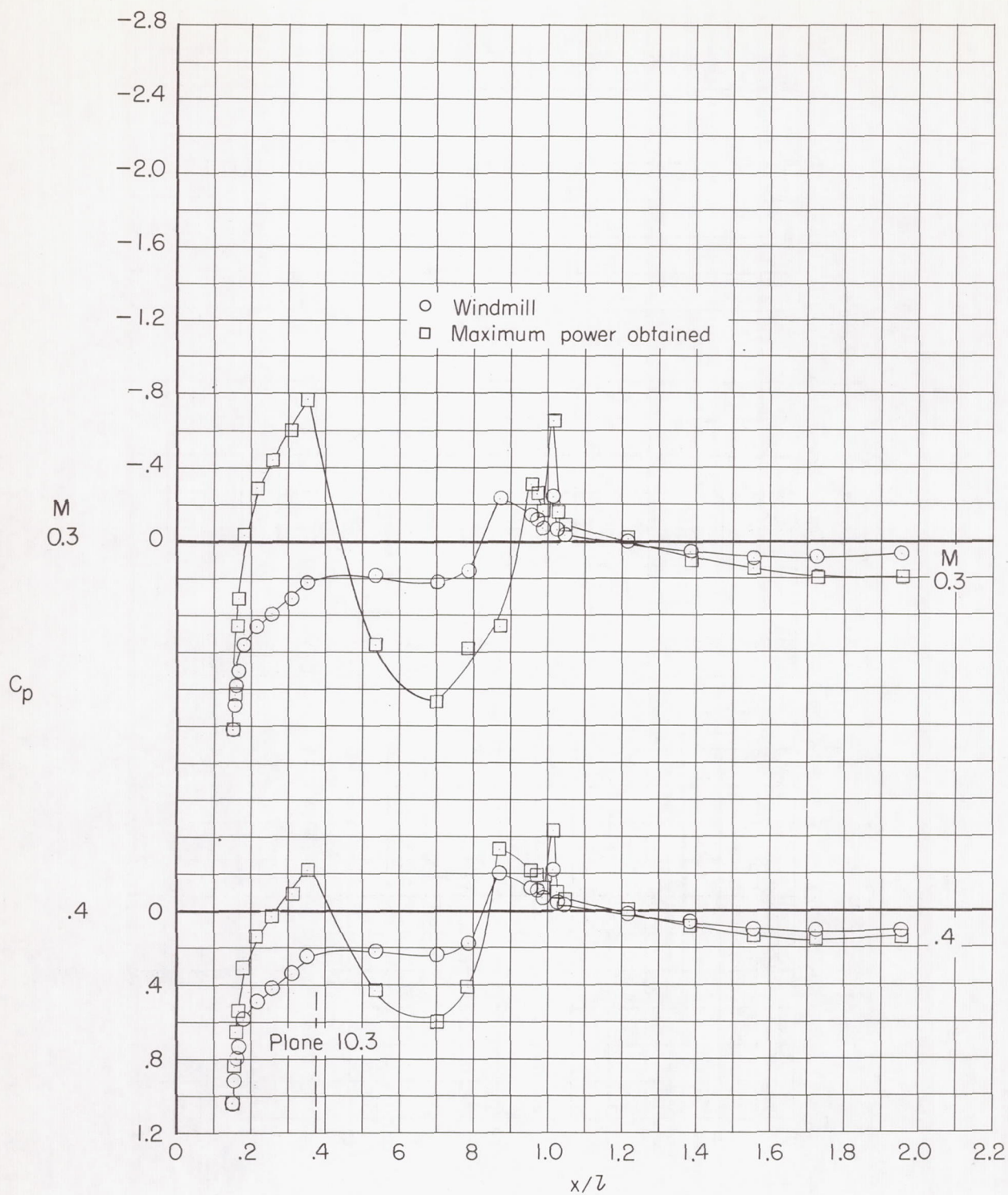
(a) $\theta = 0^\circ$. Concluded.

Figure 59.- Continued.



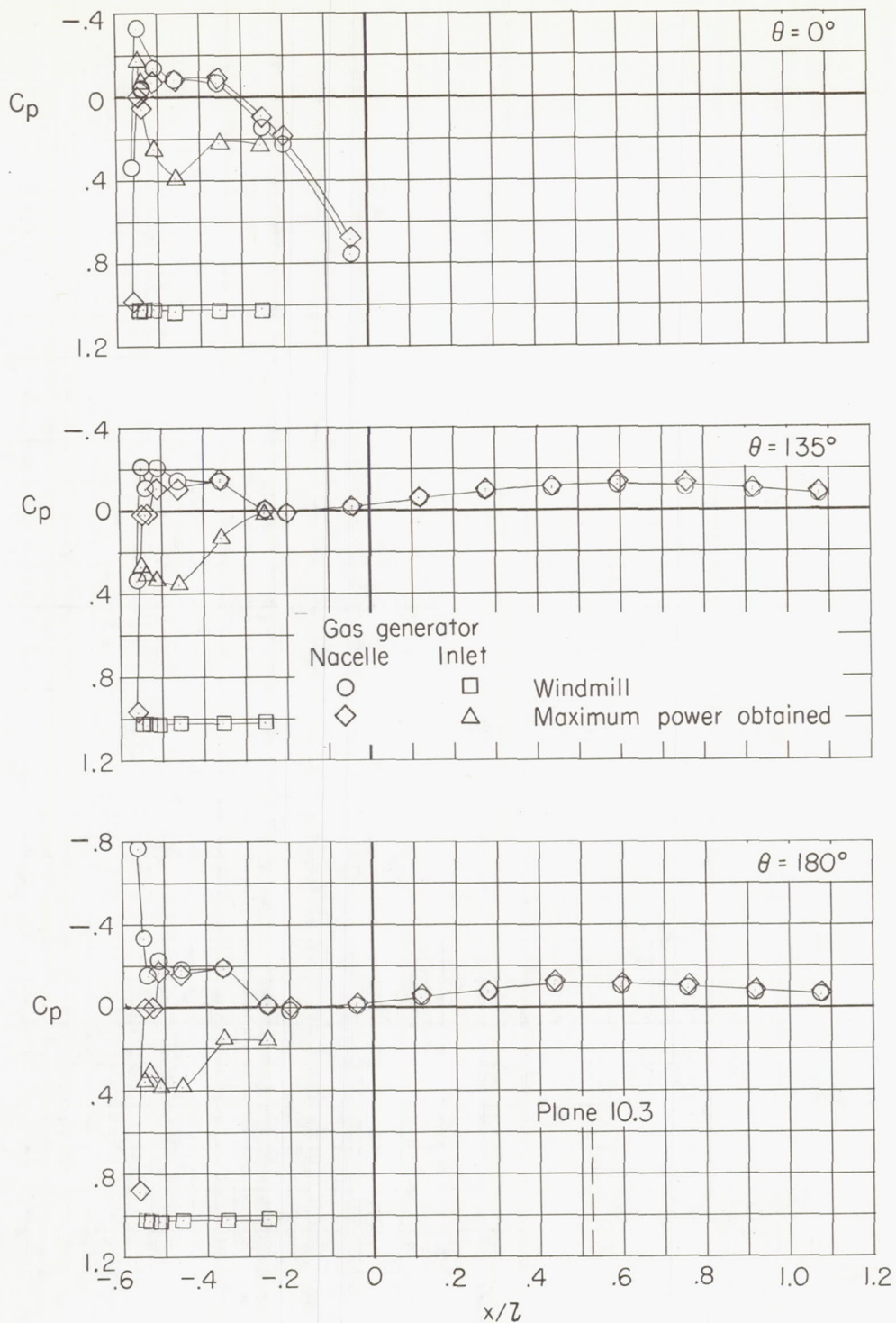
(b) $\theta = 180^\circ$.

Figure 59.- Continued.



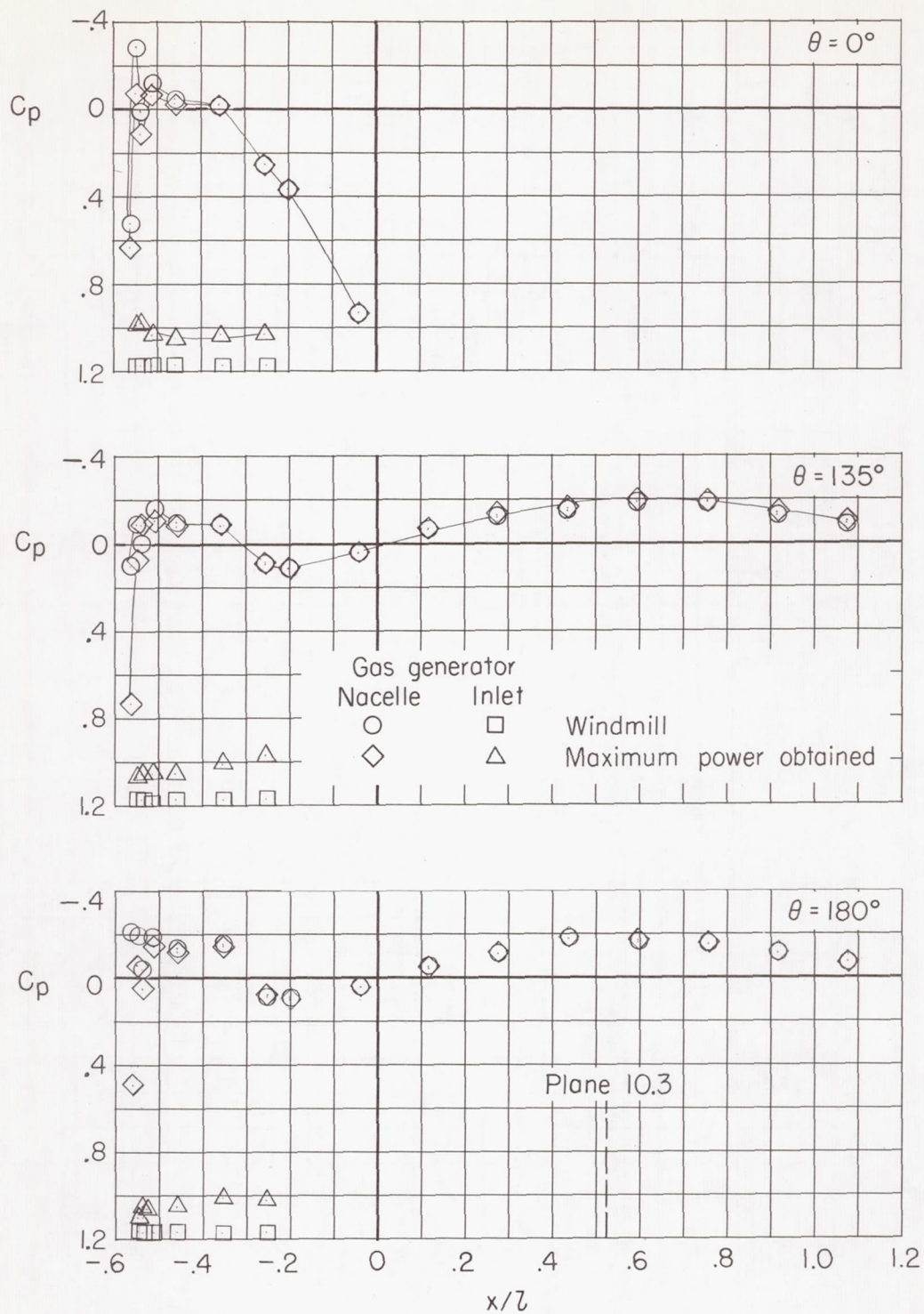
(b) $\theta = 180^\circ$. Concluded.

Figure 59.- Concluded.



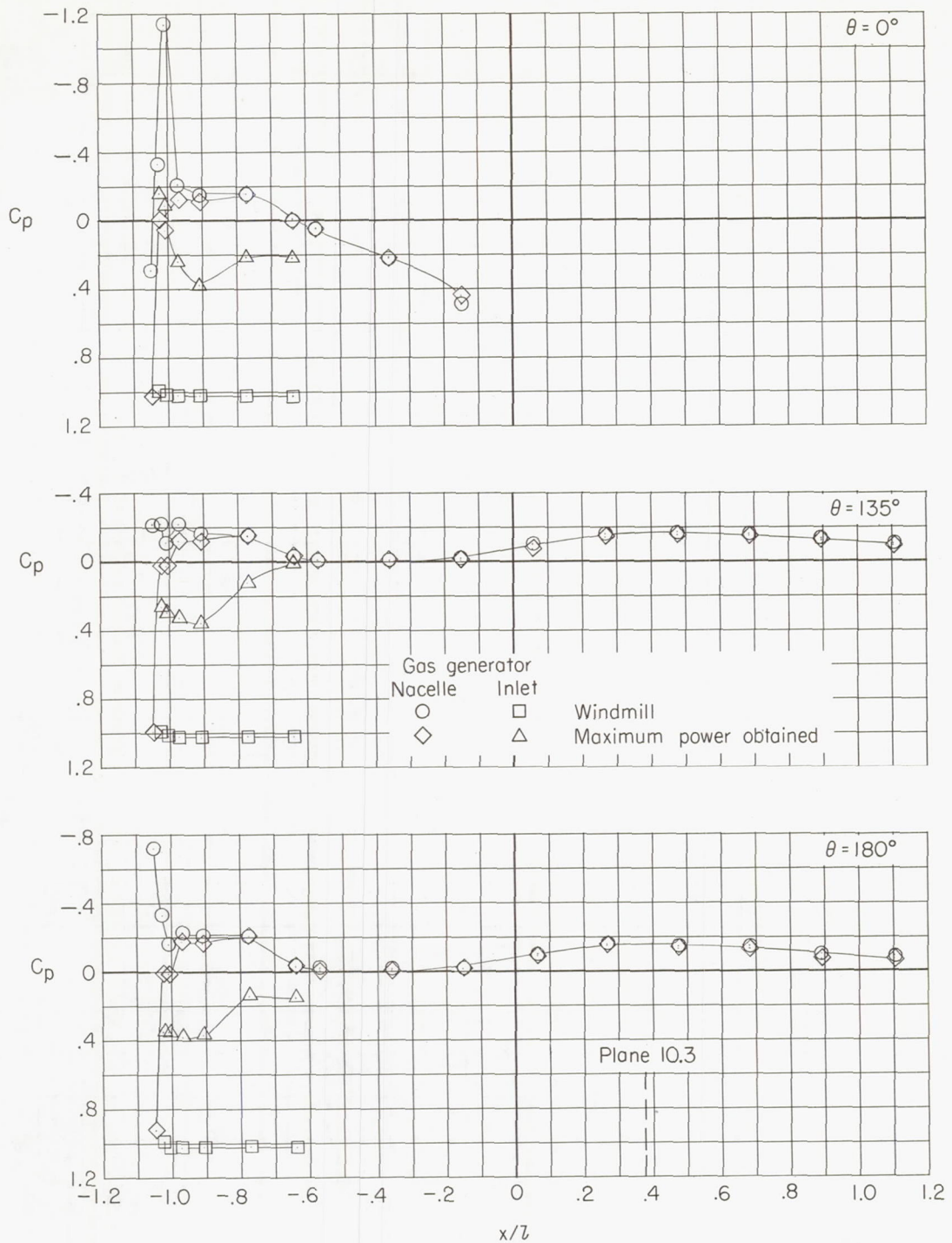
(a) $M = 0.30$; $N_F/\sqrt{\sigma} = 97.0$ percent.

Figure 60.- Gas-generator-inlet and nacelle pressure distributions for configuration 144.



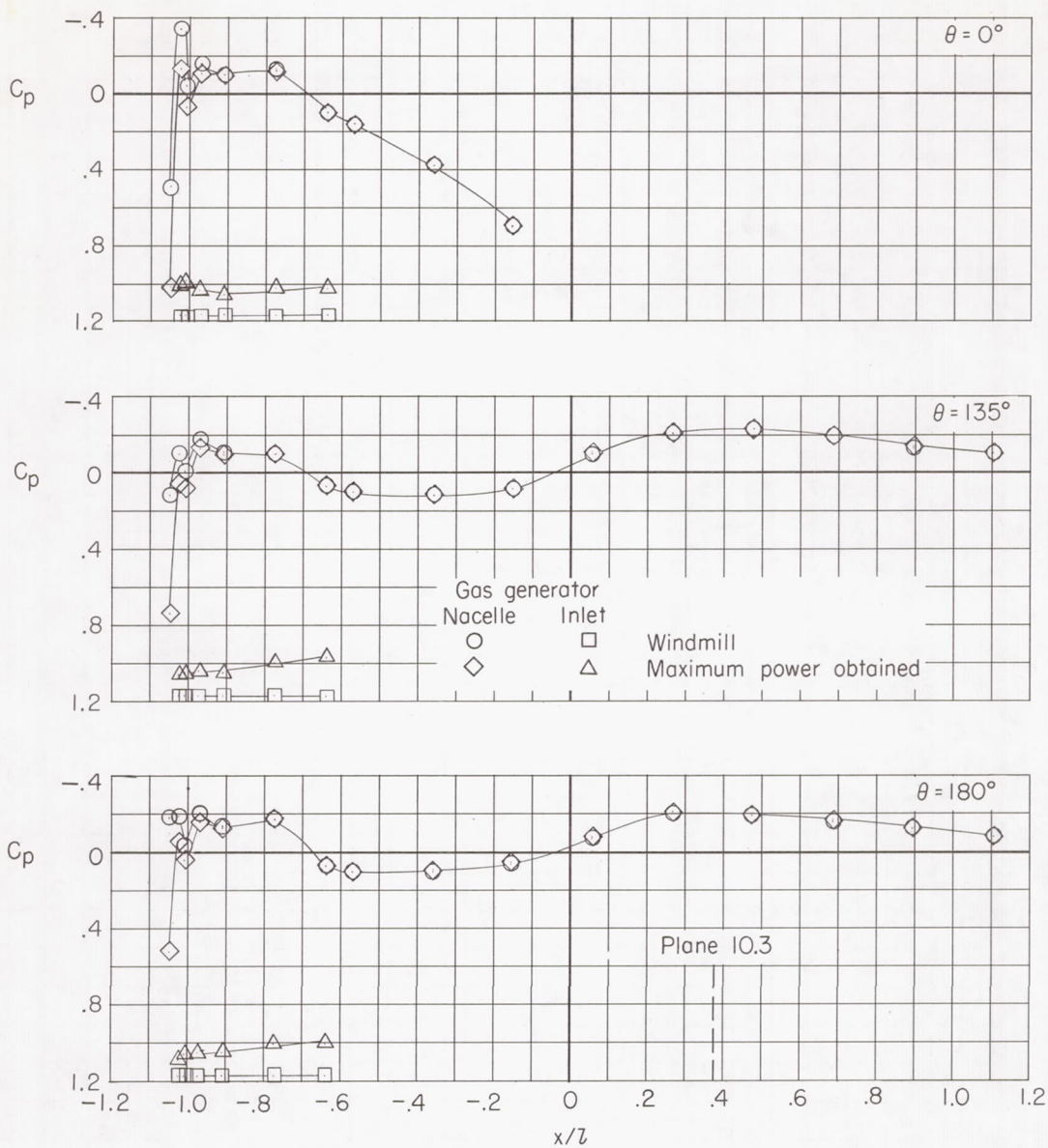
(b) $M = 0.80$; $N_F/\sqrt{\sigma} = 87.6$ percent.

Figure 60.- Concluded.



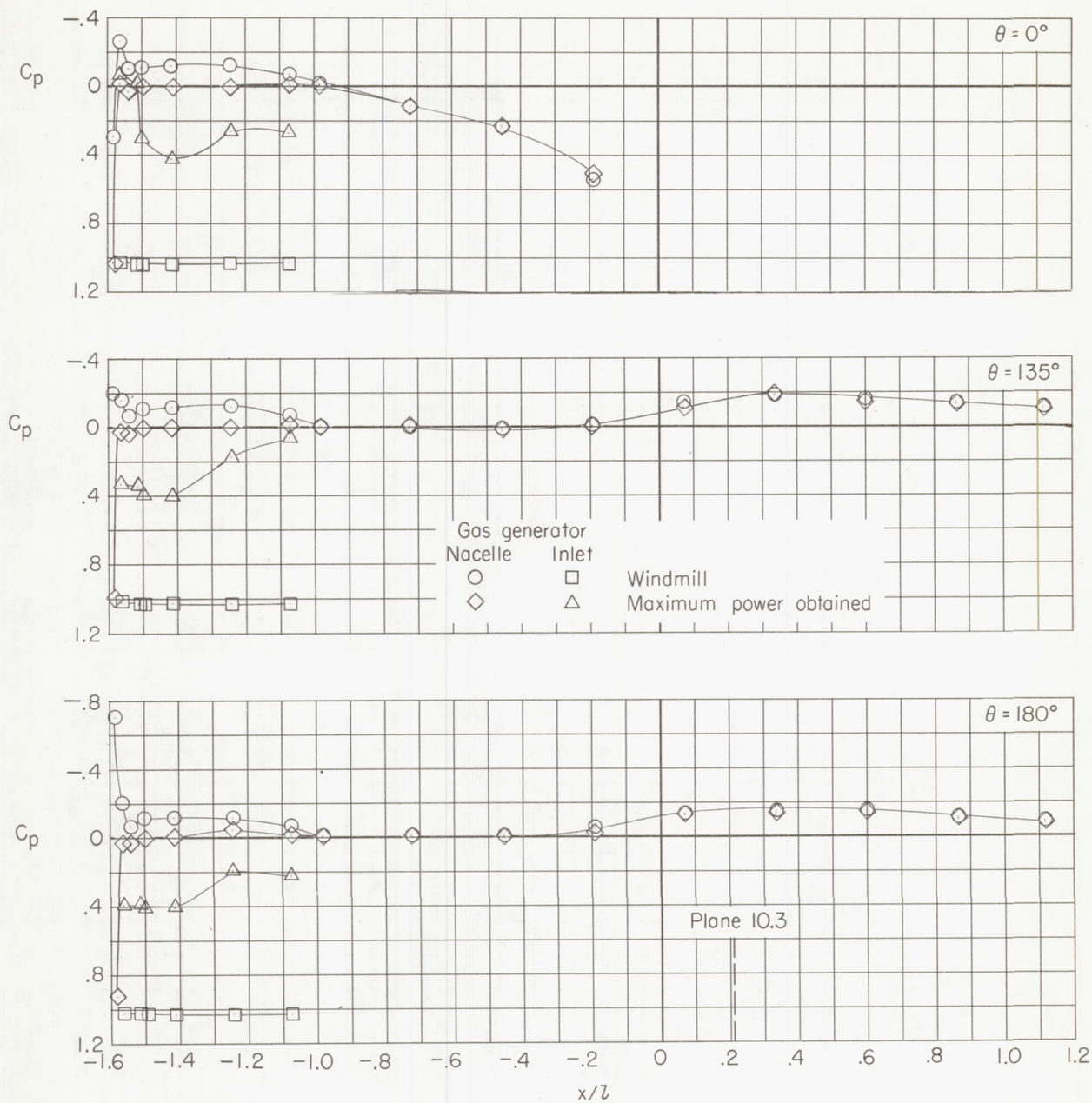
(a) $M = 0.30$; $N_F/\sqrt{\sigma} = 98.5$ percent.

Figure 61.- Gas-generator-inlet and pressure distributions for configuration 244.



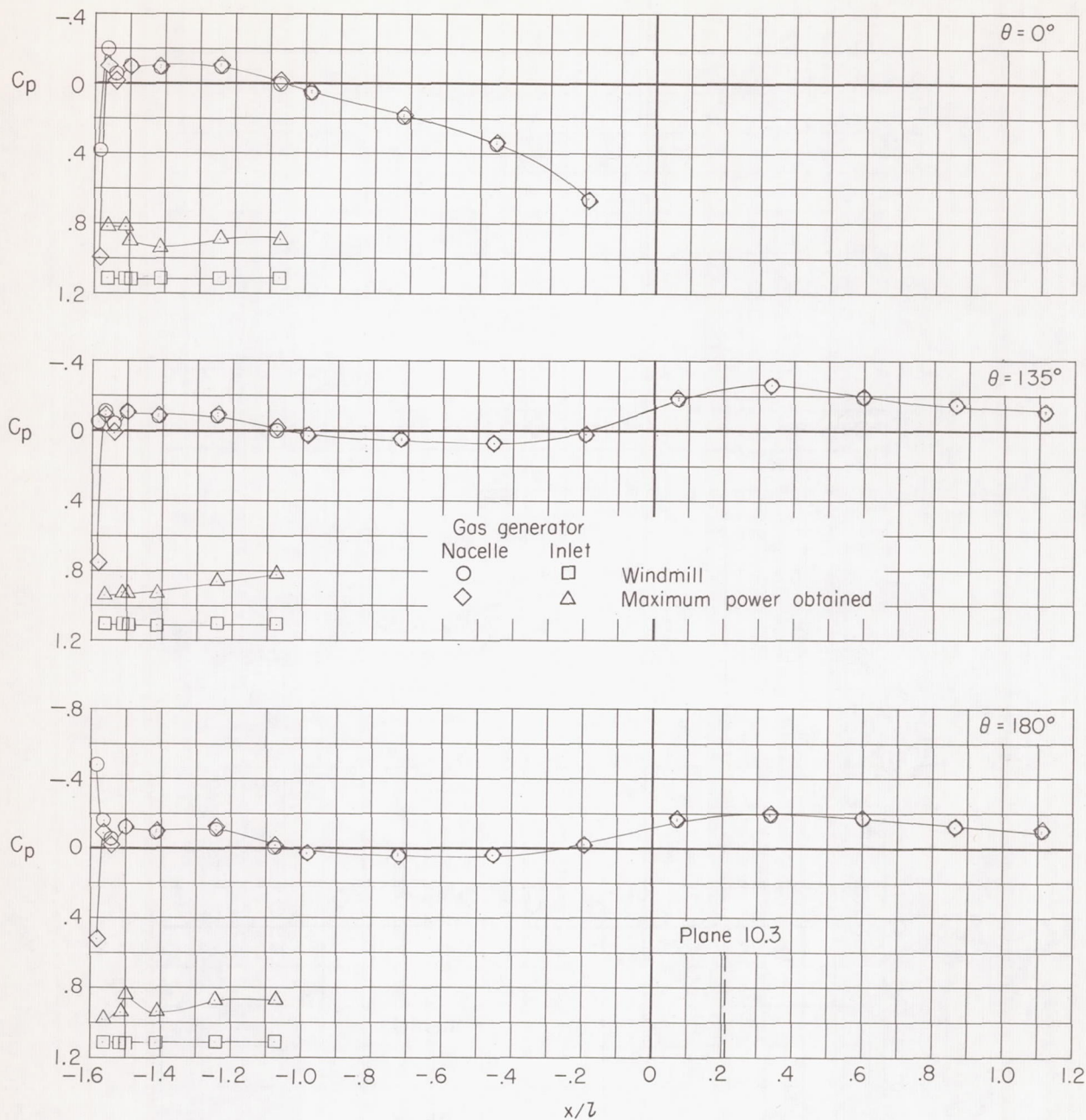
(b) $M = 0.80$; $N_F/\sqrt{\sigma} = 87.5$ percent.

Figure 61.- Concluded.



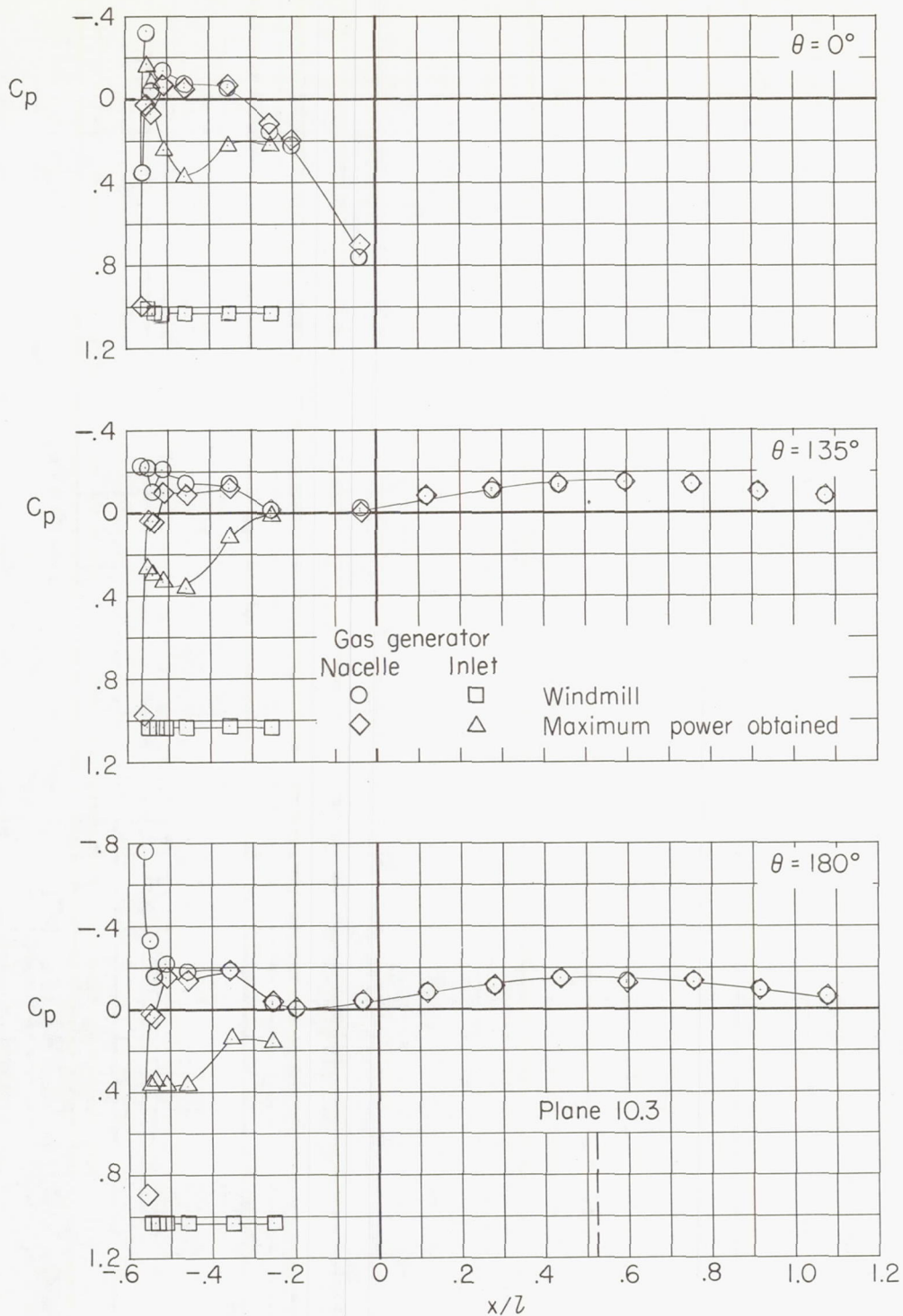
(a) $M = 0.30$; $N_F/\sqrt{\sigma} = 94.8$ percent.

Figure 62.- Gas-generator-inlet and nacelle pressure distributions for configuration 344.



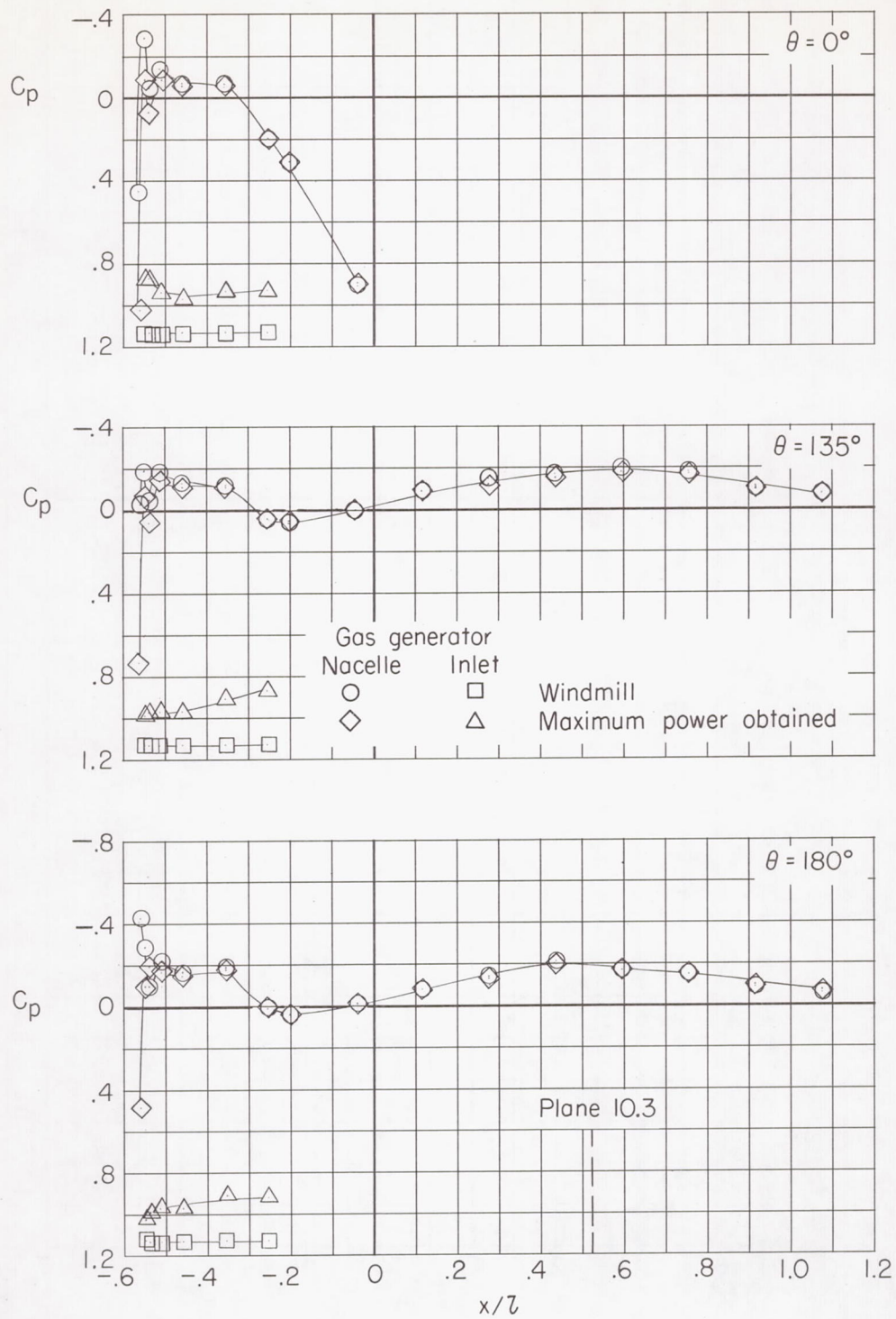
(b) $M = 0.65$; $N_F/\sqrt{\sigma} = 91.7$ percent.

Figure 62.- Concluded.



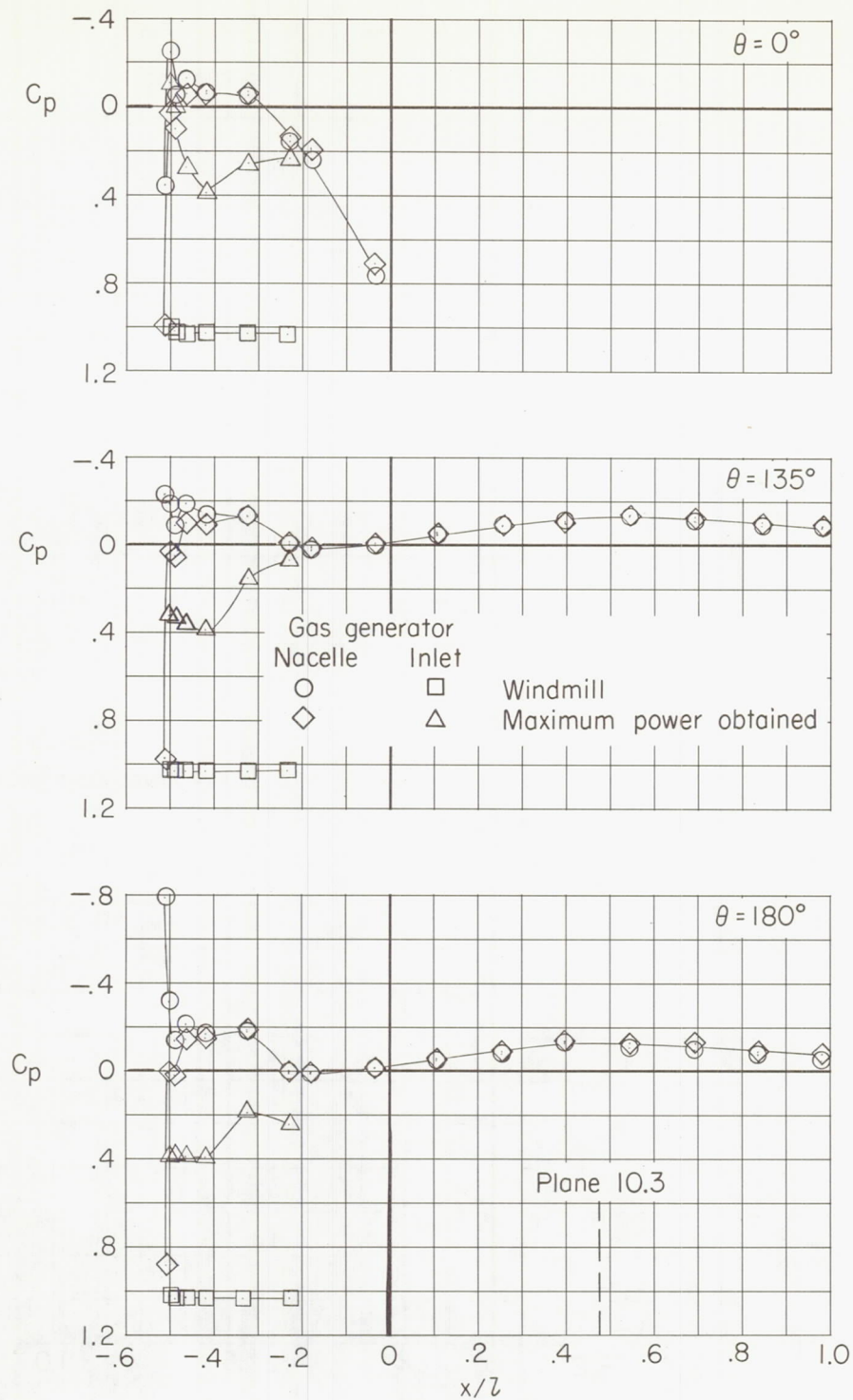
(a) $M = 0.30$; $N_F/\sqrt{\sigma} = 98.1$ percent.

Figure 63.- Gas-generator inlet and nacelle pressure distributions for configuration 123.



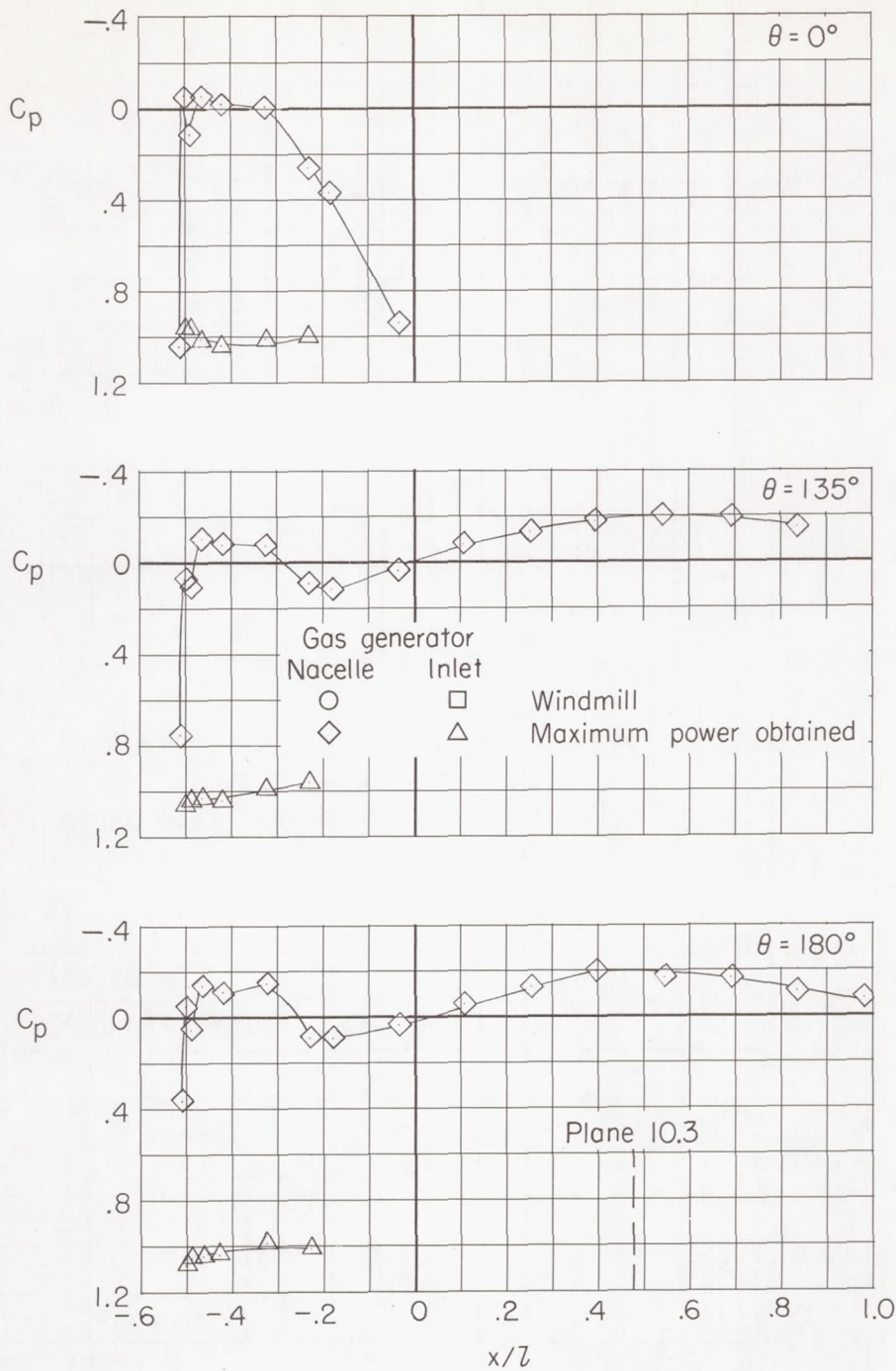
(b) $M = 0.70$; $N_F/\sqrt{\sigma} = 90.6$ percent.

Figure 63.- Concluded.



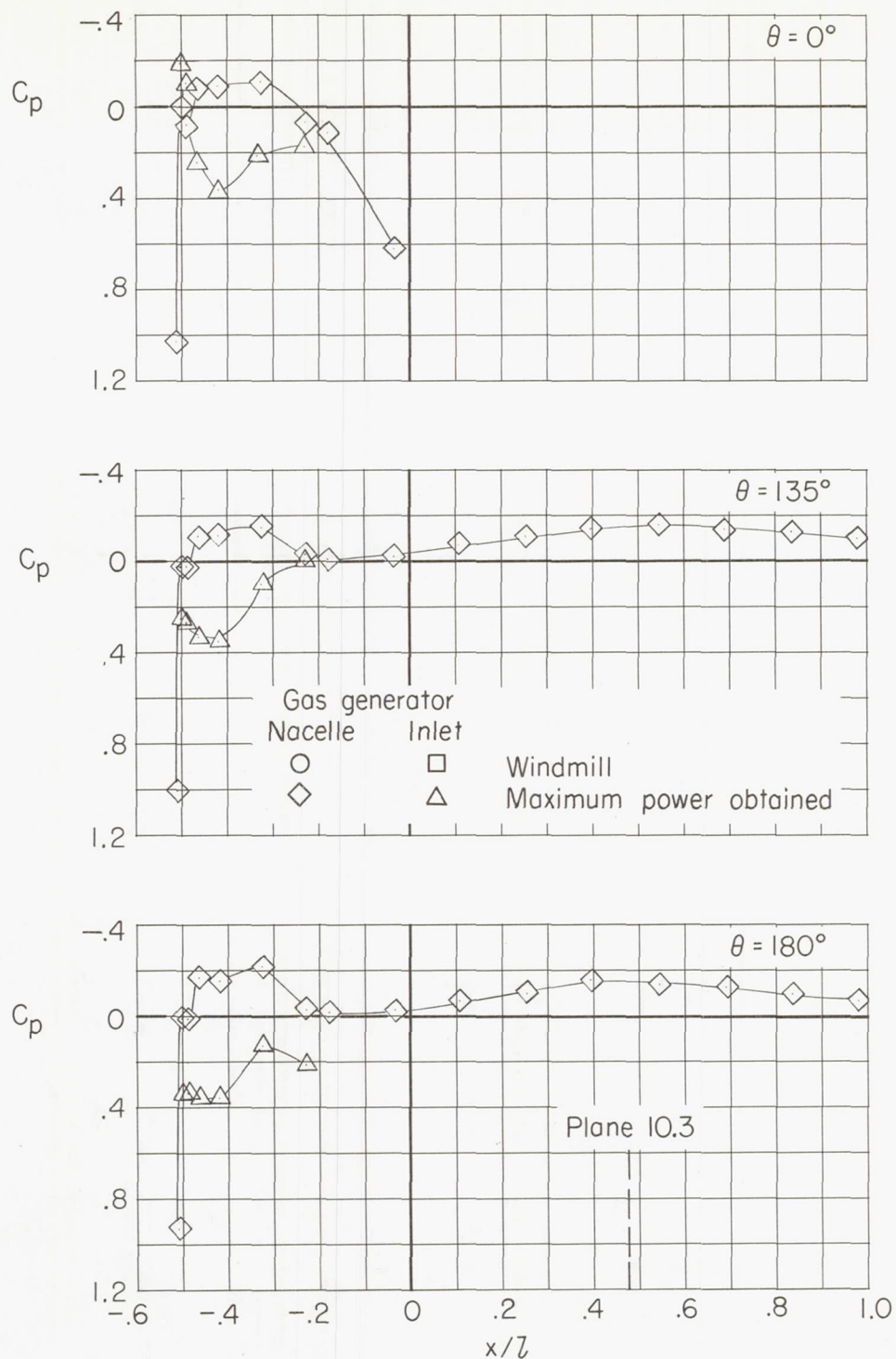
(a) $M = 0.30$; $N_F/\sqrt{\sigma} = 95.8$ percent.

Figure 64.- Gas-generator-inlet and nacelle pressure distributions for configuration 113.



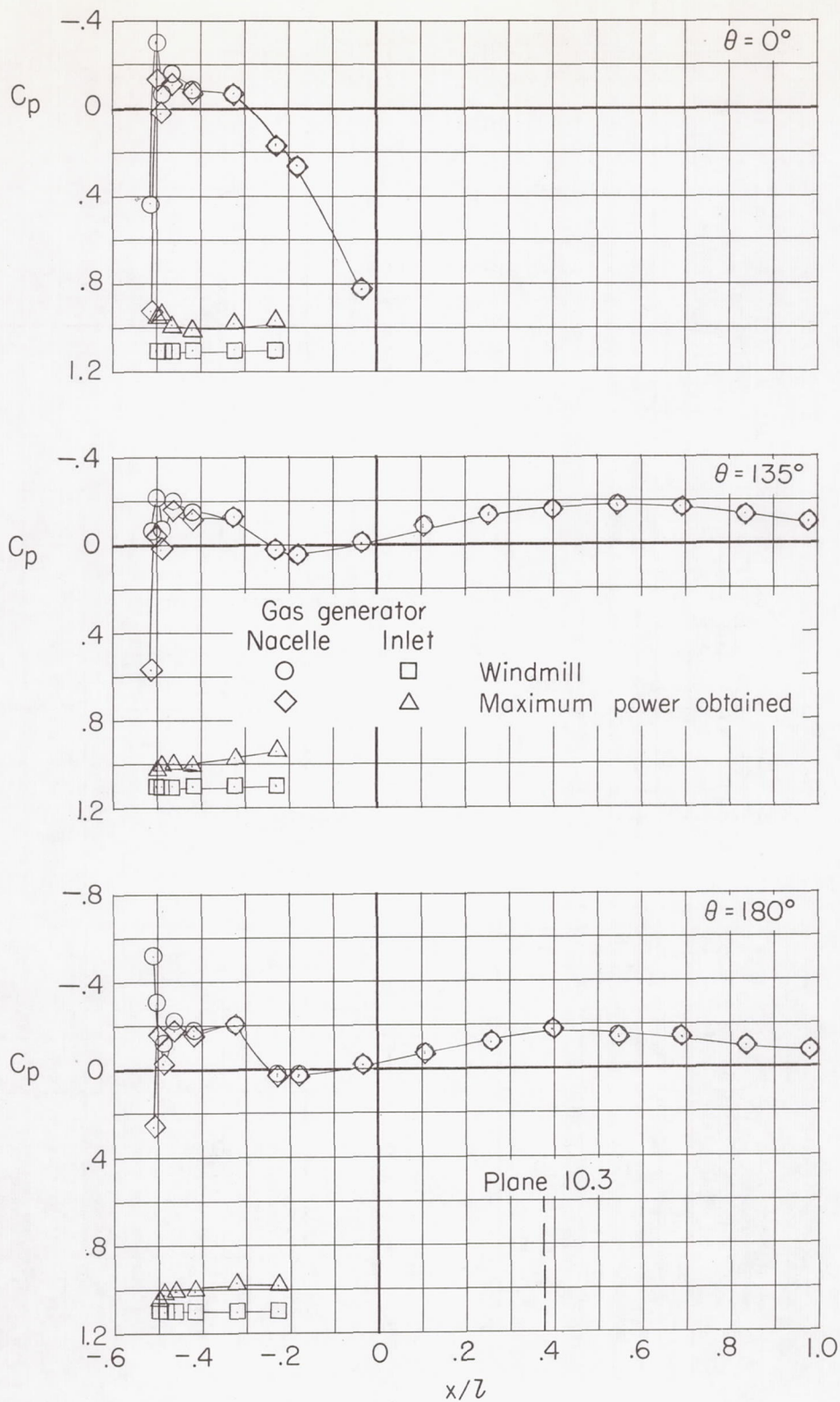
(b) $M = 0.80$; $N_F/\sqrt{\sigma} = 90.8$ percent.

Figure 64.- Concluded.



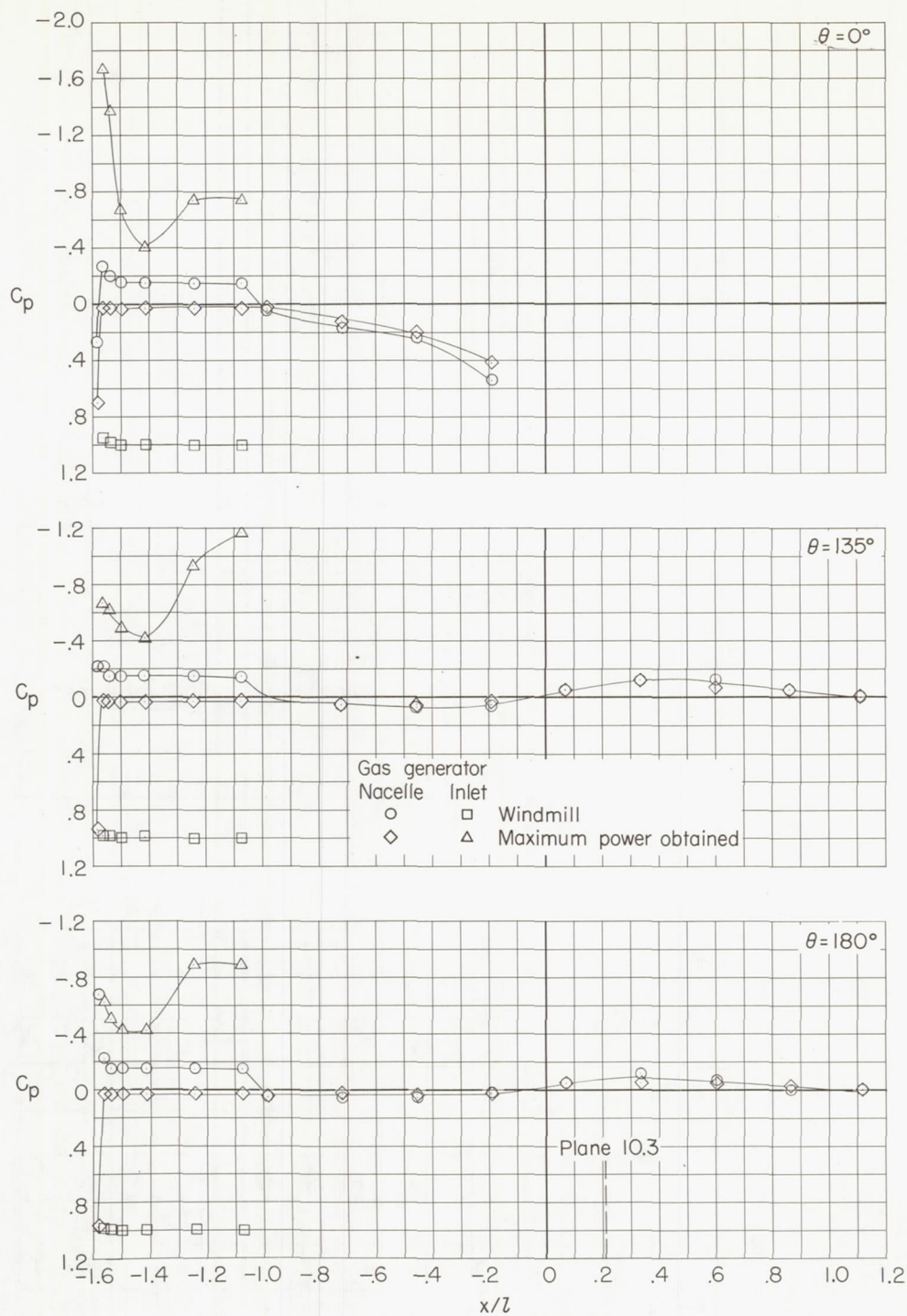
(a) $M = 0.30$; $N_F/\sqrt{\sigma} = 96.8$ percent.

Figure 65.- Gas-generator-inlet and nacelle pressure distributions for configuration 112.



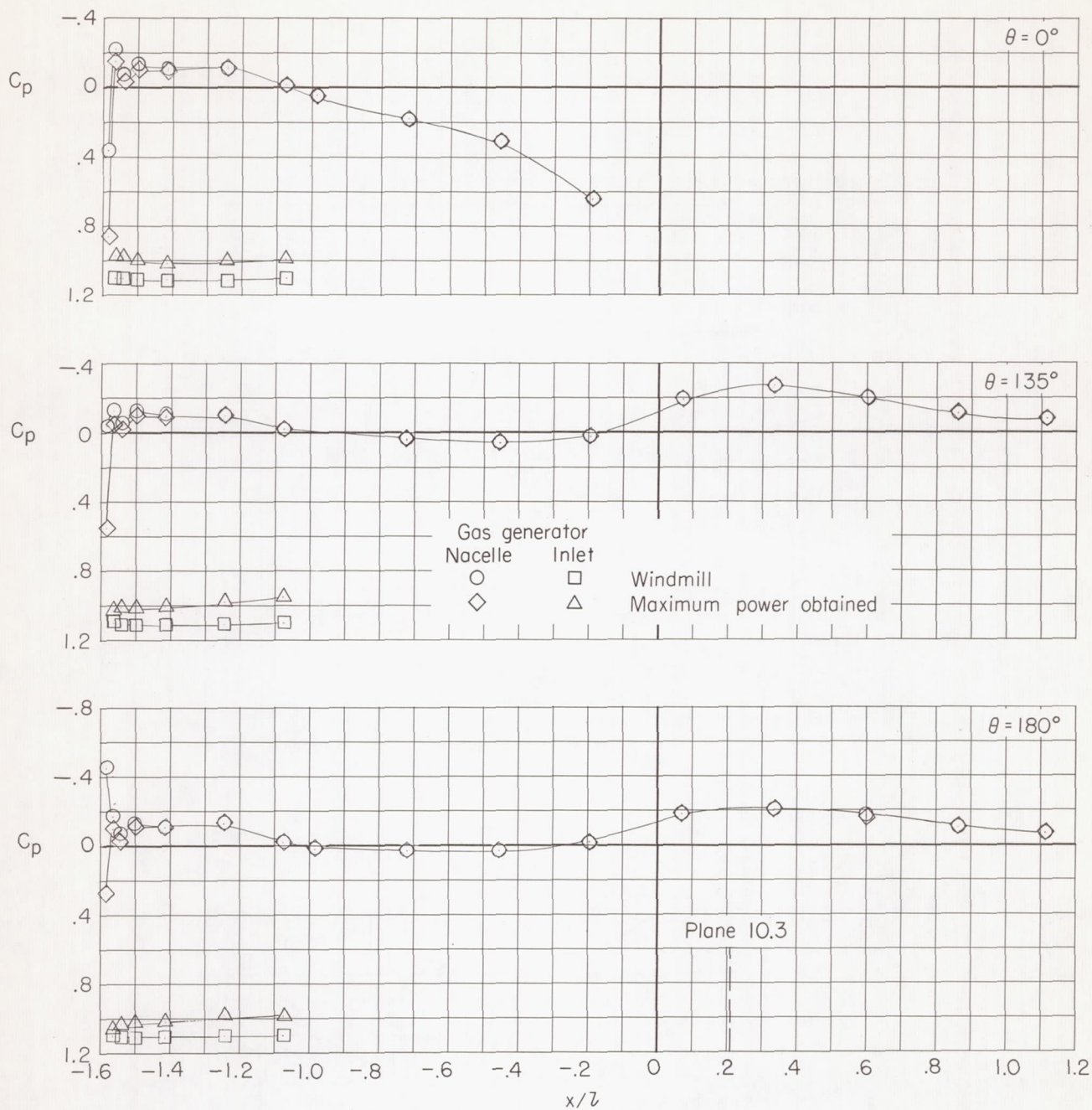
(b) $M = 0.65$; $N_F/\sqrt{\sigma} = 77.0$ percent.

Figure 65.- Concluded.



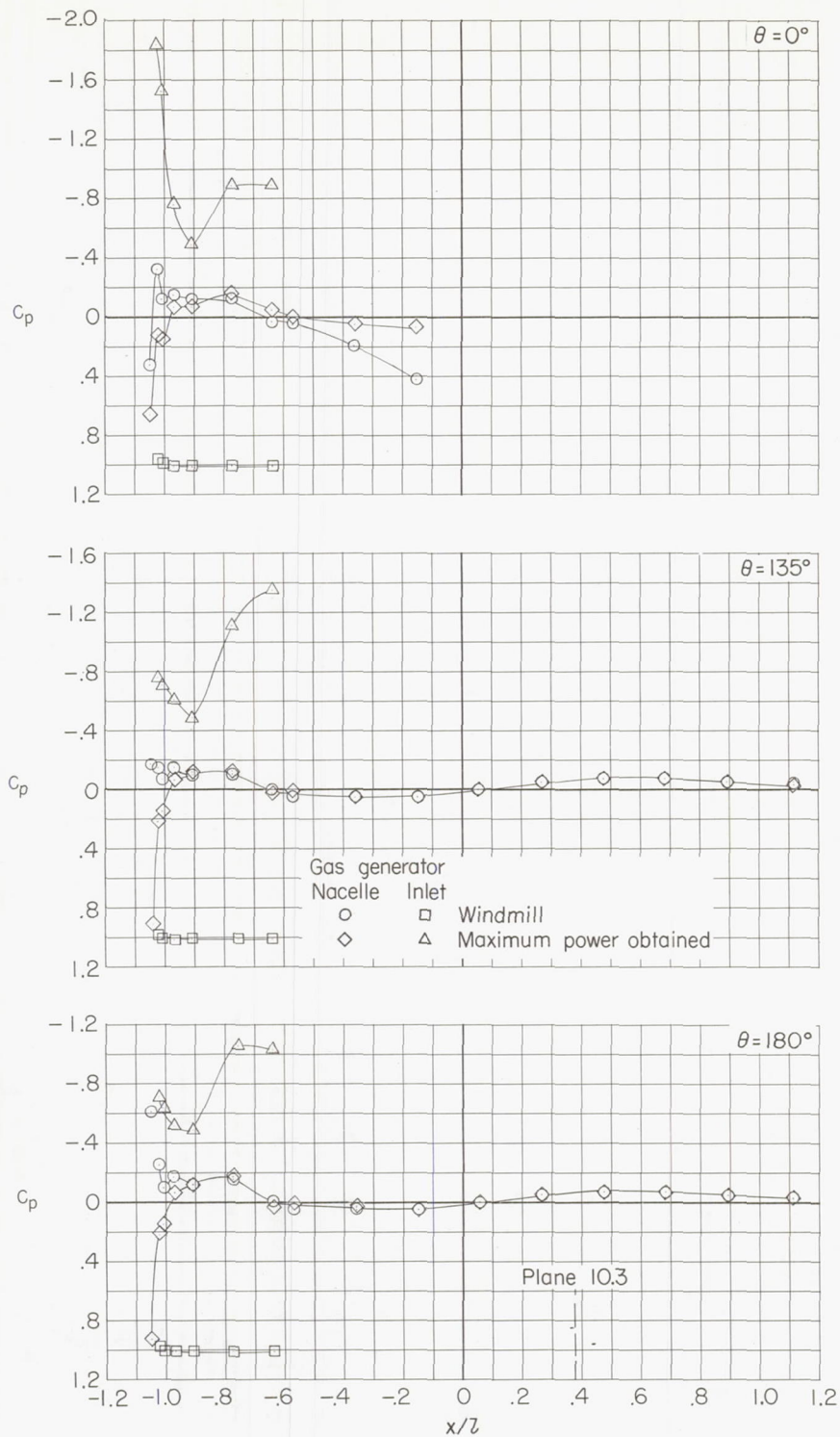
(a) $M = 0.20$; $N_F/\sqrt{\sigma} = 97.8$ percent.

Figure 66.- Gas-generator-inlet and nacelle pressure distributions for configuration 322.



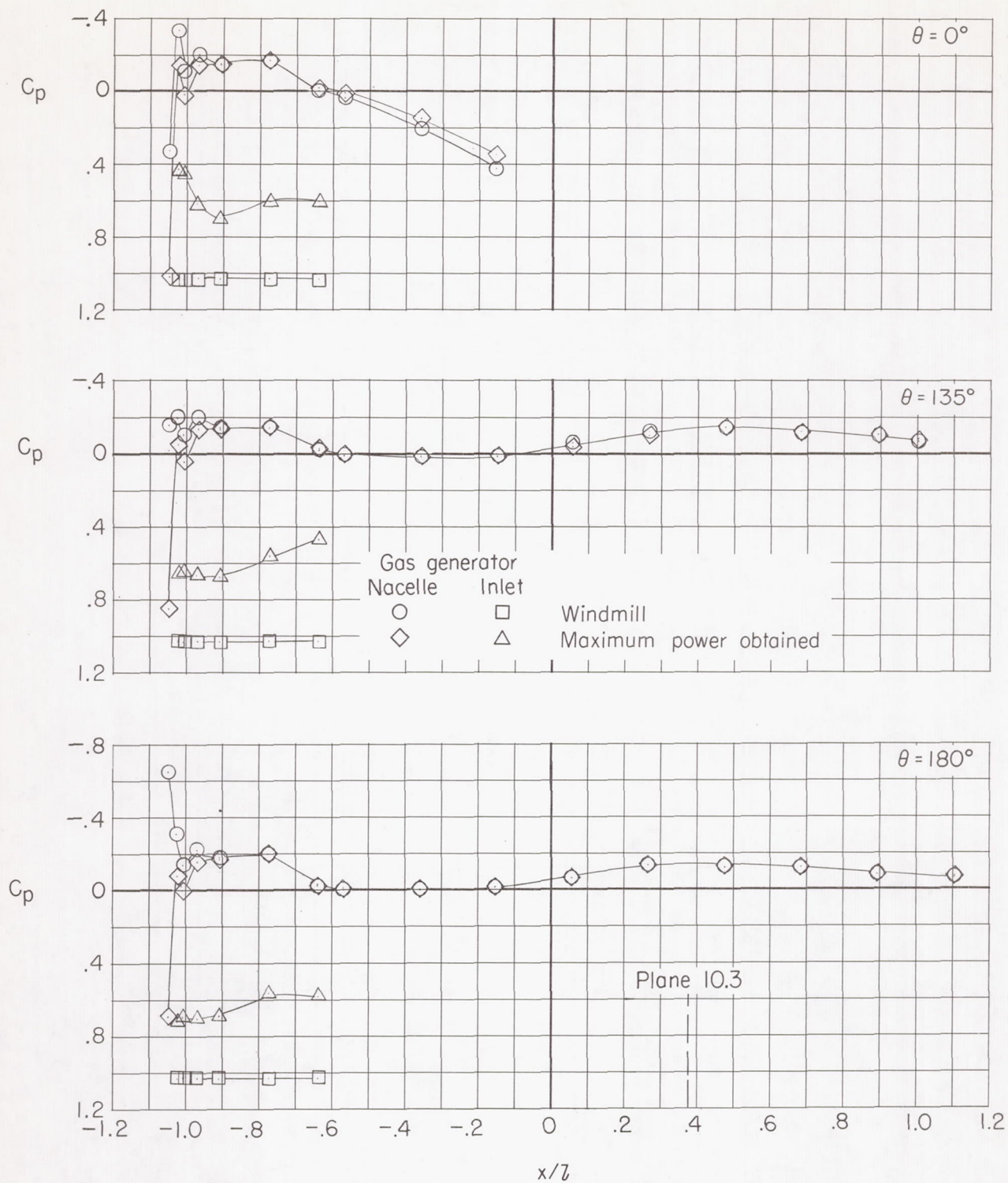
(b) $M = 0.65$; $N_F/\sqrt{\sigma} = 76.5$ percent.

Figure 66.- Concluded.



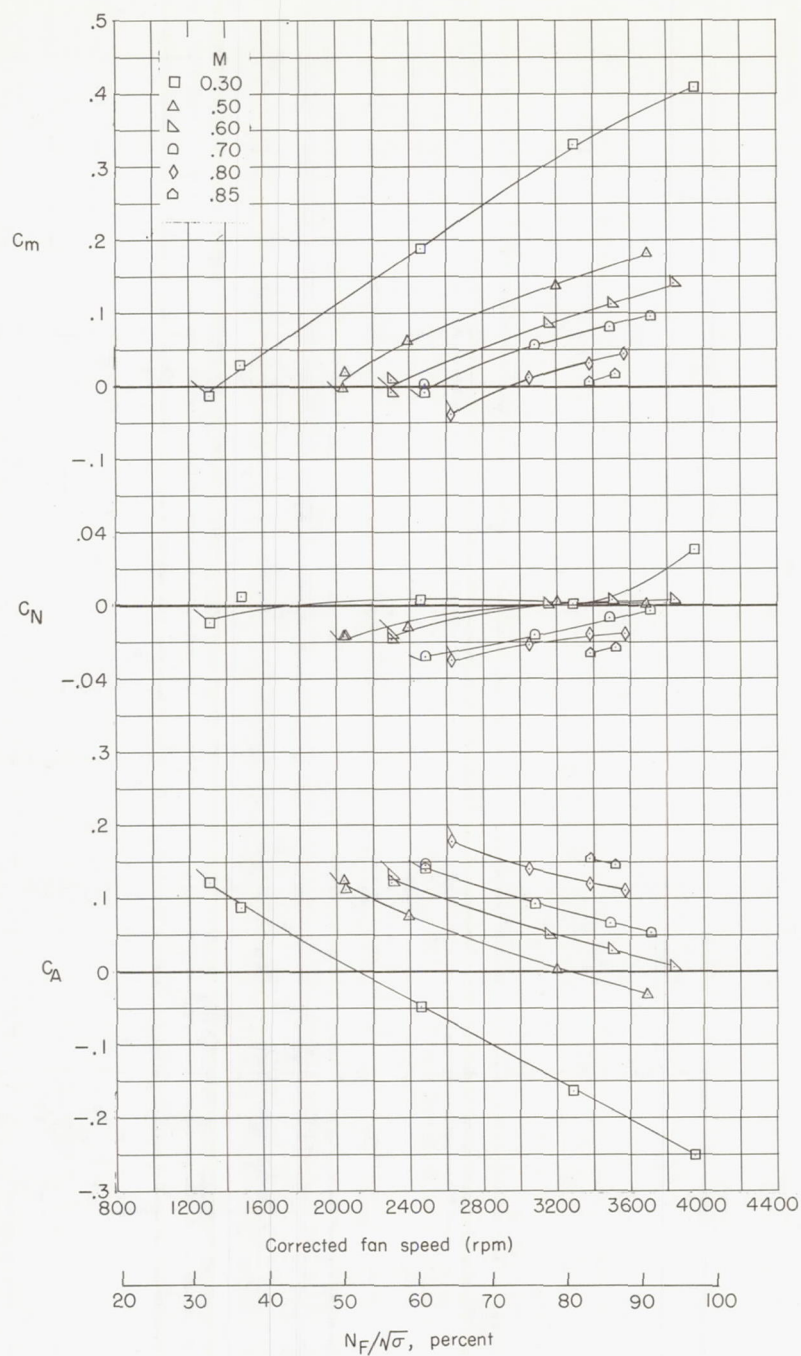
(a) $M = 0.20$; $N_F/\sqrt{\sigma} = 97.2$ percent.

Figure 67.- Gas-generator-inlet and nacelle pressure distributions for configuration 243.



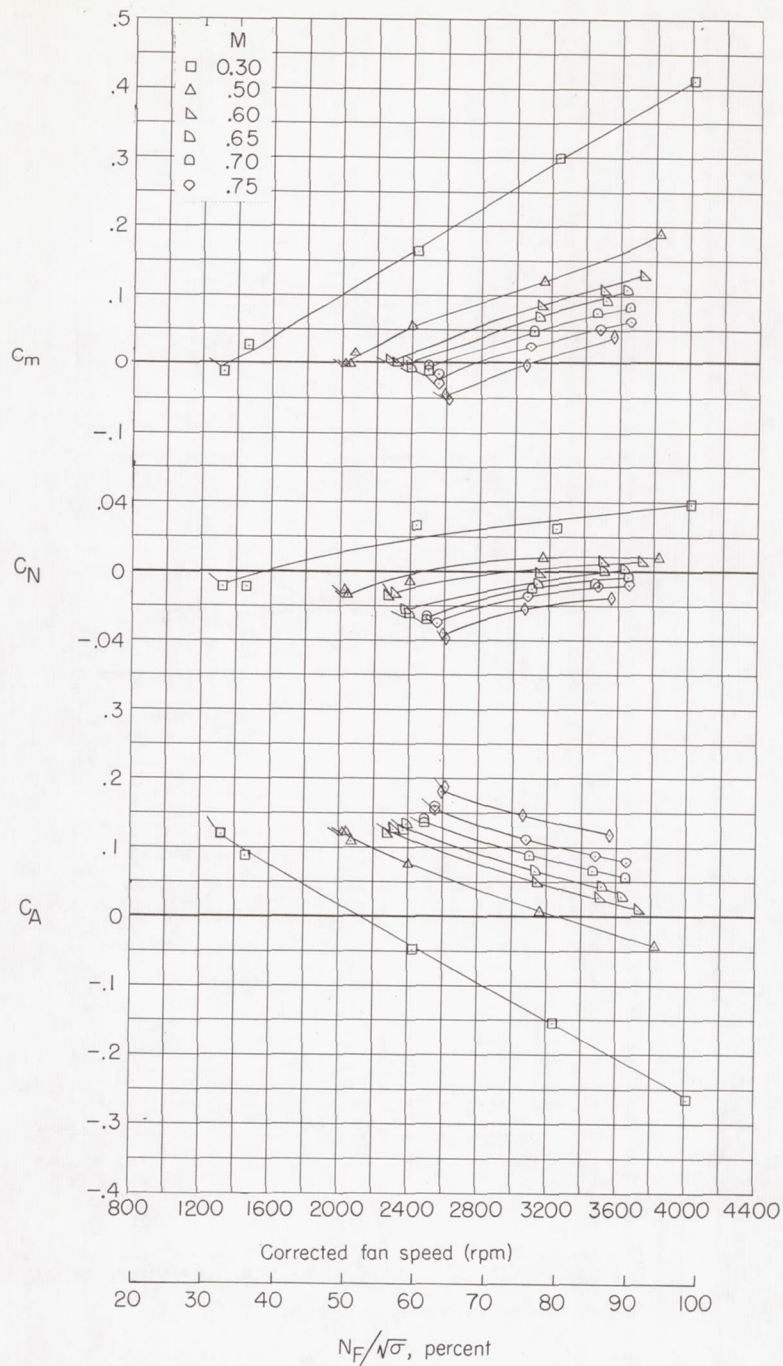
(b) $M = 0.40$; $N_F/\sqrt{\sigma} = 97.1$ percent.

Figure 67.- Concluded.



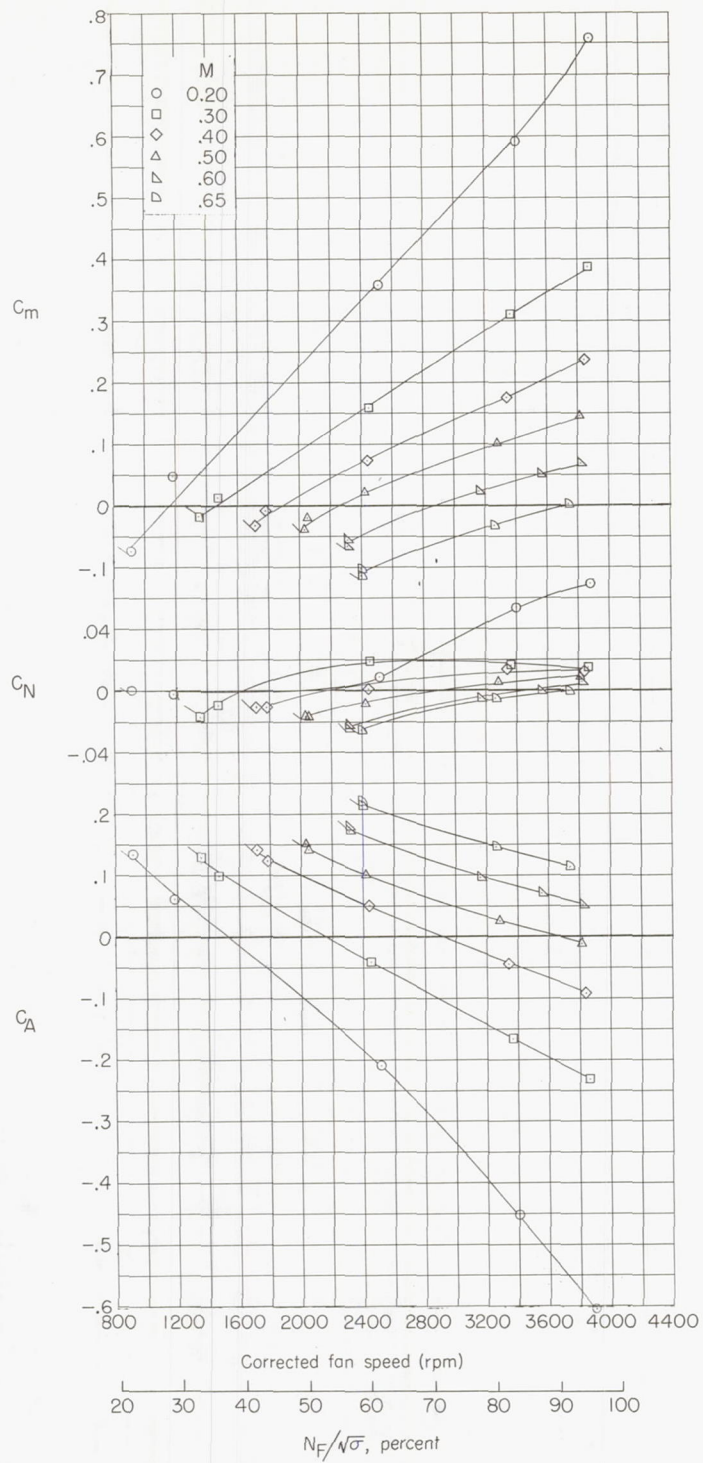
(a) Configuration 144.

Figure 68.- Aerodynamic characteristics of the various configurations tested as measured by force balance. Flagged symbols indicate windmill conditions.



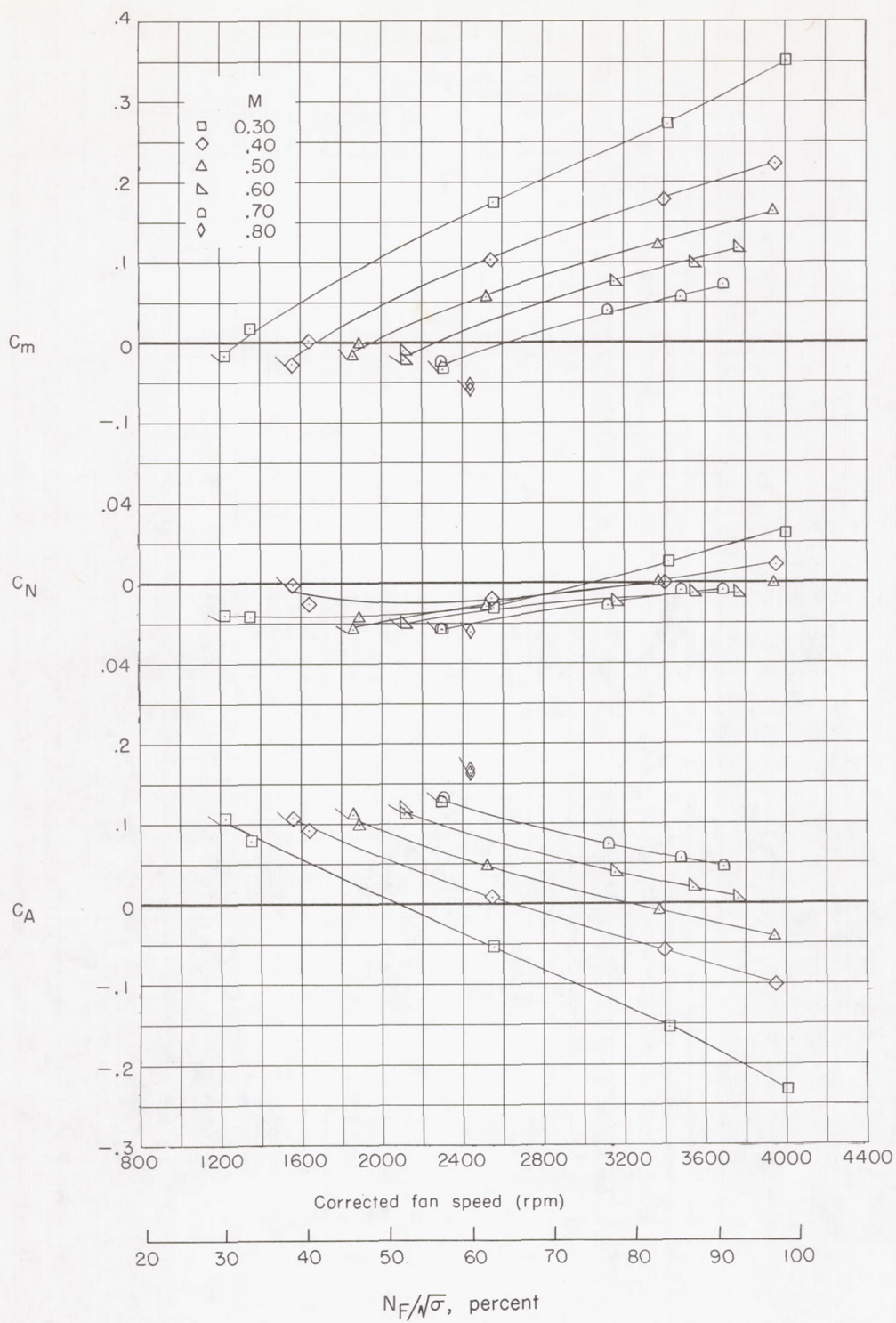
(b) Configuration 244.

Figure 68.- Continued.



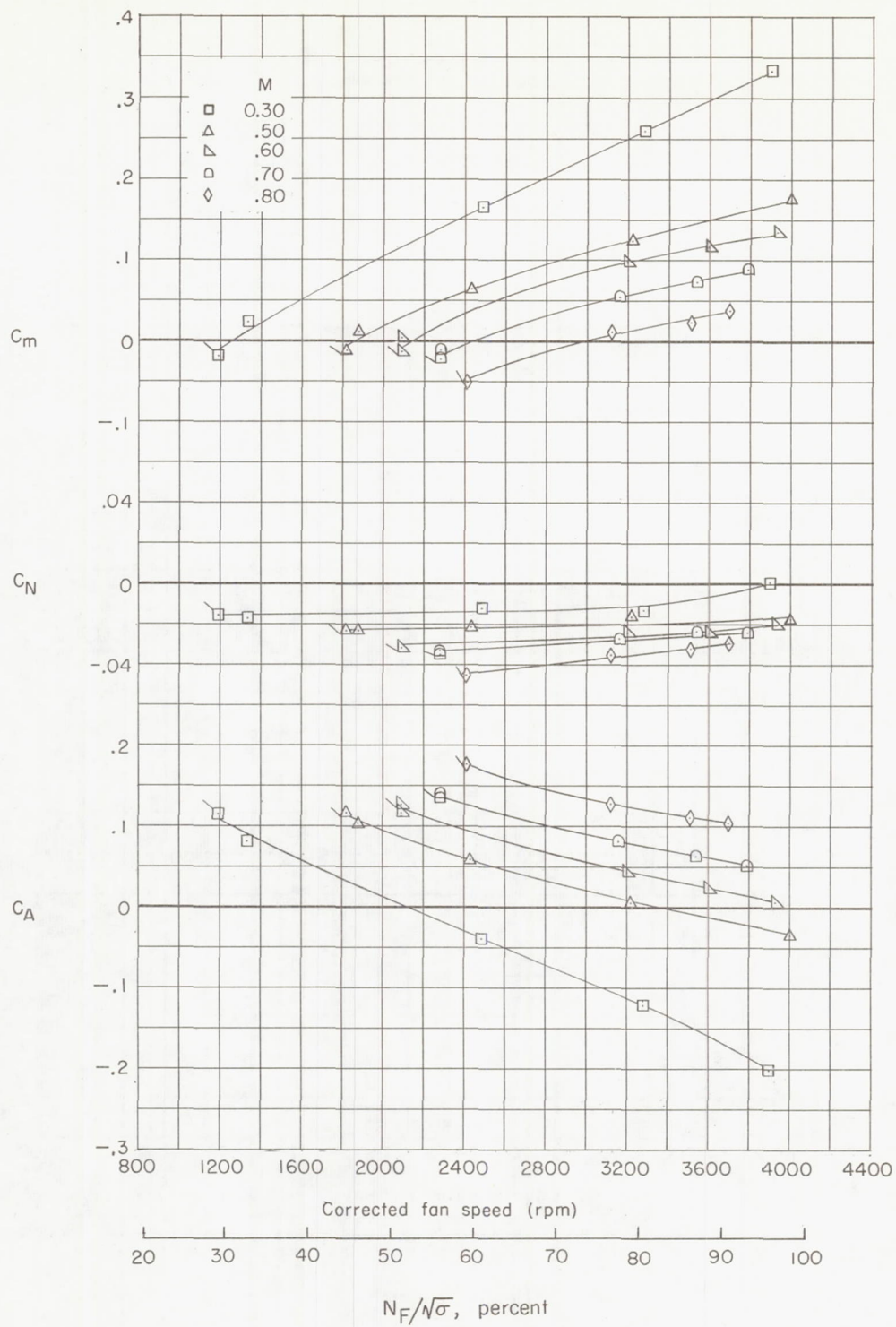
(c) Configuration 344.

Figure 68.- Continued.



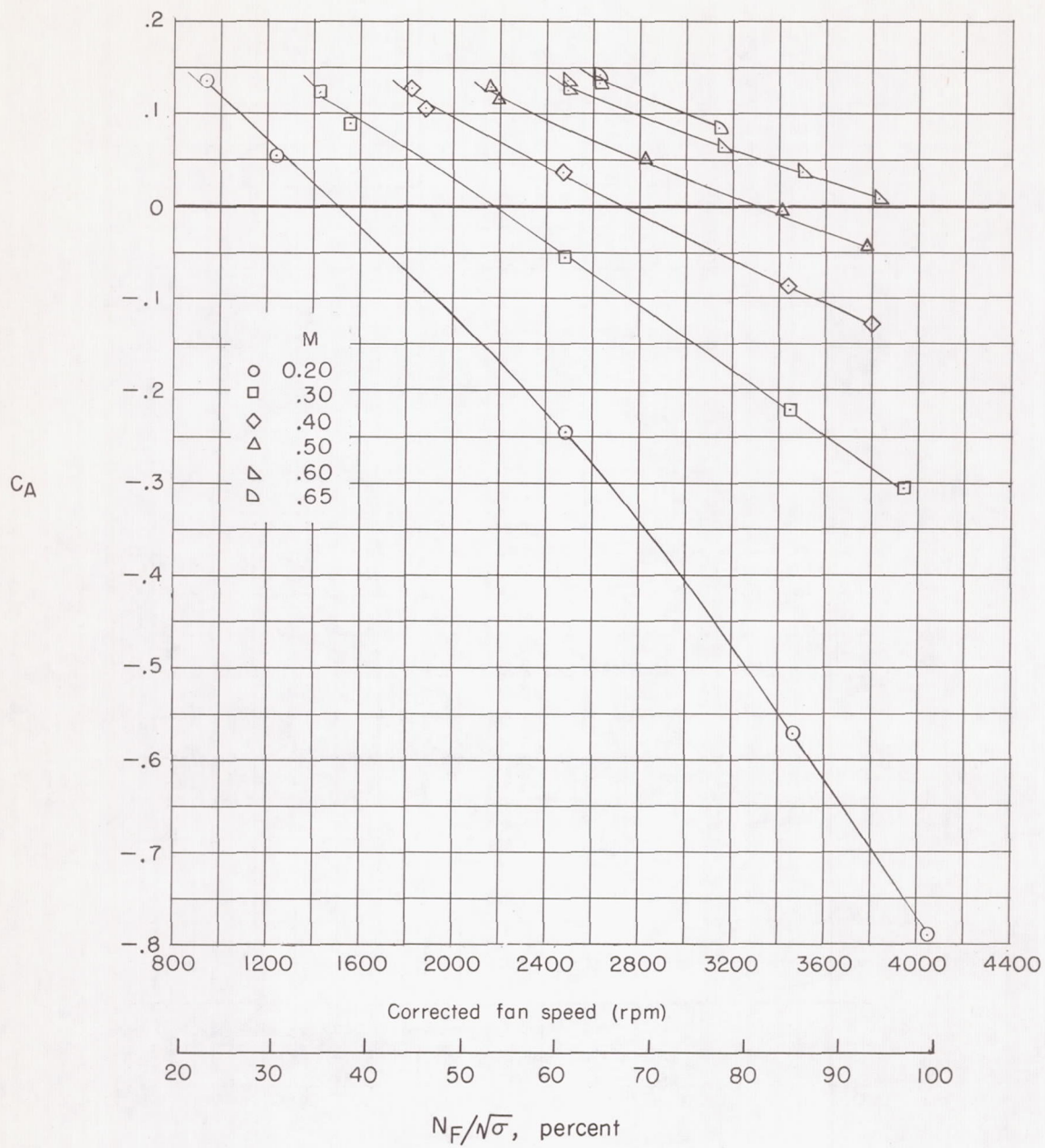
(d) Configuration 123.

Figure 68.- Continued.



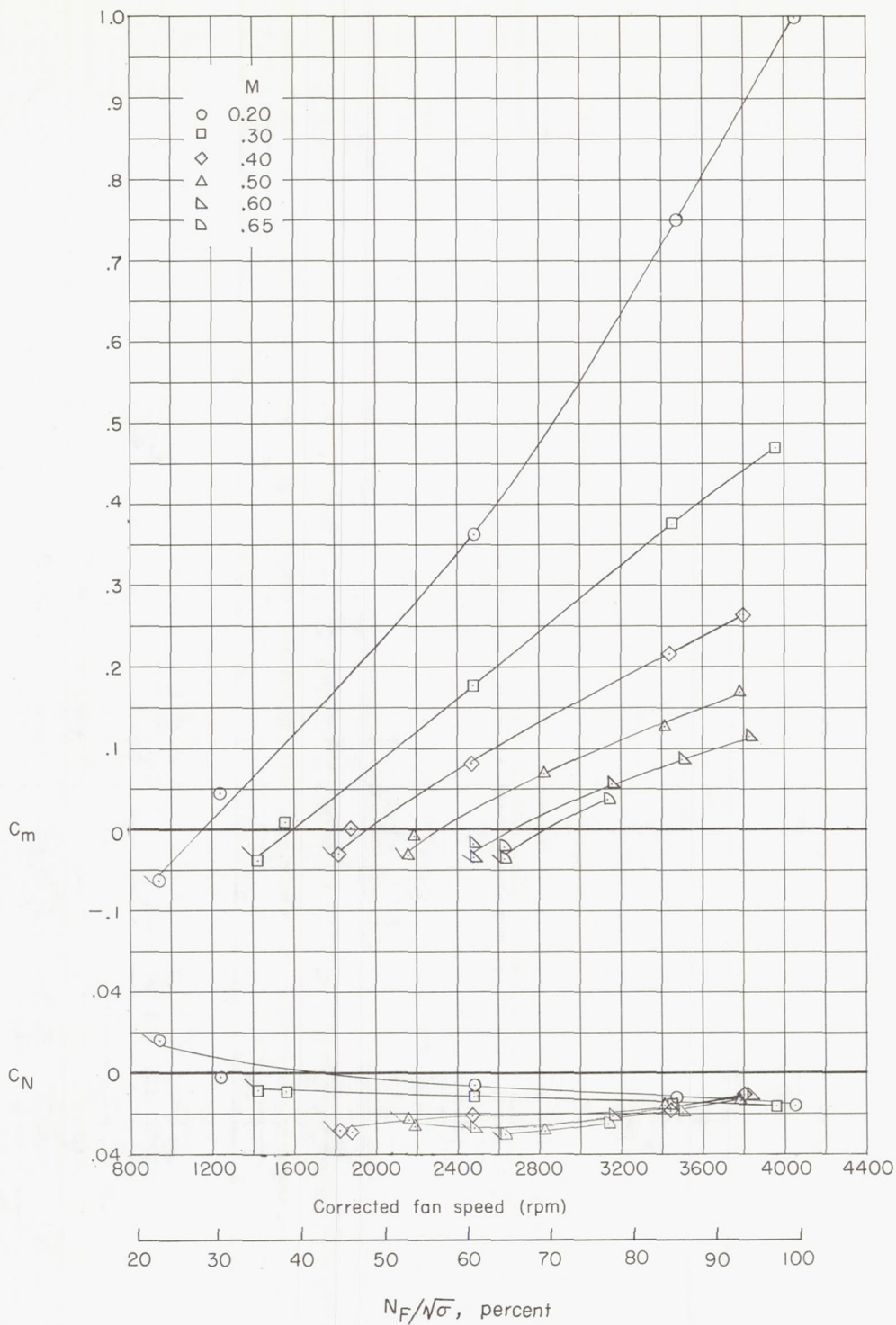
(e) Configuration 113.

Figure 68.- Continued.



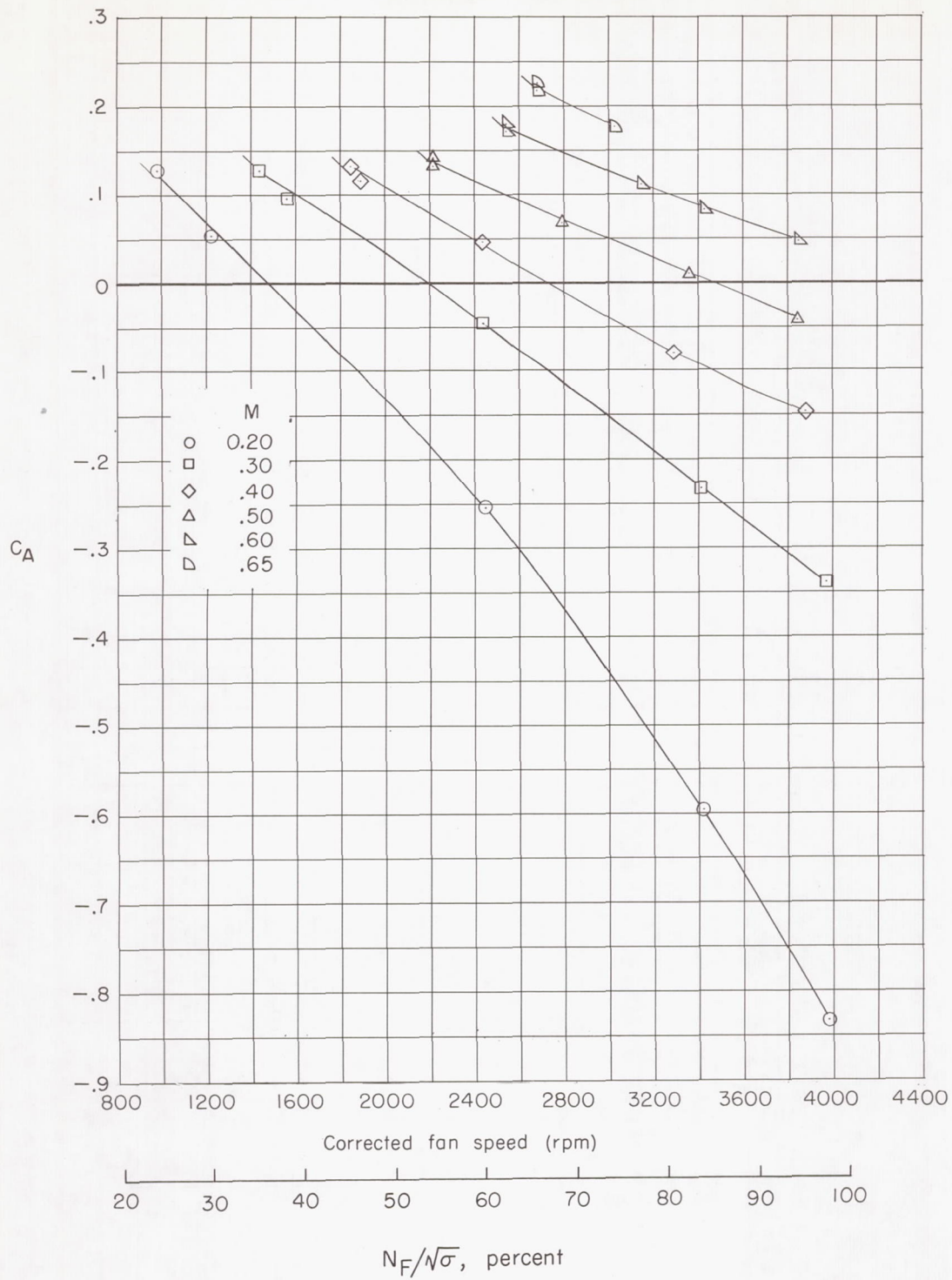
(f) Configuration 112.

Figure 68.- Continued.



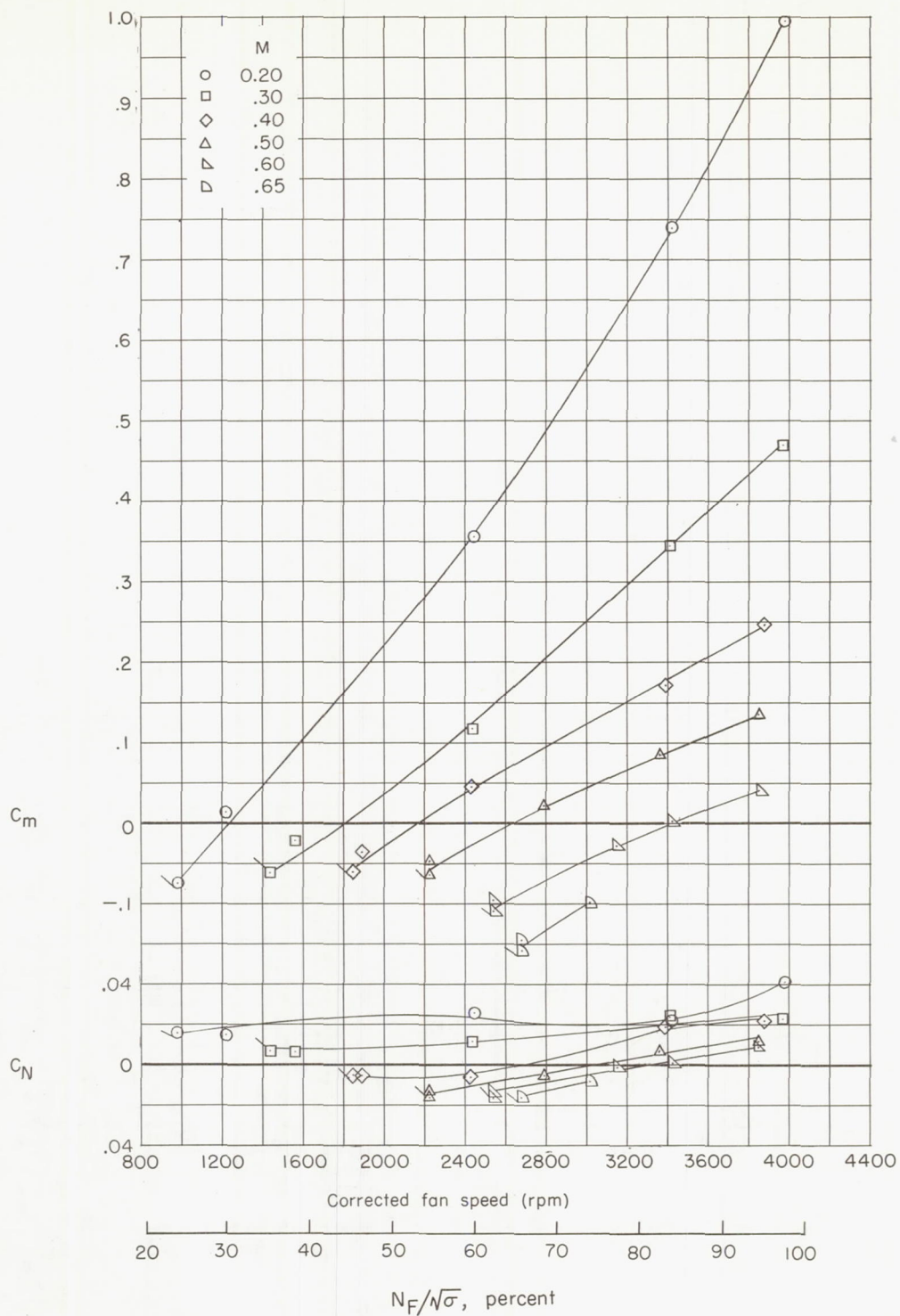
(f) Configuration 112. Concluded.

Figure 68.- Continued.



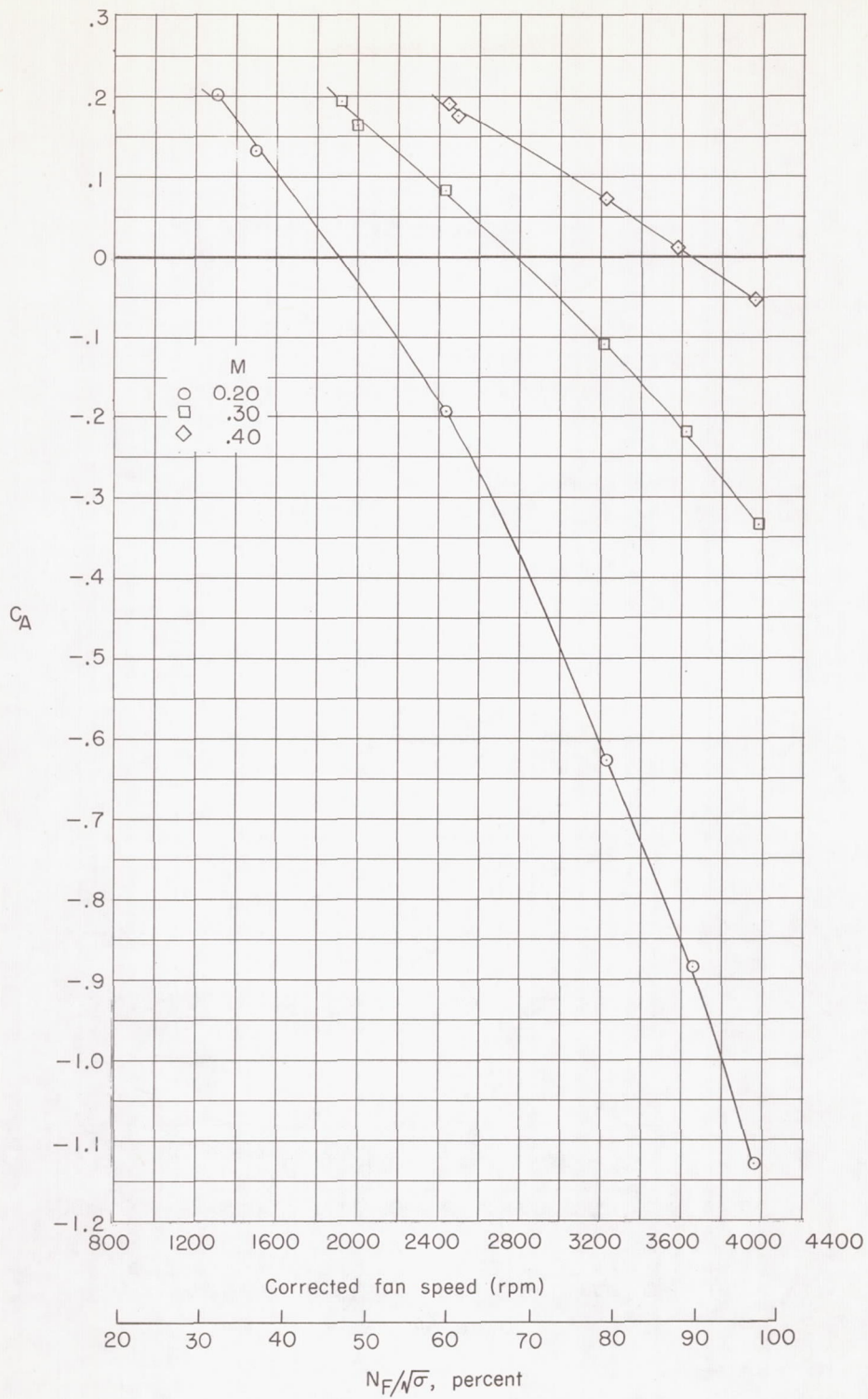
(g) Configuration 322.

Figure 68.- Continued.



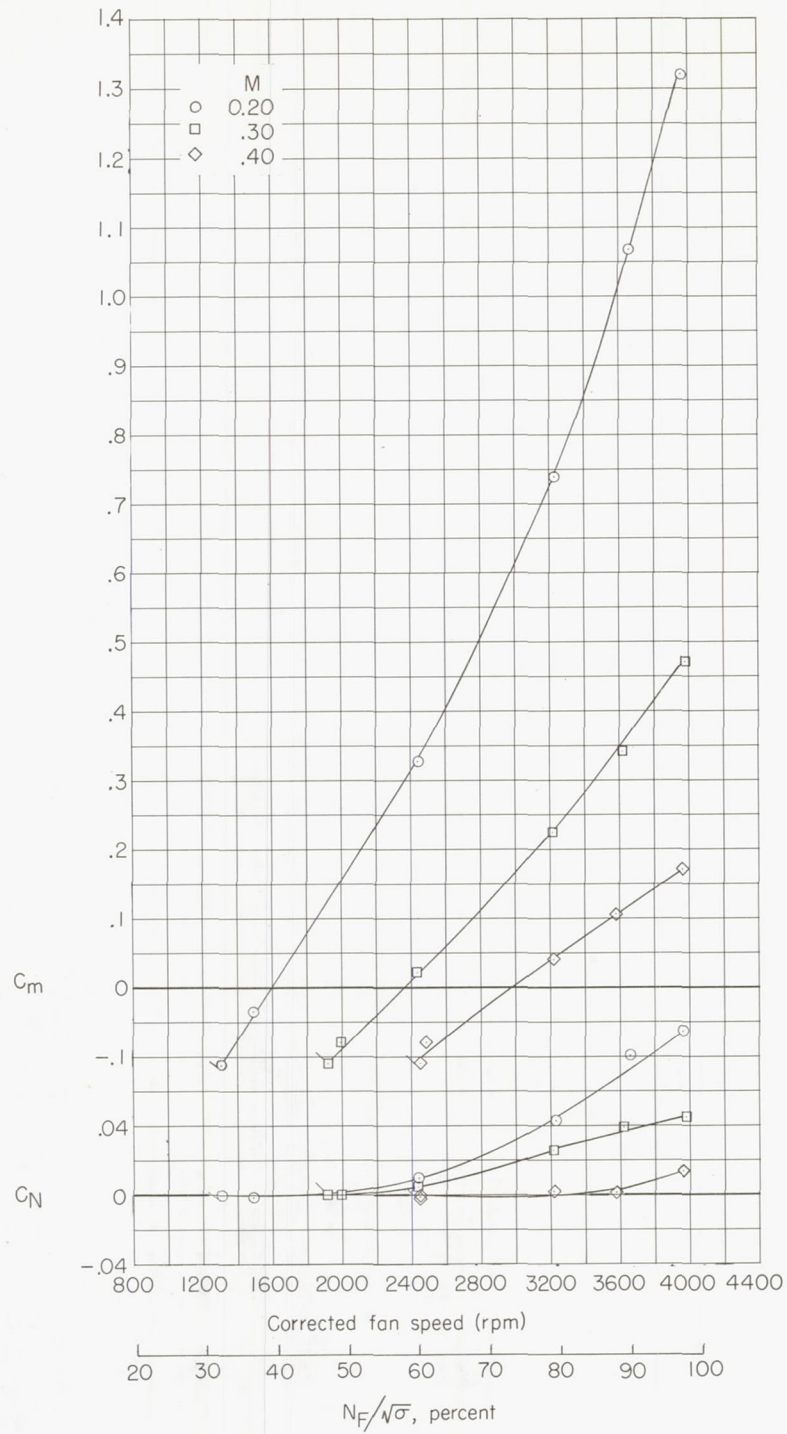
(g) Configuration 322. Concluded.

Figure 68.- Continued.



(h) Configuration 243.

Figure 68.- Continued.



(h) Configuration 243. Concluded.

Figure 68.- Concluded.

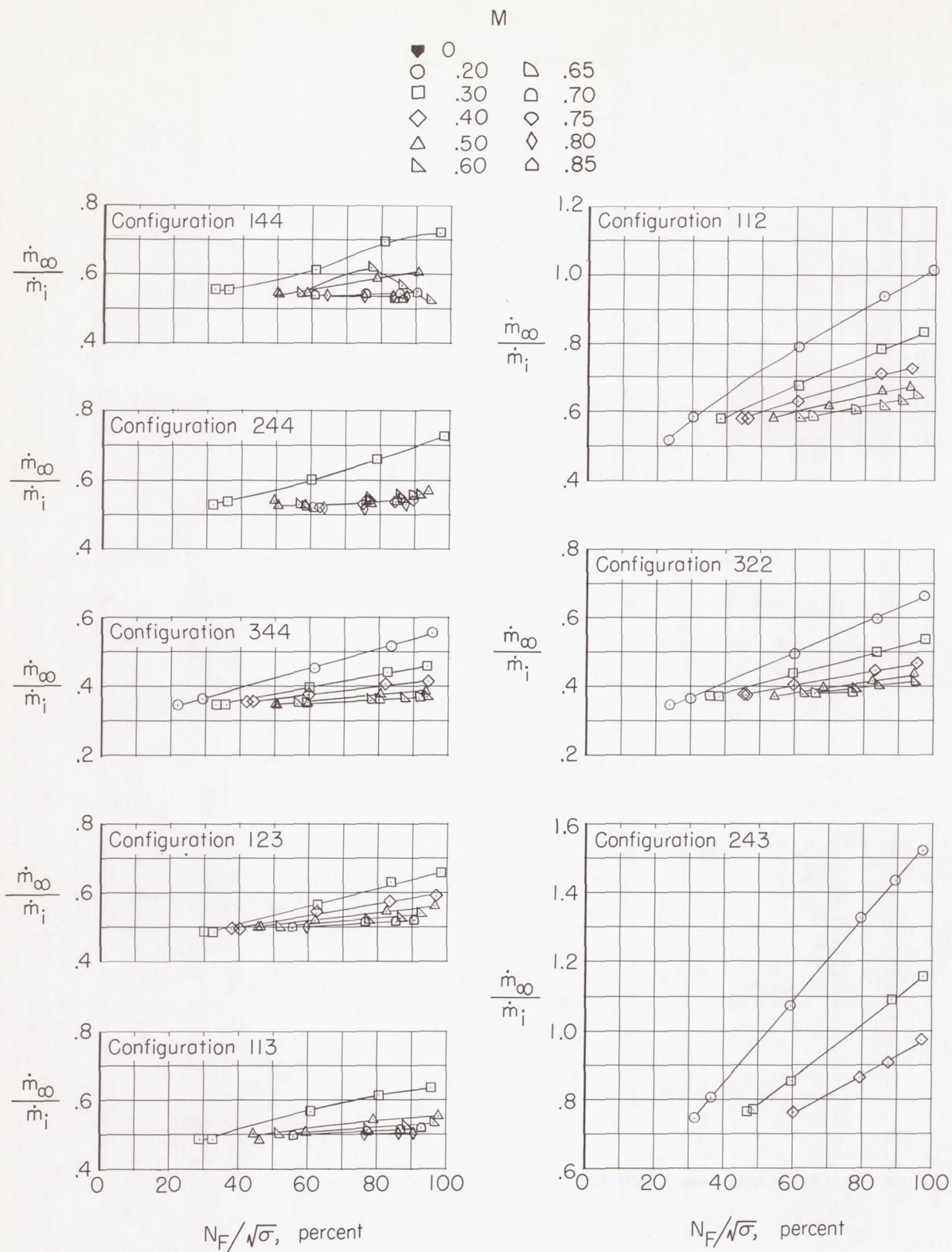
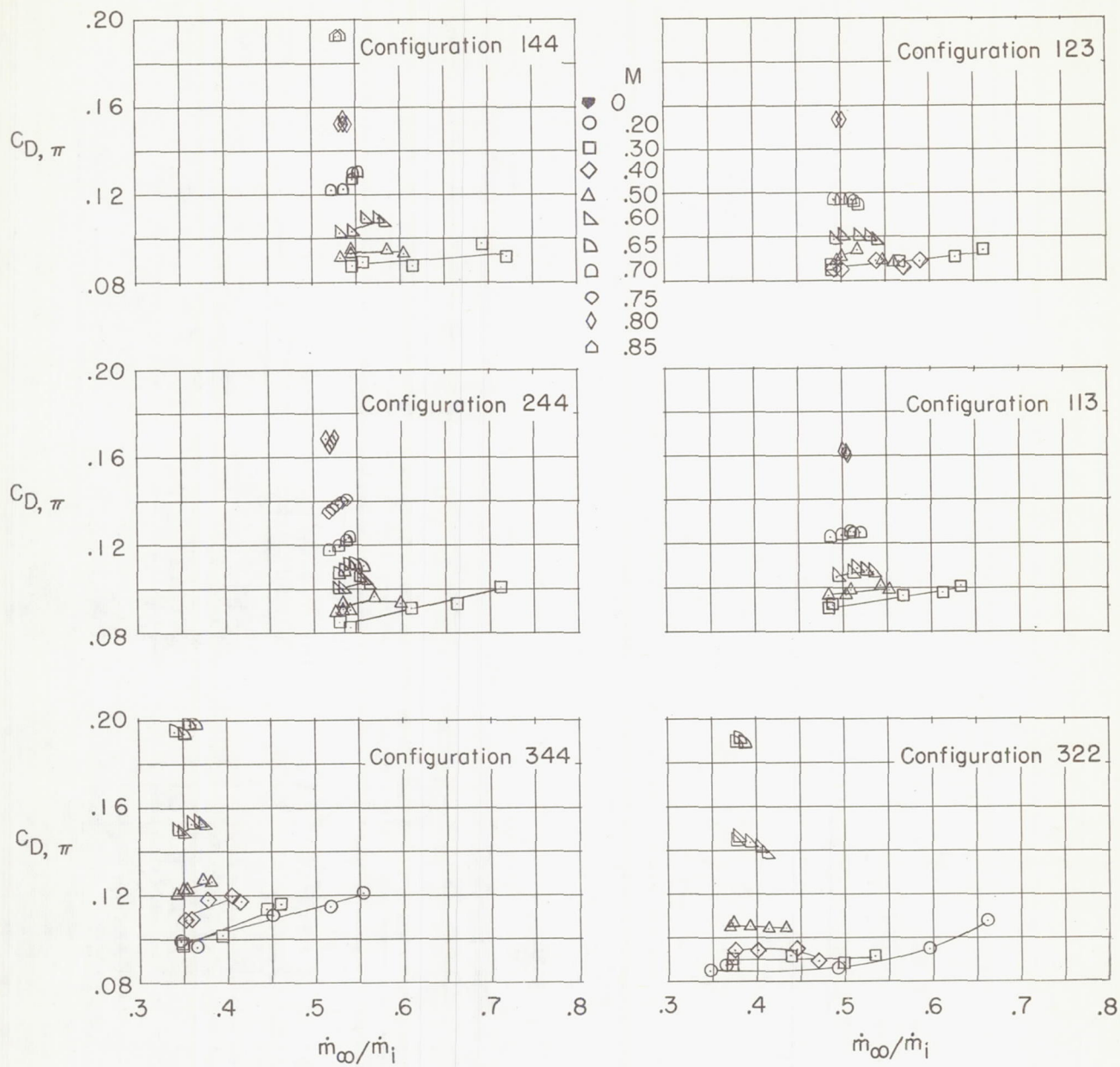
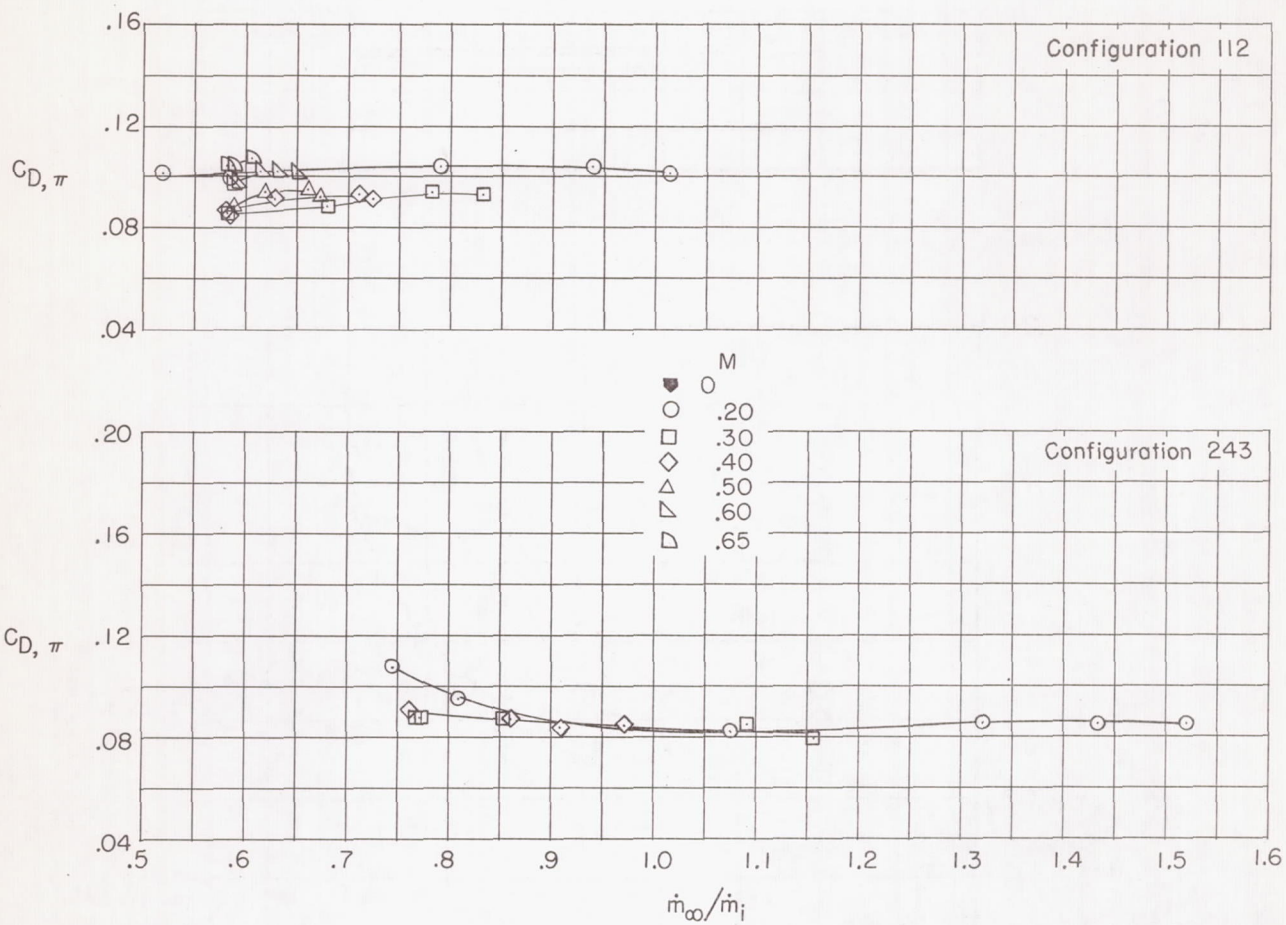


Figure 69.- Variation of mass-flow ratio with fan speed for the various configurations tested.



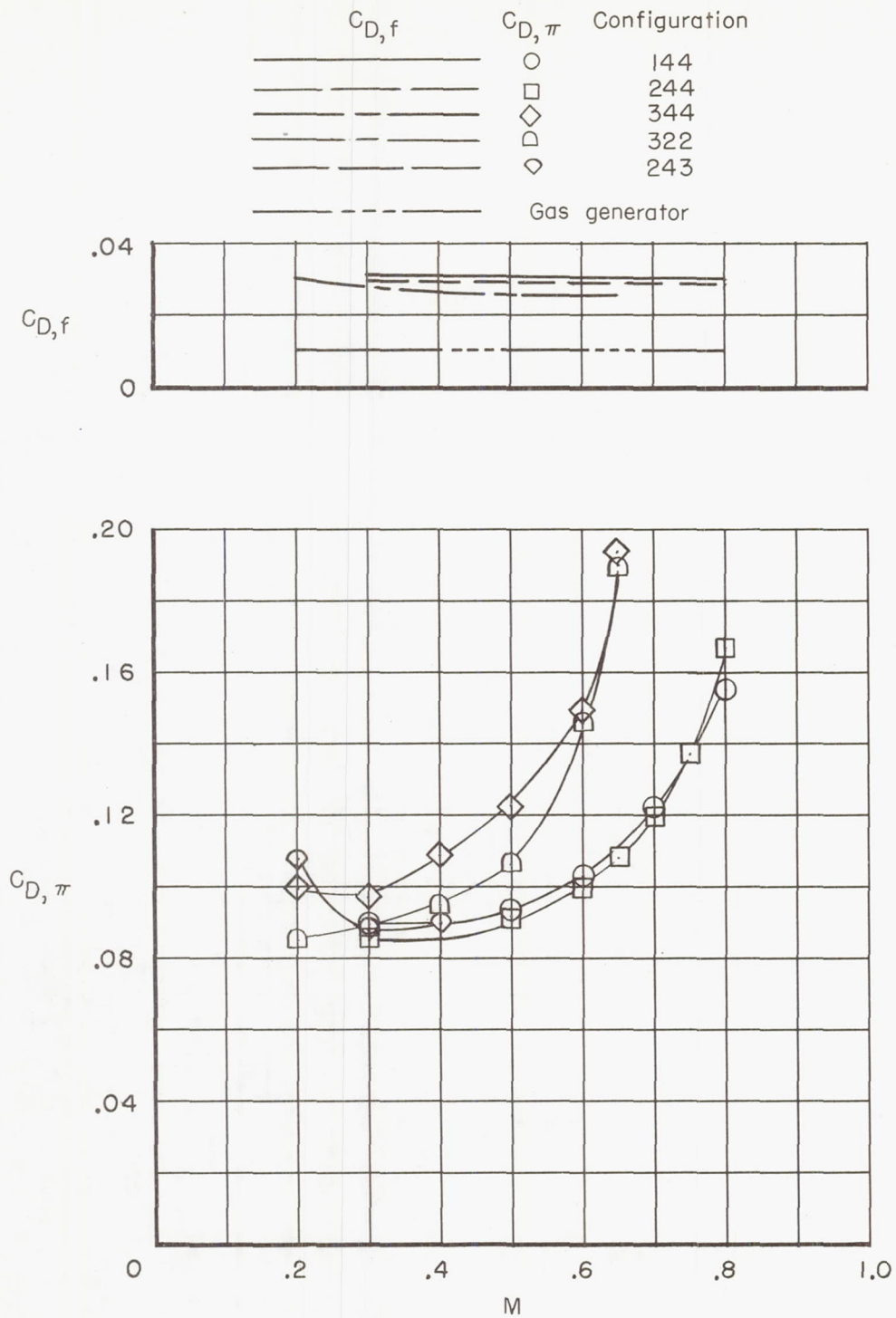
(a) Configurations 144, 244, 344, 123, 113, and 322.

Figure 70.- Variation of total nacelle-drag coefficient (fan nacelle plus engine nacelle) with mass-flow ratio for the various configurations tested.



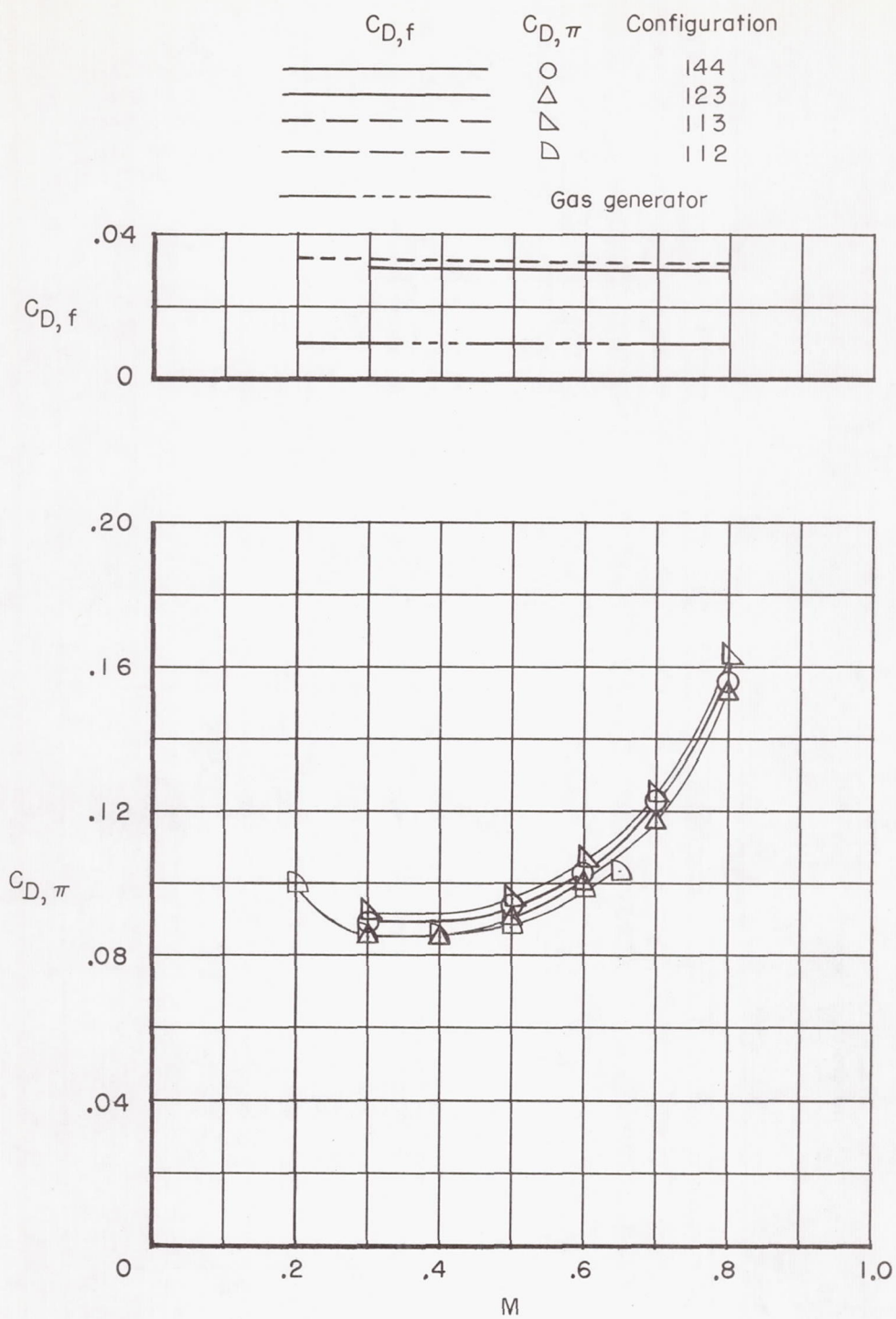
(b) Configurations 112 and 243.

Figure 70.- Concluded.



(a) Fan-nacelle comparison.

Figure 71.- Variation of windmill nacelle-drag coefficient with Mach number.



(b) Afterbody comparison.

Figure 71.- Concluded.

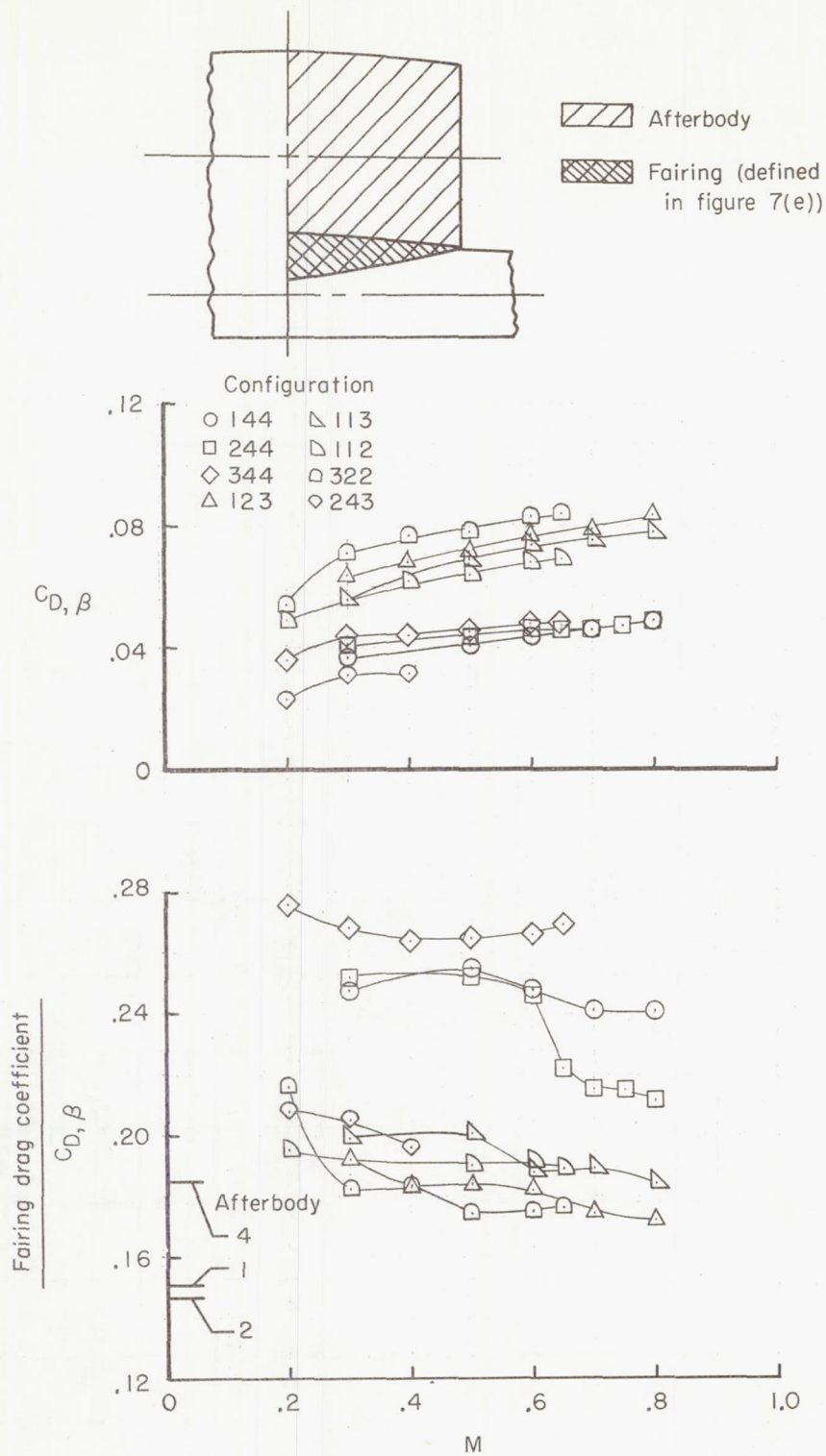


Figure 72.- Summary of windmill afterbody-drag characteristics for the various configurations tested. Tick marks indicate ratio of fairing projected area to total afterbody projected area.

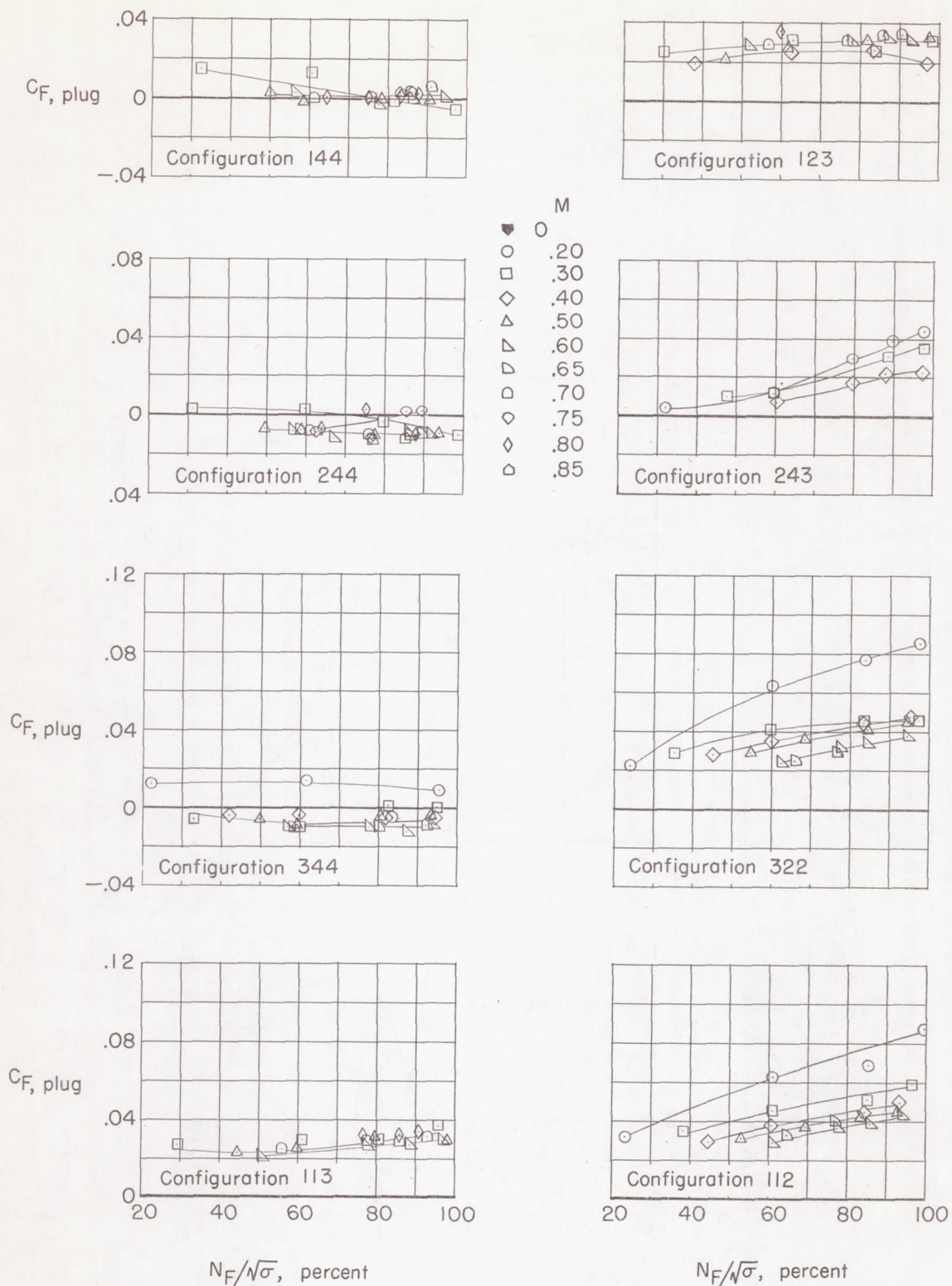


Figure 73.- Plug thrust coefficient characteristics for the various configurations tested.

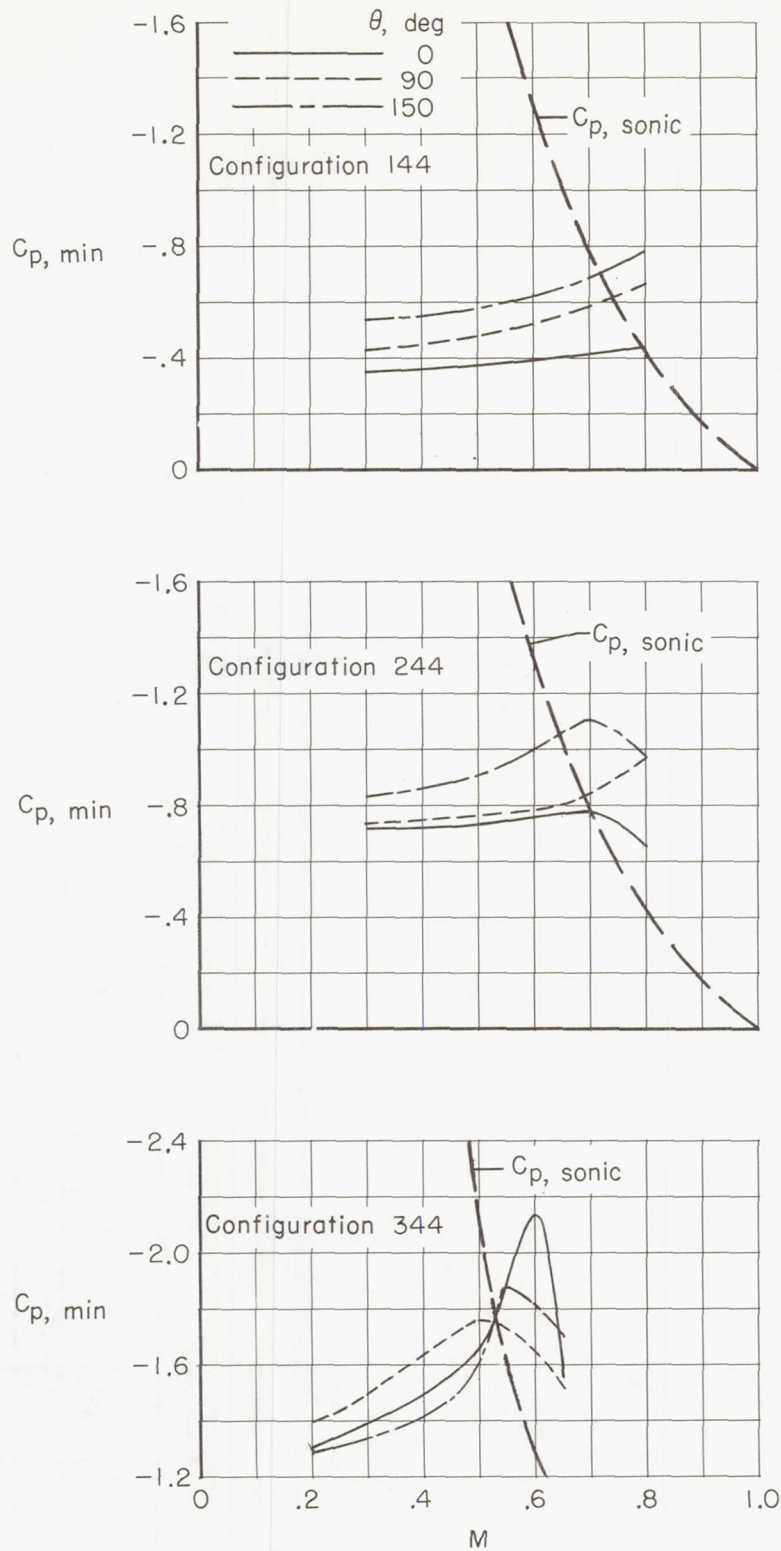


Figure 74.- Comparison of fan-nacelle peak negative pressure coefficient for configurations 144, 244, and 344 at windmill conditions.

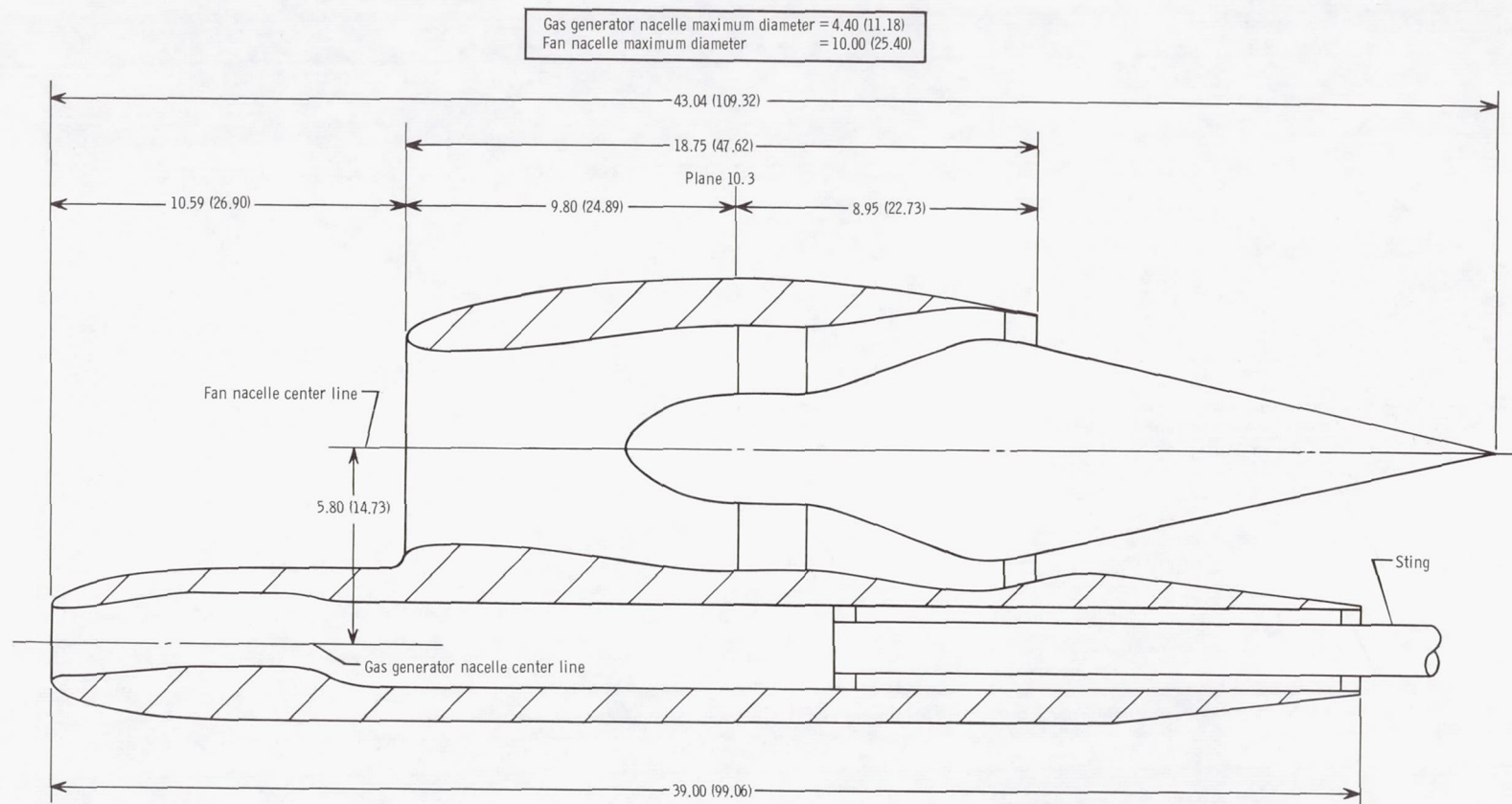


Figure 75.- Sketch of 1/5-scale model of configuration 123. All dimensions in inches (parentetical dimensions in centimeters).



Figure 76.- Photograph of 1/5-scale model of configuration 123.

L-65-5659

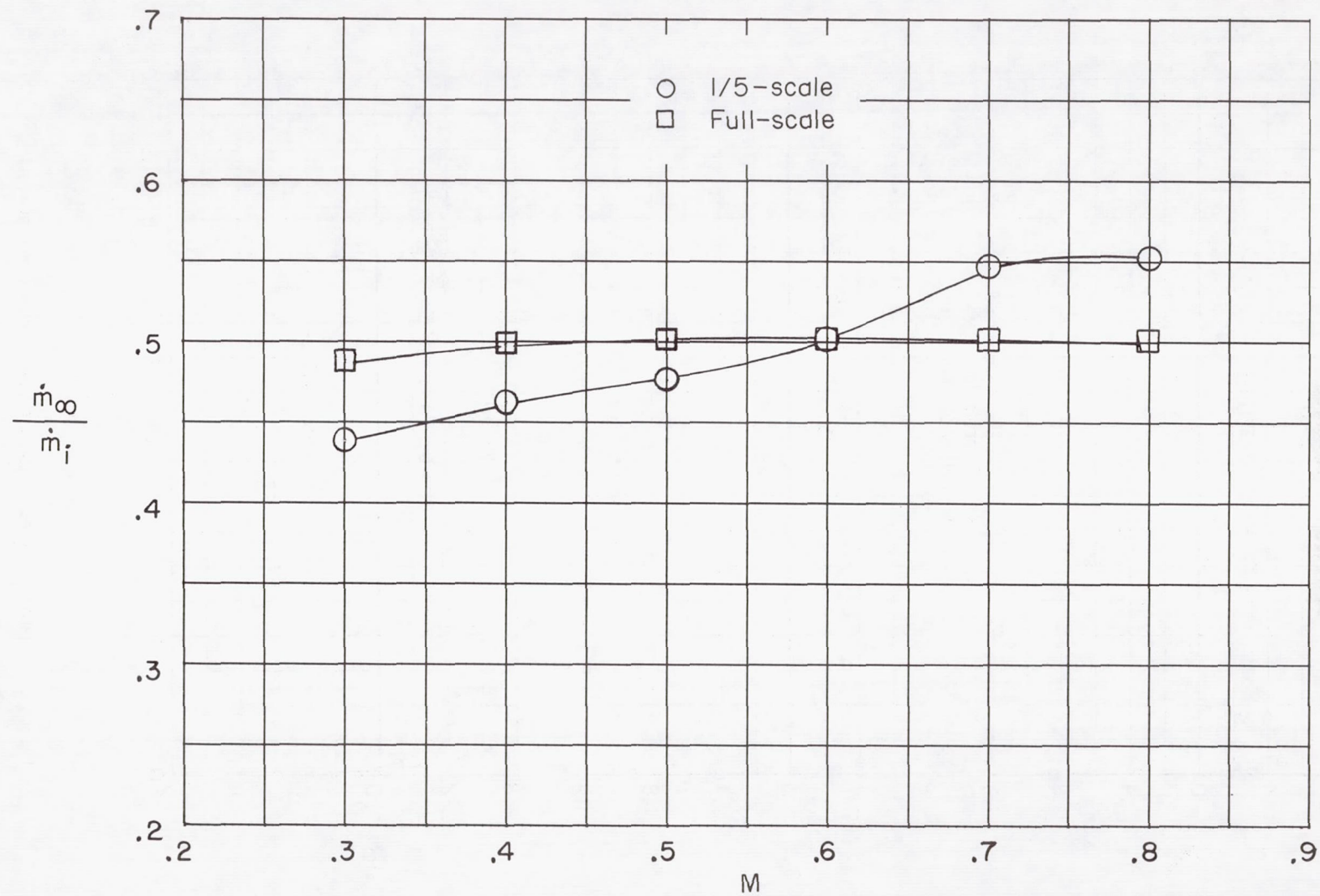
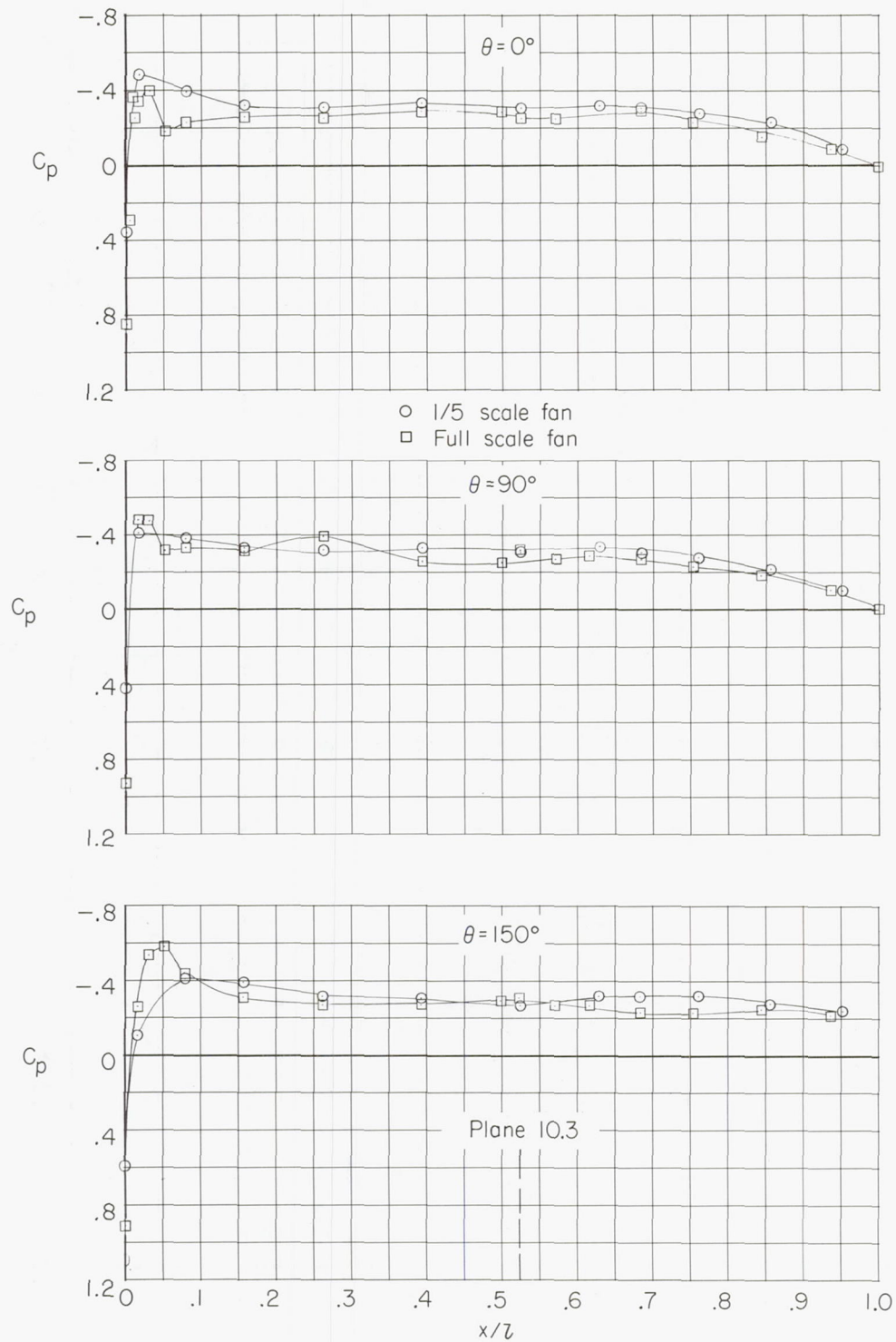
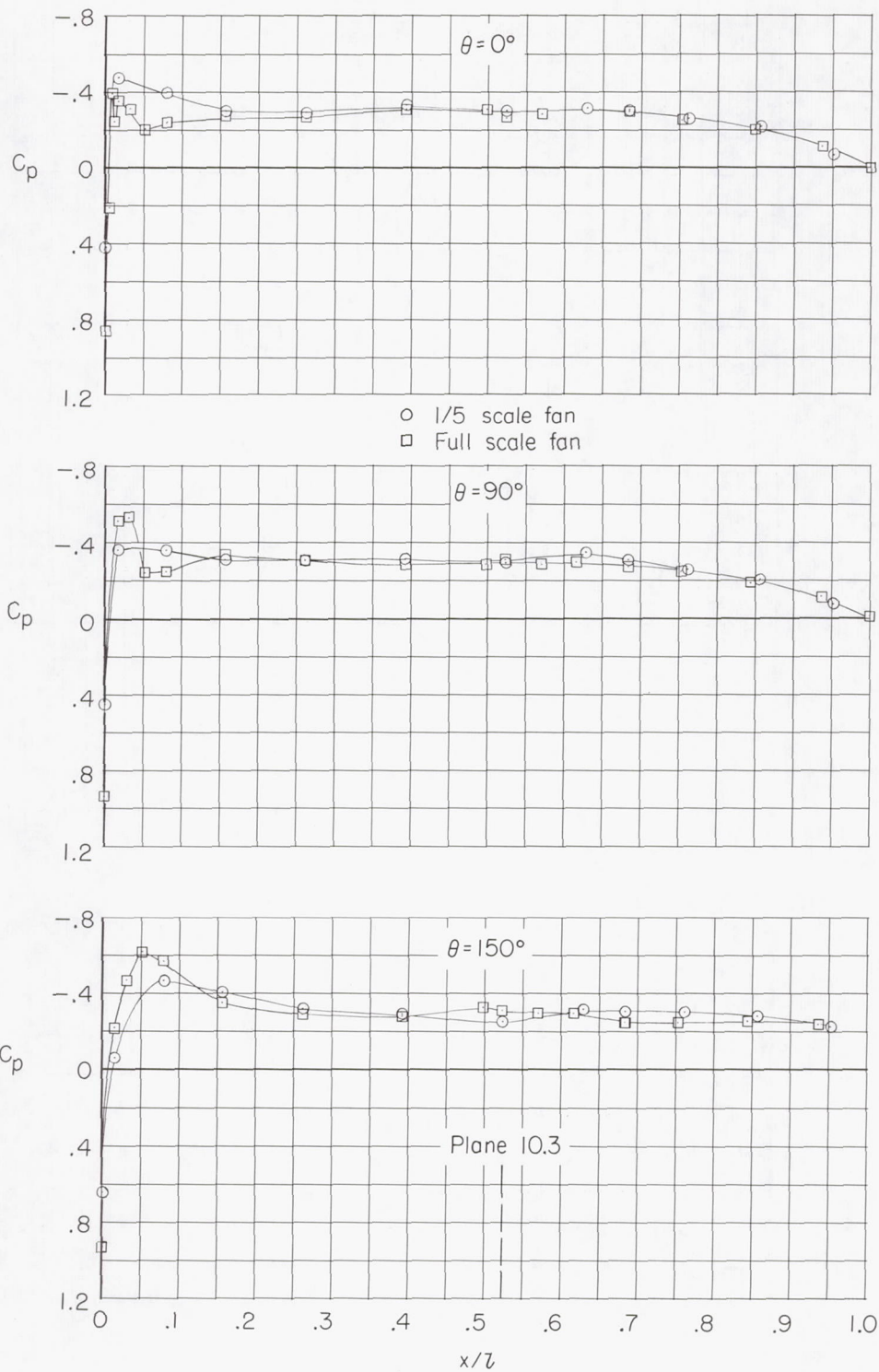


Figure 77.- Comparison of mass-flow ratio of full scale and 1/5 scale of configuration 123.



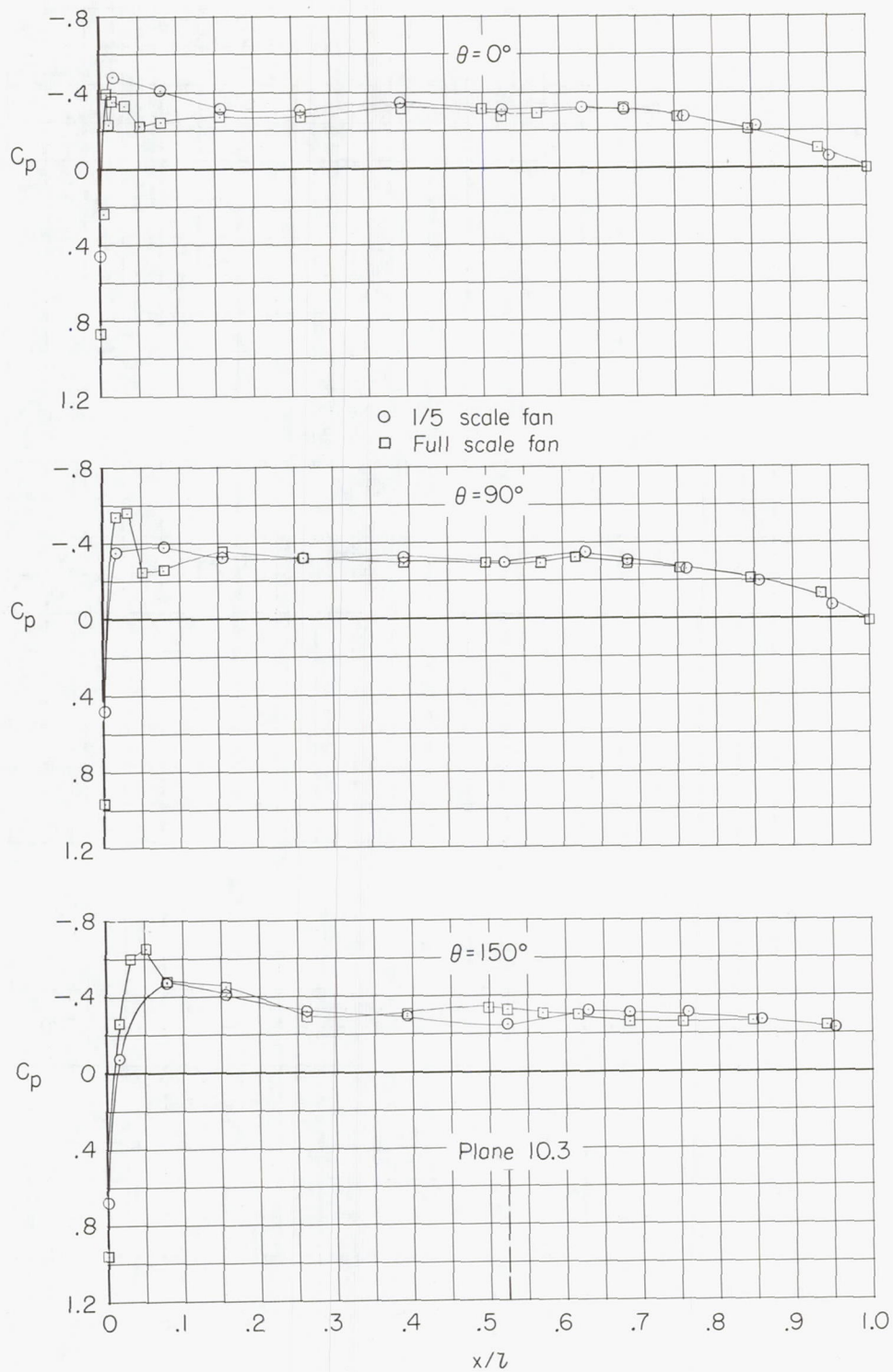
(a) $M = 0.30$.

Figure 78.- Comparison of fan-nacelle pressure distributions of configuration 123.



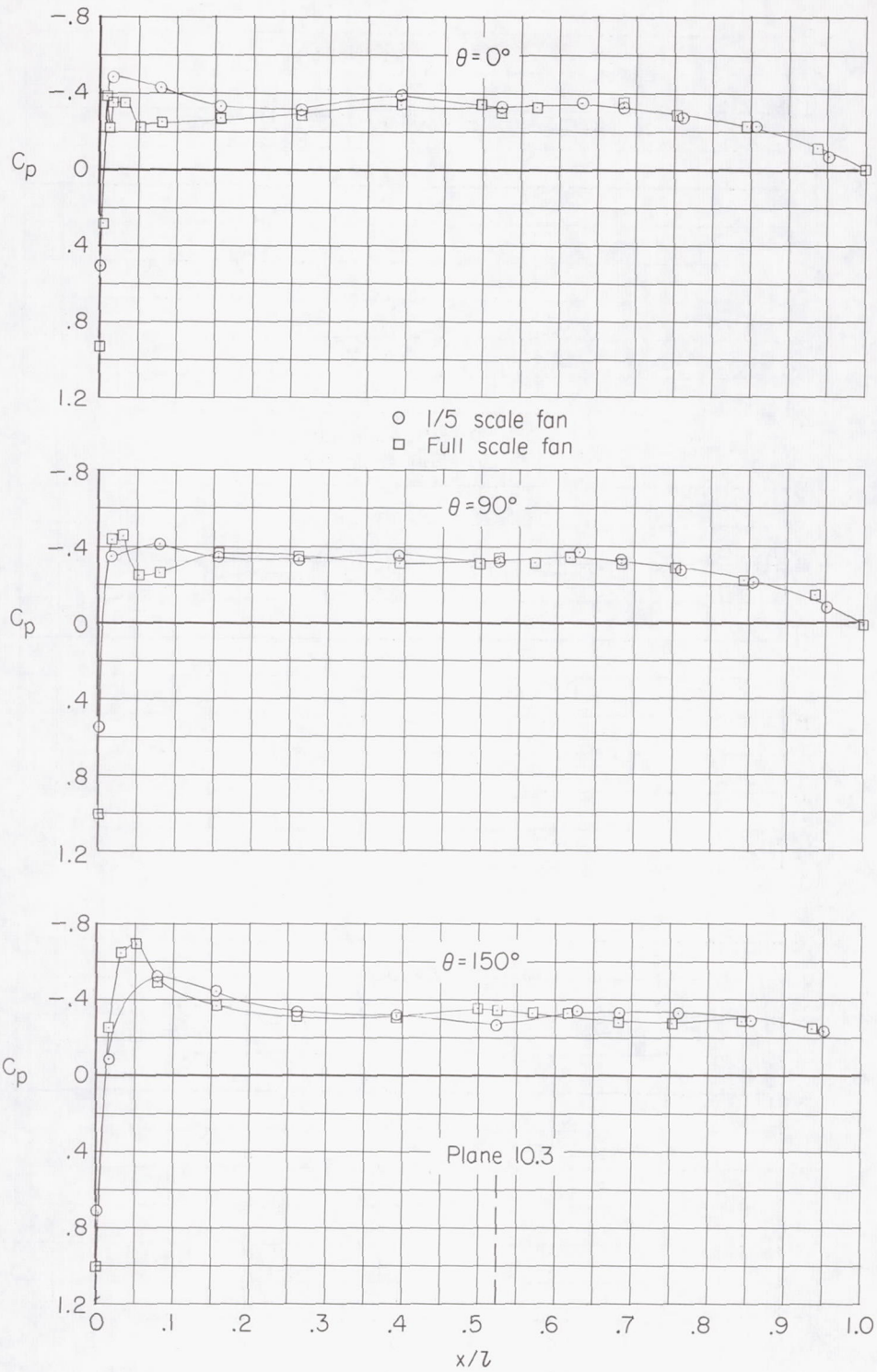
(b) $M = 0.40$.

Figure 78.- Continued.



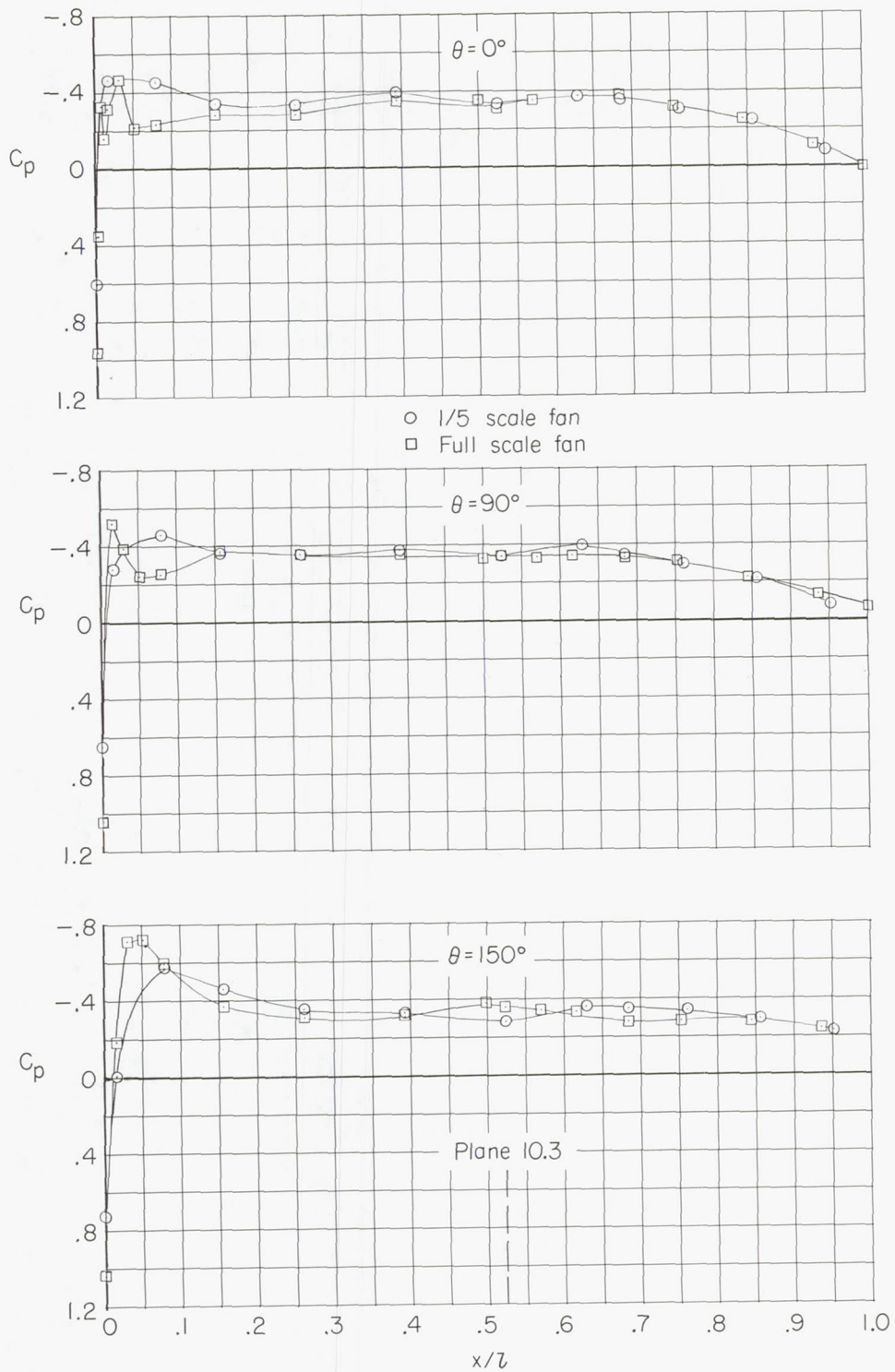
(c) $M = 0.50$.

Figure 78.- Continued.



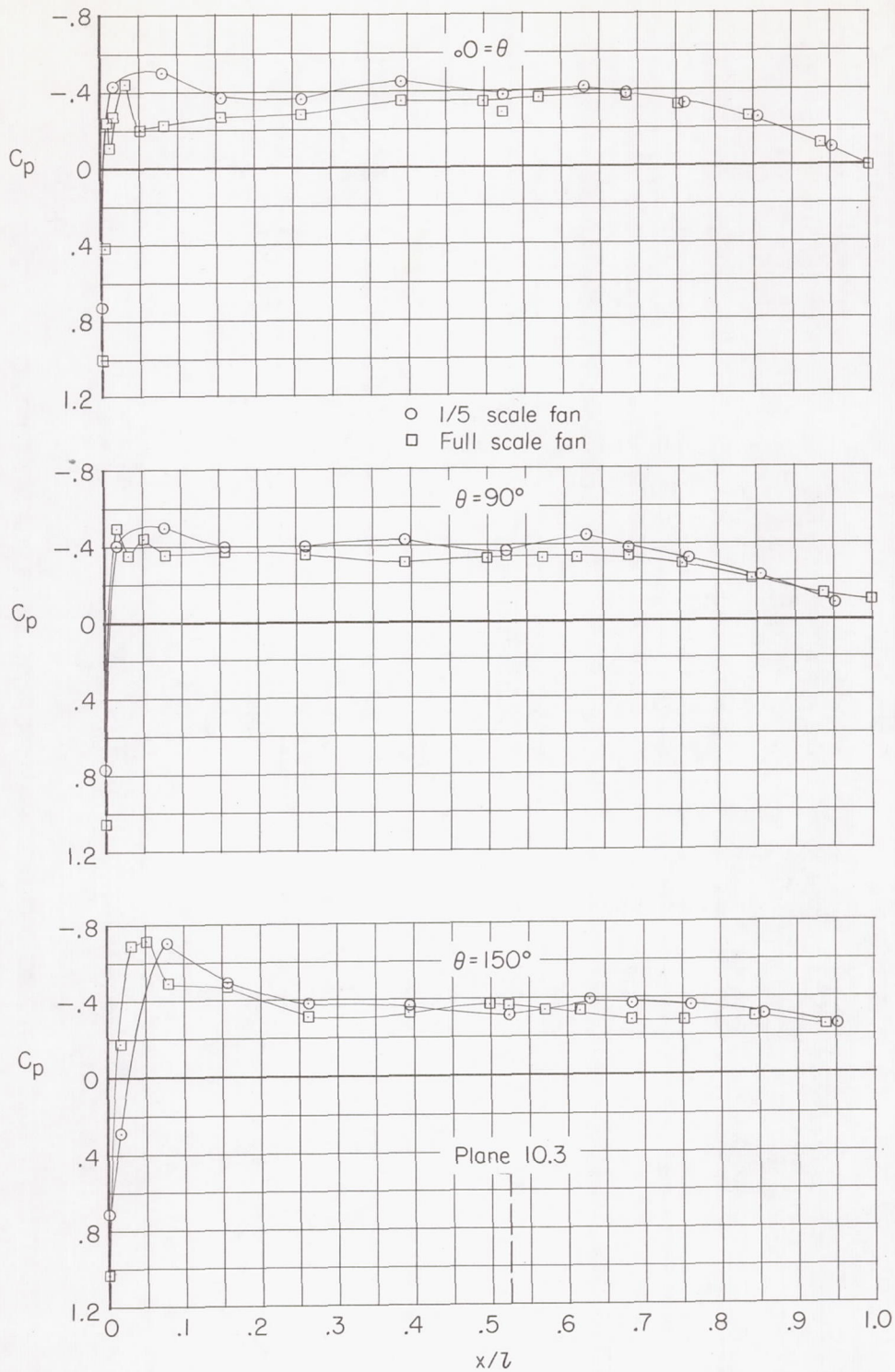
(d) $M = 0.60$.

Figure 78.- Continued.



(e) $M = 0.70$.

Figure 78.- Continued.



(f) $M = 0.80$.

Figure 78.- Concluded.

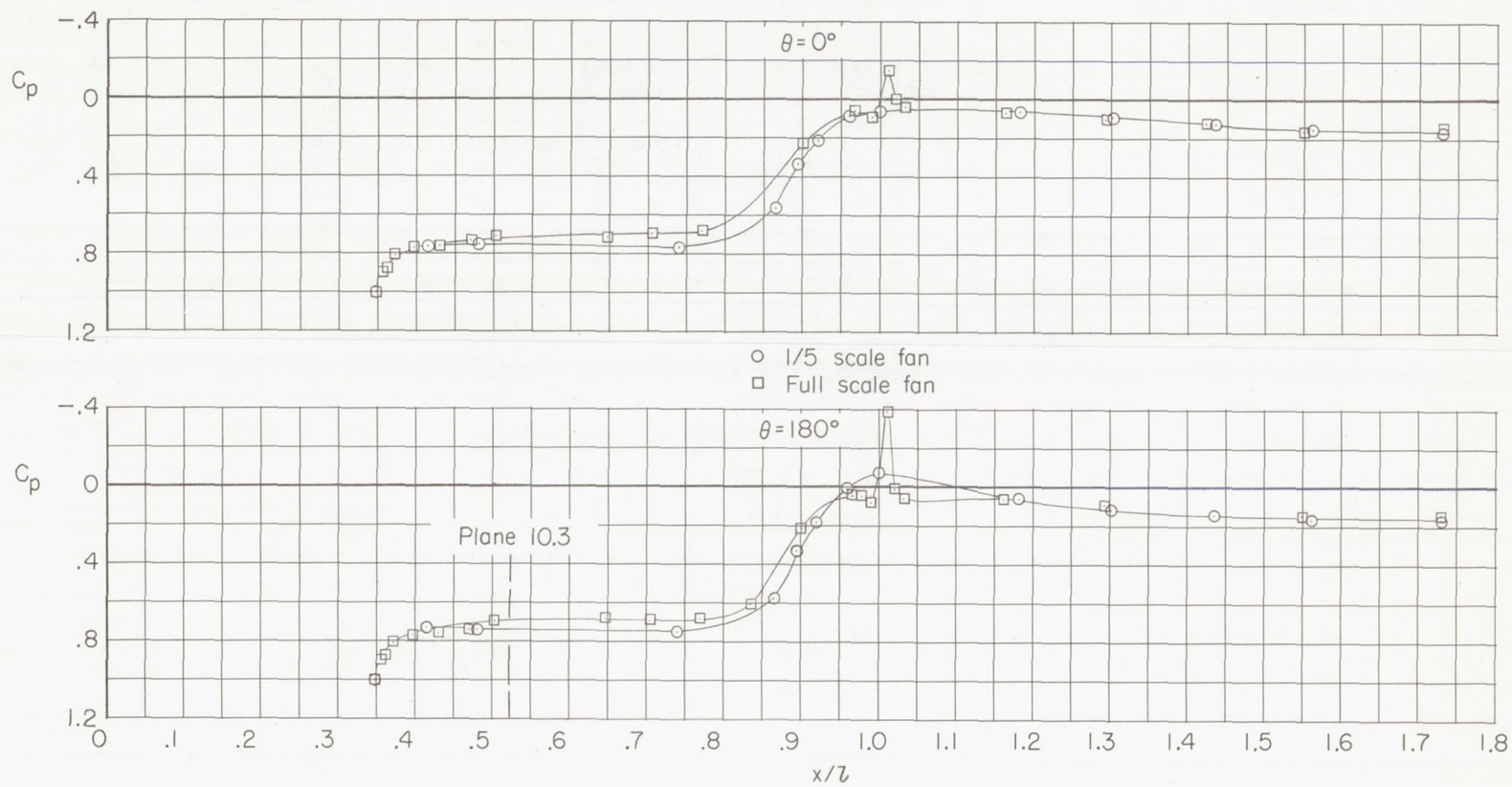
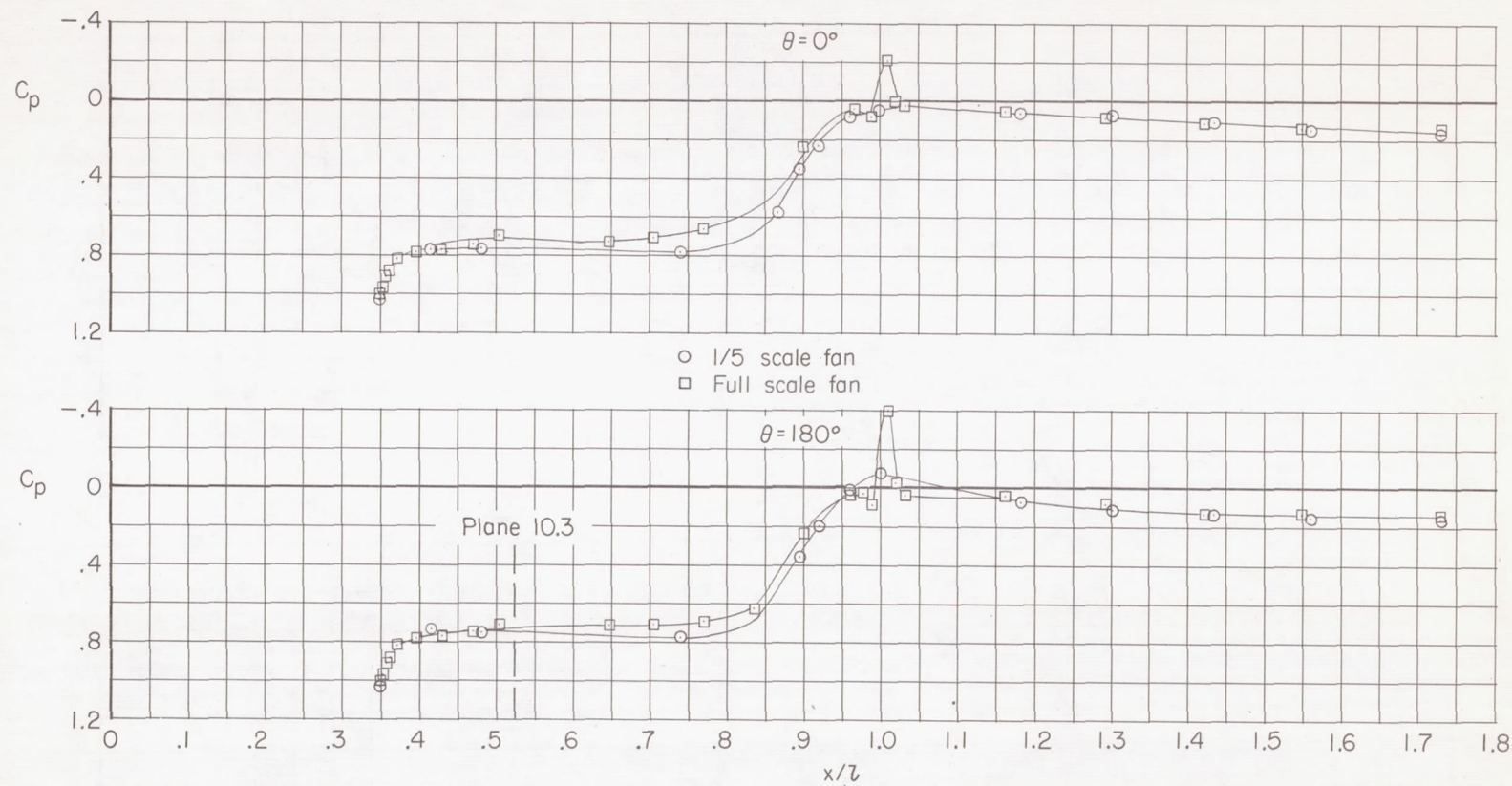
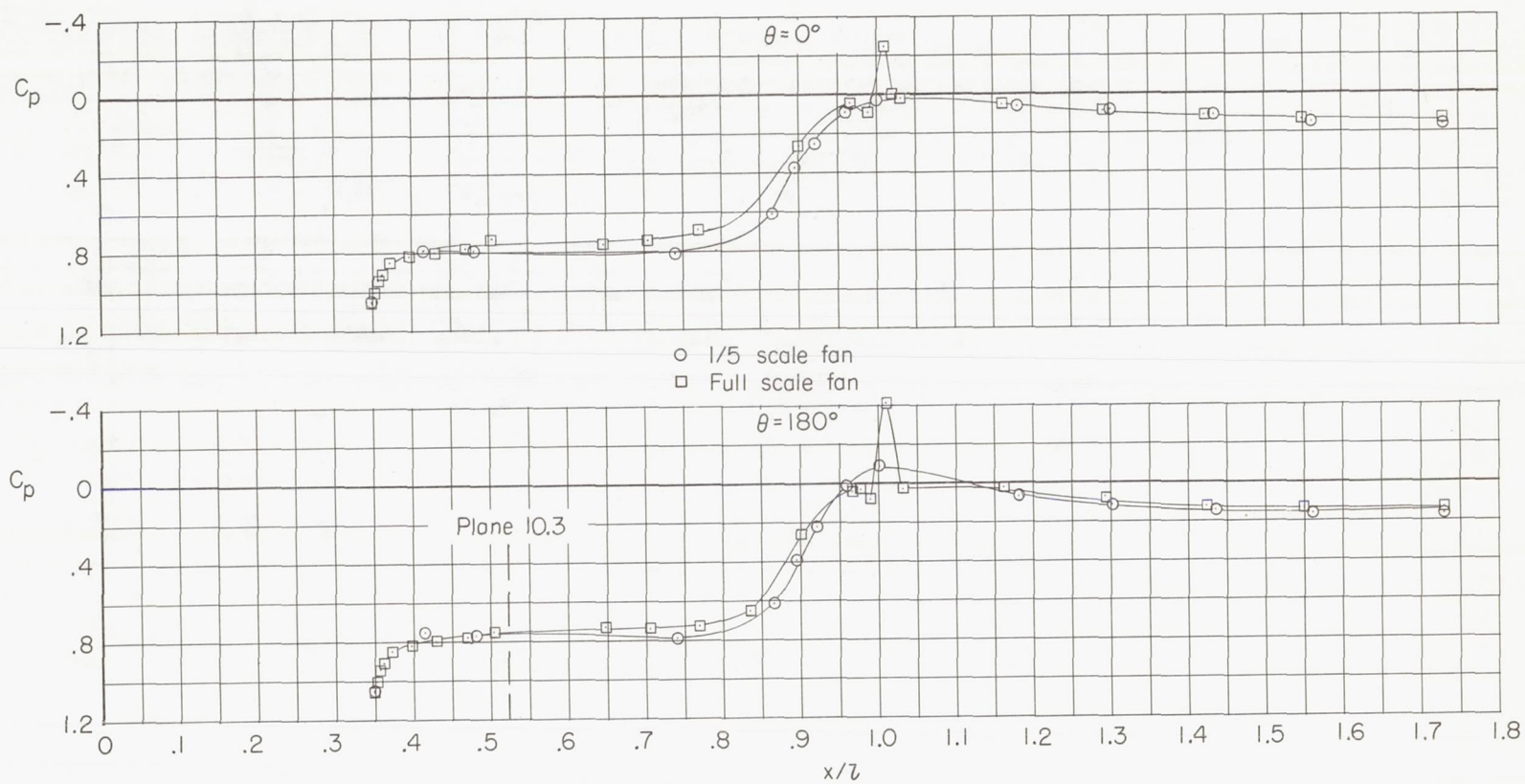
(a) $M = 0.30$.

Figure 79.- Comparison of fan-bulldozer-plus-plug pressure distributions of configuration 123.



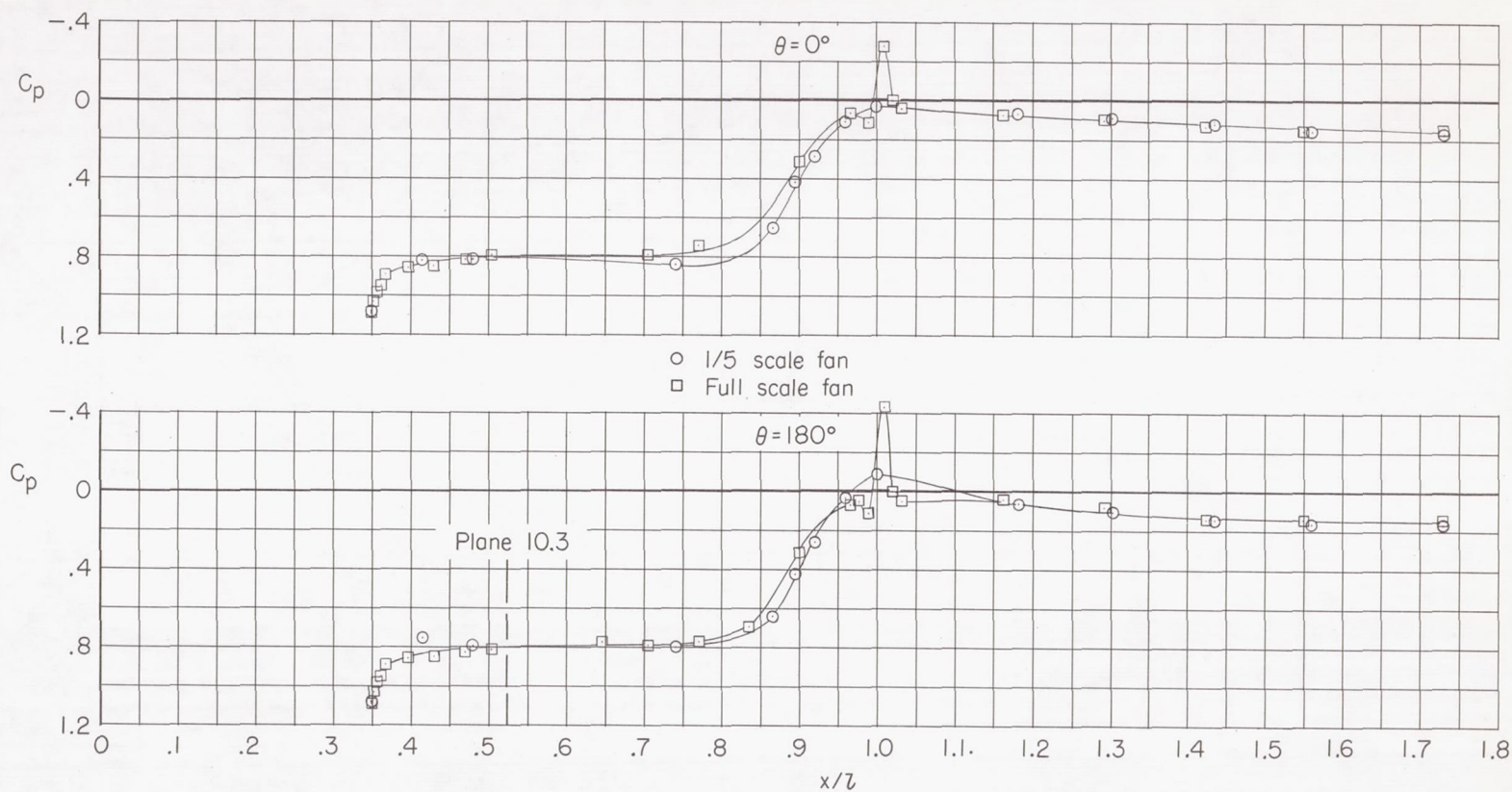
(b) $M = 0.40$.

Figure 79.- Continued.



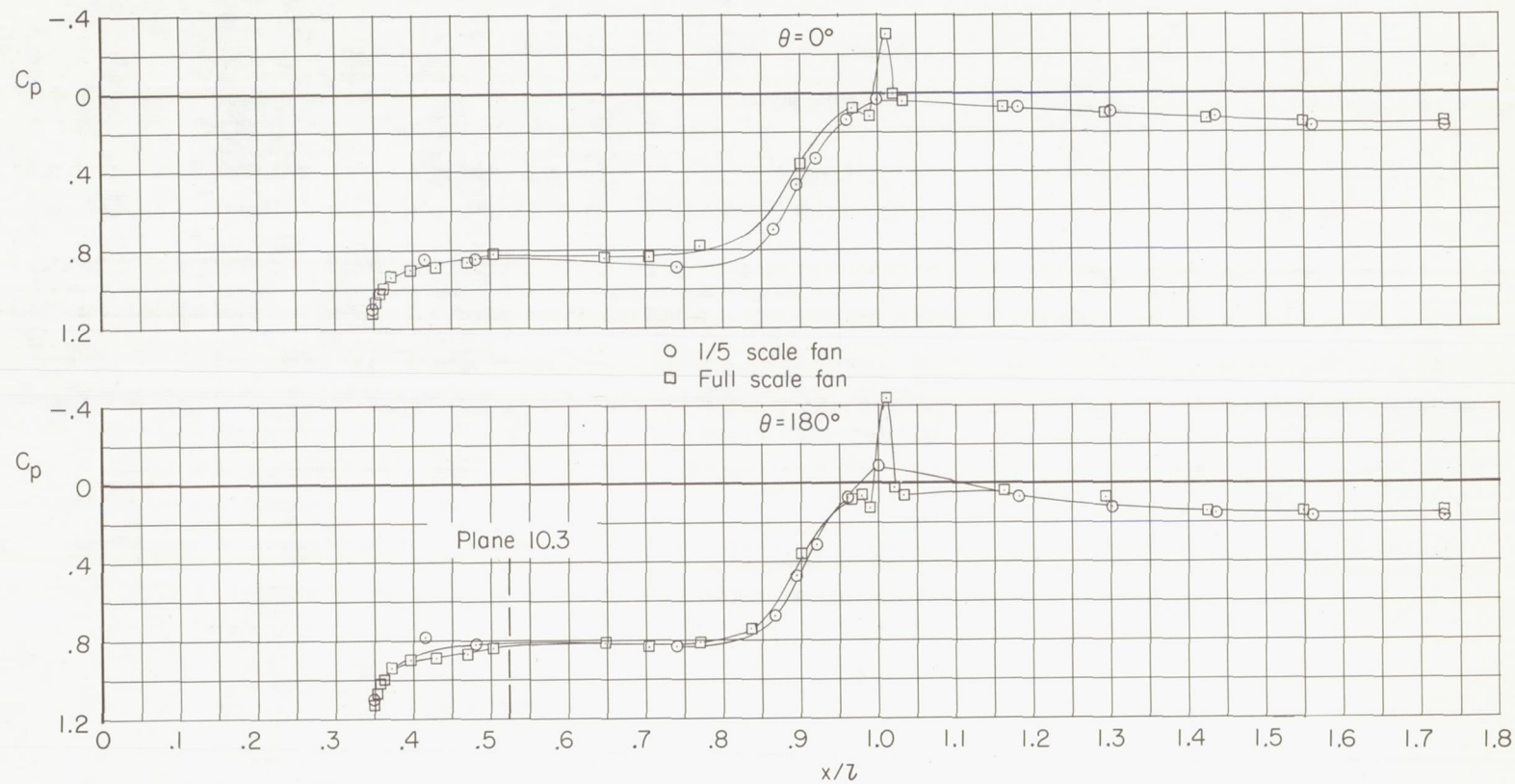
(c) $M = 0.50$.

Figure 79.- Continued.



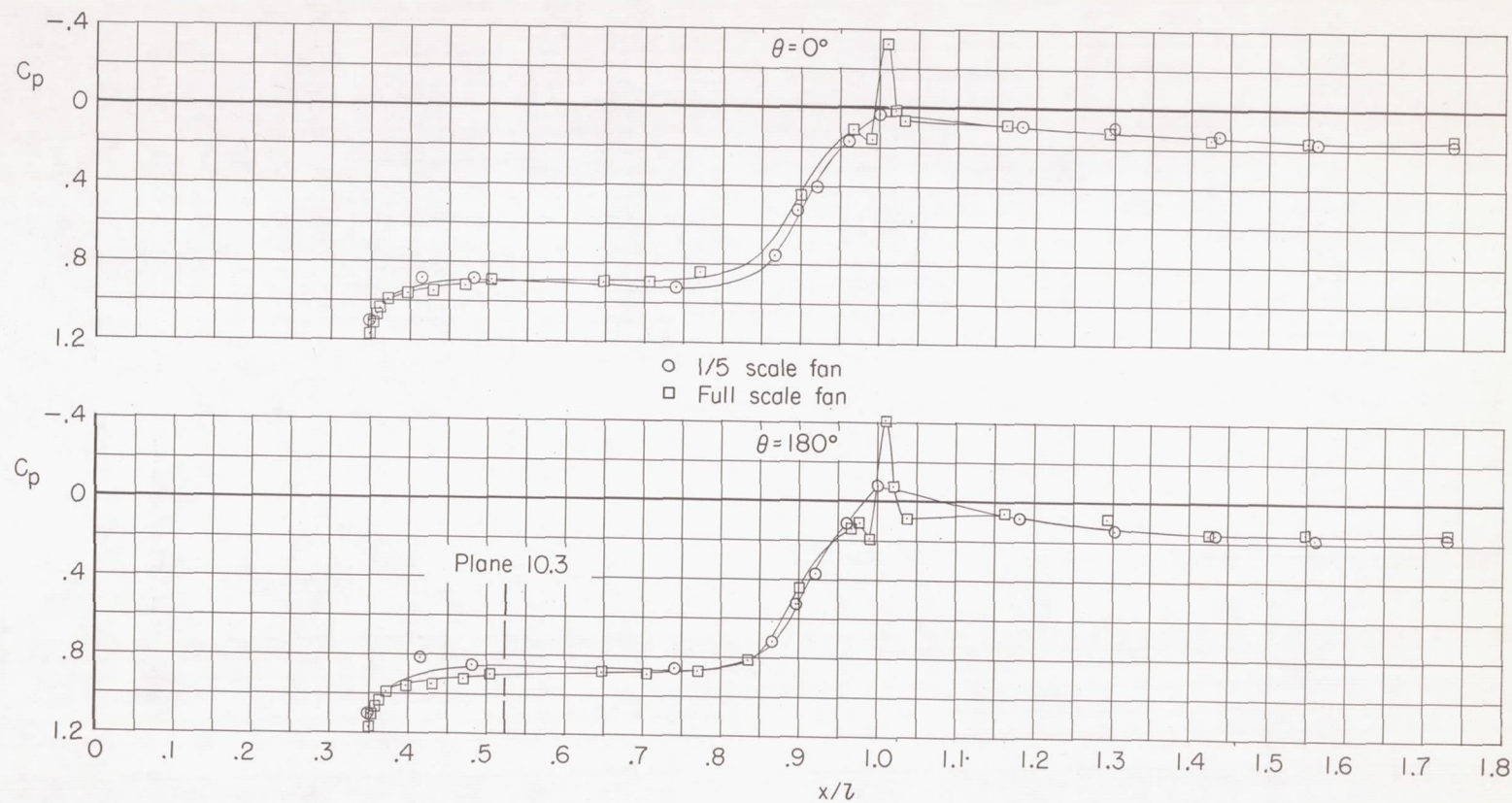
(d) $M = 0.60$.

Figure 79.- Continued.



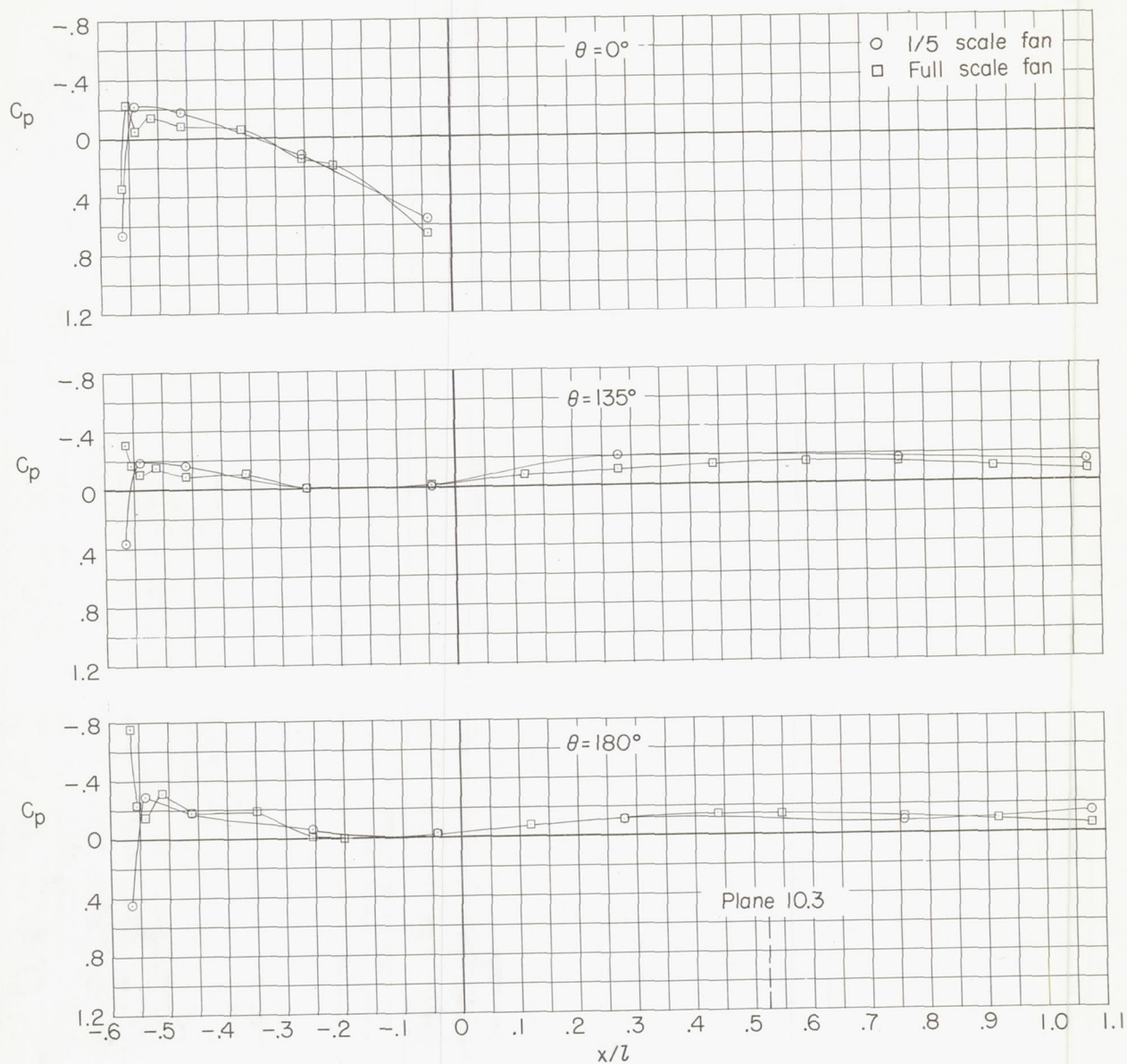
(e) $M = 0.70$.

Figure 79.- Continued.



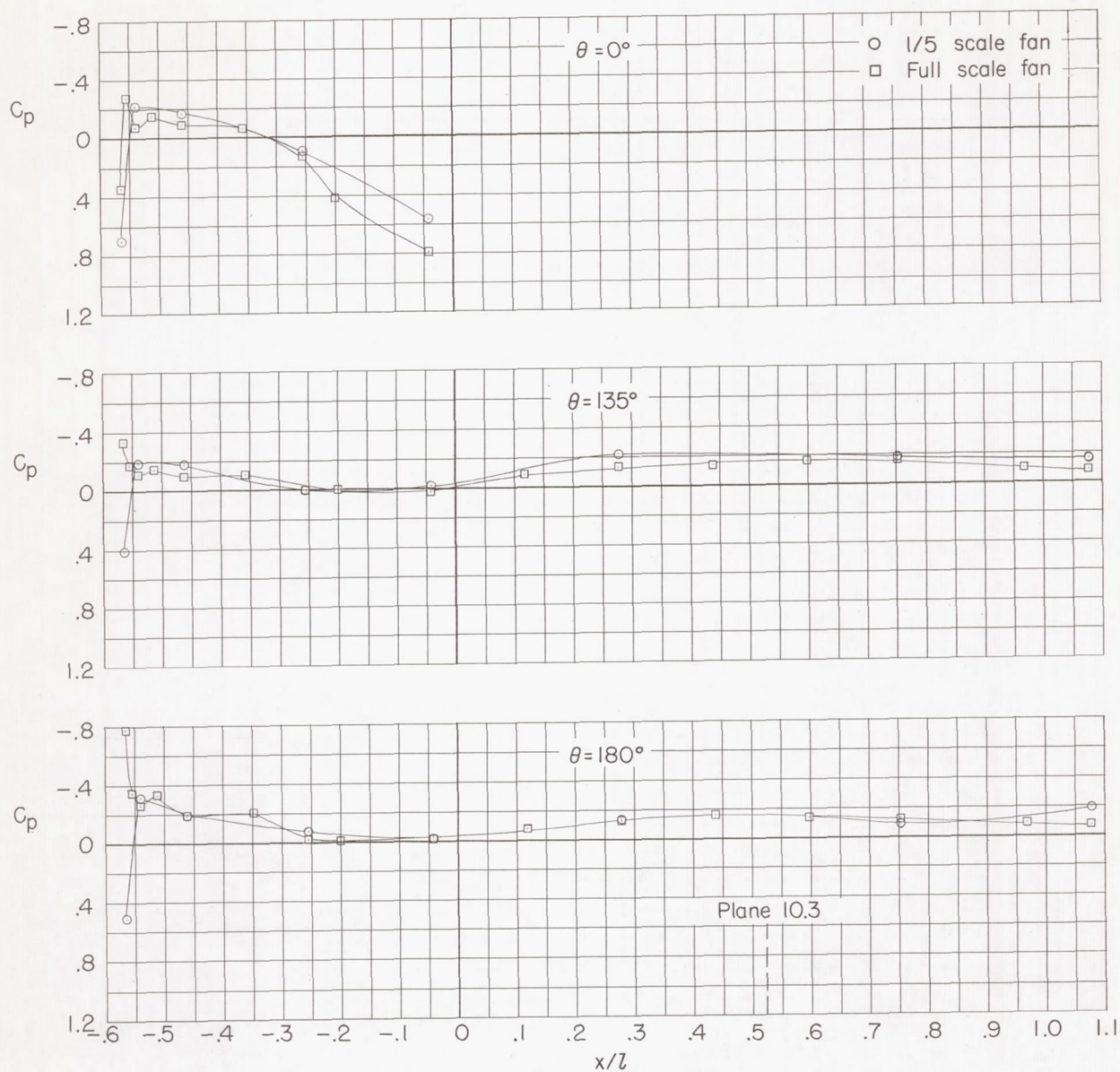
(f) $M = 0.80$.

Figure 79.- Concluded.



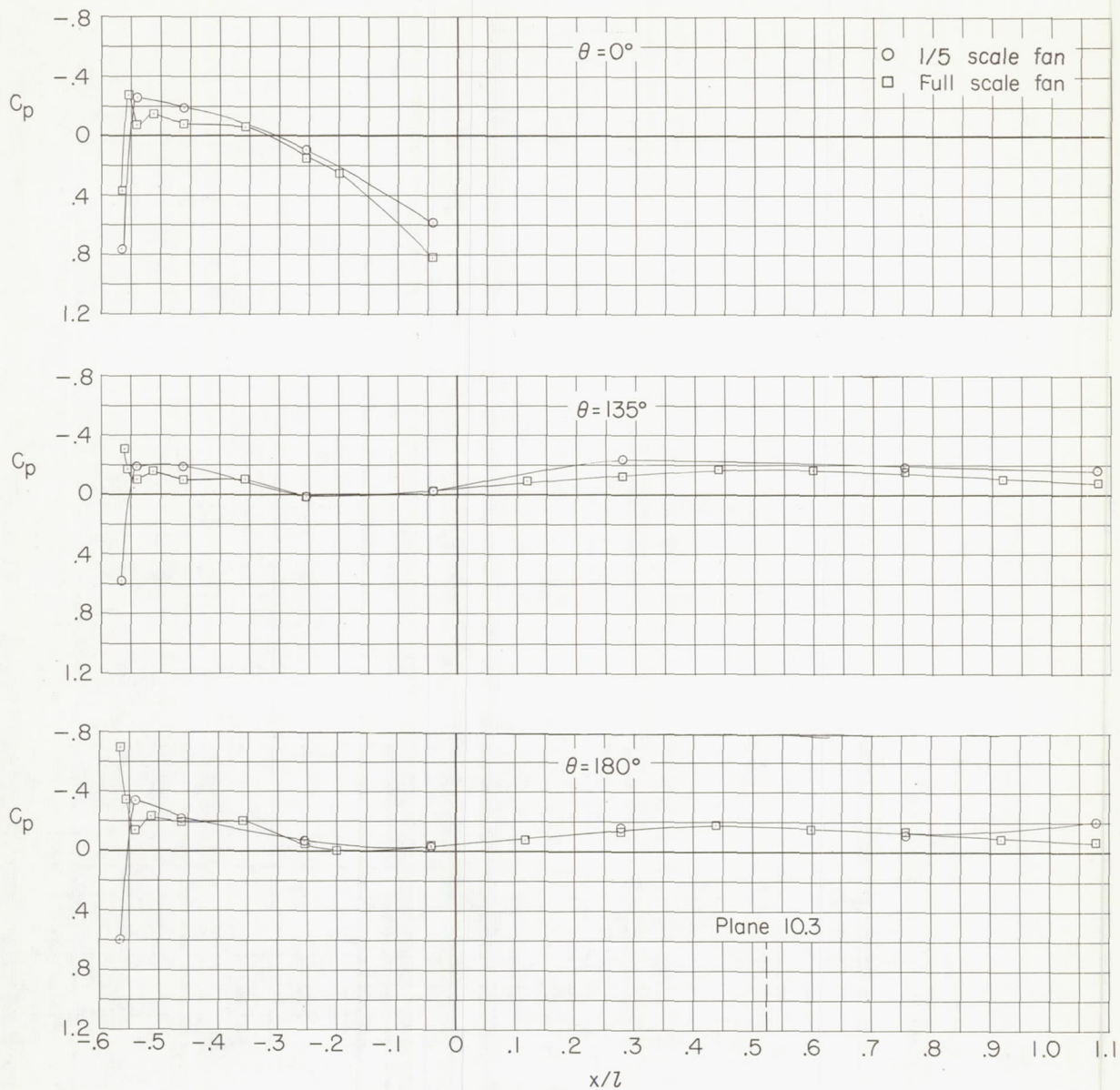
(a) $M = 0.30$.

Figure 80.- Comparison of gas-generator-nacelle pressure distributions of configuration 123.



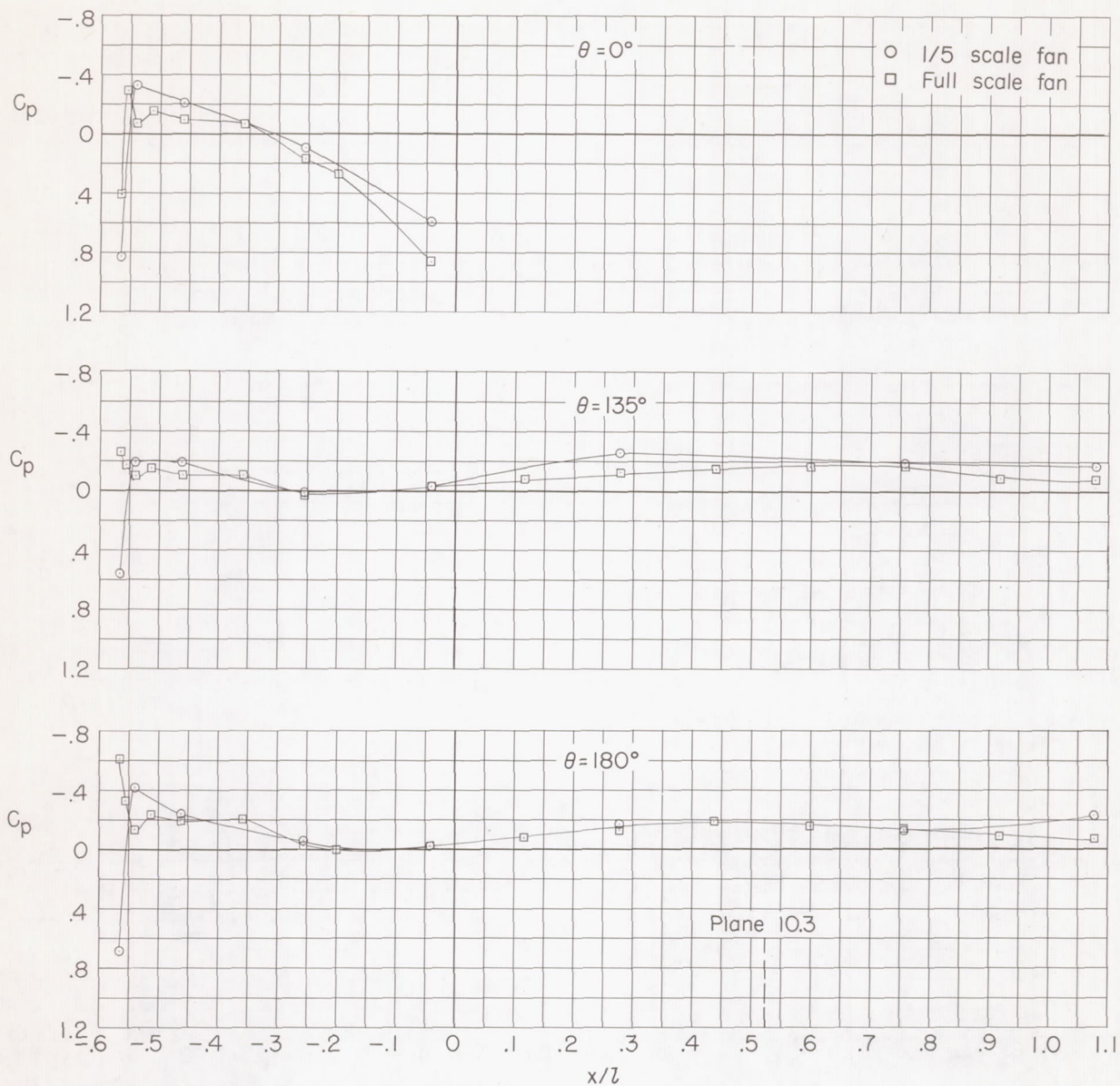
(b) $M = 0.40$.

Figure 80.- Continued.



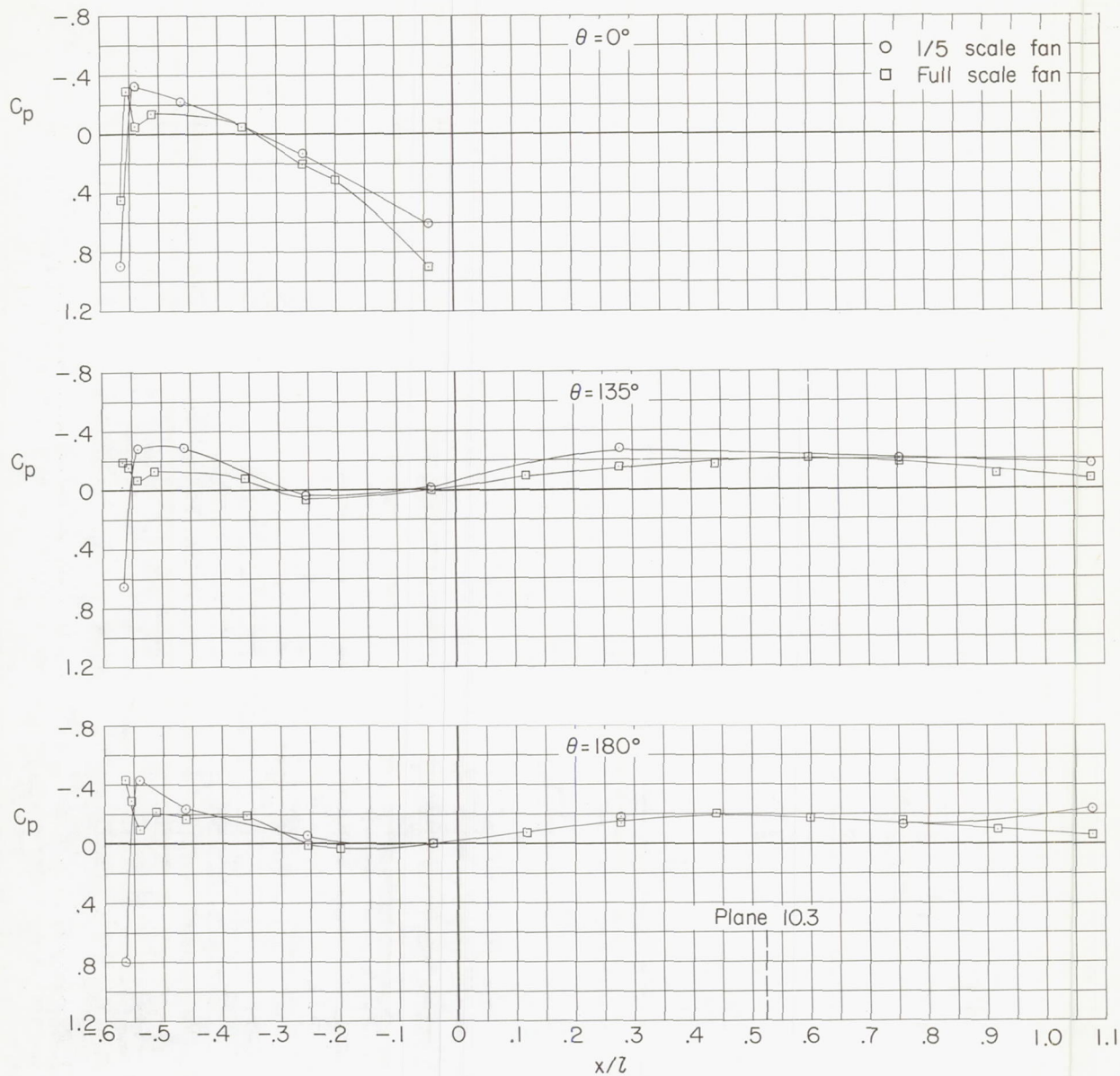
(c) $M = 0.50$.

Figure 80.- Continued.



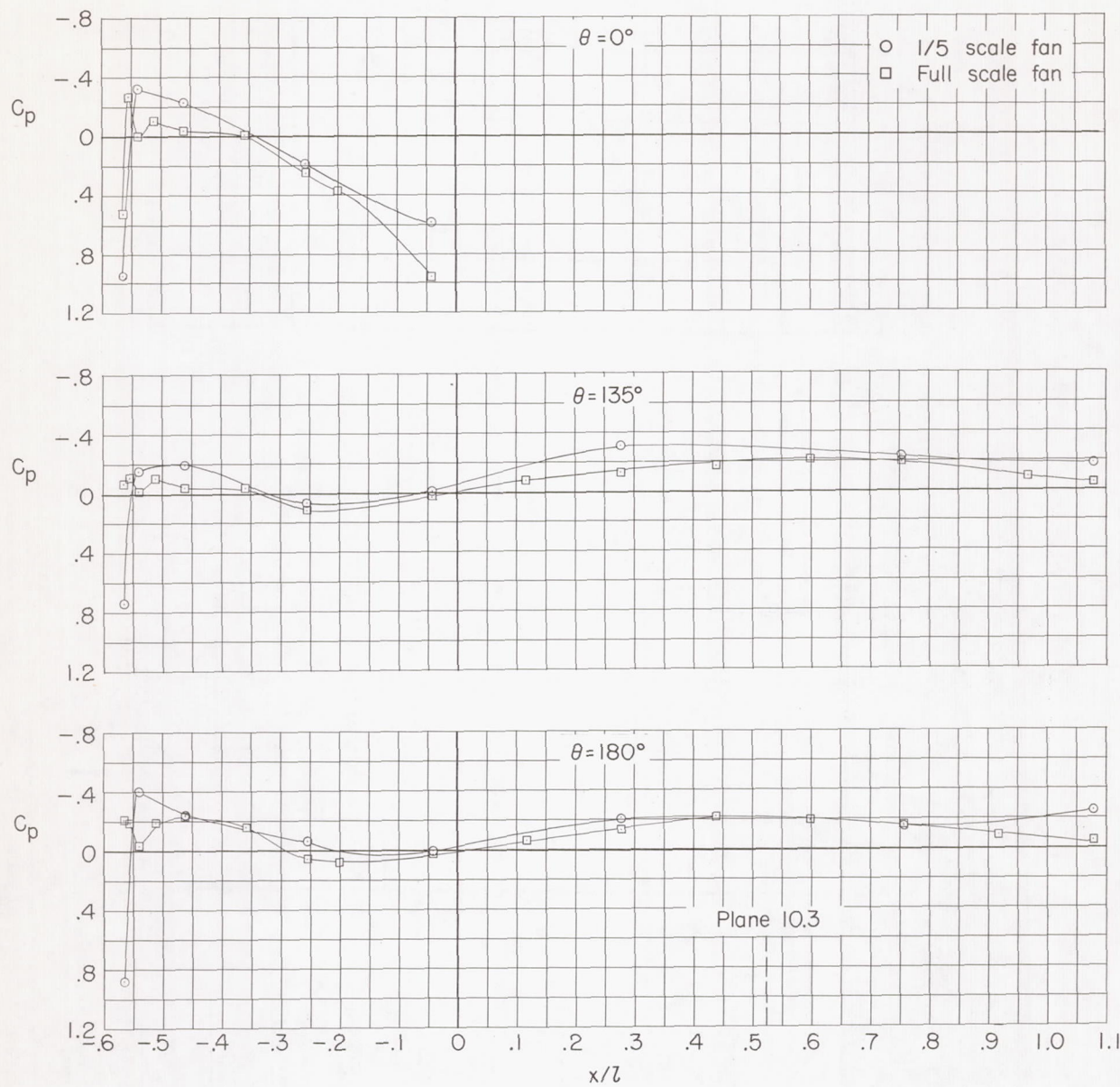
(d) $M = 0.60$.

Figure 80.- Continued.



(e) $M = 0.70$.

Figure 80.- Continued.



(f) $M = 0.80$.

Figure 80.- Concluded.

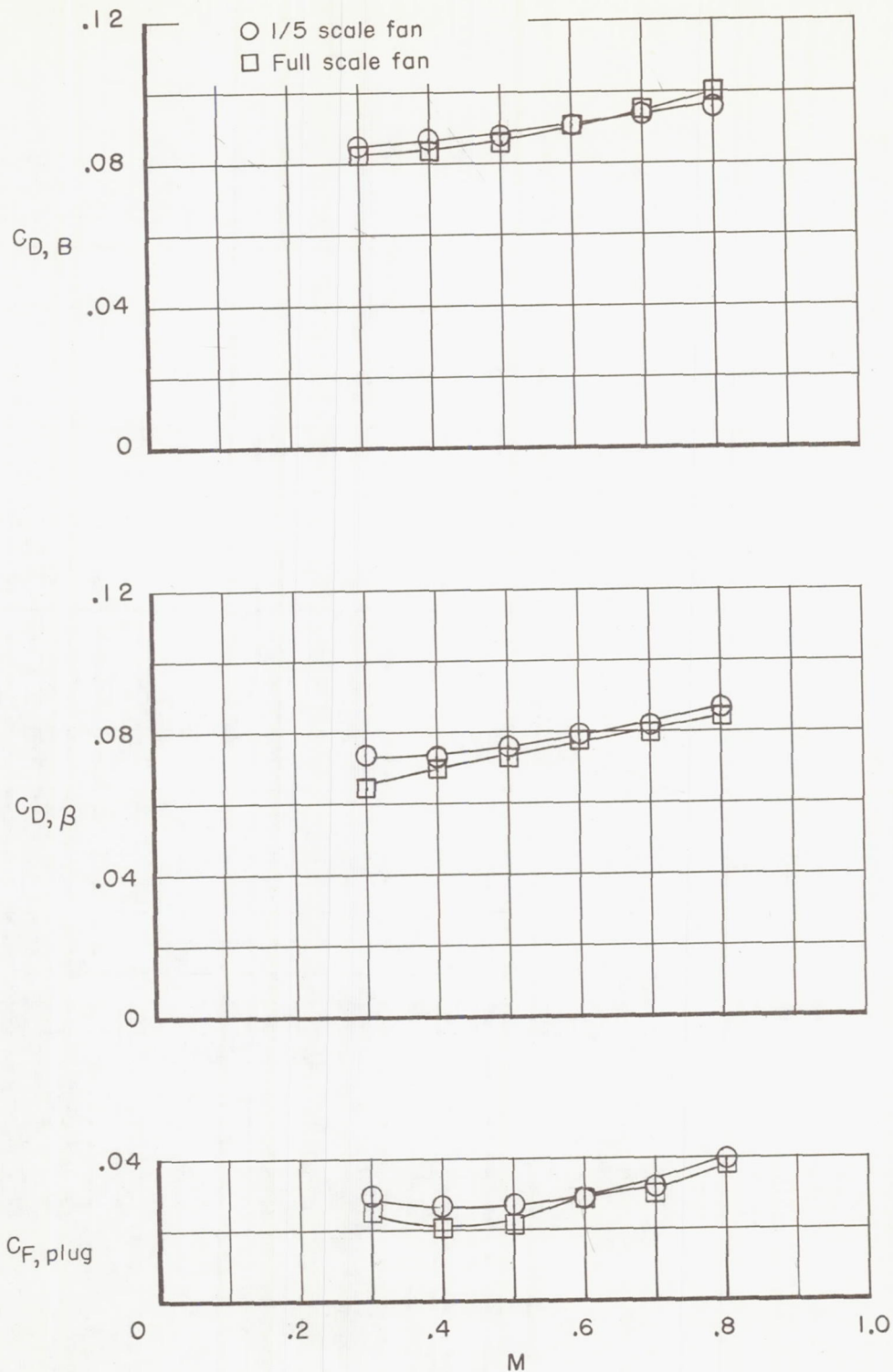


Figure 81.- Comparison of bulletnose and afterbody drag coefficients and plug thrust coefficients of configuration 123.